



**HAL**  
open science

# Geo-electrical methods for hydrogeological studies – capabilities and limits for the analysis of deep-seated landslides and mountainous watersheds

Myriam Lajaunie

► **To cite this version:**

Myriam Lajaunie. Geo-electrical methods for hydrogeological studies – capabilities and limits for the analysis of deep-seated landslides and mountainous watersheds. Earth Sciences. Université de Strasbourg, 2020. English. NNT : 2020STRAH003 . tel-03765045

**HAL Id: tel-03765045**

**<https://theses.hal.science/tel-03765045>**

Submitted on 30 Aug 2022

**HAL** is a multi-disciplinary open access archive for the deposit and dissemination of scientific research documents, whether they are published or not. The documents may come from teaching and research institutions in France or abroad, or from public or private research centers.

L'archive ouverte pluridisciplinaire **HAL**, est destinée au dépôt et à la diffusion de documents scientifiques de niveau recherche, publiés ou non, émanant des établissements d'enseignement et de recherche français ou étrangers, des laboratoires publics ou privés.

## Université de Strasbourg

École doctorale n° 413 : Sciences de la Terre et Environnement  
**Ecole et Observatoire des Sciences de la Terre / Institut de Physique du Globe de Strasbourg**

*Thèse présentée et soutenue publiquement par*

**MYRIAM LAJAUNIE**

le 30 juin 2020

pour l'obtention du grade de : **Docteur de l'Université de Strasbourg**  
discipline et spécialité : **Sciences de la Terre et de l'Univers - Géophysique**

### **Geo-electrical methods for hydrogeological studies – capabilities and limits for the analysis of deep-seated landslides and mountainous watersheds**

#### **Jury :**

GARAMBOIS Stéphane	Prof.	Université-Grenoble-Alpes, ISTerre, Grenoble, France	<i>Rapporteur</i>
GUERIN Roger	Prof.	Sorbonne Université, METIS, Paris, France	<i>Rapporteur</i>
BERTRAND Catherine	Dr. Hab.	Université de Franche-Comté, Besançon, France	<i>Examinatrice</i>
MARQUIS Guy	Prof.	Université de Strasbourg, EOST, Strasbourg, France	<i>Examineur</i>
MALET Jean-Philippe	Dr. Hab.	Université de Strasbourg, EOST, Strasbourg, France	<i>Co-directeur</i>
SAILHAC Pascal	Prof.	Université Paris-Sud Orsay, GEOPS, Orsay, France	<i>Co-directeur</i>



---

## Remerciements

Je souhaite remercier ici de nombreuses personnes qui ont été moteurs, soutien ou qui ont participé de près ou de loin à la réalisation de ma thèse.

Je remercie tout d'abord mes deux directeurs de thèse, Jean-Philippe Malet et Pascal Sailhac, pour m'avoir donné l'opportunité de réaliser ce travail. Merci Jean-Philippe pour ton suivi avisé, ton soutien, ton impulsion et ta confiance, pour m'avoir offert la possibilité de rencontrer de nombreuses équipes afin de compléter ma formation au travers de collaborations variés. Merci Pascal de m'avoir introduite aux méthodes électromagnétiques ! Merci pour les nombreuses discussions autour des différentes méthodes géo-électriques, j'essaierai de conserver un regard plein de prudence et d'esprit critique sur les données et les traitements géophysiques.

Je remercie les membres de mon jury, qui ont acceptés de lire et d'évaluer mon travail : merci à Roger Guerin et Stéphane Garambois, les rapporteurs de mon manuscrit, ainsi qu'à Guy Marquis, Catherine Bertrand, Julien Gance et Adrian Flores Orozco.

Je remercie également mon comité de suivi de thèse, constitué de Christian Camerlynck, Myriam Schmutz et Véronique Durand, comité qui m'a apporté de précieux conseils afin de limiter un dispersement trop important, guidant ainsi l'avancement de ma thèse.

Ce travail de thèse a été l'occasion pour moi d'échanges et de collaborations avec des membres de différents laboratoires. Aux côtés de ces personnes, j'ai beaucoup appris sur les domaines de l'hydrogéologie, de la géochimie, de la modélisation numérique et la géophysique. Un grand merci à Catherine Bertrand, Pierre Nevers et Thibaut Garin pour le temps passé sur le versant de Séchilienne à poser des capteurs, et pour votre participation précieuse au travail d'interprétation du modèle géophysique. Je remercie Julien Gance, pour m'avoir donné l'occasion d'utiliser des FullWavers, et de traiter ce beau jeu de données acquises à Séchilienne. Merci de m'avoir guidée dans le traitement et l'inversion des données. Un grand merci à Sheldon Warden dont l'accompagnement tout au long de ma thèse (et les relectures si efficaces !), l'aide sur le terrain, et les discussions autour des mesures CSAMT m'ont été d'une grande aide. Sheldon : à plus dans l'bus !

Merci à Nolwenn Lesparre, pour les informations fournies sur les observations géophysiques sur le bassin versant du Strengbach, et pour la discussion autour de l'interprétation des données de CSAMT.

Je remercie vivement Stéphanie Gautier dont la disponibilité, les discussions sur le glissement de terrain de Lodève et les relectures attentives ont été précieuses ! Je remercie également Nataliyah Denchik pour les nombreux échanges, pour m'avoir donné accès à de nombreuses données du glissement de Lodève et pour les explications sur les données du monitoring hydrogéochimique et pétrophysique en puits.

A big thank you to Adrian Flores Orozco, I had a great pleasure working with you and learning your technique in the context of the TDIP time-lapse experiment. Thank you for receiving me in your team for a couple of weeks, and for spending time to guide me through TDIP data processing. I would like to thank the whole geophysics team of TU Wien: Jakob, Theresa (thanks for the help in the field!), Matthias, Timea, I had a great time with you! Acknowledgements are addressed to Robert Delhaye, with whom I had the pleasure to realize CSAMT field work at the Lodève landslide. Thank you so much for this rich exchange. Thanks are also addressed to members of the DIAS Geophysics team: Duygu Kyian and Colin Hogg. Permitting me to use your current source T3 in November 2018 spared me a great deal of trouble!

A special thanks to Raphael Rochlitz, you gave me access to custEM and guide me through its installation and use with such great availability and patience ! This software was a great advantage in my PhD and I had a real pleasure testing and using it !

Je souhaite également remercier François Bretaudeau, pour avoir pris du temps pour m'expliquer le fonctionnement de PolyEM3D, pour m'y avoir donné accès, et m'avoir donné accès à du temps de calcul pour réaliser mes tests de calculs directe et inverse.

Je souhaite remercier les collègues de l'IPGS avec qui j'ai interagi de près ou de loin : merci à Pierre-Daniel Matthey, Yassine Abdelfettah, Maksim Bano, Gilbert Ferhat, Matthias Zillmer, Jean-François Girard, Marie-Claire Pierret, Renaud Toussaint, Jacques Hinderer.

Enfin, il me semble important de remercier l'équipe du Mésocentre de l'Université de Strasbourg, d'abord pour

---

avoir accepté de faire plusieurs essais dans l'installation de Fenics, et ensuite pour la disponibilité et la mise à disposition gracieuse des serveurs de calcul : merci à Michel Ringenbach et David Brusson.

Une pensée toute particulière aux doctorants et contractuels de l'IPGS avec qui j'ai partagé plein de beaux moments : Nolwenn, vive l'Islande et l'alignement de sondes mag avec des bouts de ficelle !! Guigui, la preuve que les géants aussi aiment les mines ;-) merci pour tous les bons moments ! Alexandre et Frédo, mille mercis pour votre aide à Pégairolles ! Tour à tour, vous avez bravé les vents glacials et tumultueux de l'Hérault en hiver pour me permettre de réaliser mon expérience de CSAMT time-lapse ! Quentin, plein de souvenirs sur le Strengbach !! Tom, vive le swing et les montagnes !! Shahar, merci pour ta sagesse, ton humour et tes propos toujours plein d'équilibre :) Catalina, Josipa, Bérénice, Romain, une pensée chaleureuse à vous ! Mathilde !!! On en a partagé des choses en 3 ans ! à commencer par un bureau. Merci pour tous les chouettes moments, les tisanes, les rigolades ! Je n'oublierai jamais ton éternuement hors norme <3 Huge thanks, Kushnahadi for your repeated and precious help in the field, both in Séchilienne and Lodève! Merci à tous ceux qui sont passés par la team landslides pendant ma thèse, et avec qui j'ai partagé de bons moments sur le terrain, en conférence, à fête de la science... : Clément, Floriane, Alexandre, Odin, Pierrick, et les nombreux étudiants de passage !

Parce que la vie, ce n'est pas juste la thèse, et que je n'aurais certainement pas pu mener à bien mon doctorat sans une bonne dose d'amitié, d'amour, d'acrobaties, d'arts martiaux, d'artichauts... je remercie ici tous mes amis (dont certains ont déjà été mentionnés) et mes proches, dont la présence et le soutien ont été si nécessaires et agréables ! Tout d'abord mes frères et soeurs de pratique : j'ai appris tant de choses à vos côtés ! Merci aux zouzoux de la Team Licorne pour les longues heures de sauts, de portés, de gainage, de tambour et de gong (\*\*dong dong dondong dong dong \*\*) et pour la magie des danses ! Merci également aux copains de bagarre du samedi aprèm. Merci Erwin pour m'avoir tant appris, et pour nous permettre de nous interroger sur notre pratique, de l'orienter vers ce qui nous convient, loin de la position dogmatique de certaines écoles. Merci pour m'avoir permis de travailler ma structure et mon mental, et pour avoir aiguisé ma curiosité martiale. Merci aux Girls : Carole, Cindy, Virginie, Sandra et Mymy. Merci à Wenziz, Franck, Gui, les M&M, Solène, Nathan, Antoine, Ivan, Victoria, Clims, Kik et Zouille et tous les autres ! Pour citer le Maître : je vous aime ! Merci à vous également, mes amis de lycée (Le Paysage D'Une Beauté Accordée) avec qui je passe encore de si bons moments ! Gatou, Anne-Laure, Cédric, Caroline, Fabinou, Papy !! Merci à mes amis EOSTiens avec qui j'ai passé mes meilleures années étudiantes ! Mama, Théthé, Nawal, Lacrouts, Huhu, Annanaze, Beubeu <3 I address a special thanks to Pradip Kumar Maurya, I have so many good memories with you, in the field, discovering the IP world or simply drinking Tuborgs. I am glad that we kept in touch during these four years !

Merci Frank pour m'avoir souvent accueillie chez vous pendant mes années d'école et le début de ma thèse. D'ici, je te remercie, Françoise, pour les moments passés avec toi, je garde ces souvenirs au chaud dans mon coeur. Merci à Eric et Guillaume pour m'avoir reçue à Montpellier, quand j'y étais de passage, c'était de très bon moments. Chris, à ta manière un peu spéciale, tu es présent, je t'adresse ici une pensée toute particulière. Enfin, vous m'avez soutenue sans relâche : merci Papou, Moumoune, Rébecca et Paul d'être là inconditionnellement quand je perds le moral. Merci pour votre immense soutien et vos conseils ! Merci aussi pour vos relectures. Merci, enfin et surtout, pour tous les moments et les choses que l'on partage !



---

## Résumé

L'écoulement de l'eau dans le sous-sol est contrôlé par la structure et la micro-structure des roches, sédiments et sols constitutifs du milieu. La structure générale du sous-sol est souvent complexe, car elle est issue d'une dynamique longue (tectonique, héritage glaciaire) qui a abouti à la morphologie du paysage, ainsi qu'à la distribution spatiale et la structure des géo-matériaux, et a été, par la suite, façonnée par des processus mécaniques (fragmentation, gonflement), chimiques (altération, dissolution) et biologiques. Les circulations de l'eau dans ce type de milieux sont permises non seulement par l'infiltration dans la matrice mais également par l'écoulement le long d'un ensemble de discontinuités (failles, fissures) formant des chemins préférentiels d'écoulement. Ainsi, la compréhension des processus d'écoulement et du stockage de l'eau nécessite une caractérisation structurale du milieu à des échelles spatiales très variables (pouvant aller de l'échelle du pore à celle de failles) parfois à des profondeurs importantes (kilométriques).

Ce travail de thèse concerne l'analyse de trois types d'aquifères. Les aquifères cristallins altérés constituent des réservoirs d'eau qui peuvent s'étendre à des profondeurs importantes, selon le degré d'altération de la roche. Les réservoirs de socle fracturés constituent des milieux complexes dans lesquels les propriétés d'écoulement sont très variables spatialement, et selon l'échelle d'observation. Enfin, les aquifères sédimentaires sont constitués de strates aux propriétés hydrogéologiques variables. Ce travail évalue les capacités de méthodes géophysiques à caractériser de tels aquifères lorsque ceux-ci sont situés à des profondeurs importantes (hectométriques) et dans des configurations où la topographie présente d'importantes variations.

Les méthodes géo-électriques permettent de caractériser et d'imager les variations de certaines propriétés électriques du sous-sol, en particulier la résistivité électrique. Ces propriétés électriques sont reliées à certaines propriétés structurales, pétrophysiques et hydrologiques du milieu, pouvant fournir un certain nombre d'informations sur la structure et la lithologie du sous-sol, ainsi que sur son contenu ou les circulations d'eau dans le sous-sol.

La caractérisation géophysique de la subsurface par des méthodes sensibles à la structure du sous-sol, sa lithologie ou son contenu en eau permet d'améliorer la compréhension du milieu et de lever des incertitudes quant à son fonctionnement hydrogéologique. De nombreuses méthodes hydrogéophysiques ont été développées dans ce but, fournissant une information structurale et/ou hydrologique.

Un certain nombre de méthodes géo-électriques existe, chacune se fondant sur un contexte théorique et des mises en applications spécifiques. Ces méthodes sont caractérisées par des définitions de la sensibilité et de la résolution qui dépendent de la physique sur laquelle la méthode se base, ainsi que des dispositifs de mesure mis en place. Ainsi, selon le site d'étude, le choix de la méthode et de sa mise en application est réalisé en fonction du type d'objet à imager. La réalisation de ce type d'études dans les contextes étudiés requiert une résolution et une profondeur d'investigation suffisantes. Par ailleurs, les mesures, souvent affectées par la topographie de la surface doivent pouvoir être interprétées malgré ces éventuelles distorsions.

Les défis que représentent l'étude des réservoirs étudiés reposent sur 1/ les profondeurs d'investigation à atteindre, 2/ la dimensionnalité des structures 3/ les résolutions fines nécessaires pour imager des structures de petite taille 4/ la sensibilité générale aux objets géologiques (lithologie et hydrogéologie) 5/ la prise en compte de la topographie dans les modélisation de données.

Cette thèse a pour objectif d'examiner les possibilités d'application de méthodes géophysiques, et de tester leur efficacité dans le contexte précis des trois types d'aquifères mentionnés. Pour ce faire, des protocoles de mesures statiques ou time-lapse ont été mis en place et appliqués sur trois sites tests correspondant aux trois types de réservoirs étudiés. La sensibilité des méthodes dans les contextes d'étude a été évaluée par le biais de travaux de modélisation numérique. En particulier, les questions de résolution, de profondeur d'investigation, et de sensibilité géologique ont été investiguées.

La méthode CSAMT, méthode électromagnétique en ondes planes, permet, en théorie, une bonne sensibi-

---

lité verticale, et des profondeurs d'investigation de plusieurs centaines de mètres selon le type de milieu. Cette méthode est cependant difficile à appliquer de manière dense et à modéliser (donc à interpréter) dans des milieux où la topographie varie beaucoup. Elle sera donc adéquate à l'étude de milieux pseudo-tabulaires. La question de l'influence de la topographie sur les données CSAMT est en particulier soulevée dans ce travail.

Les méthodes de tomographie de résistivité électrique, habituellement appliquées à la caractérisation des premiers 50 m du sous-sol, peuvent, par l'utilisation de nouveaux dispositifs de mesures en réseau de capteurs indépendants, être appliquées avec des résolutions décimétriques et des profondeurs d'investigations de l'ordre de quelques centaines de mètres. En ERT, les outils de modélisation et d'inversion permettent la modélisation de dispositifs de mesure flexibles ainsi que la description fine des variations topographiques.

La méthode de polarisation provoquée permet quant à elle d'étendre l'étude géo-électrique du sous-sol non plus seulement à la caractérisation de la résistivité électrique, mais également de la chargeabilité du milieu, c'est-à-dire de la capacité du milieu à emmagasiner l'énergie électrique, puis à la restituer progressivement. En hydrogéophysique, cette propriété est particulièrement intéressante car elle permet de distinguer des milieux contenant de fortes quantités d'argile de milieux non argileux contenant de l'eau, ce qui est difficilement réalisable avec la seule caractérisation de la résistivité électrique.

Les méthodologies de suivi temporel de ces paramètres par les différentes méthodes énoncées présente l'intérêt majeur de pouvoir distinguer le signal géophysique provoqué par la structure et la lithologie (considéré comme statique dans les milieux étudiés) du signal provoqué par la présence d'eau, dynamique du fait de variations de la quantité d'eau, de sa répartition dans le milieu, de sa composition chimique et de sa température. L'observation des variations du signal peut enfin permettre de réaliser un suivi de l'eau à la suite d'événements météorologiques, permettant la modélisation hydrogéologique du milieu.

Dans les réservoirs cristallins altérés, l'eau circule et peut être stockée dans la zone endommagée, qui présente une porosité et une perméabilité bien plus importantes que la roche saine. Ce type de milieu peut être assimilé à un milieu relativement continu avec des propriétés hydrogéologiques, et géo-électriques qui varient progressivement en gradient avec la profondeur, et de manière très homogène latéralement. L'utilisation de méthodes de caractérisation électromagnétiques en ondes planes y est donc adaptée, car ces méthodes permettent des profondeurs d'investigation importantes, ainsi qu'une bonne sensibilité verticale.

La méthode CSAMT, qui utilise une source contrôlée, a été choisie pour étudier ce type de milieu, car elle est peu sensible au bruit, qui est particulièrement important dans les méthodes EM en ondes planes utilisées pour l'étude de la proche surface (premier kilomètre). Si cette méthode, de par sa bonne résolution verticale et sa grande profondeur d'investigation, semble idéale pour étudier ce type de milieu, la présence de topographie, l'étude de milieux à l'échelle de versants et la modélisation des données restent des défis d'importance dans la mise en place de la méthode.

Le bassin-versant granitique du Strengbach est un bassin versant de montagne de petite taille, localisé dans les Vosges. Étudié depuis 1986 et équipé de 7 puits sur son entière superficie, ce bassin versant a fait l'objet de nombreuses études et caractérisations hydrogéophysiques. La limite de ce bassin versant en profondeur est difficile à évaluer au vu d'études géophysiques passées et des observations en forage, et semble s'étendre à des profondeurs de plus de 80 m. Ce site a été sélectionné pour les nombreuses connaissances accumulées, ainsi que pour l'existence de nombreuses données, permettant potentiellement de contraindre les observations.

Dans les réservoirs de socle fracturés, l'hétérogénéité provient des contextes tectoniques et gravitaires particuliers complexifiant la structure du milieu par la présence de failles, de fractures et de discontinuités à divers échelles et dans plusieurs directions. Les structures y sont tridimensionnelles, et les échelles de variation des propriétés sont variables. Dans le contexte de glissements de terrains, ces réservoirs sont partie intégrante de versants de montagne, et la topographie de la roche endommagée est souvent celle de la surface. Ce type de milieu requiert donc une caractérisation 3D à grande échelle (i.e. à l'échelle du versant), et la présence de topographie y ajoute un défi supplémentaire, du point de vue des campagnes de mesures, de l'analyse des données et de leur modélisation.

Pour étudier et imager, à l'échelle du versant, un milieu qui présente de telles caractéristiques, il est nécessaire de déployer un dispositif de mesures dense, qui permette l'analyse et la modélisation 3D des propriétés électriques du milieu. La tomographie de résistivité électrique 3D à grande échelle a été choisie, en utilisant un

---

réseau dense de résistivimètres autonomes, apportant la flexibilité nécessaire sur le terrain, ainsi que des outils de modélisation et d'inversion de données flexibles, permettant la modélisation d'anomalies complexes et de variations topographiques importantes.

Pour étudier ce genre de réservoirs, le glissement de terrain de Séchilienne a été choisi. Le glissement de terrain de Séchilienne est un glissement impliquant un volume de roche important, situé dans le massif de Belledonne. Ce versant instable met en jeu une roche mica-schisteuse localement fracturée et endommagée de manière conséquente, et ce, jusqu'à des profondeurs importantes (150 à 200 m). Les nombreuses connaissances accumulées sur ce site, ainsi que l'existence de nombreuses données, ont permis d'évaluer la qualité du modèle géophysique.

Les réservoirs sédimentaires sont caractérisés par la présence de contrastes de perméabilité entre unités stratigraphiques, qui contrôlent l'importance de l'infiltration vis à vis de l'écoulement le long de couches. La présence de matériaux très peu perméables, tels que des argiles, permet la rétention et le stockage de l'eau dans les réservoirs sédimentaires. L'étude géophysique de tels milieux est complexe lorsque la variabilité verticale est importante vis-à-vis de la résolution verticale de la méthode géophysique utilisée. En particulier, lorsque les réservoirs sont situés en profondeur, où la résolution des méthodes géophysiques de surface est amoindrie, détecter les variations lithologiques fines est, *a priori*, un défi important. Lors de caractérisation géo-électrique, la présence d'argile dans le milieu rend l'étude délicate, car l'argile est difficilement différenciable de l'eau du point de vue de la résistivité électrique.

Pour répondre à cette problématique, des méthodologies de suivi temporel ou mesures 'time-lapse' ont été mises en place. Des mesures time-lapse de CSAMT et de polarisation provoquée en domaine temporel (TDIP) ont été appliquées à l'étude de ce type d'aquifères. Le choix de ces deux méthodes est justifié par 1/ une bonne résolution verticale, pour le CSAMT et 2/ une sensibilité des paramètres géophysiques aux différentes lithologies successives, pour le TDIP.

Le glissement de terrain de Pégairolles a été choisi pour développer ces deux méthodologies. Le glissement de terrain de Pégairolles est un glissement lent (3-4 mm par an) et profond (50 à 60 m) localisé dans une vallée bordant les causses du Larzac. Ce glissement, constitué d'un empilement de roches sédimentaires, notamment marneuses, argileuses et évaporitiques, est apparenté, du point de vue de son fonctionnement, à un grand nombre d'instabilités localisées dans cette région : lors d'événements pluvieux intenses, appelés épisodes Cévenols, l'eau qui s'infiltré dans les couches argileuses et évaporitiques du milieu est présumée déstabiliser le milieu et entraîner des glissements de terrain. Parce qu'il est très lent et que peu de dommage y est attendu, le glissement de terrain de Lodève constitue un bon site test pour le développement et l'étude d'outils, notamment géophysiques, permettant le suivi et la compréhension du comportement hydrogéophysique du sous-sol pour des contextes similaires de milieux argileux.

L'utilisation du CSAMT dans la caractérisation des aquifères cristallins a entraîné le développement d'une méthodologie d'acquisition de traitement et d'analyse de la donnée de CSAMT, qui se sont montrées efficaces dans ce contexte. L'analyse de la distortion topographique a abouti à une méthode de correction de ces distortions, appliquée à l'étude du bassin versant du Strengbach. Parce que les observations faites sont interprétées jusqu'à 200 m de profondeur, aucune donnée additionnelle n'a permis d'évaluer les modèles 1D de résistivité obtenus.

L'utilisation d'un réseau dense de résistivimètre dans le cas de l'étude d'aquifères de socles fracturés s'est révélée une méthodologie de très intéressante, permettant des profondeurs d'investigation importantes. L'analyse de la sensibilité des mesures a été réalisée par le biais de la modélisation numérique. La zone densément fracturée dans le versant a pu être clairement délimitée dans le modèle de résistivité. Les observations ont permis la localisation du drain majeur du versant de Séchilienne, et ont mis en évidence l'existence d'aquifères perchés temporaires, permis par une double porosité dans le milieu fracturé.

L'analyse des variations temporelles de données de CSAMT pour l'étude de réservoirs sédimentaires a été réalisée sur 5 mois, à raison d'une série de mesures par mois, et a permis l'observation de variations temporelles cohérentes vis-à-vis des événements météorologiques. Cependant les données présentant des caractéristiques difficilement interprétables avec le dispositif de mesures 1D mis en place, les variations observées sur la donnée apparente n'ont pas pu être inversées, limitant les possibilités d'interprétation.

---

L'analyse des variations temporelles du signal de polarisation provoquée a montré une sensibilité importante à des variations émanant des premiers 20 m du sous-sol. Ces variations, parce que mal contraintes du point de vue de la nature de la polarisation, et du point de vue de la faible fréquence temporelle de répétition, n'ont pu être filtrées. Pour autant, cette méthode semble prometteuse, du point de vue de la zone de sensibilité relativement étendue et de la bonne résolution, à condition de réaliser des mesures à haute fréquence de répétition, en déterminant, au préalable, la nature de la polarisation par la mesure du spectre complet de polarisation.

# Contents

<b>Introduction</b>	<b>1</b>
<b>1 Context and research questions</b>	<b>4</b>
1.1 Water storage and flow in rock reservoirs . . . . .	5
1.1.1 Different types of water reservoirs . . . . .	5
1.1.2 Why is water reservoirs characterization important? . . . . .	5
1.1.3 How to characterize water reservoirs? . . . . .	6
1.1.4 Focus on catchment and landslide reservoirs . . . . .	6
1.2 Geoelectric investigations in hydrogeophysics . . . . .	8
1.2.1 Electrical properties of rocks - electrical resistivity imagery . . . . .	8
1.2.2 Basic notions in geophysics . . . . .	10
1.2.3 Electric and electromagnetic methods . . . . .	11
1.2.4 Use of these methods in the context of hydrogeophysical studies . . . . .	16
1.3 Investigating the potential of hydrogeophysical methods for the large-scale studies . . . . .	17
1.3.1 General context and main questions . . . . .	17
1.3.2 State of the art . . . . .	18
1.4 Methodology . . . . .	20
1.4.1 Characterization of a deep crystalline weathered aquifer . . . . .	20
1.4.2 Deep characterization of a fractured hard-rock reservoir . . . . .	21
1.4.3 Characterization and monitoring of deep sedimentary clayey aquifers . . . . .	21
1.4.4 Support projects and partner groups for this work . . . . .	23
1.5 References . . . . .	25
1.5.1 References to internet websites . . . . .	28
<b>2 Data measurement and processing: notions and challenges</b>	<b>29</b>
2.1 Electric and electromagnetic processes in earth materials . . . . .	30
2.1.1 Electric, dielectric and magnetic parameters . . . . .	30
2.1.2 Electromagnetic propagation and diffusion . . . . .	30
2.1.3 Electrical conduction . . . . .	31
2.1.4 Polarization of geo-materials . . . . .	31
2.2 Presentation and use of CSAMT . . . . .	32
2.2.1 Basic notions in CSAMT . . . . .	32
2.2.2 Field methodology . . . . .	35
2.2.3 Data analysis and processing . . . . .	38
2.2.4 Common distortions in CSAMT . . . . .	44
2.2.5 Modeling of CSAMT data . . . . .	46
2.2.6 Validity of CSAMT in some exemplary cases: numerical modeling tests . . . . .	51
2.2.7 Challenges in CSAMT . . . . .	54
2.3 Presentation and use of DC and IP methods in this thesis . . . . .	55
2.3.1 Electrical Resistivity Tomography . . . . .	55
2.3.2 Induced Polarization . . . . .	58
2.4 References . . . . .	63

2.4.1	References to internet websites . . . . .	65
<b>3</b>	<b>Imaging weathered crystalline aquifers: the deep structure of the Strengbach catchment using sparse CSAMT soundings</b>	<b>66</b>
	Introduction . . . . .	67
3.1	The Strengbach catchment . . . . .	67
3.1.1	The site . . . . .	67
3.1.2	General methodology developed at the Strengbach catchment observatory . . . . .	68
3.2	Field methodology . . . . .	71
3.2.1	Measurement setup . . . . .	71
3.2.2	Data processing . . . . .	73
3.2.3	Data quality control . . . . .	73
3.3	Data analysis and computation of apparent resistivity curves . . . . .	74
3.3.1	Polarization of the fields . . . . .	74
3.3.2	Dimensionality analysis . . . . .	75
3.3.3	Computation of the apparent resistivity curves . . . . .	75
3.4	Topographic effect . . . . .	80
3.4.1	Evaluation of topographic distortions . . . . .	80
3.4.2	A procedure to correct the topographic effect . . . . .	80
3.4.3	Test of the procedure: should we correct the apparent data from topographic effects . . . . .	82
3.5	1D inversion . . . . .	86
3.5.1	Methodology . . . . .	86
3.5.2	Inversion tests . . . . .	87
3.5.3	Inversion results . . . . .	88
3.6	Interpretation and discussion . . . . .	92
3.7	Conclusions and perspectives . . . . .	94
3.8	References . . . . .	95
3.8.1	References to internet websites . . . . .	95
<b>4</b>	<b>Imaging fractured aquifers: the deep 3D structure of the S�echilienne landslide using Resistivity - Distributed Automated System (R-DAS)</b>	<b>96</b>
	Introduction . . . . .	97
4.1	The S�echilienne landslide . . . . .	97
4.1.1	Geological and geomorphological setting . . . . .	98
4.1.2	Hydrogeological setting . . . . .	98
4.1.3	Landslide kinematics . . . . .	100
4.2	Geophysical instrumentation and data . . . . .	100
4.2.1	Resistivity-DAS: electrical measurement devices and acquisition setup . . . . .	100
4.2.2	Data quality control . . . . .	101
4.3	Methodology . . . . .	103
4.3.1	Data extraction and pre-processing . . . . .	103
4.3.2	Data filtering . . . . .	103
4.3.3	Inversion strategy . . . . .	106
4.3.4	Sensitivity tests . . . . .	107
4.4	Geophysical modeling: quality of the inversion model . . . . .	110
4.4.1	Inversion results . . . . .	110
4.4.2	Mean resistivity model and stability analysis . . . . .	110
4.4.3	Interpretability of the geophysical model . . . . .	112
4.5	Discussion: geological and hydrogeological interpretation of the 3D resistivity model . . . . .	115
4.5.1	Identification of geological and geomorphological structures . . . . .	115
4.5.2	Identification of hydrological structures . . . . .	115
4.6	Conclusion and perspectives . . . . .	118

4.7	References . . . . .	119
4.7.1	References to internet websites . . . . .	120
<b>5</b>	<b>Imaging deep sedimentary aquifers: Time-lapse hydrogeological study of the Pégairolles landslide with CSAMT and TDIP methods</b>	<b>121</b>
	Introduction . . . . .	122
5.1	The Lodève landslide . . . . .	122
5.1.1	Geological, structural and meteorological context at the Lodève landslide . . . . .	123
5.1.2	Long term meteorological, hydrogeological, geochemical and geophysical monitoring of the slope . . . . .	125
5.1.3	Hydrogeological, hydrochemical and meteorological time-lapse observations . . . . .	128
5.2	Methodology . . . . .	131
5.2.1	Time-lapse CSAMT . . . . .	131
5.2.2	Time-lapse TDIP . . . . .	131
5.3	Analysis and observations of the CSAMT time-lapse data . . . . .	133
5.3.1	Field setup . . . . .	133
5.3.2	Validity of time-lapse measurements in CSAMT . . . . .	137
5.3.3	Data analysis and processing . . . . .	142
5.3.4	Analysis of the apparent resistivity curves . . . . .	144
5.3.5	Discussion . . . . .	147
5.4	Analysis and observations with TDIP time-lapse data . . . . .	148
5.4.1	TDIP measurements at Lodève landslide . . . . .	149
5.4.2	Data quality . . . . .	150
5.4.3	Data processing . . . . .	151
5.4.4	Data inversion . . . . .	156
5.4.5	Analysis of temporal variations of the complex resistivity model . . . . .	161
	Conclusion . . . . .	165
5.5	References . . . . .	167
5.5.1	References to internet websites . . . . .	168
<b>6</b>	<b>Conclusion and perspectives</b>	<b>169</b>
6.1	Conclusions . . . . .	170
6.1.1	Characterization of deep crystalline weathered aquifers . . . . .	170
6.1.2	Characterization of fractured bedrock aquifers . . . . .	171
6.1.3	Characterization of deep sedimentary aquifers . . . . .	172
6.2	Perspectives . . . . .	173
6.2.1	Methodological perspectives in CSAMT . . . . .	173
6.2.2	Methodological perspectives in DC and IP . . . . .	175
6.3	References . . . . .	176
<b>A</b>		<b>I</b>
A.1	Analyse de la polarisation des champs électromagnétiques . . . . .	II
A.2	Caractérisation du glissement de terrain de Lodève par mesures TDIP 2D et 3D . . . . .	VII
A.3	Caractérisation de la structure 3D du glissement de terrain de Lodève par la méthode CSEM . . . . .	XI
A.3.1	Méthodologie de mesure . . . . .	XI
A.3.2	Analyse de la qualité et traitement des données . . . . .	XI
A.3.3	POLYEM3D : CSEM modeling and inversion software . . . . .	XIII
A.3.4	Application au jeu de données du glissement de terrain de Lodève . . . . .	XV
A.3.5	Results . . . . .	XVI
A.4	References . . . . .	XX

# List of Figures

1	Three different types of water reservoirs: a. weathered bedrock aquifers; b. fractured multi-porosity and multipermeability reservoirs; c. sedimentary aquifers: stacked independant aquifers	3
1.1	Range of resistivity values for different rock materials - from <a href="#">Loke [2013]</a>	8
1.2	Measurement principle in electrical methods - from Critex	12
1.3	Layout of a standard MT station (Vector configuration) - ©Moombarriga Geoscience	14
1.4	Natural magnetic field power spectrum and AMT dead-band (in blue)- modified from <a href="#">Constable [2007]</a>	15
1.5	Summary of geoelectrical methods capabilities in termes of resolution and depth of investigation, and related depth of observation in different contexts of hydrogeological studied	17
1.6	Methodology established in this thesis	24
2.1	Spatial variations of the angle between the electric and the magnetic field generated by an infinitesimal dipole grounded on a uniform half-space. The x and y coordinates are expressed in terms of induction numbers: the metric distances are normalized by the skin depth $\delta$ ; c. logarithmic ratio of computed apparent resistivity with far field formula over modeled resistivity; this figure shows where the far field assumption is valid. The white lines are the iso-distance of $\delta$ and $4\delta$ from the infinitesimal transmitter, and show that for homogeneous half spaces, the far field assumption is valid at distances larger than $4\delta$ where the logarithmic ratio is close to zero.	35
2.2	Measurement layout in CSAMT: a transmitting dipole is set a few kilometers away from the site, and the measurement of the resulting EM fields are measured. Several measurement configurations can be used: a. if the polarization of the magnetic and electric field can be estimated <i>a priori</i> , one can choose to recorded the fields exclusively in their resp. direction of polarization; b. in "vector measurements", the 3 components of the magnetic induction and the two horizontal components of the electric field are recorded; c. if the magnetic induction field is expected to be spatially stable, and is recorded in the vicinity of the station, one can choose to record only the horizontal electric field.	36
2.3	Example of measured raw time series with fundamental frequency of 711 Hz. From top to bottom: transmitted signal, raw electrical field towards North, and East, raw magnetic field towards North, East, and downward	38
2.4	Example of measured raw time series with fundamental frequency of 5120 Hz. From top to bottom: transmitted signal, raw electrical field towards North, and East, raw magnetic field towards North, East, and downward	38
2.5	Processing workflow of the CSAMT data	40
2.6	Example of raw spectrum of recorded signals related to a transmitted signal of fundamental frequency of 711 Hz.	41
2.7	Example of dynamic response of an AMTC magnetic coil	41
2.8	Calibrated amplitude spectrum of a measured sequence at 711 Hz	42
2.9	Calibrated phase spectrum of a measured sequence at 711 Hz	42
2.10	Example of signal detection on a calibrated amplitude spectrum. The red circles are the detected and extracted signals	43

2.11 Example of polarization ellipse: the horizontal projection of the field describes an ellipsoid section in time . . . . .	43
2.12 Modulus of the filtered electric and magnetic transfer functions . . . . .	44
2.13 Phase of the filtered electric and magnetic transfer functions . . . . .	44
2.14 Apparent resistivity and phase curves computed from eq. 2.17; this computation suggests a 1D layered medium and is not valid here . . . . .	45
2.15 Apparent resistivity and phase curves when accounting for possible 2D and 3D objects eq. 3.1 . . . . .	45
2.16 Example of polarization of the magnetic field and direction of in-phase ( $H_{\phi}$ ) and quadrature ( $H_Q$ ) signals . . . . .	46
2.17 Computation mesh used to evaluate the influence of the resistivity at the transmitter location on the apparent resistivity curve . . . . .	52
2.18 Apparent resistivity curves computed with the Cagniard formula for three different cases of resistivity at the location of the transmitter. The limit of the far field is around 700 Hz. In the far field, The resistivity of the ground at the location of the transmitter influences the apparent resistivity only below the far field limit around 700 Hz, as expected by the CSAMT theory. . . . .	52
2.19 Synthetic apparent resistivity and phase curves at ten stations at 6500 to 9000 m from the transmitter on a flat homogeneous earth ( $500 \Omega.m$ ) . . . . .	53
2.20 Propagative topographic effect: synthetic apparent resistivity and phase curves at 6500 to 9000 m from the transmitter on a homogeneous earth ( $500 \Omega.m$ ) affected by topographic changes in the area between the transmitter and the stations . . . . .	53
2.21 Diffusive topographic effect: synthetic apparent resistivity and phase curves at 7 stations at 6500 to 9000 m from the transmitter on a homogeneous earth ( $500 \Omega.m$ ) affected by topographic changes in the area between the transmitter and the stations . . . . .	54
2.22 Diffusive topographic effect: synthetic apparent resistivity and phase curves computed with the components of the electric and magnetic fields tangential to the local surface topography . . . . .	54
2.23 Applications of CSAMT to hydrogeological studies; a. from <a href="#">Wynn et al. [2016]</a> , 1D CSAMT sounding and inverted resistivity model permitting the location of two superposed water reservoirs; b. Time-lapse CSAMT study by <a href="#">Falgàs et al. [2006]</a> to evaluate the evolution of salt water intrusion in a coastal aquifer system . . . . .	55
2.24 Principle of 3D DCIP measurement from <a href="#">Maurya et al. [2017]</a> : a set of ERT profiles are installed in parallel and connected to the device through switch boxes separating each profiles into two parts. In this way, all electrodes of a quadrupole do not necessarily belong to the same profile, providing a 3D sensitivity . . . . .	57
2.25 Principal of use of IRIS Instruments FullWaver systems: each independent unit (node) records the electrical voltage at the terminals of two orthogonal dipoles. The transmitter and receivers are all synchronized by GPS - IRIS Instruments . . . . .	57
2.26 3D resistivity model obtained by <a href="#">Maurya et al. [2017]</a> to locate the contamination of a shallow aquifer related to the storage of waste in a landfill - from <a href="#">Maurya et al. [2017]</a> . . . . .	58
2.27 Schematic of the polarization of the electrical double layer at the surface of silicate grains (membrane polarization) - from <a href="#">Attwa and Ali [2018]</a> . . . . .	59
2.28 Amplitude and negative phase IP spectrum of four different Cole-Cole models; the red curve is the reference model and the three other curves present the effect of changing, one by one, each parameter of the model . . . . .	60
2.29 Time domain and frequency domain measurements techniques of the induced polarization - from <a href="#">Revil et al. [2012]</a> . . . . .	61
2.30 TDIP study of a clayey landslide from <a href="#">Gallistl et al. [2018]</a> : real conductivity profile (top) and imaginary conductivity profile (bottom) . . . . .	63

3.1	Maps of the Strengbach catchment: a. location of the boreholes, springs, meteorological stations and hydrogeological instrumentations (Riverlab, supraconducting gravimeter), b. lithological map, c. map of the microgravimetric variations over the catchment and d. water volume inferred from NMR soundings over the catchment, modified from <a href="#">Pierret et al. [2018]</a> (a., b. and d.) and <a href="#">Masson et al. [2012]</a> (c.) . . . . .	69
3.2	2D resistivity model of the Strengbach catchment from electrical resistivity tomography ( <a href="#">Gance et al. [2020]</a> (in preparation)). The northern slope presents lower resistivity values than the southern one, suggesting a more intense weathering of the northern rock. At depth, the absence of an increase of the resistivity with depth suggests that the sensitivity limit of the survey does not reach the bottom of the catchment. . . . .	70
3.3	Presentation of the field methodology: a. map of the layout (transmitter and receiver-stations) at the Strengbach catchment, b. station layout, c. geological map of the site with location of the CSAMT stations (modified from <a href="#">Pierret et al. [2014]</a> ) - the tower marked in red is a mast transmitting radio signals - and d. cylindrical coordinates in the analytical computation of the fields. . . . .	72
3.4	Polarization of the electric and magnetic fields over the Strengbach catchment from the ten measurement stations at Tx frequencies of 711, 2560 and 7680 Hz. . . . .	74
3.5	Measured (a.) and modeled (b.) magnetic fields at 1024 Hz. The modeled magnetic fields (b.) are computed over a homogeneous flat medium (represented in red) and a homogeneous medium affected by the true topography (computation with <i>custEM</i> – represented in blue) . . . . .	75
3.6	Graphs of the variation of the angle $\alpha$ between the electric and magnetic fields with the frequency over the Strengbach catchment, for each of the 10 stations. In each subfigure, the black line shows the variations of $\alpha$ in the case of a flat, 1D medium: depending on the stations location, the angle $\alpha$ presents values different from $90^\circ$ at low frequency when the EM signals are not a plane wave signals. . . . .	76
3.7	Impedance amplitude curves ( $Z_{11}$ in black and $Z_{21}$ in blue) for all ten stations. The grey zones correspond to the noisy high frequency part of the curves, ignored in the inversions . . . . .	77
3.8	Cagniard apparent resistivity curves for all ten stations. The grey zones correspond to the noisy high frequency part of the curves, ignored in the inversions. . . . .	78
3.9	Phase curves for all ten stations. . . . .	79
3.10	Maps of the topographic effects at the ten CSAMT stations. Left: topographic effect for a homogeneous subsurface with $\rho = 100 \Omega.m$ , Right: topographic effect for a homogeneous subsurface with $\rho = 1000 \Omega.m$ . The presented effect ratios were computed at 5 different frequencies represented as 5 concentric circles, the smallest one corresponding to highest frequencies. . . . .	81
3.11	Example of topographic effect simulated (station 10): a. Cagniard apparent resistivity for homogeneous flat and non-flat earth at $100 \Omega.m$ , b. Cagniard apparent resistivity for homogeneous flat and non-flat earth at $1000 \Omega.m$ and c. topographic effect $t$ for resistivities of 100 and $1000 \Omega.m$ . . . . .	81
3.12	Example of topographic effect simulated (station 3): a. Cagniard apparent resistivity for homogeneous flat and non-flat earth at $100 \Omega.m$ , b. Cagniard apparent resistivity for homogeneous flat and non-flat earth at $1000 \Omega.m$ and c. topographic effect $t$ for resistivities of 100 and $1000 \Omega.m$ . . . . .	82
3.13	Model used to test the efficiency and requirement of topographic corrections at the Strengbach catchment: a. top view with transparency to locate the anomalous plate and b. cross section . . . . .	83
3.14	Example of uncorrected, corrected and mean corrected apparent resistivity curves (station 10 - synthetic data) . . . . .	83
3.15	Example of uncorrected, corrected and mean corrected apparent resistivity curves (station 3 - synthetic data) . . . . .	84
3.16	Example of inversion tests of synthetic data: a. uncorrected (blue) and corrected (red) synthetic data, b. inverted models from uncorrected data with a coarse vertical discretization and c. inverted models from corrected data with a coarse vertical discretization . . . . .	84
3.17	Example of inversion tests of synthetic data: a. uncorrected (blue) and corrected (red) synthetic data, b. inverted models from uncorrected data with a thin vertical discretization and c. inverted models from corrected data with a thin vertical discretization . . . . .	85

3.18	Example of inversion tests of synthetic data: a. uncorrected (blue) and corrected (red) synthetic data, b. inverted models from uncorrected data with a coarse vertical discretization and c. inverted models from corrected data with a coarse vertical discretization . . . . .	85
3.19	Example of inversion tests of synthetic data: a. uncorrected (blue) and corrected (red) synthetic data, b. inverted models from uncorrected data with a thin vertical discretization and c. inverted models from corrected data with a thin vertical discretization . . . . .	86
3.20	1D inversion of the CSAMT data: a. example of data fit for the standard error model (station 9), b. example of data fit for the adjusted error model (station 9), c. set inverted models when changing the initial model and the error model and mean model (station 9), d. mean inverted model at the ten stations. The colors relate to the stations as in subfigure e. . . . .	89
3.21	Comparison between inversions of data uncorrected from topographic distortion, inversion of corrected data and inversion realized on a thin discretized model (29 layers) at station 5. . . . .	90
3.22	Inverted models for the ten stations. The number and color of the models related to the number and color of the stations in fig. 3.20. The first layers were compared when possible with the local 1D ERT models at neighbouring profiles (stations 1, 8 and 10) . . . . .	90
3.23	Map of the horizontal sections at 15, 30 and 60 m depth of the inverted models. . . . .	91
3.24	Map of the horizontal sections at 100, 250 and 450 m depth of the inverted models. . . . .	91
3.25	Example of filtered transfer functions recorded at the Strengbach catchment: a drop of the electrical transfer function towards high frequency is clearly visible at frequencies above 4000 Hz. . .	93
3.26	CSAMT field measurements of the electrode contact resistance effect with various contact resistances - from <a href="#">Zonge and Hughes [1985]</a> . . . . .	94
4.1	Morphology of the S�echilienne slope: (a) Geomorphological setting (fault model from <a href="#">Barf�ety et al. [1972]</a> and <a href="#">Vengeon [1998]</a> - appendices I and II) and location of boreholes and water sampling points; (b) Location of the portable Full-Waver resistivity measurements and of the 2D ERT profiles acquired by <a href="#">Le Roux et al. [2011]</a> ; (c) Lithological profile of the unstable slope obtained from core samples from the SC1 and SC2 boreholes, related time-lapse inclinometer observations and their respective interpretation ( <a href="#">Duranthon et al. [2013]</a> ). . . . .	99
4.2	Photographs of the monitoring equipment and of the measurement sites: (a) V-FullWaver unit at position FW9; (b) Zoom on the plugs for the three measurement channels on a V-FullWaver unit; (c) Zoom on the control screen of a V-FullWaver unit; (d) Remote electrode fully watered with a highly conductive salted mixture. . . . .	102
4.3	Example of raw voltage time series and impact of spike noise filtering: (a) Location of the stations FW3 and FW21 at the top and base of the investigated area; (b) Example of one day of measurement at stations FW3 and FW21 (data from the second day of measurements); (c) Example of spikes in the measured voltages recorded during a thunderstorm; (d) Effect of spike noise filtering on the decay curve: the unfiltered decay curve in red displays some spikes, efficiently filtered by the despiking procedure (black curve). . . . .	102
4.4	Methodological flowchart. . . . .	104
4.5	Distribution of voltage observations: (a) Distribution of the measured electric potential (in mV); (b) Distribution of contact resistance values and deviation in the measured potential; (c) Distribution of the number of stack for each data and (d) Distribution of the apparent resistivity values. . . . .	105
4.6	Data filtering: (a) Distribution of topographic effects and filtering of extreme values ( $t > 6$ and $t < -4$ ); (b) Distribution of geometrical factors (in red: geometrical factors of the data presenting extreme values of topographic effects): extreme topographic effect is often related to high geometrical factor; (c) Distribution of relative error on the apparent resistivity values. . . . .	105
4.7	Exemplary results of the synthetic tests - vertical cross section and top view - for tests 1 to 5 (a.), tests 6 to 9 (b.), tests 10 to 12 (c.) test 13 (d.) and tests 14 to 16 (e.). The cubes delimited by white wireframes are the anomalous bodies. . . . .	108

4.8	Comparison of the inverted models. First line: Inversion results for strong regularizations (LAMBDA = 20): a. distribution of resistivity values in the set of inverted models (one line corresponds to one inverted model); and an example of inverted model (initial resistivity = 200 $\Omega$ .m, fine mesh), with the top view b. and horizontal slices at 250 m depth (the whitened area corresponds to the part of the model where the topography is below the slice) and at 500 m depth. Second line: Inversion results for weak regularizations (LAMBDA = 2): e. distribution of resistivity values in the set of inverted models; an example of inverted model (initial resistivity = 200 $\Omega$ .m, fine mesh), with the top view f. and horizontal slices at 250 m depth (g.) and at 500 m (h.); i. location of the major faults (black lines), measurement (blue dots) and injection (red dots) points and unstable area (purple zone) regarding the inverted model; top view (j.) and horizontal slices at 250 m (k.) and 500 m (l.) of the data coverage (mean of sensitivity, <a href="#">Günther et al. [2006]</a> ). . . . .	111
4.9	Mean resistivity model and standard deviation model. Horizontal slices at the topographic surface at the elevations 1050, 950, 850, 750, 650, 550, 450 m (asl). . . . .	113
4.10	Comparison of the 3D resistivity models (left and center) to the 2D inverted models (right: c. and f.) of <a href="#">Le Roux et al. [2011]</a> , profiles ET3 (top) and ET4 (bottom). The 3D model is sliced at the location of the 2D investigation profiles. Two 3D-resistivity models are considered: the mean resistivity model computed from all stable inverted models (a. and d.), and a mean resistivity model computed from all stable models obtained with a weak regularization (b. and e.) . . . . .	114
4.11	3D representation of the interpreted model (mean model computed on the logarithmic resistivity of the set of selected inverted models) superimposed to the geological map of the slope ( <a href="#">Barf�y et al. [1972]</a> ). The squares represent the resistivity (log10) of the surface waters sampled in spring or at surface runoff locations. The black lines represent the major faults. . . . .	116
4.12	Resistive and conductive anomalies observed at the S�chilienne slope. (a) Top view of the extracted resistivity anomaly (resistivity above 10 <sup>3</sup> $\Omega$ .m), the black line is the location of the cross-section in (b) and the black circle is the part of the resistive anomaly located outside of the unstable area; (b) Vertical cross-section of the mean resistivity model showing the transition at depth from the resistive anomaly to the more conductive background; (c) Top view of the extracted conductive anomaly (resistivity below 10 <sup>2.4</sup> $\Omega$ .m i.e. 250 $\Omega$ .m), the black line is the location of the cross-section in (d); (d) Vertical cross-section of the mean resistivity model showing the conductive vertical patterns expanding from the surface down to a major deep conductive anomaly, (e) Acquisition setup: injection points in red and potential electrodes in blue, the unstable area is highlighted in purple. . . . .	117
4.13	Hydrogeological measurements during the year 2017 and hydrogeological concept. (a) precipitation recorded over the year 2017 at Mont Sec; (b) Water electrical conductivity and discharge in the unstable zone, recorded at the G710 gallery; (c) Electrical conductivity and water level recorded in the stable zone. Hydrogeological conceptual model of the S�chilienne slope for periods of high-flow (d.) and low-flow (e.) (modified from <a href="#">Vallet et al. [2015]</a> ). . . . .	118
5.1	Topographic map of the region surrounding P�gairolles-de-l'Escalette - The Lod�ve landslide is marked by a yellow patch . . . . .	124
5.2	Aerial view of the Lod�ve landslide (Google Earth satellite image) . . . . .	125
5.3	Geological and morphological context at the Lod�ve landslide (A); Interpretative scheme of the hydrogeological behavior of the slope (B) - from <a href="#">Denchik et al. [2019]</a> . . . . .	126
5.4	General lithology of the Trias and Lower Jurassic period which correspond to the regional context of the Lod�ve valley and local lithology from analysis of borehole core samples at the slope of the Lod�ve landslide - inspired by <a href="#">Denchik et al. [2019]</a> . . . . .	127
5.5	Variability of the total cumulative pluviometry between Les Plans station and P�gairolles station between March and September 2019 . . . . .	128
5.6	Long term variations of the petrophysical and hydrochemical properties of the water at four levels isolated by a multi-packer system in the WestBay borehole and correlation with the total rain from 2012 to mid-2019; completed from <a href="#">Denchik et al. [2019]</a> . . . . .	129

5.7	Long-term monitoring since 2012: pressure gradient between each following isolated levels in the WestBay borehole (bottom figure) and related rainfall (top figure); The separation between the two aquifers is clearly observable in the pressure gradient between the 45 and 48 m. . . . .	130
5.8	Preliminary SIP observation: resistivity and phase inverted from borehole/surface measurements at 1 Hz. The red line suggest a local loss of sensitivity of IP, potentially due to a decrease of resistivity.	133
5.9	Map of the CSAMT time-lapse experiment: transmitter site and measurement stations . . . . .	134
5.10	Map of the measurement stations: the full-stations record the 3-component magnetic field and the 2 horizontal components of the electric field (2 of the 8 full-stations were not recorded in November); the electrical stations record only the two horizontal components of the electric field. The time-lapse TDIP profile presented later in this chapter is marked as a dotted line. . . . .	134
5.11	Variations of pluviometry (total rain), water pressure and water electrical conductivity during the CSAMT time-lapse experiment. . . . .	135
5.12	Photographs of the survey: a. V8 measurement unit with its battery ; b. the site of Pégairolles de l'Escalette - view from the south; c. the transmitter station: the white box at the right is the current source, the small grey box at the left is the transmitter controller, the metal stake at the back is one of the injection electrodes; d. to face the autumnal rain, a shelter was build with broom sticks, plastic foil and garbage bags; e. the injection site: the dipole was set along a large conductive ground field along a river, close to the village of Les Pradines . . . . .	136
5.13	Synthetic apparent resistivity and phase curves computed from models 1, 2, 3 and 4 (Tbl. 5.1). The far field limit is observed at 400 Hz. . . . .	138
5.14	Inversion results of the four synthetic data, without "temporal" constraint . . . . .	139
5.15	Inversion results of the four synthetic data, with both vertical and "temporal" constraints . . . . .	139
5.16	Meshes used to evaluate the importance of channeling effects . . . . .	141
5.17	Influence of the channeling effect on the polarization of the magnetic field in the context of the two meshes from fig. 5.16: a large elongated anomaly beneath the transmitting dipole can disrupt the polarization of the electric and magnetic field at the site. . . . .	141
5.18	Polarization of the magnetic field at all repeated stations over the five months of the experiment at 5120 Hz. Two stations, which related signals are represented in grey, present very erratic polarizations. . . . .	142
5.19	Scatter plot showing the distribution of the polarization angle against the amplitude for each detected frequency at a specific station and at a specific time-period. Red dots are the data point removed by the filtering procedure. . . . .	143
5.20	Polarization of the magnetic field at all repeated stations over the five months of the experiment at 5120 Hz after applying the filtering procedure . . . . .	143
5.21	Filtered apparent resistivity curves measured in November (light green), December (light blue), January (dark blue) and March (purple) at the 8 full stations. The figures on the bottom line present an import noise content at high frequencies. Only the figures of the top line are selected for the interpretation. . . . .	145
5.22	Filtered phase curves measured in November (light green), December (light blue), January (dark blue) and March (purple) at the 8 full stations. The stations order is the same as in fig. 5.21. Only the phase from the four interpreted station are unfolded. . . . .	146
5.23	Electric and magnetic transfer functions at one of the noisy stations . . . . .	148
5.24	Variations of the rainfall at Pégairolles-de-l'Escalette, water pressure and water electrical conductivity during the TDIP time-lapse experiment. The total rain and effective rain computed following <a href="#">Oudin et al. [2005]</a> are presented. . . . .	149
5.25	Map of the TDIP profiles measured in 2019 . . . . .	150
5.26	Workflow of the TDIP time-lapse processing . . . . .	151
5.27	Principle of the neighbour analysis algorithm to filter the pseudosections from outliers; scatter plots of the mean resistivity (a.) and phase (b.) values of the nearest 10 neighbours of each data points versus the resistivity and phases values of the data point itself, for all data points in blue, and for the kept data points in orange). Logarithmic apparent resistivity (c.) apparent phase (d.), logarithmic electrical potential (e.) and current intensity (f.) pseudosections. . . . .	152

5.28	Results of the outliers filtering procedure by neighbour analysis of the pseudo-sections: pseudo-sections previous to outliers filtering (a. and b.) and after outliers filtering (c. and d.) . . . . .	153
5.29	Pseudosections of filtered dipole-dipole data with various selectiveness regarding deep apparent data: maximum admitted offsets of 70 m (a. and b.) 40 m (c. and d.) and 25 m (e. and f.) . . . . .	154
5.30	Distribution of resistivity values and phases in the 3 dipole-dipole measurements after full data processing (maximum admitted offset in the quadrupoles: 40 m) . . . . .	155
5.31	Pseudo sections of filtered multiple-gradient data for T1 (a. and b.), T2 (c. and d.) and T3 (e. and f.)	155
5.32	Variation of apparent parameters for the dipole-dipole data (maximum admitted offset in the quadrupoles: 40 m) between March (T1), July (T2) and October (T3); ( $\log(\rho(T_{n+1}) - \log(\rho(T_n))$ and $\phi(T_{n+1}) - \phi(T_n)$ ) . . . . .	156
5.33	Distribution of resistivity values and phases in the 3 multiple-gradient measurements after full data processing. . . . .	158
5.34	Pseudosections of filtered multiple-gradient data for March (a. and b.), July (c. and d.) and October 2019 (e. and f.) . . . . .	158
5.35	Variation of apparent parameters for the multiple-gradient data between March (T1), July (T2) and October (T3); ( $\log(\rho(T_{n+1}) - \log(\rho(T_n))$ and $\phi(T_{n+1}) - \phi(T_n)$ ) . . . . .	158
5.36	Inversion results at the 3 time-periods - the black line on each model represents the line at 40 m below the surface, to roughly locate were to expect the water head; the grey shaded zone corresponds to the area where the profile is not a straight line, and where the data are expected to be slightly distorted. Bottom-left figure: Interpretation scheme related to the resistivity models . . .	160
5.37	Variations in time of the models. The percentage difference of the resistivity in y relative to x (y,x) is $100 \cdot (\log(\rho_y) - \log(\rho_x)) / \log(\rho_x)$ . An increase of $\rho$ is expressed in blue, a decrease is expressed in red. An increase of the absolute phase ( $ \Phi $ ) is expressed in blue, a decrease is expressed in red . .	161
5.38	Extracted vertical logs from the inverted resistivity (left) and phase (right) models, at $x = 150, 200$ and $250$ m. . . . .	162
5.39	Conceptual scheme proposed from the temporal and vertical variations of the pressure at the four levels packered . . . . .	162
5.40	Influence of the water saturation on the imaginary part of the complex conductivity in the case of a sand/clay mixture with 10% of clay - by <a href="#">Breede et al. [2012]</a> . In the frequency range between 10 mHz and 1 Hz, the influence of the saturation on the polarization is none linear. . . . .	163
5.41	Inverted ERT profile measured along the slope in April 2019 with a GEOMON instrument: the lateral variability and bubble shapes of conductive and resistive anomalies in the first 20 to 30 m suggest a high variability in the cementation of the scree slope deposits . . . . .	165
6.1	Colocated AMT (red curve and red dotted curve - at high frequency) and CSAMT sounding (blue and black dotted curves - at lower frequencies) at the Strengbach catchment . . . . .	174
6.2	Frequency band of the IP phenomena and of plane wave induction EM methods. Inspired from <a href="#">Okay [2011]</a> . . . . .	174
A.1	Ellipse in the plan $\{0, e_x, e_y\}$ . . . . .	II
A.2	Schema précisant la géométrie du problème : un dipôle émetteur centré en O génère une densité de courant source $\mathbf{J}$ , la mesure est réalisée au point M, et une anomalie de résistivité est localisée en A. La base $\{e_{r1}; e_{\theta1}\}$ est le repère polaire local en M centré en O. De même, on définit le repère local en A : $\{e_{r2}; e_{\theta2}\}$ et le repère polaire local en M, centré en A : $\{e_{r3}; e_{\theta3}\}$ . . . . .	V
A.3	profil altimétrique et carte horizontale du profil 2 . . . . .	VII
A.4	Pseudo-section des résistivités et phases apparentes, filtrée des résistivités apparentes négatives et des phases positive, sur la base du calcul de $k$ à une dimension (i.e. en supposant que le profil est linéique). Des anomalies apparaissent clairement, sur la pseudo-section des résistivités apparentes, aux endroits où le profil forme des coudes. (mesures réciproques) . . . . .	IX

A.5	Pseudo-section des résistivités et phases apparentes, filtrée des résistivités apparentes négatives et des phases positive, sur la base du calcul de $k_{2D}$ . De nombreuses anomalies de la figure précédente disparaissent. On note sur le profile des phases apparentes un mauvais contact sur une électrode, qui présente systématiquement des polarisations élevées (le long d'une forme en V inversé). . . . .	IX
A.6	Pseudo-section des mesures réciproques traitées (calcul de $k_{2D}$ , suppression des résistivités apparentes négatives et phases apparentes positives et suppression des données aberrantes) . . . .	X
A.7	Pseudo-section des mesures normales traitées (calcul de $k_{2D}$ , suppression des résistivités apparentes négatives et phases apparentes positives et suppression des données aberrantes) . . . . .	X
A.8	Carte de la campagne de CSEM en champs proche: stations de mesure et dipôles d'émission . . .	XII
A.9	Carte de polarisation du champ magnétique généré par le dipôle 1 orienté Est-Ouest. Les mesures figurent en bleu, et la modélisation pour un milieu homogène plan à 1000 Ohm.m est représentée en noir. . . . .	XII
A.10	Carte de polarisation du champ magnétique généré par le dipôle 2 orienté Nord-Sud. Les mesures figurent en bleu, et la modélisation pour un milieu homogène plan à 1000 Ohm.m est représentée en noir. . . . .	XII
A.11	Signal émis à l'émetteur (en rouge) et fonctions de transfert (amplitude à gauche phase à droite) électriques et magnétiques du milieu . . . . .	XIII
A.12	Diagrammes d'Argand pour une des stations mesurées. . . . .	XIV
A.13	Les quatre grilles testées pour le calcul direct et inverse. La flèche noire indique la direction du Nord	XV
A.14	Grille sélectionnée pour le calcul direct et inverse. . . . .	XVI
A.15	Exemple de calcul direct sur une grille trop faiblement discrétisée entre l'émetteur et le site (Seules les amplitudes positives apparaissent). . . . .	XVII
A.16	Exemple de calcul direct sur une grille suffisamment discrétisée entre l'émetteur et le site (Seules les amplitudes positives apparaissent). . . . .	XVIII
A.17	Exemple de modèle après 4 itérations. Les stations sont représentées par des points. . . . .	XIX

# List of Tables

2.1	Characteristics of the current source T3 for different load resistances and the 3 setting modes corresponding . . . . .	37
2.2	Characteristics of the signal transmitted by the T3 and measured by the V8 and 3-ER: fundamental frequencies, sampling frequency and theoretical harmonics produced relative to the sampling frequency, to stay below the Nyquist criterion . . . . .	39
3.1	Measurement characteristics of System-2000 instruments used in this survey . . . . .	73
3.2	Mean apparent resistivity from 4000 to 500 Hz and resistivity used to compute the topographic effect t for each recorded station . . . . .	85
3.3	Data misfit range for each stations . . . . .	88
4.1	Values of parameters used in the inversion models. . . . .	107
4.2	Synthetic tests: location, dimensions, context and resistivity values of the simulated anomalies. . . . .	109
5.1	Characteristics of the four models used to evaluate the sensitivity of CSAMT measurements and to test the 1D time-lapse inversion . . . . .	137
5.2	Evolution of the number of data (and percentage of remaining data at each step) throughout the processing for the different datasets . . . . .	153

# Introduction

## Introduction

Water flows in the subsurface are primarily controlled by the structure and micro-structure of the rock matrix, and by the spatial extension of more or less permeable zones. In many cases, the general structure of the subsurface is complex, arising from a long term dynamics, that set the spatial distribution and structure of geological materials (tectonics, heritage from the glacial era) or from chemical (alteration dissolution) and biological processes. In numerous cases, the water flow occurs not only through the rock matrix but also along preferential paths formed by a net of discontinuities (faults, fissures) and function of the petrophysical characteristics of the rock matrix. For these reasons, when trying to establish the flow processes, one should often characterize them at various spatial scales, and, sometimes, at important depths (100 to more than 1 km).

There are many societal issues that require an understanding of the functioning of hydrogeological systems, and of the flow properties of the subsurface. Among these issues, one could count agriculture and land use, soil degradation and erosion problems, management of landslide and slope instability, water resource management (quality and quantity of the resource), and exploitation of geothermal energy. These issues imply the study of hydrogeological systems at various scales, from the study of very near surface processes (irrigation, soil degradation, land use: first meter to first 10 m) to very deep processes, for example in geothermal exploitation (kilometers).

Characterizing the subsurface in terms of physical parameters sensitive to the soil structure, moisture or water content permits to increase the understanding the hydrogeological functioning of a site. To this end, hydrogeophysical techniques were developed, using all the range of geophysical methods that provide insights in the hydrogeological or structural features of the subsurface with the appropriate resolution. Parameters such as the seismic wave propagation speed, the density, the electrical resistivity and the magnetic resonance are very sensitive to the amount of water in the pore space. The electrical resistivity of rock and soils is in fact influenced by the presence of water, its composition, its temperature. This dependency is particularly increased when the rock matrix is much more resistive than the fluid, and electrical response of the rock is dominated by the electrical conduction in the pore fluid.

The purpose of this thesis is to study the contribution of electric and electromagnetic methods in the establishment of hydrogeological models. The focus is made on the application to three types of reservoirs: deep weathered crystalline aquifers, fractured hard-rock aquifers and sedimentary aquifers with high clay content (fig. 1). These applications necessitate studies at the slope scale, from 100 m to 1 km depth. This work brings forward three specific methods: Electrical Resistivity Tomography (ERT), Induced Polarization (IP) and Frequency Domain (FD) Controlled Source Electro-Magnetic methods (CSEM) and more specifically Controlled Source Audio-frequency Magneto-Tellurics (CSAMT). These methods rely on different physical processes, and are sensitive to the electrical and dielectric properties of the ground. If these methods are routinely used for specific applications (small-scale hydrogeophysics (20 to 30 m depth) for ERT and IP, mining and geothermal exploration for CSAMT), their application to large-scale hydrogeological studies necessitate adaptation and developments.

For all three types of reservoirs, the pertinence of the dimensionality of the survey is studied and discussed. The possibility of increasing the physical sensitivity (higher resolution, sensitivity at greater depths) and the geological sensitivity (sensitivity to a specific object) in combining different types of information is systematically evaluated and valuable additional data are exploited when possible. Finally, the possibility of understanding hydrogeological processes by observing the time variations that these processes produce in the geophysical signal (time-lapse methodology) is explored.

This manuscript is organized in 5 chapters, framed by this introductory section, and a final conclusive section.

The 1<sup>st</sup> chapter is an introduction to the subject of this thesis. The general context of hydrogeological studies of the three types of aquifers is presented, as well as the challenge that each of them presents. The use of geoelectrical methods in the context of hydrogeological studies is presented. Finally, the main questions that conducted my work during these three years are extensively presented, as well as the protocols implemented in order to answer part of these questions.

The 2<sup>nd</sup> chapter sets the technical methodology developed to answer the questions addressed in this thesis. The geo-electrical methods used in the thesis are extensively presented as well as the potential developments and specific applications of the thesis.

In the 3<sup>rd</sup> chapter, the deep structure of a granitic catchment is explored with the Controlled Source Audio-frequency MagnetoTelluric (CSAMT) method. In weathered crystalline catchments, the limit of weathering of the bedrock at depth often defines the limit of hydrogeological reservoir. At the Strengbach catchment, the weathering limits at depth could not be identified by exploring the first 30 m of the catchment with Electrical Resistivity Tomography imagery. The application of CSAMT presented in chapter 3 allowed to image this weathering limit.

In the 4<sup>th</sup> chapter, the complex slope-scale structure of a deep rock slide is imaged. To realize this large scale study, a set of synchronized 3-channels DC resistivity node-sensors was used, referred to as Resistivity-Distributed Antenna System (R-DAS). This methodology allowed a thin sampling all over the slope of the Séchienne landslide. The produced data could be inverted in 3D with a thin description of the topography, providing a large scale 3D resistivity model of the slope.

The challenge that represents the geo-electrical study of clayey sites is addressed in the 5<sup>th</sup> chapter in the particular perspective of landslide study, as clay material are in some cases very prone to slide. The Lodève landslide is a deep, slow moving clayey landslide, where the sliding layer is located at more than 50 m depth, and is composed of an alternation of clay and evaporitic materials. Repeated CSAMT measurements were realized throughout the autumn and winter, when the system relaxes and discharges from intense autumnal rains. The induced polarization signal of this clayey-evaporitic slide was studied with 2D TDIP measurements, adapting the array to be sensitive to the first 80 m. Measurements were repeated at three different moments during the spring, summer and autumn period, and the resulting time-lapse measurements were interpreted.

Last, the conclusion summarizes the main developments and findings of the thesis and highlights some remaining questions. Perspectives are proposed for future investigations.

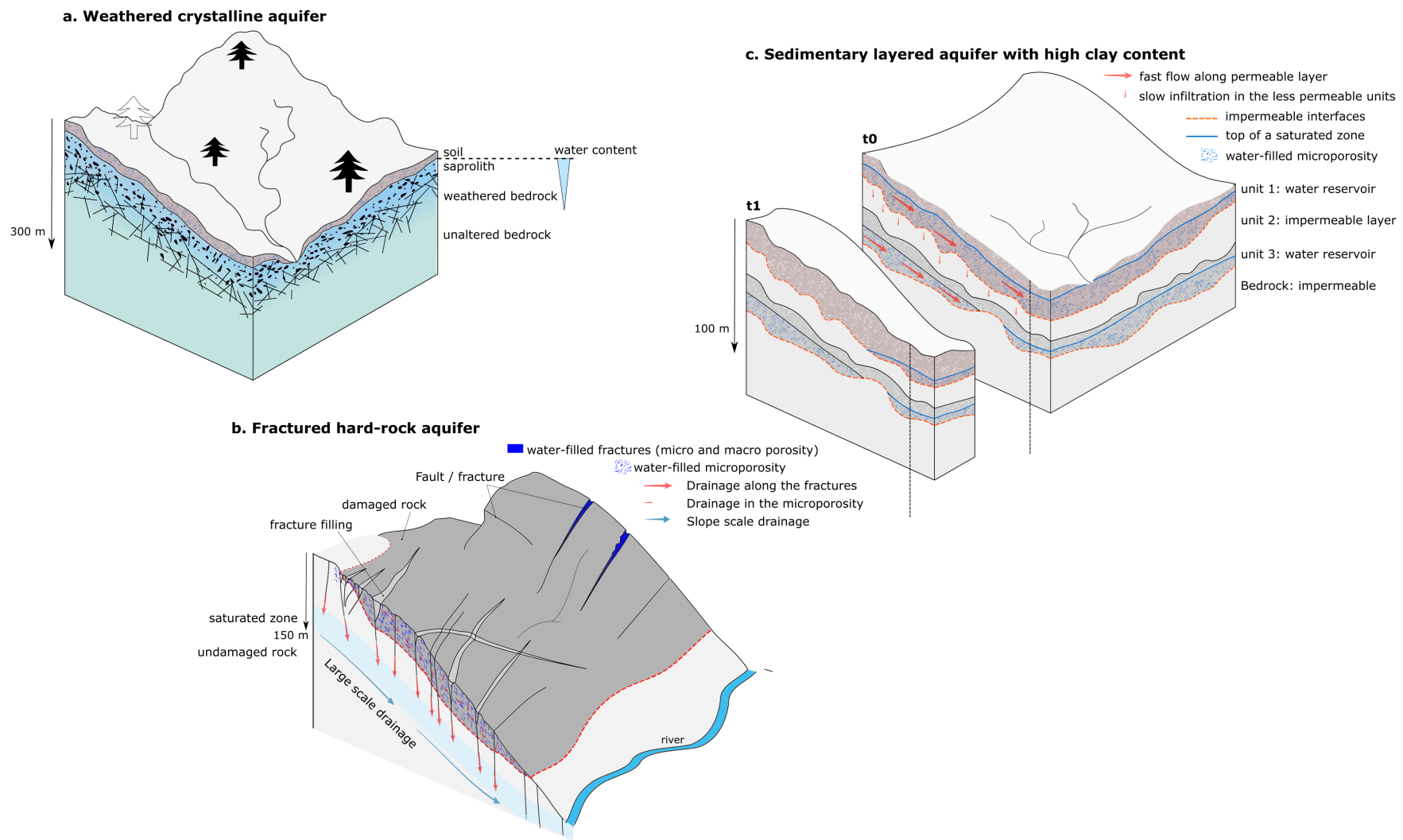


Figure 1: Three different types of water reservoirs: a. weathered bedrock aquifers; b. fractured multi-porosity and multipermeability reservoirs; c. sedimentary aquifers: stacked independant aquifers

# **Chapter 1**

## **Context and research questions**

## 1.1 Water storage and flow in rock reservoirs

### 1.1.1 Different types of water reservoirs

Water reservoirs designate any volume of water contained in an enclosing rock. Water reservoirs constitute water resource, and can be anthropogenic (artificial) or natural (Şen [2014]). Aquifers are natural water reservoirs located in the subsurface, contrary to lakes, for example. They are formed by the pore space in rock formations. This thesis focuses on this last type of water reservoirs contained in the rock matrix.

When meteoric water infiltrates the subsurface, it is driven by gravity and capillary forces through the rock fabric, depending on the structure and microstructure of the rock. The part of the subsurface where the hydrogeological processes occur is the critical zone (Lin [2010]). It is the zone of the Earth crust concerned by the water and chemical exchanges, necessary to sustain the natural ecosystems and to provide water and nutrients to vegetal and animal species. It is also the zone of the subsurface that can be influenced or altered (chemically, mechanically) by meteorological processes and that can be more generally degraded and disrupted in response to external atmospheric or anthropogenic forcing. The human activity depends upon this critical zone through occupation and exploitation. This critical zone extends from the Earth surface down to the bottom of the ground water reservoirs. In many contexts, only a few tens of meters are involved, however, in specific cases, the water flow and storage processes can extend down to a few hundreds of meters. In the following, the term subsurface is a generic term employed to designate the first kilometer of the crust, embedding the critical zone.

The diversity of morphological, lithological and structural contexts observable in the Earth subsurface provides as many different types of hydrogeological structures permitting the storage of water in the rock fabric. These different contexts define different types of reservoirs. One can distinguish for example sedimentary reservoirs (porous aquifers) from crystalline reservoirs (fissures hard-rock aquifers) (Collin [1991]). Sedimentary reservoirs are constituted of successions of sub-horizontal stacked layers of sedimentary rocks, of variable permeability. In such reservoir, the infiltration rate depends on the permeability of the successive layers, in relation to the effective permeability of each layer (fig. 1.c).

In crystalline reservoirs, the water storage is possible in damaged, fractured or weathered zones of increased porosity (micro- of macro-porosity) permitting the water to infiltrate and to be stored in the rock. Among crystalline reservoir, the distribution of macro and micro-porosity and the processes that built this porosity also define different types of reservoirs. If the weathering processes are relatively smooth and regular over a slope or a catchment, such reservoir can be assimilated to a 1D layered medium, where the progressive decrease of damage through weathering defines the progressive decrease of stored water. In such reservoirs, the water at depth is expected to be less mobilized than the water in the near surface. The deeper the water, the less impact it will have on the short terms / high frequency water transfers (fig. 1.a).

In the opposite to weathered crystalline reservoirs, fractured crystalline reservoirs are crossed by localized and large-scale features such as faults. This type of reservoirs present vertical as well as horizontal conductive and impermeable structures, and the water flow is much more complex. In such reservoirs, the nature of the flow can radically change when looking at different spatial scales, and the fractures provoke important discontinuities in the flow and storage regime (fig. 1.b).

### 1.1.2 Why is water reservoirs characterization important?

Understanding the hydrogeological functioning of the subsurface is fundamental in many different contexts and requires to determine the static and dynamic properties of the subsurface (Şen [2014]).

The hydrogeological modeling finds applications in many domain: agriculture and land use (Brakensiek [1979]), soil degradation and erosion problems (Martínez-Murillo et al. [2013]), management of landslide and slope instability (Tacher et al. [2005], Guglielmi et al. [2000]), water resource management (Folch et al. [2011]), and exploitation of geothermal energy (Jeanne et al. [2014]). Such modeling permits for example to predict and understand the conditions necessary to flooding and mud flow, salt water intrusion in coastal areas or anthro-

pogenic water contamination in industrial area.

Each of these domains focuses on specific hydrogeological properties. For example, in agriculture and land use domains, the focus is made on irrigation and supply systems, and moisture properties of soils. In water resource management, the quantity and quality of the resource is studied, and the temporal evolution of the resource in dry periods is of primary interest. The exploitation of geothermal energy is based on the circulation of water in the hot rock system, through networks of fractures, the permeability of the fractures system is therefore at stake.

### 1.1.3 How to characterize water reservoirs?

This section gives an overview on the main parameters that are commonly used, in hydrogeology, to describe static and dynamic intrinsic hydrogeological properties of the rock, as well as time dependent hydrogeological characteristics.

The capacity of a rock to store water is directly related to its effective porosity, the part of the porosity involved in water drainage. The porosity is the percentage of the pore volume in a unit volume of rock. A storage zone is also described in terms of its boundaries. Indeed, for a rock material to store water, it necessitates the rock to be surrounded, at least at its bottom and, to some extent, laterally, by impermeable media (or less permeable, by a few orders of magnitude, than the host rock), for the water to remain in this reservoir.

This brings us to the definition of permeability, which describes, the speed of the fluid through the pore space, when applying a unit pressure. It is an oriented parameter, that often presents an anisotropy (direction of faults or fissures more permeable than the orthogonal directions) (Darcy law).

The parameter that describes the amount of water present in the pore-space is the saturation, defined as the ratio of volume of water located in the pore space to the total pore space (in percent).

The quantity of water effectively present in the rock depends on both a short terms and longer terms history of water infiltration and water flow in the system (water input and water output). If the rock is locally saturated, the system {rock + water} is called an aquifer. The water level is then a measure of the 'size' of the aquifer. Above an aquifer, the rock can be more or less saturated in water and more or less permeable, defining the confinement of the aquifer.

The hydrogeological modeling aims at describing and predicting in detail the response of the system (catchment, unstable slope, aquifer, dyke/dam, geothermal system) to various types of inputs (meteoric water in a certain amount, with a certain chemistry (related to pollution)). This response (variation in water content and distribution) results in the infiltration and runoff processes, which must be modeled.

### 1.1.4 Focus on catchment and landslide reservoirs

#### Catchment studies

Catchments define delimited hydrological systems that gather the meteoric waters and conduct them, either by infiltration and flow through the subsurface or by surface run-off, towards a unique outlet. Catchments are stable water reservoirs where quantities of water transit, causing sediment transport, weathering and general rock-water interaction. The evolution of catchments are very long-term processes, occurring at decade to century scales.

In catchment hydrogeology, the system is studied at a scale where it is possible to establish the water balance, as all meteorological water entering the system is expected to converge towards a unique outlet (Pierret

[et al. \[2018\]](#)).

By doing so, it is possible to study the interaction between land-cover and hydrogeology and to describe eventually the medium in a much more complete manner. Indeed, the functioning of a catchment depends on its altitude, topography, vegetation cover and the related biochemical processes, the nature of the soil, its exposure to sun, and its underground characteristics. Processes such as absorption, evaporation and evapotranspiration can be accounted in the balance, permitting an increased accuracy in modeling the response of the system and the possible variations of the water resource. In turn, the establishing such balances allows studying the weathering processes induced by the water flow (from rainfall and snow melt), in a specific vegetation context, by monitoring the sediment and solute transport.

The subsurface properties play an important role in the water balance. The speed of the underground flow, the possible storage zones and their availability may influence the restitution time of the water, i.e. the time spent by the infiltrated water in the system. Furthermore, the preferential flow paths are expected to reshape the lateral limits of the catchment, primarily defined as the crest limits. The structure and micro-structure of the subsurface must therefore be accounted for in the modeling of catchments.

In this context, geophysical surveying can allow establishing a large-scale geological and structural model of the subsurface, identify storage zones, and distinguish altered and non-altered areas. The ANR project HydroCriZStO (2016-2020) aims at developing multidisciplinary tools to study catchments, joining a geophysical, a hydrogeology and a chemical approach.

## **Hydrogeology and landslides**

The hydrology plays an essential role in slope instability, either by inducing damages to the rock (long term process) or by triggering the instability (short term process). This role can be a cumulative damaging (alteration) along weak fractures, a rapid increase of the water pressure localized in weak zones of the subsurface (for example, intense rain events can provoke rock falls of toppling), or a loss of the cohesion inside an unconsolidated or dissolvable rock fabric (provoking mudflow at the surface, or rotational slides along the weakened layer at depth).

A few classes of landslides can be distinguished. In each of them, the role of water is very different. In the context of rocky landslides, the water can have a long term damaging action (weathering, dissolution), and can also induce brutal over-pressure along weakened fissures. On the opposite, clayey landslides are sensitive to variations of stress, and have the particularity to undergo brutal variations of the viscosity of few orders of magnitude (liquefaction) when the stress level exceeds certain threshold defined notably by the water content ([Khalidoun et al. \[2009\]](#)).

Studying the hydrogeology in the context of landslides primarily aims at modeling the response of a slope to variations of mechanical stress induced by the water when stored, or when flowing through the ground. The hydromechanical properties of the subsurface vary a lot depending on the geological and structural context, and the weakened zone can be located at various depths, affecting in turn different volumes of rock. Identifying these contexts requires to establish the spatial variations in damaging, storage capacity of the rock, and major flow paths, and to analyze the possible interaction of the water with the rock fabric.

By observing the response of the slide to specific meteorological input, one can get ground information on its functioning, establishing potential correlations between surface displacements and variations of the meteorology (rainfall). Geophysical imagery can permit to identify the underground structure, establishing the spatial extent of the damaged zones and the volumes at stake, the location of an unstable sliding layers, water-storage zones and major flow paths. In this context, the ANR project HydroSlide (2016-2019) ('Hydro-geophysical observations for an advanced understanding of clayey landSLIDES') aims at bringing forward the hydro-geophysical analysis of clayey landslides to better understand the water fluxes in the subsoil, and to model the hydrome-

canical response of the slides.

### Characterization and imagery of water reservoirs

It is very common to establish the hydrogeological properties of a given aquifer by drilling wells and record locally the local hydraulic head. The realization of pumping experiments, possible if several wells are drilled over the studied area, can help infer dynamic properties of an aquifer. These methods however cannot provide accurate information on the spatial variability of the properties and particularly on preferential flow path between the boreholes: borehole observations remain very local.

Geophysics offers a panel of imaging and characterization methods, based on the evaluation of specific physical parameters, that are somehow related to the lithology, structure or hydrogeology. In the particular case of hydrogeological studies, a few geophysical parameters can provide information on the water content, moisture, distribution of reservoirs, in the subsurface. The seismic waves velocity, the very small variations of the gravity field, the electrical resistivity, the magnetic resonance are examples of parameters and physical mechanisms that are influenced by the presence of water, and that can, in turn, give information on the presence of water in the subsurface. These parameters and mechanisms are leveraged in the specific discipline of hydrogeophysics.

## 1.2 Geoelectric investigations in hydrogeophysics

### 1.2.1 Electrical properties of rocks - electrical resistivity imagery

The ability of a material to conduct or, on the opposite, to retain an electrical current flow is described by the electrical conductivity ( $\sigma$  in [S/m]) and respectively by its opposite, the electrical resistivity ( $\rho = \frac{1}{\sigma}$  in [ $\Omega m$ ]). This property is primarily related to the composition of the material and to its structure.

In earth sciences, the electrical resistivity has been extensively used since the beginning of the twentieth century to characterize and image the subsurface. This parameter presents the advantage of varying over nine orders of magnitude for different structures, compositions and water saturations of the rock material.

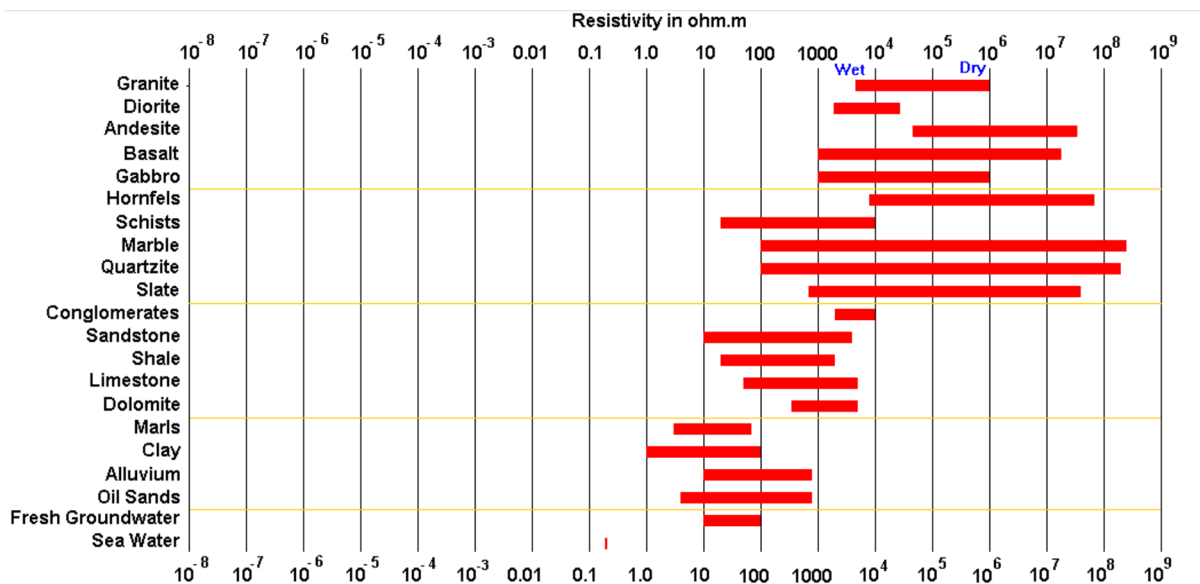


Figure 1.1: Range of resistivity values for different rock materials - from Loke [2013]

Many studies presented syntheses on the ranges of electrical resistivity values observed for different types of rocks. Loke [2013] presents and emphasizing through fig. 1.1, for several types of rocks, the range of resistivity

that the rocks can present from dry to wet state.

Indeed, when conduction occurs in the subsurface, two different processes occur: the current flows through electronic conduction processes in the solid rock matrix, and through electrolytic processes in the pore fluid. In porous rocks, the conductivity of the pore fluid is often higher by orders of magnitude than the conductivity of the rock matrix. In such situations, the overall resistivity of the material is primarily controlled by the conductivity of the fluid, which reflects in fig. 1.1.

The nature of the pore phase (gas, air and liquid) influences a lot the macroscopic electrical resistivity. For any rock, an increase of the porosity will result, if the pore-space is dry, in an increase in resistivity, the air being an electrical insulator. In addition, for a specific type of rock, the variations in the composition of the rock (percentage of some specific minerals, such as metal minerals, clay minerals) contribute in decreasing the electrical resistivity of the rock matrix. Characterizing the resistivity of the subsurface allows therefore being sensitive to the spatial variations of the petrophysical nature of the rock, its structure and micro-structure, and its water-content.

In addition to the electrical resistivity other geo-electrical parameters are interesting to characterize. If the ground can conduct the current, it can also, similarly to a capacitance, store the electrical energy during polarization phenomena. These processes are microscopic processes occurring at the scale of the surface of grains, or at the interface of bodies of very different resistivity, or of different dielectric properties. This phenomenon provides specific signals of lower amplitude regarding standard DC resistivity methods and that depends on the frequency. Studying it can provide, depending on the degree of complexity of the analyses, either one additional imaging parameter, or a full spectral response to be analysed and interpreted in terms of micro-structure and interface properties.

There exist a few geophysical techniques that allow to infer the electrical resistivity of the subsurface, and a great deal of manners of applying them in the field. Historically, the first method ever used was the electrical method, applied successfully for the first time at the beginning of the twentieth century. Shortly afterwards, the polarizability of rocks was brought to light and studied. This gave rise to the induced polarization method, which gives access to a frequency dependant complex resistivity. In parallel to these galvanic methods, electromagnetic induction techniques were developed and used to infer the resistivity anomalies in the subsurface based on a very different methodology.

Because of the numerous parameters influencing the electrical resistivity of a rock, it is rarely possible to directly interpret a resistivity model in terms of porosity, water content, or geological structure without complementary knowledge. When interpreting a resistivity model, strong prior information, or complementary geophysical characterization is needed. Nevertheless, empirical laws were established to link electrical properties to hydrogeological or petrophysical properties of the rock, providing, in specific cases, constraints on some parameters. The Archie law (Archie [1942]) constitutes, for non-clayey sedimentary materials, a relation between the bulk electrical resistivity, the resistivity of the pore fluid, the porosity, the cementation factor and the formation factor. Similar laws exist in very specific context (Waxman and Smits [1968]).

The constant development of instruments increased the sensitivity and resolution capacity of the methods. In electrical methods, two-dimensional measurements were eased by the development of multi-channels recorders, and the field methodologies pushed further into multi-dimensional studies (3D, 4D). At the same time, the rise and developments of computers allowed the formulation and solving of complex inverse problems, which played an important role in the interpretation of electrical resistivity data, as it allowed to model complex resistivity models.

These general developments led to the production of a few 3D modeling and inversion softwares, addressed to each of the different electric and electromagnetic methods and providing solution for the study of complex underground structures. At present time, a few general objectives, given hereafter, can be isolated as major topics of research and developments in geophysics:

1. increase of the depth of investigation and the resolution of the measurements to resolve complex structures
2. joint interpretation of geophysical datasets, or geophysical and non geophysical datasets, data integration
3. development of time-lapse methodology (field wise, and interpretation wise), data fusion, and data integration

## 1.2.2 Basic notions in geophysics

Most electrical and EM imaging techniques are based on the observation of the response of the subsurface to a physical signal, either originating from natural processes (passive methods), or actively generated by the field operator (active methods). The subsurface is considered as a filter, which characteristics depend on the micro and macroscopic physical properties of the ground. Its response to a set of input signals carries information on the subsurface and permits to characterize it.

The theories linking an input signal, the measured response and a physical property of the subsurface are often complex, and the transfer function characterizing the subsurface filter is rarely linear. One must often rely on mathematical tools to extract the information from the measured signal.

The property estimated from a measurement is always an apparent measure, i.e. produced by the combination of each infinitesimal unit volume to which the measurement is sensitive. It is therefore an averaged measure over the entire sensible volume. Apparent measures do not express the thin variations that are presents in the subsurface, and that contribute to the apparent values, but provide very smoothed information. Retrieving the real variations of the imaged property requires the combination of a large number of apparent properties measured with various sensitivity in neighbouring areas, such that all measurements share a part of their sensitive volume. It is then possible to decompose the apparent measure into a series of localized contribution. This step corresponds to the data inversion process. A dense spatial sampling of the measurements is then needed to retrieve, through the inversion process, a model of the effective property, and of its spatial variations.

Any geophysical investigation can be characterized in terms of physical sensitivity, geological sensitivity, resolution, and depth of investigation.

### • Sensitivity to the imaged physical property

The sensitivity of a survey, called here physical sensitivity, defines the ability of the method (in a specific context of measurement, processing and site properties) to resolve any variation of the property at any location in the subsurface. The jacobian matrix represents the impacts on the measurements of infinitesimal variations in the model (eq. 1.1), is a measure of the sensitivity in the context of a specific model, and of a survey layout.

$$J_{i,j} = \frac{\partial d_i}{\partial x_j} \quad (1.1)$$

In eq. 1.1,  $d$  designats the data,  $x$  designats the parameter in the model space,  $i$  is the data indexation and  $j$  is the indexation of the model parameters.

### • Geological sensitivity

In contrast with the physical sensitivity, the geological sensitivity could be used to highlight the fact that a geological (structural or hydrogeological) object targeted in a study will not necessarily present a significant geophysical contrast with its surrounding rock, depending on the physical property used to image the subsurface. For this reason, the geophysical method, hence the imaged physical property must be adequately chosen given the expected properties of the object to be imaged.

### • Resolution

It is the finesse at which a variation of the physical property can be detected. The resolution varies spatially

over the model and generally decreases far from the receivers and transmission units. In particular, for surface measurements, the deepest zones are often less resolved than near surface zones. The overall resolution of a survey depends on the data coverage and the noise level.

In EM methods, the resolution is very variable depending on the governing process (propagative or diffusive). When diffusion dominates, the volume contributing to the measurement is spread and the resolution is relatively low. When, on the contrary, propagative processes dominate, the volume involved in the propagation is narrower, and focused around a ray, giving the opportunity of higher resolutions.

- **Depth of investigation (DOI)**

It is the characteristic depth below which the measurement will not resolve any variation of the imaged property. The accurate determination of the depth of investigation is discussed in several articles and several methodologies exist, based for example on the *a posteriori* computation of the jacobian matrix (Oldenburg and Li [1999], Christiansen and Auken [2012]).

- **Non-uniqueness of the solution of the inverse problem**

The interpretation of the geophysical data implies the resolution of an inverse problem. This step is an attempt at identifying the best geophysical model that can explain the measured data.

Because measuring a signal requires to sample it (which is equivalent to applying filters both in space and time), the datasets are necessarily incomplete. For example, when conducting surface measurements, the data are all measured at the surface of a unique planar limit of the model. Because of that, the sensitivity of a survey is restricted to a limited area, affected by a limited resolution.

In fact, for one inverse problem, there exist an infinity of solutions. This issue is referred to as non-uniqueness of the solution of the inverse problem. To solve this problem, prior information provided by expert geologists for example and regularization constraints are used in the inversion process, to reduce the variety of possible models.

- **Non-uniqueness of the interpretation**

Once the best model has been computed, fitting at the same time the prior information and the data, and presenting a reasonable roughness, the exciting task of the interpretation can begin. Once more, however, an issue complicates the work: the non-uniqueness of the interpretation of the geophysical model.

Most physical parameter results from several characteristics, among which the chemistry, petrophysics, structure, hydrogeology characteristics and more. For this reason, a specific variation of the imaged parameter cannot be univocally related to a unique geological, structural and hydrogeological context. For example, a conductive anomaly detected in a resistive background rock could be explained by the presence of water, of conductive ore, or the local presence of clay.

In such situations, the combination of several methods, and several parameters to characterize the subsurface can allow solve this non-uniqueness, and orientate the interpretation.

### 1.2.3 Electric and electromagnetic methods

#### Electrical resistivity tomography

Electrical Resistivity Tomography (ERT) is probably the most common method in hydrogeophysics. Ohm's law establishes the relation between the voltage at the terminals of a resistance, the intensity of the current and the resistance itself. In the same manner as Ohm's law applies at the terminal of a resistance, the spatial variations of the voltage at the surface of the earth induced when injecting a current between two grounded electrodes depends on the distribution of more or less resistive objects in the subsurface. In ERT, the galvanic measurement of the electrical potential at different points of the earth surface when injecting a known current between two points permits to infer the spatial variations of electrical resistivity in the subsurface.

Two injection electrodes are connected to a current source and grounded in two locations (electrodes A and B in fig. 1.2). A windowed current  $I(t)$  is applied in the ground through this device, and the resulting potential difference between two potential electrodes (M and N) is measured. A, B, M and N form a quadrupole. Each

quadrupole provides a measurement of apparent resistivity (mean resistivity over the sensitive area) computed with eq. 1.2, where  $\Delta V$  is the potential difference between the two potential electrodes,  $I$  is the injected current, and  $k$  is the geometrical factor (eq. 1.3), specific to the electrodes layout, in the case of a half-space.

$$\rho_{app} = \frac{\Delta V \cdot k}{I} \quad (1.2)$$

$$k = \frac{2\pi}{\left(\frac{1}{AM} - \frac{1}{AN} - \frac{1}{BM} + \frac{1}{BN}\right)} \quad (1.3)$$

The sensitivity in direct current (DC) galvanic methods depends on the resistivity of the subsurface and on the electrodes layout (geometrical factor). Generally, the sensitivity at depth is increased with the conductivity of the medium, and with the size of the electrodes arrangements and the resolution is increased by decreasing the electrode spacing.

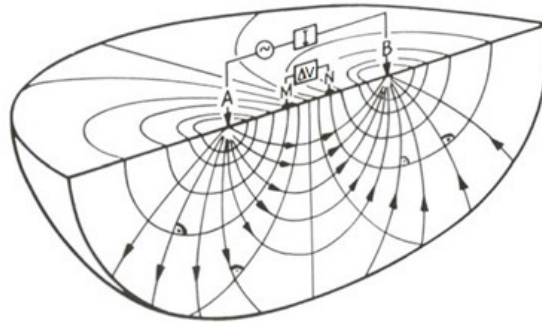


Figure 1.2: Measurement principle in electrical methods - from Critex

In the most usual case, the measurements are taken along 2-dimensional profiles using multi-electrodes systems, assuming that the structures are stretched infinitely in the direction perpendicular to the profile. Recently, several field methodology were developed to realize 3D measurements, and the software capabilities to solve complex 3D problems were developed in parallel (see chapter 4).

The measurement and processing techniques in ERT were adapted to conduct electrical measurements along the walls of boreholes. Electrical logging can be realized by moving a galvanic probe inside a borehole and sampling at different depths, or by using a multi-electrodes system, and fixing electrodes in the cement of the borehole to ensure a long term contact.

### Induced polarization (IP)

The induced polarization is an extension of the DC electrical method, that focuses on polarizability of the subsurface. Indeed, the electrical properties of the subsurface are not limited to conduction properties, but also include storage properties. When applying a potential between two surface point, such as in the ERT measurement technique, polarization phenomena may occur in the subsurface. These storage properties can be used to characterize the subsurface, as they often relate to the microstructural, hydrogeological chemical and lithological properties of the rock. In practice, this method consists in characterizing the complex conductivity of the subsurface such as in eq. 1.4, where  $\rho'$  and  $\rho''$  are resp. the real and imaginary part of the resistivity, and  $\Phi$  is the phase, which only takes negative values.

$$\rho = \rho' + i\rho'' = |\rho| e^{i\Phi} \quad (1.4)$$

**Penetration depths of the IP method: the challenge of a low noise level:** In theory, the penetration depth of the induced polarization method is related to the electrodes spacing, in the same manner as in the DC-ERT technique. In practice, the signals to measure (decay curve in the off time in the time domain, phase shift and impedance in the frequency domain) are very thin signals that requires low noise levels in order to be recorded.

For this reason, the depth of investigation of an IP survey is often lower than the depth of investigation of the DC ERT survey conducted with an equivalent array. The data recorded with large quadrupoles might be particularly sensitive to intense noise, depending on the array type (Binley and Kemna [2005]).

## Electromagnetic induction methods

In electromagnetic induction methods, the analyses of the subsurface spectral response to a mono- or finite-frequencies electromagnetic input signal is realized and is expected to provide estimates of apparent resistivity values, in the different contexts of the five methods presented hereafter.

### • The magnetotelluric (MT) method

Historically, the first frequency domain EM induction method to be studied and developed was the natural source MT method. In the 50th, in parallel, the French physicist Louis Cagniard, the soviet mathematician and physicist Andrei Tikhonov and two Japanese physicists, Harayama and Rikitake, described the MT method for its ability to solve the resistivity variations of the subsurface, offering the possibilities of reaching targets of hundreds of kilometers depth (Cagniard [1953], Tikhonov [1950]).

This method derives directly from the EM propagation equations, and exploits, in an homogeneous medium, the relation between the magnetotelluric impedance tensor  $Z$  and the apparent resistivity  $\rho$  of the sensitive medium.

The magnetotelluric impedance transfer function is the transfer function between the magnetic and electric fields (eq. 1.5, where  $*$  is the inner product). It describes, for any given medium, the horizontal electrical response of the subsurface to any given magnetic signal from a plane wave (Chave and Jones [2012]). In the frequency domain, the impedance transfer function takes its spectral form: the magnetotelluric impedance tensor (eq. 1.6). The MT impedance tensor is a complex, frequency dependent, second order tensor.

$$E(t) = z * H(t) \quad (1.5)$$

$$\begin{bmatrix} E_X \\ E_Y \end{bmatrix} = \begin{bmatrix} Z_{XX} & Z_{XY} \\ Z_{YX} & Z_{YY} \end{bmatrix} \begin{bmatrix} H_X \\ H_Y \end{bmatrix} \quad (1.6)$$

If the subsurface is a flat layered half-space, the impedance tensor simplifies as a single component tensor: the diagonal elements are null, and the off-diagonal elements are the opposite to one another (eq. 1.7 and 1.8). In this specific configuration of the subsurface, the off-diagonal elements only depends on the frequency of the EM signals, and the apparent resistivity of the subsurface (eq. 1.9). For this reason, the magnetotelluric method has the ability of solving the apparent resistivity of the subsurface.

$$E_X = Z_{XY}H_Y \quad (1.7)$$

$$E_Y = Z_{YX}H_X \quad (1.8)$$

Eq. 1.9 is the Cagniard formula, where  $\rho_{app}$  is the apparent resistivity,  $\omega$  is the pulsation and  $\mu$  the magnetic permeability.

$$Z_{xy} = \rho_{app} \omega \mu e^{-i\frac{\pi}{4}} \quad (1.9)$$

$$\delta_s = \sqrt{\frac{2\rho}{\mu\omega}} \approx 503 \sqrt{\frac{\rho}{f}} \quad (1.10)$$

As for most EM induction methods, the sensitivity of the MT method is controlled by the skin depth  $\delta_s$  (eq. 1.10), which depends on the resistivity of the subsurface  $\rho$ , the magnetic permeability of the subsurface  $\mu$  and the pulsation  $\omega$  or equivalently the frequency  $f = \omega/2\pi$  of the signal. Hence, the frequency of the signal will determine the size of the sensitive medium to which the computed apparent resistivity can be attributed. The resistivity of the subsurface influences both the resolution and the depth of investigation. The appropriate frequency range to study the near surface (first tens of meters down to a few hundreds of meters) is the audio

frequency range (1 Hz - 10 kHz). For this reason, the use of MT to near surface observations is referred to as Audio Magneto-Tellurics (AMT)

In case of 2D or 3D structures, the MT impedance tensor takes a more complex form, the diagonal elements turns non-null. A dense data sampling (regarding the frequency measured) is then necessary, and 2D or 3D inversion methodology can be employed to interpret the data and create a model of the effective resistivity (Kelbert et al. [2014]).

**Field setting:** The magnetic measurement is generally realized using a set of two or three magnetic induction coils, to measure the 2 horizontal components or the 3-components of the magnetic field. The coils are oriented along the North, East and downward directions with a compass and leveled. Fluxgate sensors can also be used. As they are very sensitive to the temperature, and because the MT measurement can take a few days, particularly when targeting low frequencies, the magnetic coils can be protected from sun beams and wind by burying them and covering them with dust, grass and foam. The electrical measurements are realized by grounding two orthogonal electrical dipole of large dimension (100 m or more) depending on the depth to be modeled. An example of station layout is proposed in fig. 1.3.

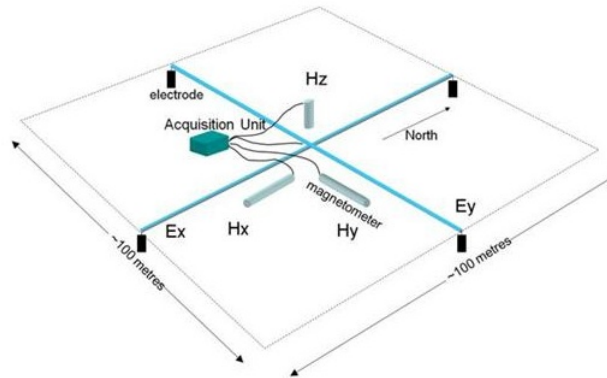


Figure 1.3: Layout of a standard MT station (Vector configuration) - ©Moombarriga Geoscience

**The MT source signals:** In MT, the source signals are EM plane waves, originating from the earth and solar electric or magnetic activity. The low frequency source signals are produced by the solar activity (solar wind and solar storm affecting the earth magnetic field) and the earth core activity. The high frequency source signals ( $> 1$  Hz) are produced by remote thunderstorms, generating waves carried by the wave guide between the earth surface and the ionosphere (Constable [2016]). The source signals are assumed to be randomly distributed, and to hit the station with random polarizations, to permit the full resolution of the MT impedance tensor.

The fig. 1.4, modified from Constable [2007], presents the power spectrum of natural magnetic signals with its many contributions. It shows a clear decrease of signal strength between 1 and 5 kHz, a frequency range referred to as AMT dead-band. This low signal strength is related to a low rate of signal emission, which occurrences are, in addition, difficult to predict. For this reason, AMT measurements are difficult to process and the uncertainties attributed to MT impedance values between 1 and 5 kHz are high, particularly when measured in areas affected by important anthropogenic noise. To face this issue, processing methods were developed to compute the MT impedance tensor, reducing as much as possible the uncertainty of the estimations. Different processing methodologies were discussed by Jones et al. [1989] who demonstrated the effectiveness of "robust methods" based on a specific statistical analysis of the error (residual) aiming at reducing the influence of outliers in the estimation of the tensor (for example, Chave and Thomson [1989] developed a popular tool based on the Jackknife method). More recently, Larnier et al. [2017] proposed a methodology based on continuous wavelet transforms to detect and extract the AMT signal.

Aside from these processing techniques, the limitations related to the low signal strength led to the development of a measurement technique involving the use of a controlled source. In the CSAMT method, a controlled source (usually a grounded electrical dipole) is located and powered as far as possible from the studied site in

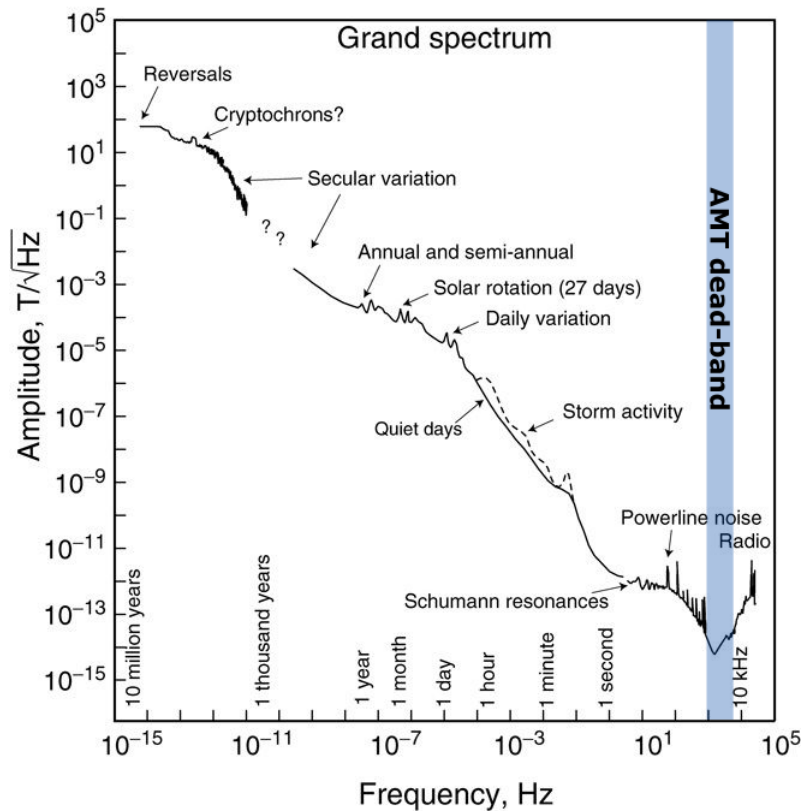


Figure 1.4: Natural magnetic field power spectrum and AMT dead-band (in blue)- modified from [Constable \[2007\]](#)

order to reproduce the far field signals used in the MT analysis.

• **The controlled source audio-MT (CSAMT) method**

The lack of source signals in the AMT dead-band compelled the geophysicists to consider the use of a remote controlled source to measure the impedance tensor. [Goldstein and Strangway \[1975\]](#) presented, in the case of a 1D layered medium containing an upper layer on top of an homogeneous half-space, the equations of the EM fields relative to grounded electrical transmitting dipole a quasi-static signal, in the situation when the transmitter-receiver offset is large regarding the wave number ( $r \gg k$ ). They demonstrate how to solve the two-layers problem analytically, and presented computation results on synthetic case scenario, as well as field data.

The equations of the electromagnetic fields produced by diverse types of sources were developed in [Ward and Hohmann \[1988\]](#), [Bannister \[1966\]](#) derived the "far field" approximation of these equations, and [Zonge and Hughes \[1991\]](#) synthesized, from the general formulations related to a grounded electrical dipole in an homogeneous half-space, the ability of CSEM to provide apparent resistivity estimations both in the far field and in the near field.

**Depth of investigation:** The sensitivity is once again determined as a function of the skin depth. If the plane wave hypothesis is fulfilled for a certain frequency, the investigation depth will be defined by the resistivity of the subsurface and the frequency of the source signal. Since the condition to be in the far field domain expresses in terms of ratio of the transmitter / receiver offset over the skin depth, the limiting factor in terms of investigation depth is in the end the transmitter receiver offset, which will determine the lowest frequency for which the recorded signal can be assimilated to a far field signal.

• **The radio-MT or very low frequency method (RMT or VLF)**

The radio-MT method is based on the same plane wave hypothesis and the same measurement and interpretation methodology as in the MT method. In Radio-MT, the source signal is very low frequency (VLF) radio

signals of anthropogenic sources (15 - 250 kHz), which are spread more or less densely depending on the studied location (Pedersen et al. [2006]). The measurement devices are the equivalent of MT measurement devices, only adapted to record higher frequency ranges. The computation of the apparent resistivity is based on eq. 1.9 and the sensitivity is as well computed through the skin depth. This method aims at identifying the near surface variations of the apparent resistivity (sensitivity from 10 to 40 m for a subsurface of 100  $\Omega m$ ).

- **The controlled source electromagnetic method (CSEM)**

In the near and transitional field of an electromagnetic source, the fields carry information on the subsurface both below the stations and below the transmitter. In such context, the MT impedance tensor cannot only be explained by the resistivity anomalies below the receiver station. The interpretation of near and transitional field data requires a complete modeling of the subsurface, including the area where the transmitting dipole is grounded and, to a lesser extent, the area that separates the transmitter and the receivers, as these zones contribute to the electric and magnetic responses.

This specific context, that requires to model the source in the inversion, relates to the Controlled Source EM method (CSEM). Because the source is modeled, there is no requirement on measuring both the electric and the magnetic field. The exclusive inversion of the electrical (or magnetic) transfer function can allow solving the resistivity variations in the subsurface.

- **The low induction number method (LIN)**

The low induction number method is a controlled source method adapted to the study of the first ten meters of the subsurface. This method focuses on the particular case where the induction number is low ( $B = r/\delta_s$ ), meaning that the source - receiver offset  $r$  is small regarding the skin depth  $\delta_s$ . This method is therefore a specific case of the CSEM method, where only near field data are measured.

A magnetic input signal is transmitted from a small-size coil and the response is measured by a similar coil located a few meters away from the transmitting coil. The measured response is the sum of the primary field - produced by the transmitter - and the secondary field corresponding to the response of the subsurface structure. In such configuration, the subsurface apparent conductivity  $\sigma_a$  can be computed from the ratio of secondary field ( $H_Q$ : quadrature response) to primary field ( $H_p$ : response in phase with the transmitter) as in eq. 1.11, where  $\omega$  is the pulsation,  $r$  is the transmitter - receiver distance and  $\mu_0$  is the magnetic permeability of the empty space.

$$\sigma_a = \frac{4000}{\omega r^2 \mu_0} \left( \frac{H_Q}{H_p} \right) \quad (1.11)$$

## 1.2.4 Use of these methods in the context of hydrogeophysical studies

In the case of the three different types of aquifer mentioned in the first subsection, the spatialization of the hydrogeological parameter is required to accurately model the functioning of the reservoirs. In particular, the critical zone requires multi-scale analysis, from metric to kilometeric scale. The broad range of scale involved in the hydrogeological functioning of a catchment requires the combination of several observation methods. Diagraphy and borehole geophysical methods, of very high vertical resolution, limit the observations to areas where a borehole was drilled. On the contrary, surface geophysical observations have a much lower vertical resolution, but permit the spatial extension of local borehole observations.

Among the different informative scales of observation, the observation of large scales (decametric - hectometric) trends and variations is particularly challenging. It requires the deployment of instrument over an important surface area, at location where the installation of devices can be rather challenging (topography). The adequate methods must be chosen and the field layout must be carefully designed, depending on the required resolution, and on the dimension, size and depth of the object to image (fig. 1.5).

In addition, the sensitivity to the geophysical variations at important depth is often limited by the power of the source signal, the presence of noise and the measurement layout. Reaching a depth of investigation of more than a few tens of meters is challenging in many sites.

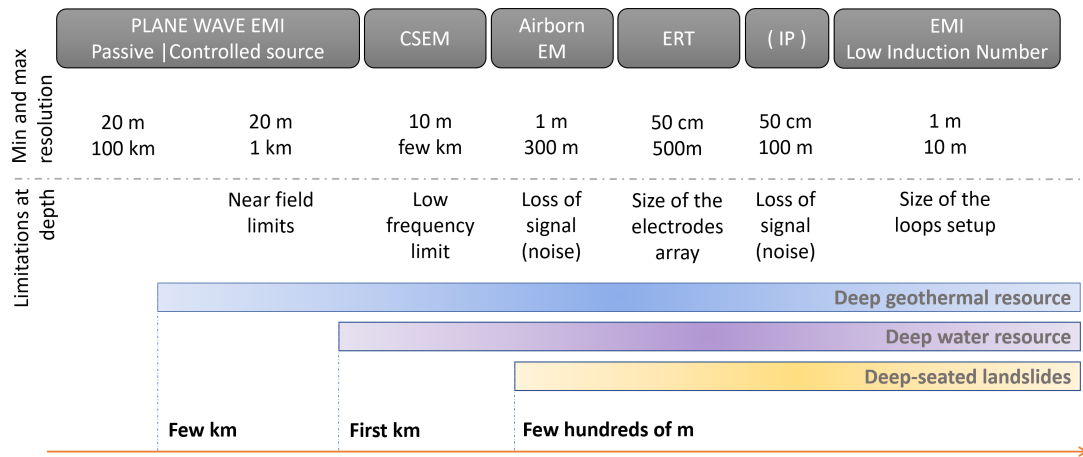


Figure 1.5: Summary of geoelectrical methods capabilities in terms of resolution and depth of investigation, and related depth of observation in different contexts of hydrogeological studied

## 1.3 Investigating the potential of hydrogeophysical methods for the large-scale studies

### 1.3.1 General context and main questions

The study of water reservoirs sometimes requires the characterization of the subsurface at important depths. The question that is explored in this thesis is: **what are the capabilities of geo-electrical measurements to characterize and image deep structures and water reservoirs?**

Crystalline and sedimentary reservoirs define two different types of medium. In crystalline reservoirs, the fracturing, fissuring and weathering of the rock defines the reservoir space. The study of the structure (1D, layered) and the study of the hydrogeology are therefore strongly related. In the context of sedimentary layered reservoirs, the limits of layers do not necessarily define reservoir limits, but the layered structures and the absence of lateral discontinuity ensure a lateral regularity in the reservoir. The different layers define units of variable micro-structures and permeabilities, featuring highly variable hydrogeological behaviors.

The three types of reservoirs that are considered in this work can be summarized, from a structural point of view, with three elementary contexts:

1. Progressive variation of the properties with depth (weathered crystalline reservoirs, fig.1.a)
2. Vertical and horizontal variations of the properties (fractured hard-rock reservoirs, fig.1.b)
3. Numerous, successive and sharp variations of the properties with depth (layered sedimentary reservoirs, fig.1.c)

Regarding the geo-electric aspect of such different contexts, this distinction has another reason: hard-rock are generally more resistive than sedimentary rocks (fig. 1.1). For this reason, the presence of water in the rock matrix of sedimentary aquifers might be more difficult to identify than the water trapped in the fissures and arena of metamorphic rocks. In sedimentary contexts, the spatial analyses of water content by means of resistivity modeling can be difficult, particularly in presence of clay minerals, as the rock matrix also will present low resistivity values. A way of isolating the hydrogeological signal in such context is to observe its variation through time.

**1. How to characterize deep crystalline weathered reservoir ?**

- Can such reservoirs be considered as 1D structures? How to ensure a large DOI ?

**2. How to characterize and image deep fractured hard-rock crystalline reservoirs?**

- How to capture the large scale variations (slope-scale) in a 3D resistivity model ? How to ensure a large DOI ?

**3. How to characterize and image deep sedimentary and clayey aquifers?**

- Can such reservoirs be assimilated to 1D structures?
- What are the monitoring possibilities (what measurement repeatability, sensitivity to variations can we expect; at which repetition rate)?

### 1.3.2 State of the art

#### Imaging and characterizing the structure of deep hydrogeological objects with geo-electrical methods

In the context of hard-rock crystalline reservoirs, the study of the structure and of the hydrogeology are strongly related. In geophysics, the dimension of structures composing the subsurface is a key point that influences the choice of methodology employed to study certain sites. A layered or pseudo-layered environment suggests sedimentary deposits barely disrupted after deposition or low tectonic impact and lateral homogeneity in the damaging processes of hard-rock. On the contrary, complex 3D structures suggest lateral inhomogeneity in the damaging processes and high impact of tectonics processes. These two contexts must be treated differently, as they define two different geophysical challenges. The lateral resolution is mostly related to the density of spacial sampling. The vertical deep resolution relies more on the type of geo-electrical methods and the intensity of the source signal it uses.

**• Deep characterization of weathered crystalline aquifers**

Geoelectrical methods have the capability of detecting anomalies from the first meters down to hundreds of kilometers depth. The kilometric sensitivity in geoelectric methods is exclusively reached by plane wave EM induction and ‘full-field’ controlled source EM (CSEM) methods. For this reason, these methods are often favored in the study of the geothermal resource, or the monitoring of deep geothermal exploitation ([Geiermann and Schill \[2010\]](#), [Abdelfettah et al. \[2014\]](#), [Árnason \[2015\]](#), [Coppo et al. \[2016\]](#), [Darnet et al. \[2019\]](#)), which are the hydrogeological situations that require the deepest sensitivity. In such context, the objects to observe are located at a few kilometers depth and are defined with a low resolution.

Deep aquifers can generally be considered as pseudo-1D objects, such that the plane wave methods are interesting methods for characterizing them. A few published articles present the study of deep crystalline aquifers in the context of water resource management. [Falgàs et al. \[2005\]](#) present the study of the plutonic catchment of La Soutte (France), applying AMT and ERT to the hydrogeological characterization up to 300 m depth. [Darnet et al. \[2019\]](#) identified the limits at depth of weathering of a granitic catchment combining CSEM, MT and seismic methods. In these two examples, the plane wave and CSEM methods showed good capability to resolve the deep electrical resistivity model.

If plane wave methods present the huge advantage of good sensitivity at large depth (up to 100 km depth) and a fairly good vertical resolution, they are, however, very sensitive to some distortion effects that can occur in the context of hydrogeological studies. The presence of topography is one of them. Another common one is the static distortion, or static shift of the apparent resistivity soundings, produced by near surface heterogeneities.

In particular, the impact of a 3D topography on these methods is known to exist, sometimes causing severe distortion in the estimation of the resistivity ([Baranwal et al. \[2011\]](#), [Kalscheuer et al. \[2013\]](#), [Ren et al. \[2013\]](#), [Árnason \[2015\]](#)). In the domain of controlled source methods, several theoretical works discussed and ana-

lyzed the topographic effect for very simple cases of hills (Lin et al. [2018]). Badea et al. [2001] and Stalnaker [2005] both developed a finite element 3D modeling code and modeled the topographic effect in CSEM measurements. In many studies, however, the topography impact is only mentioned and is seldom explored. The presence of topography also increase the difficulties in instruments installations.

- **Deep characterization of densely fractured hard-rock aquifers**

The characterization of complex 3D reservoirs on the contrary requires methods with high lateral resolution, that technically allow dense sampling in the field and that provide a better near-surface sensitivity. To realize such investigations, the previously evoked methods must be densely used throughout the site of interest. A common way of proceeding is to densely equip a site of electrical nodes, and to conduct CSEM surveys without measuring the magnetic field. This allows to gain a considerable amount of time, and is not always possible because it requires to possess a large number of magnetic sensors. For very larger-scale investigations (few  $km^2$ ), airborne EM methods allows very thin spatial sampling along the line of flights (in the order of one sounding every 25 m) and possibly good lateral coverage, in case of 3D investigations, with depths of penetration of a few hundreds of meters. On a purely structural geological study, Raingard et al. [2018] obtained DOI of 150 m on igneous rocks (Basalt and Andesites). In the context of aquifer mapping, again in volcanic systems, d'Ozouville et al. [2008] imaged a perched aquifer system in 3D with DOI of 400 m.

Finally, large-scale ERT measurements are commonly applied to image structures until 50 - 100 m depth, providing high 2D resolution. However, the depth of investigation is generally constrained by the size of electrode arrays and the length of the multi-core cables. In addition, the usual measurement methodology requires that the structures are 2-dimensional. Lately, research and development were made into developing setups to obtain good 3D sensitivity. Among these setups and measurement technique, the use of Resistivity Distributed Autonomous Systems permit a tremendous increase of the depth of investigation, and spacial extent of ERT surveys. This method is based on the deployment of autonomous 3-channels resistivimeters all over the survey area. These instruments, developed by IRIS Instruments<sup>®</sup> (FullWaver system), are synchronized through GPS signal: the ERT surveys are no longer limited by the length of heavy multi-core cables.

### **Isolating the hydrogeological signals and detecting water circulation through time-lapse methodologies**

Hydrogeological reservoirs and vadose zones are time varying objects as they respond to meteorological inputs and gravitational water flow. In most water reservoirs, the main evolution of the hydrogeological state occurs at a yearly scale, involving seasonal meteorological variations: the variation of pluviometry throughout the year and the variations in temperature (influencing the evapo-transpiration processes and impacts on the effective water infiltrating the subsoil) lead to the alternation of high and low water flow periods. Long term local evolution of the meteorology related to long term global climate change are as well expected to influence the water reservoir cycles.

In addition to these general temporal evolution, some variations can be observed in specific cases: exploited reservoirs can evolve in response to the variations in intensity of extraction, coastal reservoirs can evolve in response to the tidal processes, and extremely dynamic reservoirs can undergo variation of the structure of the reservoir itself.

When the geophysical measurements are accurately sensitive to the 'state' of the hydrogeological body, it is possible to record the evolution of the imaged object. For each of the studied object, the critical issue is the choice of the rate of repetition of the measurements. This rate must be adapted to the evolution rate of the phenomenon to be observed, but must also account for the rest of the variations occurring at the time and spatial scale observed, in order to avoid bias in the interpretation. For shallow objects (first 10 to 30 m), time-lapse methodologies are often realized with ERT techniques, or with Low induction number EM measurements, fast to deploy and easy to repeat. Borehole time-lapse observation also constitute interesting localized observations, for which automated monitoring systems exist.

In the context of this work, the focus is made on the monitoring of deep hydrogeological objects with surface measurements. In geophysical prospection, increasing the depth of investigation generally goes hand in hand with reducing the resolution, which must be good if one wants to interpret temporal variations. In addition, the

variations in the geophysical signal results in variations of the sensitivity that must be assessed through modeling. For these reasons, the time-lapse investigation of deep layers from surface measurements is a challenge.

Time-lapse methodologies are very often employed with many geophysical, geochemical and hydrogeological methods, at different time-scale and with different aims. ERT is very commonly used for the monitoring of the first tens of meters of the subsurface. It is used in simple context of monitoring aquifers in order to record the variation of water-head, to follow the melting of ice-sheets (Doetsch et al. [2015]), but also in tracers experiments (Doetsch et al. [2012]), and controlled infiltration experiments (Travelletti et al. [2012]) to help understand the underground flow process.

In the context of landslides, Gance et al. [2016] presents a permanent monitoring setup based on the high temporal repetition of ERT measurements along a profile, allowing the detection of infiltration paths. This monitoring experiment involved a specific monitoring instrument: the GEOMON<sup>4D</sup> (Supper et al. [2014]). Because of ground displacements, such context implies to correct the data from the displacements undergone by the electrodes. Wilkinson et al. [2016] showed how this displacement could actually be accounted for in the inversion, imposing large constraints on the direction and the spacial regularity of the displacements and Uhlemann et al. [2017] utilized this technique to correct 4D-ERT data applied to monitor the evolution of soil moisture during a landslide reactivation.

In these examples, the ERT setups were adapted to shallow studies (first tens of meters). For deeper investigation ranges, the measurements must be adapted or the method must be changed. MT and CSEM were reported several times to be successful in the realization of deep time-lapse experiments. Darnet et al. [2018] presented a monitoring experiment at the active geothermal field of Reykjanes, to image the response of the reservoir to the electricity production away from the boreholes. They however noted the complexity of using MT in environments affected by high industrial noise.

In the context of aquifer studies, Falgàs et al. [2006] published results of time-lapse measurements in the context of a coastal aquifer, where CSAMT measurements were successfully used, jointly with seismic tomography data, to observe the variations of salinity of the underground water in a confined granite aquifer, denoting sea water infiltration.

In the context of landslides, the monitoring experiments found in the literature mainly focus on very shallow observations (Travelletti et al. [2012], Altdorff and Dietrich [2014], Gance et al. [2016], Flores Orozco et al. [2019]).

## 1.4 Methodology

### 1.4.1 Characterization of a deep crystalline weathered aquifer

The first challenge is the specific context of pseudo-1D structures. When the subsurface can be, at first order, assimilated to a succession of stacked horizontal layers or units, the investigation requires a thin vertical resolution, but the sensitivity to lateral variation is not a requirement. Such context can be found in sedimentary aquifer and more generally in the context of many stable reservoirs. In such case, the investigation concerns in particular the vertical location and delineation of units, and large-scale lateral variations in the geophysical and geo-structural properties.

In order to explore the first axe of research, the controlled-source AMT method was applied to test the ability of this method to characterize the deep structure of crystalline weathered aquifers. The assumption is made that the medium, in such context, can be assimilated to 1D medium, and that the realization of few soundings, inverted independently in 1D, can be sufficient to capture the structure and spatial extent of the reservoir (fig. 1.6).

#### Characterization of the granitic catchment of the Strengbach using CSAMT

The granitic catchment of the Strengbach, in the Vosges mountains (France) (chapter 3) was selected to test this methodology. This catchment is characterized by an intense weathering of the bedrock. The limits of

weathering at depth could not be identified by 2D ERT profiles. This catchment presents the huge interest to be the object of long term multi-disciplinary studies, that lead to an important quantity of geophysical data recorded over its area, and the existence of 8 boreholes over the site. It is indeed one of the observation sites of the French Hydro-Chemical Observatory for the Environment OHGE (Observatoire Hydro-Géochimique de l'Environnement<sup>©</sup>) and the experimental site chosen to conduct an ANR project: HydroCriZStO (HYDRO-geochemical behavior of CRITICAL Zone at STrengbach Observatory), (2016-2020), which is one of the supporting project of this work.

In this context, this work also benefited from the support from the CRITEX project (Challenging equipment for the spatial and temporal exploration of the critical zone, ANR-11-EQPX-0011) which aims at the multi-disciplinary development of tools and methodologies for the study of the critical zone.

### 1.4.2 Deep characterization of a fractured hard-rock reservoir

The second challenge relates to the geo-electrical characterization of complex multi-dimensional and multi-scale structures. Such contexts are more specific to highly fractures and damaged hard-rock (Jomard et al. [2010]). In particular, rocky landslides often involve high degrees of damaging, induced both by weathering process and local tectonics. In this second context, the 3D nature of the subsurface structures requires the deployment of 3D survey methodologies and good lateral as well as vertical resolution is required. The methodology established to characterize such medium is the use of a novel large-scale 3D ERT measurement methodology: resistivity distributed automated systems (R-DAS). The measurement principal is the use of small autonomous measurement units or nodes distributed all over the survey area, with flexible inter-nodes distances (fig. 1.6).

#### 3D ERT imagery of the Séchilienne unstable slope

To test this second methodology, the Séchilienne landslide was chosen. The landslide of Séchilienne is a deep seated hard rock instability, that involved a complex structure, shaped by the tectonic and glacial heritage and by weathering processes. At Séchilienne, the subsurface water flow channelized by large faults, and contribute to the instability of the slope. The limits at depth of the fractured rock, the distribution of faults and their impacts on the slope hydrogeology are key points to improve the modeling of the slope. The Séchilienne landslide was object to many studies in the past to improve the knowledge on the hydrogeological processes, and on the mechanical impact of water flow in the triggering of this instability. A long term hydrochemical monitoring methodology provided information on the water flow paths at the slope scale, borehole data (core samples analysis, diagraphy) had been locally acquired. The structures of the slope (main faults) was analyzed from surface and tunnels observations, and wedged by geophysical imagery. In order to explore the second question, a 3D geo-electrical characterization of the Séchilienne landslide at the scale of the unstable slope (chapter 4) was realized with R-DAS of Fullwaver sensors (IRIS Instruments). This work was supported by the French Landslide Observatory OMIV (Observatoire Multi-disciplinaire des Instabilités de Versants<sup>©</sup>), and involved the important support from the instrumentation company IRIS Instruments.

### 1.4.3 Characterization and monitoring of deep sedimentary clayey aquifers

The study and characterization of deep sedimentary aquifers with high clay content is the last challenge of this thesis, as it implies an important vertical variation of the structural, lithological and hydrogeological properties. Such variations can be difficult to decipher from surface geophysical measurements, particularly when the structures of interest are located at large depth, where surface measurements are usually coarsely resolved and affected by a larger uncertainty. In such context, the application of monitoring experiments can allow the isolation of the pure hydrogeological signal (temporally varying). Two methodologies are proposed: 1D CSAMT time-lapse measurements and time-domain IP time-lapse measurements (fig. 1.6).

- **Time-lapse CSAMT measurement to characterize deep sedimentary aquifers**

Because of the decoupling between the transmitter and the receivers signals in far field CSAMT method, this

method is expected to be suited to time-lapse measurements. In near field CSEM on the contrary, the resistivity below the transmitter is important, and variations of this resistivity could importantly bias the time-lapse observation. In addition, the high vertical resolution of CSAMT seems particularly appealing in the context of pseudo-1D layered subsurface, as a unique sounding repeated at some frequency rate could be sufficient to provide main information on the evolution of the groundwater table.

However, few CSAMT time-lapse studies could be found in the literature (Falgàs et al. [2006], Ranganayaki et al. [1992]). For this reason, it seemed particularly interesting to test the capability of CSAMT to monitor the changes of apparent resistivity at depth.

Following the CSAMT methodology applied at the Strengbach catchment, a few question raised from the use of CSAMT to monitor the hydrogeological variations in the subsurface.

1. What possibilities offers the CSAMT method in the hydrogeological monitoring of pseudo-1D sites?
2. Is the stability regarding the characteristics of the transmitter an advantage in the measurements setup and methodology?
3. Is the vertical resolution enough to record and interpret resistivity variations related to the hydrogeological processes?

#### • Time-lapse IP measurement

Because clay has a high adsorption capacity (cation exchange capacity in the case of clay), the electrical resistivity of clay materials is rather low, making it difficult to distinguish between high clay content and high water content. The large cation exchange capacity of clay, and the resulting double layer at the surface of clay minerals makes it a very polarizable material. Hence, measuring the induced polarization signal often allows to remove the uncertainty regarding the interpretation of conductive anomalies in the subsurface.

If few examples of characterization of clayey landslides with IP can be found in the literature (Flores Orozco et al. [2018], Gallistl et al. [2018], Marescot et al. [2008]) accompanied by laboratory studies on the evolution of IP signatures of clayey materials with deformation and stress such as in clayey landslides (Ghorbani et al. [2009], Maineuil et al. [2018]), the application of field time-lapse IP data to landslides is rare. Time-lapse TDIP measurements is therefore the last methodology applied in this thesis for its potential to characterize deep sedimentary aquifer with high clay content, with the challenge of deep penetration depths.

### **Time-lapse study of the Lodève landslide to monitor the recharge processes related to heavy rain events**

The Lodève landslide is a slow moving and deep rotational instability (the unstable layer is expected at 60 m depth). The instability is triggered by intense rain events and by the infiltration and flow process in evaporitic and clayey layers from the Rhaetian and Norian era. The site is monitored through borehole measurements, combining data on the water chemical, electrical and mechanical properties and the realization of high-frequency electrical resistivity borehole monitoring (twice a day). At the Lodève landslide, the effort consists in relating the temporal variations observed in the hydrogeology to the evolution of the pluviometry, in order to model the hydrogeological response of the slope. The two time-lapse methodologies proposed previously were developed and tested at the Lodève landslide, and are the subject of chapter 5.

Because of both the existing measurement setups running at the Lodève landslide, and the very slow damage of the slope, this site seems particularly interesting to develop time-lapse measurements methodologies. The Lodève landslide is instrumented and studied as part of an experiment site for the French Landslide Observatory OMIV (Observatoire Multi-disciplinaire des Instabilités de Versants) and these two experiments were both supported by the ANR project HYDROSLIDE (High frequency hydrogeophysical observations for a better understanding of landslides mechanical behaviour, ANR-15-CE04-0009, 2016 - 2019).

**1. How to characterize deep crystalline weathered reservoir?**

- Can such reservoirs be considered as 1D objects at the resolution of CSAMT measurements?
- Can CSAMT resolve this type of structures at depth?
- How much does the presence of topography influence the apparent measurements?

**2. How to characterize and image deep fractured hard-rock crystalline reservoirs?**

- What depth of investigation can provide R-DAS measurements?
- What resolution can be obtained in the application to the Séchilienne landslide?
- Do such 3D models allow to image the different objects (faults, reservoirs) of the slope ?

**3. How to characterize and image deep sedimentary and clayey aquifers?**

- Can such reservoirs be assimilated to 1D structures?
- Is the resolution at depth high enough to characterize and monitor the variations of water head?

**1.4.4 Support projects and partner groups for this work**

This work has been supported by two research projects funded by the French Research Agency (ANR)

- HYDROLSIDE (High frequency hydrogeophysical observations for a better understanding of landslides mechanical behaviour, ANR-15-CE04-0009) - [2017-2019], coordinated by the EOST (Jean-Philippe Malet) which aim was to develop innovative geophysical methods for the slope scale and time-lapse analysis of landslide behavior.
- HYDROCRIZTO (HYDRO-geochemical behavior of CRITICAL Zone at STrengbach Observatory, ANR-15-CE01-0010) [2017-2020], coordinated by the EOST and the LHYGES (Marie-Claire Pierret) which aim was to develop joint methodologies combining geophysical, geochemical and hydrogeological approaches to improve the characterization and modeling of catchments.

The work is part of the large-scale equipment project CRITEX (Challenging equipment for the spatial and temporal exploration of the critical zone, ANR-11-EQPX-0011) which aims at the multi-disciplinary development of tools and methodologies for the study of the critical zone. In particular, the use of the CSAMT equipment in this work was enabled by the CRITEX project.

This work further benefited from national research and observation infrastructures:

- the French Landslide Observatory OMIV (Observatoire Multi-disciplinaire des Instabilités de Versants)
- the French Hydro-Chemical Observatory for the Environment OHGE (Observatoire Hydro-Géochimique de l'Environnement)

Collaboration and partnerships were established with

- the company IRIS Instruments<sup>®</sup> (Julien Gance) which gave the opportunity of the deployment of Full-Waver instruments at the Séchilienne Landslide (chapter 4)
- the Department of Geophysics at the Technical University of Vienna (Adrian Flores-Orozco), which permitted the realization of the TDIP time-lapse study at the Lodève landslide (chapter 5)
- Geoscience Montpellier (Stephanie Gautier), which permitted the access to extensive data on the Lodève landslide (chapter 5)
- the Department of Geophysics of the DIAS (Robert Delhaye), through a methodological exchange in field, instrumentation and processing techniques in CSAMT (chapter 5)

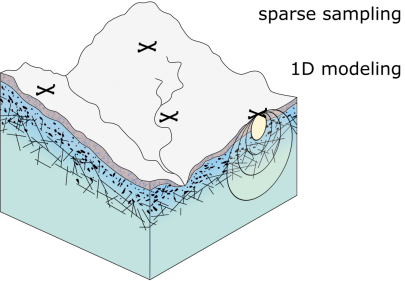
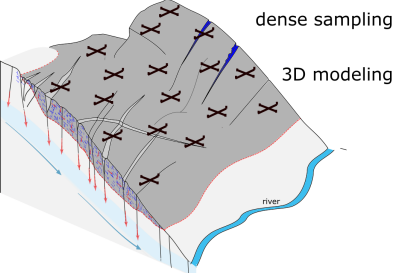
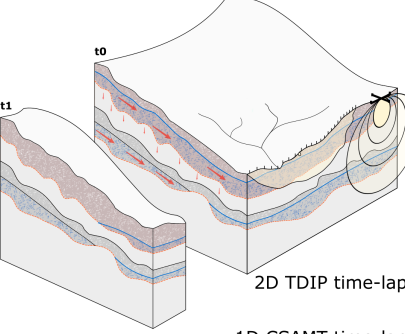
<p><b>Weathered hard-rock aquifer</b></p>  <p>sparse sampling 1D modeling</p>	<p><b>Challenges</b></p> <p>Important depth (&gt; 100 m)</p> <p>Important topographic variations</p> <p>Large-scale characterization</p>	<p><b>Proposed methodology</b></p> <p>Testing the ability of plane-wave controlled source methods : CSAMT - 1D</p> <p><b>Application site</b></p> <p>Strengbach granitic catchment: observing the limits of weathering at depth, expected below 30 m depth -</p> <p>200 Ohmm &lt; <math>\rho</math> &lt; 5000 Ohmm - <b>dmax</b> = 300 m</p> <p><b>Additional data on the site</b></p> <p>2D ERT - RMP - Borehole resistivity - Diagraphy</p>
<p><b>Multi-permeability fractured hard-rock aquifer</b></p>  <p>dense sampling 3D modeling</p>	<p><b>Challenges</b></p> <p>3D structures (horizontal &amp; vertical)</p> <p>Multi-permeable reservoir</p> <p>Important topographic variations</p> <p>Slope-scale imagery in 3D</p>	<p><b>Proposed methodology</b></p> <p>Testing the ability of a large-scale ERT methodology : use of resistivity distributed automated systems</p> <p><b>Application site</b></p> <p>Séchilienne landslide: densely fractured unstrable slope - variations of the damaging at the slope scale -</p> <p>100 Ohmm &lt; <math>\rho</math> &lt; 3000 Ohmm - <b>dmax</b> = 150 m</p> <p><b>Additional data on the site</b></p> <p>2D ERT - Diagraphy - borehole core samples - hydrogeological and hydrochemical surveying</p>
<p><b>Sedimentary aquifer with high clay content</b></p>  <p>2D TDIP time-lapse 1D CSAMT time-lapse</p>	<p><b>Challenges</b></p> <p>Important vertical variability</p> <p>High clay content</p> <p>heterogeneous clay content</p> <p>Important temporal variability</p>	<p><b>Proposed methodology</b></p> <p>Time-lapse observations with 1D CSAMT and TDIP methods</p> <p><b>Application site</b></p> <p>Lodève landslide: clayey and evaporitic landslide in the Trias and Jurassic sedimentary units -</p> <p>20 Ohmm &lt; <math>\rho</math> &lt; 500 Ohmm - <b>dmax</b> = 80 m</p> <p><b>Additional data on the site</b></p> <p>Borehole geochemical and petrophysical monitoring - analysis of borehole core samples - one 2D ERT profile</p>

Figure 1.6: Methodology established in this thesis

## 1.5 References

- Abdelfettah, Y., Sailhac, P., Schill, E., and Larnier, H. (2014). Preliminary magnetotelluric monitoring results at Rittershofen. In *3rd European geothermal workshop, Karlsruhe*, pages 15–16.
- Altdorff, D. and Dietrich, P. (2014). Delineation of areas with different temporal behavior of soil properties at a landslide affected Alpine hillside using time-lapse electromagnetic data. *Environmental Earth Sciences*, 72(5):1357–1366.
- Archie, G. E. (1942). The electrical resistivity log as an aid in determining some reservoir characteristics. *Transactions of the AIME*, 146(01):54–62.
- Árnason, K. (2015). The static shift problem in MT soundings. In *Proceedings world geothermal congress*.
- Badea, E. A., Everett, M. E., Newman, G. A., and Biro, O. (2001). Finite-element analysis of controlled-source electromagnetic induction using Coulomb-gauged potentials. *Geophysics*, 66(3):786–799.
- Bannister, P. R. (1966). Quasi-static fields of dipole antennas at the earth's surface. *Radio Science*, 1(11):1321–1332.
- Baranwal, V. C., Franke, A., Börner, R.-U., and Spitzer, K. (2011). Unstructured grid based 2-d inversion of VLF data for models including topography. *Journal of Applied Geophysics*, 75(2):363–372.
- Binley, A. and Kemna, A. (2005). Dc resistivity and induced polarization methods. In *Hydrogeophysics*, pages 129–156. Springer.
- Brakensiek, D. L. (1979). *Field manual for research in agricultural hydrology*. Number 224. Department of Agriculture, Science and Education Administration.
- Cagniard, L. (1953). Basic theory of the magneto-telluric method of geophysical prospecting. *Geophysics*, 18(3):605–635.
- Chave, A. D. and Jones, A. G. (2012). Introduction to the magnetotelluric method. *The magnetotelluric method: Theory and practice*, pages 1–18.
- Chave, A. D. and Thomson, D. J. (1989). Some comments on magnetotelluric response function estimation. *Journal of Geophysical Research: Solid Earth*, 94(B10):14215–14225.
- Christiansen, A. V. and Auken, E. (2012). A global measure for depth of investigation. *Geophysics*, 77(4):WB171–WB177.
- Collin, J. (1991). Groundwater, a common asset that should be managed in common. Proceedings and review of the colloquium, Paris 1990. *Hydrogeologie (France)*.
- Constable, C. (2007). Geomagnetic spectrum, temporal. *Encyclopedia of Geomagnetism and Paleomagnetism*, Springer, Dordrecht, The Netherlands.
- Constable, C. (2016). Earth's electromagnetic environment. *Surveys in Geophysics*, 37(1):27–45.
- Coppo, N., Darnet, M., Harcouet-Menou, V., Wawrzyniak, P., Manzella, A., Bretaudeau, F., Romano, G., Lagrou, D., and Girard, J.-F. (2016). Characterization of deep geothermal energy resources in low enthalpy sedimentary basins in Belgium using electro-magnetic methods—csem and mt results.
- Darnet, M., Dezayes, C., Girard, J., Baltassat, J., Lerouge, C., Reuschlé, T., Coppo, N., Bretaudeau, F., Porte, J., and Lucas, Y. (2019). Geophysical signature of the transition zone between the sedimentary cover and the basement: an analogue approach to help de-risking geothermal prospects. *arXiv preprint arXiv:1905.07897*.
- Darnet, M., Wawrzyniak, P., Coppo, N., Nielsson, S., Schill, E., and Fridleifsson, G. (2018). Monitoring geothermal reservoir developments with the Controlled-Source Electro-Magnetic method—A calibration study on the Reykjanes geothermal field. *Journal of Volcanology and Geothermal Research*.
- Doetsch, J., Ingeman-Nielsen, T., Christiansen, A. V., Fiandaca, G., Auken, E., and Elberling, B. (2015). Direct current (dc) resistivity and induced polarization (ip) monitoring of active layer dynamics at high temporal resolution. *Cold Regions Science and Technology*, 119:16–28.
- Doetsch, J., Linde, N., Vogt, T., Binley, A., and Green, A. G. (2012). Imaging and quantifying salt-tracer transport in a riparian groundwater system by means of 3d ERT monitoring. *Geophysics*, 77(5):B207–B218.
- d'Ozouville, N., Auken, E., Sorensen, K., Violette, S., de Marsily, G., Deffontaines, B., and Merlen, G. (2008). Extensive perched aquifer and structural implications revealed by 3d resistivity mapping in a Galapagos volcano. *Earth and Planetary Science Letters*, 269(3-4):518–522.
- Falgàs, E., Ledo, J., Benjumea, B., Queralt, P., Marcuello, A., Teixidó, T., and Arango, C. (2006). Imaging ground water resources of a mediterranean coastal aquifer using seismic and csamt data. In *Symposium on the Application of Geo-*

- physics to Engineering and Environmental Problems 2006*, pages 863–870. Society of Exploration Geophysicists.
- Falgàs, E., Marquis, G., Sailhac, P., Ledo, J., Queralt, P., and Béhaegel, M. (2005). Aquifer imaging using csamt and ert. In *Near Surface 2005-11th European Meeting of Environmental and Engineering Geophysics*, pages cp–13. European Association of Geoscientists & Engineers.
- Flores Orozco, A., Gallistl, J., Bückler, M., and Williams, K. H. (2018). Decay curve analysis for data error quantification in time-domain induced polarization imaging. *Geophysics*, 83(2):E75–E86.
- Flores Orozco, A., Kemna, A., Binley, A., and Cassiani, G. (2019). Analysis of time-lapse data error in complex conductivity imaging to alleviate anthropogenic noise for site characterization. *Geophysics*, 84(2):B181–B193.
- Folch, A., Menció, A., Puig, R., Soler, A., and Mas-Pla, J. (2011). Groundwater development effects on different scale hydrogeological systems using head, hydrochemical and isotopic data and implications for water resources management: The Selva basin (ne Spain). *Journal of Hydrology*, 403(1-2):83–102.
- Gallistl, J., Weigand, M., Stumvoll, M., Ottowitz, D., Glade, T., and Orozco, A. F. (2018). Delineation of subsurface variability in clay-rich landslides through spectral induced polarization imaging and electromagnetic methods. *Engineering Geology*, 245:292–308.
- Gance, J., Malet, J.-P., Supper, R., Sailhac, P., Ottowitz, D., and Jochum, B. (2016). Permanent electrical resistivity measurements for monitoring water circulation in clayey landslides. *Journal of Applied Geophysics*, 126:98–115.
- Geiermann, J. and Schill, E. (2010). 2-d magnetotellurics at the geothermal site at Soultz-sous-Forêts: Resistivity distribution to about 3000 m depth. *Comptes Rendus Geoscience*, 342(7-8):587–599.
- Ghorbani, A., Cosenza, P., Revil, A., Zamora, M., Schmutz, M., Florsch, N., and Jougnot, D. (2009). Non-invasive monitoring of water content and textural changes in clay-rocks using spectral induced polarization: A laboratory investigation. *Applied Clay Science*, 43(3-4):493–502.
- Goldstein, M. and Strangway, D. (1975). Audio-frequency magnetotellurics with a grounded electric dipole source. *Geophysics*, 40(4):669–683.
- Guglielmi, Y., Bertrand, C., Compagnon, F., Follacci, J., and Mudry, J. (2000). Acquisition of water chemistry in a mobile fissured basement massif: its role in the hydrogeological knowledge of the La Clapière landslide (Mercantour massif, southern Alps, France). *Journal of Hydrology*, 229(3-4):138–148.
- Jeanne, P., Rutqvist, J., Vasco, D., Garcia, J., Dobson, P. F., Walters, M., Hartline, C., and Borgia, A. (2014). A 3d hydrogeological and geomechanical model of an enhanced geothermal system at The Geysers, California. *Geothermics*, 51:240–252.
- Jomard, H., Lebourg, T., Guglielmi, Y., and Tric, E. (2010). Electrical imaging of sliding geometry and fluids associated with a deep seated landslide (La Clapière, France). *Earth Surface Processes and Landforms: The Journal of the British Geomorphological Research Group*, 35(5):588–599.
- Jones, A. G., Chave, A. D., Egbert, G., Auld, D., and Bahr, K. (1989). A comparison of techniques for magnetotelluric response function estimation. *Journal of Geophysical Research: Solid Earth*, 94(B10):14201–14213.
- Kalscheuer, T., Bastani, M., Donohue, S., Persson, L., Pfaffhuber, A. A., Reiser, F., and Ren, Z. (2013). Delineation of a quick clay zone at Smørgrav, Norway, with electromagnetic methods under geotechnical constraints. *Journal of Applied Geophysics*, 92:121–136.
- Kelbert, A., Meqbel, N., Egbert, G. D., and Tandon, K. (2014). Modem: A modular system for inversion of electromagnetic geophysical data. *Computers & Geosciences*, 66:40–53.
- Khaldoun, A., Moller, P., Fall, A., Wegdam, G., De Leeuw, B., Méheust, Y., Fossum, J. O., and Bonn, D. (2009). Quick clay and landslides of clayey soils. *Physical Review Letters*, 103(18):188301.
- Larnier, H., Sailhac, P., and Chambodut, A. (2017). Detection and characterization of lightning-based sources using continuous wavelet transform: application to audio-magnetotellurics. *Geophysical Journal International*, 212(1):103–118.
- Lin, C., Tan, H., Wang, W., Tong, T., Peng, M., Wang, M., and Zeng, W. (2018). Three-dimensional inversion of CSAMT data in the presence of topography. *Exploration Geophysics*, 49(3):253–267.
- Lin, H. (2010). Earth’s critical zone and hydrogeology: concepts, characteristics, and advances. *Hydrology and Earth System Sciences*, 14(1):25.
- Loke, M. (2013). Tutorial: 2-d and 3-d electrical imaging survey Revision date: 8th of march 2013. *Geomoto Software*. (<http://www.geomotosoft.com/>).

- Maineult, A., Jougnot, D., and Revil, A. (2018). Variations of petrophysical properties and spectral induced polarization in response to drainage and imbibition: a study on a correlated random tube network. *Geophysical Journal International*, 212(2):1398–1411.
- Marescot, L., Monnet, R., and Chapellier, D. (2008). Resistivity and induced polarization surveys for slope instability studies in the Swiss Alps. *Engineering Geology*, 98(1-2):18–28.
- Martínez-Murillo, J., Nadal-Romero, E., Regüés, D., Cerdà, A., and Poesen, J. (2013). Soil erosion and hydrology of the western Mediterranean badlands throughout rainfall simulation experiments: A review. *Catena*, 106:101–112.
- Oldenburg, D. W. and Li, Y. (1999). Estimating depth of investigation in dc resistivity and ip surveys. *Geophysics*, 64(2):403–416.
- Pedersen, L. B., Bastani, M., and Dynesius, L. (2006). Some characteristics of the electromagnetic field from radio transmitters in europe. *Geophysics*, 71(6):G279–G284.
- Pierret, M.-C., Cotel, S., Ackerer, P., Beaulieu, E., Benarioumlil, S., Boucher, M., Boutin, R., Chabaux, F., Delay, F., Fourtet, C., Friedmann, P., Fritz, B., Gangloff, S., Girard, J.-F., Legtchenko, A., Viville, D., Weill, S., and Probst, A. (2018). The Strengbach catchment: A multidisciplinary environmental sentry for 30 years. *Vadose Zone Journal*, 17(1).
- Raingear, A., Reninger, P.-A., Thiery, Y., Lacquement, F., and Nachbaur, A. (2018). 3d geological modelling coupling AEM with field observations. In *Proceedings of the 7th International Workshop on Airborne Electromagnetics, Kolding, Denmark*, pages 17–20.
- Ranganayaki, R., Fryer, S., and Bartel, L. (1992). Csamt surveys in a heavy oil field to monitor steam-drive enhanced oil recovery process. In *SEG Technical Program Expanded Abstracts 1992*, pages 1384–1384. Society of Exploration Geophysicists.
- Ren, Z., Kalscheuer, T., Greenhalgh, S., and Maurer, H. (2013). A goal-oriented adaptive finite-element approach for plane wave 3-d electromagnetic modelling. *Geophysical Journal International*, 194(2):700–718.
- Şen, Z. (2014). *Practical and applied hydrogeology*. Elsevier.
- Stalnaker, J. L. (2005). *A finite element approach to the 3D CSEM modeling problem and applications to the study of the effect of target interaction and topography*. PhD thesis, Texas A&M University.
- Supper, R., Ottowitz, D., Jochum, B., Kim, J.-H., Römer, A., Baron, I., Pfeiler, S., Lovisolò, M., Gruber, S., and Vecchiotti, F. (2014). Geoelectrical monitoring: an innovative method to supplement landslide surveillance and early warning. *Near Surface Geophysics*, 12(1):133–150.
- Tacher, L., Bonnard, C., Laloui, L., and Parriaux, A. (2005). Modelling the behaviour of a large landslide with respect to hydrogeological and geomechanical parameter heterogeneity. *Landslides*, 2(1):3–14.
- Tikhonov, A. (1950). On determining electrical characteristics of the deep layers of the Earth's crust. In *Doklady*, volume 73, pages 295–297.
- Travelletti, J., Sailhac, P., Malet, J.-P., Grandjean, G., and Ponton, J. (2012). Hydrological response of weathered clay-shale slopes: Water infiltration monitoring with time-lapse electrical resistivity tomography. *Hydrological Processes*, 26(14):2106–2119.
- Uhlemann, S., Chambers, J., Wilkinson, P., Maurer, H., Merritt, A., Meldrum, P., Kuras, O., Gunn, D., Smith, A., and Dijkstra, T. (2017). Four-dimensional imaging of moisture dynamics during landslide reactivation. *Journal of Geophysical Research: Earth Surface*, 122(1):398–418.
- Ward, S. H. and Hohmann, G. W. (1988). Electromagnetic theory for geophysical applications. In *Electromagnetic Methods in Applied Geophysics: Volume 1, Theory*, pages 130–311. Society of Exploration Geophysicists.
- Waxman, M. H. and Smits, L. (1968). Electrical conductivities in oil-bearing shaly sands. *Society of Petroleum Engineers Journal*, 8(02):107–122.
- Wilkinson, P., Chambers, J., Uhlemann, S., Meldrum, P., Smith, A., Dixon, N., and Loke, M. H. (2016). Reconstruction of landslide movements by inversion of 4-d electrical resistivity tomography monitoring data. *Geophysical Research Letters*, 43(3):1166–1174.
- Zonge, K. L. and Hughes, L. J. (1991). Controlled source audio-frequency magnetotellurics. In *Electromagnetic Methods in Applied Geophysics: Volume 2, Application, Parts A and B*, pages 713–810. Society of Exploration Geophysicists.

### 1.5.1 References to internet websites

Moombarriga Geoscience<sup>©</sup> - <http://moombarriga.com.au/index.php/magnetotelluric-surveys-mt/>  
Observatoire Hydro-Géochimique de l'Environnement<sup>©</sup> 2014-2020 EOST - <http://ohge.unistra.fr/?lang=fr>  
OMIV<sup>©</sup> 2018 - <http://eost.u-strasbg.fr/opomiv/>  
IRIS Instruments<sup>©</sup> 1991-2016 - <https://www.iris-instruments.com/>

## **Chapter 2**

### **Data measurement and processing: notions and challenges**

Chapter 1 brought forward a few main questions, that led this thesis. Each question relates to a specific context of observation (dimension of the subsurface structures, lithology, variations of the surface topography) and is explored with specific methods. Three main geoelectric investigation technics are used: CSAMT, ERT and IP. In this chapter, these methods are presented, as well as the applications realized in this thesis.

## 2.1 Electric and electromagnetic processes in earth materials

The electric and electromagnetic processes that are exploited in geo-electrical methods (electric and electromagnetic methods) are presented in the following section.

### 2.1.1 Electric, dielectric and magnetic parameters

Three main parameters influence the electric and magnetic response of a material. In eq. 2.1, 2.2 and 2.3,  $\mathbf{E}$  designates the electric field,  $\mathbf{J}$  is the current density vector,  $\mathbf{D}$  is the electric displacement,  $\mathbf{B}$  is the magnetic field and  $\mathbf{H}$  is the magnetization field.

$$\mathbf{E} = \rho \mathbf{J} \quad (2.1)$$

$$\mathbf{D} = \epsilon \mathbf{E} \quad (2.2)$$

$$\mathbf{B} = \mu \mathbf{H} \quad (2.3)$$

$\rho$  is the electrical resistivity of the subsurface expressed in  $\Omega\text{m}$ . It characterizes how intense is the conduction in response to the application of an electric field (eq. 2.1). Rock materials present resistivity values ranging approximately from 10 to 10000  $\Omega\text{m}$  (fig. 1.1 chapter 1). The inverse of the electrical resistivity, the electrical conductivity,  $\sigma$ , is expressed in  $\text{S/m}$  and is used very often to characterize the pore fluid.

$\epsilon$  is the dielectric permittivity in  $\text{F/m}$ , that mainly impacts the high frequency EM response of the subsurface. It characterizes the polarization of the matter, and is frequency dependent. Commonly, one considers the relative permittivity  $\epsilon_r = \epsilon/\epsilon_0$ , where  $\epsilon_0$  is the dielectric permittivity of the vacuum. In geo-materials,  $\epsilon$  takes values from 3 to 40, depending on the lithology and water content. Crystalline rocks present lower values than sedimentary ones, and the water content tends to increase the permittivity. The dielectric permittivity of water is around 80.

$\mu$  is the magnetic permeability, expressed in  $\text{H/m}$ .  $\mu$  expresses the magnetization produced in a material placed in a magnetic field. This property is related, such as the dielectric permittivity, to the atomic structure of the matter. In most geo-materials,  $\mu$  takes values very close to the magnetic permeability of the vacuum:  $\mu_0 = 4\pi 10^{-7} \text{H/m}$ . The assumption is often made that  $\mu = \mu_0$ . Some rocks however present magnetic properties. Magnetic rocks characterized by  $\mu > \mu_0$  are classified as ferromagnetic when they present a spontaneous magnetization (generally associated to  $\mu \approx 5\mu_0$ ) or paramagnetic when no intrinsic magnetization is present. Diamagnetic materials on the contrary, are characterized by  $\mu < \mu_0$ , which means that the aimantation of the matter is opposed to the local magnetic field. Magnetic materials in the crust are of limited amount. The magnetic permeability influences the entire spectrum of the EM response, and can produced very local (crustal) anomalies of the earth magnetic field. The presence of magnetic objects in the subsurface is investigated in magnetic methods, a passive geophysical method that maps from the surface the 3 components of the magnetic field, in which the local perturbation due to local anomalies can be observed.

### 2.1.2 Electromagnetic propagation and diffusion

The Maxwell equations, governing the electromagnetism phenomena, permit to write, in the frequency domain, the general propagation / diffusion equations of the electromagnetic fields in the absence of local source

term:

$$\Delta \mathbf{E} - k^2 \mathbf{E} = 0 \quad (2.4)$$

$$\Delta \mathbf{H} - k^2 \mathbf{H} = 0 \quad (2.5)$$

where  $k = \sqrt{\epsilon\mu\omega^2 - i\sigma\mu\omega}$  is the electromagnetic wave number, function of  $\rho$ ,  $\epsilon$   $\mu$  and the pulsation:  $\omega = 2\pi f$ .

### Electromagnetic propagation

At high frequency, such that  $\epsilon\omega \gg \sigma$ ,  $k \approx \sqrt{\epsilon\mu\omega^2}$  and the solution of eq. 2.4 and eq. 2.5 corresponds to a propagative solution. The electromagnetic signal propagates as a wave, at a velocity  $V = \frac{1}{\sqrt{\mu\epsilon}}$ .

The absorption of the energy by the medium is controlled by the attenuation coefficient  $\alpha$  (eq. 2.6).

$$\alpha = \omega \left[ \frac{\mu\epsilon}{2} \left( \sqrt{1 + \left( \frac{\sigma}{\omega\epsilon} \right)^2} - 1 \right)^{\frac{1}{2}} \right] \quad (2.6)$$

The attenuation depends on both the frequency of the signal and the conductivity of the medium, such that a signal at higher frequency attenuates faster, and a high conductivity of the medium does not allow a deep penetration of the wave. As an indicator, at the frequency considered in EM methods ( $10^{-3} < f < 10^9$ ), in the air, the electromagnetic signal propagates.

### Electromagnetic diffusion

At lower frequency, when  $\epsilon\omega \ll \sigma$ ,  $k \approx \sqrt{-i\sigma\mu\omega}$  and the EM waves diffuse in the matter, with an attenuation given by the skin depth  $\delta$  (eq. 2.7).

$$\delta = \sqrt{\frac{2\rho}{\mu\omega}} \quad (2.7)$$

Generally, in earth materials, one considers that EM signals propagates at frequencies above 10 MHz (Geo-radar method) and diffuses below 500 kHz (EM induction methods).

## 2.1.3 Electrical conduction

At the low frequency limit, the electromagnetic signals, allowed and maintained by the variation of the electric and magnetic fields and the resulting induction phenomena, disappear. Only direct current (DC) conduction can exist. In such context, only the electrical resistivity influences the electric state.

The electrical resistivity is frequency dependant, and the conduction response of a rock is expected to change if the injected current is a DC signal, or if it is a periodic signal at a certain frequency.

## 2.1.4 Polarization of geo-materials

At higher frequency, as the conduction phenomenon persists, another phenomenon emerges: electrical polarization of the matter. This polarization can be an accumulation of charges at both sides of a conduction or dielectric barrier, i.e. at the frontier between two media of different electrical resistivity or different dielectric permittivity resp., or an in-homogeneous distribution of charges at the surface of an adsorbing grain, induced by an electrical field. In rock materials, these two phenomena occur usually at frequencies from  $10^{-3}$  to  $10^4$  Hz (Kemna et al. [2012]).

In an homogeneous material, the polarization is described by the dielectric permittivity. In the subsurface, the origin of polarization arises not only from the properties of each materials, but also from the variations of properties from one grain to the next, from one unit to the next, or from the matrix to the pore fluid. In geophysics, the polarization can be described in different ways

- a complex frequency dependant resistivity
- a complex frequency dependant dielectric permittivity
- very rarely, a complex frequency dependant magnetic permeability

## 2.2 Presentation and use of CSAMT

The CSAMT method is a plane wave EM induction method derived from the passive MT method. A controlled source is used to produce a plane wave EM signal at the studied site. The far field impedance tensor, independent of the nature, location and orientation of the source, is recorded at the site, providing an estimation of the apparent resistivity. CSAMT is characterized by large depths of investigations and good vertical resolution (Zonge and Hughes [1991]). The use of a controlled source ensures that the signal will emerge from the noise. The CSAMT proved to be efficient in numerous cases, reducing greatly the uncertainty in the computation of the MT impedance tensor, with respect to MT measurements more likely to be affected by cultural noise. In particular, successful applications are to be noticed, mainly in mineral exploration, geothermal research and volcanology, and in oil exploration. Applications in the context of hydrogeological studies are rather rare (Falgàs et al. [2005], Falgàs et al. [2006], Wynn et al. [2016]). The use of a controlled source however brings problems related to source effects (Zonge and Hughes [1991]). Here are three different kinds of source effects:

- Because there is a technical limit on the distance from the site at which the transmitter can be set, due to the limited power of the transmitter (in the order of 10 kW), the far field condition is not always valid for the entire frequency-range sampled. In the near field, the MT impedance tensor turns dependant on the location of the transmitter, on its polarization, and, to a certain extent on the resistivity below the transmitter.
- The topographic variations are expected to distort the EM signals. The topographic effect at the location of the site (effect on diffusive process) was object to some studies (Ren et al. [2013], Kalscheuer et al. [2013]) and a non-horizontal transmitting dipole is expected to modify the source signals, potentially invalidating the theory of CSAMT (Lin et al. [2018]). Another topographic effect concerns the distortion due to topographic variations between the transmitter to the studied site, affecting the EM propagation. This last effect is seldom mentioned. In the far field, the signal reaching the station is assumed to be carried by the EM wave propagating in the air, the subsurface being diffusive at the frequencies used. A none-flat topography between transmitter and receivers may distort the EM fields. This point is studied and discussed in chapter 3.
- The MT method assumes randomly distributed sources, with a set of independent random polarizations. It is very difficult, in practice, to record data from different source signals, and thus to have a robust estimate of the impedance tensor. Many times, a unique transmitting dipole is used, which does not allow a full determination of the impedance tensor.

In this thesis, the CSAMT method was employed in contexts where the general morphology and characteristics of the sites (topography, limited access to power source) were limiting the measurements possibilities (transmitter location and polarization and spatial sampling). The case of a simple measurement setup is considered, where a unique transmitting of small size is used, located at the limit distance of validity of the far field. Different ways of extracting the information contained in 1D-CSAMT data (isolated soundings) were explored.

### 2.2.1 Basic notions in CSAMT

The basis of the CSAMT method originate from the MT method. In MT, the measurement of the plane wave magnetic and electric fields produced by natural remote sources permit to compute the magnetotelluric impedance tensor. The MT impedance tensor gives access to the apparent resistivity of the subsurface, including, in addition, information on the dimensionality of the subsurface anomalies. The MT measurement is strongly dependant on the occurrence and strength of the source signals. In the audio frequency band (10 Hz – 10 kHz), adequate to study the near surface (first kilometer) the sources are of very low intensity, and the MT measurements are strongly affected by the noise level. In this context, the CSAMT method was developed, with the challenge of reproducing in the field, with a controlled source, the same plane wave signal as the source signals used in MT. In other words, the measurements must be made in the far field of an EM source signal.

### Near field and far field in CSAMT

The far field domain corresponds to the domain where the measured frequencies are high enough so that the induction number is large,  $B \gg 1$ .  $B$  is defined by  $B = r/\delta$  where  $r$  is the transmitter-receiver offset and  $\delta$  is the skin depth. In the far field case, the impedance tensor does not depend on the source polarization and location, and an apparent resistivity tensor can be computed from the impedance tensor, that only depends on local resistivity. The impedance tensor presents the advantage of carrying information on the dimensionality of detectable bodies.

The theory of the CSAMT method has been widely studied and commented in the literature (Cagniard [1953], Zonge and Hughes [1991], Boerner et al. [1993], Grant Caldwell et al. [2002] and many others). Whereas the far field assumption was the basis of CSAMT, it is common that the near field must be considered in the interpretation of low frequency measurements at sites located near the transmitter. Several authors presented datasets that exhibit near field behaviors (Unsworth et al. [2000]). Simultaneously analyzing near field and far field apparent resistivity curves allows to identify the frequency range where the transition occurs by locating the intersection between the two curves (Yamashita et al. [1985]), and a methodology based on modeling CSAMT data continuously from the near to the far field can be used as a tool for near field corrections (Bartel and Jacobson [1987]).

### Impedance tensor

The MT impedance tensor is a frequency-dependent complex tensor of second order. This tensor, which is the first step to computing apparent resistivity and phase, contains, in the general case, four components, from which two independent invariants can be extracted. When the subsurface is composed of horizontal stacked layers, this tensor simplifies into two dependent anti-diagonal components (one is opposite to the other).

In this section, we will use the formalism from Grant Caldwell et al. [2002]. This formalism relies on the expression of the electrical and magnetic fields response tensors, two tensors that describe the EM responses to an impulsive current density vector  $\mathbf{J}$  (in  $A.m^{-2}$ ) produced by a horizontal grounded dipole (specific controlled source context), to finally retrieve the far field results of the MT method, and generalize them to transition and near field contexts.

$$\begin{aligned}\mathbf{E} &= \tilde{\rho}_a \mathbf{J} \\ \mathbf{H} &= \tilde{\xi} \mathbf{J}\end{aligned}\tag{2.8}$$

$\tilde{\rho}_a$  and  $\tilde{\xi}$  are the frequency domain tensors representing the transfer functions of the ground according to which an impulse current density is filtered into the electric and magnetic fields responses respectively. Both tensors are frequency dependent and follow very specific behaviors in the low frequency and high frequency limits. In particular, in their high frequency asymptotic behavior (i.e. in the far field limit), they both turn to be independent of the source location and polarization.

Regardless of the domain, the relation between the electric and magnetic signals can be formulated by eq. 2.9, introducing the magnetotelluric impedance tensor  $\tilde{Z}$  (eq. 2.10)

$$\mathbf{E} = \tilde{\rho}_a \mathbf{j} = \tilde{\rho}_a \tilde{\xi}^{-1} \tilde{\xi} \mathbf{j} = \tilde{Z} \mathbf{H}\tag{2.9}$$

$$\tilde{Z} = \tilde{\rho}_a \tilde{\xi}^{-1}\tag{2.10}$$

### Electric and magnetic response tensors

The electric response tensor  $\tilde{\rho}_a$  depends on the ground apparent resistivity. At high and low frequency (i.e. in the far and near fields), this tensor exclusively depends on the apparent resistivity. The principle of MT methods is to resolve this tensor.

In the MT method, the MT impedance tensor describes the electrical response of the ground to a far field magnetic signal. It is a two-input-two-output linear system (eq. 2.9), with the horizontal magnetic field as the

‘input’ signal and the horizontal electric field as the ‘output’ signal (e.g. [Rodriguez et al. \[1996\]](#)). We consider indeed the (primary) magnetic field to be very weakly influenced by the resistivity anomalies in the ground, in contrast to the electric field, which carries a significant amount of information on these anomalies. For this reason, we will consider in the following the magnetic response tensor of a homogeneous half space, expressed, in a polar coordinate system, as:

$$\tilde{\xi} = r/2 \begin{bmatrix} 0 & ikr(I_0K_1 - I_1K_0) - 6I_1K_1 \\ I_1K_1 & 0 \end{bmatrix} \quad (2.11)$$

$I_0$ ,  $I_1$ ,  $K_0$  and  $K_1$  are the modified Bessel functions of first and second kind, of the underlying variable  $ikr/2$ ,  $k$  being the wave number in a homogeneous half space and  $r$  the transmitter-receiver offset. Note that the 1D assumption makes it very easy to invert the magnetic response tensor.

In the near field,  $\tilde{\xi}$  simplifies into a form that only depends on the transmitter-receiver offset,  $r$ . In the far field on the contrary, the dependency of  $\tilde{\xi}$  on  $r$  vanishes and  $\tilde{\xi}$  only depends on the skin depth ([Grant Caldwell et al. \[2002\]](#)). The asymptotic behavior of  $\tilde{\xi}$  allows to obtain the usual far field and near field formula to compute the apparent resistivity in homogeneous half spaces, introduced in [Cagniard \[1953\]](#) and [Zonge and Hughes \[1991\]](#) (eq. 2.12). Because magnetic measurements usually consist in measurement of the flux density, a reformulation of the formula is proposed by [Cagniard \[1953\]](#) and [Zonge and Hughes \[1991\]](#) in the far field, changing the factor  $i\omega\mu_0$  by the factor  $i5f$ . In the near field, a similar reformulation brings the factor  $\frac{10^4}{2\pi r}$ , implying no longer a frequency but a distance dependency. The correct formula when measuring  $Z$  from the flux density in nT and the electric field in mV/km are given in eq. 2.12 and 2.13 for the far field and the near field cases resp. for a homogeneous half space.

$$Z(kr \gg 1) = i5f \tilde{\rho}_a(kr \gg 1) \quad (2.12)$$

$$Z(kr \ll 1) = \frac{10^4}{2\pi r} \tilde{\rho}_a(kr \ll 1) \quad (2.13)$$

where the asymptotic formulations of  $\tilde{\rho}_a$  are:

$$\tilde{\rho}_a(kr \ll 1) = \rho \begin{bmatrix} 1 & 0 \\ 0 & 1 \end{bmatrix} \quad (2.14)$$

$$\tilde{\rho}_a(kr \gg 1) = \rho \begin{bmatrix} 1/2 & 0 \\ 0 & 2 \end{bmatrix} \quad (2.15)$$

By injecting the chosen formulation of  $\tilde{\xi}$  into eq. 2.10, a general relation between impedance tensor, resistivity tensor and magnetic response tensor is given in eq. 2.16, valid regardless of the measurement domain, when the impedance tensor is expressed in mV/km/nT. This expression of the MT impedance tensor extends the usual far field MT impedance tensor in the transitional and near field, introducing at the same time the context of full-field CSEM techniques.

$$\tilde{Z}\tilde{\xi} = \frac{2\pi r}{10^4} \begin{bmatrix} Z_{xx} & Z_{xy} \\ Z_{yx} & Z_{yy} \end{bmatrix} \begin{bmatrix} 0 & ikr(I_0K_1 - I_1K_0) - 6I_1K_1 \\ I_1K_1 & 0 \end{bmatrix} = \tilde{\rho}_a \quad (2.16)$$

## 2D and 3D impedance tensor

When the ground includes 2D or 3D structures producing resistivity anomalies, the impedance tensor is formed by 4 independent components. A thorough analysis of the full impedance tensor can provide valuable information, its anti-diagonality and symmetry properties contain indeed information on the dimensionality of the underground structures. In MT, the multiple sources used in a measurement are assumed to be randomly oriented, and the problem if oversampled provides constrains to all four components of the full impedance tensor. In CSAMT, to solve the four coefficients, two independent transmitting dipoles producing independent density current vectors, are needed in order to resolve the full impedance tensor.

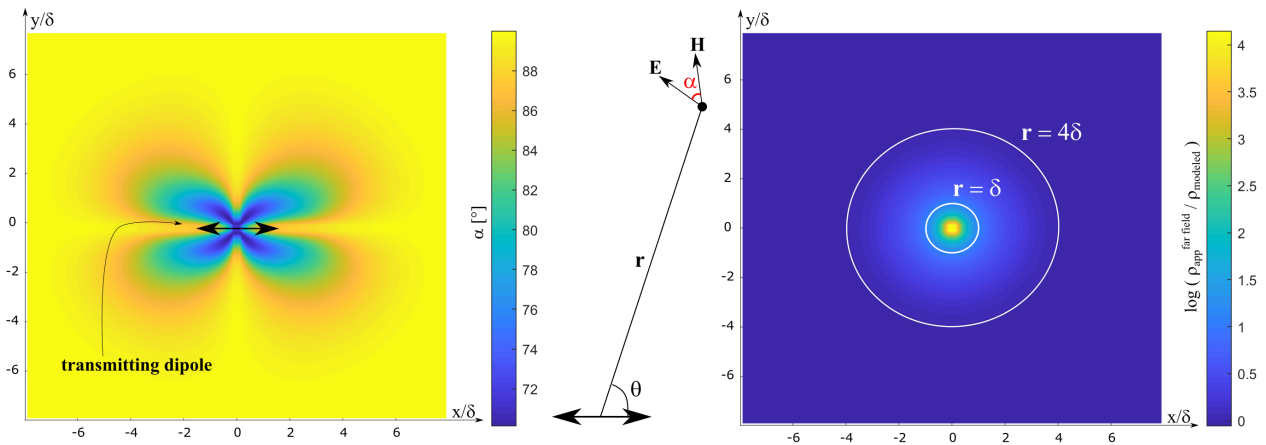


Figure 2.1: Spatial variations of the angle between the electric and the magnetic field generated by an infinitesimal dipole grounded on a uniform half-space. The  $x$  and  $y$  coordinates are expressed in terms of induction numbers: the metric distances are normalized by the skin depth  $\delta$ ; c. logarithmic ratio of computed apparent resistivity with far field formula over modeled resistivity; this figure shows where the far field assumption is valid. The white lines are the iso-distance of  $\delta$  and  $4\delta$  from the infinitesimal transmitter, and show that for homogeneous half spaces, the far field assumption is valid at distances larger than  $4\delta$  where the logarithmic ratio is close to zero.

The use of a unique transmitter only allows to interpret the subsurface in terms of 1D resistivity variations. The measurements no longer allow to get information on 2D and 3D anomalies, and only a dense spatial sampling can provide information on the 2D and 3D resistivity variations by means of a 2D or 3D inversion procedure.

### Orthogonality of the EM fields

If the orthogonality of the fields is expected at high induction numbers, it is not necessarily the case in the transitional and near fields (Boerner et al. [1993], Grant Caldwell et al. [2002]). This is demonstrated in particular by the fact that the 1D MT impedance tensor in the near field is not anti-symmetric. In fact, the angle  $\alpha$  between the electric and magnetic fields in all three domains can be computed from the general form of the impedance tensor given by Grant Caldwell et al. [2002]. This angle is a function of the distance to the transmitter, and the angle  $\theta$  formed by the axis of the transmitting dipole and the axis from the center of the dipole to the measurement station (Fig 2.1). In the far field, when  $\alpha$  is different than  $90^\circ$ , it results in non null diagonal elements in the impedance tensor and it is to be interpreted in terms of dimensionality of the subsurface. The map in fig. 2.1 presents the spatial variations of this angle  $\alpha$ . The coordinates are the metric coordinates normalized by the skin depth, in order to express the variation of the angle univocally regarding the frequency of the signal and the resistivity of the ground. The coordinates are therefore the induction number (dimensionless). In the far field, on top of a 1D layered earth, for any value of  $\theta$ , the angle  $\alpha$  in radia is  $\pi/2$ . In the near and transitional fields however, alpha varies from  $70^\circ$  to  $90^\circ$  (fig. 2.1).

## 2.2.2 Field methodology

### Standard layout in CSAMT

The CSAMT instrument setting is composed of two components: the transmitting part and the receivers part. A source signal is created by injecting an alternating current at a certain frequency into the ground through the transmitting dipole, while the electric and magnetic responses are recorded at the receiver station.

The transmitter station is usually composed of a high power current or tension source connected to a grounded electrical dipole and powered by the main current or a power generator. Usually, a current source is chosen to deliver the signal, to ensure the stability of the current in the dipole wire.

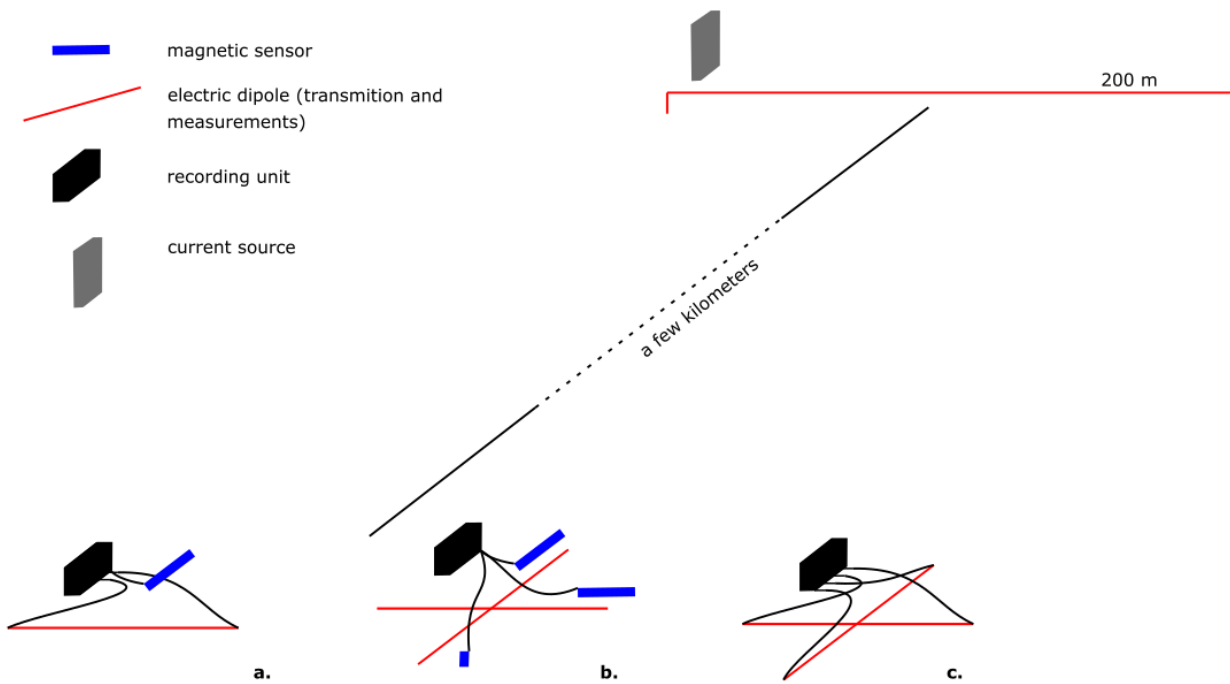


Figure 2.2: Measurement layout in CSAMT: a transmitting dipole is set a few kilometers away from the site, and the measurement of the resulting EM fields are measured. Several measurement configurations can be used: a. if the polarization of the magnetic and electric field can be estimated *a priori*, one can choose to recorded the fields exclusively in their resp. direction of polarization; b. in "vector measurements", the 3 components of the magnetic induction and the two horizontal components of the electric field are recorded; c. if the magnetic induction field is expected to be spatially stable, and is recorded in the vicinity of the station, one can choose to record only the horizontal electric field.

To ensure the strength of the source signal, the current source is connected to a very large dipole (a few hundreds of meters). A large flat area must be found, at a good location such that 1/ the grounds resistivity must be low, and the contact must be of good quality, for the device to work on its ideal domain and the power to be high) and 2/ the polarization and location of the dipole is such, that the signal reaching the studied site can be assimilated to plane wave signals. The transmitter must be installed a few kilometers from the site, to respect the far field assumption. For example, if the lowest frequency transmitted is 100 Hz, and the medium is expected to have a resistivity around  $500 \Omega \cdot \text{m}$ , the transmitter could be safely installed at 6 km from the site, which would be sufficient to ensure that  $r > 4\delta$  (Zonge and Hughes [1991]).

The recording station, at the very least, must be composed of a grounded dipole to measure one horizontal component of the electrical field, and one magnetic coil, oriented horizontally, orthogonal to the grounded dipole (fig. 2.2.a). However, such configuration is only suited if two non-parallel transmitting dipoles are used (see 2.2.3). In most cases, a vector configuration (similar to the MT measurements) is used: the two components of the electric field and the 3 components of the magnetic field are recorded (fig. 2.2.b).

Two orthogonal electrical dipoles of a few tens of meters are grounded to the subsurface. The use of unpolarizable electrodes can be required for low frequency measurements (below 10 Hz). Similarly to MT, magnetic induction coils are generally used to realize the magnetic measurements. Three coils are set orthogonal to one another, oriented towards the North, the East and downwards respectively, and leveled. The orientation must be accurately realized, as errors in the orientation of the coil will produce errors in the computation of the impedance tensor. If low frequencies are measured, it is crucial to protect the magnetic coils from wind and sun beams by burying them partially or completely in the ground, and covering them with grass, foams and dust. A sketch of CSAMT measurement station is proposed in fig. 2.2.

**Instrumentation**

The fields methodology set up in the following CSAMT survey was developed on a set of instruments manufactured by the company Phoenix Geophysics ©: the **System 2000.net**. This system is a complete CSAMT set of instruments (current source, transmitter monitor unit, receiver units and magnetic coils), composed of GPS synchronized units. Each unit is controlled by a set of control-file prepared by the user, and loaded into the system via SD cards. The different units can communicate, if close enough to one another, with radio signals at 2.4 GHz. The radio transmission is interesting to monitor and display on screen the quality of the signals recorded by any unit, but is not necessary. It is often problematic, as the presence of obstacles between two boxes obstructs the radio signal.

• **TX - T3 current source**

The T3 is a current source which can provide, in the optimal conditions, a maximum power of 3 kW, 9 A of output current and 1.1 kV of output voltage (tbl. 2.1). It can be powered by current sector (50 Hz of 60 Hz, 200-240 V), power generator, or batteries (12, 24, 48 or 72 V). When powered by batteries, the transmitter T3 act as a tension source, and the output tension is linearly linked to the input tension. It is then more suited for transmitting via a magnetic loop.

The T3 works on 3 different modes, which intensity and voltage characteristics are presented in table 2.1.

• **RXU-Transmitter Monitor**

The transmitter control unit plays two roles in the Phoenix Geophysics instrument setting. Connected to the GPS signal, it allows a better accuracy in time estimation, and a better synchronisation than the T3 alone, that only contains an internal clock. Secondly, this unit can impose the transmission of specific sequences of signal (Scan of a set of ordered frequencies, during a chosen amount of time), designed by the operator. These sequences are passed into the transmitter unit via a SD-card, in a formatted control-file. The injected current is recorded by the unit and stored in the same SD-card during transmission.

• **V8 receiver units**

The main receiver unit of the **System 2000.net** is the V8 unit, characterized by 4 independent electrical channels and 3 magnetic channels. The recordings are characterized by a maximum sampling frequency of 24 kHz. During measurement, the injection sequence imposed to the transmitter must be indicated to the V8 in a control-file, and the recording window and sampling frequencies are adapted depending on this transmitted sequence, as shown in table 2.2. The GPS synchronization ensures the synchronicity of the transmitter monitor unit and the recording unit. All units from this system are powered by external battery. The V8 has a display screen allowing to verify the quality of the recordings while measuring.

**AMTC magnetic coils:** The AMTC magnetic coils are induction coils manufactured by Phoenix Geophysics, and specifically designed for "high frequency" recordings, with a dynamic range from 10 s to 12000 Hz. AMTC coils present a flat response from 2 Hz to 6 kHz.

• **3-ER receiver units**

When the magnetic field is assumed to be stable enough over the survey area, systematic recordings of it is not necessary. Instead a unique 3C-magnetic recording can be used for a few close electrical stations if recorded at

load resistance		output current	min output voltage	mode
min	suggested max			
30 Ω	600 Ω	0.05 - 9 A	300 V	<b>1</b>
120 Ω	1200 Ω	0.05 - 5 A	600 V	<b>2</b>
900 Ω	2000 Ω	0.05 - 1.3 A	1100 V	<b>3</b>

Table 2.1: Characteristics of the current source T3 for different load resistances and the 3 setting modes corresponding

the same time. The 3-ER receiver units only record the electrical field, on 3 independent channels (fig. 2.2.c). They allow to complete a vector CSAMT survey with additional recordings of the electrical field, with a noticeable gain of time. The sampling and programming characteristics of the 3-ER unit are similar to those from the V8 units, the recordings are also stored on SD cards.

• **Transmitted signal**

For each transmitted frequency, a specific windowed signal of a specific length is transmitted a few times (10 to 15). For frequencies of 711 and 5120 Hz, the respective windowed source signal are shown in the first subfigure of fig. 2.3 and fig. 2.4. For some of the fundamental transmitted frequencies, the frequency samplings and current-waveform allow the transmission of harmonic signals (tbl. 2.2).

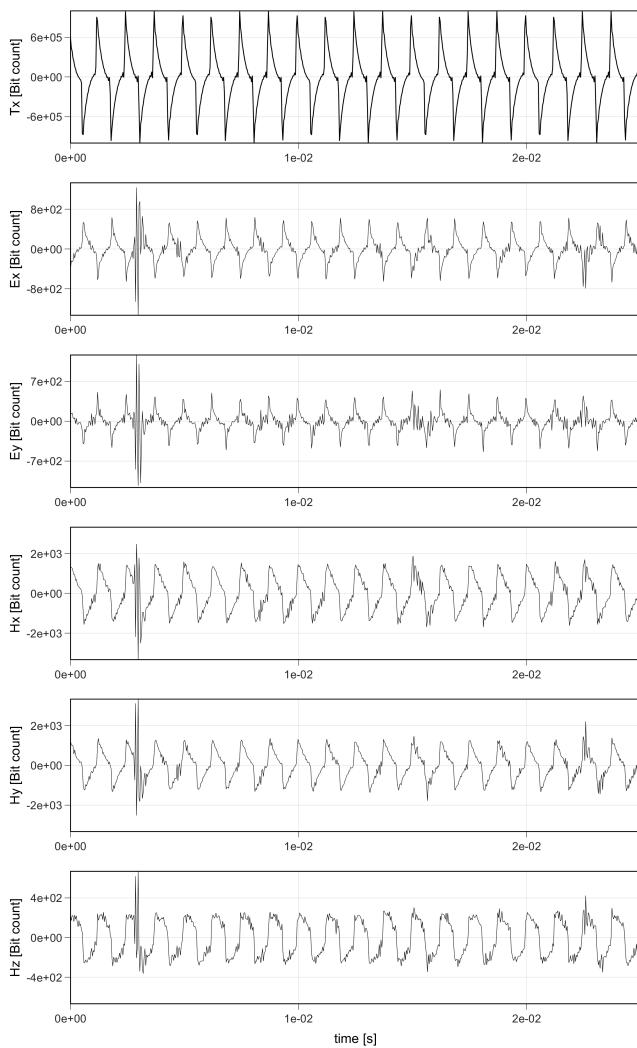


Figure 2.3: Example of measured raw time series with fundamental frequency of 711 Hz. From top to bottom: transmitted signal, raw electrical field towards North, and East, raw magnetic field towards North, East, and downward

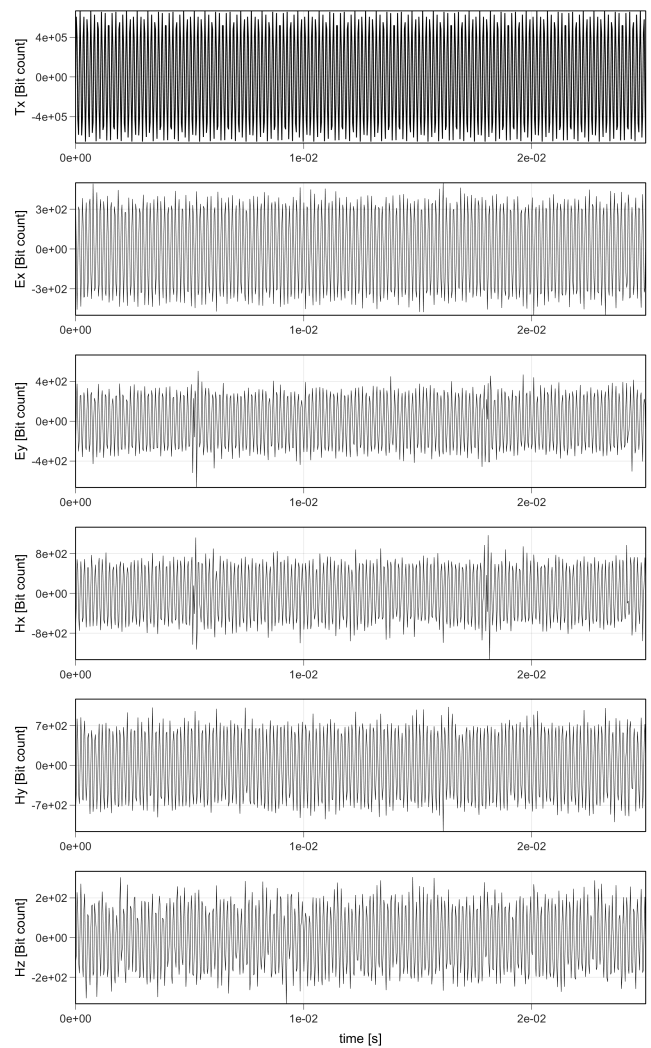


Figure 2.4: Example of measured raw time series with fundamental frequency of 5120 Hz. From top to bottom: transmitted signal, raw electrical field towards North, and East, raw magnetic field towards North, East, and downward

**2.2.3 Data analysis and processing**

In order to fully analyse the data and control the processing, set of processing scripts were developed in Matlab language. The entire processing workflow is presented in this section as well as in fig. 2.5.

<b>Transmitted frequency</b>	512 Hz	711.11 Hz	1024 Hz	1280 Hz	1920 Hz	2560 Hz
<b>Sampling frequency</b>	2400 Hz	24000 Hz	24000 Hz	24000 Hz	24000 Hz	24000 Hz
<b>Possible harmonics</b>		→ h16	→ h11	→ h9	→ h6	→ h4
<b>Transmitted frequency</b>	3840 Hz	5120 Hz	7680 Hz	9600Hz		
<b>Sampling frequency</b>	24000 Hz	24000 Hz	24000 Hz	24000 Hz		
<b>Possible harmonics</b>	→ h3	→ h2				

Table 2.2: Characteristics of the signal transmitted by the T3 and measured by the V8 and 3-ER: fundamental frequencies, sampling frequency and theoretical harmonics produced relative to the sampling frequency, to stay below the Nyquist criterion

### Common processing steps

The different processing steps are realized in the spectral domain. Each recorded sequence (or time-series) is processed independently such that, for a unique frequency, several independent estimations of the MT impedance tensor is made. The processing scheme include the extraction and conversion of raw time-series to the spectral domain, calibration and extraction of the signal. Finally, the impedance tensor and apparent resistivity is computed.

#### • Data extraction

The raw data are the time-series, in bit-count, of the recorded electric and magnetic responses related to the source signal. These time-series are extracted from the instrument in a compressed format owned by Phoenix Geophysics. A set of software are delivered by the company, allowing to extract the raw time-series and the control-files in ascii format. Examples of raw time-series are given in fig. 2.3 and fig. 2.4. These two figures present raw time-series related to the fundamental transmitted frequencies of 711 and 5120 Hz respectively. As presented in table 2.2, these two signals were recorded with the same sampling frequency: 24000 Hz. With such sampling frequency, the signal at 711 Hz is very well sampled, rich of harmonics and permits in theory to record 15 harmonic frequencies in ideal noise conditions. On the opposite, the signals at 5120 Hz is poor of harmonics, and can only provide 1 harmonic frequency, according to the Nyquist criterion.

#### • Computation of the spectra

The raw time-series are transposed in the spectral domain through a Fourier transform. Examples of raw amplitude spectrum are given in fig. 2.6. In figure 2.6, a high frequency bump can be observed in all measured components. This bump corresponds to temporary natural audio frequency signals, probably produced by a remote thunder storm. This high frequency signal could be extracted and processed, following MT processing techniques in order to extract a small part of the natural MT response.

#### • Data calibration

Magnetic coils are dynamic filters: a raw signal is amplified and phase-shifted depending on its frequency. A dynamic calibration must therefore be applied to the data depending on calibration functions attributed to each sensor. An example of dynamic response of AMTC coils is given in fig. 2.7. The raw data are in bit-count. A static calibration must be applied to the electric and magnetic data, to convert the raw data in the correct physically meaningful units (usually in [mV/km] and [nT] for the electric and magnetic fields respectively). Example of calibrated amplitude and phase spectra are presented in fig. 2.8 and fig. 2.9 resp. (note the important similarity in shape between calibrated and uncalibrated spectra, unabled by the very flat response, both in amplitude and

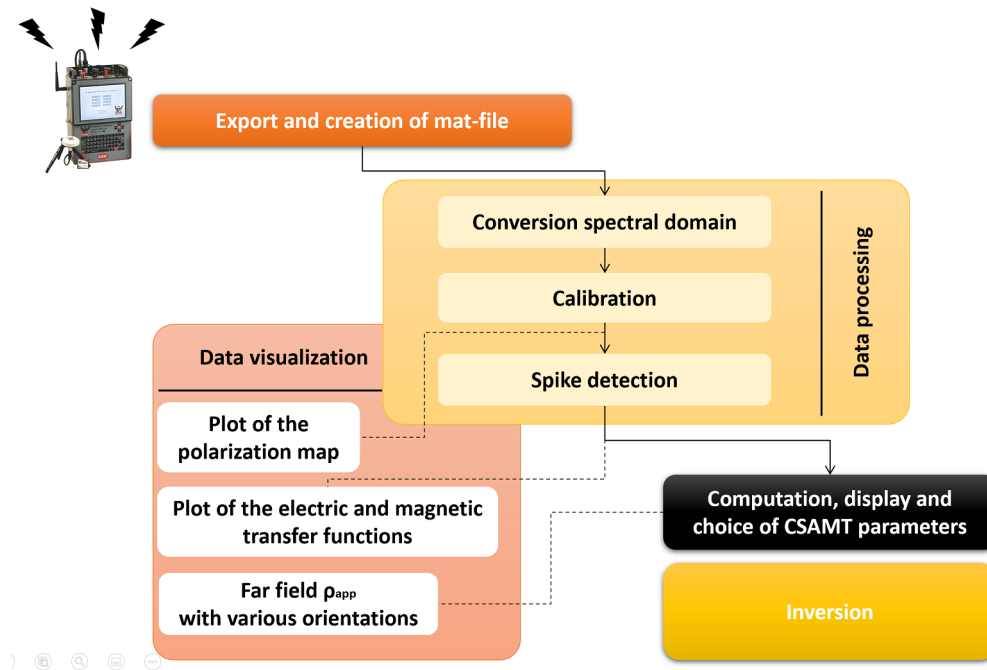


Figure 2.5: Processing workflow of the CSAMT data

phase, of the instrument between  $10^1$  and  $10^4$  Hz).

#### • Signal detection and filtering

The calibrated spectra contain more or less noise. If the signal is strong enough regarding the noise level, clear picks can be observed at the transmitted frequencies, as well as at harmonic frequencies. Because the detection of harmonic signals highly depends on the noise level, an automatic picking script was developed. It consists in a sliding window detector, based on detection of values exceeding the mean value over the window + 3 times the standard deviation. An example of detected picks is presented in fig. 2.10. It can be seen from this figure that not only harmonic signals are detected, but also signals of different unknown origins, potentially related to close sources. These signals must therefore not be accounted for in the interpretation.

### Data visualization and quality control

The exploration and analyses of the data are essential to evaluate the data quality and help selecting the strategy to adopt in order to reduce the sensitivity to noise. This exploration is realized by plotting the data in certain ways. For example, it can be interesting to represent the polarization of the recorded fields in a map, or to look in details at the electric and magnetic transfer functions.

#### • Polarization ellipses

For each field, the two horizontal components are rarely in phase. This is reflected in a elliptical polarization of the magnetic field (fig. 2.11). The polarization ellipse is characterized by a major axis and a minor one. Because of the strong attenuation that the signals are expected to undergo in the rock materials, it is expected that the major axis would mainly relate to the primary field, and the minor axis correspond to the secondary field. In a flat layered earth, the magnitude of the minor axis regarding the magnitude of the major axis can be associated to the importance of 2D or 3D objects in the subsurface (because related to the secondary field). However, it is possible also to related large minor axis to topographic effects.

In the near field, it is expected that the major response is related to the in-phase component of the field (in-phase regarding the transmitted signal), and the minor axis corresponds to the quadrature signal and is the secondary field, generated by local anomalies. In the far field, the primary field is not in phase with the transmitted signal. In an homogeneous flat earth, the primary horizontal fields are actually phase shifted of  $\pi/4$

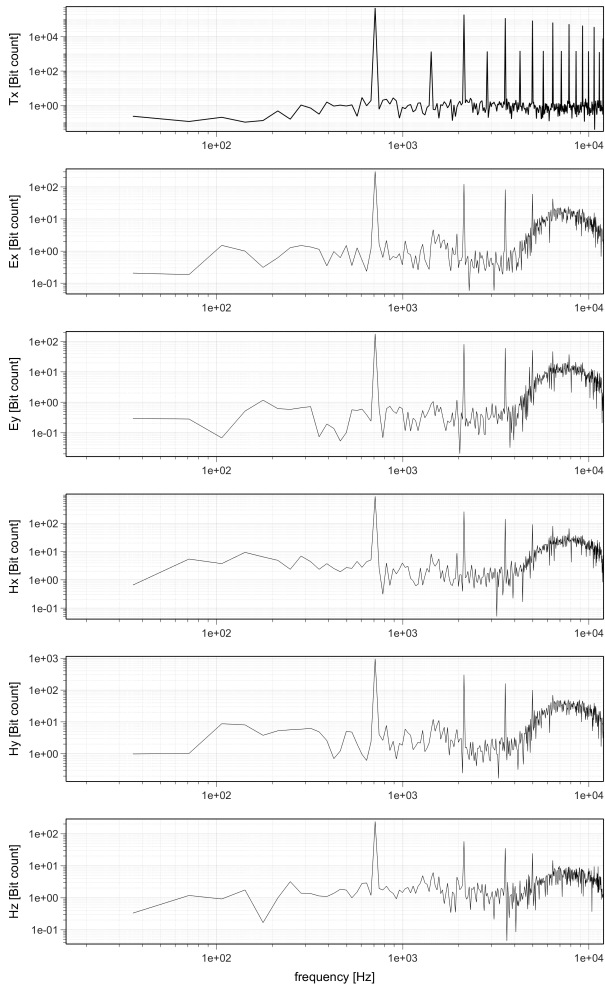


Figure 2.6: Example of raw spectrum of recorded signals related to a transmitted signal of fundamental frequency of 711 Hz.

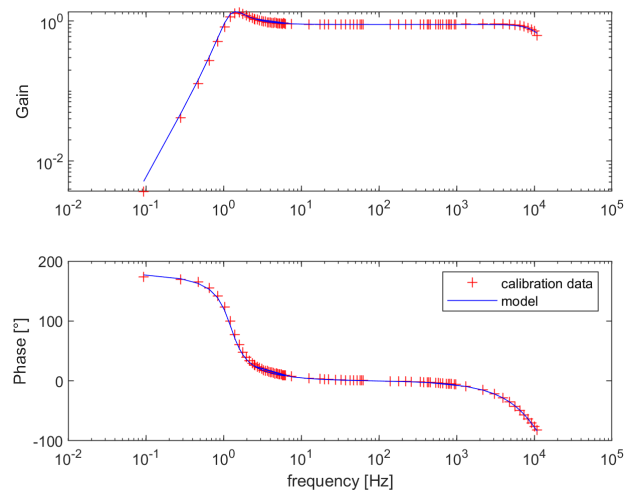


Figure 2.7: Example of dynamic response of an AMTC magnetic coil

regarding the transmitted signal.

Mapping the polarization of the fields over the entire area allows 1/ to observe the stability and coherence of the recorded fields over the site, 2/ to evaluate the stability in time of the transmitted signals, related to the transmitter quality and of the response, related to transient noise.

• **Electric and magnetic transfer functions**

Another important step to evaluate the data quality is to plot, separately, the amplitude and phase transfer functions of the electric and magnetic fields, such as in fig. 2.12 and 2.13. This can permit to observe which components and which fields are mostly affected by noise, for example.

**Computation of the apparent resistivity**

• **Resolution of the MT impedance tensor with two dipoles**

If the medium is a 1D layered earth, with no 2D nor 3D anomaly, a unique transmitter could in theory be used, the generated horizontal E and H fields would be orthogonal and  $Z_{xy}$  and  $Z_{yx}$  could be simply deduced by eq. 2.17, where  $\bar{X}$  designates the complex conjugate of X.

$$\bar{Z}_{xy} = \frac{E_x}{H_y} \qquad \bar{Z}_{yx} = \frac{E_y}{H_x} \qquad (2.17)$$

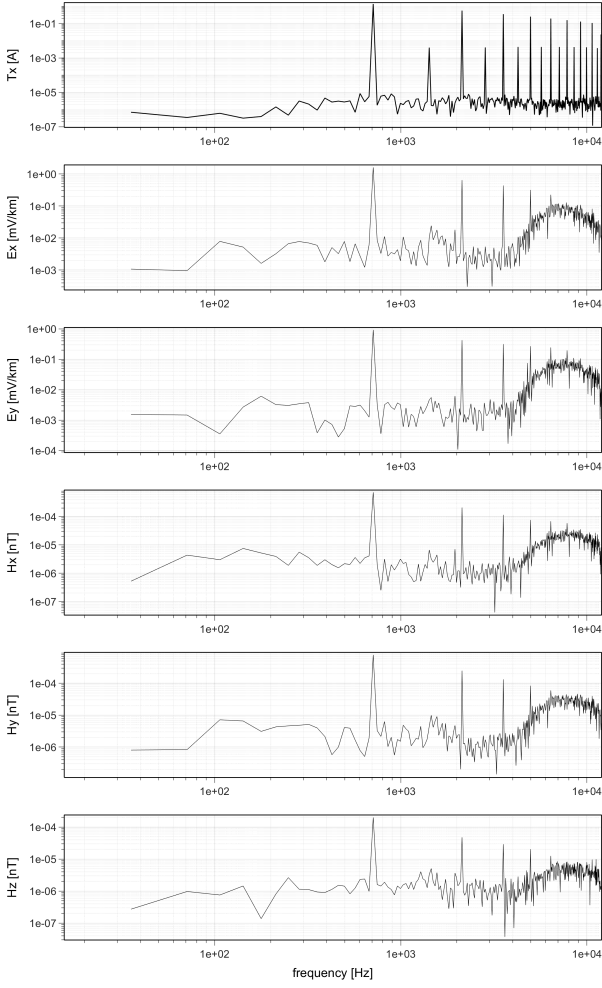


Figure 2.8: Calibrated amplitude spectrum of a measured sequence at 711 Hz

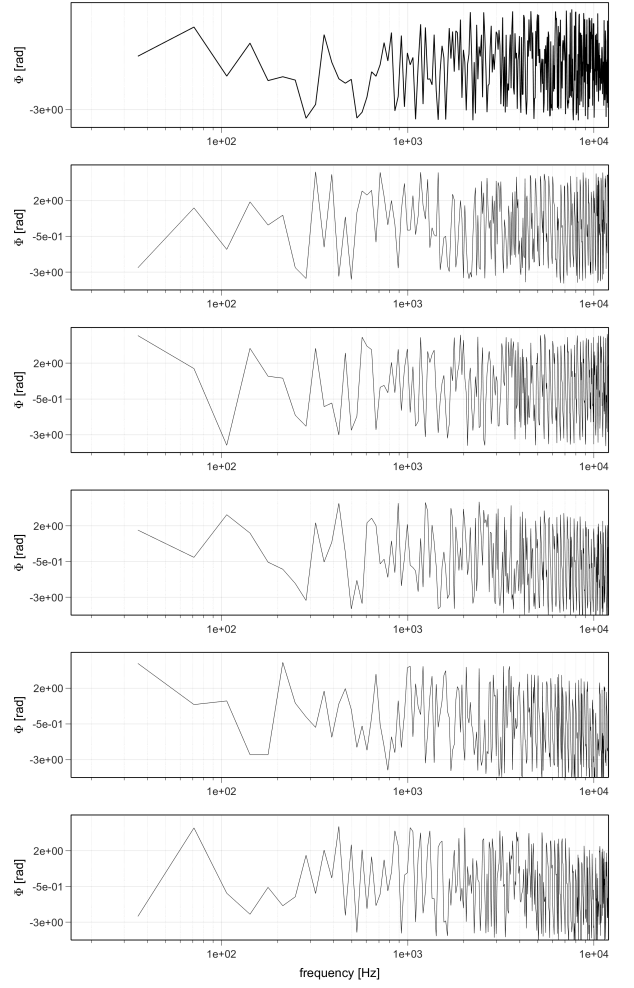


Figure 2.9: Calibrated phase spectrum of a measured sequence at 711 Hz

When the subsurface is not a 1D layered earth, the impedance tensor is composed of 3 independent components. In such case, the information brought by a single transmitting dipole is not sufficient. To obtain the full tensor at a certain location, the magnetic field must be recorded in the two horizontal directions, or at least along two non-parallel directions. This implies the use of two non-parallel transmitting dipole, ideally producing orthogonal magnetic field on the site. The full MT impedance tensor can then be computed following eq. 2.18, where S1 and S2 designate the two sources used successively to produce the two sets of EM responses.

$$\begin{aligned}
 \overline{Z}_{xx} &= \frac{E_x^{S1} H_y^{S2} - E_x^{S2} H_y^{S1}}{H_x^{S1} H_y^{S2} - H_x^{S2} H_y^{S1}} & \overline{Z}_{xy} &= \frac{E_x^{S2} H_x^{S1} - E_x^{S1} H_x^{S2}}{H_x^{S1} H_y^{S2} - H_x^{S2} H_y^{S1}} \\
 \overline{Z}_{yx} &= \frac{E_y^{S1} H_y^{S2} - E_y^{S2} H_y^{S1}}{H_x^{S1} H_y^{S2} - H_x^{S2} H_y^{S1}} & \overline{Z}_{yy} &= \frac{E_y^{S2} H_x^{S1} - E_y^{S1} H_x^{S2}}{H_x^{S1} H_y^{S2} - H_x^{S2} H_y^{S1}}
 \end{aligned}
 \tag{2.18}$$

Note that this use of two orthogonal source H-fields is related to the MT hypothesis that the natural sources are randomly oriented and come from random directions.

The apparent resistivity curves can be inferred following the Cagniard formula (Cagniard [1953]).

#### • Resolution with a unique dipole

If only one transmitting dipole is used in the field, the information is incomplete and does not allow to compute

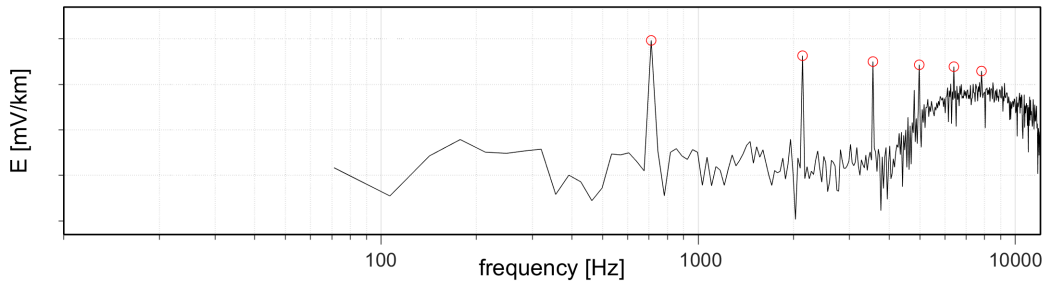


Figure 2.10: Example of signal detection on a calibrated amplitude spectrum. The red circles are the detected and extracted signals

a full impedance tensor. We propose a method to estimate the apparent resistivity and the "degree" of 2D effects present in incomplete CSAMT measurements. If, for example, the input magnetic field produced by the transmitting dipole is polarized along the  $x$  axis, the measurement will only enlighten the first column of the impedance tensor (eq. 3.1). The complete tensor will remain unresolved, but the components  $Z_{xx}$  and  $Z_{yx}$  of the impedance tensor can still be fully computed. If  $Z_{xx}$  is much smaller than  $Z_{yx}$  (one or two orders of magnitude), one can consider that the 2D effects are negligible, and the apparent resistivity can be computed from  $Z_{yx}$ .

$$\begin{bmatrix} E_x \\ E_y \end{bmatrix} = \begin{bmatrix} Z_{xx} & - \\ Z_{yx} & - \end{bmatrix} \begin{bmatrix} H_x \\ 0 \end{bmatrix} \quad (2.19)$$

The figures 2.14 and 2.15 present the apparent resistivity and phase curves computed from the EM responses in fig. 2.12 and 2.13, when assuming a real 1D layered medium and following eq. 2.17 (fig. 2.14) and when accounting for possible 2D or 3D effects and following eq. 3.1 (fig. 2.15).

• **Near field computation of the apparent resistivity: use of cylindrical coordinates**

The theory of EM fields suggests that the apparent resistivity curve of a layered half-space can also be resolved using the near field impedance tensor. This computation implies orienting the field along the cylindrical-coordinates vector, with the center of the frame located at the center of the transmitter [ $e_r, e_\theta$ ] (eq. 2.13, eq. 2.35). This computation requires however the use of two orthogonal dipoles. In addition, it is expected from non-far field data to be highly influenced by anomalies in the transmitter area. For this reason, near field EM signals are simply ignored in this work.

• **Extraction of primary and secondary signals**

The theory of CSAMT is developed in the context of a layered earth. However, when the subsurface includes 2D or 3D structures, or when the surface topography is not flat, a "secondary field" component is measured, and the polarization ellipse produced by the superposition of the two components is clearly measured.

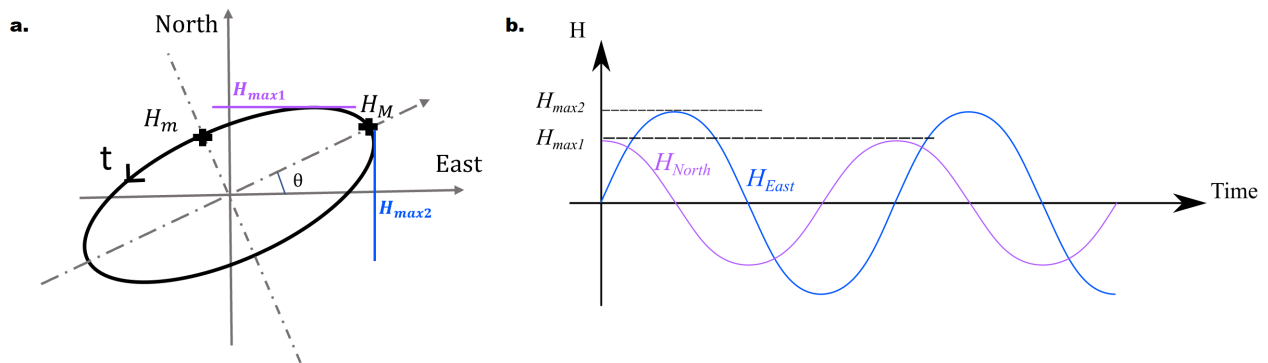


Figure 2.11: Example of polarization ellipse: the horizontal projection of the field describes an ellipsoid section in time

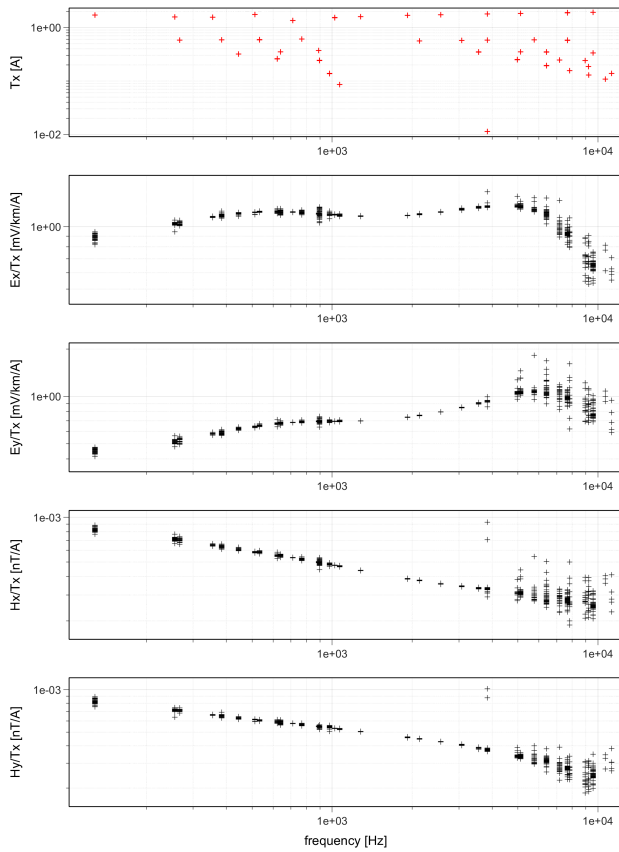


Figure 2.12: Modulus of the filtered electric and magnetic transfer functions

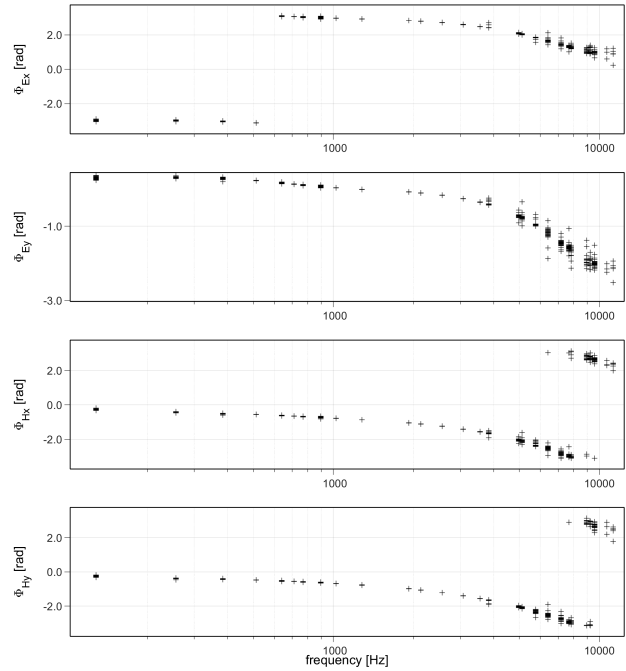


Figure 2.13: Phase of the filtered electric and magnetic transfer functions

In order to be as less affected as possible by the secondary responses, an attempt at isolating the primary magnetic field was made. In the far field, the primary magnetic field  $H_{\mathcal{P}}$  produced by a grounded electric dipole is expected to be phase-shifted by  $\pi/4$  with respect to the electrical current injected in the transmitter dipole (Ward and Hohmann [1988]). The secondary magnetic field  $H_{\mathcal{Q}}$  should be phase shifted by  $3\pi/4$  with respect to the transmitter.

The two directions in which the horizontal magnetic field is phase shifted of  $\pi/4$  and  $3\pi/4$  regarding the transmitter were computed (details of the computation in the appendix A.1.). The direction of primary and secondary components turned out to be non-orthogonal (fig. 2.16), leading to questions regarding the validity of this decomposition. Theoretical considerations on the phase of a secondary field showed in fact that in a general case, the secondary field is not necessarily in quadrature regarding the primary field (appendix A.1.), this method was therefore abandoned.

## 2.2.4 Common distortions in CSAMT

Because the success of a CSAMT survey relies on the validity of a set of hypothesis, some of them being quite challenging to satisfy in field experiment (far field hypothesis, relative flatness of the surface, relative simplicity in the dimension of the underground structures), it is very useful to possess tools to evaluate, previous to conducting a field survey, the validity of these hypothesis, or the impact of invalid hypothesis. Some numerical modeling tools are presented in the next paragraphs, followed by preliminary results on synthetic examples.

Numerical modeling tools are presented in this paragraph, as I adapted them to the specific task of decision-making tool in the perspective of a CSAMT field survey.

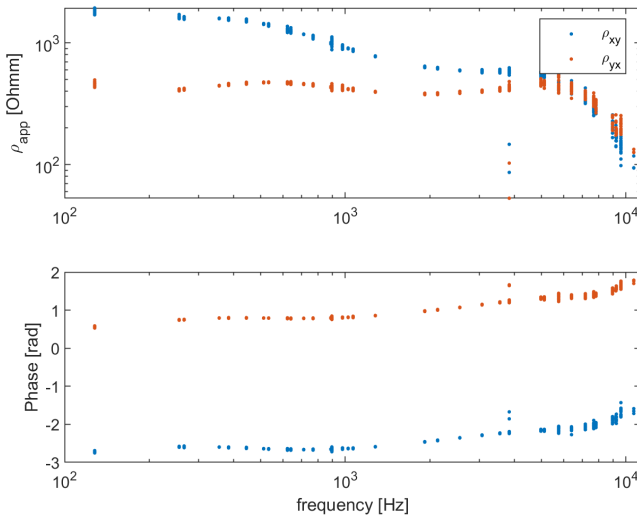


Figure 2.14: Apparent resistivity and phase curves computed from eq. 2.17; this computation suggests a 1D layered medium and is not valid here

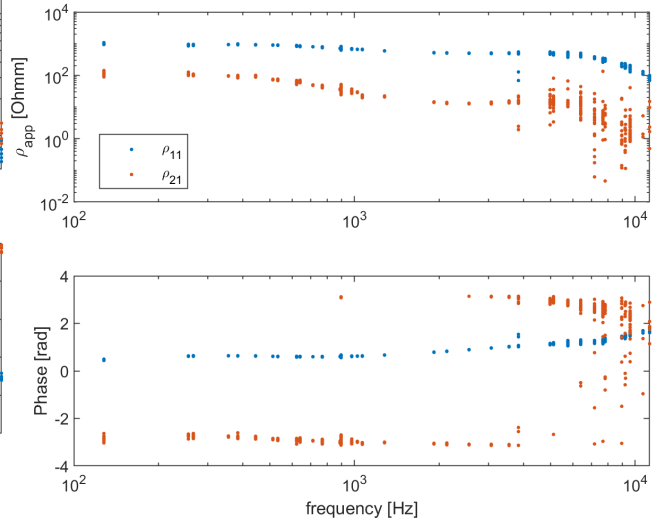


Figure 2.15: Apparent resistivity and phase curves when accounting for possible 2D and 3D objects eq. 3.1

### • Topography

Variations of the surface topography can be seen as a 3D effect. It is expected to impact the diffusion and propagation of the EM signal. The realization of modeling experiments is important in the case of topographic variations in order to evaluate the effects of the topography on the fields. This is described in particular in chapter 3 of this thesis.

### • Near surface distortions

Near surface distortion are to be expected when realizing galvanic measurements of the electric field ([Árnason \[2015\]](#)). These distortions are produced by near surface anomalies of small size, at a smaller scale than the finest resolution of the measurement. In MT and CSAMT methods, where the magnetotelluric impedance tensor is the bases of the investigation, these distortions act as a static shift (independent of the frequency) of the impedance curve upwards or downward in log-space. These anomalies impact the entire frequency range sampled, and can hardly be identified by very high frequency measurements.

It is very current to resolve the static shift by completing the survey with non galvanic measurements (transient EM (TEM) measurements, for example) to resolve the shallow variations of resistivity of the subsurface and wedge the apparent resistivity curves with airborne TEM data ([Delhaye et al. \[2017\]](#)).

Another methodology consist in comparing the mean apparent resistivity of neighbouring soundings, assuming that the mean apparent resistivity should vary very smoothly and thinly amongst neighbouring stations ([Sternberg et al. \[1985\]](#)).

### • Induced polarization

If the subsurface contains a polarizable object (presence of clay), distortions should be expected in the measured apparent resistivity and sensitivity of the CSAMT measurement. A polarizable object should cause a delay in the EM response, delay that should depends on the frequency, altering the EM measurements ([Kratzer and Macnae \[2012\]](#)).

### • Sensitivity and depth of investigation

In CSAMT, the habit is to consider that the sensitive volume is directly given by the skin depth  $\delta$ , or, more precisely, by the ratio of the skin depth to the square root of two. The belief that low frequency data ensure directly a certain DOI might be too simplistic. As suggested by [Boerner et al. \[1993\]](#), after data inversion, the sensitivity might be reevaluated by means of synthetic sensitivity tests, that evaluate the impact of a small variations of the

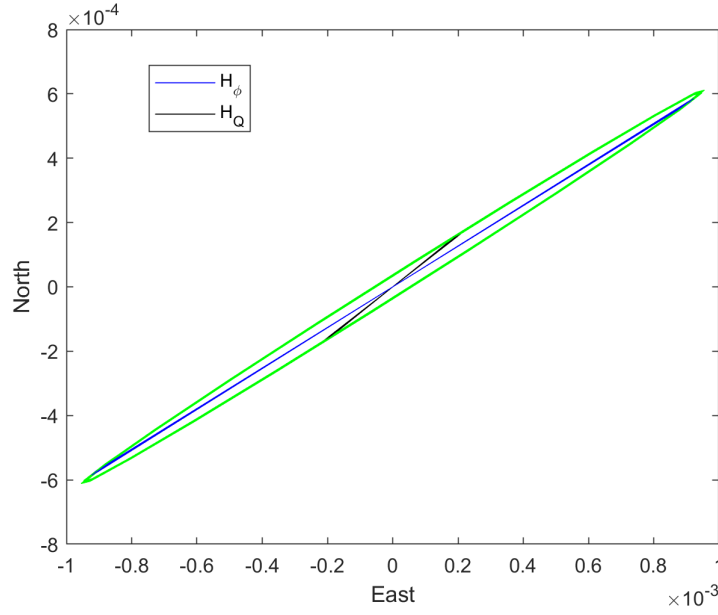


Figure 2.16: Example of polarization of the magnetic field and direction of in-phase ( $H_\phi$ ) and quadrature ( $H_Q$ ) signals

model on the data, through numerical modeling.

## 2.2.5 Modeling of CSAMT data

### Electric and magnetic field produced by a grounded electrical dipole

The electric and magnetic field follow the Maxwell's equations, and comply to the constitutive equations of electromagnetism. The displacement currents are neglected and the assumption of an absence of magnetic source is made. The equation of diffusion and propagation of electromagnetism can easily be derived from the Maxwell's equations, and provide, in the case of an electrical current density source, the equation 2.20.

$$\begin{aligned}\nabla \wedge \mathbf{E} + i\mu\omega\mathbf{H} &= \mathbf{0} \\ \nabla \wedge \mathbf{H} - (\sigma + i\epsilon\omega)\mathbf{E} &= \mathbf{J}\end{aligned}\quad (2.20)$$

The expressions are given in the spacial and frequency domain,  $\mu$  is the magnetic permeability of the medium,  $\sigma$  is its electrical conductivity,  $\epsilon$  its dielectric permittivity and  $i = \sqrt{-1}$ .  $\mathbf{E}$  designates the electrical vector field,  $\mathbf{H}$  the magnetic vector field, and  $\mathbf{J}$  is the source current density.

In order to formulate and compute the electric and magnetic fields generated by a grounded electrical dipole powered with an alternating current, one can refer to the Schelkunoff potential vector relative to an electrical source,  $\mathbf{A}$ , which, in the absence of any magnetic source, fully constraints the electromagnetic fields (eq. 2.21, eq. 2.22).

$$\mathbf{E} = -i\mu\omega\mathbf{A} + \frac{1}{\sigma + i\epsilon\omega}\nabla(\nabla \cdot \mathbf{A}) \quad (2.21)$$

$$\mathbf{H} = \nabla \wedge \mathbf{A} \quad (2.22)$$

where  $\mathbf{A}$  satisfies the equation:

$$\Delta\mathbf{A} + k^2\mathbf{A} = \mathbf{J} \quad (2.23)$$

where  $k$  is the wavenumber:  $k = \sqrt{\omega^2\mu\epsilon - i\omega\mu\sigma}$ .

$\mathbf{A}$ , expressed in [A], represents the EM response to a certain source, relatively to a certain medium. One can separate, in the expression of  $\mathbf{A}$ , the source term and the Green's function, which can be associated to the

filtering action of the space, and relate to its electromagnetic properties ( $\mu, \sigma$  and  $\epsilon$ ). This is made by re-writing  $\mathbf{A}$  as a convolution product, in the space and time domain, of the Green's function of the medium in  $[m^{-1}]$  and the source term  $\mathbf{J}$  ( $[A.m]$ ), as in eq. 2.24.

$$\mathbf{A}(x, y, z, t) = G(x, y, z, t) * \mathbf{J}(x, y, z, t) \quad (2.24)$$

#### • Description of the source

The source term can be express at different levels of detail: an infinitesimal polarized source can be considered a good model in many cases. The source is then expressed as in eq. 2.25. To describe more accurately a long electrical dipole source, one can choose to sum up a series of infinitesimal dipole, all oriented along the dipole to be modeled.

$$\mathbf{J}(x, y, z, \omega) = I L \mathbf{e}_1 \delta(x) \delta(y) \delta(z) \delta(\omega) \quad (2.25)$$

where  $I$  is the intensity of the current flowing in the dipole,  $L$  is the length of the dipole, and  $\mathbf{e}_1$  is the direction vector of the dipole.  $\delta$  is the dirac function.  $\mathbf{J}$  can be written as a product of two independent functions, one of the space coordinates, and one of the pulsation  $\omega$ , such that:

$$\mathbf{J}(x, y, z, \omega) = \mathbf{e}_1 S_s(x, y, z) S_f(\omega) \quad (2.26)$$

According to [Singh and Mogi \[2010\]](#), for short linear dipoles, when the source-receiver offset is large enough ( $r > 5L$ ), the formulation of the infinitesimal dipole is acceptable to describe the source. [Streich et al. \[2011\]](#) suggest that the validity of this previous statement depends on the source frequency. In other cases, the dipole can be modeled by integration of infinitesimal dipoles along the dipole-wire.

In the following, the assumption is made of a mono-frequency source:  $S_f(\omega) = \delta(\omega_0)$ .

#### • Green's function

The Green's function is defined as the solution of eq. 2.23 for an impulsive source term in space and time:  $J(x, y, z, t) = \delta(x, y, z) \delta(t)$ . By re-writing eq. 2.23 in the frequency domain, we obtain eq. 2.27 and its solution in the Fourier domain in eq. 2.28 ( $x \rightarrow k_x, y \rightarrow k_y, z \rightarrow k_z$ ).

$$\Delta G(x, y, z, t) + k^2 G(x, y, z, t) = -\delta(x, y, z) \delta(t) \quad (2.27)$$

$$G(k_x, k_y, k_z, \omega) = \frac{1}{k_x^2 + k_y^2 + k_z^2 - k^2} \quad (2.28)$$

In an infinite homogeneous medium, the Green's function is easy to obtain by applying the inverse Fourier transform, providing eq. 2.29, where  $r$  is the cylindrical first coordinate.

$$G_\infty = \frac{e^{-ikr}}{4\pi r} \quad (2.29)$$

providing the solution:

$$\mathbf{A}_\infty = \int_V \frac{e^{-ik|r-r'|}}{4\pi|r-r'|} \mathbf{J}(r') dV' \quad (2.30)$$

In the roughest hypothesis, the earth can be represented as an homogeneous conductive half-space, below a resistive air half-space. In the homogeneous half-space and 1D-layered earth cases, the invariance in  $z$  is lost, and a discontinuity along a plan ( $z = z_0$ ) is introduced. Because the resistivity and permittivity distributions present a cylindrical symmetry about the vertical  $z$  axis, it is common to express the Green's function in the Hankel space, by means of Hankel transforms ([Bannister \[1966\]](#), [Anderson \[1979\]](#), [Ward and Hohmann \[1988\]](#), [Boerner et al. \[1993\]](#)). The Green's function, expressed in the space and frequency domain in eq. 2.27 can be transformed in the Fourier space as in eq. 2.28.

$$\frac{\partial G(k_x, k_y, z, \omega)^2}{\partial^2 z} + [k_x^2 + k_y^2 - k^2] G(k_x, k_y, z, \omega) = -\delta(z) \quad (2.31)$$

$$G(k, \lambda) = \frac{1}{4\pi} \int_0^\infty \frac{\lambda}{u} e^{-u|z|} J_0(\lambda k) du \quad (2.32)$$

G follows an equation of propagation along the z axis. To solve this equation, it is common to make use of the Hankel transform of G, particularly adapted to the cylindrical geometry. The potential vector **A** can be obtained by solving the integral on  $\lambda$  numerically (Anderson [1979]) where  $\lambda$  is the horizontal wave number and  $\rho$  is the radial distance to the point source.

#### • Homogeneous half-space

In the case of an homogeneous half-space, for an impulsive source in space and frequency, the EM solution of the EM fields are provided and commented among others by Zonge and Hughes [1991]. Eq. 2.37 presents the general expressions of the EM fields for a homogeneous half-space projected in a cylindrical space  $\{e_r, e_\phi, e_z\}$ .  $I_0, I_1, K_0$  and  $K_1$  are the modified Bessel functions of order 0 and 1, and of first (I) and second (K) kind.

$$\begin{aligned} E_r &= \frac{Idl \cos \phi}{2\pi \sigma r^3} [1 + e^{-ikr} (1 + ikr)] \\ E_\phi &= \frac{Idl \sin \phi}{2\pi \sigma r^3} [2 - e^{-ikr} (1 + ikr)] \\ E_z &= \frac{i\mu_0 \omega Idl \cos \phi}{2\pi r} \left[ I_1\left(\frac{ikr}{2}\right) K_1\left(\frac{ikr}{2}\right) \right] \\ H_r &= \frac{Idl \sin \phi}{2\pi r^2} \left[ 3I_1\left(\frac{ikr}{2}\right) K_1\left(\frac{ikr}{2}\right) + \left(\frac{ikr}{2}\right) \cdot \left( I_1\left(\frac{ikr}{2}\right) K_0\left(\frac{ikr}{2}\right) - I_0\left(\frac{ikr}{2}\right) K_1\left(\frac{ikr}{2}\right) \right) \right] \\ H_\phi &= \frac{-Idl \cos \phi}{2\pi r^2} \left[ I_1\left(\frac{ikr}{2}\right) K_1\left(\frac{ikr}{2}\right) \right] \\ H_z &= \frac{-3Idl \sin \phi}{2\pi k^2 r^4} [1 - e^{-ikr} (1 + ikr - 1/3 k^2 r^2)] \end{aligned} \quad (2.33)$$

#### Far field domain ( $r \gg \delta$ )

When the transmitter - receivers offset is large enough such that  $r \gg \delta$ , the EM fields can be assimilated to plane wave signals and the far field condition is met. The equations simplifies as in eq. 2.34.

$$\begin{aligned} E_r &= \frac{Idl \cos \phi}{2\pi \sigma r^3} \\ E_\phi &= \frac{Idl \sin \phi}{2\pi \sigma r^3} \\ E_z &= \frac{\sqrt{(\mu_0 \omega)} Idl \cos \phi}{2\pi \sqrt{\sigma} r^2} e^{i\pi/4} \\ H_r &= \frac{Idl \sin \phi}{2\pi \sqrt{\mu \sigma \omega} r^3} e^{-i\pi/4} \\ H_\phi &= \frac{-Idl \cos \phi}{2\pi \sqrt{\mu \sigma \omega} r^3} e^{-i\pi/4} \\ H_z &= \frac{-3Idl \sin \phi}{2\pi \mu \sigma \omega r^4} e^{-i\pi/2} \end{aligned} \quad (2.34)$$

In this situation, the MT impedance tensor is decoupled from the source medium and is linearly related to the subsurface apparent resistivity, as is described in the Cagniard formula: the MT methodology applies. The sensitivity is still given by the skin depth.

**Near field domain ( $r \ll \delta$ )**

On the opposite, when  $r \ll \delta$ , the expressions of the EM fields simplify as in eq. 2.35.

$$\begin{aligned}
 E_r &= \frac{I dl \cos \phi}{\pi \sigma r^3} \\
 E_\phi &= \frac{I dl \sin \phi}{2\pi \sigma r^3} \\
 E_z &= \frac{i\mu_0 \omega I dl \cos \phi}{4\pi r} \\
 H_r &= \frac{I dl \sin \phi}{4\pi r^2} \\
 H_\phi &= \frac{-I dl \cos \phi}{4\pi r^2} \\
 H_z &= \frac{I dl \sin \phi}{4\pi r^2}
 \end{aligned} \tag{2.35}$$

In the near field, the ratio defined by the MT impedance tensor is no longer a property of the subsurface (independent of the signal used to measure it), as it depends on the location and polarization of the signal transmitter. The equations 2.35 suggest, following eq. 2.36 that the apparent resistivity of the subsurface can still be deduced from near field data. This is true if the subsurface is homogeneous. However, the dependency upon the transmitter position and location induces necessarily also a dependency upon the resistivity beneath the transmitting dipole.

$$\begin{aligned}
 \frac{E_r}{H_\phi} &= \frac{-4}{\sigma r} = \frac{-4\rho}{r} \\
 \frac{E_\phi}{H_r} &= \frac{2}{\sigma r} = \frac{2\rho}{r}
 \end{aligned} \tag{2.36}$$

In fact, the near field interpretation of the impedance tensor is fairly complicated. In most cases, lateral variations are expected over distances of a few kilometers, which are the typical transmitter-receivers offset in the case of CSAMT studies. Even in the near field of the transmitter, it is very likely to observe variations of resistivity from the transmitter location to the studied site. Because in the near field, the MT impedance tensor is not decoupled from the source, near field measurements turn sensitive to the structures below the transmitter and in between the transmitter and the receiver.

In the literature, different conditions are proposed to ensure that an EM signal generated by a horizontal grounded dipole is a plane wave signal. These conditions concern the transmitter receiver offset  $r$  relative to the skin depth  $\delta$ . [Goldstein and Strangway \[1975\]](#) propose that the condition  $r > 3\delta$  ensures the validity of the far field condition, [Zonge and Hughes \[1991\]](#) proposes the condition  $r > 4\delta$ . In practice, because an homogeneous subsurface is very unlikely, the condition that defines the far field domain cannot be straightforwardly deduced. In fact, this transition depends in particular on the resistivity at the transmitter location (see the tests at the end of the section). Discussion on the far field limit can be found on chapter 3 and 5 of this thesis.

**• 1D layered half space**

As in MT, the Cagniard formula of the apparent resistivity as a function of the MT impedance tensor is still valid in the case of a 1D-layered medium. To solve the equations of the EM fields generated by a grounded dipole when the ground is composed of infinite horizontal layers, one usually formulate the problems using Hankel transforms, particularly suited to cylindrical symmetries. The computation of the fields back to space and frequency domain provide integral formula function of the transverse electric and transverse magnetic reflection coefficients  $r_{TE}$  and  $r_{TM}$  resp. relative to the layered space and of the modified Bessel functions of first and second kind,  $I_N$  and  $K_N$ . The equation 2.37 is extracted from [Streich et al. \[2011\]](#) and is relative to a

specific description of the source dipole.

$$\begin{aligned}
 E_x = -z_0 \frac{Idl}{4\pi} & \left( \int_0^\infty [e^{-u_0(z+h)} + r_{TE} e^{u_0(z-h)}] \frac{\lambda}{u_0} J_0(kr) dk \right. \\
 & \left. - \frac{Idl}{4\pi} \frac{\partial}{\partial x} \int_0^\infty [(e^{-u_0(z+h)} - r_{TE} e^{u_0(z-h)}) \frac{u_0}{y_0} \right. \\
 & \left. - e^{-u_0(z+h)} + r_{TE} e^{u_0(z-h)}] J_1(kr) dk \right]
 \end{aligned} \tag{2.37}$$

These integral formulations must be evaluated numerically. To do so, convolution technics are generally used, associated to specific digital filters (Anderson [1979]).

#### • 2D and 3D structures in the subsurface

When the subsurface is more complex and includes 2-dimensional (2D) or 3-dimensional (3D) structures, the fields cannot be formulated and computed analytically. The equations must be reformulated, using adequate operators to solve the differential forms and the space must be locally discretized to employ a numerical computation methodology.

The modeling of the EM fields in the presence of 2D or 3D structures is often realized by decomposing the fields into a primary field, which corresponds to the theoretical fields produced by the source in a 1D medium, and a secondary or perturbation field, which corresponds to the signal produced by anomalies of the subsurface in response to the primary field.

Two main families of numerical methods are very common in solving complex differential problems: the finite volume and the finite elements methods.

Other methods can be employed, for example, Hanneson and West [1984] decomposed the current induced by the primary field on a thin conductive plate onto a family of low order polynomial functions, fixing the boundary conditions and solved the integral equations; Hohmann [1975] presented a similar example where the computation of the secondary field produced by a cubic anomaly in a 1D layered space is realized by assimilating the body to a scattered current density volume, and computing integral equations related to such secondary source numerically. He emphasizes the simplicity of the numerical solution regarding finite difference or finite element methods, but this method exclusively works if the subsurface contains a series of simple anomalies, and not for complex 3D media.

**Finite difference methods:** In the finite difference method, the space is discretized in parallelepiped cells of various size. The differential operators are replaced in the equations by finite difference operators, taking care that the continuity equations are respected at the interface of the cells.

**Finite element methods:** In the finite element computation, the space is discretized in irregular cells of flexible forms (for example tetrahedral cells). The equations are re-formulated in the weak formulation. The method consists in decomposing the fields in a linear combination of a set of independent functions such that the error in the solving of the differential equations at the nodes of the mesh is as low as possible. This is made by inverting a sparse matrix of very large size.

**CustEM: computation of controlled source EM data:** CustEM<sup>®</sup> is an "open-source toolbox for customizable 3D finite-element modeling of controlled-source electromagnetic data" (Rochlitz et al. [2019]). It was recently developed at the LIAG, Hannover, and allows the computation of electric and magnetic fields produced by different types of transmitters (grounded dipoles, vertical and horizontal magnetic loops). Written in fortran and python, it is based on the Fenics Project. <sup>®</sup> library for the finite element computation. CustEM uses in particular the parallel solver mumps, and can be launched in parallel with MPI. The modeling work is realized in three steps:

1. the creation of the mesh (creation of a surface with flexible topography, locally refined at the transmitter and the receivers, inclusion of structures (cubes, plate) in the subsurface, and scaling of the mesh)
2. the computation of the fields, launched with mpi and based on the parallel solver mumps. The computation is made with polynomial interpolation functions of order 1 or 2. During the time of this work,

a total electric field approach was recommended instead of a total magnetic field approach for performance issues. However, the software is designed to allow both total and secondary fields approach for the electric and magnetic fields, as well as a gauged-potential approach. The secondary field approach is reserved to flat topography models with 1D structures.

3. the export of the computed responses at the chosen frequencies, stored in binary files.

CustEM can ensure a good accuracy for frequencies below 10 kHz, which is the usual high frequency limit of our CSAMT surveys.

**ModEM: computation of the MT response:** ModEM is a 3D finite volume modeling software designed and developed initially at the Oregon State University (Egbert and Kelbert [2012], Kelbert et al. [2014]), later on commercialized to private contractors but kept freely available for academic applications. This software allows an accurate modeling and inversion of MT data in a flexible range of environments (3D, topography). As the free version only permit a finite element modeling, it is to be noted that the thin description of rough topographic variations implies the use of very heavy grids. Practically, ModEM computes the induction response to a plane wave signal in terms of full impedance tensor and tipper.

Technical developments concerning the CSAMT method were realized as part of this doctoral work. This chapter presents and details the measurement and processing methodology developed. Numerical modeling aspects are discussed, and some general synthetic tests are presented.

## 2.2.6 Validity of CSAMT in some exemplary cases: numerical modeling tests

In this section, the numerical modeling software CustEM is used to demonstrate a few general and interesting results regarding the CSAMT method. The influence of the conductivity below the transmitting dipole, and the influence of topography are evaluated and discussed. To do so, the electric and magnetic fields produced by a large electrical dipole were computed in each configurations, and the Cagniard formula was systematically applied to the measured fields at locally refined stations. Responses were computed for 14 to 15 frequencies regularly log-spaced from 25 Hz to 15 kHz.

### Influence of the transmitter site on the near field and far field signal

For this test, an horizontal dipole of 200 m in the x direction was modeled on

1. an homogeneous half-space at 500  $\Omega.m$
2. the same homogeneous half space as in 1. with a large cubic anomaly located 20 m below the surface, of size [x=2000 m, y=1000 m, z=1980 m] and of resistivity 2000  $\Omega.m$
3. the same half space with the same anomaly as in 2., but with an anomaly-resistivity of 50  $\Omega.m$

The computation was realized from 2500 to 3500 m away from the source, so that each station would record both far field and near field data ( $\delta_{min} \approx 90m$ ,  $\delta_{max} \approx 2250m$ ), with a station modeled every 50 m (fig. 2.17).

The apparent resistivity curves (fig. 2.18) showed 3 important observations:

1. As expected, the near field / far field transition frequency is independent of the resistivity below the transmitter
2. As expected, the resistivity bellow the transmitter does not influence the far field apparent resistivity, but influences a lot the near field apparent resistivity.
3. In fact, the far field / near field transition is difficult to detect as soon as the resistivity near the transmitter varies from the resistivity at the site, because then, the near field part of the curve is not a straight slope.
4. A sort of resonance is observable at the transition between near field and far field, that seems decreased when the resistivity at the transmitter is low, increasing the stability of the resistivity estimation near the transition frequency.

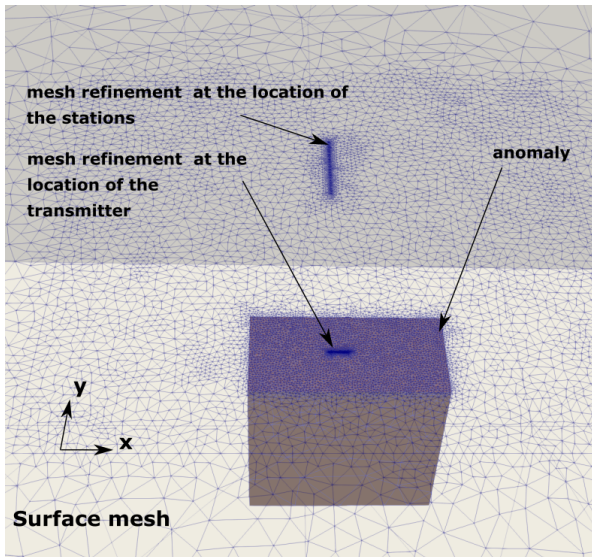


Figure 2.17: Computation mesh used to evaluate the influence of the resistivity at the transmitter location on the apparent resistivity curve

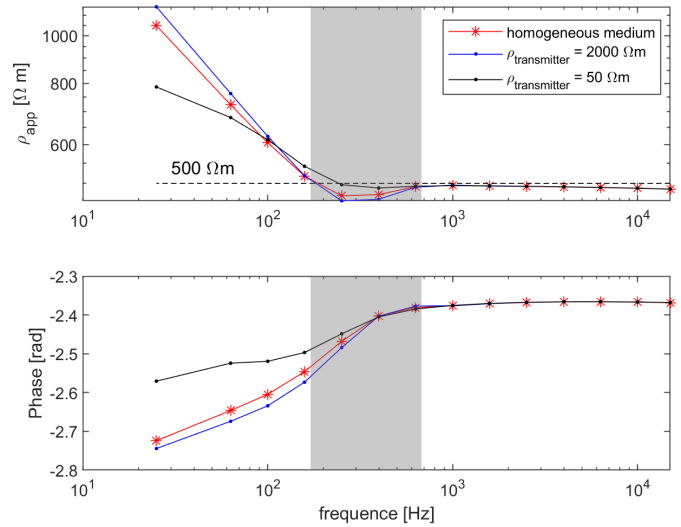


Figure 2.18: Apparent resistivity curves computed with the Cagniard formula for three different cases of resistivity at the location of the transmitter. The limit of the far field is around 700 Hz. In the far field, The resistivity of the ground at the location of the transmitter influences the apparent resistivity only below the far field limit around 700 Hz, as expected by the CSAMT theory.

### Influence of the topography in the propagative processes

The propagation of the signal from transmitter to receiver is expected to be influenced by the surface topography, inducing distortion in the data. To evaluate this effect, far field CSAMT data were computed on a synthetic model affected by a 2D topography. A 200 m long transmitting dipole was modeled, oriented in the y direction. A wavy topography was modeled in the x direction, from 1000 to 6000 away from the transmitting dipole, depicting two small hills of 600 m height (fig.2.20). The grounds resistivity was set constant at 500  $\Omega$ .m. Estimation of the electric and magnetic field were realized from 6000 to 9700 m away from the source, on the other side of the "hills", with one refined "station" every 50 m. As a control test, the same computation was realized on an equivalent synthetic setup, modeling this time a flat homogeneous space at 500  $\Omega$ .m (fig. 2.19).

The synthetic apparent resistivity curves are shown in fig. 2.20 at three of the modeled station, located at the foot of the hill and 1850 m and 3700 m away from the foot of the hill. Distortion are observed in most station, are the most severe at the stations close to the foot of the hill and do not completely vanish far from the hills. But as the effect close to the hills particularly affects the low frequencies, the effect at the most remote stations only affect the highest frequencies.

### Influence of the topography in the diffusive processes

The topography below the station is assumed to impact the diffusive process, causing distortion in the apparent resistivity curves. [Árnason \[2015\]](#) argued that severe topography can cause static distortion in the AMT and MT data, sometimes difficult to depict. In the following test, a 2D topographic profile was modeled, assuming for a local flat earth at the location of each modeled station (the horizontal components of the electric and magnetic fields are considered) (fig. 2.21).

The following observations were made:

1. No static effect was observed, but rather a frequency dependant effect. The topography affects not only the apparent resistivity, but the phase shift as well.
2. The effect seems very distinctive regarding the location of the station in the topography: foot of a hill

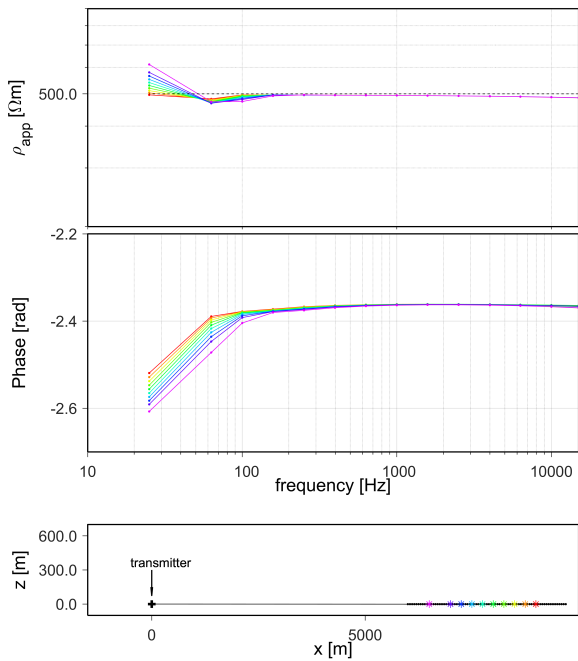


Figure 2.19: Synthetic apparent resistivity and phase curves at ten stations at 6500 to 9000 m from the transmitter on a flat homogeneous earth ( $500 \Omega.m$ )

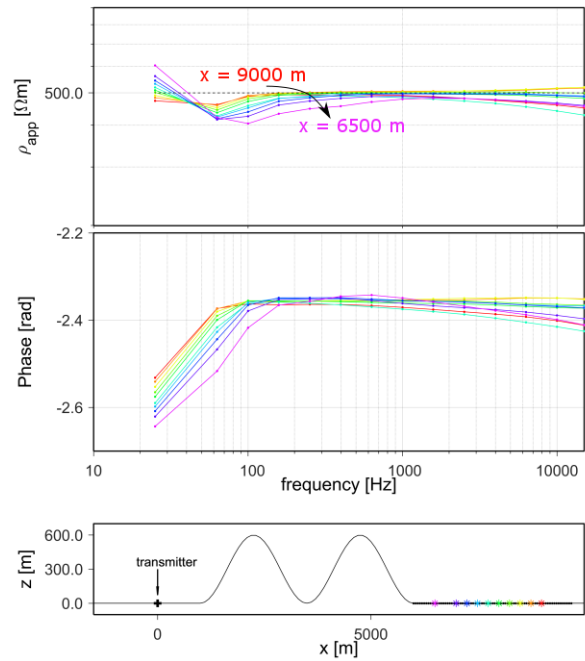


Figure 2.20: Propagative topographic effect: synthetic apparent resistivity and phase curves at 6500 to 9000 m from the transmitter on a homogeneous earth ( $500 \Omega.m$ ) affected by topographic changes in the area between the transmitter and the stations

- (green - orange shading), at the middle of a slope (blue shading) or close to the summits (pinkish shading)
- 3. At high frequency the summit and valley stations seem more affected. At low frequency, all stations are more or less affected.
- 4. In comparison with the previous test, the diffusive effect seem to be of much more importance than the propagative effect (more than 40 % error for the diffusive effect against maximum 20 % for the propagative effect)

Because the modeled topography has locally a certain slope, an additional test was made, considering this time the components tangential to the surface topography to compute the apparent resistivity curves (magnetic field oriented along the slope: fig. 2.22). Considering the tangential fields in the computation makes more sense regarding the theory of MT, where the earth surface has the effect of orienting any incident plane wave in the direction normal to local surface interface, hence where the fields tangential to the surface will carry the MT information. This test is expected to provide a different estimation of apparent resistivities regarding fig. 2.21 for the stations along the slopes: in blue shadings.

We can observe that this new computation mainly influences the middle blue station, noted  $S_x$  in fig. 2.21. For this station, the apparent resistivity increases a lot at low frequency, probably impacted by diffusive process that were initiated on the first size of the hill, noted 'Slope 1', adding a signal not accounted for in the MT theory. The absence of such signal at high frequency is explained by the fact that the skin depth, lower at higher frequency, causes the diffusive signal to vanish away from the surface 'Slope 1', hence on the other size of the hill. This low frequency distortion should be nonexistent in the case of a hill of much larger width.

### Discussion on the possibilities of correcting CSAMT data from topographic distortions

As shown in the previous paragraphs, the topographic distortion in CSAMT is two folds, provoked both in the propagation of the EM signal in the air, along the surface topography and in the diffusive processed. Both effects affect the electric and magnetic fields. Several possibilities exist to get rid of such unwanted effects. The first

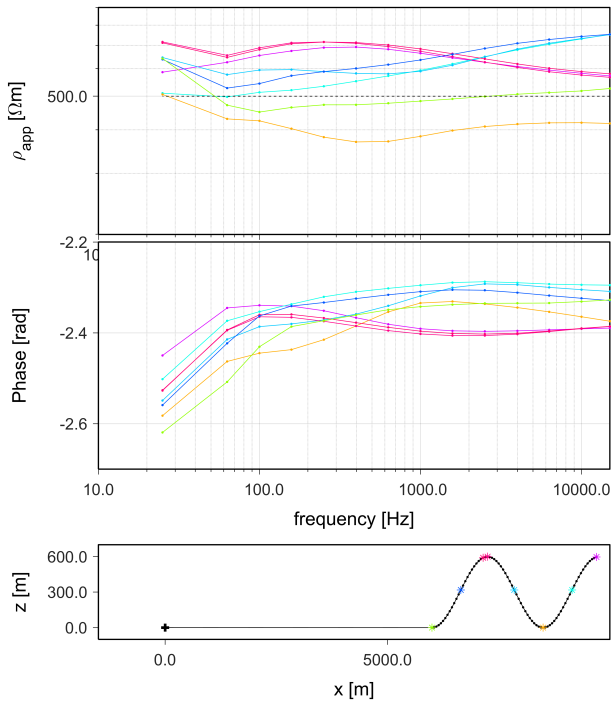


Figure 2.21: Diffusive topographic effect: synthetic apparent resistivity and phase curves at 7 stations at 6500 to 9000 m from the transmitter on a homogeneous earth ( $500 \Omega.m$ ) affected by topographic changes in the area between the transmitter and the stations

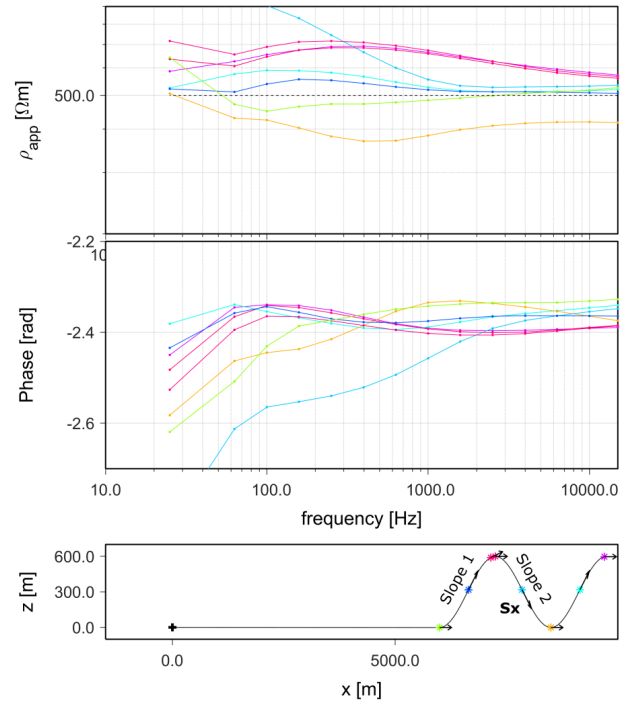


Figure 2.22: Diffusive topographic effect: synthetic apparent resistivity and phase curves computed with the components of the electric and magnetic fields tangential to the local surface topography

one is a correction of the apparent data, by applying a correction coefficient obtained with specific strategies based on numerical modeling. The second possibility is to model the topography and take it into account in the data inversion, updating the topographic effect as the iterative inversion goes on (Lin et al. [2018]). The second methodology is clearly more accurate, because the topographic effect will be progressively better determined as the inverted model gets closer and closer to the true model (at least in the good inversion scenario). It however requires a 3D inversion forward modeling with modeling of the transmitter in the inversion scheme.

## 2.2.7 Challenges in CSAMT

There are four challenges associated to the use of CSAMT in this work. The first challenge is the one of the observation of a signals related to the hydrogeology and the presence of water. The resistivity contrasts are not always expected to be very important.

Besides, the use of CSAMT in this work is always related to an assumption of pseudo-1D dimensionality of the subsurface. The methodology developed strongly relies on the validity of this assumption. Related to this second dimensionality challenge, the validity of the method in case of strong topography is explored, as well as the possibilities of correcting from topographic effects.

Third, the realization of CSAMT surveys in mountainous environments brings forth the challenge of finding reasonable source location.

Last, the challenge of time-lapse measurements is addressed. Being sensitive the 1-D variations related to small changes of water height in a layer located around 35 m depth requires very low noise levels, and, more importantly, requires to ensure that the variations of apparent resistivity observed are well related to local changes, and are not to be attributed to changes of the transmitting signal for example, or change in topographic effect.

Fig. 2.23.a illustrates the application of CSAMT to the location of groundwater, through the example of the study from Wynn et al. [2016]. Two areas of decreased resistivity are identified in the 1D inverted CSAMT model as two aquifers. Fig. 2.23.b presents the results from a 2D time-lapse CSAMT study by Falgàs et al. [2006], one of

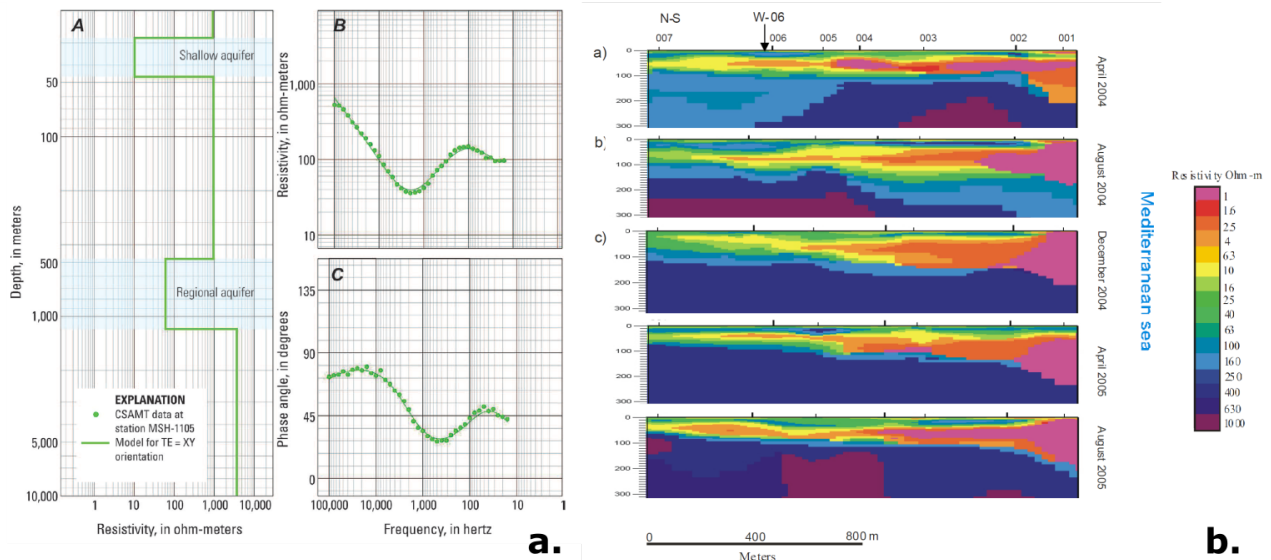


Figure 2.23: Applications of CSAMT to hydrogeological studies; a. from Wynn et al. [2016], 1D CSAMT sounding and inverted resistivity model permitting the location of two superposed water reservoirs; b. Time-lapse CSAMT study by Falgàs et al. [2006] to evaluate the evolution of salt water intrusion in a coastal aquifer system

the few time-lapse CSAMT studies found in the literature, to monitor the evolution of an intrusion of salt water in a coastal aquifer. This two two exemplary studies depict the possible use of CSAMT in hydrogeophysics.

## 2.3 Presentation and use of DC and IP methods in this thesis

### 2.3.1 Electrical Resistivity Tomography

#### Invention and first applications

The electrical method was invented at the beginning of the twentieth century when Conrad Schlumberger successfully applied, in 1912, a method imagined and formalized simultaneously by several geophysicists. C. Schlumberger realized surface maps of equipotential curves produced when injecting a current in the ground between two grounded electrodes, using potentiometers, galvanometer, or even a ringing phone, indicating when the two measurement points were at the same potential.

At the early stage of the technique, the anomalies were detected through the abnormal form of the equipotential curves regarding the theoretical equipotentials of a layered half space. The method was limited to the detection of an abnormal body in a 1D layered earth, and the surface topography and water content were influencing drastically the measurements.

#### Basis of the method

The Electrical Resistivity Tomography (ERT) method consists in mapping the variations of the electrical potential generated at the surface of the earth when applying a voltage difference between two points at the earth surface. These variations of electrical potential at the surface results from the distribution of objects of variable electrical resistivity and structure (layers, intrusion, fissures, fluid reservoirs, etc.) in the subsurface.

#### Measurement techniques

An ERT survey is composed of a set of measurements of apparent resistivity values attributed to intersected volumes of sensitivity. Each of these measurements are realized using a specific quadrupole composed of two injection electrodes and two potential electrodes (chapter 1). The measurement array designate the set of

quadrupoles successively used in the survey.

- **Resolution, depth of investigation and lateral extent of a survey**

The sensitivity in ERT depends mainly on the resistivity distribution in the subsurface. For example, the injected current will preferentially flow in the conductive layers, increasing the sensitivity to conductive layers. In addition, the presence of a resistant layer close to the surface tends to reduce the possibilities of injecting a high current intensity in the ground, reducing the possibilities of current flow in deeper layers.

The depth of investigation of an ERT measurement is additionally controlled by the geometry of the quadrupole (distance between the two potential electrodes and the two injection electrodes). The depth of investigation of a survey is therefore related to the lateral extent of the measurement setup. The resolution of a measurement as well depends on the geometry of the quadrupole. The overall resolution, lateral and vertical extent of the resistivity model depends on the measurement array used in the survey.

- **2D measurements**

In the most usual case, the measurements are taken by aligning the electrodes along a profile, which permits to realize '2-dimensional' profiles: such measurements are sensitive to variations of the electrical resistivity in the direction of the profile, and require that the structure are of infinite extension laterally from the profile. This measurement technique was enabled and favored by the successful development of multi-channels instruments and the use of multi-core cables to connect sets of aligned electrodes to the instrument.

In 2D-ERT, there exists a few typical measurement arrays with specific sensitivity characteristics, that constitute a guideline for ERT field measurements. For example, the dipole-dipole array consists in keeping constant, equal and small the distances between the potential electrodes and between the current electrodes, and scanning the profile by changing the location of both couples of electrodes. The multiple gradient array consists in injecting the current between two electrodes relatively distant from one another, and placing successively the potential electrodes at different locations in the area in between the injection electrodes.

- **3D measurements**

Lately, research and development were made into developing setups to obtain good 3D sensitivity. Three types of setup can roughly be distinguished in the literature:

1. The pseudo-3D characterization consists in the successive realisation of a large number of overlapping or parallel 2D profiles over the studied area and to interpret and invert them together to permit the computation of a 3D model (Uhlenmann et al. [2017]).
2. Maurya et al. [2017] proposed a methodology to realize full 3D measurements, involving a set of profiles installed in parallel, all successively connected by half to the main instrument by the use of switch-boxes. This setup allowed to gain sensitivity in the direction orthogonal to the profiles regarding pseudo-3D methods by the use of non-aligned quadrupoles (fig. 2.24). Maurya et al. [2017] used this device for the DCIP characterization of contamination plumes over surfaces of  $m^2$ , reaching depth on penetrations of 45 to 50 m.
3. The use of distributed antennas or measurements nodes, common in seismology and in CSEM methods, allows the realization of a full 3D characterization, without constraints on the distribution of sensors. This type of setup presents the huge advantage of liberating the field operators from the heaviness of large multi-core cables, enabling a large scale deployment and allowing measurements in areas with local limited access (example of IRIS Instruments<sup>©</sup> Fullwaver system in fig. 2.25).

## Challenges

The electrical method has been extensively developed since it was first used, a hundred of years ago. The latest developments to be noticed in ERT imagery are 1/ the development of measurement methodologies to allow for 3 dimensional surveys at different scales, and 2/ the related developments of software to permit the modeling and inversion of DC resistivity measurements on various type of objects (from finite size laboratory samples and laboratory experimental setups to complex subsurface affected by topography). Nowadays, the development of multi-channels instruments allow easy and fast measurements in most field contexts.

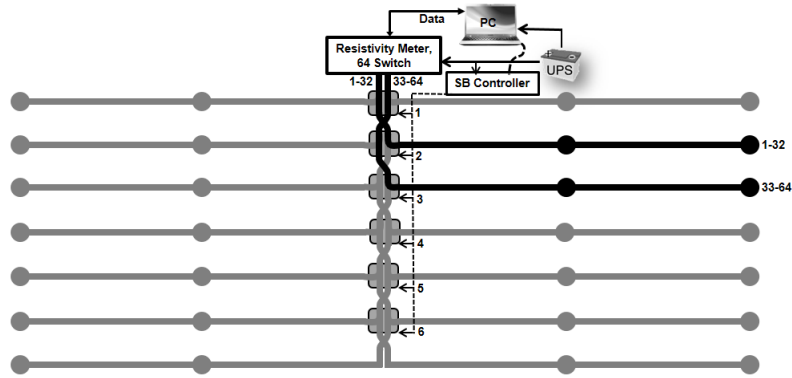


Figure 2.24: Principle of 3D DCIP measurement from Maurya et al. [2017]: a set of ERT profiles are installed in parallel and connected to the device through switch boxes separating each profiles into two parts. In this way, all electrodes of a quadrupole do not necessarily belong to the same profile, providing a 3D sensitivity

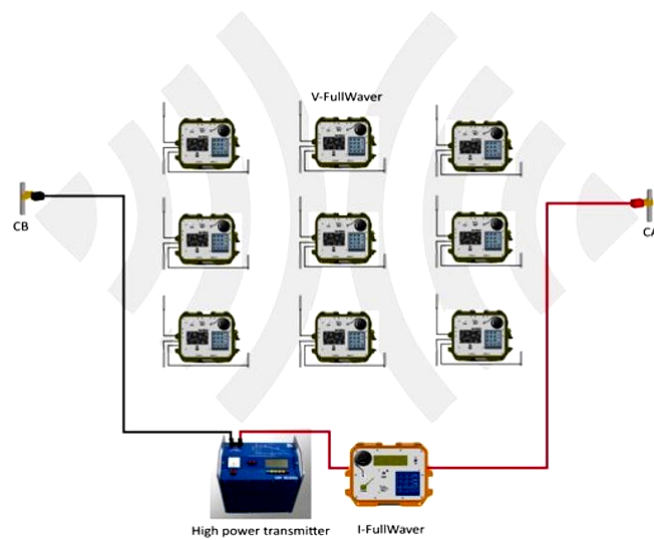


Figure 2.25: Principal of use of IRIS Instruments FullWaver systems: each independent unit (node) records the electrical voltage at the terminals of two orthogonal dipoles. The transmitter and receivers are all synchronized by GPS - IRIS Instruments

3D surveys are increasingly realized, particularly in the field of hydrogeophysics. However, such studies so far were based on multi-channel instruments, limiting the spatial extend of the surveys. Nevertheless, 3D ERT provided very informative resistivity models in numerous cases. Figure 2.26 presents for example the 3D resistivity model obtained by Maurya et al. [2017] in the study of a contamination plume in a shallow aquifer, due to the storage of waste in a landfill.

**Large scale ERT and important DOI:** The characterization of the subsurface electrical resistivity over a large surface area is still quite rare, because until now, the size of the ERT surveys are often limited by the limited length and heaviness of multi-core cables (fig. 2.25). For the same reason, the depths of investigation of ERT surveys rarely exceed 100 m depth, and most of the time focus on the first 30 to 50 m of the subsurface.

**Topography:** Conducting ERT studies in environments presenting rough topographic variations presents a double challenge: it makes the survey difficult, some areas being difficult to reach and to equip and it makes the data modeling difficult, requiring the use of flexible computation meshes.

The recent development of modeling and inversion software provided adaptable modeling possibilities, al-

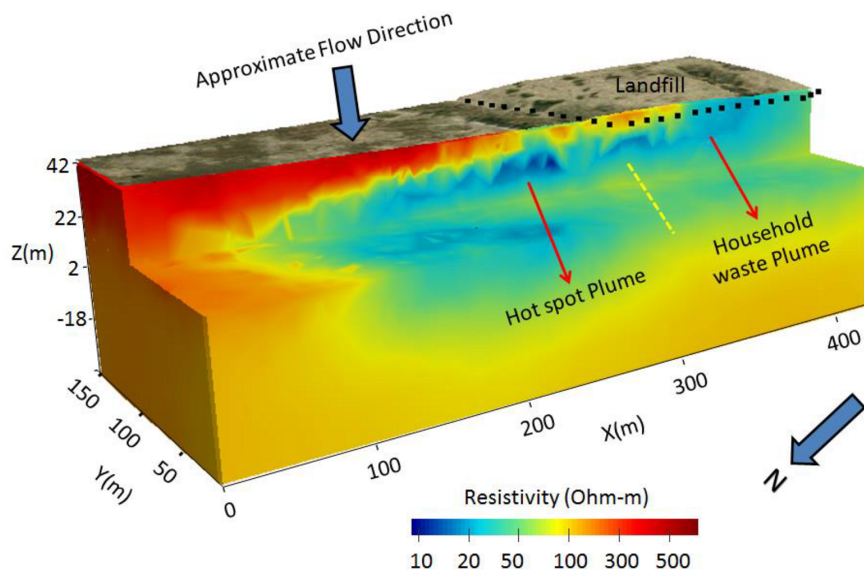


Figure 2.26: 3D resistivity model obtained by [Maurya et al. \[2017\]](#) to locate the contamination of a shallow aquifer related to the storage of waste in a landfill - from [Maurya et al. \[2017\]](#)

lowing to run the computations on flexible meshes, modeling of unconventional electrodes array and accounting for topographic variations (For example BERT, PyGimli, Res3DInv).

**The Resistivity-Distributed Automated Systems: IRIS Instruments Fullwaver systems:** Recently, the company IRIS Instruments developed a new equipment to realize 3D survey both in ERT and TDIP. The instrument rely on nodes measurements of the potential, using a network of GPS-synchronized portable units. This measurement methodology is referred to as "Resistivity - Distributed Automated Systems": R-DAS and is schematically presented in fig. 2.25.

## 2.3.2 Induced Polarization

### Discovery and first applications

While surveying a site searching for ore deposits, Conrad Schlumberger observed that the electrical potential induced in the subsurface by the circulation of the input current did not go instantaneously to zero as the input current was shut down. Instead, it turned to a small percentage of the potential induced during injection, then decreased more or less slowly. C. Schlumberger identified this phenomenon as polarization process. First considered as a noise, this induced polarization turned into a new exploration method, as it was recognized to provide valuable information, particularly in the research of minerals.

### Polarization phenomena in the subsoil

Three different types of polarization occur in the subsurface.

The first process is the one discovered initially by C. Schlumberger: the metal-polarization, also referred to as 'electrode polarization'. This polarization is lead by the presence of metal minerals in the subsurface and is produced by the interaction between two conductive bodies presenting different conduction processes. When a metal grain is in a pore filled with fluid, the conduction in the fluid, which is an electrolytic conduction, will occur at a different timescale than the conduction in the metal mineral, which is an electronic conduction (circulation of free charges in the mineral). This difference of conduction will lead to the accumulation of charges at the fluid/grain interface, producing a polarization signal in particular after the current turnoff, or, similarly,

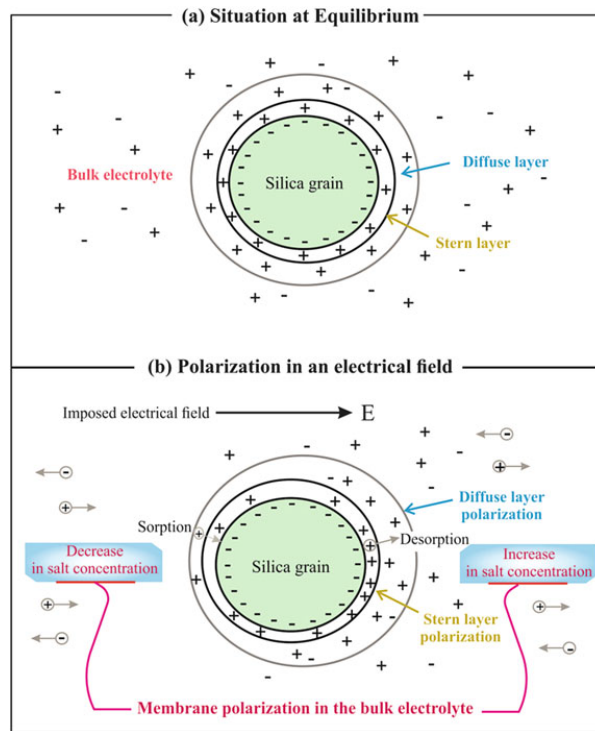


Figure 2.27: Schematic of the polarization of the electrical double layer at the surface of silicate grains (membrane polarization) - from Attwa and Ali [2018]

a delay in the restitution of energy.

A second polarization phenomenon can occur in the presence of clay particles in a fluid saturated rock. It is called the membrane polarization. Clay minerals are constituted of silicate ions (for example:  $(Si_2O_7)^{6-}$ ) and the electro-neutrality of clay mineral is ensured by the adsorption of ions ( $H^+$  for example). This adsorption leads to a very specific electronic structure at the interface of the clay minerals: the double or triple electronic layers (fig. 2.27.a). When a current flows through the rock material, the potential applied will disturb the structure of the double layer, as in fig. 2.27.b, producing, after the current turnoff, a polarization signal (Okay et al. [2014]).

The last type of polarization is referred to as Maxwell-Wagner polarization, or interface polarization and occur generally at the interface of two bodies of different electrical and dielectric properties (insulating body vs conducting body), where charges will accumulate when applying a potential difference between two points in the ground.

### Interpretation of the IP information

Induced polarization in the subsurface is a complex phenomenon, that incorporates different phenomena. The usual procedure when interpreting the IP information is to extract the modulus and the phase of the data, or, quasi-equivalently the real and imaginary part of the data. In a general manner, one considers that the modulus is dominated by the conduction processes (conduction in the pore fluid) and the phase relates to the surface conduction processes, the polarization at grain/fluid interface.

### Mathematical modeling

The polarization of a material is physically described as a complex impedance, and a spectral extension of the apparent resistivity. The resistivity of the medium is no longer a static real value, but is a complex value, dynamic as it depends on the frequency of the input signal. When the frequency tends to the DC limit, the

amplitude of the complex resistivity tends to the classical resistivity (DC resistivity), and the phase tends to zero (see Cole-Cole model, fig. 2.28). The complex resistivity is usually studied from  $10^{-3}$  Hz to  $10^4$  Hz (Kemna et al. [2012]).

There are many ways to describe and model the polarizable behavior of a medium.

A usual way to proceed with field induced polarization (IP) data is to choose one of the existing analytical models, and to estimate its parameters by means of data inversion. Notwithstanding the lack of a clear physical meaning, analytical models offer an intermediate interpretation tool to identify the link between an IP signal, and the geological, structural or geochemical characteristics of the ground.

The Cole-Cole model is a 4-parameters description (eq. 6.1, fig. 2.28), allowing generally a close fit to the measured signal. The Constant Phase Angle (CPA) model involves only 2 parameters (eq. 2.39), providing as unique polarization variable the phase shift of the complex resistivity. Those models are two prevailing analytical descriptions of the complex resistivity spectrum, used for both frequency domain (FD) and time domain (TD) modeling. Recently, the maximum phase angle model was proposed by Fiandaca et al. [2018].

$$\zeta_{\text{Cole-Cole}} = \rho \left( 1 - m_0 \left( 1 - \frac{1}{1 + i\omega\tau} \right) \right) \quad (2.38)$$

$$\zeta_{\text{CPA}} = K(i\omega)^{-b} \quad (2.39)$$

Even though the Cole-Cole model is often successful to describe induced polarization data-sets, the parameters involved in the model do not have a clear physical meanings. The Cole-Cole model, as any other phenomenological model, does not ensure to represent every type of polarization, and could, for this reason, bias the interpretation (Florsch et al. [2012]). The simplicity represented in such canonical models do not picture well the high variety of polarization in rock materials.

For this reason, other methods have been proposed to describe the polarization signal. For example, Florsch et al. [2012] proposed to fit the data to a distribution of the relaxation times, as it was identified to be closely related to the distribution of grain-size (Revil and Florsch [2010]).

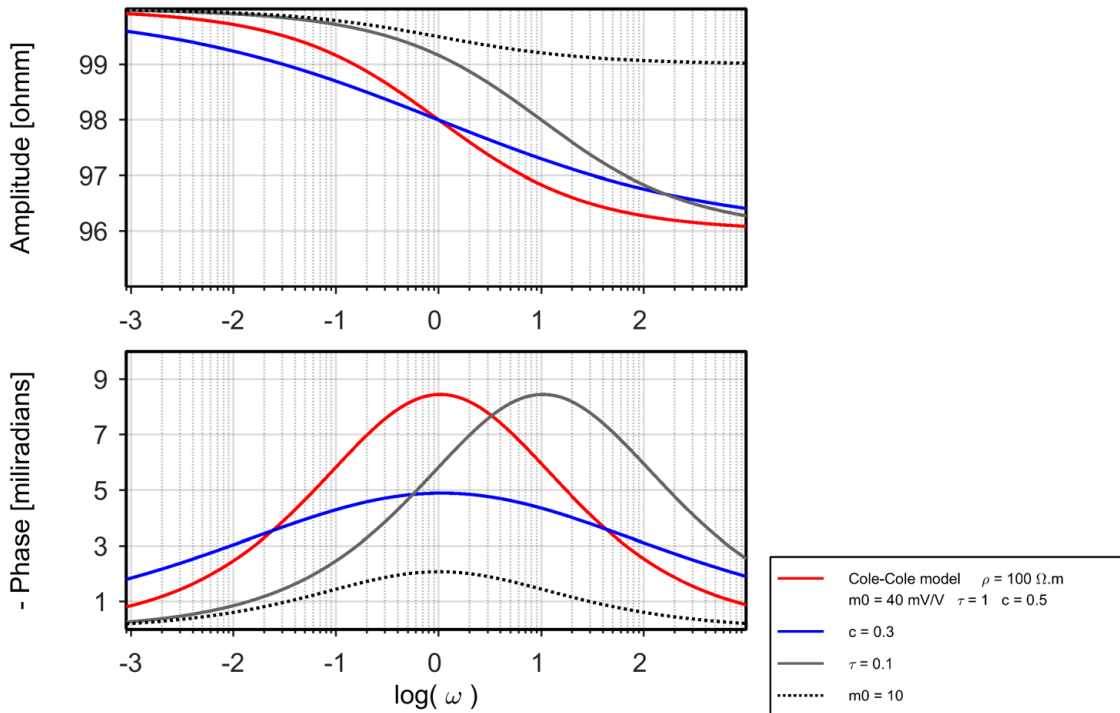


Figure 2.28: Amplitude and negative phase IP spectrum of four different Cole-Cole models; the red curve is the reference model and the three other curves present the effect of changing, one by one, each parameter of the model

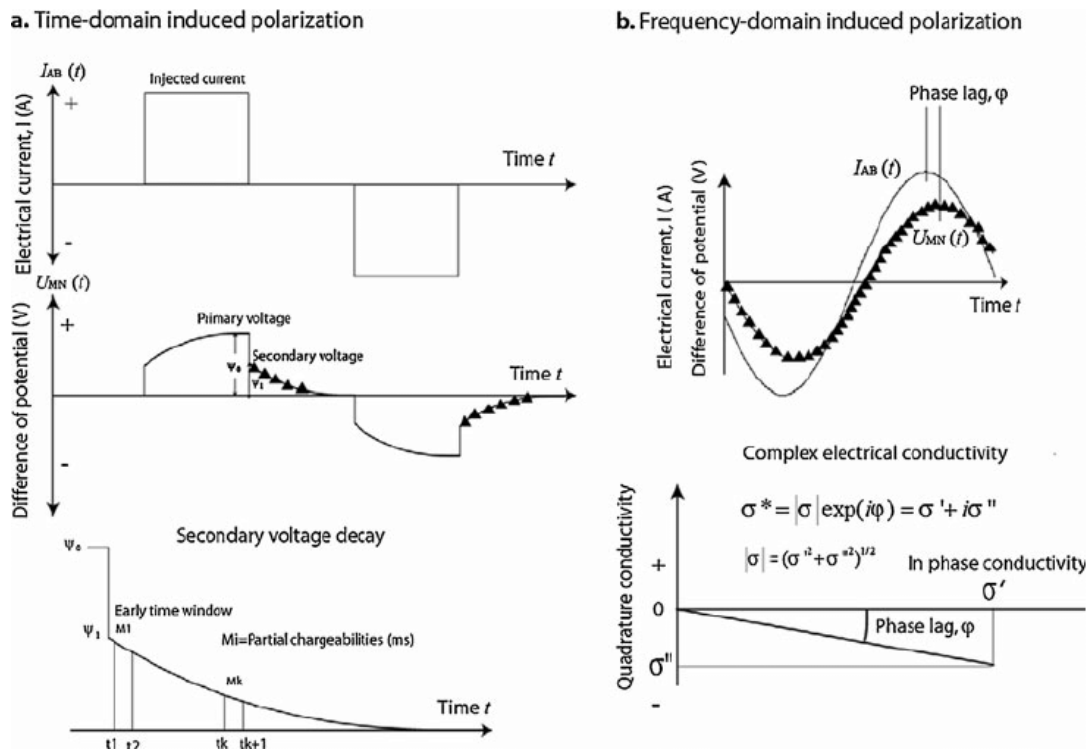


Figure 2.29: Time domain and frequency domain measurements techniques of the induced polarization - from [Revil et al. \[2012\]](#)

Laboratory experiments are often associated to the field measurements to identify the polarization response of different known units and to understand how variation of properties of interest (porosity, size of grain, temperature of water, etc.) can influence the IP response.

### Field methodology

#### Time domain and frequency domain measurements:

In time domain (TDIP), the induced polarization results in a transient response after any change of regime (from off to on, for example) of a galvanically induced current. In the frequency domain, it results in a phase shift in the steady electrical response to an induced current alternating periodically (fig. 2.29).

The setup used to realize induced polarization measurements is similar to the one used in ERT. A set of current and injection electrodes are grounded to the soil, and a set of spatialized measurements are realized successively considering different quadrupoles and following specific measurement arrays (Wenner - Schlumberger, multiple-gradient, dipole-dipole, pole-dipole, etc.).

The measurement of the induced polarization can be realized in the time-domain, or in the frequency domain. The time-domain measurements consist in measuring the transient response after turning off the injected current. Typically, the injected current is a windowed current, often 50% duty cycle (fig. 2.29), allowing among other an easy filtering for transient passive phenomena inducing noise (self potential). The measured decay curves can be windowed and transformed to the spectral domain to obtain the complex resistivity transfer function. Another method is to compute the integral chargeability (air below the decay curve) and to convert it into a value analogue to a phase shift. A full spectrum cannot be obtained, but the polarization is rather used to bring a new parameter in the imaging and characterization of the subsurface.

The frequency domain measurement (SIP for spectral IP) consists in the injection of periodically alternating current, at various frequency, the amplitude and phase shift of the response is then measured, for each input frequency (fig. 2.29) and the transfer function of the complex resistivity can directly be plotted, point by point.

**Common sources of noise in IP:** The measurement of the induced polarization is subject to two major noise sources.

- When realizing measurements at low frequencies (below 1 Hz), a phenomenon of polarization occurs at the surface of metallic potential electrodes, that pollute the data. To resolve this issue, unpolarizable electrodes are used, consisting in porous pot (ceramic) filed with an electrolyte in which a solid electrode dives, connected to the measurement wire. [Petiau and Dupis \[1980\]](#). Instead of a single-step contact made between two elements of contrasting resistivity (the metal electrode and the soil), provoking the polarization, the contact is made in two steps: first between the metal and the electrolyte and then between the electrolyte and the soil. In this second contact, the use of a fluid maximizes the contact surface area with the soil, reducing the potential of accumulation of charges at this soil/ fluid contact.
- At frequency above 1 Hz, the EM coupling effect is expected to distort significantly the IP measurements. This effect comes mainly from the mutual inductance (cross-talk) between the cables. It is favored by the use of long cables, hence by large electrodes spacing. For a specific array, this effect increases linearly with the frequency. It is possible to reduce it by separating the cables as much as possible or limiting the length of the electrode array, or by using specific cables-arrangements ([Schmutz et al. \[2014\]](#) or Fullwaver systems). Another methodology consists in modeling this effect and to correct the data from it, or to account for this effect in the inversion ([Ghorbani et al. \[2009\]](#)).

**Time-domain IP - full decay analysis versus integrated chargeability:** To characterize fully the polarization response of the different units constituting the subsurface, multi-frequency estimation of the polarization transfer function must be obtained. To do so, either frequency domain measurements, or full decay analysis of time-domain IP data must be recorded. Analysis of core samples and granulometry information can also be used in an attempt at interpreting precisely the IP information in terms of microstructure and poral content.

Nevertheless, a full characterization is not necessarily required, and the IP method can be used at a single frequency, providing an additionnal parameter to image the surface, and to possibly detect anomalous objects. When the full decay curve is not well sampled, and that the correct filters are not applied to the curve, only a small part of it can be retrieved. In such context, the significant part of the spectrum usually retrieved from full wave data cannot be obtained, and strong assumptions must be made. If the response is expected to be close to a constant phase angle response, one can compute the parameters of the constant phase angle model, and interpret them. If not, the integral chargeability can be converted into a unique phase, by following [Kemna et al. \[1997\]](#). The information carried by the data cannot be interpreted as full IP behavior, but rather as a sampling of the response at one frequency. Either complementary data can allow to locate this response in a more complete IP information (for example: timelapse TDIP measure interpreted at the light of a full SIP survey at one time period). If not, then the IP information permits exclusively a different "lightning" of the subsurface, taking advantage of an extra parameter regarding a DC resistivity survey.

## Challenges

In the context of this thesis, the IP method is considered in the context of deep sedimentary layered aquifers. The challenge resides in the sensitivity at depth (30 to 80 m) and the ability to 1/ distinguish the different units stacked at these depths, with various clay content and local high evaporites content. 2/ deploying a time-lapse methodology, to allow observing the variations of water height and possible water/rock interactions.

The first point requires high signal to noise ratio, and depends highly on the properties of the subsurface. In a similar context of clay-rich landslides, [Gallistl et al. \[2018\]](#) presents an extensive joint IP and EMI methodology, adequate for shallow applications (first 20 m). Fig. 2.30 shows one of the resulting figures of the survey, where the sliding plane is delineated both by the increase in real and complex conductivity. In their study, [Gallistl et al. \[2018\]](#) note the high sensibility of the imaginary part of the conductivity to the size of clay particles.

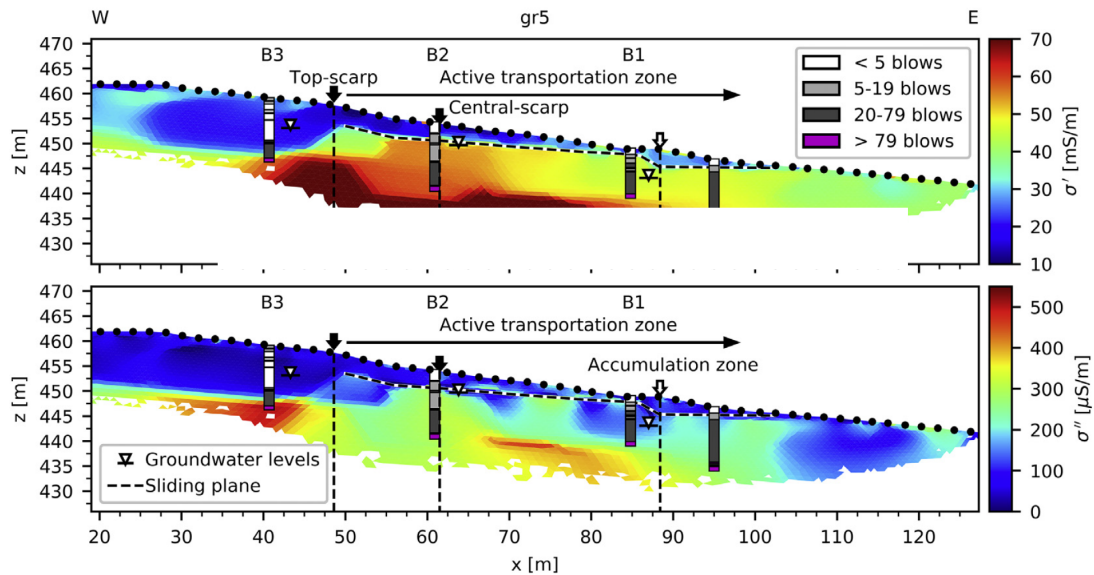


Figure 2.30: TDIP study of a clayey landslide from Gallistl et al. [2018]: real conductivity profile (top) and imaginary conductivity profile (bottom)

## 2.4 References

- Anderson, W. L. (1979). Numerical integration of related hankel transforms of orders 0 and 1 by adaptive digital filtering. *Geophysics*, 44(7):1287–1305.
- Árnason, K. (2015). The static shift problem in MT soundings. In *Proceedings world geothermal congress*.
- Attwa, M. and Ali, H. (2018). Resistivity characterization of aquifer in coastal semiarid areas: An approach for hydrogeological evaluation. In *Groundwater in the Nile Delta*, pages 213–233. Springer.
- Bannister, P. R. (1966). Quasi-static fields of dipole antennas at the earth's surface. *Radio Science*, 1(11):1321–1332.
- Bartel, L. and Jacobson, R. (1987). Results of a controlled-source audiofrequency magnetotelluric survey at the Puhimau thermal area, Kilauea volcano, Hawaii. *Geophysics*, 52(5):665–677.
- Boerner, D. E., Kurtz, R. D., and Jones, A. G. (1993). Orthogonality in CSAMT and MT measurements. *Geophysics*, 58(7):924–934.
- Cagniard, L. (1953). Basic theory of the magneto-telluric method of geophysical prospecting. *Geophysics*, 18(3):605–635.
- Delhaye, R., Rath, V., Jones, A. G., Muller, M. R., and Reay, D. (2017). Correcting for static shift of magnetotelluric data with airborne electromagnetic measurements: a case study from Rathlin basin, northern Ireland. *Solid Earth*, 8(3):637.
- Egbert, G. D. and Kelbert, A. (2012). Computational recipes for electromagnetic inverse problems. *Geophysical Journal International*, 189(1):251–267.
- Falgàs, E., Ledo, J., Benjumea, B., Queralt, P., Marcuello, A., Teixidó, T., and Arango, C. (2006). Imaging ground water resources of a mediterranean coastal aquifer using seismic and csamt data. In *Symposium on the Application of Geophysics to Engineering and Environmental Problems 2006*, pages 863–870. Society of Exploration Geophysicists.
- Falgàs, E., Marquis, G., Sailhac, P., Ledo, J., Queralt, P., and Béhaegel, M. (2005). Aquifer imaging using csamt and ert. In *Near Surface 2005-11th European Meeting of Environmental and Engineering Geophysics*, pages cp–13. European Association of Geoscientists & Engineers.
- Fiandaca, G., Madsen, L. M., and Maurya, P. K. (2018). Re-parameterisations of the Cole–Cole model for improved spectral inversion of induced polarization data. *Near Surface Geophysics*, 16(4):385–399.
- Florsch, N., Camerlynck, C., and Revil, A. (2012). Direct estimation of the distribution of relaxation times from induced-polarization spectra using a Fourier transform analysis. *Near Surface Geophysics*, 10(6):517–531.
- Gallistl, J., Weigand, M., Stumvoll, M., Ottowitz, D., Glade, T., and Orozco, A. F. (2018). Delineation of subsurface variability in clay-rich landslides through spectral induced polarization imaging and electromagnetic methods. *Engineering*

- Geology*, 245:292–308.
- Ghorbani, A., Camerlynck, C., and Florsch, N. (2009). Cr1div: A Matlab program to invert 1d spectral induced polarization data for the Cole–Cole model including electromagnetic effects. *Computers & Geosciences*, 35(2):255–266.
- Goldstein, M. and Strangway, D. (1975). Audio-frequency magnetotellurics with a grounded electric dipole source. *Geophysics*, 40(4):669–683.
- Grant Caldwell, T., Bibby, H. M., and Brown, C. (2002). Controlled source apparent resistivity tensors and their relationship to the magnetotelluric impedance tensor. *Geophysical Journal International*, 151(3):755–770.
- Hanneson, J. and West, G. (1984). The horizontal loop electromagnetic response of a thin plate in a conductive earth: Part i—computational method. *Geophysics*, 49(4):411–420.
- Hohmann, G. W. (1975). Three-dimensional induced polarization and electromagnetic modeling. *Geophysics*, 40(2):309–324.
- Kalscheuer, T., Bastani, M., Donohue, S., Persson, L., Pfaffhuber, A. A., Reiser, F., and Ren, Z. (2013). Delineation of a quick clay zone at Smørgrav, Norway, with electromagnetic methods under geotechnical constraints. *Journal of Applied Geophysics*, 92:121–136.
- Kelbert, A., Meqbel, N., Egbert, G. D., and Tandon, K. (2014). Modem: A modular system for inversion of electromagnetic geophysical data. *Computers & Geosciences*, 66:40–53.
- Kemna, A., Binley, A., Cassiani, G., Niederleithinger, E., Revil, A., Slater, L., Williams, K. H., Orozco, A. F., Haegel, F.-H., Hördt, A., et al. (2012). An overview of the spectral induced polarization method for near-surface applications. *Near Surface Geophysics*, 10(6):453–468.
- Kemna, A., Räckers, E., and Binley, A. (1997). Application of complex resistivity tomography to field data from a kerosene-contaminated site. In *3rd EEGS Meeting*, pages cp–95. European Association of Geoscientists & Engineers.
- Kratzer, T. and Macnae, J. C. (2012). Induced polarization in airborne EM. *Geophysics*, 77(5):E317–E327.
- Lin, C., Tan, H., Wang, W., Tong, T., Peng, M., Wang, M., and Zeng, W. (2018). Three-dimensional inversion of CSAMT data in the presence of topography. *Exploration Geophysics*, 49(3):253–267.
- Maurya, P. K., Rønne, V., Fiandaca, G., Balbarini, N., Auken, E., Bjerg, P. L., and Christiansen, A. V. (2017). Detailed landfill leachate plume mapping using 2d and 3d electrical resistivity tomography—with correlation to ionic strength measured in screens. *Journal of Applied Geophysics*, 138:1–8.
- Okay, G., Leroy, P., Ghorbani, A., Cosenza, P., Camerlynck, C., Cabrera, J., Florsch, N., and Revil, A. (2014). Spectral induced polarization of clay-sand mixtures: Experiments and modeling. *Geophysics*, 79(6):E353–E375.
- Petiau, G. and Dupis, A. (1980). Noise, temperature coefficient, and long time stability of electrodes for telluric observations. *Geophysical Prospecting*, 28(5):792–804.
- Ren, Z., Kalscheuer, T., Greenhalgh, S., and Maurer, H. (2013). A goal-oriented adaptive finite-element approach for plane wave 3-d electromagnetic modelling. *Geophysical Journal International*, 194(2):700–718.
- Revil, A. and Florsch, N. (2010). Determination of permeability from spectral induced polarization in granular media. *Geophysical Journal International*, 181(3):1480–1498.
- Revil, A., Karaoulis, M., Johnson, T., and Kemna, A. (2012). Some low-frequency electrical methods for subsurface characterization and monitoring in hydrogeology. *Hydrogeology Journal*, 20(4):617–658.
- Rochlitz, R., Skibbe, N., and Günther, T. (2019). *custom*: Customizable finite-element simulation of complex controlled-source electromagnetic data. *Geophysics*, 84(2):F17–F33.
- Rodriguez, B. D., Stanley, W. D., and Williams, J. M. (1996). Axial structures within the Reelfoot rift delineated with magnetotelluric surveys. Technical report.
- Schmutz, M., Ghorbani, A., Vaudelet, P., and Blondel, A. (2014). Cable arrangement to reduce electromagnetic coupling effects in spectral-induced polarization studies—reducing EM coupling effects for SIP. *Geophysics*, 79(2):A1–A5.
- Singh, N. and Mogi, T. (2010). Emdpler: A f77 program for modeling the EM response of dipolar sources over the non-magnetic layer earth models. *Computers & Geosciences*, 36(4):430–440.
- Sternberg, B. K., Washburne, J. C., and Anderson, R. G. (1985). Investigation of MT static shift correction methods. In *SEG Technical Program Expanded Abstracts 1985*, pages 264–267. Society of Exploration Geophysicists.
- Streich, R., Becken, M., and Ritter, O. (2011). 2.5 d controlled-source EM modeling with general 3d source geometries.

*Geophysics*, 76(6):F387–F393.

Uhlemann, S., Chambers, J., Wilkinson, P., Maurer, H., Merritt, A., Meldrum, P., Kuras, O., Gunn, D., Smith, A., and Dijkstra, T. (2017). Four-dimensional imaging of moisture dynamics during landslide reactivation. *Journal of Geophysical Research: Earth Surface*, 122(1):398–418.

Unsworth, M. J., Lu, X., and Watts, M. D. (2000). Csamt exploration at Sellafield: Characterization of a potential radioactive waste disposal site. *Geophysics*, 65(4):1070–1079.

Ward, S. H. and Hohmann, G. W. (1988). Electromagnetic theory for geophysical applications. In *Electromagnetic Methods in Applied Geophysics: Volume 1, Theory*, pages 130–311. Society of Exploration Geophysicists.

Wynn, J., Mosbrucker, A., Pierce, H., and Spicer, K. (2016). Where is the hot rock and where is the ground water—using CSAMT to map beneath and around Mount St. Helens. *Journal of Environmental and Engineering Geophysics*, 21(2):79–87.

Yamashita, M., Hallof, P., and Pelton, W. (1985). Csamt case histories with a multichannel CSAMT system and near-field data correction. In *SEG Technical Program Expanded Abstracts 1985*, pages 276–278. Society of Exploration Geophysicists.

Zonge, K. L. and Hughes, L. J. (1991). Controlled source audio-frequency magnetotellurics. In *Electromagnetic Methods in Applied Geophysics: Volume 2, Application, Parts A and B*, pages 713–810. Society of Exploration Geophysicists.

### 2.4.1 References to internet websites

IRIS Instruments © 1991-2016 - <https://www.iris-instruments.com/v-fullwaver.html>

PHOENIX GEOPHYSICS © 2006 - <http://phoenix-geophysics.com/home/>

CustEM © 2016-2018 - R. Rochlitz - <https://custem.readthedocs.io/en/latest/index.html>

FEniCS Project. © - 2019 - <https://fenicsproject.org/>

## **Chapter 3**

# **Imaging weathered crystalline aquifers: the deep structure of the Strengbach catchment using sparse CSAMT soundings**

The work presented in this chapter is based on Lajaunie, M., Sailhac, P., Warden, S., Mathey, P.-D. (submitted): "Discussion on the near field and far field approximations in the CSAMT method: application to the Strengbach catchment", *Earth, Planets and Space*

## Introduction

This chapter addresses the methodological challenge of characterizing deep weathered crystalline aquifers with geoelectrical methods. Weathered crystalline rocks constitute porous media of variable permeability, where water can circulate and be stored. The spatial extent and storage capacity of crystalline aquifers are respectively defined by the spatial extent of the weathered rock and by the degree of damaging. The degree of weathering of the rock is expected to decrease with depth. In this thesis, we hypothesize that weathered crystalline aquifers can be assimilated to 1D objects. A methodology based on 1D CSAMT measurements is proposed in order to study them. This methodology was tested and applied at the granitic Strengbach catchment, in the Vosges mountains.

The Strengbach catchment has been studied for many years in the context of a multidisciplinary project gathering geological, hydrogeological, geochemical and geophysical analysis, in order to develop methodologies to model functioning of mountainous catchments.

Ten CSAMT soundings were realized, distributed over the surface of the catchment in a sparse sampling. The data were analysed and processed, and numerical modeling was used to evaluate the importance of topographic distortion on the data. A method for correcting the data from topographic distortion was proposed, tested and applied to the data. The data were inverted in 1D, providing ten 1D models of the Strengbach catchment, and allowing the detection of the limits of weathering.

## 3.1 The Strengbach catchment

### 3.1.1 The site

#### Geological and hydrogeological characteristics

The Strengbach catchment is a granitic catchment of relatively small size (0.8 km<sup>2</sup>) in the Vosges Mountains (France). Located at an altitude comprised between 880 and 1150 m, it is characterized by slopes of 15 % in mean, up to 30 %. The land cover is mainly commercially managed forest (at 90 %), composed of spruce and beech stands (Pierret et al. [2018]).

The Strengbach catchment is covered by 1 m thick acidic podzols overlaying 1 to 9 m of granitic saprolite. The bedrock is mainly composed of granite from the late Paleozoique era, except at the northern summits, where gneiss and granito-gneiss outcrop. The southern and western slopes are marked by veins of microgranites. Characterized by different degrees of hydrothermal alteration (fig. 3.1.b). The bedrock is considered heterogeneous and presents preferential flow paths.

The catchment counts four permanent springs and the main outlet is the Strengbach stream, that flows towards south east (fig. 3.1.a).

#### Main questions about the Strengbach catchment

In 1986 a great monitoring effort was initiated at the Strengbach catchment. The aim, at that time, was to study the influence of acid rain on the forest ecosystems (Dambrine et al. [1998]). Meteorological, hydrological and geochemical repeated measurements were realized and are still repeated in that context. Later, the study of this small-scale forest catchment was broaden to address more general questions related to the functioning of catchments. The instrumentation was enhanced throughout the years, geophysical observations were realized and four main questions were brought forward:

- What is the general functioning of the catchment and which water resource does it represent?
- How do the soil, plants and atmosphere interact, and how do these interactions relate to weathering processes and influence the fertility of the soil?
- What is the sedimentary dynamics of the catchment?
- How to quantify the response of the system to perturbations such as climate change and acid rain?

### 3.1.2 General methodology developed at the Strengbach catchment observatory

#### Multi-disciplinary experiments: hydrogeological, hydrochemical and geophysical instrumentation

The complete understanding of the catchment functioning seems to involve different strata (atmosphere and vegetation, soil, subsurface), which interact with one another. For this reason, a multidisciplinary methodology was developed at the Strengbach catchment.

The long-term monitoring effort started in 1986 was continued until now. A meteorological station records among other things the rainfall, the snow cover, the temperature as well as the atmospheric pressure. Seven cumulative rain gauges were installed all over the catchment.

The amount of water flowing through the outlet was monitored, as well as the discharge from the four permanent springs. The stream water and the spring water were collected at least every two weeks since 1986, and object to chemical analysis. In 2018, a *RiverLab* was installed at the outlet, to sample and analyze at high temporal frequency the water.

Experiments were developed to study the weathering processes in the different horizons of soil (Wild et al. [2019])

In 2012 and 2013, seven boreholes were drilled (F1A, F1B, F5, F6, F7, F8 and F9 in fig. 3.1.a). These boreholes brought information on the deep structure of the catchment and its potential role in the water fluxes: optical and acoustic loggings were realized, gamma ray emissions were recorded and core samples were collected allowing to infer locally the lithology up to a depth of 121 m. Laboratory analysis of the core samples were realized (porosity, permeability, formation factor, surface conductivity,  $V_p$ ,  $V_s$ ). Analysis of the physical and chemical properties of the boreholes water were realized (pH, Eh, conductivity, temperature, salinity). The boreholes F1A, F1B and F5 do not have a metal casing, allowing the realization of electrical and EM geophysical loggings (Electrical resistivity, NMR, self potential, georadar tomography). Seismic borehole measurements were also realized in 2016.

MRS and gravimetry surface measurements were realized, an optic fiber was installed to record the variations of temperature and soil moisture in the first meters of the soil. Collocated seismic and ERT profiles were realized all over the catchment to characterize its structure. AMT measurements were also conducted, characterized by an important noise level.

Time-lapse observations of the gravity field were realized regularly since 2014 with a relative gravimeter, on 17 stations, enriched since 2018 by repeated measurements with a supraconducting gravimeter, measuring continuously the relative gravity field with a very high accuracy (a few  $\mu\text{Gal}$ ).

#### Main hydrogeological observations

Several observations, relevant for this work, were made on the structure and composition of the catchment. First, it was noticed from hydrochemical studies that the hydrothermal alteration of the granitic bedrock is stronger in the northern slope than in the southern slope (Pierret et al. [2014]). The altered granite on the northern slope is characterized by larger amounts of quartz, white mica, clay, and iron oxide than the altered granite on the southern slope. Moreover, higher clay content was noticed in the soil (top layer) of the northern slope than in the southern slope.

Doukoure [2019] observed from full waveform acoustic logging, vertical seismic profiling and drilling data that the limit at depth of the damaged granite to an undamaged granite is around 25 m, and varies from 15 to 40 m, but noticed that fractures are still noticeable below those depth (around 40, 60 and 80 m), with non-negligible apertures, suggesting possible damaging at larger depth.

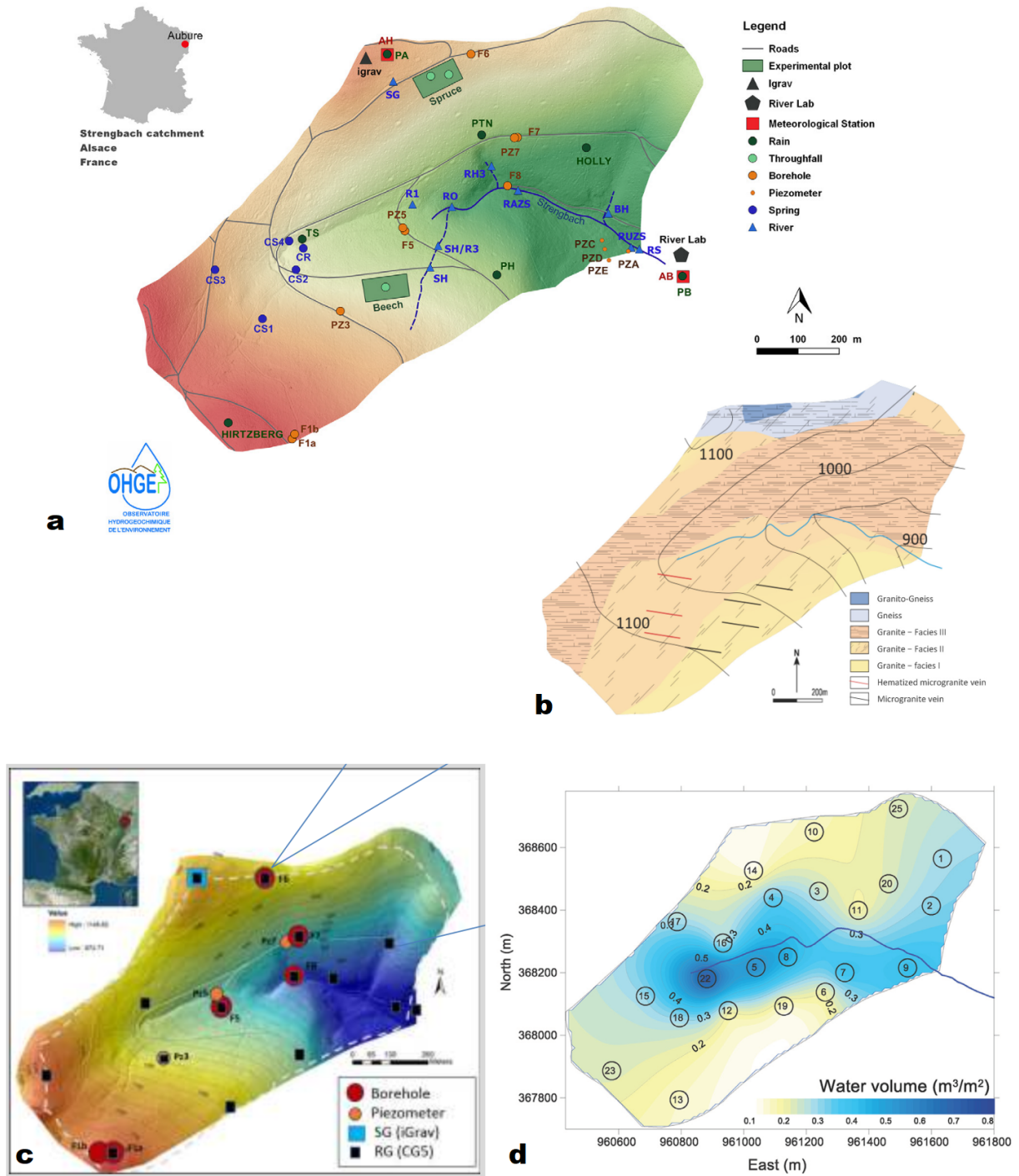


Figure 3.1: Maps of the Strengbach catchment: a. location of the boreholes, springs, meteorological stations and hydrogeological instrumentations (Riverlab, supraconducting gravimeter), b. lithological map, c. map of the microgravimetric variations over the catchment and d. water volume inferred from NMR soundings over the catchment, modified from [Pierret et al. \[2018\]](#) (a., b. and d.) and [Masson et al. \[2012\]](#) (c.)

### Context of this work

The first analysis at the Strengbach catchment focused on the first ten meters of the subsurface, assuming that the hydrogeology at the site was controlled by these first upper layers. On such assumptions, a numerical model of water flow was realized (Weill et al. [2017]), based on the hypothesis that the water flows only in the soil and in the damaged granite. The surface topography and the assumed topography of the interface between undamaged and damaged granite were modeled over the catchment, and the computation could model the flow regime observed at the outlet in response to a certain meteorological event by choosing the right permeability for each layer. However, one could legitimately question the role of the "damage granite in the groundwater flow, since tilted faults and fissures are noticed until large depth in the boreholes. In addition, the spatial variations of alteration of the rock is expected to have an impact on the hydrogeological functioning, and the question was raised on the limits of weathering at depth, and the location of a transition towards a sound rock.

The multi-disciplinary methodology developed at the Strengbach catchment extended the study to depth of 20 to 30 m. A catchment-scale 2D ERT survey was realized (Gance et al. [2020] (in preparation)), aiming at locating the spatial limits of bedrock weathering and therefore at pinpointing the limits at depth at which the rock is no longer involved in the hydrogeological functioning of the catchment. The series of 19 ERT profiles provided a series of 2D resistivity models (fig. 3.2), resolved until a depth of 20 to 30 m, revealing a clear variation of resistivity between the northern and the southern slope, supporting the observation of different degrees and nature of damaging between the northern and southern slopes. Lateral variations of the resistivity are locally noticeable, suggesting that the subsurface is more complex than initially hypothesized. However, the low resistivity observed at large depth does not seem to decrease at the deepest zones reached by the tomography, suggesting that the limit of weathering is located deeper than the DOI of the survey.

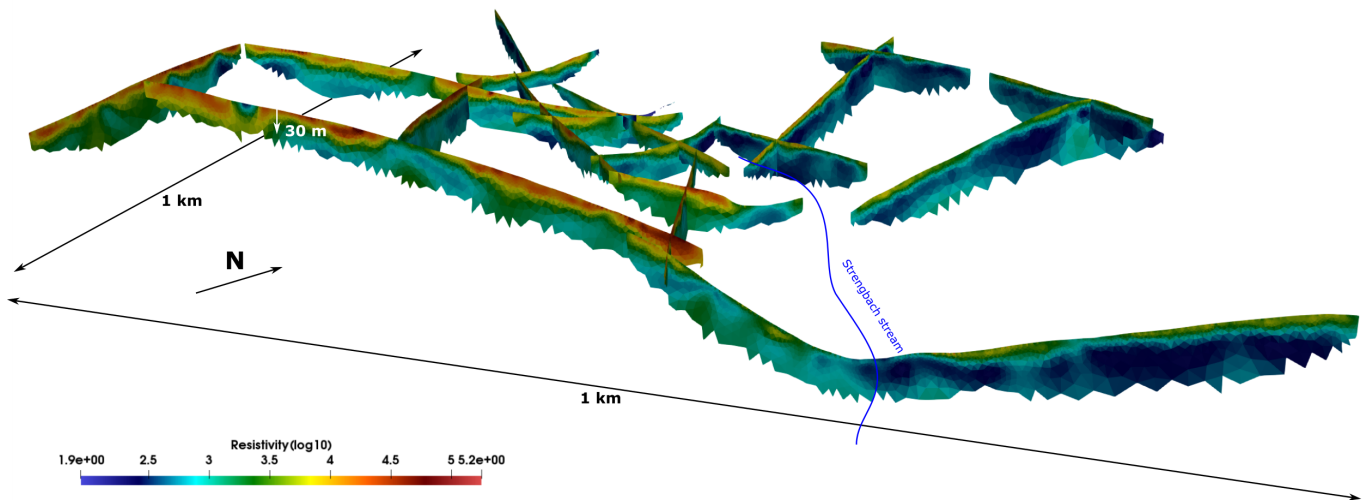


Figure 3.2: 2D resistivity model of the Strengbach catchment from electrical resistivity tomography (Gance et al. [2020] (in preparation)). The northern slope presents lower resistivity values than the southern one, suggesting a more intense weathering of the northern rock. At depth, the absence of an increase of the resistivity with depth suggests that the sensitivity limit of the survey does not reach the bottom of the catchment.

The analysis of MRS data suggested that water was still present in small quantity, at depths around 30 m. In addition, the drilling of the boreholes revealed, while drilling as well as through loggings (acoustic loggings, optical and sonic televiewer and borehole-GPR) that the weathering of the granitic bedrock had propagated down to important depths, and granitic sand as well as large faults were identified at important depths.

The question of a limit of weathering turned exciting. AMT measurements were realized in 2015 at 7 stations but the signal-to-noise ratio was insufficient. In this context, CSAMT was considered as a valuable method to allow the characterization of the deep structure of the catchment.

Even if the deeper porous zones in the granite should not have a great influence on the seasonal functioning of the rock, it could be of importance in the long term functioning of the catchment, and is also relevant in the determination of the lateral limits of the catchment, as deep fault networks of faults could bring in or carry out significant amounts of water.

## **3.2 Field methodology**

### **3.2.1 Measurement setup**

The measurement layout at the Strengbach catchment is presented in fig. 3.3. A single 200 m-long transmitter dipole was set nearly 3 km north of the site, at an altitude of approximately 650 m, and vector measurements (full horizontal electric and magnetic fields, fig. 3.1.b) were realized at 10 stations. Data were acquired using Phoenix Geophysics<sup>®</sup> instrument devices (V8 receiver, 3ER units, T3 current transmitter and RXU transmitter controller). A vector measurement methodology was applied, accounting for both horizontal components for the electric field, and all three components for the magnetic field (fig. 3.3.b).

The frequencies of the transmitted signals are presented in Table 1. The injected current intensity ranged between 1 and 2 A depending on the frequency, and the electrical contact between the ground and the current source was realized by two long copper electrodes with a minimum of 80 cm in the ground and a diameter of 22 mm, daily salt-watered. Data were collected using a single V8 measurement unit, with two 14 m electrical dipoles, and three AMTC coils.

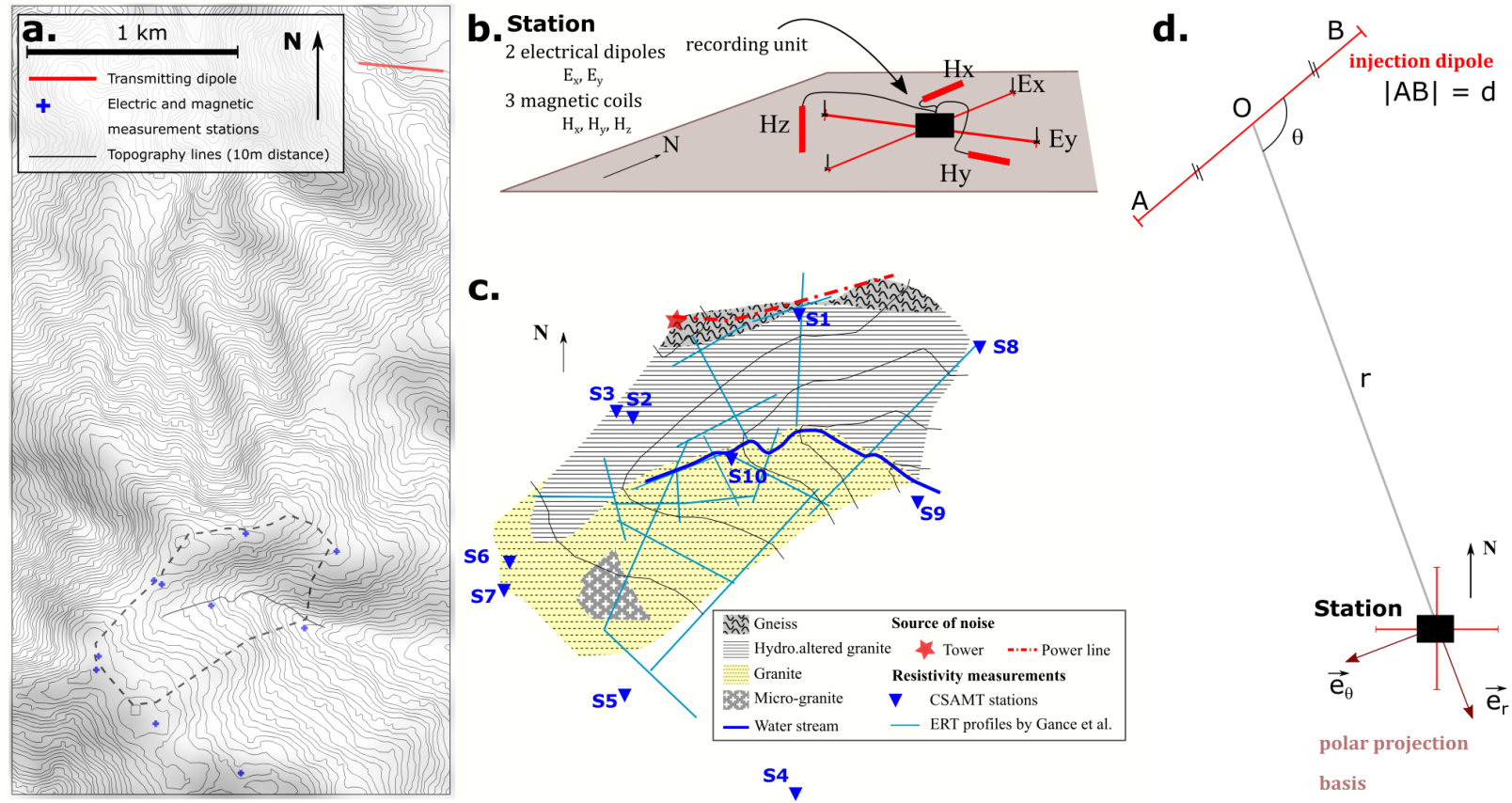


Figure 3.3: Presentation of the field methodology: a. map of the layout (transmitter and receiver-stations) at the Strengbach catchment, b. station layout, c. geological map of the site with location of the CSAMT stations (modified from Pierret et al. [2014]) - the tower marked in red is a mast transmitting radio signals - and d. cylindrical coordinates in the analytical computation of the fields.

The 10 transmitted fundamental frequencies range from min 11 Hz and maximum 512 Hz to 9600 Hz and are regularly log-spaced. The measurements consist of a set of time-series recorded over windows of 600 to 750 samples, at a sampling rate of 2400 or 24000 Hz. For each transmitted frequency, several data windows were recorded during each acquisition. Table 3.1 describes the details of the sampling during a complete recording.

Frequencies [Hz]	11.11	16	22.22	177.78	128	88.89	64	44.44	32
Sampling rate [Hz]	150	150	150	2400	2400	2400	2400	2400	150
Number of windows	11	4	2	2	5	3	5	2	4
Number of samples per windows	675	600	675	675	600	675	600	1080	600

256	355.56	512	711	1024	1280	2560	3840	5120	7680	9600
2400	2400	2400	24000	24000	24000	24000	24000	24000	24000	24000
5	2	11	5	11	11	11	11	11	11	11
600	675	600	675	750	750	750	750	750	750	750

Table 3.1: Measurement characteristics of System-2000 instruments used in this survey

### 3.2.2 Data processing

The procedure used to process the CSAMT data is the one presented in chapter 2 (fig. 2.5). This procedure was developed and applied using MATLAB. The data were extracted and converted to spectral domain by computing the Fourier transform of each time-series independently. The data were then calibrated and converted in nT for the magnetic field and in mV/km for the electrical field.

Because transmitted signals from Phoenix Geophysics instrument T3 are not mono-frequential and contain harmonics, the processing includes a frequency domain detection of signals, i.e. the detection of the spikes in the amplitude spectra of both fields, by means of sliding window detection.

Our experience showed that slight variations in the intensity of the transmitter signal can occur, due for example to variations of the contact resistance, causing variations in the measured signals. Moreover, the variation in noise content and nature over the different time-series may cause the signal to be unevenly detected through time amongst the time-windows. For this reason, a simple stack could then reduce the quality of the data. Our CSAMT data analysis strategy was therefore based on the independent processing of all time-series, providing, for each detected frequency, 3 to 50 estimations of the impedances. The mean value and standard deviation of the impedances were then computed. This allows assessing the stability of the estimated impedance tensor as the dispersion in the computed amplitude and phase spectrum of the impedance transfer function provides a direct quantification of data uncertainty. Finally, only data points detected at transmitted frequencies or their harmonics are kept in the dataset. Some unwanted frequencies seem very often detected, that must be filtered, as the origin of these signal is unknown. Outliers corresponding to frequencies where all data points do not respect the general smoothness of the impedance curve or apparent resistivity curve were detected and removed manually, as well as isolated data points, i.e. data points at frequencies for which less than 3 data point have been detected.

### 3.2.3 Data quality control

For each transmitted frequency, the dispersion of all detected data points, expressed as a standard deviation, gives a first quantification of the data quality.

Additionally, the use of harmonic signals provides a much higher spectral resolution in the apparent resistivity and impedance tensor spectrum. The smoothness of the spectrum can therefore be used to assess the measurement quality.

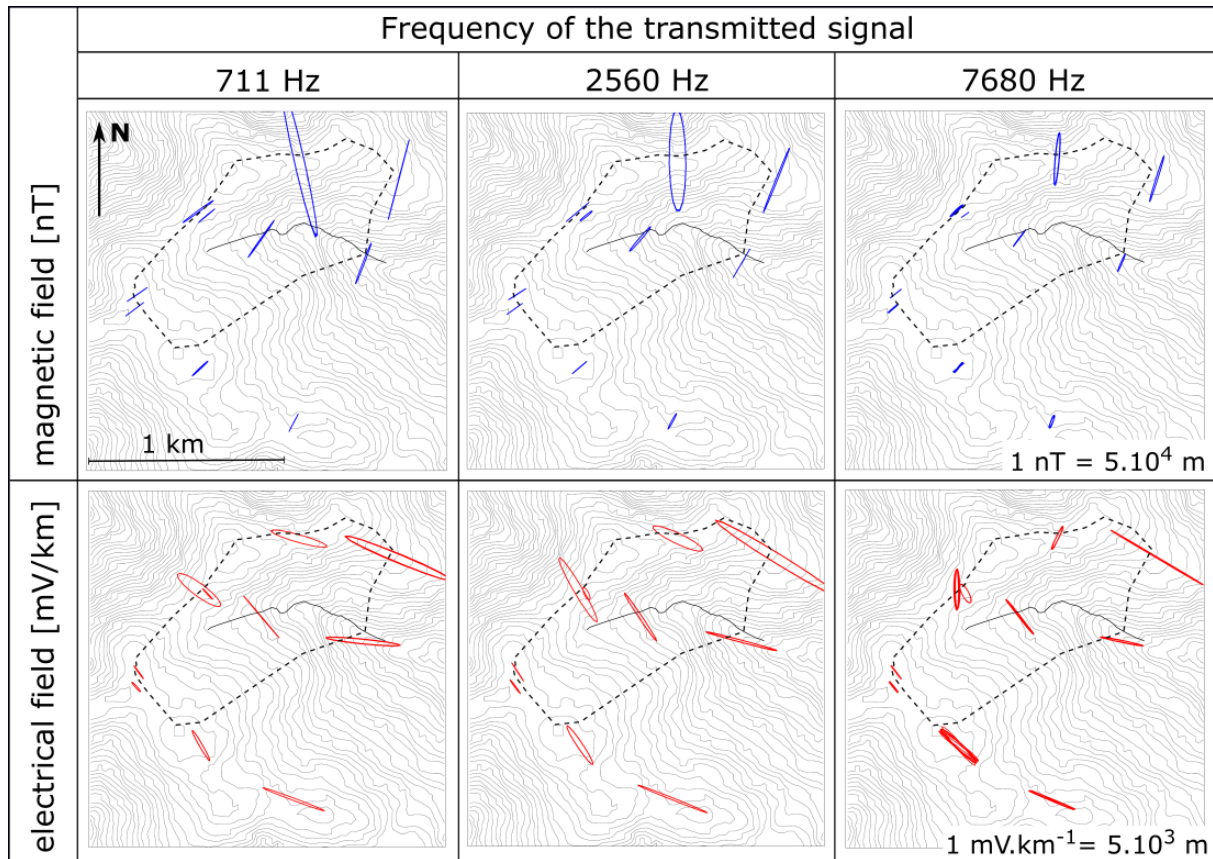


Figure 3.4: Polarization of the electric and magnetic fields over the Strengbach catchment from the ten measurement stations at Tx frequencies of 711, 2560 and 7680 Hz.

### 3.3 Data analysis and computation of apparent resistivity curves

A thorough analysis of the recorded signals is presented in this section, based on the analysis of the dimensionality of the subsurface estimated from the polarization of the field.

#### 3.3.1 Polarization of the fields

In the far field, the magnetic field is expected to be homogeneously polarized all over the survey area. Non-homogeneous polarization can be produced by near field effects, strong topographic variations, very conductive or magnetic objects in the surrounding of the station or noise.

Fig. 3.4 presents the polarization for both magnetic and electric field for 3 transmitted frequencies (711, 2560 and 7680 Hz). Focusing on the magnetic field, the polarization appears to be quite stable over the range of frequencies. The topographic effect on the polarization of the magnetic field was modeled, by comparing the signals produced by a grounded dipole over a homogeneous flat half space with those produced by a grounded dipole over a homogeneous medium for which the actual topography was modelled (fig. 3.5.b). A resistivity of  $2000 \Omega.m$  was modeled in both cases and at a transmitted frequency of 1024 Hz.

Fig. 3.5 shows that most magnetic field polarization can be explained by the topography. The station 1 presents an unexpected amplitude and polarization regarding the two modeled magnetic fields. This might be explained by the presence of a power line buried close to the station (fig. 3.3), inducing some noise in the data, or acting as a local conductive anomaly. The stations 2 and 3 seem less influenced by the topography than what is observable from the custEM modeling. In fact, these two stations seem rather close to the flat earth modeling in terms of polarization.

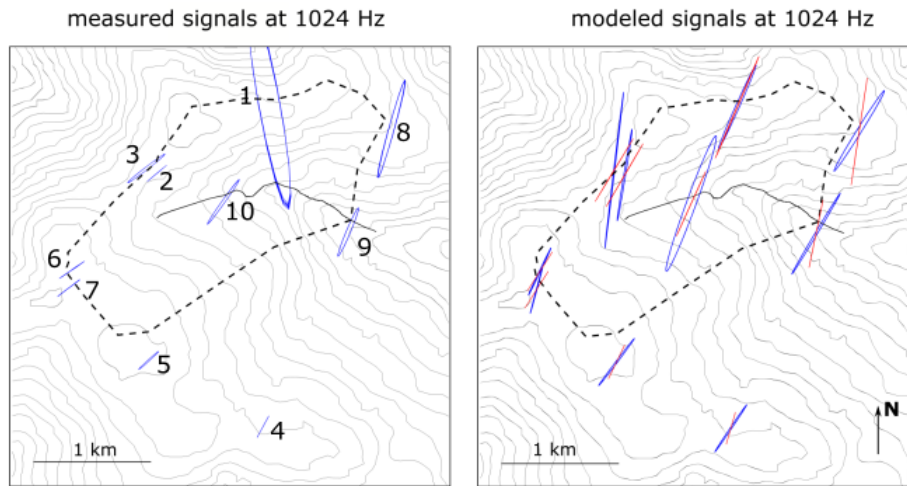


Figure 3.5: Measured (a.) and modeled (b.) magnetic fields at 1024 Hz. The modeled magnetic fields (b.) are computed over a homogeneous flat medium (represented in red) and a homogeneous medium affected by the true topography (computation with custEM – represented in blue)

### 3.3.2 Dimensionality analysis

The electric field presented in fig. 3.4 shows very clearly the influence of 2D structures on the data over most stations: the non-orthogonality of the E field with regards to the H field implies therefore that one of the diagonal elements is non zero. This becomes clear when rotating the impedance tensor such that the first coordinate matches the direction of the main H field. This case scenario leads to eq. 3.1, where  $E_1$  being not null,  $Z_{11}$  turns to be non-null as well. The importance of 2D structures can therefore be deduced from the amplitude of  $Z_{11}$  relative to  $Z_{21}$

$$\begin{bmatrix} E_1 \\ E_2 \end{bmatrix} = \begin{bmatrix} Z_{11} & - \\ Z_{21} & - \end{bmatrix} \begin{bmatrix} H_1 \\ 0 \end{bmatrix} \quad (3.1)$$

The angle  $\alpha$  between the electric and magnetic fields quantifies the importance of the component  $Z_{11}$  relative to  $Z_{21}$  and characterizes the influence of 2D and 3D structures in the measured data. This angle, which, in the homogeneous case, is  $90^\circ$  in the far field (fig. 2.1), is presented for our dataset in fig. 3.6. The angle values range from  $70^\circ$  to  $90^\circ$  for most stations, except for stations 1, 2 and 3, which all present low values of  $\alpha$  on some frequency ranges. At high frequencies, where the far field hypothesis is known to be valid, the non-orthogonality between electrical and magnetic fields are interpreted as 2D effect. This 2D effect is expected as a result of the topographic variations, but can also be produced by geological, hydrological structures, or by anisotropy. This analysis is limited to the far field, since the near field implies, for a homogeneous half space, the angle  $\alpha$  to be different from  $90^\circ$ . In the near field, the angle can then be modeled for example assuming the medium to be a homogeneous half space (fig. 2.1), but one should be careful since the transition field implies an increasing sensitivity to the area surrounding the transmitter: additional effects can then contribute to the angle  $\alpha$ .

### 3.3.3 Computation of the apparent resistivity curves

Because a single transmitter was used in the CSAMT measurements, the impedance and apparent resistivity curves were computed using eq. 3.1. The resulting curves of impedance tensors, apparent resistivity and phase are presented in fig. 3.7, 3.8 and 3.9 resp..

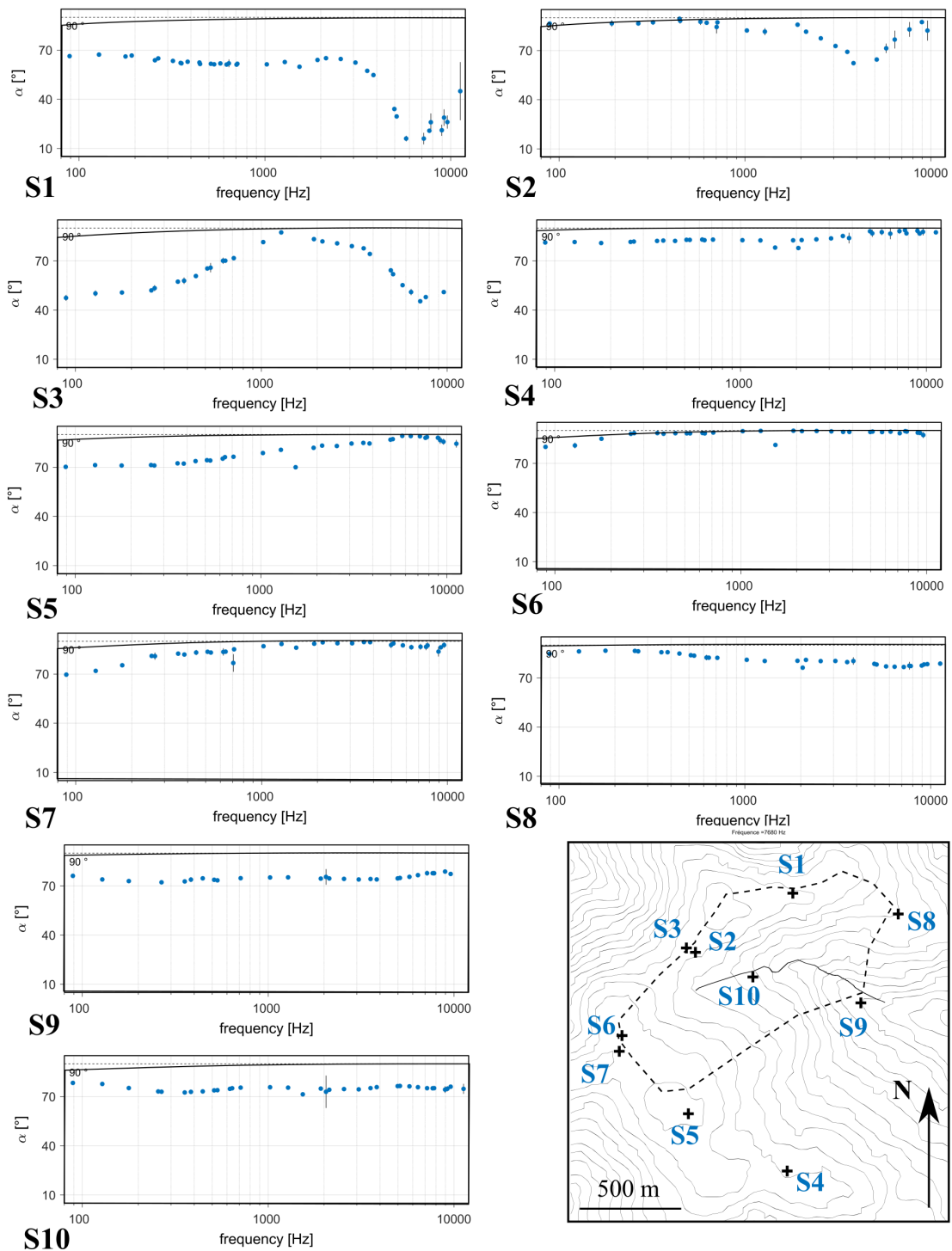


Figure 3.6: Graphs of the variation of the angle  $\alpha$  between the electric and magnetic fields with the frequency over the Strengbach catchment, for each of the 10 stations. In each subfigure, the black line shows the variations of  $\alpha$  in the case of a flat, 1D medium: depending on the stations location, the angle  $\alpha$  presents values different from  $90^\circ$  at low frequency when the EM signals are not a plane wave signals.

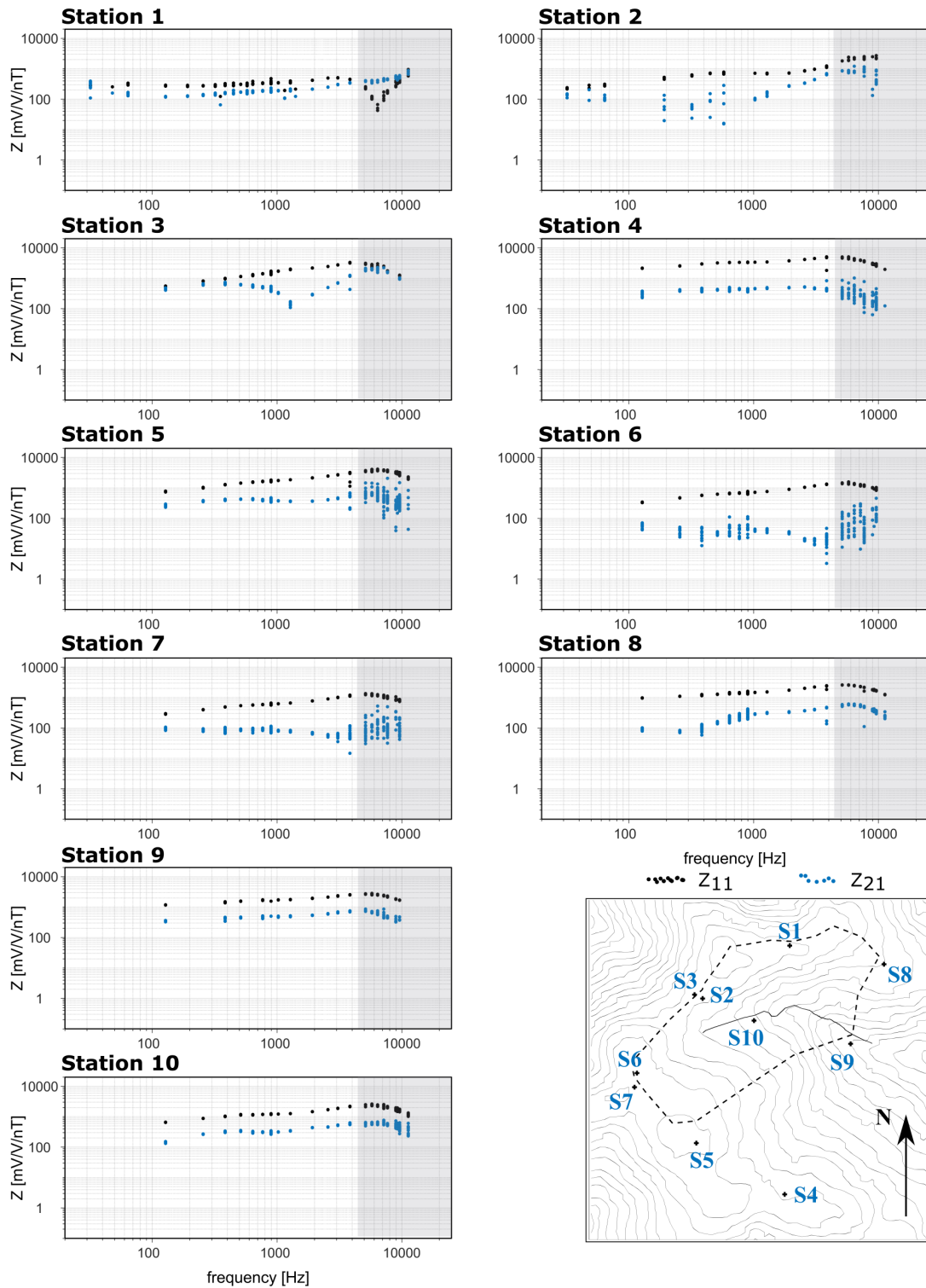


Figure 3.7: Impedance amplitude curves (Z11 in black and Z21 in blue) for all ten stations. The grey zones correspond to the noisy high frequency part of the curves, ignored in the inversions

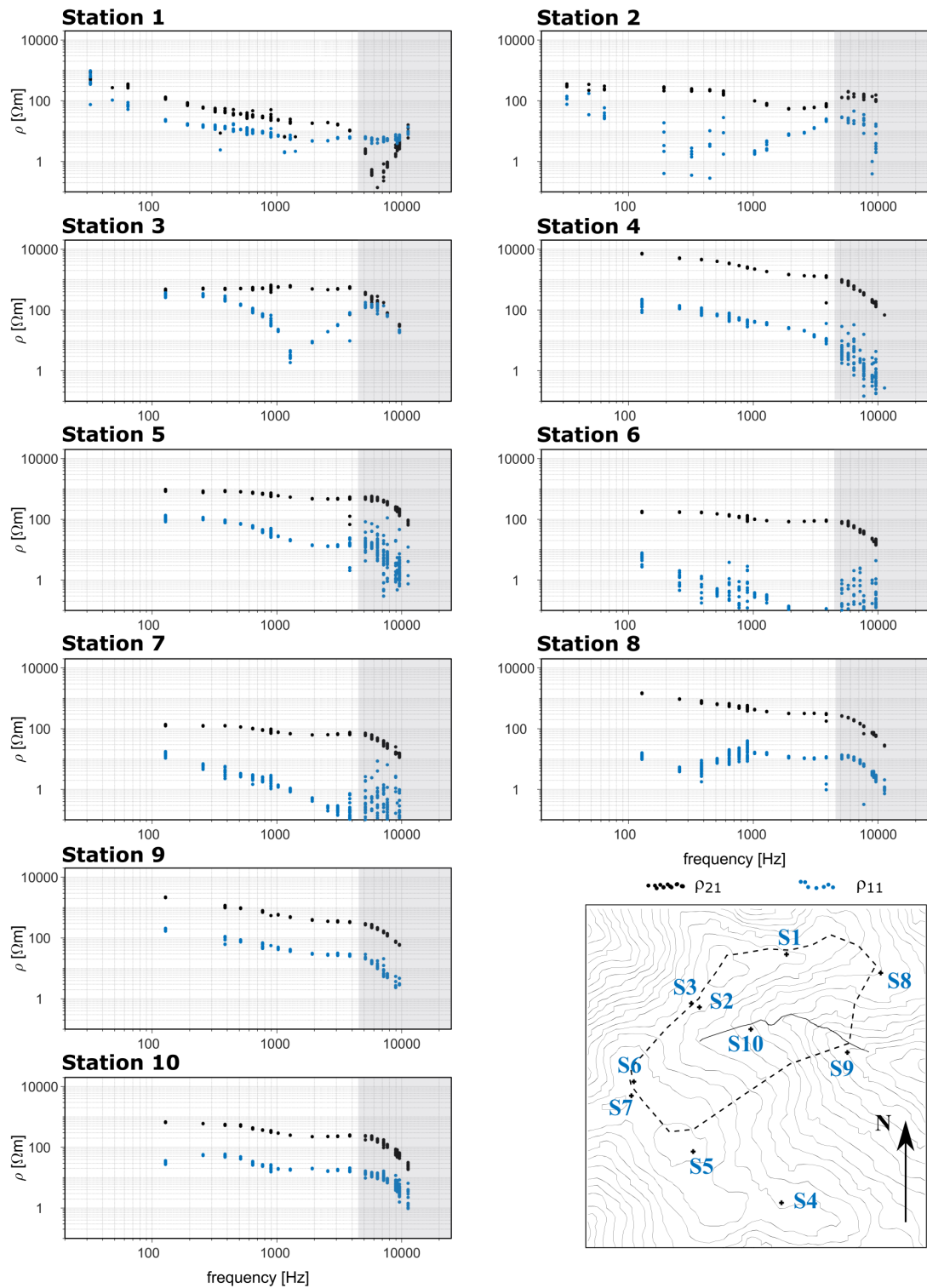


Figure 3.8: Cagniard apparent resistivity curves for all ten stations. The grey zones correspond to the noisy high frequency part of the curves, ignored in the inversions.

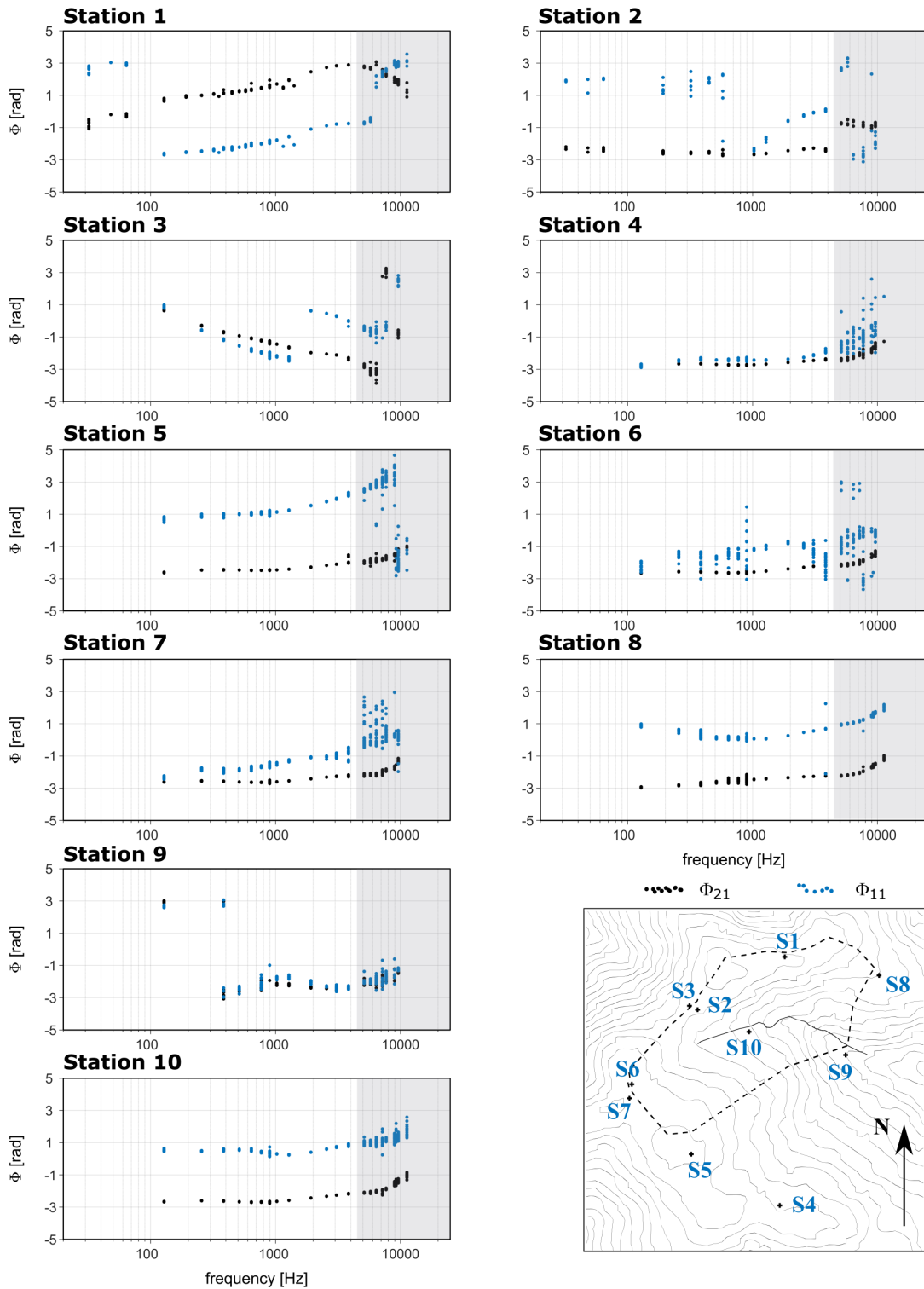


Figure 3.9: Phase curves for all ten stations.

## 3.4 Topographic effect

### 3.4.1 Evaluation of topographic distortions

The topographic effect at the Strengbach catchment was evaluated by means of numerical modeling. The software CustEM (Rochlitz et al. [2019]) was used to compute synthetic data related to homogeneous earth affected by the true topography of the Strengbach catchment. A total E field approach and a polynomial discretization of second order of the field were used in every custEM tests presented in this work. Two homogeneous models were built at 100 and 1000  $\Omega$ .m and the far field apparent resistivity values related to the two models were computed at each measurement stations, applying the Cagniard formula.

An expression of the topographic effect is proposed here, called  $t$  (eq. 3.2) and defined as the ratio of the apparent resistivity computed while including the topography in the computational model, over the apparent resistivity computed for a flat earth with the same setup (analytical computation). In this way, no near field effect is accounted for in the topographic effect ratio. The topographic effect ratios associated to the two resistivity models at 100 and 1000  $\Omega$ .m resp. were evaluated for each station at 15 modeled frequency between 25 and 15000 Hz.

$$t = \frac{\rho_{app,topo}}{\rho_{app,flat}} \quad (3.2)$$

The two maps in figure 3.10 show the topographic effect  $t$  for different frequencies at each station as concentric colored circles. The smallest circles correspond to the highest frequencies. These maps show that the topographic effect is variable from station to station, but is relatively stable over the far field frequency range for each station independently (the different concentric circles are difficult to tell apart). It has to be noted that the effect increases at low frequency, at the far field limits. The effect seems generally higher when the subsurface resistivity is 1000  $\Omega$ .m, but that might be related to the fact that the far field limit occurs at much higher frequency in a more resistive medium. The produced errors are generally lower than 10 % in the far field. It seems that the most affected stations are stations 2 and 3, affected by a topographic effect  $t > 1$ , and station 4, affected by a topographic effect  $t < 1$ . In addition, no obvious relation between the local shape of the topography (local summit, valley, convexity or concavity of the topography) and the topographic effect ( $t > 1$  or  $t < 1$ ) appears.

### 3.4.2 A procedure to correct the topographic effect

Some stations present important topographic effects, provoking either a static or a dynamic shift of the apparent resistivity curve (fig. 3.11 and 3.12). For this reason, it seemed pertinent to correct this effect at least at first order for the stations the most affected. The following procedure is proposed to correct the apparent resistivity curves.

The distortion ratio computed in the previous paragraph for a subsurface at 100 and 1000  $\Omega$ .m are the actual correction coefficients for homogeneous subsurfaces at 100 and 1000  $\Omega$ .m resp.. Indeed, for any homogenous medium at  $\rho_h$ , applying  $t_{\rho_h}$  as in eq. 3.3 fully corrects from the topographic effect.

$$\rho_{corr} = \rho_{meas.} \frac{\rho_{flat}}{\rho_{custEM}} = \rho_{meas.} \frac{1}{t} \quad (3.3)$$

The idea of the correction proposed hereafter is based on the assumption that, if the apparent resistivity of a 1D medium is bounded, the amount of topographic effect might as well be bounded accordingly to the range of resistivity in the subsurface. If so, it should be possible to range the amount of topographic effect, to correct accordingly the apparent resistivity curve (or, equivalently, the MT impedance) and to evaluate the uncertainty related to the correction. More specifically, several cases can be distinguished. If the correction coefficient  $t$  for a medium at 100  $\Omega$ .m is very close to the one for a medium at 1000  $\Omega$ .m (station 10, fig. 3.11.c), one could assume that the effect is not very sensitive to the resistivity. Correcting any apparent resistivity curve with apparent resistivity in the range between 100 and 1000  $\Omega$ .m should be done with a great degree of confidence, and a low uncertainty could be attributed to the data. If, on the contrary, the two correction coefficients are very different (station 3, fig. 3.12.c), one could try, if possible, to narrow the range of apparent resistivity values

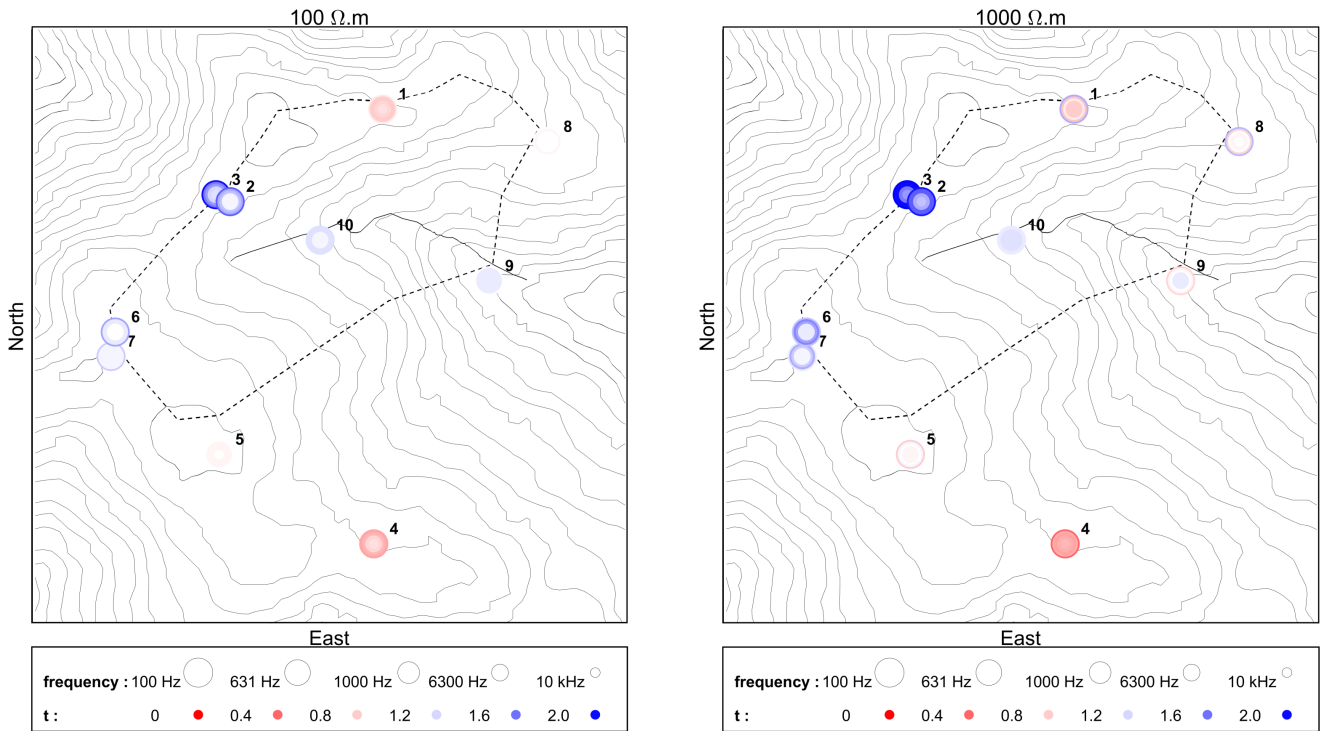


Figure 3.10: Maps of the topographic effects at the ten CSAMT stations. Left: topographic effect for a homogeneous subsurface with  $\rho = 100 \Omega.m$ , Right: topographic effect for a homogeneous subsurface with  $\rho = 1000 \Omega.m$ . The presented effect ratios were computed at 5 different frequencies represented as 5 concentric circles, the smallest one corresponding to highest frequencies.

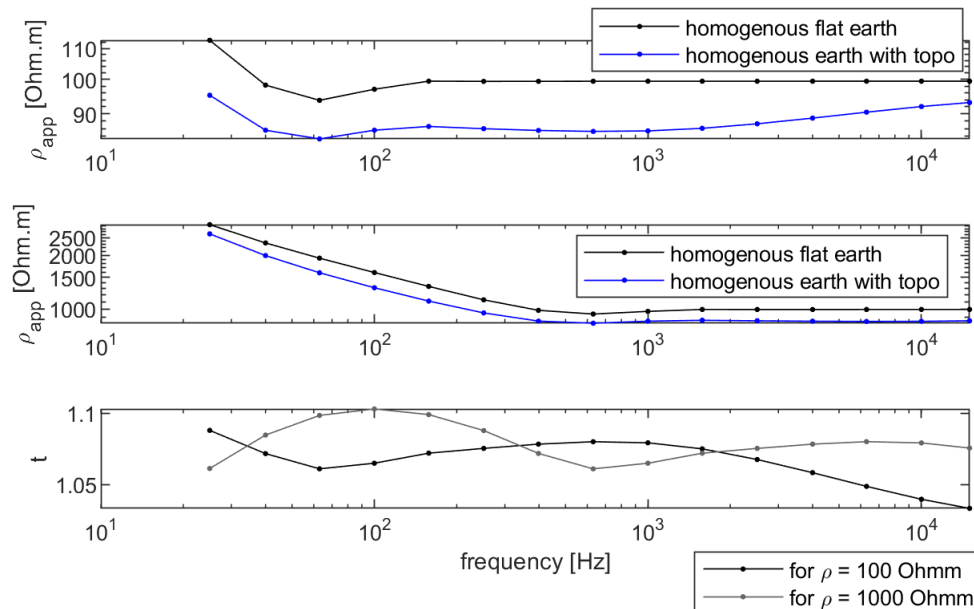


Figure 3.11: Example of topographic effect simulated (station 10): a. Cagniard apparent resistivity for homogeneous flat and non-flat earth at  $100 \Omega.m$ , b. Cagniard apparent resistivity for homogeneous flat and non-flat earth at  $1000 \Omega.m$  and c. topographic effect  $t$  for resistivities of  $100 \Omega.m$  and  $1000 \Omega.m$

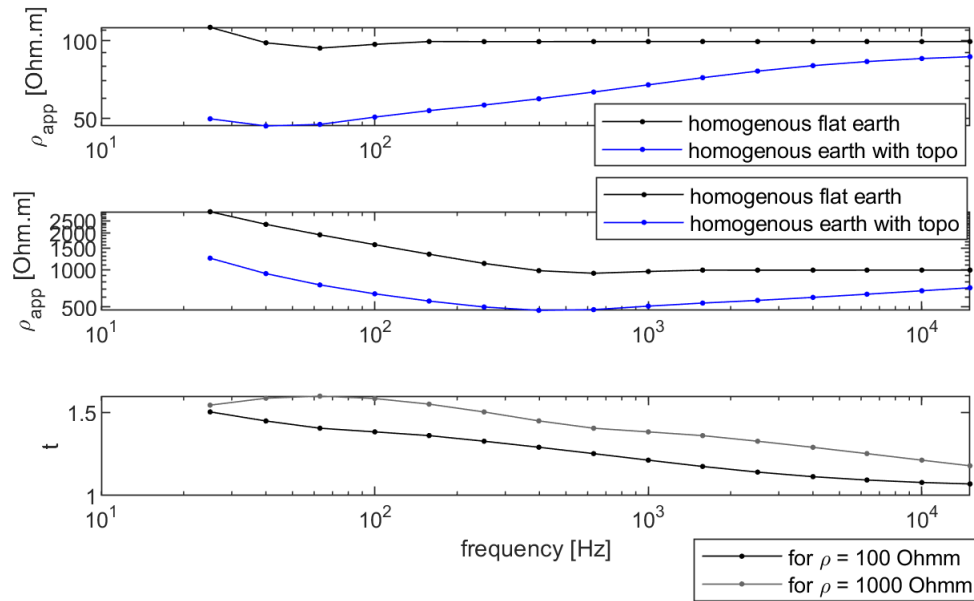


Figure 3.12: Example of topographic effect simulated (station 3): a. Cagniard apparent resistivity for homogeneous flat and non-flat earth at 100  $\Omega$ .m, b. Cagniard apparent resistivity for homogeneous flat and non-flat earth at 1000  $\Omega$ .m and c. topographic effect  $t$  for resistivities of 100 and 1000  $\Omega$ .m

to consider for the corrections. If this is not possible because the measured apparent resistivity curve varies over the entire range of values initially considered (here between 100  $\Omega$ .m and 1000  $\Omega$ .m), a correction could be proposed, but would be characterized by a very low degree of confidence, and the data would be characterized by a high uncertainty.

To further evaluate the possibility of topographic correction, and test the proposed correction method, synthetic data were computed on a model of the Strengbach catchment at the same locations than the measured stations. A model including a plate anomaly of 80 m thick at 100 m below the lowest station and extending over the survey area was built (fig. 3.13) and synthetic data were computed with *custEM*. The background resistivity was 1000  $\Omega$  and the anomaly was at 100  $\Omega$ .m.

Fig.3.14 compares the synthetic apparent resistivity curve from station 10 (located in a local valley) uncorrected, and corrected from the topography with the two corrections. It appears that the two correction act in a very close manner, as a shift, suggesting that the topographic effect as that station 1/ is significant and 2/ is not too dependant upon the resistivity of the subsurface. In such context, a correction can be reasonably applied. Because the two corrections are very close, one could simply chose to correct using the  $t_{100}$ , which would be less affected by the near field, or by a mean of the two corrections.

Fig. 3.15 on the contrary shows two very different corrections for the two resistivities. In such context, a methodology can consist in computing the mean of the two corrected apparent resistivity curves.

### 3.4.3 Test of the procedure: should we correct the apparent data from topographic effects

Additional synthetic tests were realized to evaluate the efficiency of the topographic corrections. The computed and corrected data were inverted using the 1D inversion scheme presented in section 3.5 previous and after applying the topographic correction, and the inversion results were compared. Fig. 3.16, 3.17, 3.18 and 3.19 present the inversion results for the two stations affected the most by the topography (stations 7 and 8 in fig. 3.10) and for two levels of discretizations (13 and 30 layers). It appears that the correction helps on the stability and accuracy of the inversion above the anomaly and improves the location of the anomaly. However, it can be noted that in both cases (with and without correction, the resolution below the anomaly is low, and the

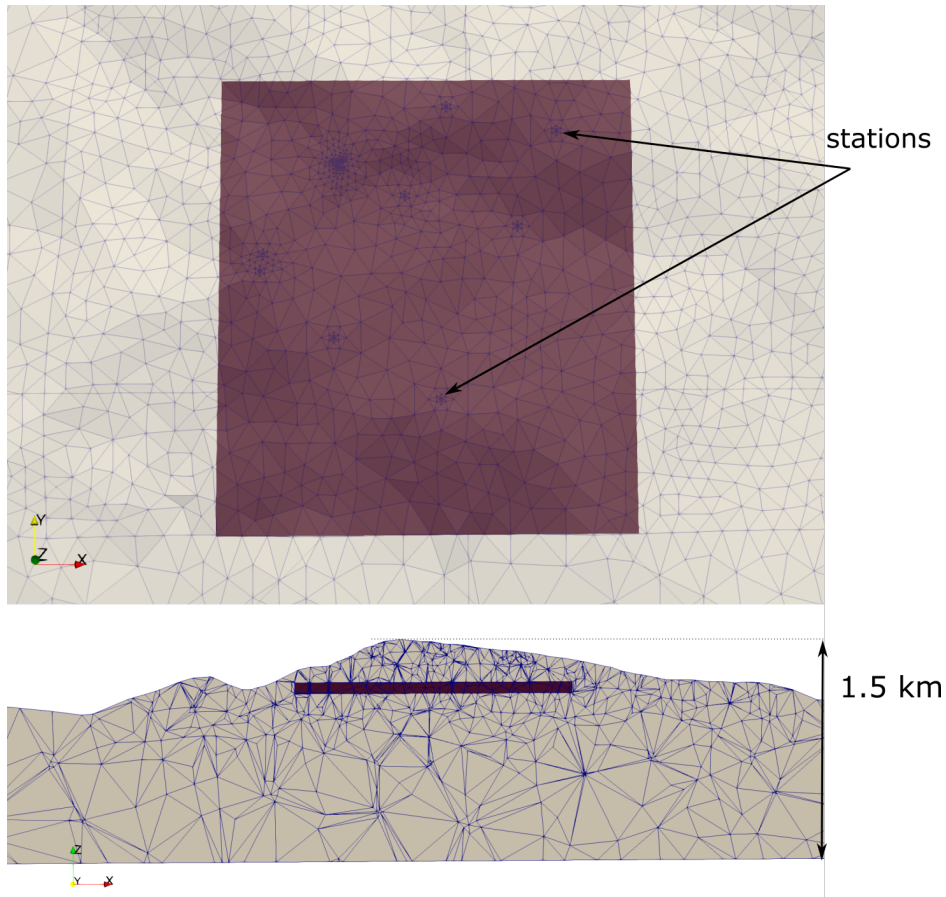


Figure 3.13: Model used to test the efficiency and requirement of topographic corrections at the Strengbach catchment: a. top view with transparency to locate the anomalous plate and b. cross section

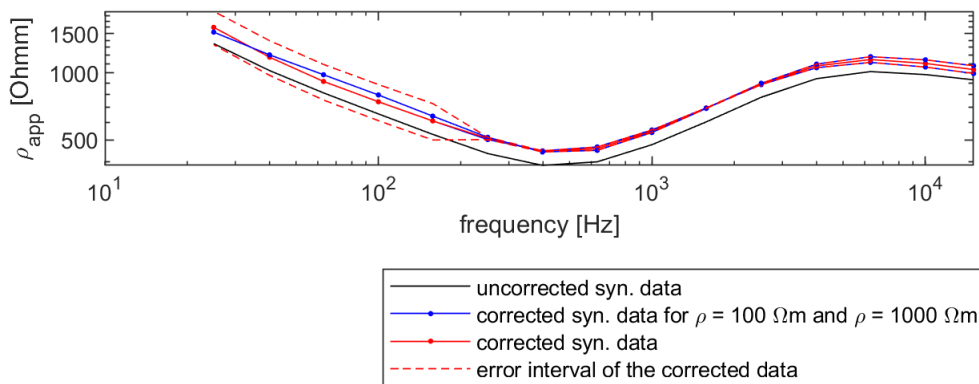


Figure 3.14: Example of uncorrected, corrected and mean corrected apparent resistivity curves (station 10 - synthetic data)

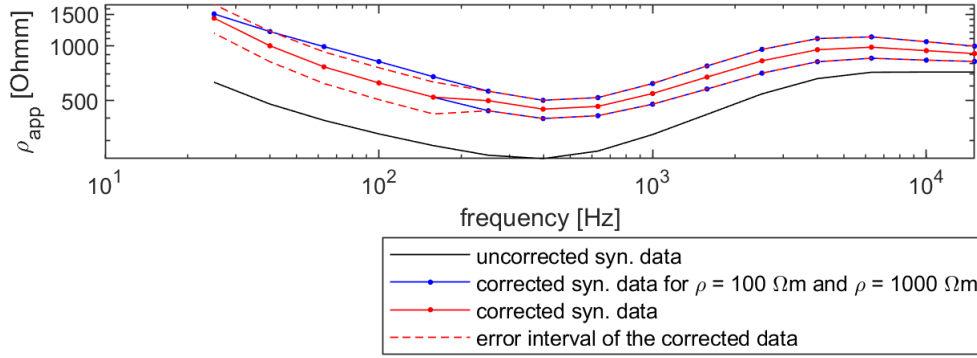


Figure 3.15: Example of uncorrected, corrected and mean corrected apparent resistivity curves (station 3 - synthetic data)

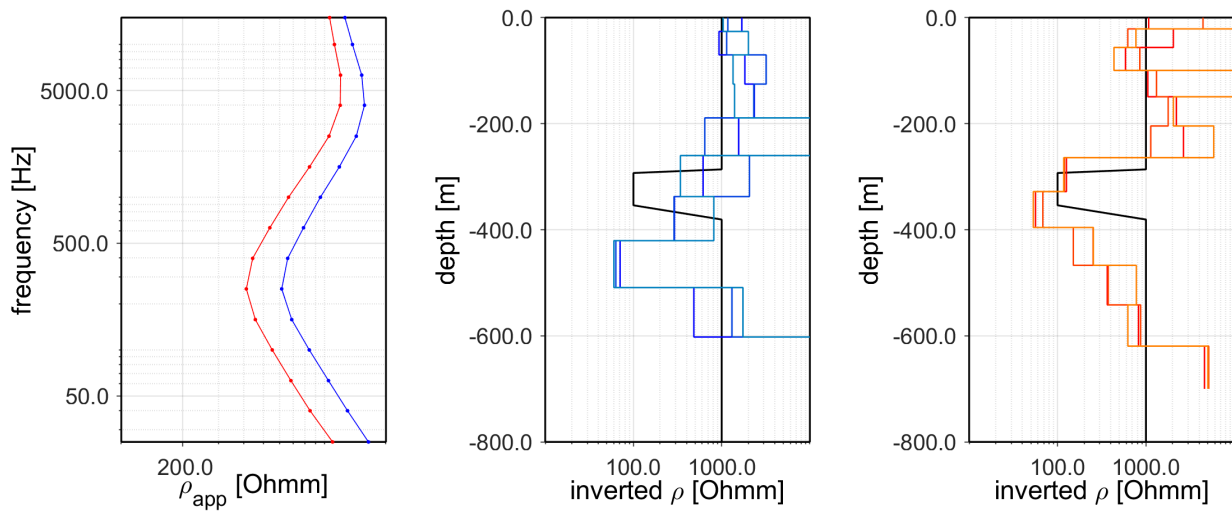


Figure 3.16: Example of inversion tests of synthetic data: a. uncorrected (blue) and corrected (red) synthetic data, b. inverted models from uncorrected data with a coarse vertical discretization and c. inverted models from corrected data with a coarse vertical discretization

true resistivity is not recovered.

In conclusion, it appears that the topographic distortion is not negligible, and should be accurately modeled and taken into account. The correction methodology proposed in this work seems to efficiently correct from the distortion in the context of the Strengbach catchment, even though this correction procedure has a variable accuracy among the stations.

In the following, the data considered are corrected from topographic distortion by applying eq. 3.3 with a correction coefficient  $t$  attributed to a single resistivity, chosen for each station depending on their apparent resistivity curve. This choice was made because the resistivity range presented in each data is relatively narrow for frequencies between 4000 and 400 Hz, which are the highest frequencies considered in the inversion. The resistivity values chosen for each station were selected to be close to the arithmetic mean of apparent resistivities from 4000 to 500 Hz for each station, tout en keeping the number of numerical computation (hence apparent resistivities to test) low. These selected values are given for each station in table 3.2, together with the mean of apparent resistivities recorded from 4000 to 500 Hz.

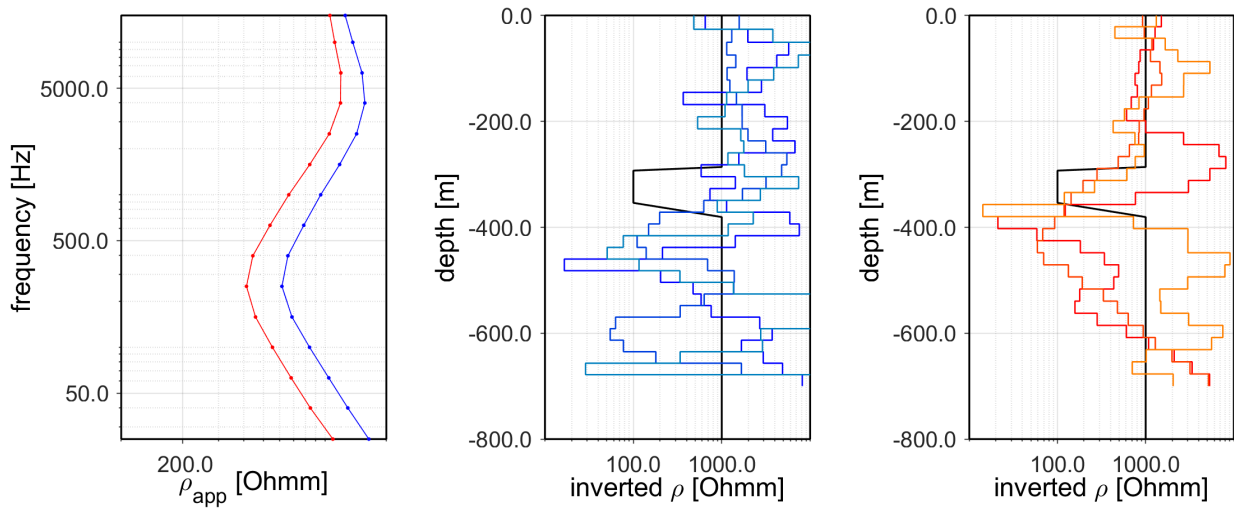


Figure 3.17: Example of inversion tests of synthetic data: a. uncorrected (blue) and corrected (red) synthetic data, b. inverted models from uncorrected data with a thin vertical discretization and c. inverted models from corrected data with a thin vertical discretization

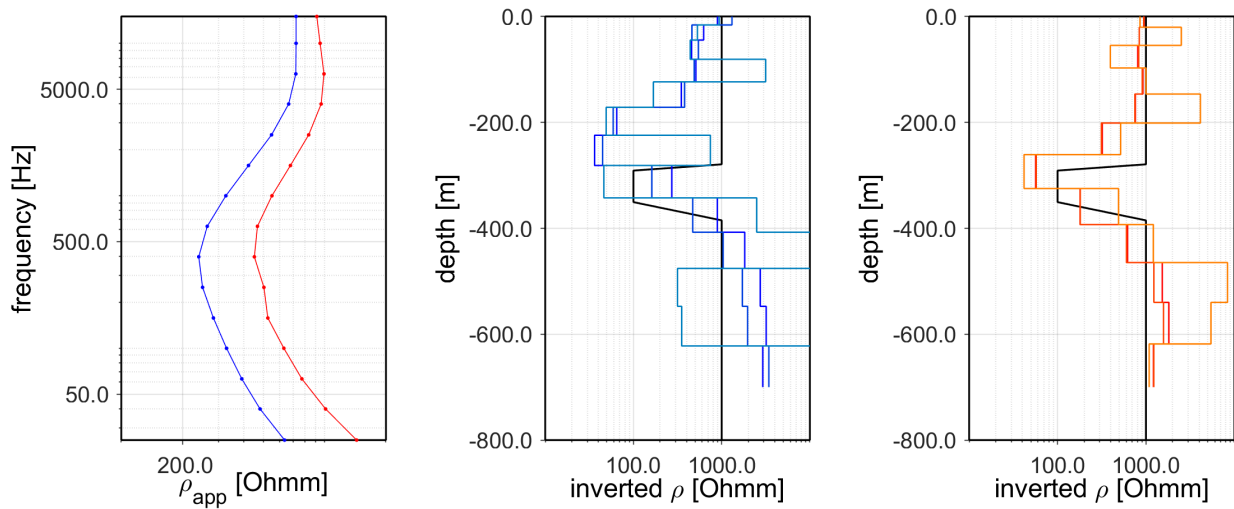


Figure 3.18: Example of inversion tests of synthetic data: a. uncorrected (blue) and corrected (red) synthetic data, b. inverted models from uncorrected data with a coarse vertical discretization and c. inverted models from corrected data with a coarse vertical discretization

Stations	mean resistivity	correction resistivity	Stations	mean resistivity	correction resistivity
Station 1	25	100	Station 6	113	100
Station 2	92	100	Station 7	85	100
Station 3	562	650	Station 8	471	350
Station 4	2400	1000	Station 9	576	650
Station 5	644	650	Station 10	340	350

Table 3.2: Mean apparent resistivity from 4000 to 500 Hz and resistivity used to compute the topographic effect t for each recorded station

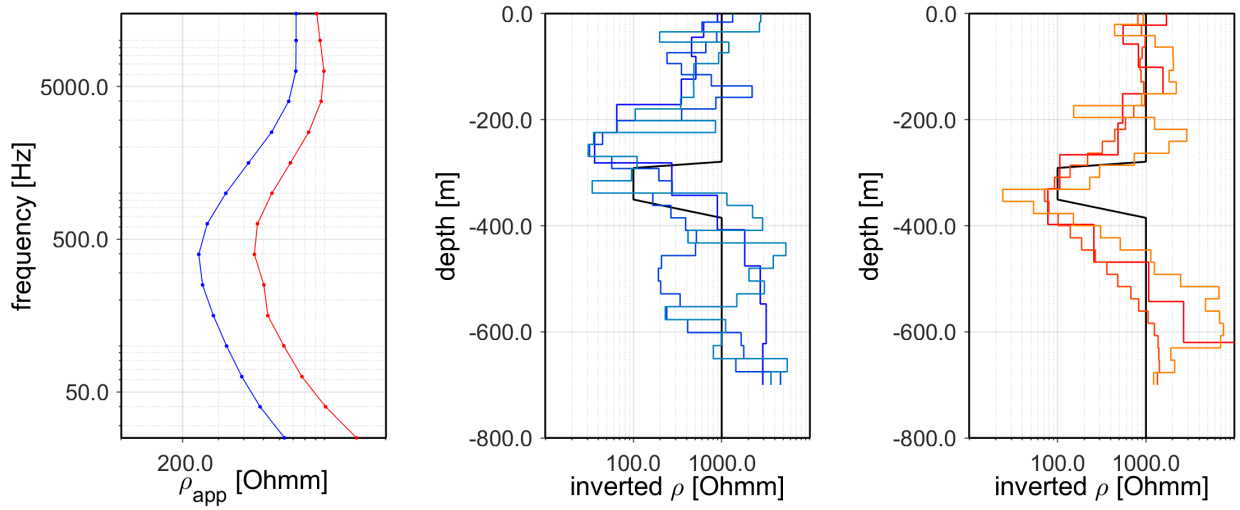


Figure 3.19: Example of inversion tests of synthetic data: a. uncorrected (blue) and corrected (red) synthetic data, b. inverted models from uncorrected data with a thin vertical discretization and c. inverted models from corrected data with a thin vertical discretization

## 3.5 1D inversion

### 3.5.1 Methodology

The data were inverted in 1D for frequencies smaller or equal to 3840 Hz. For higher frequencies, the data are affected by a high uncertainty and the apparent resistivity systematically drops, for unidentified reasons, leading to very poor fit in the inversion. Only the apparent resistivity curves were taken into account in the cost function, no attempt at fitting the phase has been made.

#### Uncertainty

The data uncertainty could be evaluated through three different aspects. First, the dispersion of the apparent resistivity data points at each frequency provides an analysis of the measurements uncertainty. Second, a simple analytical computation can provide an analysis of the error at the transition between the far field domain and the near field domain. Last the topography error could be evaluated through synthetic analysis (see previous section), providing a topographic error. A formulation of the uncertainty, including contribution of the data intrinsic dispersion, the near field uncertainty, and a topographic uncertainty when the topographic correction is realized is summarized in eq. 3.4 (where  $\sigma_\rho$  designates the standard deviation of the series of apparent resistivity at a specific frequency).

$$\frac{\delta\rho}{\rho} = \frac{\sigma_\rho}{\rho} + \frac{|\rho_{FarField} - \rho_{mod}|}{\rho_{mod}} + \frac{|\rho_{flat} - \rho_{topo}|}{\rho_{flat}} \quad (3.4)$$

$$\rho_{inv} = \rho \left( 1 \pm \frac{\delta\rho}{\rho} \right) \quad (3.5)$$

Because the correction of the topography presented in the previous section was proven useful, apparent data were corrected from the topographic effects, so that the error related to the topographic effect was ignored in the inversion.

The data uncertainty (related to the data dispersion at each frequency) was evaluated by computing the standard deviation of all data points for each frequency. Frequencies at which less than three data points were detected were removed from the dataset because the data were not sampled enough for a reasonable estimation

of the uncertainty. The error committed by the far field interpretation of transitional field data is not considered here, although we expect this error to be quite important at low frequencies, for some of the stations. For this reason, an adjusted data uncertainty has been evaluated, based on numerical modeling. The electric and magnetic fields generated by an infinitesimal dipole have been computed for a homogeneous flat earth, which resistivity equals the apparent resistivity computed at the frequency where the transition seem to occur,  $f_c$ . The error committed when considering the far field formula has been computed (misfit) for each frequency. A new uncertainty has been computed by adding this misfit to the standard uncertainty, computed from the data dispersion.

### Inversion scheme

The inversion procedure consists in the minimization of the cost function (eq. 3.6). In eq. 3.6,  $\Phi$ , the cost, depends on two terms. The misfit term (first term in the right side) is the norm L2 of the data misfit, where  $d_{calc}$  and  $d_{obs}$  are the logarithm of the computed and observed apparent resistivity resp. and  $\sigma_d$  is the uncertainty attributed to the logarithmic resistivity. The regularization term (second term in the right side) controls the smoothness of the model and is computed as the L2 norm of the model gradient, multiplied by the regularization term  $\lambda$ .

The MATLAB function *fminsearch* (Lagarias et al. [1998]) was used to explore the model space. The maximum number of iterations was set at 50000, number that was never reached.

$$\Phi = \left\| \frac{d_{calc} - d_{obs}}{2\sigma_d} \right\|_2 + \lambda \left\| \frac{\Delta_m}{h} \right\|_2 \quad (3.6)$$

$$misfit = \left\| \frac{d_{calc} - d_{obs}}{2\sigma_d} \right\|_2 \quad (3.7)$$

The vertical discretization has been chosen depending on the high and low frequency limits of  $\rho_a$ . The regularization coefficient was chosen by realizing a set of quick inversions for a chosen set of coefficients ranging from  $10^{-5}$  to  $10^4$  and choosing the regularization that provides the best inversion both in terms of misfit and model smoothness. The final quality of the model (misfit) is characterized by the root mean squared error on the natural logarithm of the resistivity.

In order to test the stability of the inversion, for each data, three different inversions were tested with different homogeneous initial models, based on the mean apparent resistivity and the apparent resistivity at the lowest and highest measured frequency. For each of these initial models, inversions were realized accounting for the standard and the adjusted data uncertainty. The spread of the resulting eight models has been considered as an indicator of the stability of the inversion. A confidence interval around the mean models is estimated by computing the standard deviation of the models resistivity for each layers (fig. 3.20).

### 3.5.2 Inversion tests

After correcting the apparent data from the topographic effect a few tests were realized to estimate the quality of the inversions. In particular, 3 key elements were evaluated:

1. the parametrization (thickness of the first layer, limit depth of the inverted model)
2. the error model
3. the formulation of the loss function (formulation of the regularization part, norms used for the data fit and the regularization)

The stability of the inversion when changing the parametrization was evaluated. The vertical discretization was refined from 12 to 28 layers and the regularization scheme was optimized to allow the inversion to work properly. The fine inverted models were then compared with the coarse ones presented in the previous paragraph, showing generally good consistencies, but smoother transitions between the different "units" observed (fig. 3.21.c).

The interpreted data were corrected from the topographic effect previous to inversion. However, the uncorrected data were also inverted to evaluate the variability in terms of inverted model induced by the topographic effect on real data showing that the inverted models were very similar, particularly when using a coarse parametrization, inducing coarse confidence degree in the inverted models (fig. 3.21.a. and b.).

Finally, inversions were realized with a thinner vertical discretization (29 layers), and a stronger regularization. Because the parametrization and regularization of such inversions must be very finely controlled in order to retrieve an acceptable model regarding both the data fit and the regularization, these inversions were taking a longer time than the inversions presented as results. Fig. 3.21 presents a comparison between models obtained by inverting the data from station 5: 1/ uncorrected from topographic distortions, 2/ corrected from topographic distortions and 3/ corrected data with a thinner vertical discretization. It shows that 1/ the three inversion models are very close, and show the same variations, and the same resistivity values, 2/ very thin variations at the surface observed in the coarse models might be only due to a lack of regularization, 3/ in the context of this specific station, the topographic correction does not play a huge role after data inversion and 4/ the variability between inverted models obtained with the thin discretization (fig. 3.21.c) is impressively low until 500 m depth regarding the coarser discretization (fig. 3.21.b), suggesting that this degree of discretization is needed to fully exploit the data content. This last point also suggests that the limit depth of confidence for this station is 500 m, below this depth, the data do not permit to resolve accurately the 1D model.

### 3.5.3 Inversion results

Most inverted data resulted in models with acceptable misfit values (tbl. 3.3). A few data could however not be well fitted, reflecting the fact that data acquired over a 2D or 3D structures cannot be fitted adequately by a 1D model (Stations 1 and 3, as expected from the dimensionality analysis in section 3.3.2). The interpreted models are represented in fig. 3.20.c.. Fig. 3.22 presents the confidence interval obtained for each model following the above described strategy. All models seem very stable when changing the parametrization and initial model, and are resolved with good confidence.

Table 3.3: Data misfit range for each stations

Station 1	10.51 - 18.44	Station 6	0.73 - 2.39
Station 2	1.28 - 1.34	Station 7	0.85 - 1.04
Station 3	3.04 - 5.38	Station 8	0.82 - 2.70
Station 4	0.78 - 2.22	Station 9	0.86 - 1.84
Station 5	0.97 - 1.7	Station 10	1.38 - 2.79

All station present a clear and progressive increase of the resistivity starting around 60 to 80 m depth. The highest resistivity are obtained at depths of 80 to 250 m. Most stations present a decrease of resistivity at high depths (200 to 400 m depth). The stations 6 and 7, located close to a summit of the catchment, clearly show lower resistivity values, and the resistive zone is shifted towards smaller depth. On the contrary, the stations 4 and 8 seem to present higher resistivity values and a deeper increase of the resistivity. These observations could be explained by static shifts, which effects would be to shift the apparent resistivity curve and to shift anomalies along the z axis after the inversion.

A comparison was made with the resistivity obtained from the 2D-ERT models, when such models were available close to the stations (black dotted lines in stations 1, 8 and 10 in fig. 3.22), showing that the ERT models often present higher resistivity than CSAMT. No further analysis is proposed, as the ERT and CSAMT data were measured at different times, and that no meteorological record could allow comparing the hydrogeological state of the soil.

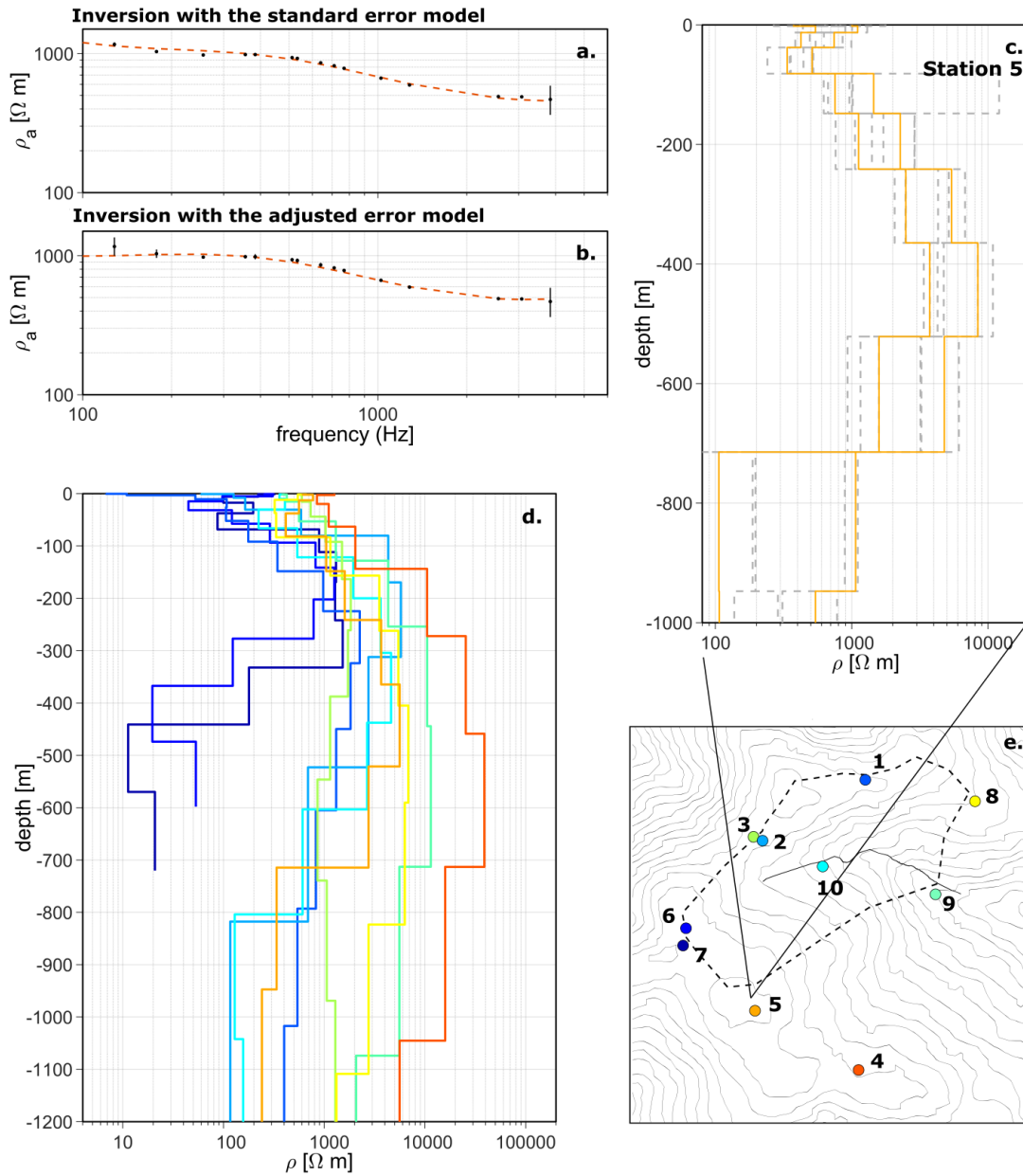


Figure 3.20: 1D inversion of the CSAMT data: a. example of data fit for the standard error model (station 9), b. example of data fit for the adjusted error model (station 9), c. set inverted models when changing the initial model and the error model and mean model (station 9), d. mean inverted model at the ten stations. The colors relate to the stations as in subfigure e.

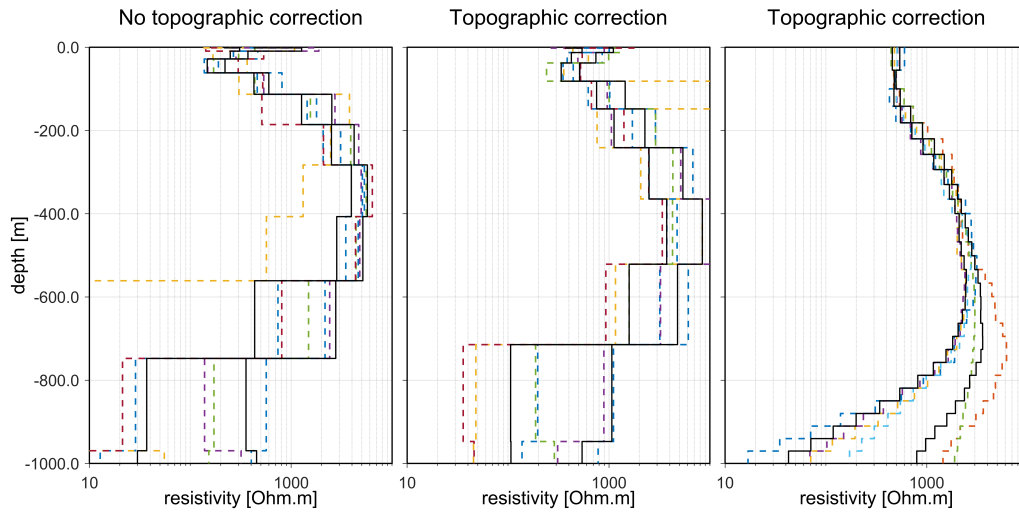


Figure 3.21: Comparison between inversions of data uncorrected from topographic distortion, inversion of corrected data and inversion realized on a thin discretized model (29 layers) at station 5.

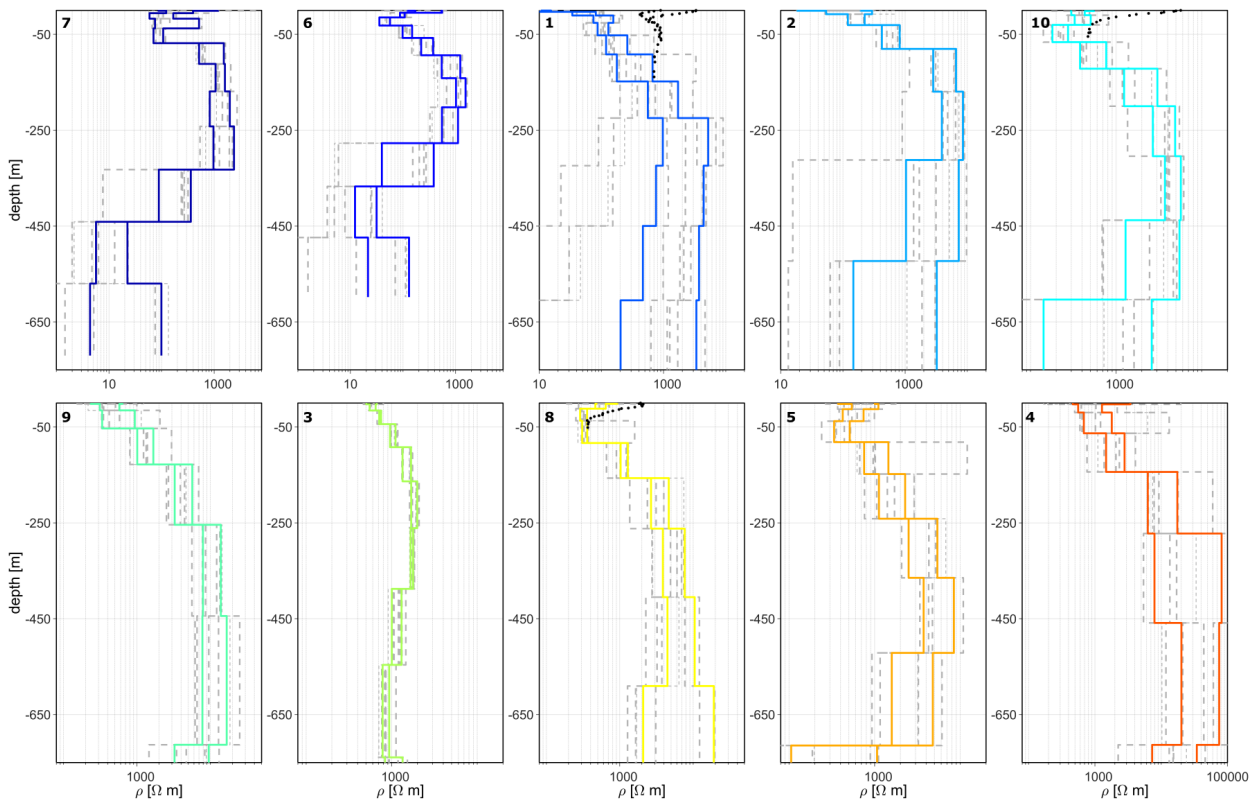


Figure 3.22: Inverted models for the ten stations. The number and color of the models related to the number and color of the stations in fig. 3.20. The first layers were compared when possible with the local 1D ERT models at neighbouring profiles (stations 1, 8 and 10)

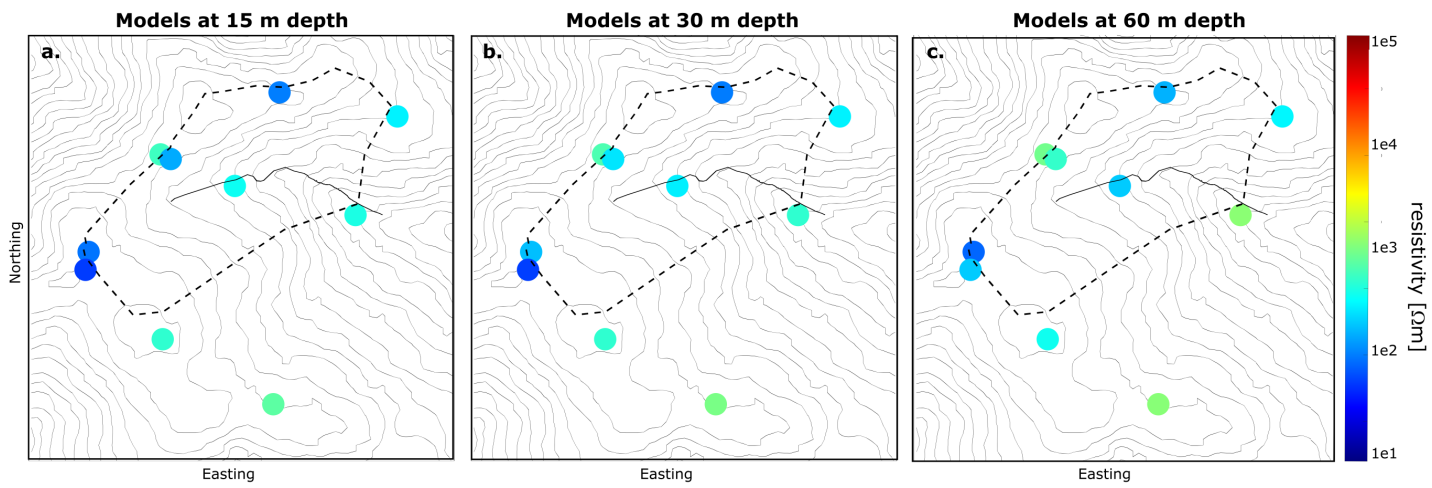


Figure 3.23: Map of the horizontal sections at 15, 30 and 60 m depth of the inverted models.

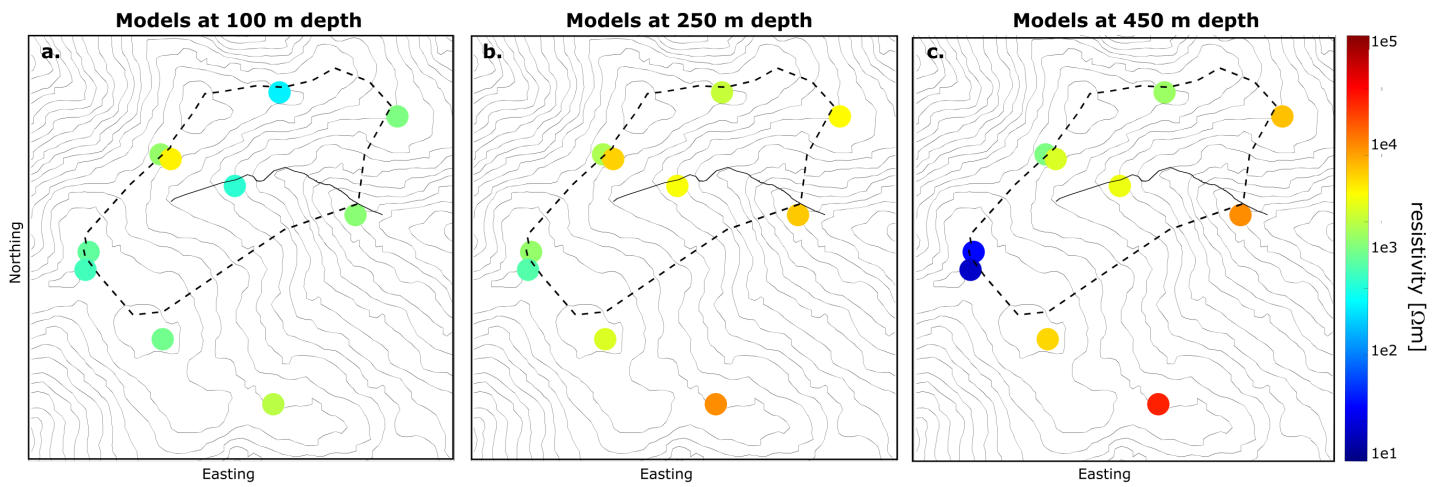


Figure 3.24: Map of the horizontal sections at 100, 250 and 450 m depth of the inverted models.

## 3.6 Interpretation and discussion

The increase of the resistivity between 80 and 250 m depth observed in all models is interpreted as the decrease of weathering, allowing to estimate the limits at depth of the aquifer. The maximum resistivity values observed at each station vary importantly over the catchment, from one station to the other: the granite at the West (stations 6 and 7) of the catchment seems generally more conductive than at the South (stations 4 and 5), and generally, the models seem to follow this North-West / South-East trend.

Such variations could be explained by static effects. Non-galvanic measurements of the electrical field should have been realized concurrently to the CSAMT survey to allow estimate such effects. However, the spatial coherency and regularity of this trend encourages to propose a geological explanation such as variations of the granite properties. Such hypothesis could not be validated, since the knowledge on the rock properties as such depths (below 100 m depth) is vacant.

One can notice that similar catchment-scale trends were already observed at the Strengbach catchment, concerning the shallowest part of the granite. ERT observations and analysis of the soils properties demonstrated in particular variations in the properties of the granite between the northern and the southern slope, depicting differences in the weathering processes. This characteristics results in clear North / South variations of the electrical resistivity in the first 20 to 30 m, clearly observed in the 2D ERT models of the catchment, but not observable in the CSAMT soundings, probably due to a lack of sensitivity in the near surface (all measurements at frequencies above 4000 Hz were removed).

At greater depth, a decrease of the resistivity is observed in most stations (fig. 3.22, 3.23, 3.24). However, without further sensitivity test, it is not clear if this trend is driven by the inversions or by the data, hence no interpretation of it is proposed.

A few interrogations remain. In particular, the decrease of apparent resistivity towards high frequencies systematically observed in all stations at frequencies above 4000 Hz could not be explained. Fig. 3.25 shows the electric and magnetic transfer functions of the subsurface, revealing that this trends originates from the measured electrical transfer functions. A few explanations are proposed. A high contact resistance could provoke such trend (Zonge and Hughes [1985], fig. 3.26), but as the contact resistance would vary from one station to the next, one would expect that the frequency at which this decrease occurs would as well vary. A poor contact at one cable could also produce such drop of the amplitude, but it would as well be expected to change from one station to the next. Another explanation could be a polarizability of the subsurface. The effect of induced polarization on CSAMT signals is not yet known, but one could suspect it to be very similar to the effect of a high contact resistance at the electrodes. It is known that the soil contains none negligible amount of clay, that could indeed produce such types of signals. However, this question was not further investigated, and is yet to be studied.

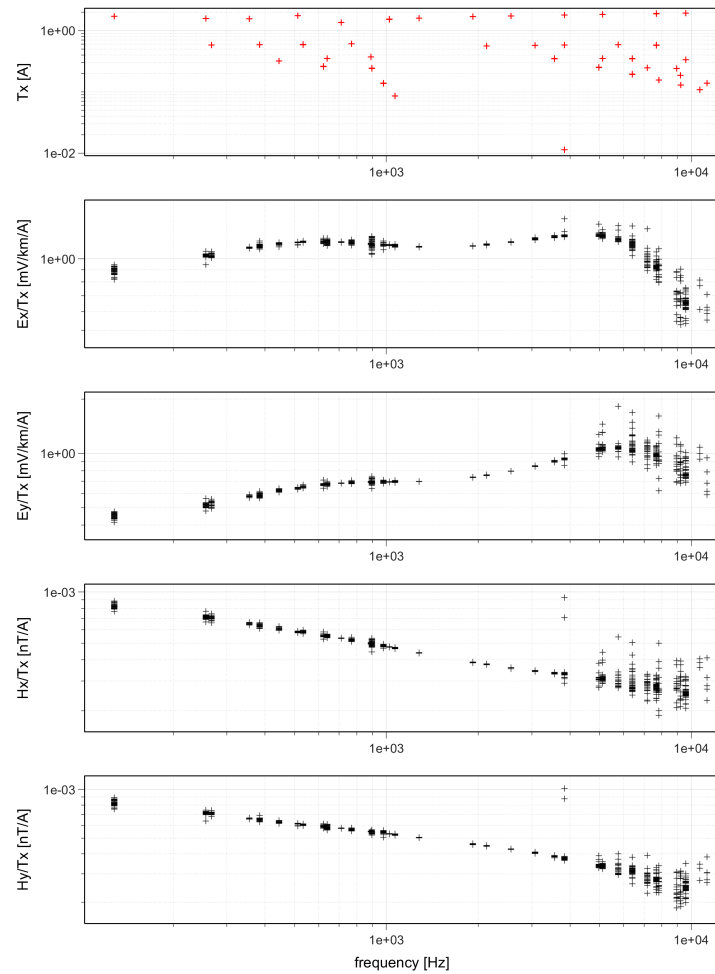


Figure 3.25: Example of filtered transfer functions recorded at the Strengbach catchment: a drop of the electrical transfer function towards high frequency is clearly visible at frequencies above 4000 Hz.

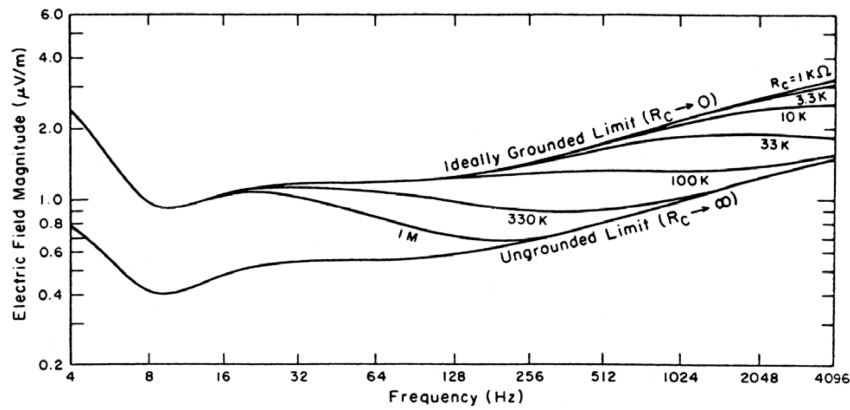


Figure 3.26: CSAMT field measurements of the electrode contact resistance effect with various contact resistances - from Zonge and Hughes [1985]

### 3.7 Conclusions and perspectives

The CSAMT method was successfully applied at the Strengbach catchment, using a 1D methodology, a sparse spatial sampling (10 stations over  $0.8 \text{ km}^2$ ) and a single transmitting dipole. An analysis of the data dimension showed that, for most stations, a 1D assumption was reasonable. Numerical modeling of the dataset allowed to estimate the topographic distortion and a correction methodology was proposed and tested on synthetic data. As this simple methodology seemed efficient, it was applied on the real data.

The apparent resistivity curves presented smooth and coherent shapes. For frequencies above 4000 Hz however, the curves presented an important decrease with frequency (more than 1 decade of resistivity per decade of frequency). These drops in the apparent resistivity seemed mainly imputable to the electrical transfer functions, but could not be explained with confidence, even though several explanations are proposed.

The data were inverted in 1D, for frequency below 4000 Hz. Low frequency data were removed when clearly identified as transitional field data. However, an adjusted error model was proposed in the inversion in order to decrease the weight of low frequency data that could potentially be affected by the transitional field. It was observed that at high frequency (above 4000 Hz), the measured apparent resistivity systematically presents strong decrease with frequency of more than one decade. This part of the data was not inverted, but was also not explained. Questions can be raised on the reason of this systematic decrease. The first layer of the subsurface is known to be a podzol containing certain minerals such as clay. This first layer is either very resistive in the southern slope, or resistive in the northern slope. One could suspect clay to provide a polarization signal. A high contact resistance could lead to such patterns in the apparent resistivity curve (through a decrease of measured electrical field towards high frequencies), however, the contact was very carefully established between the electrodes and the soil, and such effect would not be expected systematically at every stations. Last, errors in the calibration was suspected.

All inverted models presented a clear increase of the resistivity at depths from 80 to 250 m, which is interpreted as the transition from a weathered granite to an unweathered one. The limit of the weathered granite at depth appears to be shallower at the West of the catchment, and to increase towards the South-East.

It has to be noted that the maximum resistivity in each models is variable, suggesting either a spatial variation of the granite properties at depth, or a lack of constraint of the resistivity models at depth. Additional sensitivity tests could be conducted in order to evaluate the accuracy of the inverted models at depth. Last, a more exhaustive analyses of possible causes of static effect should be conducted, for example by realizing TEM sounding. This should however be done in similar meteorological and hydrogeological context as the one of the CSAMT survey, as the static effect at dry and wet periods must be different. Future CSAMT studies should systematically include inductive recordings of the electrical field, in order to analyse fully the static effects.

## 3.8 References

- Dambrine, E., Pollier, B., Poszwa, A., Ranger, J., Probst, A., Viville, D., Biron, P., and Granier, A. (1998). Evidence of current soil acidification in spruce stands in the Vosges mountains, north-eastern France. *Water, Air, and Soil Pollution*, 105(1-2):43–52.
- Doukoure, F. (2019). Acoustic measurements for the characterisation of the hard rock aquifer at the Strengbach catchment. Master's thesis, Ecole et Observatoire des Sciences de la Terre.
- Gance, J., Sailhac, P., Malet, J.-P., and Viville, D. (2020). Structure of a granitic mountain catchment inferred from electrical resistivity values. *in review*.
- Lagarias, J. C., Reeds, J. A., Wright, M. H., and Wright, P. E. (1998). Convergence properties of the Nelder–Mead simplex method in low dimensions. *SIAM Journal on optimization*, 9(1):112–147.
- Masson, F., Viville, D., Pierret, M.-C., Mouyen, M., Hecker, L., and Chabaux, F. (2012). Time-lapse microgravity study of the Strengbach catchment (Vosges mountains, France). *Comptes Rendus Geoscience*, 344(6-7):357–365.
- Pierret, M., Stille, P., Prunier, J., Viville, D., and Chabaux, F. (2014). Chemical and u–sr isotopic variations in stream and source waters of the Strengbach watershed (Vosges mountains, France). *Hydrology and Earth System Sciences*, 18(10):3969–3985.
- Pierret, M.-C., Cotel, S., Ackerer, P., Beaulieu, E., Benarioumlil, S., Boucher, M., Boutin, R., Chabaux, F., Delay, F., Fourtet, C., Friedmann, P., Fritz, B., Gangloff, S., Girard, J.-F., Legtchenko, A., Viville, D., Weill, S., and Probst, A. (2018). The Strengbach catchment: A multidisciplinary environmental sentry for 30 years. *Vadose Zone Journal*, 17(1).
- Rochlitz, R., Skibbe, N., and Günther, T. (2019). *custem*: Customizable finite-element simulation of complex controlled-source electromagnetic data. *Geophysics*, 84(2):F17–F33.
- Weill, S., Delay, F., Pan, Y., and Ackerer, P. (2017). A low-dimensional subsurface model for saturated and unsaturated flow processes: ability to address heterogeneity. *Computational Geosciences*, 21(2):301–314.
- Wild, B., Daval, D., Beaulieu, E., Pierret, M.-C., Viville, D., and Imfeld, G. (2019). In-situ dissolution rates of silicate minerals and associated bacterial communities in the critical zone (Strengbach catchment, France). *Geochimica et Cosmochimica Acta*, 249:95–120.
- Zonge, K. L. and Hughes, L. J. (1985). Effect of electrode contact resistance on electric field measurements. In *SEG technical program expanded abstracts 1985*, pages 231–234. Society of Exploration Geophysicists.

### 3.8.1 References to internet websites

PHOENIX GEOPHYSICS © 2006 - [http://phoenix-geophysics.com/home/?](http://phoenix-geophysics.com/home/)

## Chapter 4

# **Imaging fractured aquifers: the deep 3D structure of the Séchilienne landslide using Resistivity - Distributed Automated System (R-DAS)**

The work presented in this chapter is based on Lajaunie, M., Gance, J., Nevers, P., Malet, J.-P., Bertrand, C., Garin, T., Ferhat, G. (2019): "Structure of the Séchilienne unstable slope from large-scale three-dimensional electrical tomography using a Resistivity Distributed Automated System (R-DAS)" published in *Geophysical Journal International* (doi: 10.1093/gji/ggz259).

## Introduction

In this chapter, the hydrogeophysical study of deep fractured bedrock aquifers is tackled. Fractured bedrock aquifers present multi-scale porosity, preferential flow path and constitute 3D structures. The challenge of imaging such complex structures requires a dense 3D spatial sampling, and a large penetration depth. We present a methodology based on large-scale 3D electrical resistivity tomography to study such type of aquifers. This methodology takes advantage of a novel type of measurement system: Resistivity Distributed Automated Systems (R-DAS). In this chapter, such a methodology is applied to image the slope-scale resistivity variations at the Séchilienne landslide.

The structure of the Séchilienne landslide is known to be very complex. Imaging this structure at depth requires a dense spatial sampling, at a large scale ( $1\text{km}^2$ ). In such context (large topographic variations and dimensionality of subsurface structure) CSAMT and CSEM measurements are often object to important distortion effects (static shift for example), difficult to correct without additional measurements (typically TEM, or ERT). Instead, large-scale 3D ERT is expected to provide a good sensitivity to the 3D structure, using accessible methods to account for the distortion effects produced by the important topographic variations. Subject to the large size of the survey area, and a low noise level, important depth of investigations were expected to be reached ( $>200\text{ m}$ ).

### 4.1 The Séchilienne landslide

The Séchilienne slope is one of the largest and most active landslides of the European Alps with a volume estimated at ca.  $60 \pm 10\text{ M m}^3$  and depths in the range of 150 to 200 m (Le Roux et al. [2011]). The geology consists of fractured hard rocks (micaschists) with double permeability and strong spatial heterogeneities. The deformation of the slope is monitored by on-site extensometric gauges and at distance by a terrestrial radar and a total station since more than 20 years (Duranton et al. [2003]). The hydrogeological and hydrochemical processes in the fractured hard rock (water infiltration, chemical alteration) control the deformation of the unstable slope. The complex structures of the slope (fractures, spatial variation in the degree of micro-fracturation, clay deposits in the porosity) create preferential water flow paths characterized by specific geochemical signatures (Vallet et al. [2015]). In order to constrain these flow paths and understand the hydro-geomechanical response of the slope to forcing rainfall events, and to the seasonal hydrological cycle, a better knowledge of the slope structures is needed. Images of the in-depth structures of large slopes can be obtained through geomechanical modeling if the observation of the surface displacements over time allows inferring the internal mechanical process controlling the deformation (Cappa et al. [2014]) or by geophysical surveys. The latest can provide relevant information on the structures and discontinuities shaping the subsurface. Geophysical methods have been used in the past to study the Séchilienne slope (Duranton et al. [2003]; Meric et al. [2005]; Jongmans and Garambois [2007]; Helmstetter and Garambois [2010]; Le Roux et al. [2011]). Imaging the variations in the electrical properties of the Séchilienne slope has proven to be insightful for understanding the subsurface geological and hydrological properties and delineating zones with specific mechanical behaviours (Meric et al. [2005]; Le Roux et al. [2011]). However, these surveys were based on profile measurements and 2D assumptions were made, considering that the subsurface is homogeneous laterally to the profiles. This assumption allows a first-order interpretation of the data, but artefacts are locally produced by the strong gradient of the topography (locally close to  $45^\circ$ ) perpendicular to the survey line and the presence of 3D structures.

At Séchilienne, imaging complex structures at a few hundreds of meters below the surface necessitates the application of 3D electrical surveys. Such type of investigation is rarely applied to landslides because of rough topographies, presence of vegetation, and, in general, difficult access to the measurement sites. Moreover, large depths of investigation require large spacing between electrodes and therefore the spreading of several kilometers of heavy multicore cables for standard measurements with multi-electrodes resistivity meters. Most of the landslide 3D models presented in the literature were created from the interpolation of multiple 2D profiles (Travelletti and Malet [2012]; Gance et al. [2016]). Only a few examples exist where "real" 3D landslide surveys have been carried out but these investigations were limited to small depths of investigation (from 10 to 30 m: Friedel et al. [2006]; Uhlemann et al. [2017]). This study takes advantage of recently developed Resistivity Distributed Automated Systems (R-DAS) for electrical resistivity measurements. R-DAS are easily portable

and heavy cable free systems that allow overcoming the previously mentioned difficulties. 3D electrical data acquired over a large-scale array (1.5 km<sup>2</sup>) using the FullWaver system from IRIS Instruments<sup>®</sup> are presented and interpreted. The DC resistivity dataset is processed and inverted with the BERT software package (Rücker et al. [2006]; Günther et al. [2006]). A resistivity model is proposed and interpreted taking into consideration the previous geotechnical, geophysical and hydrogeological studies. The objectives of the work are 1) to propose a 3D resistivity model of the Séchilienne slope up to a depth of 500 m, 2) to discuss the quality of data and of the inversion models, and 3) to interpret the 3D resistivity model in terms of rock properties, structure and microstructure and water content. In particular, the impacts of the sparseness and quality of the resistivity measurements are discussed. Sensitivity tests are carried out to define the limits of interpretability of the models.

### 4.1.1 Geological and geomorphological setting

The Séchilienne slope is located on the right bank of the Romanche River, South East of Grenoble (Isère, France). From a geological viewpoint, the slope is part of the Paleozoic external crystalline massif of Belledonne. The substratum is mainly composed of micaschists characterized by a N-S trending sub-vertical foliation. Stratigraphically discordant carbonate deposits from the Carbonifer to the Lias eras cover micaschists located on the top East of the massif (Mont Sec) and along the massif ridge line. The slope is also locally covered by Quaternary (Würm) glacio-fluvial deposits (Vengeon [1998]; Vallet et al. [2016]). The volume of the unstable slope is estimated to 60 M m<sup>3</sup> (Le Roux et al. [2011]). The most active part of the landslide, named “Les Ruines”, is located on the eastern border of the unstable zone. Its volume is estimated at 3 M m<sup>3</sup>. The measured surface velocity is in the range of 10 cm.yr<sup>-1</sup> for most of the unstable slope to nearly 300 cm.yr<sup>-1</sup> in the active part (Dubois et al. [2014]). The landslide extends from 400 m to 1100 m elevation (Le Roux et al. [2011]) and presents steep slopes around 35° to 40° resulting from the incision by the Romanche River and the ice of the Romanche glacier during the Quaternary glaciations (Montjuvent and Winistorfer [1980]). Above 1100 m, a major head scarp about 10 m high and several hundreds of meters wide separates the Mont Sec from the northern part of the unstable zone. The morphology of the Mont Sec corresponds to a glacial plateau with local moraine deposits mixing amphibolite and gneiss clasts. To the North, the presence of peat filling locally North-South depressions with a maximum thickness of 10 m has been noticed by Legchenko et al. [2011]. To the East, a North-South fault scarp delineates the landslide boundaries. To the West and the South, no clear geomorphological evidence of landslide activity is identified. In depth, the landslide is characterized by a deep progressive deformation with a maximum depth estimated at 150 m (Le Roux et al. [2011]) which is hard to estimate due to the absence of a well-defined basal sliding surface. The geological information (identification of the faults at the surface and in the anthropogenic gallery of Electricité de France – EDF – at the base of the slope, interpretation of 2D resistivity and seismic profiles) have been summarized by Baudement et al. [2013] and integrated in a Gocad-derived 3D model used for the interpretation of the 3D resistivity model.

Two boreholes (SC1, SC2; fig. 4.1c) were drilled in 2010 in the unstable area at depths up to 150 m. Analysis of the core samples provide direct information on the lithology and fracturation of the slope. The micaschists present very local variations in the nature of the fillings (clay, calcite, sandstone, iron oxide, chlorite, quartz veins, pyrite) and in the tectonic and geochemical processes (fracturation, alteration, oxidation). Very fractured sections are observed at several depths; these sections are characterized locally by a total loss of continuity in the cores. The two boreholes do not present the same sequence of lithology and fracturation demonstrating the heterogeneity of the slope induced by the gravitational deformation.

Inclinometer observations have been acquired at least once a year in SC1 and SC2 from 2009 to 2014 (fig. 4.1c). At SC1, the vertical profile of velocity identifies two units separated by deformation surfaces at ca. -60 m and -106 m; at SC2, only one deformation surface at ca. -112 m is observed. The depth of the instability can thus be considered in the range of around -110 m (Duranton et al. [2013]).

### 4.1.2 Hydrogeological setting

The heterogeneity in fracturation and microstructure controls the location of the flow paths and the transit times (Vallet et al. [2015]). The Mont-Sec massif is characterised by a dual-permeability behaviour typical of

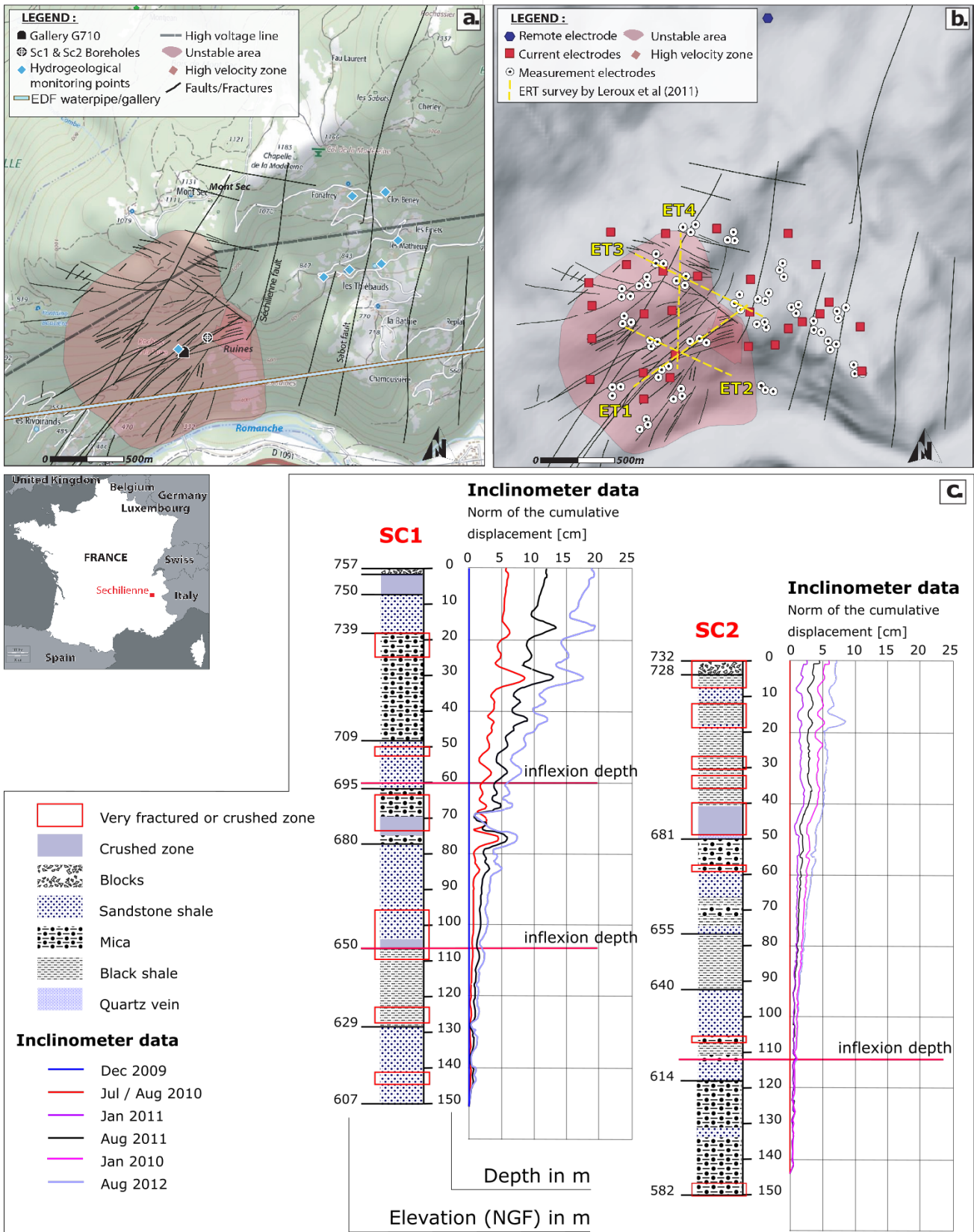


Figure 4.1: Morphology of the Séchilienne slope: (a) Geomorphological setting (fault model from Barféty et al. [1972] and Vengeon [1998] - appendices I and II) and location of boreholes and water sampling points; (b) Location of the portable Full-Waver resistivity measurements and of the 2D ERT profiles acquired by Le Roux et al. [2011]; (c) Lithological profile of the unstable slope obtained from core samples from the SC1 and SC2 boreholes, related time-lapse inclinometer observations and their respective interpretation (Duranthon et al. [2013]).

fractured rocky aquifers where permeable fractures play a major role in the drainage. High flow velocities (ranging from 0.45 to 0.84 km.day<sup>-1</sup>) are observed in the Sabot fractures and in the Séchilienne fault system) and low flow velocities (0.08 km.day<sup>-1</sup>) are observed in the less pervious micro-fracturation bypassing the main fractures (Mudry and Etievant [2007]). At the base of the slope, the EDF gallery (fig. 4.1a) acts as a major drain of the massif (Vallet et al. [2015]).

The difference in hydraulic conductivity between the unstable zone (very fractured) and the underlying stable bedrock creates a system of two-layer aquifer with a shallow perched aquifer, localized in the unstable zone, and a deep aquifer connected by major fractures. The landslide perched aquifer is temporarily and mainly discontinuous and its extent and connectivity fluctuate according to short-term recharge events through a dense network of open fractures associated to trenches and counterscarps at the surface. During the high-flow periods, a water input from the top sedimentary cover close to Mont Sec also contributes to the recharge, while during the low-flow periods, the perched aquifer is almost dry (Guglielmi et al. [2002]; Vallet et al. [2015]). The hydraulic behaviour is very contrasted between high-flow and low-flow periods (Vallet et al. [2015]). During high-flow periods, the recharge amount is sufficient to maintain the perched aquifer saturated and the numerous disconnected saturated zones are temporarily connected (Cappa et al. [2014]). A subsurface drainage of the perched aquifer occurs in these periods, mostly controlled by fractures oriented at N70. During the low-flow periods, temporarily disconnected saturated zones appear. These disconnected zones are filled after rain events but are not sustained because of the low recharge amount. The deep aquifer, which extends all over the massif, corresponds to a deep saturated zone (altitude around 550 m asl) in the fractured bedrock; the vadose zone above it is about 100 m thick (Vallet et al. [2015]).

### 4.1.3 Landslide kinematics

Changes in landslide displacement rates are controlled by rainfall events as identified by the positive correlation between antecedent cumulative precipitation and average velocities (Rochet et al. [1994]; Alfonsi [1997]). Vallet et al. [2016] identified a correlation between the water recharge (instead of the precipitation) and the surface displacement rates. Recharge variations and surface displacement rates are seasonally linked with high displacement rates during high-flow periods and low displacement rates during low-flow periods (Vallet et al. [2016]). Moreover, as hypothesized by Cappa et al. [2014], high water pressures in the deep aquifer can facilitate the rupture of the landslide due to stress transfer and frictional weakening during groundwater-level changes. So far, these results are based on few point measurements surface observations and remain difficult to spatialize, particularly at depth. In this context, the imaging of the 3D spatial variations of the electrical resistivity could be useful to confirm and enrich the previous results.

## 4.2 Geophysical instrumentation and data

To image the structure of the slope up to a depth of 500 m, a 3D resistivity tomography with an array of portable electrical automated resistivimeters has been carried out in July 2017 over an area of 2.0 km<sup>2</sup> (fig. 4.1b).

### 4.2.1 Resistivity-DAS: electrical measurement devices and acquisition setup

The FullWaver system of IRIS Instruments is composed of several autonomous receivers (V-FullWaver) and of one autonomous current recorder (I-FullWaver) connected to a 3 kW high-power transmitter (TIPIX - IRIS Instruments). The combination of the receivers and the transmitter forms a Resistivity Distributed Automated System (R-DAS). The measurement principle of the Fullwaver system is the same than the one used for multi-electrode resistivimeters (fig. 2.25). It consists in measuring the current injected by the transmitter between two current electrodes and the resulting voltage between two reception electrodes. The differences with multi-electrode systems are that:

- The transmitter and receiver systems are separated (instead of being in one box) to avoid electromagnetic interference of strong power transmitted to the receiver;

- The receiver system is composed of multiple autonomous receivers connected to a maximum of three electrodes. With this technology, the receivers are not linked together by any cable allowing the planning of 3D electrical surveys on rough topography;
- The transmitter and receivers are separated, so, instead of being synchronized to the same internal clock, the measurements are time stamped to the GNSS clock;
- The current and voltage are recorded as time series with a sampling frequency of 100 Hz, requiring to process the data afterwards with advanced signal processing techniques.

At Séchilienne, 23 V-FullWavers connected to 3 electrodes were used, forming two 50 m orthogonal dipoles, constituting a measurement network of 69 electrodes. The theoretical positioning of the electrodes was planned using orthophotographs in order to distribute the systems as regularly as possible, taking into account the rough topography and the accessibility to the measurement sites. In practice, on site, the positioning was slightly adapted. The survey was realized over five days in July 2017 in a period of high-water flows at the end of the Spring season. On site, each day, the V-FullWavers were programmed in the morning and recordings were acquired during the whole day. At the end of the day, the V-FullWavers were taken back for data collection and recharge of the battery. The current injections have been realized between a fixed remote electrode located at 1.5 km North from the investigation area, at an altitude of 1079 m asl and a mobile current electrode successively grounded at 30 locations distributed over the studied area (fig. 4.1b), at various altitudes between 51 m above and 535 m below the fixed remote electrode. The fixed remote electrode (fig. 4.2d) was buried in a forested area in a trench filled with salted water. The injection cable was set as far as possible from the reception cable in order to limit inductive and capacitive coupling effects. A great attention was paid to lower the contact resistance at the mobile current electrode (by adding 20 L of salted water) five minutes before each injection and at the remote electrode (by adding 40 L of salted water each day). The contact resistance measured between the injection and remote electrodes was in the range 0.4 to 4.0 k $\Omega$ , allowing injecting a current between 0.5 and 3.2 A. The total injection time was at least of 400 s corresponding to 100 stacks for 2 s injection duration. This duration has been increased up to 600 s (150 stacks) for the lower amperages (fig. 4.5b). At the measurement electrodes, it was not possible to add water every day because of the sharp topography and the difficult accessibility. As a consequence, the contact resistance can be relatively high with mean contact resistance of 15 k $\Omega$  and a maximum of 67 k $\Omega$ . This range of contact resistance is however not affecting the measurements because of the high input impedance of the FullWaver systems (100 M $\Omega$ ).

The position of each electrode was measured by differential GNSS using Trimble R8s receivers; the GNSS dataset was processed with the TBC (Trimble Business Centre) software. A permanent GNSS antenna belonging to the French geodetic datum (RGF93) was used to cluster the measurements to the national topographic reference. In order to achieve the best position determination, two base stations were used at close distance (1.2 km) from the site. The use of two base stations allows estimating accuracy on each position, in the range from 0.02 m to 0.60 m in the horizontal plane. The lowest accuracy corresponds to measurement points located under forest vegetation.

### 4.2.2 Data quality control

Data were measured with a good quality for the first four days of measurements. The fifth day, the measurements were realized while a thunderstorm was approaching. This is clearly visible on the voltage measurements of this day showing a lot of spikes and a charging of the soil with a sudden increase of the self-potential (fig. 4.3). All measurements were stopped when the thunder hit the mountain and started again some hours later.



Figure 4.2: Photographs of the monitoring equipment and of the measurement sites: (a) V-FullWaver unit at position FW9; (b) Zoom on the plugs for the three measurement channels on a V-FullWaver unit; (c) Zoom on the control screen of a V-FullWaver unit; (d) Remote electrode fully watered with a highly conductive salted mixture.

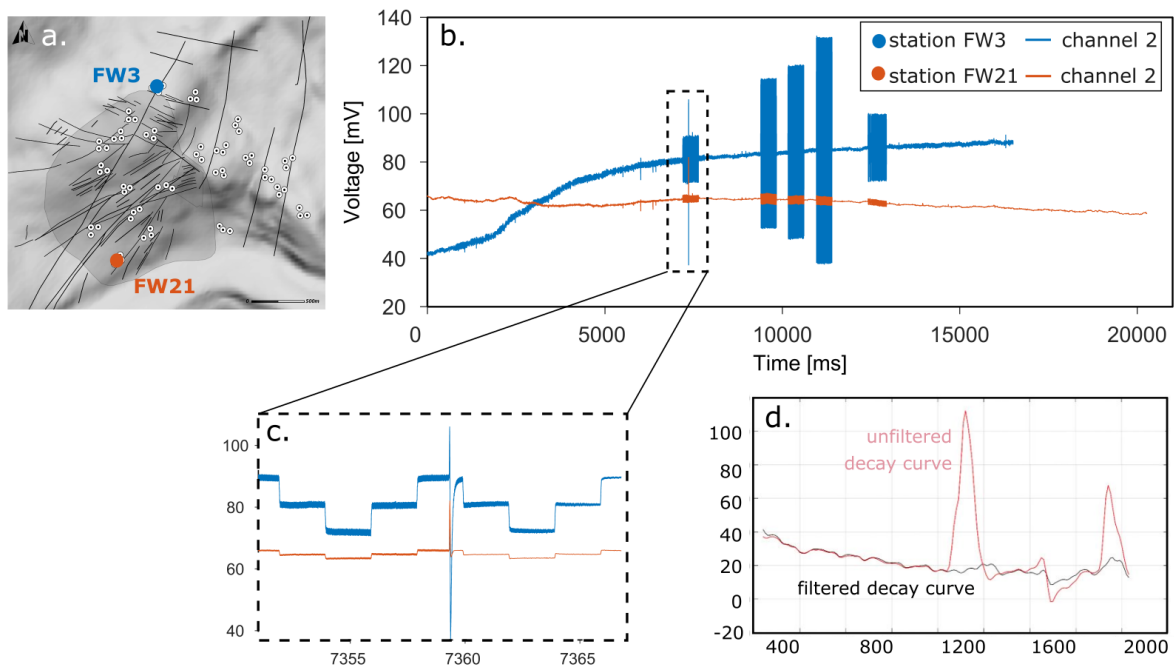


Figure 4.3: Example of raw voltage time series and impact of spike noise filtering: (a) Location of the stations FW3 and FW21 at the top and base of the investigated area; (b) Example of one day of measurement at stations FW3 and FW21 (data from the second day of measurements); (c) Example of spikes in the measured voltages recorded during a thunderstorm; (d) Effect of spike noise filtering on the decay curve: the unfiltered decay curve in red displays some spikes, efficiently filtered by the despiking procedure (black curve).

## 4.3 Methodology

The methodology to create a resistivity model of the slope consists in 1) the extraction and pre-processing of the raw data, 2) the filtering and error assessment of the data, 3) the test of inversion parameters, and 4) the sensitivity analysis of the model parameters. The four steps are presented in fig. 4.4. The software FullWave Viewer is used for pre-processing the data (step 1), and the software package BERT (Rücker et al. [2006], Günther et al. [2006]) is used for the inversion and sensitivity tests (steps 3 and 4).

### 4.3.1 Data extraction and pre-processing

The voltage data of all electrodes were processed with the IRIS Instruments software FullWave Viewer (fig. 4.3). The processing consists in resynchronizing possible unsynchronized time series, filtering spikes and self-potential jumps, stacking the different periods after synchronous detection of the fronts, computing the average voltage over a part of the injection window on the stacked period, computing the average current over a part of the injection window on the stacked period, calculating the resistance from the previous measurements, calculating the chargeability over 20 windows during the off time of the stacked period, and finally calculating the total chargeability from the 20 windows and the associated standard deviations. The data with low signal (typically  $V_p < 0.1$  mV) and high standard deviations (typically  $\text{std} > 200$  mV.V<sup>-1</sup> or 20 %) have been reprocessed manually. The measured chargeability is comprised in the range from 10 to 30 mV.V<sup>-1</sup>. This high chargeability is explained by the presence of disseminated pyrite.

### 4.3.2 Data filtering

#### Extreme topographic effects

The roughness of the slope, the presence of high slope-gradients and of sharp topographic anomalies (scarps, depressions) are impacting the computation of the apparent resistivity inducing anomalies; this is referred as the topographic effect  $t$  (Fox et al. [1980], Rücker et al. [2006]). The topographic effect  $t$  is the ratio between the approximated geometric factor for a homogeneous half space  $k_a$  and the true geometric factor  $k$  according to eq. 4.1:

$$t = \frac{k_a}{k} \quad (4.1)$$

A high-resolution Digital Surface Model (DSM), acquired from an airborne LIDAR survey (0.5 m spatial resolution) over the landslide and complemented with a lower resolution DSM (5 m) acquired by airborne stereophotogrammetry over the surrounding stable slopes are combined to obtain a realistic topography of the slope. Using the resulting DSM, sampled at a spatial resolution of 0.2 m, the  $t$ -value is computed by means of forward computation (Rücker et al. [2006]), providing a distribution of  $t$ -values (fig. 4.6a). In this study, the survey layout and the topographic variations lead to topographic effects ranging from -90 to 12. A few data display extremal topographic effect (less than -4 or more than +6) (fig. 4.6a). These data correspond mostly to situation where the geometrical factor is extremal (higher than  $10^6$  in absolute value, fig. 4.6b), therefore associated to very low potential measurements at the receivers. The associated data points - affected by a very high uncertainty - have been removed. Over 1181 data arising from the pre-processing, 14 data have been filtered because of extreme topographic effect, and 19 additional data have been filtered during the inversion because of high uncertainty. In total, 1148 data are introduced in the inversion process.

#### Effect of electrode layout on data uncertainty

Because of the unusual geometrical layout of the survey (i.e. the measurement dipoles are very small in comparison to the distance between the injection electrodes and the measurement electrodes, and the injection and measurement dipoles are rarely collinear), the uncertainty associated to the electrode positioning is a possible source of errors (Uhlemann et al. [2015]). This uncertainty propagates in the computation of the geometrical factor  $k$ , and can be highly amplified locally for specific cases of unusual (not aligned) quadrupolar geometries.

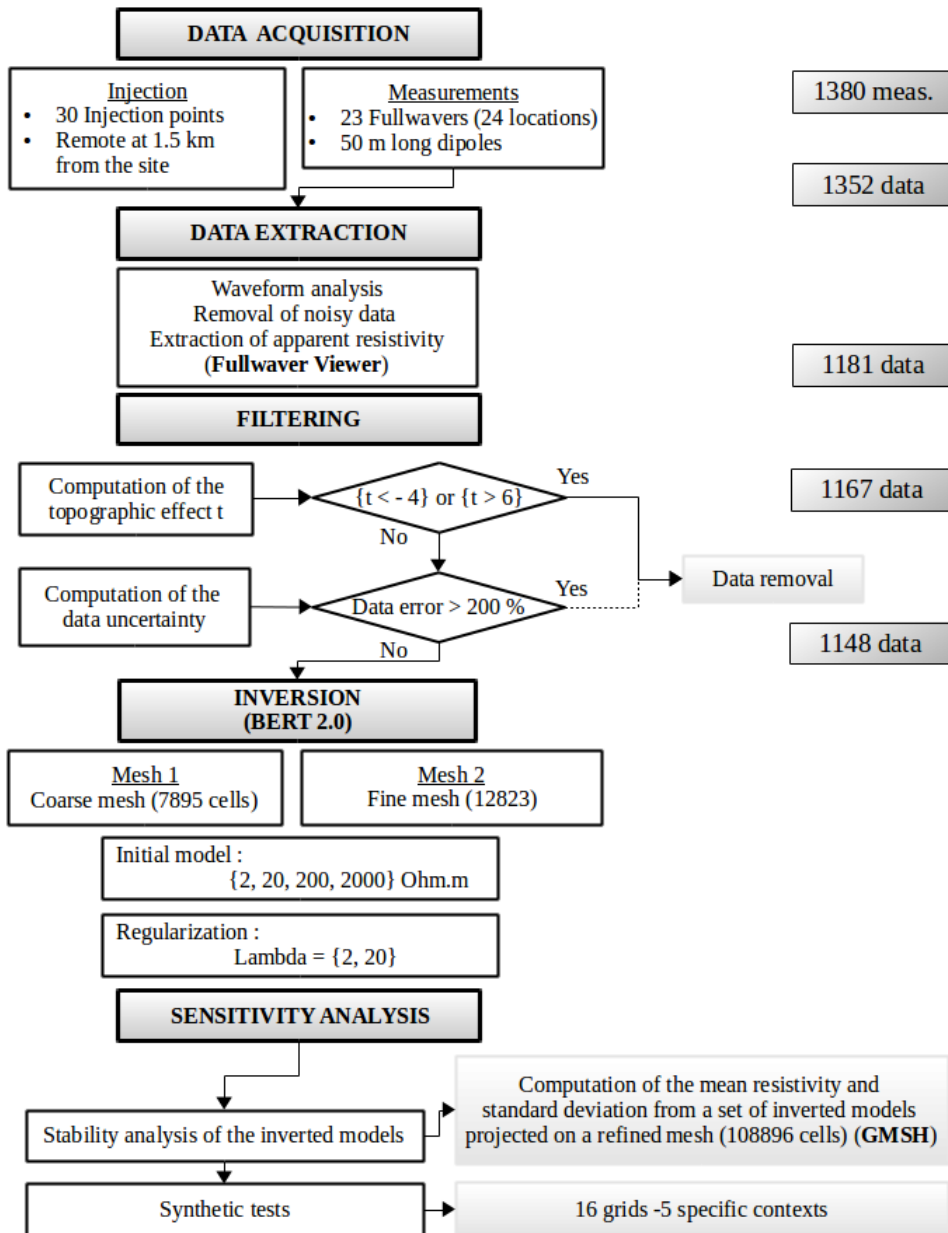


Figure 4.4: Methodological flowchart.

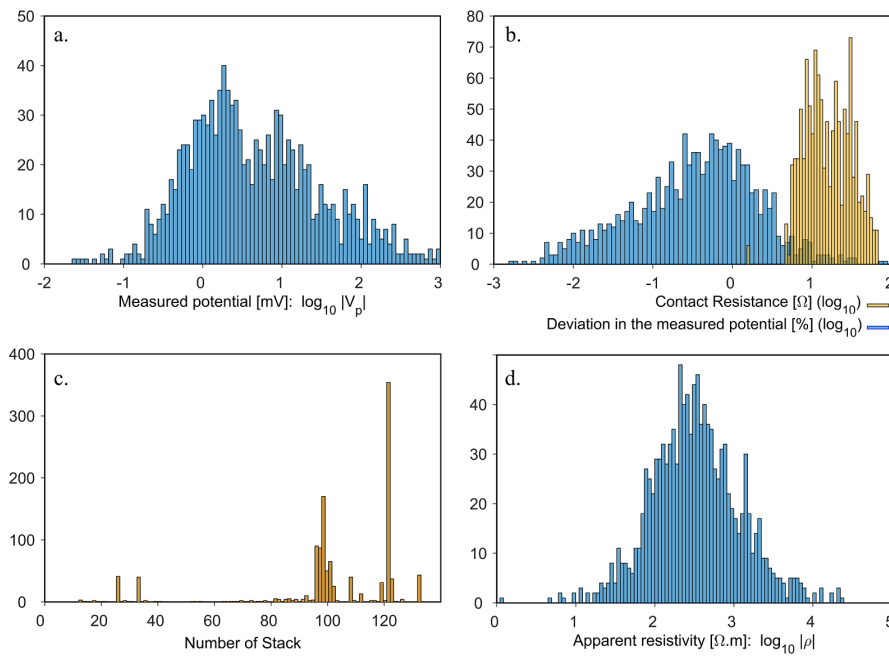


Figure 4.5: Distribution of voltage observations: (a) Distribution of the measured electric potential (in mV); (b) Distribution of contact resistance values and deviation in the measured potential; (c) Distribution of the number of stack for each data and (d) Distribution of the apparent resistivity values.

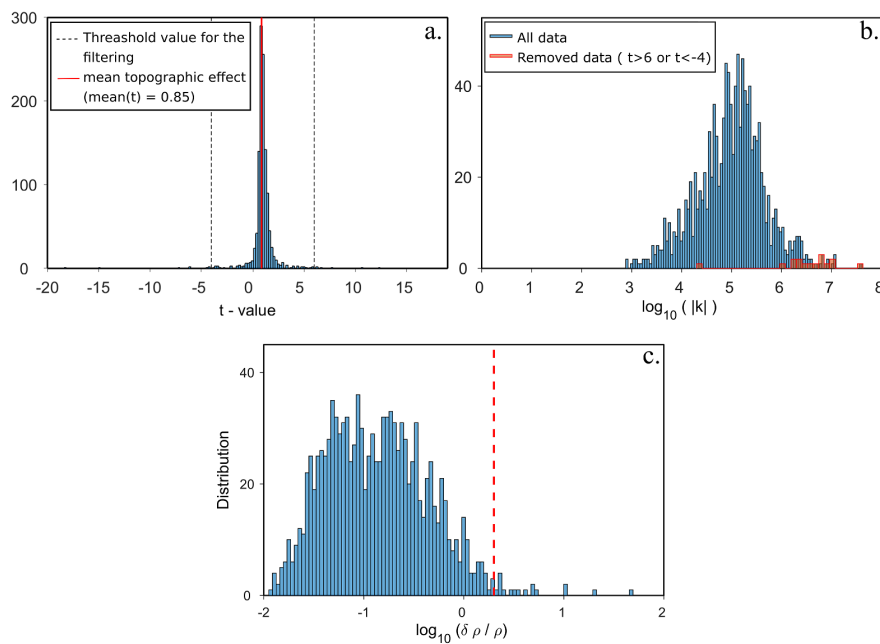


Figure 4.6: Data filtering: (a) Distribution of topographic effects and filtering of extreme values ( $t > 6$  and  $t < -4$ ); (b) Distribution of geometrical factors (in red: geometrical factors of the data presenting extreme values of topographic effects): extreme topographic effect is often related to high geometrical factor; (c) Distribution of relative error on the apparent resistivity values.

In particular, when considering quadrupoles formed by two orthogonal dipoles, one in the alignment of the other, such that the two measurement electrodes are almost equidistant from each injection electrodes, the geometrical factor of such a quadrupole is exceptionally large, and low positioning errors (up to 50 cm) cause dramatic errors in the estimation of  $k$ . Two options are available. The first one is to filter out these points. The second is to compute and use their associated uncertainty in the inversion. We chose the second option as it will damp automatically and gradually each data point weight in the inversion instead of rejecting a number of data points based on a threshold value chosen subjectively. The effect of the electrode positioning on the geometrical factor has been quantified for each quadrupole using the positioning accuracy provided by the GNSS measurements (when available) or using a constant uncertainty of 2 m around the electrode when no GNSS accuracy was available. Assuming that the topographic effect is accurately computed with BERT, the error on the geometric factor can be calculated as the error on the approximated geometric factor for a homogeneous half-space. The relative error affecting the geometrical factor is calculated with eq. 4.2 and eq. 4.3:

$$\delta k = \sum_{i,j} [\delta X_{i,j} \frac{\partial k}{\partial X_{i,j}}] \quad (4.2)$$

where  $X$  is successively each of the two horizontal coordinates for all four electrodes forming the quadrupole for which  $k$  is computed. In the sum,  $i$  is successively [A, B, M, N] and  $j = 1, 2$  scans the two horizontal coordinates, with, for example

$$\frac{\partial k}{\partial x_A} = \frac{k^2}{2\pi} \left[ \frac{x_A - x_M}{[(x_A - x_M)^2 + (y_A - y_M)^2]^{3/2}} - \frac{x_A - x_N}{[(x_A - x_N)^2 + (y_A - y_N)^2]^{3/2}} \right] \quad (4.3)$$

The derivatives with respect to the  $y$  component and to the other electrodes have similar forms. A second uncertainty arose from the accuracy of the potential measurement itself. Following Günther et al. [2006], we define this error as the sum of a fixed percentage  $\%p$  and a relative voltage error  $\frac{\delta V}{V}$ . The total error is expressed in eq. 4.4:

$$\frac{\delta \rho}{\rho} = \%p + \frac{\delta V}{V} + \frac{\delta k}{k} \quad (4.4)$$

The errors are computed using a percentage error of 1% and a voltage error  $\delta V$  of  $2.10^{-5}$  V. Data with uncertainties higher than 200% are filtered during the inversion (fig. 4.6c).

### 4.3.3 Inversion strategy

Sixteen inversions of the full dataset (Table 4.1) have been realized with the software package BERT (Rücker et al. [2006], Günther et al. [2006]). BERT is based on preconditioned conjugate gradient methods. The modeling process is realized using two meshes for the computation of the primary and secondary resistivity fields and the computation of the potential is performed with quadratic shape functions. Computations are carried out on unstructured tetrahedral meshes of  $\{340 \times 340 \times 200\}$  km<sup>3</sup> for the forward modeling and  $\{2 \times 2.7 \times 2\}$  km<sup>3</sup> for the inversion (parameter mesh). The parameter mesh covers the entire survey area, including the remote (fixed) injection electrode, and its top interface describes the true topography all over and outside the covered area. Although optimal for the dimensions of the large-scale geological and hydrogeological features of the slope, the spatially sparse and irregular sampling leads to a local lack of resolution close to the surface because of the large inter-distance between the FullWaver systems (between 50 and 200 m). In order to test the stability of the inversion process and to assess the areas unresolved by the data inversion, several parametrizations of the inversion have been tested. Sixteen inversions have been realized changing one by one three parameters controlling the inversion process:

- First, the regularization of the inversion, controlled in BERT by the parameter LAMBDA, defines the degree of spatial variation authorized by the inversion, hence the smoothness of the model. A weak regularization (here fixed at LAMBDA = 2) will integrate the data noise in the inverted model, while a strong regularization will prevent from inversion-induced noise but can also impeach the finest information content of the data to be expressed in the inverted model;

Table 4.1: Values of parameters used in the inversion models.

Regularization	Initial model (homogeneous resistivity in $\Omega.m$ )	Mesh
LAMBDA = 2	STARTMODEL = 2	Coarse: 7895 cells
LAMBDA = 20	STARTMODEL = 20	Fine: 12823 cells
	STARTMODEL = 200	
	STARTMODEL = 2000	

- Second, the initial model is considered homogeneous, with different resistivity values, allowing testing several areas of the model space. If the initial model is too far from the true model, the inversion might not succeed in updating the model to bring it closer to the true model. Moreover, if the data sensitivity is locally low (due to the sparse sampling), depending on the regularization, the inverted model might locally be mostly driven by the initial model. The variation in the initial model is therefore expected to allow detecting locally unresolved areas in the model.
- Last, the coarseness of the mesh plays a role in the quality of the modeling and in the computation of synthetic data. Coarse and fine meshes (Table 4.1) have been used in the inversions, for the purpose of detecting if differences arise regarding the accuracy of the modeling, given that a coarser model will necessarily provide a less accurate description of the topography.

From the sixteen inversions presented in Table 4.1, all 12 stable inversions (i.e. converging with reasonable misfit values and presenting stable distribution of resistivity) are selected (fig. 4.8). The mean and standard deviation of the logarithmic resistivity in the set of inverted models are computed on a refined mesh (108896 cells), on which each inverted model is projected. In the following, the resulting models are respectively referred to as ‘mean resistivity model’ and ‘standard deviation model’ (fig. 4.9). The local dispersion of resistivity values amongst all inverted models provides information on the sensitivity: only areas displaying similar resistivity values are considered resolved by the inversion, and the sensitivity can be inferred from the discrepancy in the set of inverted models. The stack of the inverted models is used to filter noise created by the inversion. Inversion results and interpretation will be presented and discussed in Section 4.4 and 4.5, taking into account the sensitivity tests performed in the following section.

#### 4.3.4 Sensitivity tests

The sensitivity of the data and of the inversion is assessed with synthetic tests. Sixteen grids have been created and the synthetic data related to our survey have been computed with BERT, with respect to the resistivity values indicated in Table 4.2. The synthetic data have been inverted with both a strong (LAMBDA = 20) and a weak (LAMBDA = 2) regularization, using an error model computed with a similar strategy as for the field data, and expressed by eq. 4.4. The mean and standard deviation models of the strongly and weakly regularized models are computed for all 16 tests. The accuracy in the location, the shape and the resistivity value of the main anomalies observed in the field inverted models are tested, as well as the possible spreading induced by the inversion process. The field inverted models display resistivity values ranging from 100 to 10000  $\Omega.m$ , and present the following characteristics: 1/ a deep conductive anomaly located at the East of the unstable zone, extending locally towards the surface and 2/ a strong resistive anomaly at the surface, all over the unstable zone at the west of the model (fig. 4.9, 4.11 and 4.12).

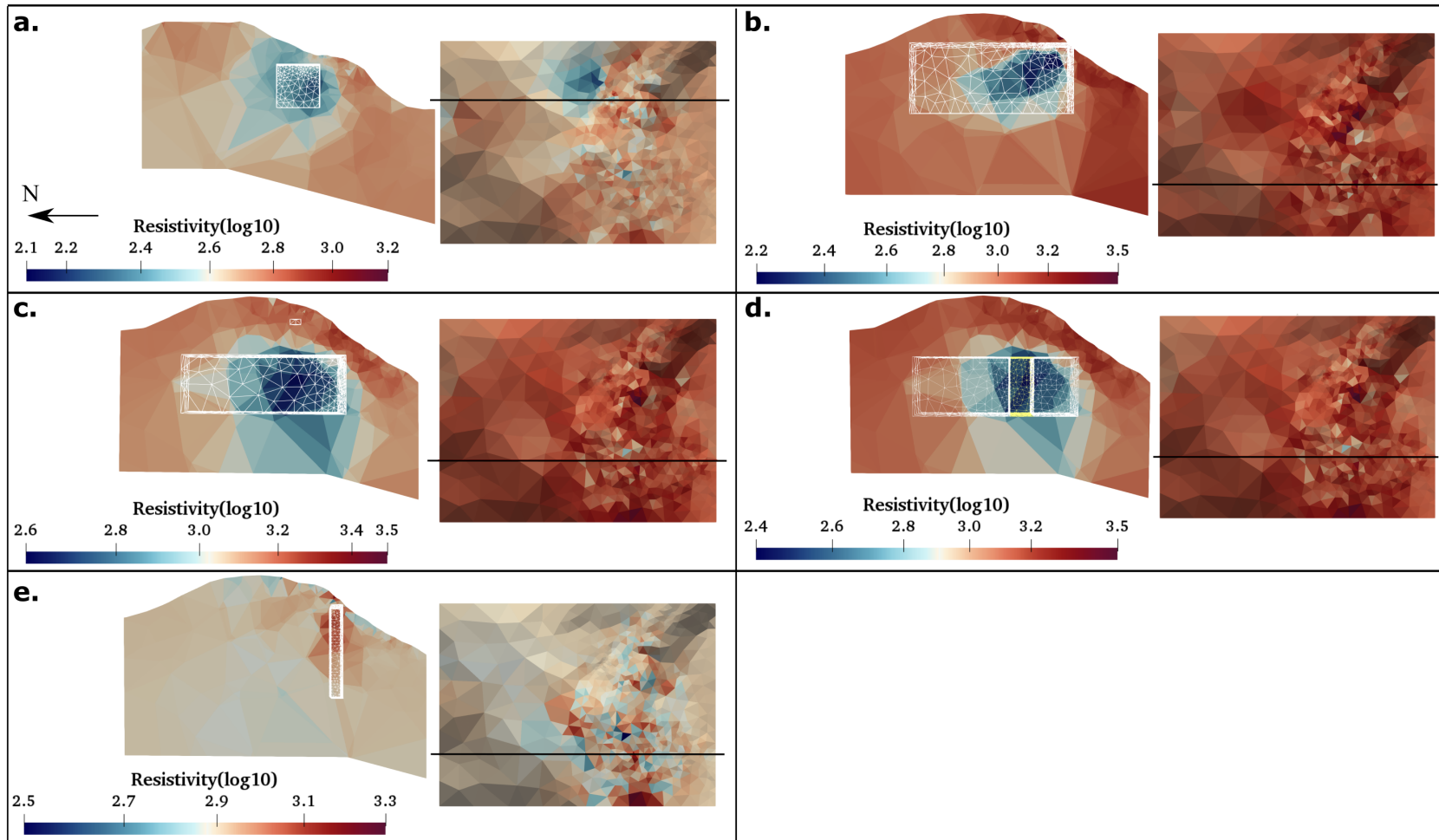


Figure 4.7: Exemplary results of the synthetic tests - vertical cross section and top view - for tests 1 to 5 (a.), tests 6 to 9 (b.), tests 10 to 12 (c.) test 13 (d.) and tests 14 to 16 (e.). The cubes delimited by white wireframes are the anomalous bodies.

Table 4.2: Synthetic tests: location, dimensions, context and resistivity values of the simulated anomalies.

Test ID	Background resistivity [ $\Omega$ .m]	Anomalous resistivity [ $\Omega$ .m]	Altitude of the anomaly (m)	Dimension of the anomaly (E x N x Z)	Context
Test 1	500	50	550	400	Eastern conductive anomaly
Test 2	500	5	550	400	Eastern conductive anomaly
Test 3	500	5	550	200	Eastern conductive anomaly
Test 4	500	5	300	400	Eastern conductive anomaly
Test 5	500	50	300	400	Eastern conductive anomaly
Test 6	1500	300	690	800 x 1000 x 200	West. resistive anomaly
Test 7	1500	300	490	800 x 1000 x 600	West. resistive anomaly
Test 8	1500	300	690	1000 x 1400 x 200	West. resistive anomaly
Test 9	1500	300	490	1000 x 1400 x 600	West. resistive anomaly
Test 10	1500	300	300	1000 x 1400 x 500	West. resistive anomaly
Test 11	1500	300	800	200 x 200 x 50	West. resistive anomaly
		300	300	1000 x 1400 x 500	West. resistive anomaly
Test 12	1500	300	885	100 x 100 x 50	West. resistive anomaly
		300	300	1000 x 1400 x 500	West. resistive anomaly
Test 13	1500	300	900	100 x 100 x 20	West. resistive anomaly
		50	300	1000 x 1400 x 500	Conductive fault
Test 14	800	2000	390	1000 x 200 x 500	Conductive fault
		2000	390	200 x 1000 x 800	Resistive fault
Test 15	800	2000	390	100 x 1000 x 800	Resistive fault
Test 16	800	2000	390	50 x 1000 x 800	Resistive fault

### Sensitivity of the model to a conductive anomaly

The synthetic tests 1 to 5 (Table 4.2) aim at simulating a finite dimension conductive anomaly at depth, located at the East of the unstable zone. A conductive cube has been introduced in a homogeneous material, affected by the topography of the slope. The objectives of the synthetic tests are 1) to define if conductive anomalies can be detected and accurately localized in the inverted models given the sharp topography, 2) to test if artifacts such as a spreading of the anomalous resistivity towards the surface are provoked by the inversion, 3) to estimate if the bottom of the anomaly is well determined and 4) to quantify if the resistivity values are well assessed. Results indicate that:

- the anomaly has to be large (of at least 200 m<sup>3</sup> at an altitude of 550 m) in order to be detected (the anomaly is always detected except in test 3, where the anomalous body is a cube with side length of 200 m);
- if it is close enough to the surface, a cubic conductive anomaly tends to spread through inversion towards the surface (a spreading is observed for tests 1 and 2 but not for tests 4 and 5). The resistivity of the spreading shape contrasts however less than the true anomaly with the background resistivity;
- the anomalous conductivity seems always largely under-estimated, over one order of magnitude;
- the spatial location is accurate and the size (especially the limits at depth) is well constrained.

### Sensitivity of the model to conductive bodies of various sizes below the Western resistive anomaly

The very damaged rocks in the unstable zone is expected to produce a very high resistivity (Le Roux et al. [2011]). The transition to the stable zone is expected to result in a decrease of the resistivity with depth. The sensitivity to an abrupt change in resistivity is evaluated with the synthetic tests, as well as the sensitivity to variation of resistivity within this deep conductive body. The detectability of small-sized conductive anomalies located close to the surface and in the resistive sector of Mont Sec is also tested.

- First, a conductive anomaly in a resistive background, located at an altitude around 800 m is simulated at the location where a transition from the resistive anomaly towards a more conductive medium is ex-

pected. Four tests are realized, changing the dimensions and the location of the conductive body (Table 4.2; tests 6 to 9). An anomaly is observed in the inverted models, at the 'true' location, but with a wrong estimation of the resistivity, which is often over-evaluated (particularly with strong regularization) and inside this anomaly, a gradient towards the 'true' resistivity value appears as an artefact. These anomalies are only detected below the area covered by the sensors. At depth, the limit of the anomaly is always detected.

- Second, anomalies of small sizes ( $< 200 \text{ m}^3$ ) located close to the surface are simulated above and in addition to the conductive anomaly simulated in test 9 (Table 4.2; tests 10 to 12). These tests indicate that such small bodies, even close to the surface, cannot be detected by the inversion.
- Third, a conductive anomaly, shaped as a vertical parallelepiped and oriented East-West, is included in the conductive anomaly simulated in test 9 (Table 4.2; test 13). Results indicate that such anomaly cannot be distinguished from the patterns obtained in test 13: a conductive anomaly is detected inside the conductive body, with wrong estimations of the resistivity values. Such pattern can thus not be detected with our measurement layout.

### Sensitivity of the model to extreme resistive anomalies corresponding to faults

Tests were further performed to assess the detectability of vertical resistive anomalies in the Western sector of the model. The context is the presence of vertical faults crossing the unstable slope. Vertical parallelepipeds of variable thicknesses have been incorporated in the grids with high resistive values (Table 4.2; tests 14 to 16). The simulations indicate that such anomalies can be detected, for all tested thicknesses (50, 100 and 200 m). At depth, the detection is limited, and the resistivity decreases at the location of the anomaly. For anomalies of 200 m thick, the modeled resistivity value is retrieved, but for thinner anomalies, the resistivity of the anomaly is largely under-evaluated. In all three cases, artefacts arise locally at the surface of the inverted model.

## 4.4 Geophysical modeling: quality of the inversion model

### 4.4.1 Inversion results

The sixteen inversions (Section 4.3, Table 4.2) converged with reasonable  $\chi^2$  values ( $0.88 < \chi^2 < 1$ ). The distribution of the resistivity values for all inverted models are presented in fig. 4.8a and 4.8e. The distributions of resistivity values are stable within the group of inverted models produced by a same regularization parameter when considering only inversion with initial models of 2, 20 and 200  $\Omega\cdot\text{m}$ . The inversions with initial model of 2000  $\Omega\cdot\text{m}$  produces models with higher resistivity values indicating that the initial model constrains largely the inversion process. Therefore, only the inverted models with initial models of 2, 20, and 200  $\Omega\cdot\text{m}$  are further considered in the analysis. From the three tested parameters controlling partly the inversion, it seems that the parameter influencing the most the resistivity model is the regularization parameter.

Two models are presented as examples for the two regularizations in fig. 4.8b, 4.8c, 4.8d, 4.8f, 4.8g and 4.8h. A weak regularization provides a patchy aspect at the surface (fig. 4.8f), partly resulting from the inversion process, but the structures at depth are stable for the set of models. A strong regularization provides very stable models (fig. 4.8a) displaying only smooth and large-scale resistivity variations. The patchy surface arising from weak regularizations is more homogeneous in the models obtained from strong regularized inversions.

### 4.4.2 Mean resistivity model and stability analysis

In order to reduce inversion-induced noise (section 4.4), as a stacking procedure, and to detect unresolved areas, the mean and the standard deviation of the logarithmic resistivity in the set of inverted field-models selected in the previous section are computed on a refined mesh (108896 cells), on which each inverted model is projected. In the following, the resulting models are respectively referred to as 'mean resistivity model' and 'standard deviation model' (fig. 4.9).

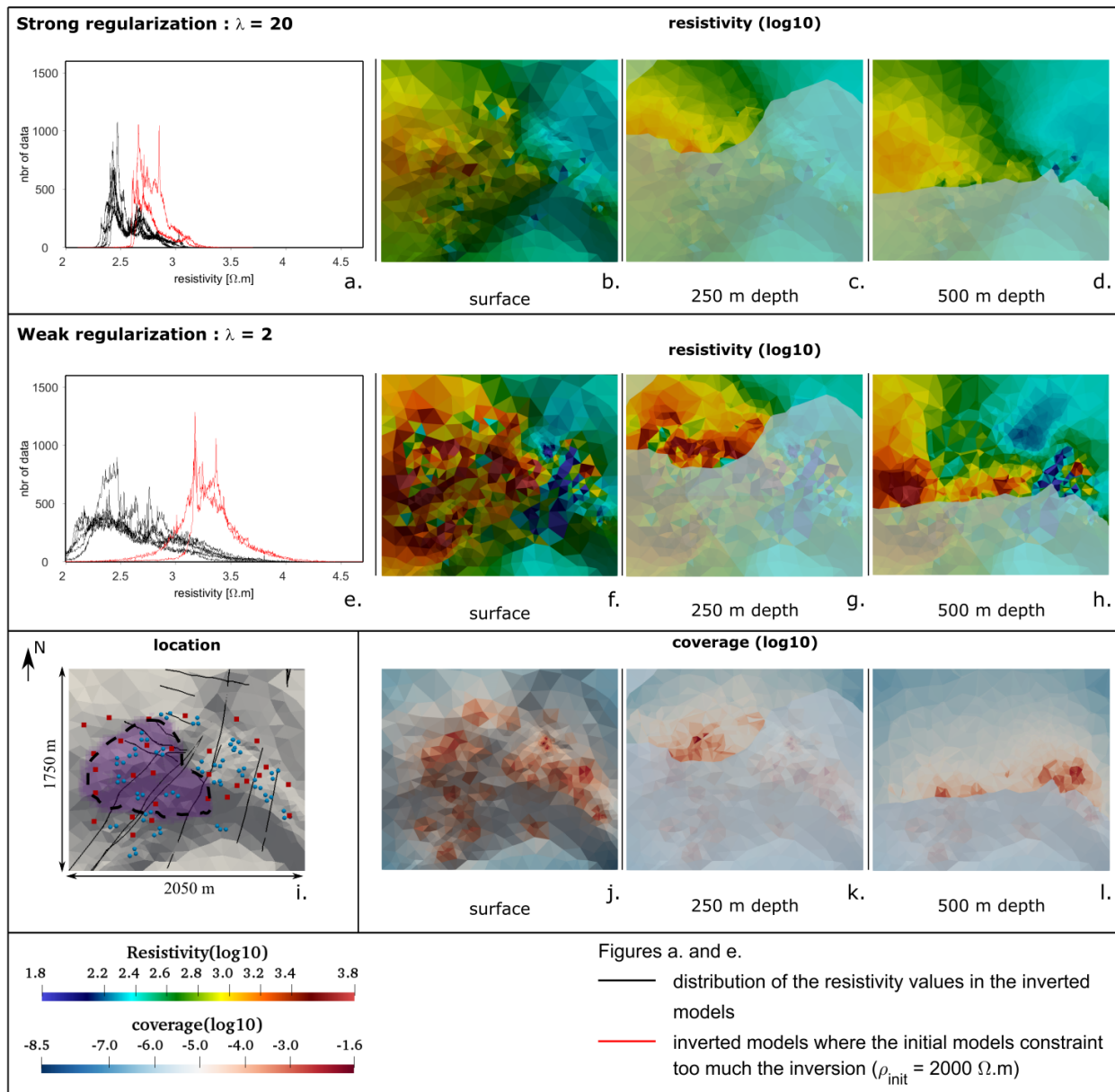


Figure 4.8: Comparison of the inverted models. First line: Inversion results for strong regularizations (LAMBDA = 20): a. distribution of resistivity values in the set of inverted models (one line corresponds to one inverted model); and an example of inverted model (initial resistivity = 200  $\Omega.m$ , fine mesh), with the top view b. and horizontal slices at 250 m depth (the whitened area corresponds to the part of the model where the topography is below the slice) and at 500 m depth. Second line: Inversion results for weak regularizations (LAMBDA = 2): e. distribution of resistivity values in the set of inverted models; an example of inverted model (initial resistivity = 200  $\Omega.m$ , fine mesh), with the top view f. and horizontal slices at 250 m depth (g.) and at 500 m (h.); i. location of the major faults (black lines), measurement (blue dots) and injection (red dots) points and unstable area (purple zone) regarding the inverted model; top view (j.) and horizontal slices at 250 m (k.) and 500 m (l.) of the data coverage (mean of sensitivity, Günther et al. [2006]).

The mean resistivity model presents resistivity values in the range [125-2500]  $\Omega$ .m and displays two characteristics:

- a strong resistive anomaly located in the first 250 m, below the surface and all over the unstable zone;
- a deep conductive area oriented along the North-South direction and located at the East of the unstable zone, with vertical conductive patterns extending from the surface down to this conductive anomaly.

Small size (100 m width) lateral variations are observed at the surface of the model particularly at the location of the resistive anomaly. Such lateral variations are expected to exist at the surface, as attested by the analysis of the two boreholes' core samples (fig. 4.1c), and seem to be detected in the mean resistivity model with the stacking procedure. The standard deviation model (fig. 4.9) presents values in the range of  $6.9 \cdot 10^{-3}$  to  $2.4 \cdot 10^{-1}$  and displays sharp variations mostly at the surface. The maximum values denote small uncertainties of less than 100 % in the resistivity value. At depth, the standard deviation model displays values below  $1.3 \cdot 10^{-1}$ , and does not allow defining the investigation limits of the dataset. Even if the resolution is poor at depth, the data still allows determining large-scale variations of the resistivity; these variations are stable from one inverted model to another, but are not interpreted in our analysis.

Locally, the 3D model is compared with 2D resistivity profiles of [Le Roux et al. \[2011\]](#) (fig. 4.10). Both the mean resistivity model and the mean model computed from all weakly regularized models (fig. 4.8a) are compared with the profiles 3 and 4 from [Le Roux et al. \[2011\]](#), fig. 4.1b. The two mean models present similar structures along the profiles. The principal difference lies in the resistivity values of the observed structures. The cross-sections from the mean model (Fig 4.10a and 4.10d) display resistivity values of 300 to 2000  $\Omega$ .m when the cross-sections from the weakly regularized mean model (fig. 4.10b and 4.10e) display resistivity values reaching 4000  $\Omega$ .m. This second model approaches closer to the values observed in the profiles from [Le Roux et al. \[2011\]](#), showing that, at this location and at this resolution, the resistivity variations brought by a weak regularization are still data-driven rather than induced by noise. Nevertheless, most of the thin variations contained in the profiles from [Le Roux et al. \[2011\]](#) are not retrieved by the 3D model, showing the resolution difference between the type of measurements presented in this work and a 2D profile with an electrode spacing of 5 m. In particular, the profile 3 displays a very conductive anomaly at the east (left hand side) of the profile reaching the top layers at 50 to 100  $\Omega$ .m, which does not appear in the 3D models. Such an anomaly is observable in the 3D model, but at much greater depth (around 300 m depth, Fig 4.12b), suggesting a difference in resolution for the two acquisitions, and a possible difference in hydrological state between the two measurements.

### 4.4.3 Interpretability of the geophysical model

Only the patterns that are stable among the set of inverted models are interpreted. Because the mean resistivity model emphasizes well these observed patterns, and partly reduces the noise introduced by weakly regularized inversions, it is used as basis for the interpretations proposed hereafter (4.9, 4.11 and 4.12). The limit of interpretability of a model depends on the size of the object of interest. The data coverage computed during the inversion consists in the sum of the absolute sensitivities. The coverage is used as absolute estimation of sensitivity and a threshold value of  $10^{-6}$  is taken as interpretability limit of the model providing a depth of investigation of around 500 m. This limit is in agreement with the lateral limits of detection inferred from the synthetic tests; however, the synthetic tests also demonstrated that for large anomalies ( $> 200 \text{ m}^3$ ), the anomaly could be detected below the depth of investigation defined by the chosen coverage limit, tested up to 1500 m. The synthetic tests indicate that only resistivity variations of more than 20 % can be interpreted. Small anomalies ( $< 200 \text{ m}^3$ ) located close to the surface are hardly detected. These limitations are caused by the low spatial sampling of the measurements; it forces us to focus on the large-scale anomalies and to address with great care the interpretation of small anomalies observed close to the surface.

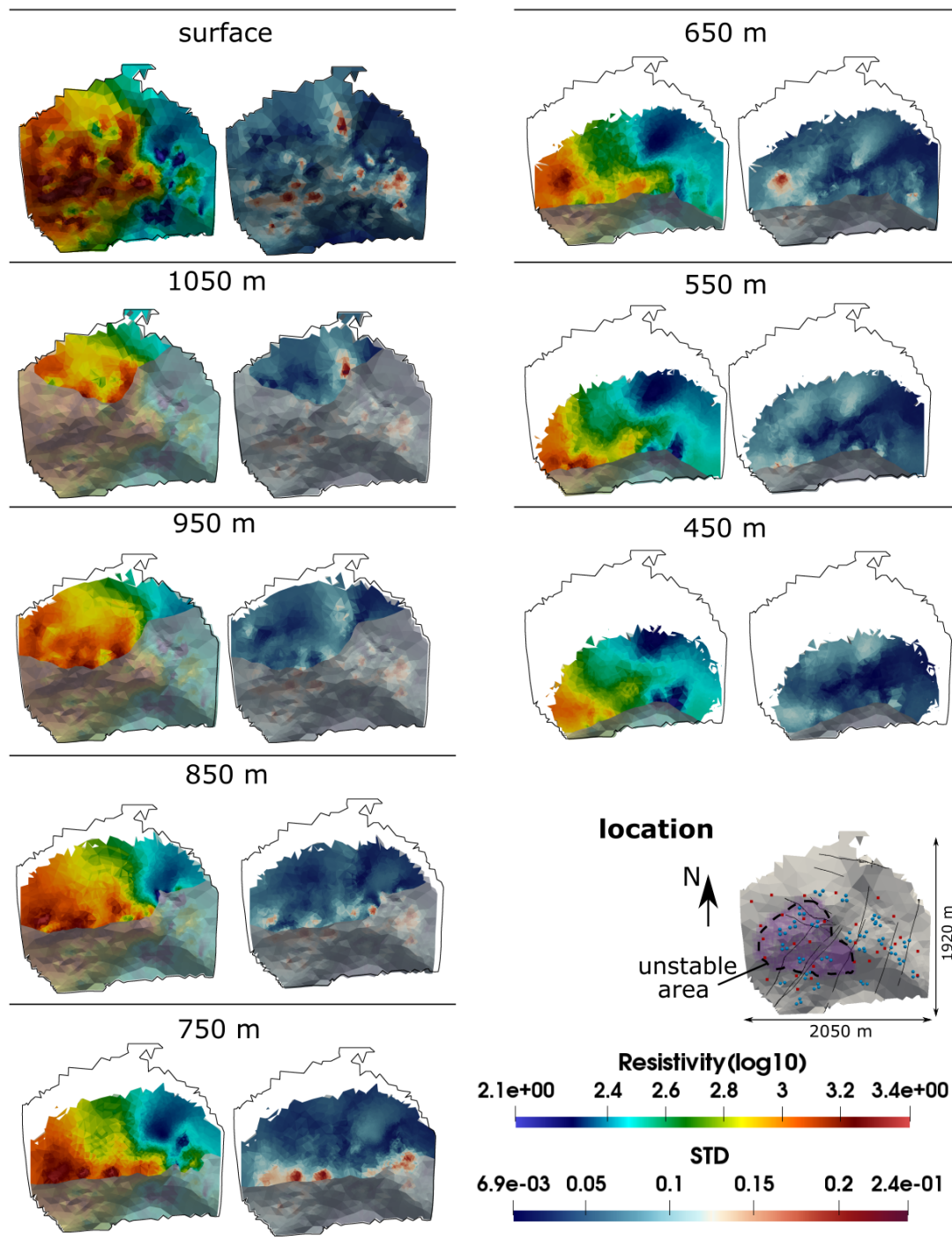


Figure 4.9: Mean resistivity model and standard deviation model. Horizontal slices at the topographic surface at the elevations 1050, 950, 850, 750, 650, 550, 450 m (asl).

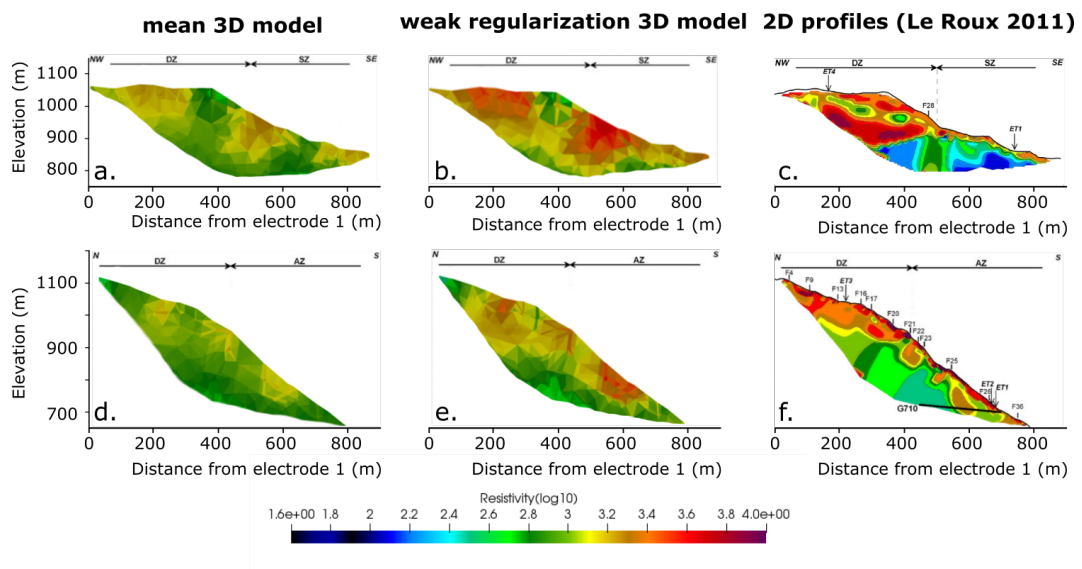


Figure 4.10: Comparison of the 3D resistivity models (left and center) to the 2D inverted models (right: c. and f.) of [Le Roux et al. \[2011\]](#), profiles ET3 (top) and ET4 (bottom). The 3D model is sliced at the location of the 2D investigation profiles. Two 3D-resistivity models are considered: the mean resistivity model computed from all stable inverted models (a. and d.), and a mean resistivity model computed from all stable models obtained with a weak regularization (b. and e.)

## 4.5 Discussion: geological and hydrogeological interpretation of the 3D resistivity model

Previous geophysical studies (Meric et al. [2005]; Le Roux et al. [2011]) identified that variations of electrical and seismic properties correspond quite well with the known delineations of structures controlling the landslide. The variations of geophysical properties are caused by changes in the macrostructure of the slope (geology, fault, crushed area, fluid chemistry) and microstructure of the media (porosity, veins, composition of the matrix, presence of clays). In particular, the highest resistivity values are detected at locations where the rock is densely fractured and damaged (Le Roux et al. [2011]). The variations of geophysical properties are also caused by water circulation and more specifically changes in the water flow regime in zones with high clay contents as identified by self-potential measurements (Meric et al. [2005]). The zones of lowest resistivity values correspond to the location of permanent ground water in the fractures and of high clay content. The anomalies observed in the 3D mean resistivity model are interpreted with complementary information (borehole core samples, fault model, water chemistry).

### 4.5.1 Identification of geological and geomorphological structures

The strong resistive anomaly in the Western sector of the model is presented in the fig. 4.12a and 4.12b. The anomaly is interpreted by Le Roux et al. [2011] as a very fractured and dry material. We expand this interpretation, suggesting, from a hydrological perspective, that the degree of fracturation in this zone makes it very permeable; this is confirmed by the absence of water sources in most of this area. The boundary at depth of this resistive anomaly can be interpreted in two ways. A decrease of the electrical resistivity with depth could correspond either to a transition to a more compact and less damaged micaschist, or to the transition from a dry to a water saturated material. The resistivity transition is located at an altitude of about 500 to 600 m, which is the known altitude of the deep aquifer. It seems therefore that the resistivity limit of 500  $\Omega$ .m corresponds to the bottom of the vadose zone. At the surface, the high resistivity patches (2500  $\Omega$ .m) align along the major faults (fig. 4.11). This observation suggests that the degree of fracturation close to the surface (50 to 200 m depending on the location) is inhomogeneous. It is possible to delineate the most damaged areas, which extend laterally from the fault planes, up to a distance of 100 m, to a less damaged material, presenting a resistivity below 1500  $\Omega$ .m. At depth (100 to 250 m), these trends seem to vanish as the resistivity drops. Because of the low resolution and the loss of detectability at depth, it is not possible to estimate the dip of the observed faults. The inclinometer observations indicate a limit of the instability at a depth of 110 m below the surface. Assuming that the resistivity variations are directly and only correlated to the structural properties of the material at this depth and can be therefore an indicator of the geomechanical behaviour, resistivity values above 1000  $\Omega$ .m could be attributed to unstable mass.

From the observation of this very resistive zone, two remarks can be made:

- From a geophysical and geomechanical point of view, the highly resistive zones should be specific to the unstable area (active zone); however, high resistivity values are also noticeable outside of the unstable area (fig. 4.12a, see the area circled in black). The high resistivity values observed in this area certainly correspond to a highly damaged zone, and it is unclear why this zone has not currently experienced high displacement rates (Chanut et al. [2013]).
- The active zone of "Les Ruines", which is the zone experiencing the highest displacement rates, does not appear as very resistive. Its resistivity is of about 1000  $\Omega$ .m while the maximum observed resistivity is of about 2500  $\Omega$ .m close to the fault planes. In the location of les Ruines, it seems that the topography and the fault segmenting the slope above this zone play a major role in the observed toppling movement.

### 4.5.2 Identification of hydrological structures

The deep conductive anomaly in the Eastern sector of the model is presented in fig. 4.12c and 4.12d. The main part of the anomaly is a slope-scale conductive trend oriented along the North/South structure of the Sabot

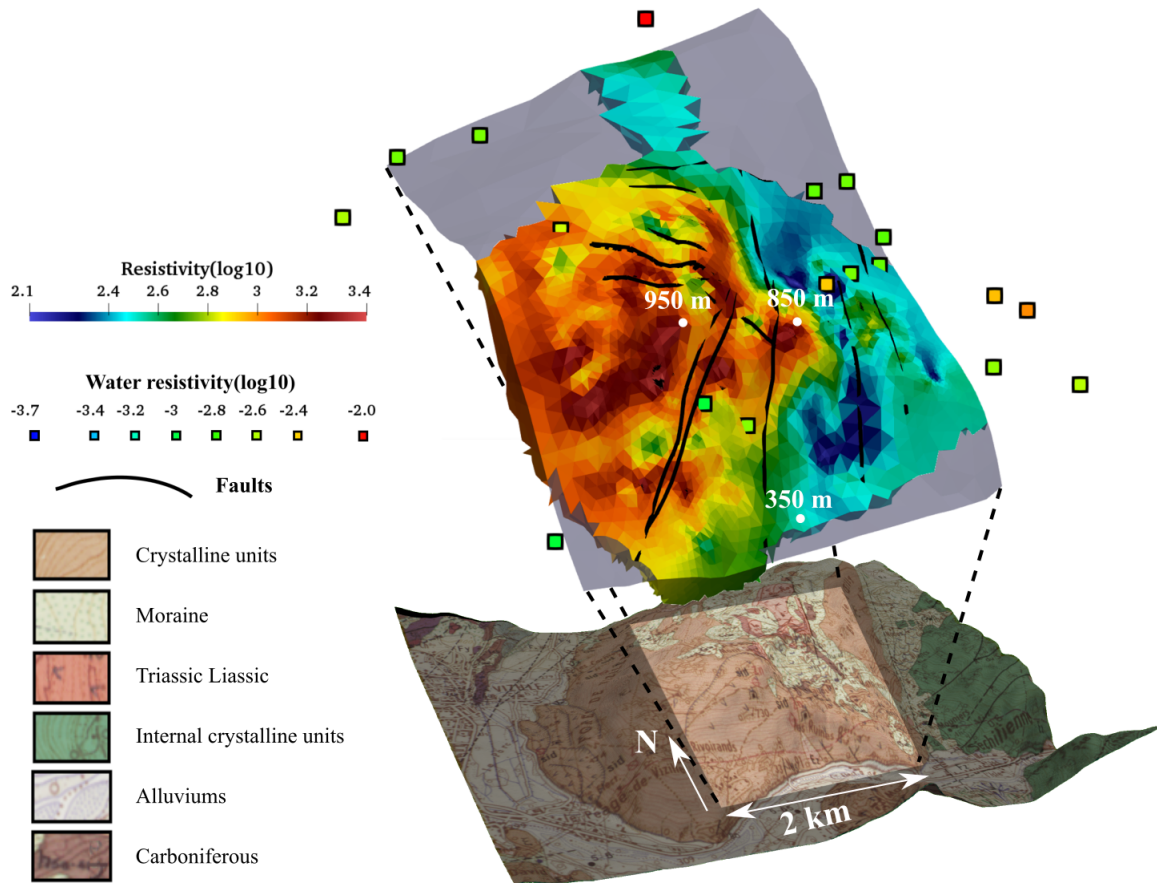


Figure 4.11: 3D representation of the interpreted model (mean model computed on the logarithmic resistivity of the set of selected inverted models) superimposed to the geological map of the slope (Barféty et al. [1972]). The squares represent the resistivity ( $\log_{10}$ ) of the surface waters sampled in spring or at surface runoff locations. The black lines represent the major faults.

fault, with resistivity values ranging from 125 to 250  $\Omega.m$ . Synthetic tests showed that large cubic resistive anomalies located in this area always have under-evaluated conductivities in the inverted models; it is therefore expected that the resistivity values obtained for this anomaly are over-estimated.

Vertical thin conductive anomalies locally extend from the surface down to the deep conductive anomaly. These vertical patterns present similar resistivity values as the main conductive anomaly. They could be discussed as the synthetic tests showed that a parallelepiped conductive anomaly at the location of the large North-South anomaly could produce, through the inversion process, a spread of the anomaly towards the surface, producing the same types of patterns as the ones observed in the inverted models. We however believe that these patterns exist, because they represent a strong anomaly, with resistivity values as low as the rest of the conductive anomaly. In the synthetic tests, the spread patterns present smaller conductivity values than the conductive anomaly producing it.

The abundance of water outflows in this area suggests a wet rock, and the possibility that water can be stored in the near surface rock. These outflows are largely sampled and documented in a geochemical monitoring of the slope (Mudry and Etievant [2007]; Vallet et al. [2015]). Vallet et al. [2015] described this area as a major drain of the massif, and concluded, from the analysis of water chemistry, that water coming from the West and the North of the fault cluster along the Sabot fault, at the location of the conductive anomaly.

In relation to the hydrological observations (fig. 4.13), we interpret these conductive anomalies in the stable area as local perched aquifers discharging downwards in the main aquifer. These perched aquifers develop during high water periods, favored by the permeability contrasts between decompressed zones of increased porosity located at the surface, and the unaltered rock. The Sabot fault acts as a drain, easing the water transfers from the perched aquifer to the main aquifer. At the end of the high waters period, the perched aquifers – constantly

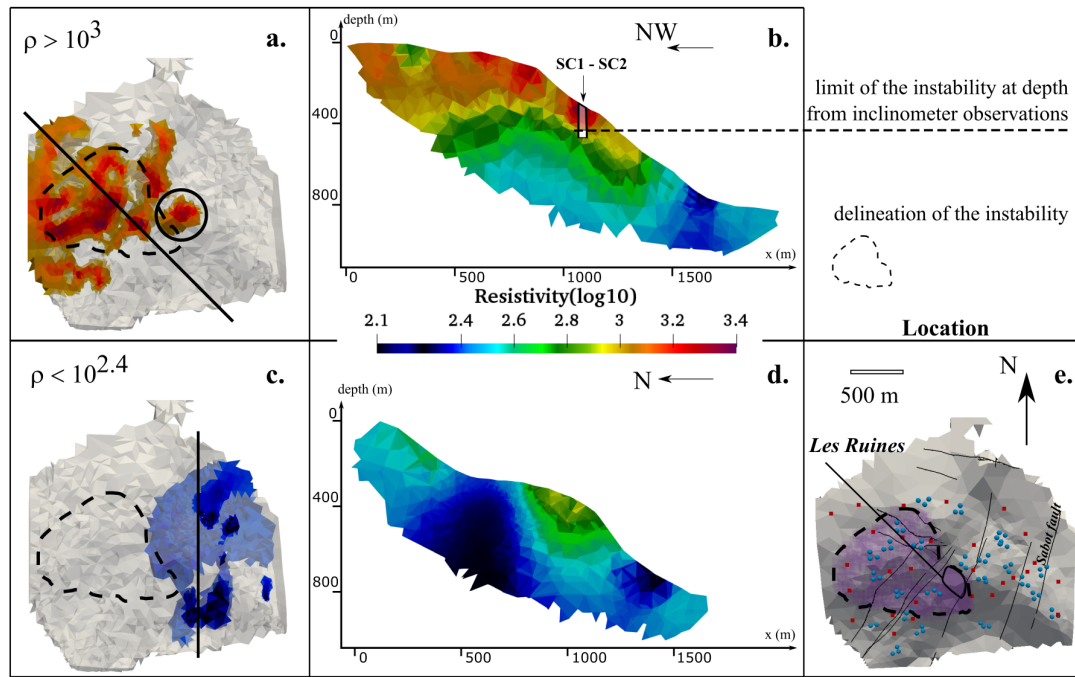


Figure 4.12: Resistive and conductive anomalies observed at the Séchilienne slope. (a) Top view of the extracted resistivity anomaly (resistivity above  $10^3 \Omega \cdot m$ ), the black line is the location of the cross-section in (b) and the black circle is the part of the resistive anomaly located outside of the unstable area; (b) Vertical cross-section of the mean resistivity model showing the transition at depth from the resistive anomaly to the more conductive background; (c) Top view of the extracted conductive anomaly (resistivity below  $10^{2.4} \Omega \cdot m$  i.e.  $250 \Omega \cdot m$ ), the black line is the location of the cross-section in (d); (d) Vertical cross-section of the mean resistivity model showing the conductive vertical patterns expanding from the surface down to a major deep conductive anomaly, (e) Acquisition setup: injection points in red and potential electrodes in blue, the unstable area is highlighted in purple.

supplied during high-flow periods by rainfall - progressively discharge in the main aquifer drained by the Sabot fault. Throughout the low-flow period, this process applies at first to the water located in the largest pores and concerns, at the end of the low-flow period, the water located in the micropores.

During the high-flow periods, the water level of the deep aquifer is directly controlled by the precipitation and the rapid infiltration, while in low-flow periods, the flow is maintained by the restitution of the water stored in the rock micro-porosity. The micro-porosity is characterized by an important capacitive function and the water presents an increased mineralization, due to its increased residence time in the rock. The joint analysis of the variation in water level and the variation of electrical conductivity (fig. 4.13c) illustrates the importance of the drainage of the micro-fissured matrix during the low-flow period, at which the increase in water conductivity is the direct consequence of the discharge of the water from the micro-fissures.

The 3D ERT survey has been conducted in July 2017 at the start of the low-flow period. At that moment, the perched aquifers are still maintained by the presence of water contained in the small-sized pores, while the water from the largest porosity has already been drained out towards the deep aquifer.

In the unstable zone, a dense network of opened fractures (as illustrated in fig. 4.13d. and e.) allows rapid groundwater flows along these preferential flow paths. In low-flow periods, similar processes as the ones described before for the stable area occur, and the water flow towards the saturated zone is enabled by the restitution of the water stored for several months in the micro-porosity of the matrix. The volume of water involved in this process is however smaller than in the stable area (the discharge is close to 0 L/h in most of the low-flow period, fig. 4.13b) highlighting a smaller storage capacity as in the stable zone.

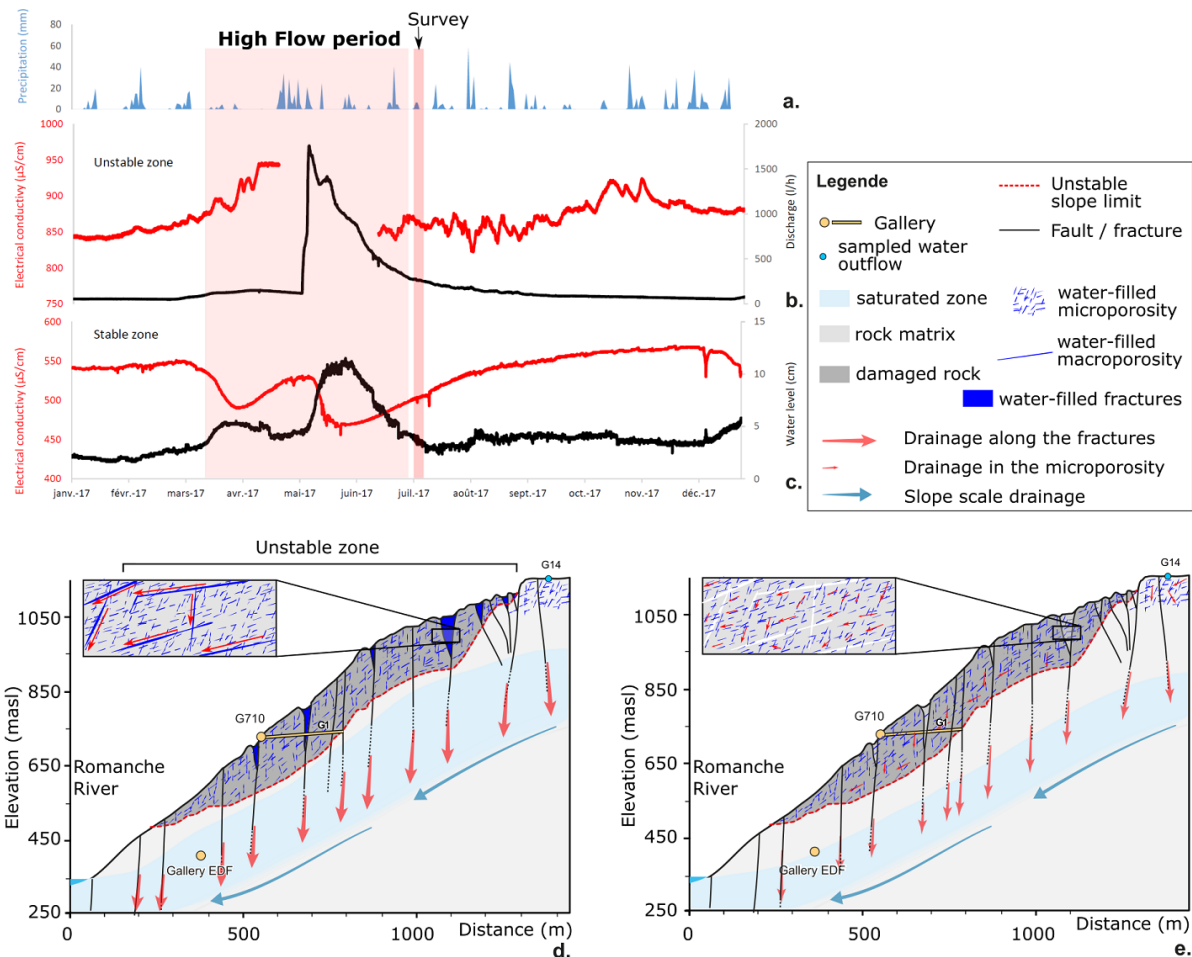


Figure 4.13: Hydrogeological measurements during the year 2017 and hydrogeological concept. (a) precipitation recorded over the year 2017 at Mont Sec; (b) Water electrical conductivity and discharge in the unstable zone, recorded at the G710 gallery; (c) Electrical conductivity and water level recorded in the stable zone. Hydrogeological conceptual model of the Séchilienne slope for periods of high-flow (d.) and low-flow (e.) (modified from Vallet et al. [2015]).

## 4.6 Conclusion and perspectives

The use of the novel R-DAS FullWaver has proven successful to infer new knowledge on the large-scale geological and hydrogeological structures of the Séchilienne slope. The scale of the study, together with the sparse and uneven sampling are uncommon in the spectrum of resistivity surveys, where a regular sampling provides sensitivity variations which are easy to capture and understand. This unusual layout led us to carry an extensive analysis of the sensitivity in order to understand the ability of our dataset to detect specific anomalies, including an analysis of the stability of the inverted models, and the realization of synthetic tests. The analysis of stability highlighted the unresolved mesh located at the surface of the model; the synthetic tests allowed identifying the main anomalies observed in the inverted models. These tests provided some remarkable results.

- First, despite the minimal electrode distances of 50 m, the dataset seemed not to be sensitive to small scale anomalies close to the surface ( $< 200 \text{ m}^3$ );
- Second, the sparse layout and the strong topography variations are prompt to produce artefacts in the inverted model;
- Third, large-scale anomalies ( $> 200 \text{ m}^3$ ) are always detected in the sensitive zone of the models.
- Fourth, the sensitive zone is defined by a threshold in the coverage value ( $10^{-6}$ ), providing a depth of investigation of 500 m. Large-scale anomalies are also detectable at greater depths within the simple

contexts simulated in the synthetic tests (for example, the inversion was sensitive to the bottom of an anomaly located at 1500 m depth);

- Fifth, the resistivity values of the detected anomalies are not correctly retrieved in the inverted model. According to the synthetic tests, anomalies seem to be under-estimated.

The unstable zone has been detected in the model as a resistive anomaly (with resistivity values  $> 1500 \Omega.m$ ) where the damage is mostly located along the major faults crossing the Mont Sec slope, until a distance of about 100 m. A large conductive anomaly at the East of the landslide (Sabot fault) is detected and interpreted as a perched aquifer. At the end of the high-flow period, when the geophysical survey was realized, these remaining perched aquifers correspond to water stored in the micro-porosity, discharging in the deep aquifer. These interpretations are in very good accordance with the hydrogeological understanding arising from hydro-chemical observations, and could be fully confirmed by repeating this analysis with measurements realized at the end of a low-flow period.

The main limitations of the work are the local poor spatial sampling. A major improvement could be to increase the number of receivers in order to densify the spatial sampling. The detectability of smaller-scale anomalies close to the surface would thus be increased. However, adding a few receivers would increase a lot the duration and effort needed for the survey, and given the rough topography and the difficulty to access the most damaged locations, some areas would necessarily remain uncovered. The presented methodology is applicable to similar contexts where the large scale geological and hydrogeological features of a site are questioned. A regular sampling, as dense and regular as possible should be considered, and sensitivity tests should also be carried out, as they have proven to be very insightful to capture the sensitivity of an inverted dataset.

## 4.7 References

- Alfonsi, P. (1997). Relation entre les paramètres hydrologiques et la vitesse dans les glissements de terrains. Exemples de La Clapière et de Séchilienne (France). *Revue française de géotechnique*, (79):3–12.
- Barféty, J., Bordet, P., Carme, F., Debelmas, J., Meloux, M., Montjuvent, G., Mouterde, R., and Sarrot Reynauld, J. (1972). Carte géologique détaillée de la France (1/50000) n 797 Vizille. *Editions du BRGM*, 38p.
- Baudement, C., Bertrand, C., Guglielmi, Y., Viseur, S., Vallet, A., and Cappa, F. (2013). Quantification de la dégradation mécanique et chimique d'un versant instable: approche géologique, hydromécanique et hydrochimique Etude du versant instable de Séchilienne, Isère (38). In *JAG-3èmes journées Aléas Gravitaires*, pages 1–6.
- Cappa, F., Guglielmi, Y., Viseur, S., and Garambois, S. (2014). Deep fluids can facilitate rupture of slow-moving giant landslides as a result of stress transfer and frictional weakening. *Geophysical Research Letters*, 41(1):61–66.
- Chanut, M.-A., Dubois, L., Duranthon, J.-P., and Durville, J.-L. (2013). Mouvement de versant de séchilienne: relations entre précipitations et déplacements. In *Acte de colloque, 1ère conférence internationale sur les risques des mouvements de terrain, Ain Draham (Tunisie)*, pages 14–16.
- Dubois, L., Chanut, M., and Duranthon, J. (2014). Amélioration continue des dispositifs d'auscultation et de surveillance intégrés dans le suivi du versant instable des Ruines de Séchilienne. *Géologues*, 182:50–55.
- Duranthon, J., Chanut, M., and Dubois, L. (2013). Ruines de Séchilienne, rapport annuel de suivi du site, avril 2012 (mars 2013). *CETE-Centre d'Etudes Techniques de LYON*, 41829(1):119.
- Duranthon, J. P., Effendiantz, L., Memier, M., and Previtali, I. (2003). Apport des méthodes topographiques et topométriques au suivi du versant rocheux instable des ruines de Séchilienne. *Revue XYZ*, 94:31–38.
- Fox, R. C., Hohmann, G. W., Killpack, T. J., and Rijo, L. (1980). Topographic effects in resistivity and induced-polarization surveys. *Geophysics*, 45(1):75–93.
- Friedel, S., Thielen, A., and Springman, S. M. (2006). Investigation of a slope endangered by rainfall-induced landslides using 3d resistivity tomography and geotechnical testing. *Journal of Applied Geophysics*, 60(2):100–114.
- Gance, J., Malet, J.-P., Supper, R., Sailhac, P., Ottowitz, D., and Jochum, B. (2016). Permanent electrical resistivity measurements for monitoring water circulation in clayey landslides. *Journal of Applied Geophysics*, 126:98–115.
- Guglielmi, Y., Vengeon, J., Bertrand, C., Mudry, J., Follacci, J., and Giraud, A. (2002). Hydrogeochemistry: an investigation

- tool to evaluate infiltration into large moving rock masses (case study of La Clapière and Séchilienne alpine landslides). *Bulletin of Engineering Geology and the Environment*, 61(4):311–324.
- Günther, T., Rücker, C., and Spitzer, K. (2006). Three-dimensional modelling and inversion of DC resistivity data incorporating topography—ii. Inversion. *Geophysical Journal International*, 166(2):506–517.
- Helmstetter, A. and Garambois, S. (2010). Seismic monitoring of Séchilienne rockslide (French Alps): Analysis of seismic signals and their correlation with rainfalls. *Journal of Geophysical Research: Earth Surface*, 115(F3).
- Jongmans, D. and Garambois, S. (2007). Geophysical investigation of landslides: a review. *Bulletin de la Société géologique de France*, 178(2):101–112.
- Le Roux, O., Jongmans, D., Kasperski, J., Schwartz, S., Potherat, P., Lebruc, V., Lagabrielle, R., and Meric, O. (2011). Deep geophysical investigation of the large Séchilienne landslide (western Alps, France) and calibration with geological data. *Engineering Geology*, 120(1-4):18–31.
- Legchenko, A., Clément, R., Garambois, S., Maury, E., Mic, L.-M., Laurent, J.-P., Desplanque, C., and Guyard, H. (2011). Investigating water distribution in the Luitel Lake peat bog using MRS, ERT and GPR. *Near Surface Geophysics*, 9(2):201–209.
- Meric, O., Garambois, S., Jongmans, D., Wathelet, M., Chatelain, J.-L., and Vengeon, J. (2005). Application of geophysical methods for the investigation of the large gravitational mass movement of Séchilienne, France. *Canadian Geotechnical Journal*, 42(4):1105–1115.
- Montjuvent, G. and Winistorfer, J. (1980). Glaciations quaternaires dans les Alpes franco-suissees et leur piedmont. *Geol. Alp*, 56:251–282.
- Mudry, J. and Etievant, K. (2007). Synthèse hydrogéologique du versant instable des ruines de Séchilienne. *Unpublished report, UMR Chrono-Environnement, University of Franche-Comté, Franche-Comté*.
- Rochet, L., Giraud, A., Antoine, P., and Evrard, H. (1994). La déformation du versant sud du Mont-Sec dans le secteur des ruines de Séchilienne (Isère). *Bulletin of the International Association of Engineering Geology-Bulletin de l'Association Internationale de Géologie de l'Ingénieur*, 50(1):75–87.
- Rücker, C., Günther, T., and Spitzer, K. (2006). Three-dimensional modelling and inversion of dc resistivity data incorporating topography—i. Modelling. *Geophysical Journal International*, 166(2):495–505.
- Travelletti, J. and Malet, J.-P. (2012). Characterization of the 3d geometry of flow-like landslides: A methodology based on the integration of heterogeneous multi-source data. *Engineering Geology*, 128:30–48.
- Uhlemann, S., Chambers, J., Wilkinson, P., Maurer, H., Merritt, A., Meldrum, P., Kuras, O., Gunn, D., Smith, A., and Dijkstra, T. (2017). Four-dimensional imaging of moisture dynamics during landslide reactivation. *Journal of Geophysical Research: Earth Surface*, 122(1):398–418.
- Uhlemann, S., Wilkinson, P. B., Chambers, J. E., Maurer, H., Merritt, A. J., Gunn, D. A., and Meldrum, P. I. (2015). Interpolation of landslide movements to improve the accuracy of 4d geoelectrical monitoring. *Journal of Applied Geophysics*, 121:93–105.
- Vallet, A., Bertrand, C., Mudry, J., Bogaard, T., Fabbri, O., Baudement, C., and Régent, B. (2015). Contribution of time-related environmental tracing combined with tracer tests for characterization of a groundwater conceptual model: a case study at the Séchilienne landslide, western Alps (France). *Hydrogeology journal*, 23(8):1761–1779.
- Vallet, A., Charlier, J.-B., Fabbri, O., Bertrand, C., Carry, N., and Mudry, J. (2016). Functioning and precipitation-displacement modelling of rainfall-induced deep-seated landslides subject to creep deformation. *Landslides*, 13(4):653–670.
- Vengeon, J.-M. (1998). *Déformation et rupture des versants en terrain métamorphique anisotrope. Apport de l'étude des Ruines de Séchilienne*. PhD thesis, Université Joseph-Fourier-Grenoble I.

#### 4.7.1 References to internet websites

IRIS Instruments © 1991-2016 - <https://www.iris-instruments.com/>

## **Chapter 5**

# **Imaging deep sedimentary aquifers: Time-lapse hydrogeological study of the Pégairolles landslide with CSAMT and TDIP methods**

The work presented in this chapter is based on Lajaunie, M., Gautier, S., Flores-Orozco, A., Malet, J.-P., Sailhac, P., Delhaye, R. (in preparation): "Geo-electrical time-lapse experiments to capture the seasonal hydrogeological dynamics of the Lodève Landslides", intended for submission in *Geofizika* or *Geophysical Journal International*.

## Introduction

In this chapter, we explore the possibilities of studying deep sedimentary aquifers. Such aquifers are generally characterized by successions of different sedimentary units of contrasting geoelectrical properties. In particular, the presence of clay layers brings very conductive units into play, making the identification of saturated and unsaturated zones challenging. In this context, the benefit of time-lapse methodologies is explored. Indeed, in the case of stable reservoirs, only temporal changes in the hydrogeology will produce temporal variations on the geophysical signal. These temporal variations concern both the amount of water in the rock and the water chemistry, which depends on the rock/water interactions (adsorption, precipitation, dissolution, etc.). To study deep sedimentary aquifers, both a high vertical resolution and a high depth of investigation are required; the CSAMT method is therefore considered in this work. A good sensitivity to the rock / water exchange processes might as well permit to distinguish more clearly the different units; the TDIP method is therefore also considered.

To test these methodologies, the Lodève landslide (Hérault, France) was selected as study site. This slow moving and deep rotational instability is constituted of overlaying clay and evaporite units and expected to be triggered by intense and brief rainfall events. Several time-lapse methodologies were developed at the Lodève landslide as part of a research project aiming at developing strategies to study and characterize clayey landslides, as they constitute an important threat in many regions of the world. The Lodève landslide presents the advantage of a very low displacement rate, allowing to deploy observation devices without risking them to suffer damages due to sliding.

Time-lapse experiments were conducted independently with the two methods. CSAMT soundings were realized and repeated during the winter 2018 - 2019 at a monthly rate at 8 different stations. The measurement possibilities (frequency rate, instrumentation) are discussed, sensitivity tests are presented, showing that the variations of signal expected at the Lodève landslide can theoretically be detected by repeated CSAMT measurements. The processing techniques are systematically presented. The processed data are presented and discussed with regards to the related meteorological chronicles. Second, a 475 m long TDIP profile was measured and repeated at seasonal time-scale, three times from March to October 2019. The processing and inversion techniques are presented. The inverted models are as well presented and discussed with regards to the related meteorological chronicles.

## 5.1 The Lodève landslide

The Lodève landslide is a slow moving (3 to 4 mm/yr) and deep (60 m) rotational instability, located in the South-East of France, 60 km North from Montpellier (Hérault department). It is located in the Lodève basin, a set of connected steephead valleys marking the southern limit of the karstic Larzac plateau (Causses du Larzac, fig. 5.1).

The instability observed at the Lodève landslide is the most common type of instability observed in the Hérault valley (Vincent and Zornette [2001]), as the same geomorphology and lithology - very prone to slides - can be found at different locations along the steephead valleys at the south of the Larzac plateau. However, if these rotational landslides are numerous in the region, their occurrence rates and displacement rates are rarely as low as at the Lodève landslide.

These rotational slides often present non-negligible correlations between the ground displacement and the meteorology. The delay between meteorological events and grounds displacement is however not constant among these slides (Vincent and Zornette [2001]), suggesting implications of the hydrogeological processes in the subsurface, inducing variations of the characteristic times of water infiltration and water retention processes, which would result in different hydro-mechanical time-responses. These slides have the potential to damage infrastructures such as roads, bridges and habitations; an investigation of these instabilities and the

damages related was published in [Vincent and Zornette \[2001\]](#). It is fundamental to understand their functioning, in particular to model the hydrogeological processes implicated, in order to capture the landslide response and the potential damages it can cause in order to adapt the infrastructures.

As the deformation and damaging is slow enough (3 to 4 mm/yr), the Lodève landslide is a very interesting candidate-site for investigating the functioning of hydraulically induced rotational landslides implying clay and evaporitic layers. This site presents indeed the great advantage of allowing to deploy a long term instrumentation, without risking to loose the instruments in a brutal acceleration of the slide. A multi-disciplinary observatory was installed in 2012, aiming at two main tasks:

1. observing the impact of seasonal and Cévenol meteorological events on the geophysical, chemical, and hydrogeological characteristics of the slide,
2. improve from these observations our knowledge on rock-water interaction,
3. improve from these observations our hydrogeological understanding of the landslide.

Three main geological units are believed to be potentially the source of the instability. These units, from the Norian to the Rhaetian era, are composed of clay, mudstone, marl and evaporitic rocks. They are expected to be located at depth from 35 m to more than 60 m. A thorough analysis of the water chemistry is expected to provide information on the different units involved in the water infiltration and in the water flow and to help deducing the water pathways. Two boreholes were drilled in 2012. In the first borehole, the chemical and petro-physical properties of the water at four different depths were repeatedly recorded at a monthly rate. In the second one, an electrical sounding was realized twice a day from 2013 up to now, providing locally high vertical and temporal resolutions on the variations of electrical resistivity at depth (from 36 to 56 m depth).

### 5.1.1 Geological, structural and meteorological context at the Lodève landslide

#### Geographical and geological context

The karstic Larzac plateau consists in a succession of upper Trias to lower Jurassic horizontal units. At its southern border, a set of rivers (among which the Lergue river) eroded the sediments cover, shaping a set of steephead valleys forming the Lodève basin. This erosion affected several units from the lower Jurassic (exclusively limestone and sandstone), to the upper Trias (clay and evaporites), which locally outcrop. The setting of the playa environment characterizing the Lodève basin is extensively described in [Lopez et al. \[2008\]](#).

The Lodève landslide is located south of the village of Pégairolles-de-l'Escalette, in the west bank of the Lergue river (fig. 5.2). The unstable slope was progressively formed by the erosion and alteration of the upper limestone and sandstone units. The local tectonics build up resulted in a series of vertical North/South faults and fractures, allowing the water infiltration down to the deeper clayey and evaporitic layers (fig. 5.3). Fig. 5.4 presents the general lithology of the upper Trias and lower Jurassic, and the specific lithology identified at the Lodève landslide from borehole core sample.

During heavy rainfall events, a portion of meteoritic water is expected to infiltrate along these flow paths, down to the clay and evaporite layers from the Norian and Rhaetian era, leading to the rapid recharge of the units, and to the onset of high pressure in the confined layers ([Denchik et al. \[2019\]](#)). The water flowing in the evaporitic units (white gypsum and anhydride) provokes a dissolution of the evaporites, as suggested by the increased amount of  $\text{SO}_4^{2-}$  and  $\text{Ca}^{2+}$  ions in the water samples collected at depth from 36 to 56 m ([Denchik et al. \[2019\]](#)), possibly leading to a decrease in the cohesion of the rock material and a decrease of the shear strength.

#### Meteorological context

The Lodève basin, as part of the Cévennes mountain range (Méditerranée region), is affected by a specific meteorological context, consisting in episodic heavy rainfall events occurring mainly at the beginning of the

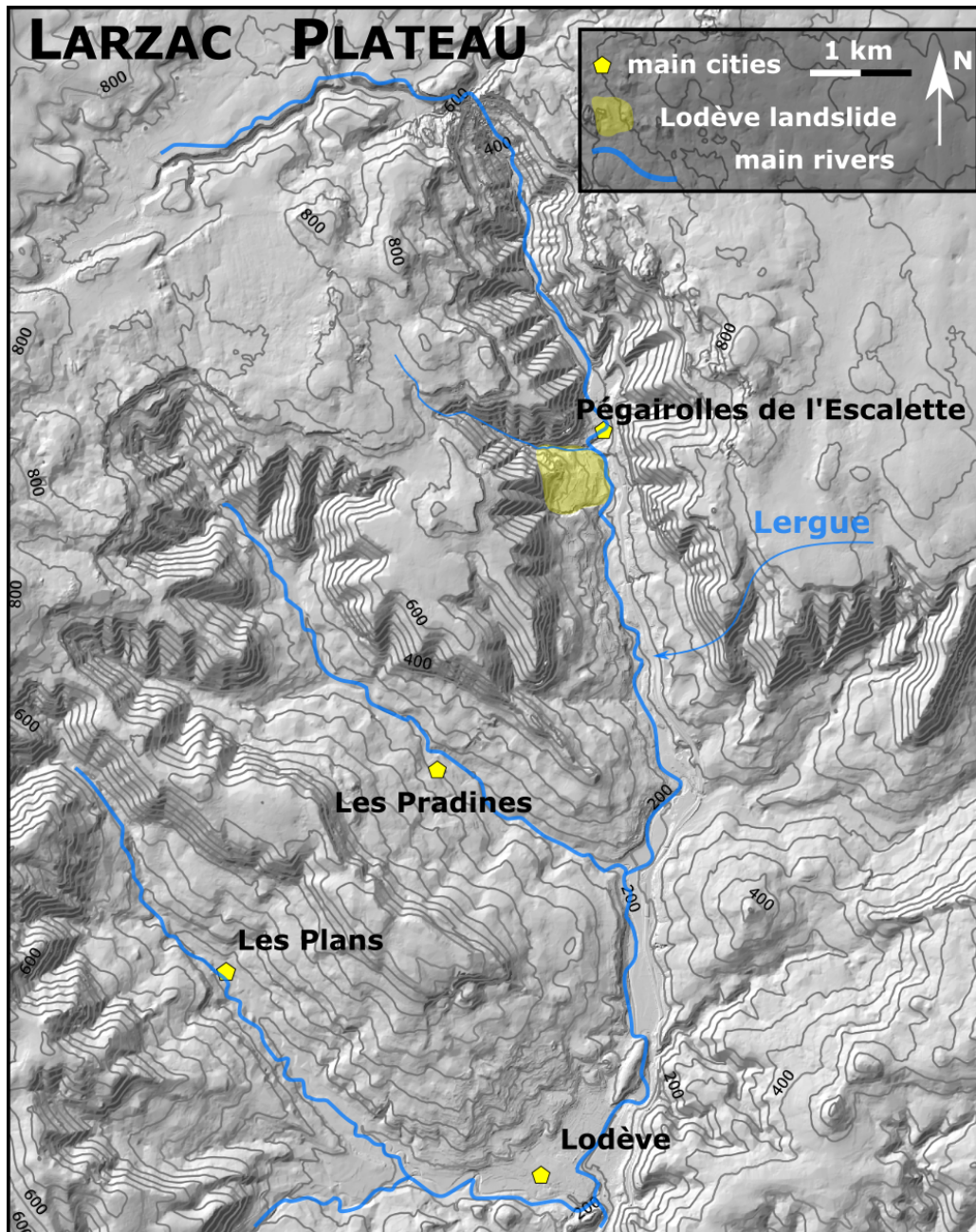


Figure 5.1: Topographic map of the region surrounding Pégairolles-de-l'Escalette - The Lodève landslide is marked by a yellow patch

autumn, called Cévenols events and more generally Mediterranean events. These episodes are characterized by a duration of generally 1 up to 3 days long, and a rain amount of 200 to 400 mm (Delrieu et al. [2004], Blanchet and Creutin [2017]), occurring after extremely dry summers.

### Hydrogeological context

Two reservoirs were identified within the slide. A first one is a semi-confined aquifer in the Norian units, potentially subject to periodic high hydrostatic pressure (Denchik et al. [2019]). The second one is an unconfined aquifer located in the Rhaetian units, with a water head around 36 m depth. These two aquifers are favored by the high permeability contrast between the overlaying units (breccia, marl and clay, evaporites). The intense rainfall events can temporarily connect them (Denchik et al. [2019]). In the upper part of the slide, large vertical faults crossing the Hettangian units are expected to contribute to the water infiltration, supplying in particular



Figure 5.2: Aerial view of the Lodève landslide (Google Earth satellite image)

the deep Norian aquifer.

At the Lodève landslide, the hydrogeology is controlled by 1/ the infiltration processes, 2/ the water circulation in the rocks and 3/ the water / rock interactions, which are made important by the high amount of claystone and evaporites.

Water/rock interactions in clay materials operate through adsorption processes, potentially leading to clay swelling. Water rock interactions in evaporitic units correspond to precipitation and dissolution processes. In both cases, the processes are very sensitive to the water pressure, and potentially play an important role in the instability.

### Morphology of the landslide

The slide is located 300 m southward of the southern entrance of the village of Pégairolles-de-l'Escalette. The slope is roughly oriented in the East - West direction. The unstable zone extends over 400 m in the North/South direction and 400 m in the East/West direction, at an altitude varying from 470 m to 280 m. The slopes are generally not very steep ( $15^\circ$  to  $20^\circ$  in mean) but locally reach  $45^\circ$  in the upper part.

The movement is essentially rotational, consisting in the slide of faulted blocs along the evaporite layer, at the slow rate of 3 to 4 mm / yr (fig. 5.3.b). The highest part displays the highest speed observed in the site. Several scarps are also visible along the slope (fig. 5.3.a).

### 5.1.2 Long term meteorological, hydrogeological, geochemical and geophysical monitoring of the slope

In order to document the behavior of clay-evaporitic landslides, the Lodève landslide was chosen as observation site and was instrumented since 2012. The main intent was to observe the hydrogeological response to the general seasonal meteorological variations and to the rapid and intense Cévenol events and to characterize the underground water circulation associated to such events as first step towards a hydromechanical modeling of the slide.

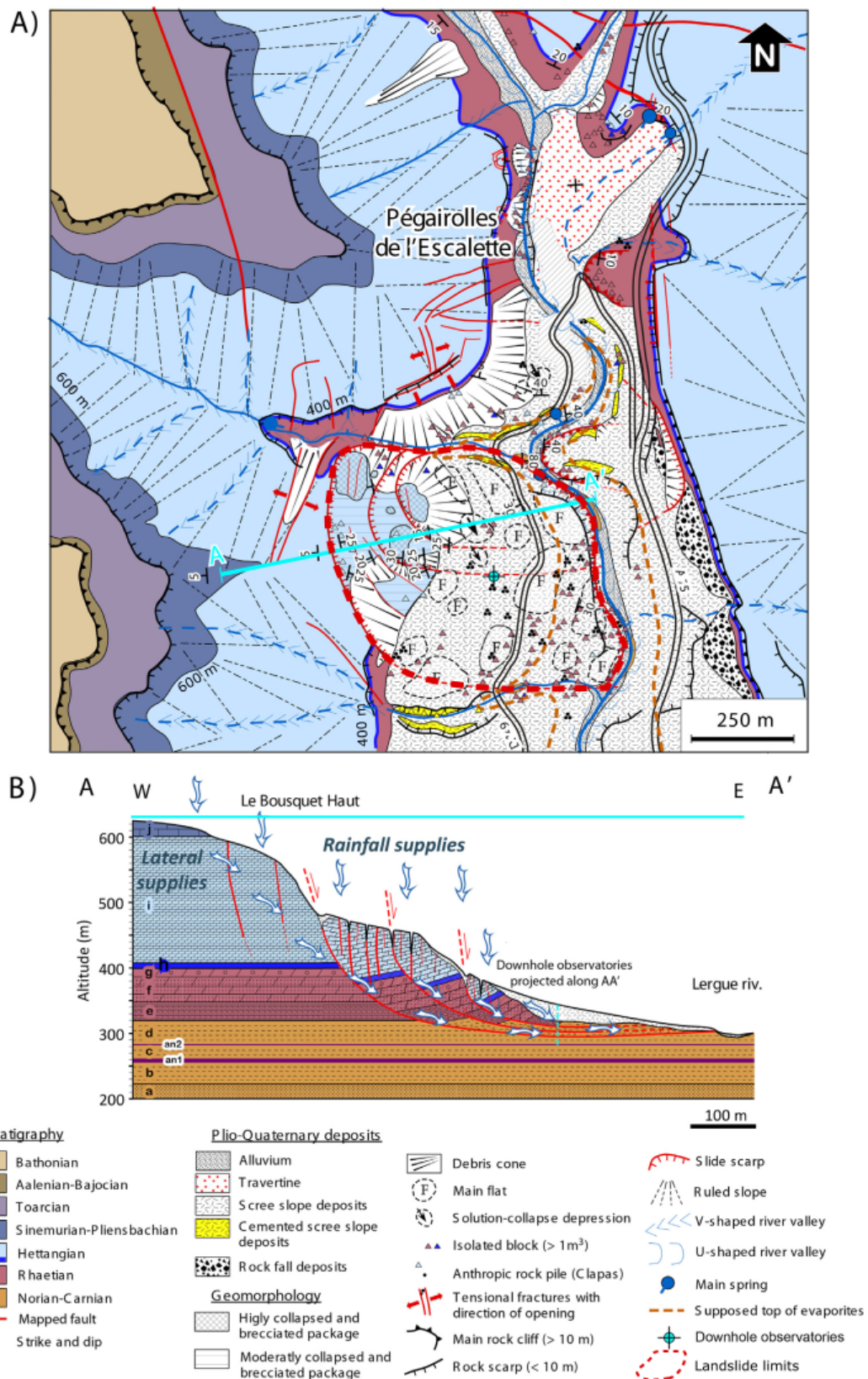


Figure 5.3: Geological and morphological context at the Lodève landslide (A); Interpretative scheme of the hydrogeological behavior of the slope (B) - from Denchik et al. [2019]

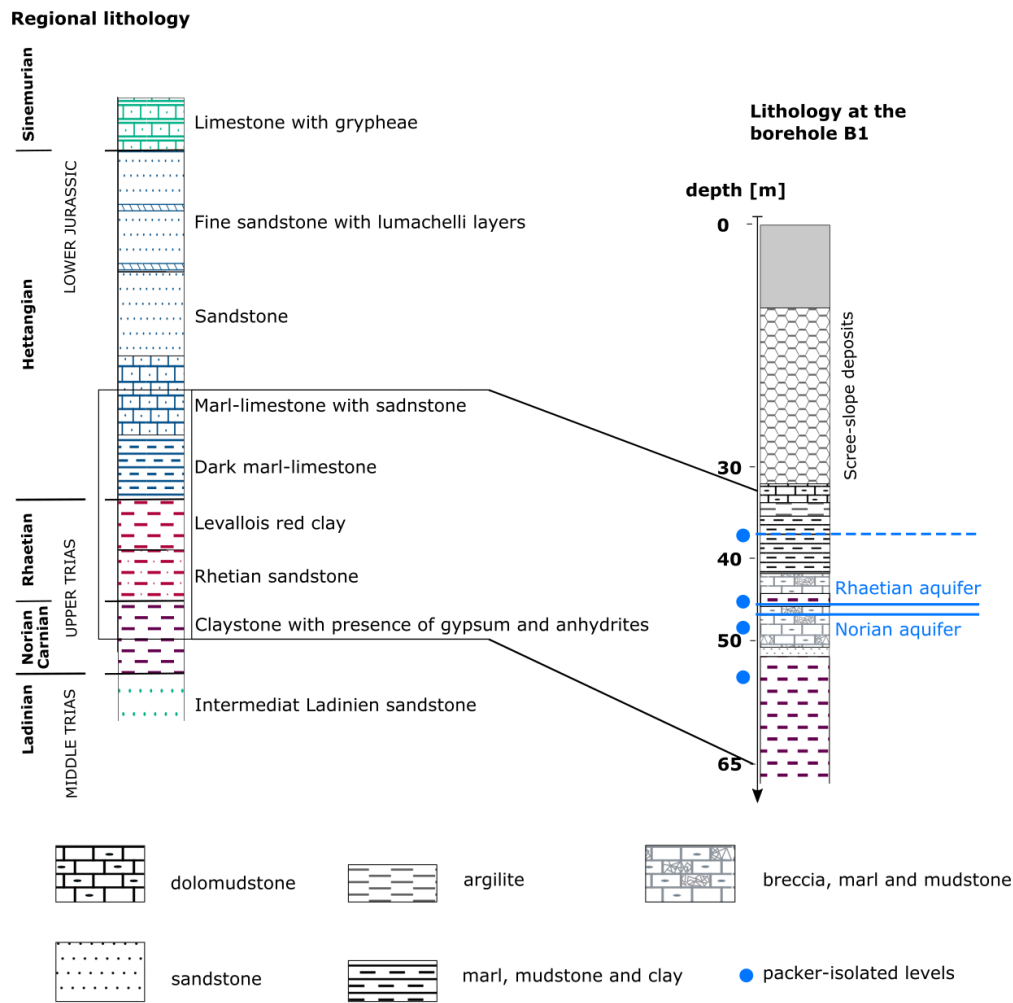


Figure 5.4: General lithology of the Trias and Lower Jurassic period which correspond to the regional context of the Lodève valley and local lithology from analysis of borehole core samples at the slope of the Lodève landslide - inspired by Denchik et al. [2019]

### Studied area

The studied area is the lower half-part of the slide, where the surface topography is characterized by a very smooth slope. This area consists in 30 m of scree slope deposits, covering a succession of mudstone, marl, clay and evaporite layers (see fig. 5.4). The topography difference between the highest (West) and lowest point (East) of the studied area is about 70 m. The site is covered with vineyards, most of which being supported by metal stakes.

Two boreholes were drilled, dedicated respectively to daily repeated geophysical logging and to water sampling and analysis of chemical, mechanical, electrical and thermal properties of the underground water, at an approximate rate of two measurements per month.

### Geophysical borehole instrumentation

A first borehole was drilled and equipped to realize daily electrical logging and repeated measurements of the cumulative strain along the borehole. The borehole was drilled up to 65 m depth, and an automated multi-electrodes system from the ImaGeau<sup>®</sup> company was installed along the hole, later cemented with bentonite, with electrodes-spacing of 1 m. The measurements are realized with a dipole-dipole array, designed to be sensitive from 31 to 53 m depth. Eight optic fibers were installed in the borehole to record the cumulative strain from 37 to 58 m depth.

## Hydrogeological and geochemical borehole instrumentation

The second borehole aims at observing the property of infiltrated and ground water. Well logs (Gamma ray, electrical resistivity, temperature and fluid electrical conductivity) were realized just after the drilling and an analysis of the borehole core samples was conducted.

Four hydrogeological units were isolated with a multi-packer WestBay system installed in the borehole. These four units correspond to the two identified aquifers: the Norian aquifer and the Rhaetian aquifer, to an evaporite-rich layer and to the deep clay-evaporitic layer (fig. 5.4). Located at 36, 45, 48 and 56 m depth, these units are object to repeated sampling of the water (irregular, minimum once every 6 weeks) and measurements of the following parameters: in-situ water pressure and temperature, electrical conductivity, pH, total organic carbon (TOC), total dissolved solid (TDS) and concentration of magnesium ( $Mg^{2+}$ ), calcium ( $Ca^{2+}$ ), sulfate ions ( $SO_4^{2-}$ ) and bicarbonate ions ( $HCO_3^-$ ). The level at 36 m depth is seldom sampled, it corresponds to the unsaturated layer and chemical measurements are only possible when the saturation of this level is sufficient.

## Meteorological instrumentation

A national meteorological observatory from Météo-France is located 6 km South-West of the slide, at the location "Les Plans" (fig. 5.1), providing recordings of the daily rainfall. A local meteorological station was installed in 2019 in the slope, providing the evolution hour per hour of the temperature, atmospheric pressure and rainfall at the location of the slide. A comparison of the recordings at the two stations from mid March and September 2019 is given in figure 5.5.

The concurrent measurement of the rainfall and the surface temperature permits to estimate potential evapotranspiration (Oudin et al. [2005]), and to deduce the effective rain infiltrating the subsurface, after evaporation and transpiration by the vegetal cover.

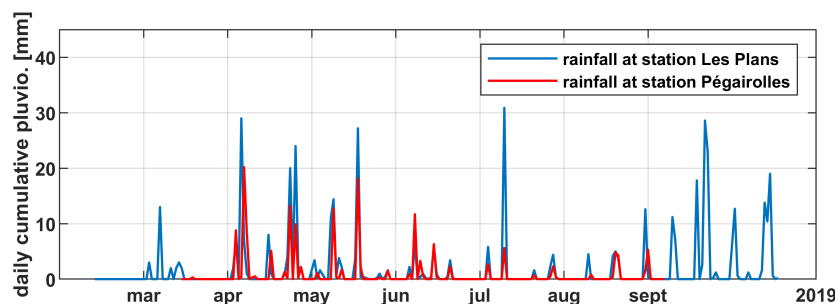


Figure 5.5: Variability of the total cumulative pluviometry between Les Plans station and Pégairolles station between March and September 2019

### 5.1.3 Hydrogeological, hydrochemical and meteorological time-lapse observations

A complete hydrochemical and mechanical monitoring was realized and can be found in Denchik et al. [2019]. This study presents the analysis and interpretations of the two downhole datasets, from 2013 to 2017. These observations are briefly resumed in the following subsection.

The two observed aquifers present two different trends regarding water pressure, ions concentration, and electrical conductivity values. Two major types of temporal variations seem to emerge from the monitoring of the four isolated units: the yearly cycle, and the short and intense Cévenol events.

The figure 5.6 presents the variations of geochemical, electrical, thermal and mechanical properties of the sampled water, with the rainfall as reference since the borehole was equipped, in 2012.

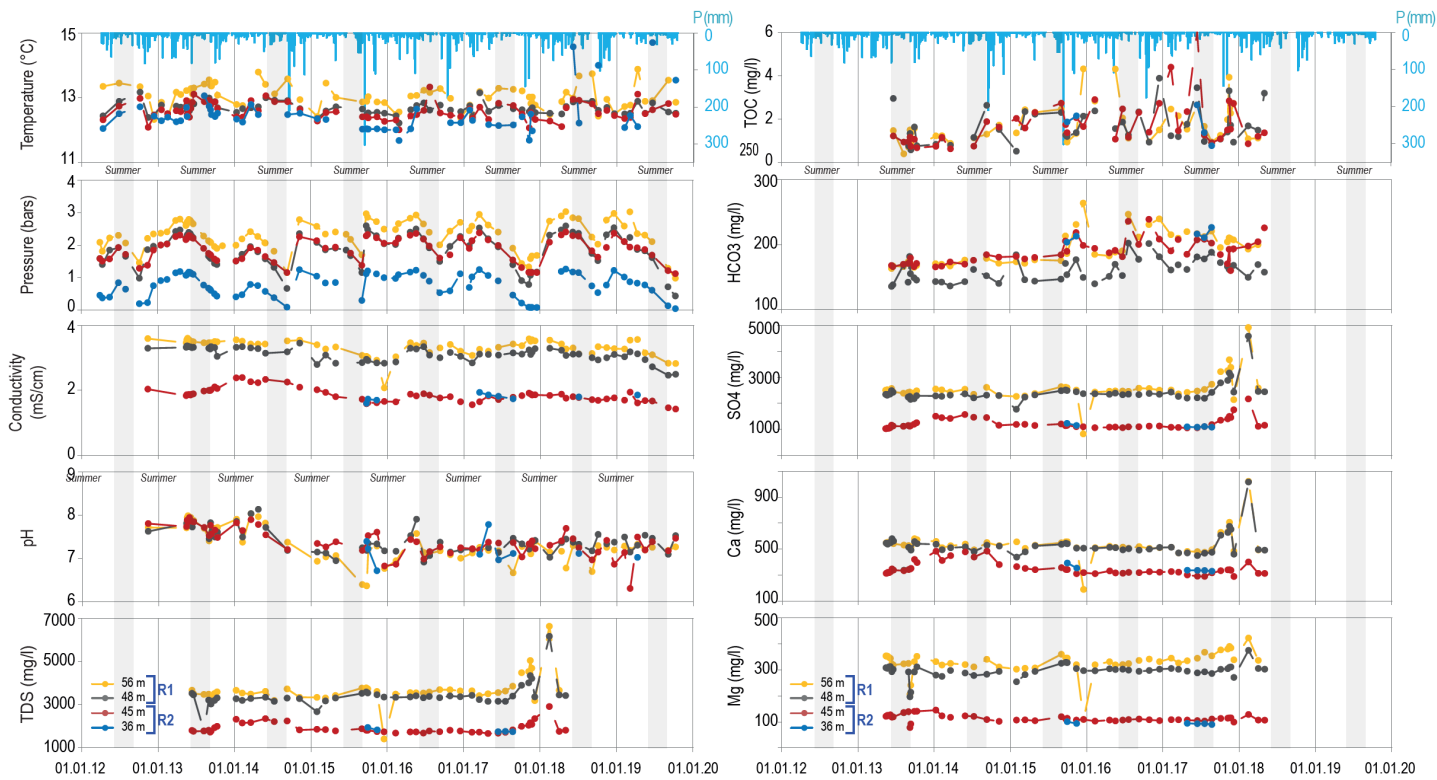


Figure 5.6: Long term variations of the petrophysical and hydrochemical properties of the water at four levels isolated by a multi-packer system in the WestBay borehole and correlation with the total rain from 2012 to mid-2019; completed from Denchik et al. [2019]

### Characterization the hydrogeological response to seasonal meteorological events

The yearly cycle is mainly observable in the variations of water pressure (fig. 5.6). This yearly trend produces an increase of the water pressure during the autumn and winter, until it starts decreasing in the late winter to spring period. The decrease of the pressure is maintained during the summer dry period, down to the minimum value, just before the occurrence of the first autumnal rain event. It can be noticed that the temporal variations of the water pressure is not regular from one level to the next one, in reference to the discordance of the shallower and the deeper aquifers. Fig. 5.7 presents the long-term pressure gradient between each consecutive monitored levels and the concurrent rainfall measured at Les Plans station, the closest meteorological station from the site providing long-term data. The variations of gradient pressure between 45 and 48 m depth are quite important and follow a clear year cycle, with important variations during Cévenol episodes. This suggests a variable saturation of the rock between 45 and 48 m and an important variability of the permeability from one unit to the next.

At the opposite, the electrical conductivity of the water barely changes in time, nor do the concentration in most chemical elements (Ca, SO<sub>4</sub>, Mg) or the TDS. The variations of HCO<sub>3</sub>, of the TOC and of the pH seem more erratic, discordant both in time and vertically.

### Characterization of short terms variations: response to the heavy rain event of 2015

The amount of water involved and the brutality of Cévenol episodes are not stable from one year to the next. In 2015, a particularly intense rain event (300 mm within one day) resulted in very fast transient variations in the concentration of most of the chemical elements sampled in the deepest sampled units. The water electrical conductivity and the concentration of Mg, Ca, SO<sub>4</sub>, TDS of the deepest unit reached values corresponding to the shallowest ones, suggesting a change in the flow regime and possible communication between the deepest and the shallowest units Denchik et al. [2019]. This was observed 3 months after the intense rain episode, suggesting

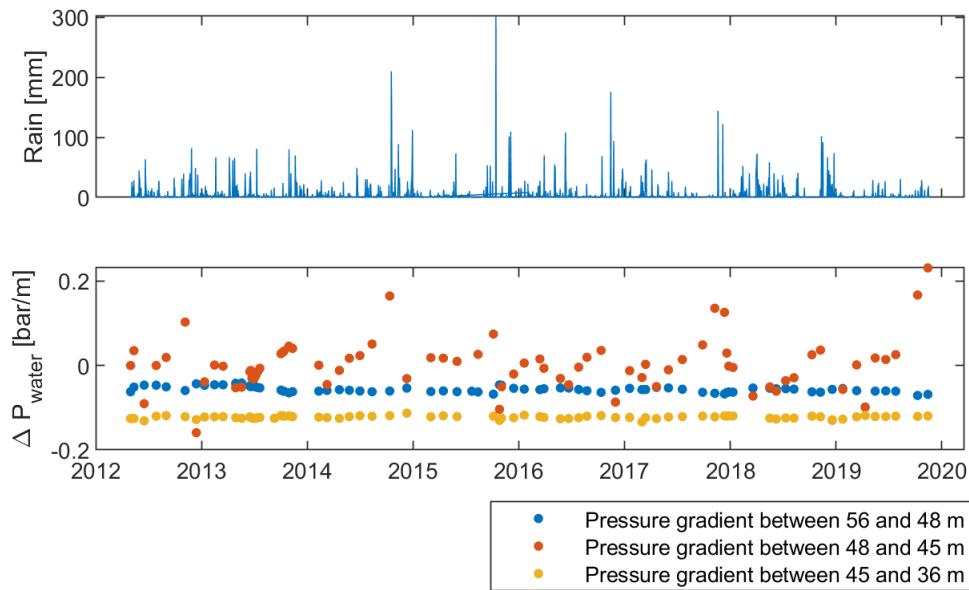


Figure 5.7: Long-term monitoring since 2012: pressure gradient between each following isolated levels in the WestBay borehole (bottom figure) and related rainfall (top figure); The separation between the two aquifers is clearly observable in the pressure gradient between the 45 and 48 m.

that the chemical response operates with a delay. However, the response to this event is recorded at a too low frequency rate (one measurement per month) to permit the observation of the full response.

### Improving the understanding of Lodève landslide through surface hydrogeophysical studies

In this work, we try to observe the response of the subsurface to the seasonal variations produced by the alternation of dry to very dry periods and wet periods. As presented previously, these yearly variations are expected should partly be driven by the variations in water pressure (or water-table). To a lesser extend, variations in the rock water interactions can be expected if intense Cévenol events such as the one in 2014 occur, resulting in variations in the water chemistry. These two aspects (variations of the water pressure (hence of the water height) and ion content are expected to be sensed in geoelectrical studies.

This work addresses the challenge of observing the yearly hydrogeological cycle, the intense recharge generated by Cévenol events and the slow discharge following it through surface measurements, in order to extend the boreholes information to the rest of the site. Time-lapse methodologies were developed base on two geophysical methods: CSAMT and TDIP.

In the CSAMT experiment, both methodological and analytical questions are explored:

1. Are 1D CSAMT time-lapse soundings suited to observe the changes of water table expected at the yearly scale at the Lodève landslide ? Is the resolution sufficient ?
2. How do these temporal changes reflect in the electrical resistivity model of the slide ?

In contexts of high clay content, the adsorption occurring at the surface of clay grain is expected to produce a polarization signal. This polarization signal, when recording properly, can help to identify the zones of high clay content, bringing constraint on the hydrogeophysical interpretation. TDIP measurements were conducted to improve the sensitivity to the lithology. In particular, a few questions are raised:

1. Do TDIP time-lapse measurements help constraining the variations of the hydrogeological model in time (variations of the water height) ?
2. What can be expected regarding the identification of evaporites ? What are the sensitivity 1/ to the rock formations themselves and 2/ to the dissolution and precipitation processes?

## 5.2 Methodology

### 5.2.1 Time-lapse CSAMT

Time-lapse methodologies using CSAMT are rarely mentioned and presented in the literature. [Darnet et al. \[2018\]](#) showed that the CSEM technique had a high sensitivity to variations of the resistivity model, and was adequate in the monitoring of a geothermal reservoir affected by high anthropogenic noise. In this analysis, the synthetic data were exploited up to the near field domain, and no discussion on the influence of the variations below the transmitter is made. [Falgàs et al. \[2006\]](#) repeated measurements along a profile to observe the variation of intrusion of salt water in a coastal aquifer. [Bartel \[1982\]](#) presented a monitoring methodology to observe in situ underground coal gasification (UCG) processes using CSAMT with extensive field tests that lead to the final monitoring methodology employed. It is expected that the good vertical resolution, the large depth of investigation and the insurance of a stable source signal provided by the controlled source, make all together CSAMT a very good candidate-method to monitor the hydrogeological reservoirs in pseudo-layered contexts.

In the following study, the ability of 1D CSAMT soundings to monitor hydrogeological variations is explored. Indeed, in a similar manner as a well, a unique sounding, repeated in time, could provide, in a layered medium, the variations of the water level.

This chapter presents a first attempt at applying in the field a time-lapse methodology. The temporal resolution and related field requirements are discussed.

#### **High temporal frequencies: requirement of automated systems**

To record the response to a Cévenol event, a high temporal resolution is required (daily or weekly measurements). [Denchik et al. \[2019\]](#) observed indeed that the response of Lodèves aquifer to the most intense Cévenol events is very focused in time and occurs within 3 months after the event.

Daily measurements require to leave the equipment on site during the experiment. If the measurements are to be realized for a long time, the systems need to run autonomously.

**The sensors:** The permanent setting of a recording unit is possible if the instrument can be programmed in advance to exit autonomously from a standby mode regularly at fixed hour to realize the measurements. Such programmings are possible with instruments such as Metronix's ADU measurement units, however, the batteries still need to be regularly checked and changed (every few days).

**The transmitter:** High power transmitters are often instruments that require a manual setting. In particular, these instruments run on very specific domains of usage regarding the output impedance that it can afford at the terminals. When the ground impedance varies (throughout the day, or throughout days), the mode of usage of the instruments often must be tuned. For this reason, a high temporal monitoring would require a self adapting current source.

The realization of such measurements requires the possibility of protecting every instruments from potential windy, wet or extremely warm ( $T > 40\text{ }^{\circ}\text{C}$ ) weather.

#### **Monitoring at monthly temporal frequencies**

The time-lapse methodology at the Lodève landslide aimed at observing the seasonal variations during late fall and winter time, expected that this long-term trend is strongly related to the intense rain episodes occurring during the autumn. At that period, the system is expected to finish its recharge led by heavy autumnal rain, and to start relaxing (fig. 5.6).

### 5.2.2 Time-lapse TDIP

In most environments, characterizing the electrical resistivity allows to detect water. The electrical resistivity can then be a measure of the amount of water in the pore space, and if the pore space is known to be filled with

water of a known electrical conductivity, the resistivity of the saturated rock can be a measure of the size of the pore space, hence the porosity (Archie [1942]).

This is however true only if the rock matrix is electrically insulating relative to the pore fluid. When it comes to conducting minerals, the Archie law is no longer valid as the matrix conductivity is not negligible regarding the fluid. In the particular case of environmental geoscience and hydrogeophysics, clay is the main formations which presence leads to such relations. In the presence of clay minerals, the electro-negativity of the mineral leads to adsorption process, that permit important surface conduction (Mitchell and Soga [1993]). The electrical resistivity of clay minerals is in the same orders of magnitude than that of water with low mineral content, leading to uncertainty in the interpretation of the resistivity models.

If this particular feature of clay is a disadvantage when characterizing the DC resistivity, it is an asset when characterizing the complex conductivity. Indeed, the adsorption occurring at the surface of clay minerals yields to the existence of an electrical double layer, that produces an intense polarization that can be measured with the induced polarization method, when applying a current (Vacquier et al. [1957]).

At the Lodève landslide, clay is present in non-negligible amount in several geological units (Carnian, Norian, Rhaetian and lower Hettangian). In particular, the amount of clay in the unstable gypsum unit is not well known. For this reason, DC resistivity presents limitations when trying to distinguish between high clay contents and important water content in the matrix pores. In contrast, induced polarization is expected to permit distinguishing the zones of high clay content from the zones of low clay content. For this reason, induced polarization time-lapse measurements were realized to improve the characterization of the site and observe the temporal variations of the signal related to the hydrogeology.

### Initial observations

In 2016, SIP data were collected at the Lodève landslide as a first attempt to characterize the polarization signal of the subsurface. At the time, the objectives were:

1. to observe the IP response of clay associated with thin evaporite layers (gypsum and anhydrides);
2. to explore the relevance of IP measurements to delineate the different units constituting the slope (in particular the evaporitic layers);
3. to explore the relevance of IP to separate the hydrogeological information (variations of water head mainly) and the lithology information, and potentially to monitor the variation of hydraulic head associated with the seasonal meteorological cycle.

The IP signal of claystone has been broadly explored in the context of various saturated sand-clay mixtures (Breede et al. [2012]), various water saturations (Ulrich and Slater [2004]) or in various contexts of induced stresses (Ghorbani et al. [2009], Maineult et al. [2018]) through laboratory experiments. The in situ measured IP signal remains however dependant on the specification of each site, because of the numerous parameters influencing the IP. Besides, the specific question of the IP signal of clay and evaporite layers is however very few studied and documented. Guinea et al. [2010] presents TDIP measurements realized over a lutite and gypsum medium in Spain, showing no particular polarizable behavior of the gypsum, but suggesting potential effects of capacitance linked to the alternation of conductive (clayey) and resistive (evaporites) layers, with potential charge accumulations at the interface.

Borehole / surface SIP measurements were realized, taking advantage of electrodes setup in the imaGeau borehole. Fig. 5.8 presents inverted models from the borehole-surface data recorded in 2016 at the Lodève landslide, at 1 Hz. The apparent modulus and phase of the complex resistivity were recorded at several frequencies, showing 1/ an increase of the conductivity with depth, attributed both to the presence of clay and marl at depth below 32 m, ad to the presence of water at depth, varying around 36 m depth; 2/ clear decrease of the phase between 27 and 45 m depth, which location correlates well with the Rhaetian unit composed of dolomudstone, marl and clay. In addition, three points are noted.

- The phase seems to be very low at depths where the clay and evaporites layers alternates (below 52 m depth); nevertheless, the sensitivity at those depths might as well be low because the borehole is only instrumented until a depth of 52 m.

- The lateral variations of phase in the polarizable units seem highly correlated to the variations of modulus at the same depths, suggesting either that the high conductivity closer to the borehole diminishes the measured chargeability, or that the inversion process dumps the phase information in the data by explaining the data with a low resistivity.
- It seems that the vicinity of the borehole presents anomalies, imputable either to the presence of the borehole (sediments reshuffled by the drilling), or to measurement issues.

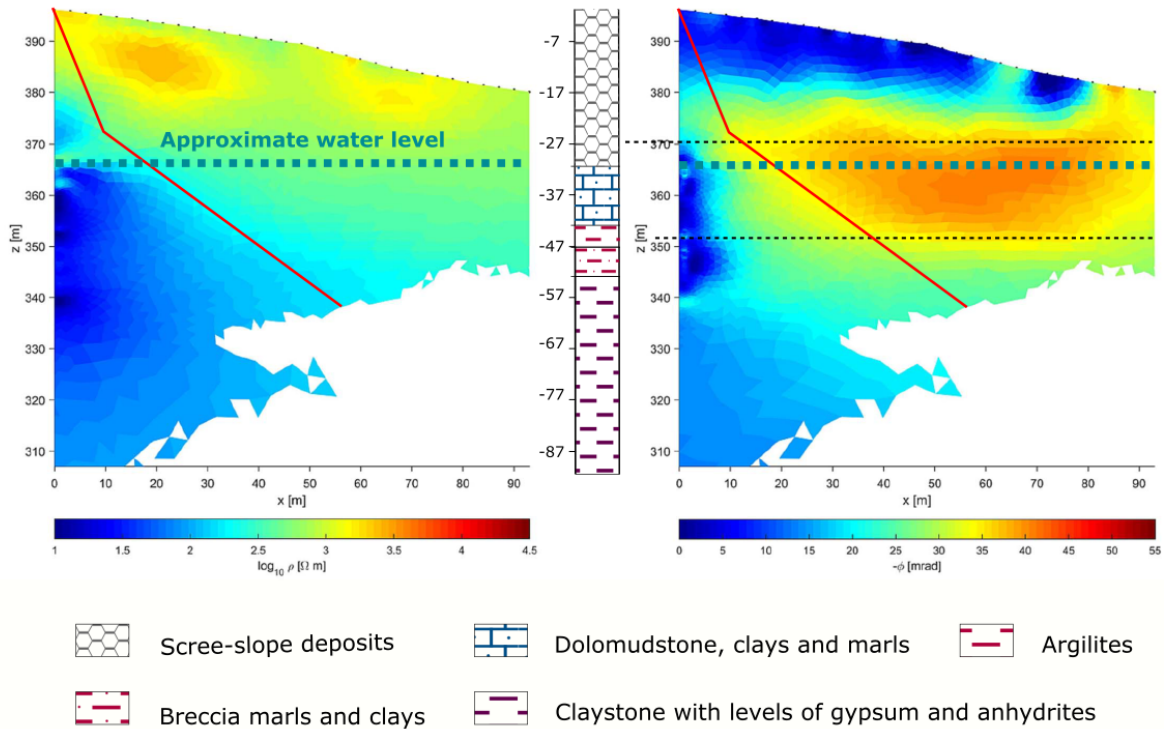


Figure 5.8: Preliminary SIP observation: resistivity and phase inverted from borehole/surface measurements at 1 Hz. The red line suggest a local loss of sensitivity of IP, potentially due to a decrease of resistivity.

At higher frequency (37.5 Hz), this zone presenting a low phase (hence polarizable) seems to be even more sharply detected, slightly shifted upwards.

This first characterization suggested a good detectability of the marl and mudstone layers and possibilities of detecting the bottom of this unit, where the chargeability seemed to decrease. These first observations suggest that the alternation of clay and evaporites layers do not particularly present a strong polarization.

These observations encouraged further investigations on the detectability of the different layers from surface measurements, as well as the possibilities to image the time varying hydrogeological signal.

## 5.3 Analysis and observations of the CSAMT time-lapse data

### 5.3.1 Field setup

The time-lapse experiment consists in a monthly repetition of the measurements at 8 full EM stations and 4 electrical stations. The time-lapse data were acquired at four time-periods, from November 2018 to March 2019. The measurements were realized every month, except in February, when no measurement could be realized due to logistic issues. Two of the 8 full-EM stations were recorded only from December.

The CSAMT setup is presented in fig. 5.9 and fig. 5.10, with the 200 m long transmitting dipole located about 3 km away from the measurement site. It can be noted that the orientation of the transmitted dipole is not

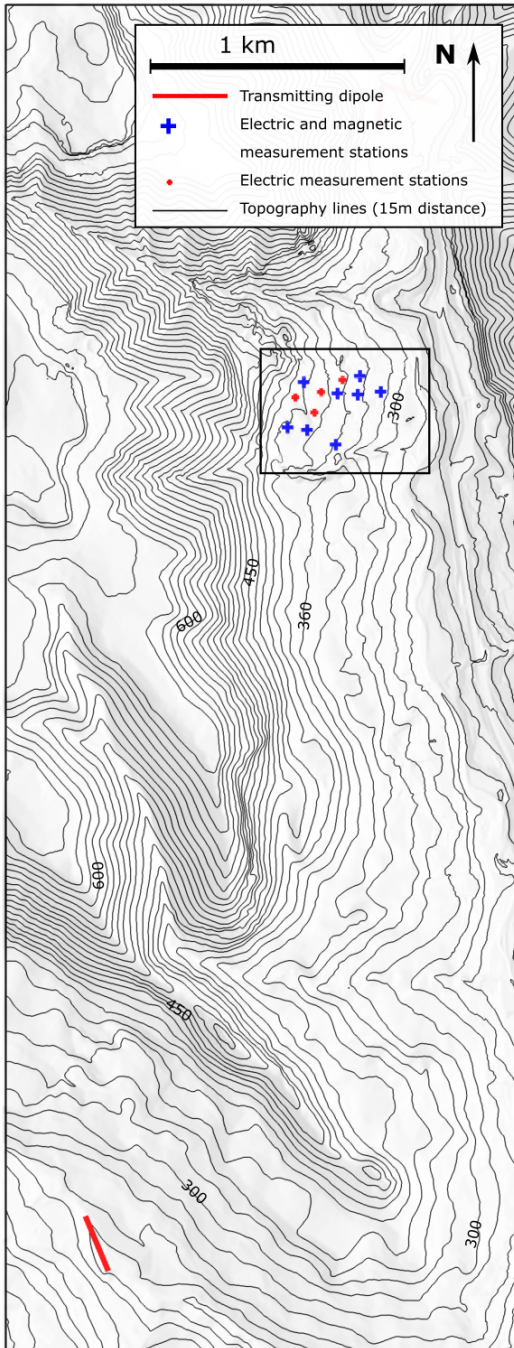


Figure 5.9: Map of the CSAMT time-lapse experiment: transmitter site and measurement stations

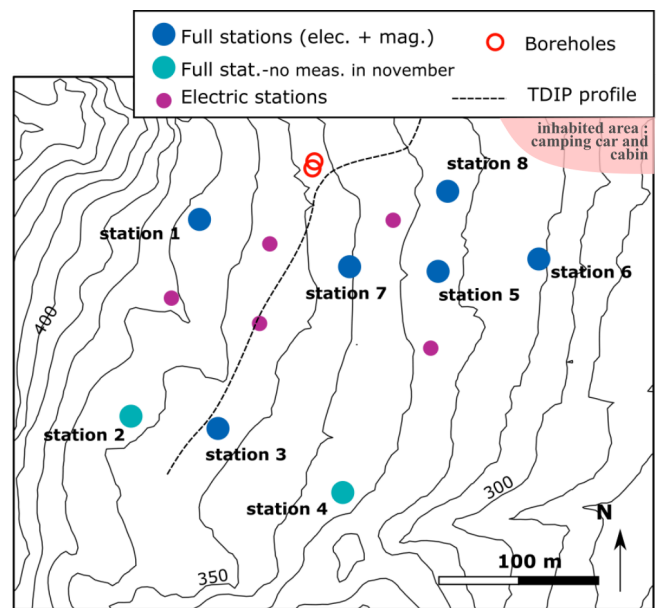


Figure 5.10: Map of the measurement stations: the full-stations record the 3-component magnetic field and the 2 horizontal components of the electric field (2 of the 8 full-stations were not recorded in November); the electrical stations record only the two horizontal components of the electric field. The time-lapse TDIP profile presented later in this chapter is marked as a dotted line.

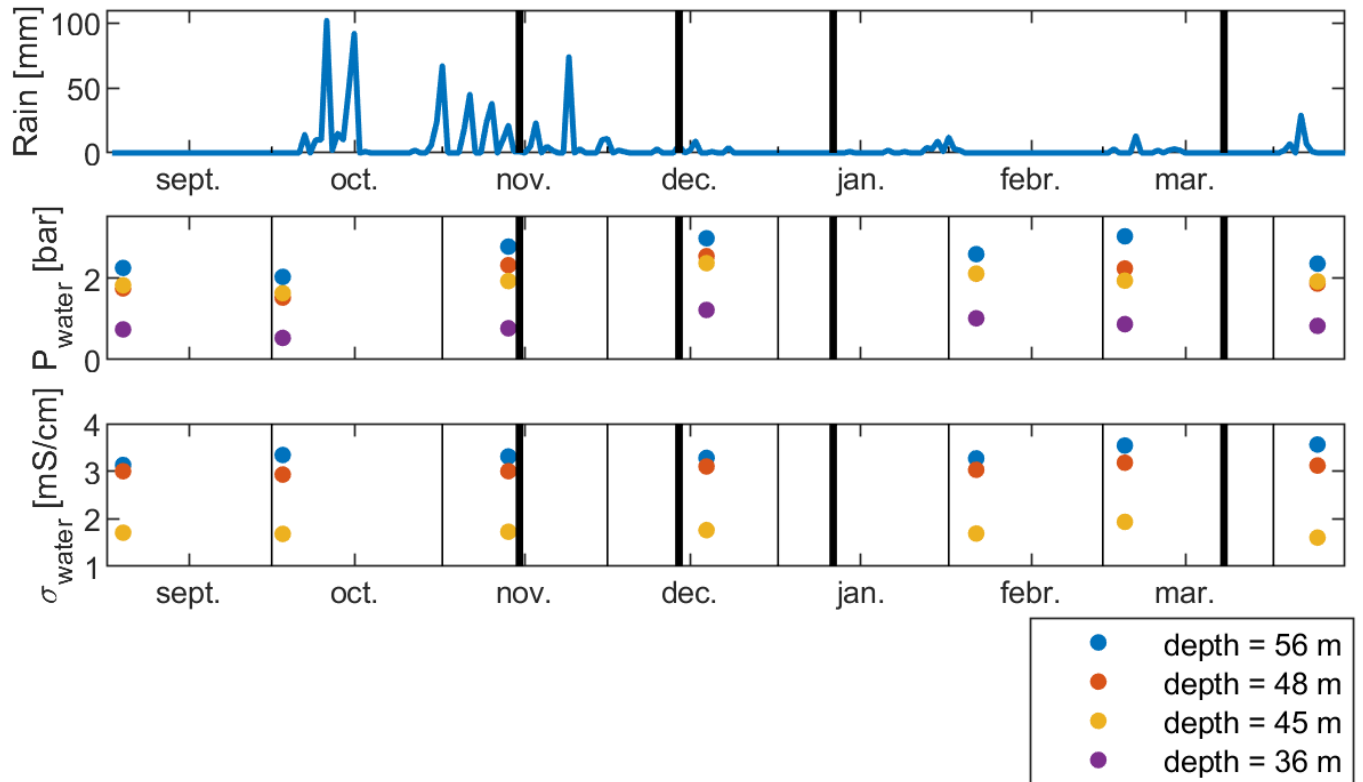


Figure 5.11: Variations of pluviometry (total rain), water pressure and water electrical conductivity during the CSAMT time-lapse experiment.

optimal given its location relative to the site. Optimally, the orientation of the dipole should be orthogonal to the line joining the transmission site and the measurement site. The timeline of the measurements is presented in fig. 5.11, where each measurement period is symbolized by a black thick vertical line.

During the first measurement period, in November, additional near field data were recorded, with a couple of transmitting dipoles located 1 km away from the site. These data were initially measured to allow realizing a 3D characterization of the slope, and 21 stations were recorded at that occasion, amongst which 13 were full electric and magnetic stations and 9 were only electrical stations. The processing and preliminary modeling of this CSEM dataset is presented in Appendix A.3.

### Time-lapse logistic

The transmitting site was set once and for all at the beginning of the experiment, along a river bench in the village Les Pradines (fig. 5.1, fig. 5.9), on alluvium deposits to ensure low contact resistances (fig. 5.12.e). Two long electrodes were grounded at the extremities of the dipole. Ground electrodes, used in buildings and houses to protect against electrical risks, were chosen as they have a large contact-surface and they are expected to last very long in the ground. These electrodes were grounded on at least 1 m length, and salt-watered at the beginning of each measurement periods. A cable was set to connect the electrodes to the current source. The electrodes and cables were left during the entire experiment. The current source ran on a 2.6 kW power generator. The routine at the beginning of each time-period was to install the transmitting site and the power generator as in fig. 5.12.c and fig. 5.12.d.

The measurement stations were recorded one by one, as only one full-EM V8 and one 3-ER receivers were used (fig. 5.9). The measurements were realized on 14 m length electrical dipoles and with 3 AMTC magnetic coils. Metal electrodes were used and left at the site for the entire time-lapse experiment. Because the slide is moving very slowly the electrodes are considered motionless for the duration of the experiment.



Figure 5.12: Photographs of the survey: a. V8 measurement unit with its battery ; b. the site of Pégairolles de l'Escalette - view from the south; c. the transmitter station: the white box at the right is the current source, the small grey box at the left is the transmitter controller, the metal stake at the back is one of the injection electrodes; d. to face the autumnal rain, a shelter was built with broom sticks, plastic foil and garbage bags; e. the injection site: the dipole was set along a large conductive ground field along a river, close to the village of Les Pradines

### 5.3.2 Validity of time-lapse measurements in CSAMT

#### Theoretical sensitivity of CSAMT to hydrogeological changes

In the time-lapse study of the Lodève landslide, the water conductivity of the unconfined aquifer is expected to remain constant. On the contrary, the water pressure, related to the hydraulic head, is expected to vary. During the autumn an increase of the water pressure is observed in response to the heavy rain events. This increase occurs for a part of the winter, before it starts decreasing progressively, to finally be at its lowest at the end of summers. In this context, we question the ability of CSAMT sounding, interpreted in 1D, to sense these small variations of the water pressure.

To answer this question, sensitivity tests were conducted to evaluate to what extent a certain variation of the model influences the apparent resistivity curve, and to evaluate if such variations can be interpreted in the inversion (i.e. if they are large enough to be interpreted as effective variations in the inverted models). Another question is: can we easily decipher a variation of the depth of the top aquifer from the variation of conductivity of the pore fluid?

Synthetic data were computed using the specific layout applied at the Lodève landslide. A conductive anomaly was modeled as a bloc located about 50 m below the surface depending on the location on the slope, extending over the entire survey area. The sensitivity to the variation of resistivity and to the depth of this anomaly was evaluated by comparing the synthetic data from 4 different models, with slight changes of 1/ the resistivity of the anomaly and 2/ the location of the top of the anomaly (Tbl. 5.1).

Model	Background	Anomaly	Depth of the top	Thickness
M1	800 $\Omega$ .m	80 $\Omega$ .m	60 m	100 m
M2	800 $\Omega$ .m	120 $\Omega$ .m	60 m	100 m
M3	800 $\Omega$ .m	80 $\Omega$ .m	65 m	100 m
M4	800 $\Omega$ .m	80 $\Omega$ .m	70 m	100 m

Table 5.1: Characteristics of the four models used to evaluate the sensitivity of CSAMT measurements and to test the 1D time-lapse inversion

The synthetic apparent resistivity curves (fig. 5.13) show that both a variation of resistivity of the anomaly (80 to 120  $\Omega$ .m) and a variation of 5 m of the depth of the anomaly result in clear variations of the apparent resistivity curve. Very small variations can also be observed on the phase curves (fig. 5.13). It seems that changing the depth of the anomaly causes the apparent resistivity curve to shift vertically, and keeps the phase unchanged (models 3 and 4). On the contrary, a variation of the resistivity of the anomaly induces dynamic variations of the apparent resistivity curve and also influences the phase (model 2). In these tests, the far field limit is observed at approximately 400 Hz.

The synthetic apparent resistivity curves were inverted and used to tune a temporally constrained inversion scheme. Fig. 5.14 and 5.15 present inversion tests conducted on the synthetic data. Fig. 5.14 presents inversion results when imposing no temporal constraint on the data. The top of the anomaly is smoothed out by the vertical constraints, but is located approximately at the correct depth for all 4 inverted models. In addition, the variations between each synthetic models are well reproduced by the inversion: the model 2 presents an anomaly more resistive than the model 1 and the pick resistivity of the models 3 and 4 are shifted downwards by approximately 10 m both from the low resistivity pick of model 1. It seems however, in the case of the models 3 and 4, that the shift of the pick comes together with an increase of the pick resistivity, and the two models can only be distinguished by a change of the resistivity of the anomaly: the variation of the depth of the anomaly, as initially modeled, is not detected. The bottom of the anomaly, well resolved in models 1 and 3, is not well resolved, in terms of resistivity value, in the models 2 and 4. At depth, below the anomaly, it seems that the inverted models show features that do not exist in the synthetic model.

If the temporal variations are expected to be of limited amplitude, constraining the amount of variations

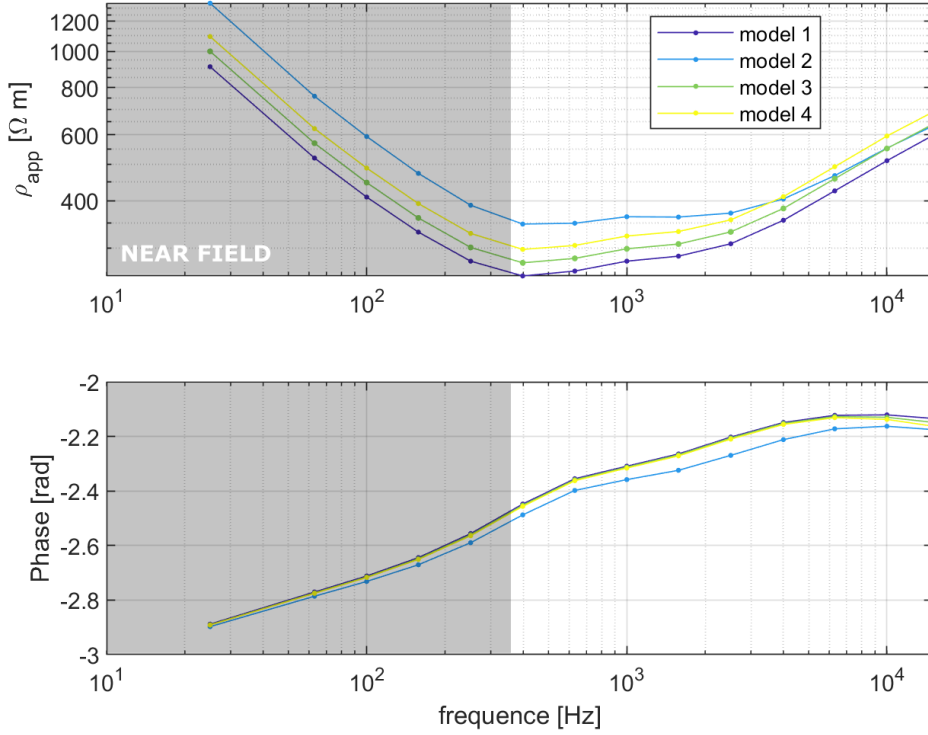


Figure 5.13: Synthetic apparent resistivity and phase curves computed from models 1, 2, 3 and 4 (Tbl. 5.1). The far field limit is observed at 400 Hz.

between the inverted models can constitute a valuable guide to constrain the inversion. A "temporally" constrained inversion scheme was tested, by imposing a weight on the variation from the inverted model at step  $i - 1$  ( $m_{T_{i-1}}$ ) and the inverted model at step  $i$  ( $m$ ), subject to the minimization, in the cost function. This new cost function (eq. 5.1) is adequate if it is known that the variations of the model are limited in time. In eq. 5.1, the temporal constraint term is normalized by a percentage  $p$  of the model at the previous iteration  $m_{T_{i-1}}$ . This percentage establishes the amount of admitted change in the model, and was set to 2 percents. Because a unique temporal constraint in the inversion is not sufficient and does not generate to vertically-smooth models, a vertical constraint was added in the cost function. The difficulty at that point was to tune the two constraints so that one would not weigh much than the other in the minimization scheme. This new time-lapse inversion was used in a loop over 5 iterations, constraining at each new iteration the inversion of the first model with the fourth inverted model at the previous iteration, to improve at maximum the coherency between the 4 inverted models.

Fig. 5.15 shows the results from a temporally constrained inversion. If the results seem coherent with the expected variations for models 1, 2 and 3, model 4 does not explain the high frequency data, because of unbalanced cost function.

$$\Phi = \left\| \frac{d_{calc} - d_{obs}}{2\sigma_d} \right\|_2 + \lambda_T \left\| \frac{\log(m_{T_{i-1}}) - \log(m)}{p \cdot \log(m_{T_{i-1}})} \right\|_2 + \lambda_{vertical} \left\| \frac{\Delta \log(m)}{p \cdot \log(m)} \right\|_2 \quad (5.1)$$

### Evaluating the effects of possible distortions

Synthetic tests were realized to verify that the effect of resistivity variations outside of the studied area would not result in the variations observed in the time-lapse experiment. The following elements were tested:

- Effect of the topography
- Effect of homogeneous changes of resistivity at the transmitter location

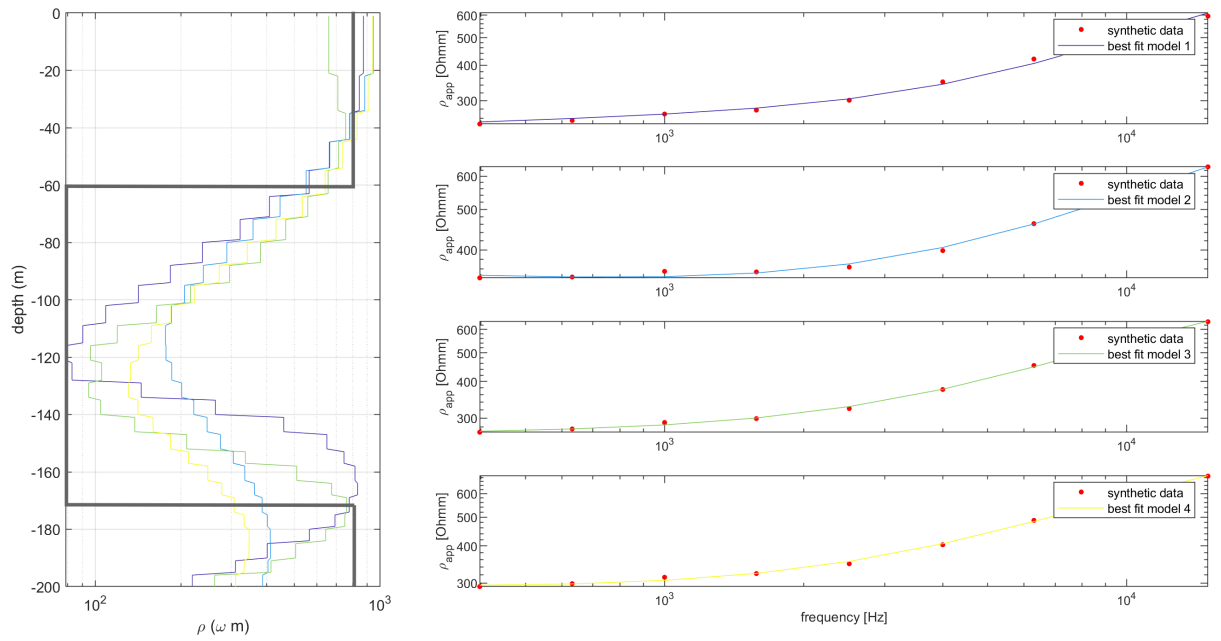


Figure 5.14: Inversion results of the four synthetic data, without "temporal" constraint

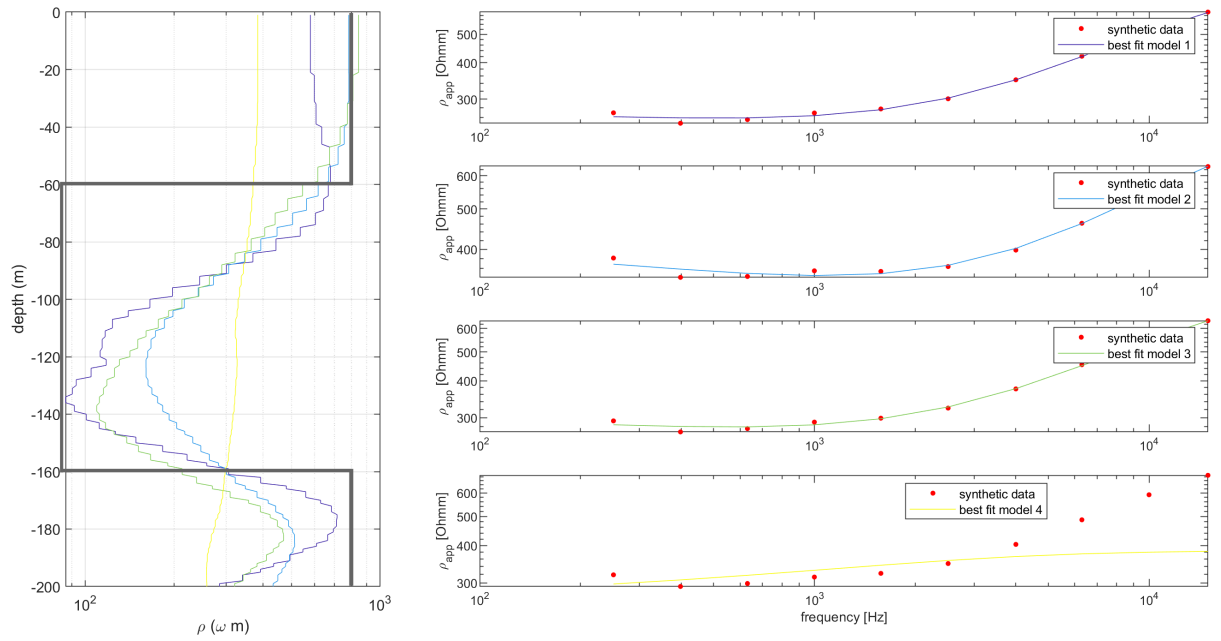


Figure 5.15: Inversion results of the four synthetic data, with both vertical and "temporal" constraints

- Channeling effect at the transmitter location (channeling of the electrical current in the ground)
- Effect of variation of high contact resistance

These effects are described and discussed in the following section.

#### • Topographic effect

In a time-lapse CSAMT campaign, a rough topography is expected to distort the data in a way that highly depends on the resistivity of the first layers. If the ground resistivity changes importantly during the time-lapse experiment, the topographic distortion is expected to change as well. At the Lodève landslide, the site is characterized by a very small and regular slope on the site, but is bordered by a cliff at the West, and an important slope at the South. The data are therefore expected to be distorted by the topography. Because the variations expected during the winter do not exceed a few percents, it is however considered that the variation of the topographic effect in the case of this experiment is negligible.

#### • Effect of homogeneous change of resistivity at the transmitter location

Only far field data are fully decoupled from the resistivity variations at the transmitter (chapter 2, fig. 2.18). Transition field data can be in some way influenced by the resistivity, and thus by the resistivity variations, at the transmitter. For this reason, it is fundamental to limit the interpretations of a time-lapse CSAMT data set to the variations observed in the far field, even if the variations of the apparent resistivity in the transitional field seem coherent with the general context of a time-lapse CSAMT survey. Otherwise, one could interpret variations actually occurring at the transmitter location.

#### • Channeling effects transmitter location

Here, the context is the one of a thin conductive anomaly at the transmitters location, that could channel the current injected by the transmitter, changing the polarization of the fields. If such channeling effects temporarily occur at the transmitter, the question is: how much will it affect the polarization of the fields in the site? If the polarization at the site varies a lot, the sensitivity of the measurements could be changed in case of 2D or 3D structures, given that the partial computation of the impedance tensor depends on the polarization of the magnetic field.

To test this effect, numerical modeling were realized with *custEM*. An homogeneous medium at 500  $\Omega$ .m was modeled, including a thin and elongated vertical anomaly at 50  $\Omega$ .m and 1 km deep below the transmitter. A few tests were realized, changing the orientation of the thin anomaly (North-South and East-West), and its width (fig. 5.16). The produced electric and magnetic fields were compared with the ones produced in the homogeneous case in terms of polarization (fig. 5.17), showing that the width of the anomaly must be really large to produce such effects (anomaly b in fig. 5.16). Such anomaly do not seem realistic, however, if a body of smaller size, but more conductive by orders of magnitudes is present in the subsurface (metallic wire), similar effect could be produced. The stability of the polarization of the fields should anyway be checked as an indicator of the data quality, and the stability of the dimensionality.

#### • Effect of variations of the contact resistance

[Zonge and Hughes \[1985\]](#) presents the effects of high contact resistances on the MT, CSAMT and IP estimation of the resistivity. They present synthetic frequency dependent electrical fields in the context of homogeneous half space, for a wide range of contact resistance. The effect results in a decrease, at high frequency, of the theoretical response, towards a asymptotic response. The greater is the contact resistance, the lower is the frequency above which the effect occurs (fig. 3.26).

At the Lodève landslide, the soil is composed of small calcareous rocks, with various degree of coherence, potentially producing high contact resistance. If the initial contact resistance is high, and decreases in time, the resulting time-lapse observation should be biased by the improvement of the contact. No bentonite was used to ensure a good contact resistance in the time-lapse experiment, but this issue turns out to be potentially very critical, not only in a time-lapse experiment. Hence, the use of bentonite to cement the electrodes and increase the contact with the ground should be systematic in future work.

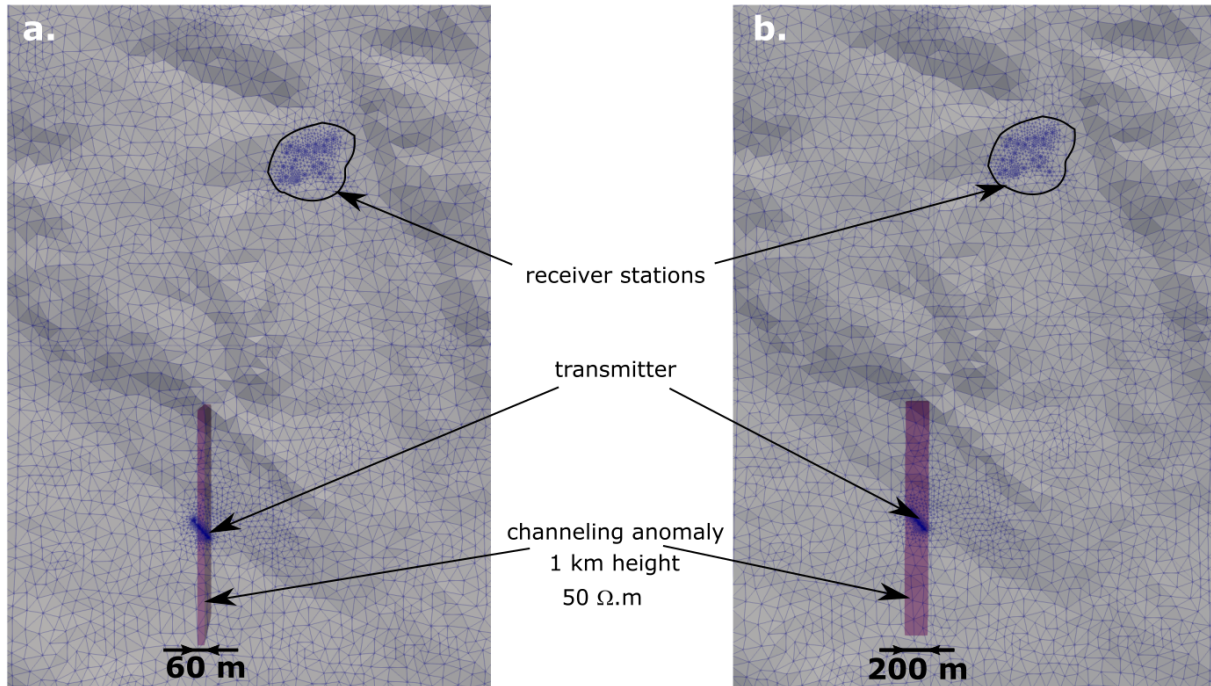


Figure 5.16: Meshes used to evaluate the importance of channeling effects

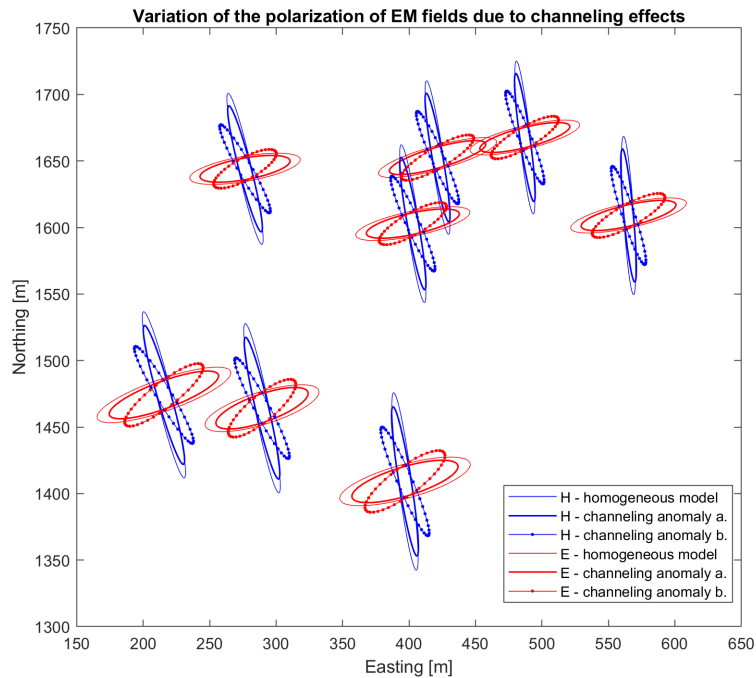


Figure 5.17: Influence of the channeling effect on the polarization of the magnetic field in the context of the two meshes from fig. 5.16: a large elongated anomaly beneath the transmitting dipole can disrupt the polarization of the electric and magnetic field at the site.

### 5.3.3 Data analysis and processing

The data were analyzed following the standard methodology (chapters 2 and 3): the extracted data were converted into raw amplitude and phase spectrum, the static and dynamic calibrations were applied, and the signal was extracted using the signal detection script. The stations where only electrical data were recorded displayed erratic and incoherent transfer functions. For this reason, these data were not analyzed so far, and are not presented in the following.

#### Noise at the measurement site

CSAMT measurements are sensitive to noise. The noise can be of several type. It can be a flaw in the instrumentation, a signal from agro-engines, transient signals due to a car passing. The proximity with the village of Pegairolles de l'Escalette could bring powerline noise (50 Hz and harmonics).

In order to characterize the noise at the survey area, the instrument was left recording for half an hour without producing any controlled signal at the transmitter. The general noise level is quite low, but some signal seem to be systematically recorded, with specific frequencies of [6464, 4032, 4800, 4736, 232] Hz. These signals are strong enough so that the pick detection procedure used to detect the transmitted fundamental and harmonic signals detects it. Note that 9600 Hz, which is the highest frequency permitted by the current transmitter, is an harmonic of 4800 Hz.

#### Polarization of the magnetic field: stability in space and time

The polarization of the recorded magnetic and electric fields are indicators of the quality of the data and of the noise content. It could also allow to detect potential near surface distortion, topographic distortion and channeling effects. For each station, the polarization at the four measurement time-periods was observed for all frequencies.

The fig. 5.18 presents the polarization of the magnetic field at the 4 time-periods at each stations at 5120 Hz. The magnetic field appears to be noisy, presenting for most sites a poor stability of the polarization ellipses, particularly in November and January. In addition to that, stations 5 and 6 (in grey in fig. 5.18) present discordant polarization compared to the neighbouring stations, all along the time-lapse experiment. This could be due to the presence of metallic structures in the vicinity of the stations. In particular, these two stations are known to be close to a grounded wire located at 1 or 2 m depth and oriented in the East-West direction over 400 m. They are also located in the vicinity of a private property, where possible engines could produce noise. Such stations cannot be included in the data interpretation, as the measurements are most likely distorted.

The noise observed in the magnetic field is also present in the electrical recordings.

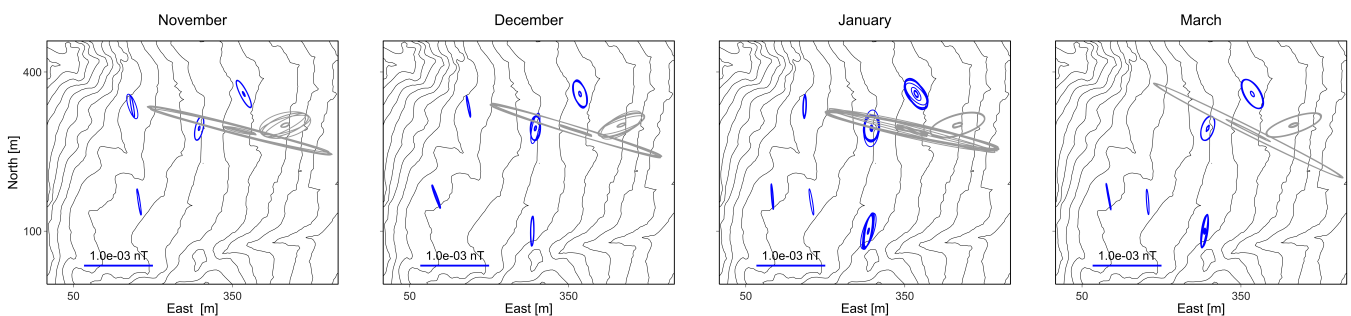


Figure 5.18: Polarization of the magnetic field at all repeated stations over the five months of the experiment at 5120 Hz. Two stations, which related signals are represented in grey, present very erratic polarizations.

Note that such instability in the recorded magnetic fields does not permit to apply the methodology initially planned, consisting in recording both full EM stations and electrical station at neighbouring locations at the same time, using the magnetic field recorded at the first station to interpret the data from the second one.

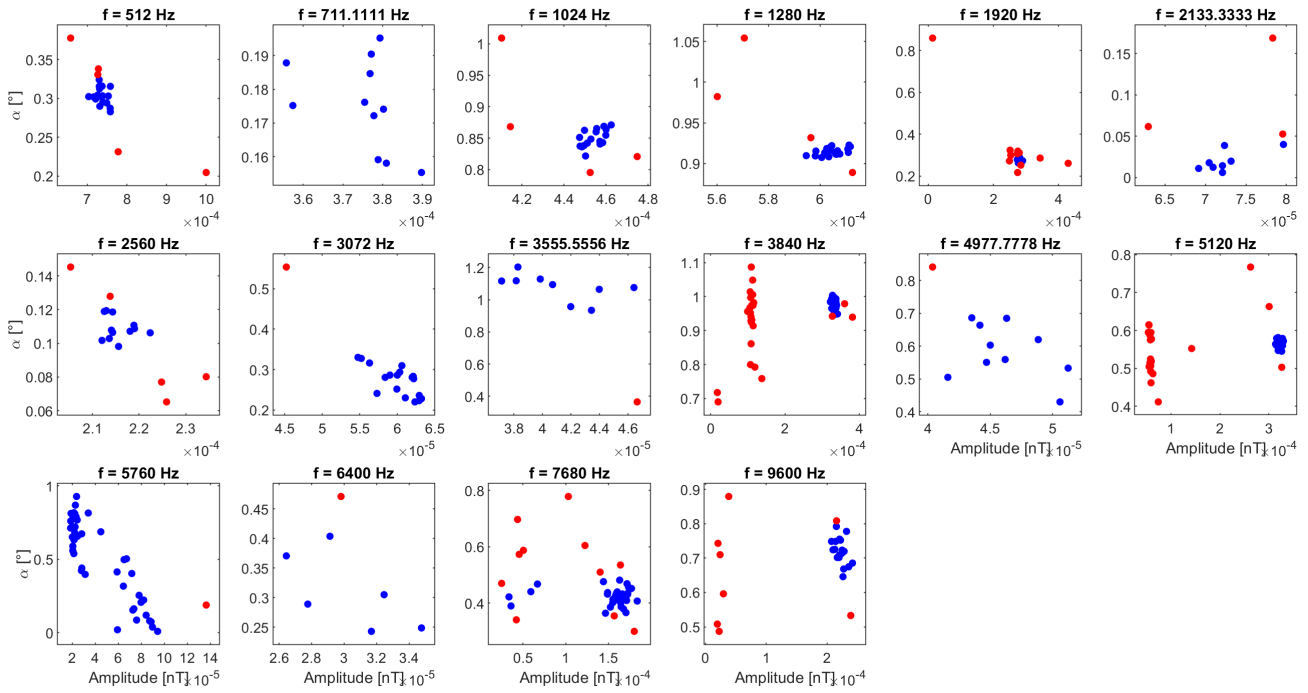


Figure 5.19: Scatter plot showing the distribution of the polarization angle against the amplitude for each detected frequency at a specific station and at a specific time-period. Red dots are the data point removed by the filtering procedure.

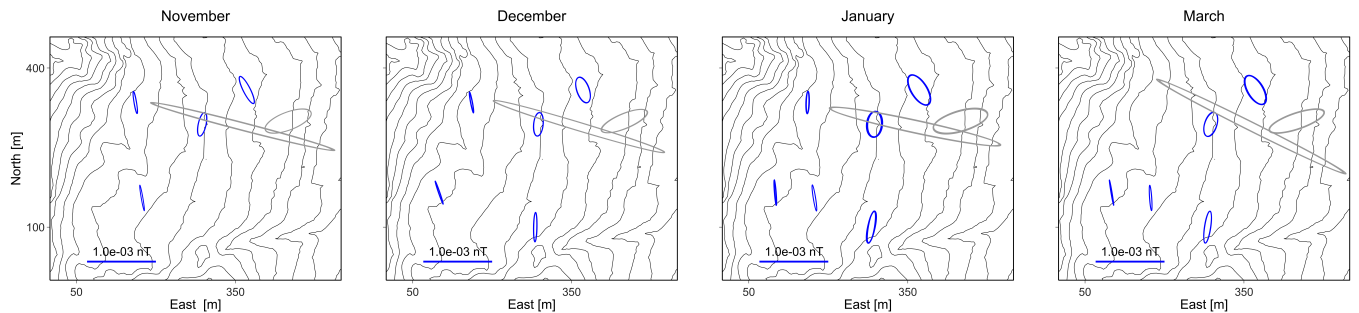


Figure 5.20: Polarization of the magnetic field at all repeated stations over the five months of the experiment at 5120 Hz after applying the filtering procedure

### Filtering procedure

The high noise content resulted in a high variability in the amplitude and phase of measured signals (fig. 5.18). The distribution of the measured signals in terms of polarization angle ( $\alpha$ ) and horizontal amplitude was analyzed, independently for each station and at each frequency (fig. 5.19), in order to evaluate the extent of the noise affecting the data. The scatter plot of the polarization angle against the maximum amplitude revealed that the variability is produced mainly by a few outliers.

When both fundamental and harmonic signals are recorded for a same frequency, the amplitude of data-points related to the fundamental frequency are much higher than the ones related to harmonic data-points. For this reason, certain frequencies display clusters of data-points in fig. 5.19, regrouped at several amplitudes (for example: 3840 Hz, 9600 Hz). When this is the case, it is observed that the clusters related to the harmonic signals, of lower amplitude, are more dispersed. In such case, only fundamental signals are selected.

Several methods were considered in order to filter the data and remove the outliers. The methodology selected is based on the computation of quartiles of the series of polarization angle and of amplitudes inde-

pendently. The procedure chosen to remove the outliers was applied independently for each time-period, each station and each detected frequency. The distribution of polarization angle and amplitude was partitioned into quartiles, defining  $Q_{1/4}$ ,  $Q_{2/4}$  the median and  $Q_{3/4}$  both for the distribution of polarization angle and amplitude. The validity of the data was evaluated as the distance of the data point to the median value, in relation to the distance between the first and third quartile, following eq. 5.2. This procedure was applied first regarding the distribution of the amplitude, for which  $x = 2$  and then regarding the distribution of the polarization angle for which  $x = 1.2$ . These specific values were selected after testing several thresholds and visually evaluating their ability to remove the observed outliers (fig. 5.19). Both values were selected based on manual tests and visual considerations. Because the amplitude is expected to vary in time if the source is slightly unstable, the admitted variations of amplitude was chosen very large. On the contrary, the polarization angle is expected to be very stable.

$$L_{inf} = Q_{2/4} - x|Q_{3/4} - Q_{1/4}| \quad (5.2)$$

$$L_{sup} = Q_{2/4} + x|Q_{3/4} - Q_{1/4}|$$

$$L_{inf} < d < L_{sup} \quad (5.3)$$

This filtering procedure reduced importantly the noise content in the data, and the effect applied, naturally, to the polarization maps (fig. 5.20), but also in the computed apparent resistivity curves (fig. 5.21).

### 5.3.4 Analysis of the apparent resistivity curves

Apparent resistivity and phase curves were computed from the filtered data for all stations (fig. 5.21 and fig. 5.22). From the final filtered data, 4 of the 8 CSAMT stations present reasonable apparent resistivity curves: for each frequency, the dispersion of the apparent resistivity is low, and the general shape of the curves is smooth. The remaining stations presented important noise levels at high frequency, suggesting the pollution of the signals by high frequency perturbation. From fig. 5.21, only the top four stations are analyzed in the following. It is noticeable that all rejected stations are located in the North-East part of the site, where there is private property (camping car and a cabin). The stations presenting the best quality are on the contrary located in the South and West of the site.

Most stations present a transition towards near field at high frequency: the far field limit is observed between 1000 and 2000 Hz, which is incoherent with the expected limit of  $d = 4\delta$ . Indeed, if we consider a subsurface of  $200 \Omega.m$ , knowing that the transmitted dipole is located more than 3 km away from the site, the expected frequency of transition would be:  $f = \rho \left(\frac{503}{4d}\right)^2 = 90 \text{ Hz}$ . This effect remains unexplained. In particular, the numerical modeling tests which reproduce the receiver and transmitter geometry, do display a far field limit at much lower frequency (400 Hz) for a higher resistivity than observed in the true apparent data, suggesting that the survey layout cannot be held responsible for this high frequency far field limit. Because of the high far field frequency limit (2000 Hz), less than one decade is interpretable, providing 7 sampled frequencies. The apparent resistivity values varying from 20 to  $200 \Omega.m$ . The general trend is an increase of the resistivity when decreasing the frequency.

#### Variations of apparent resistivity

The temporal variations seem to be mainly focused on the high frequencies (above 5000 Hz). Below 5000 Hz, the temporal variations are a shift of the curve, of limited amplitude, suggesting that most variations occur in the first 50 to 70 m. Above 5000 Hz, the temporal variations are coherent from one station to the other. These variations are a decrease of the resistivity with time until January. After January, the station 1 shows a decrease of the apparent resistivity in time, whereas the 3 next stations show an increase of the apparent resistivity. These variations are in relatively good accordance with the variations of the water pressure, which increase from 0.8 bar to 1.5 bar from November to January, and decrease down to 0.9 bar around February / March (fig. 5.11) Because temporal variations occur in the first 50 to 70 meters of the subsurface (corresponding to the highest frequencies), temporal variations of the apparent curves are expected to be observed at lower frequencies (by

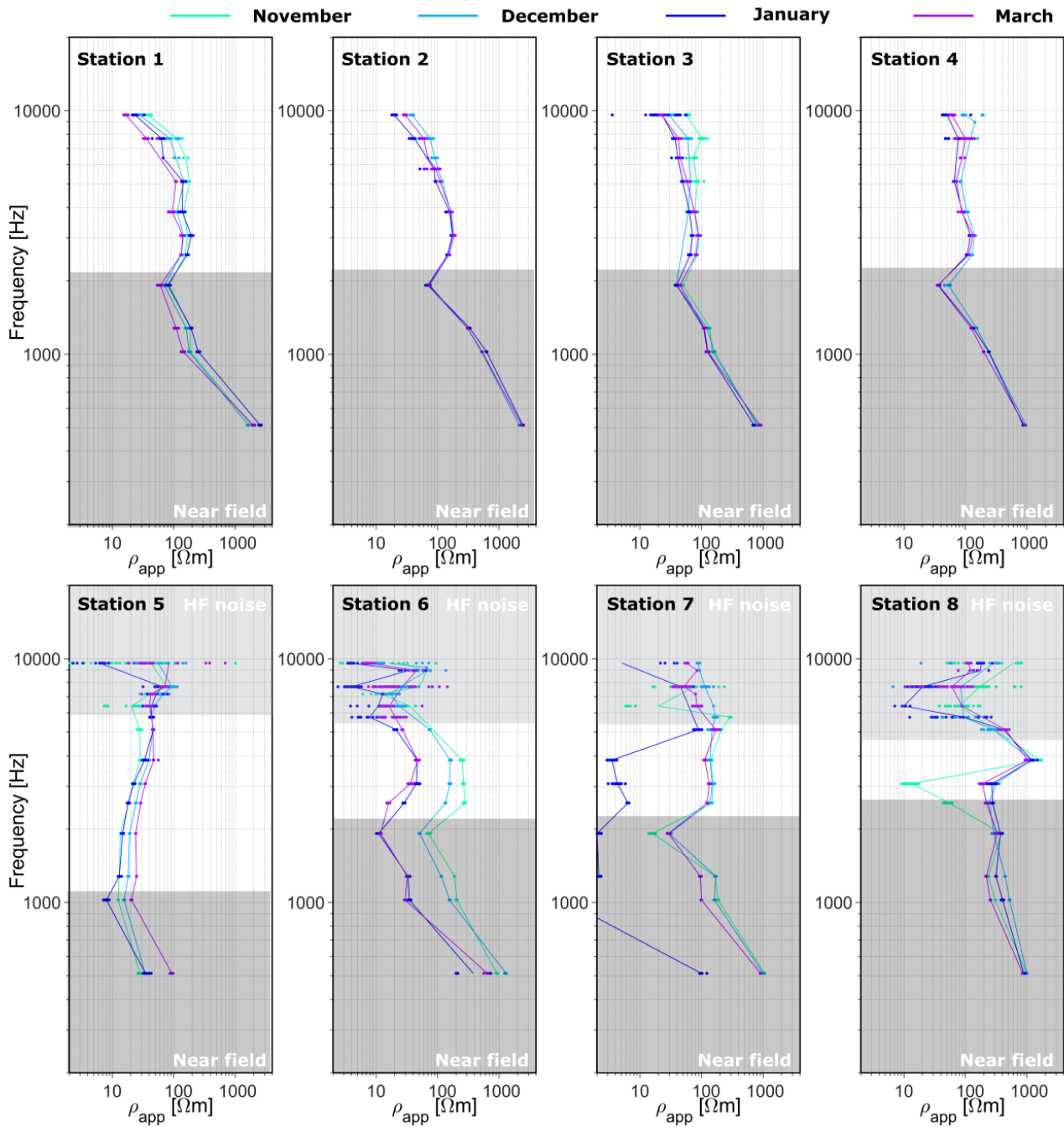


Figure 5.21: Filtered apparent resistivity curves measured in November (light green), December (light blue), January (dark blue) and March (purple) at the 8 full stations. The figures on the bottom line present an import noise content at high frequencies. Only the figures of the top line are selected for the interpretation.

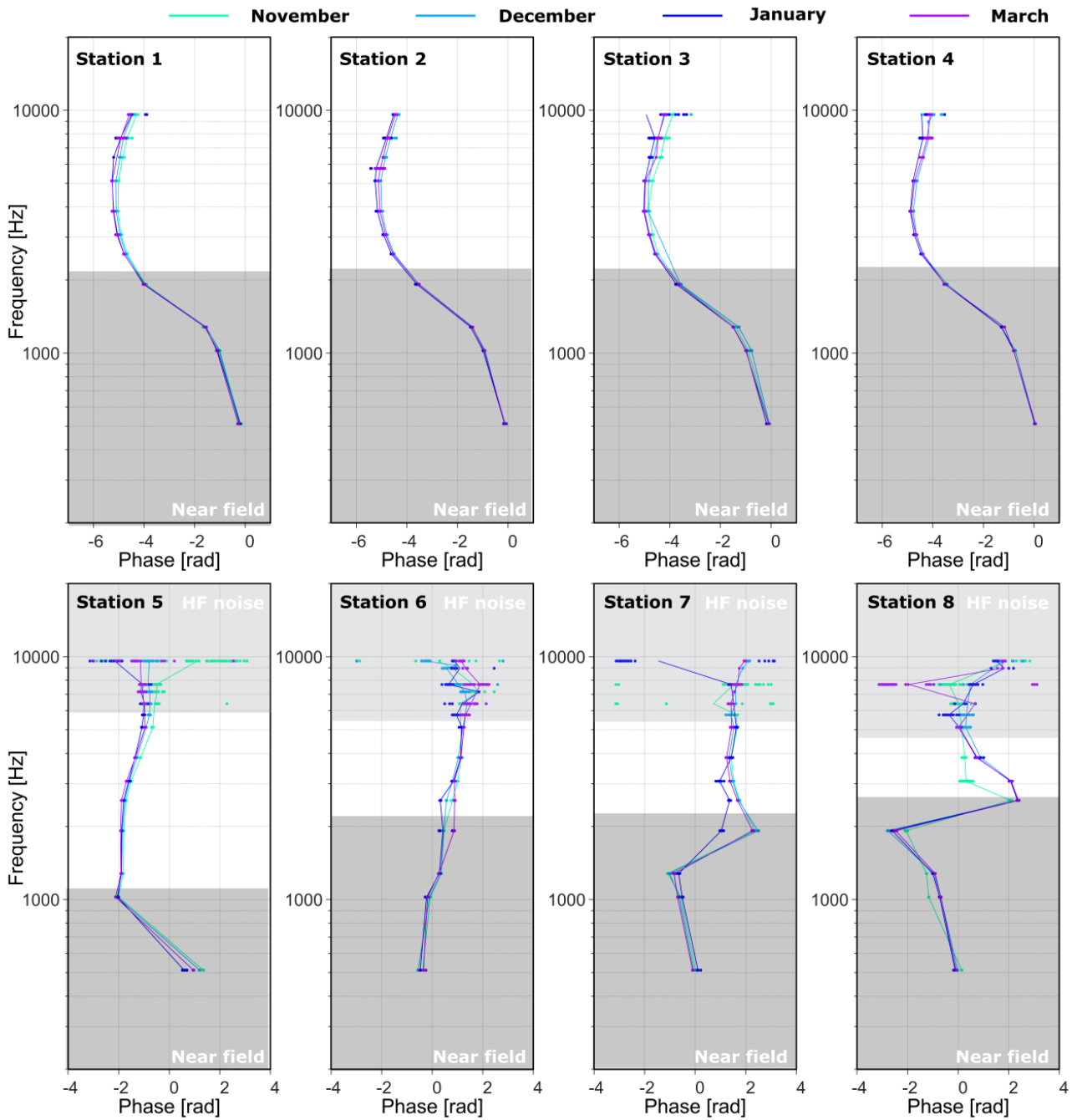


Figure 5.22: Filtered phase curves measured in November (light green), December (light blue), January (dark blue) and March (purple) at the 8 full stations. The stations order is the same as in fig. 5.21. Only the phase from the four interpreted station are unfolded.

definition and construction of the apparent parameters). Below 5000 Hz, the soundings present similar shapes at all 4 times, and a temporal shift of the curves is more or less pronounced depending on the station. These observed features are clear, yet are not possible to interpret without a proper inversion.

### **Variations of the phase**

The phase curves have very smooth shapes. The far field limit is very well marked, as an important increase of the phase around 2000 Hz.

The temporal variations of the phase are very limited, yet seem coherent from one station to the next, and consist in a decrease of the phase between November and December, between December and January, and an increase of the phase between January and March. No interpretation of the variations of the phase is proposed.

### **Discussion on the possibility to invert the data**

Despite the apparent smoothness of the apparent resistivity and phase curves obtained at the four interpreted stations, no 1D inversion could satisfactorily explain the data. Several inversion tests were made, changing the vertical discretization of the model, and adapting the regularization, inverting only the phase, or both the phase and the apparent resistivity. However, no model could explain the data. A few reasons for that are proposed:

- presence of 2D and 3D anomalies in the subsurface
- distortion of the data by external elements (metal stakes holding the vine, buried objects, fences, cables)
- distortion of the data by induced polarization effect
- an insufficient frequency sampling and a wrong balance in the data inversion

## **5.3.5 Discussion**

### **Field methodology: how to optimize the data quality?**

In this study, the analysis of the data was difficult because of an important noise contaminating four of the eight stations. This noise was quite stable in time: the affected stations presented bad data at all four sampled time-periods. The remaining data was of much better quality, and temporal variations could be observed in the apparent resistivity curves, in good agreement with the temporal evolution of the hydrogeology. A few tracks are proposed in order to improve the data quality, as a guidance for future work. This noise arises both from the magnetic and the electrical field as attested by fig. 5.23. In an environment affected by such noise levels, it might be interesting, in future work, to increase the transmission and measurement time, thus increasing the sensitivity to low amplitude signals (stacking procedure), providing a better estimation of the data uncertainty, and better filtering possibilities. In order to ensure the quality of electrical recordings, bentonite could be considered to increase the contact between the electrodes and the subsurface, limiting the polarization effects at the electrodes.

Questions remain regarding the very high frequency at which the far field limits were observed for all data, but unexplained through modeling tests.

### **Resolution, sensitivity and data inversion in CSAMT**

Difficulties were encountered in the inversion of the data as no inversion could explain correctly the data. Three possible effects are proposed: 1/ distorting effects (polarization from metal stakes and other metal elements), 2/ a bad parametrization and regularization of the inversion and 3/ 2D or 3D effects.

The second track is the question of the frequency sampling. Indeed, very thin and high vertical variations of the resistivity should be difficult to fit if too poorly sampled. This could be tested by simple 1D modeling. In the inversion, the habit is to regularize the models in order to compensate the lack of information in the data. In

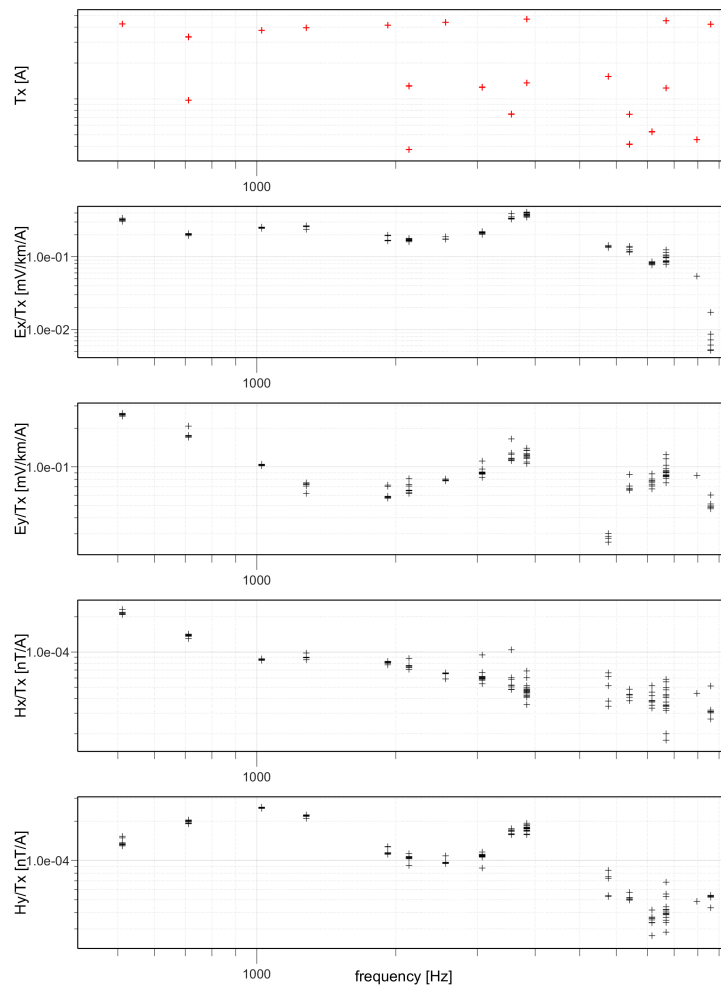


Figure 5.23: Electric and magnetic transfer functions at one of the noisy stations

CSAMT, this lack of information could simply originate from an inadequate vertical discretization of the model. In such context, having the finest frequency sampling possible is really important.

The last track is the most probable, and would result in a distortion of the apparent resistivity, leading to difficulties in the fit of the data to a 1D model.

Both effects probably occur: data 2D or 3D distortion and insufficient sampling together with inappropriate regularization.

## 5.4 Analysis and observations with TDIP time-lapse data

Measurements were realized at a seasonal scale, starting in March 2019 and targeting the alternating clay and evaporitic units identified in the borehole core samples below 30 m depth, down to more than 60 m depth. The measurements were repeated twice, in July 2019 and October 2019. The most important effect on seasonal variations at the Lodève landslide are variations in water pressure (Denchik et al. [2019]), which are in the case of unconfined aquifers is proxies of the hydraulic head. No variations are expected in the fluid conductivity nor in the fluid temperature (fig. 5.24). Hence, this time-lapse experiment explores the question of the sensitivity of TDIP measurements to variations of water-levels.

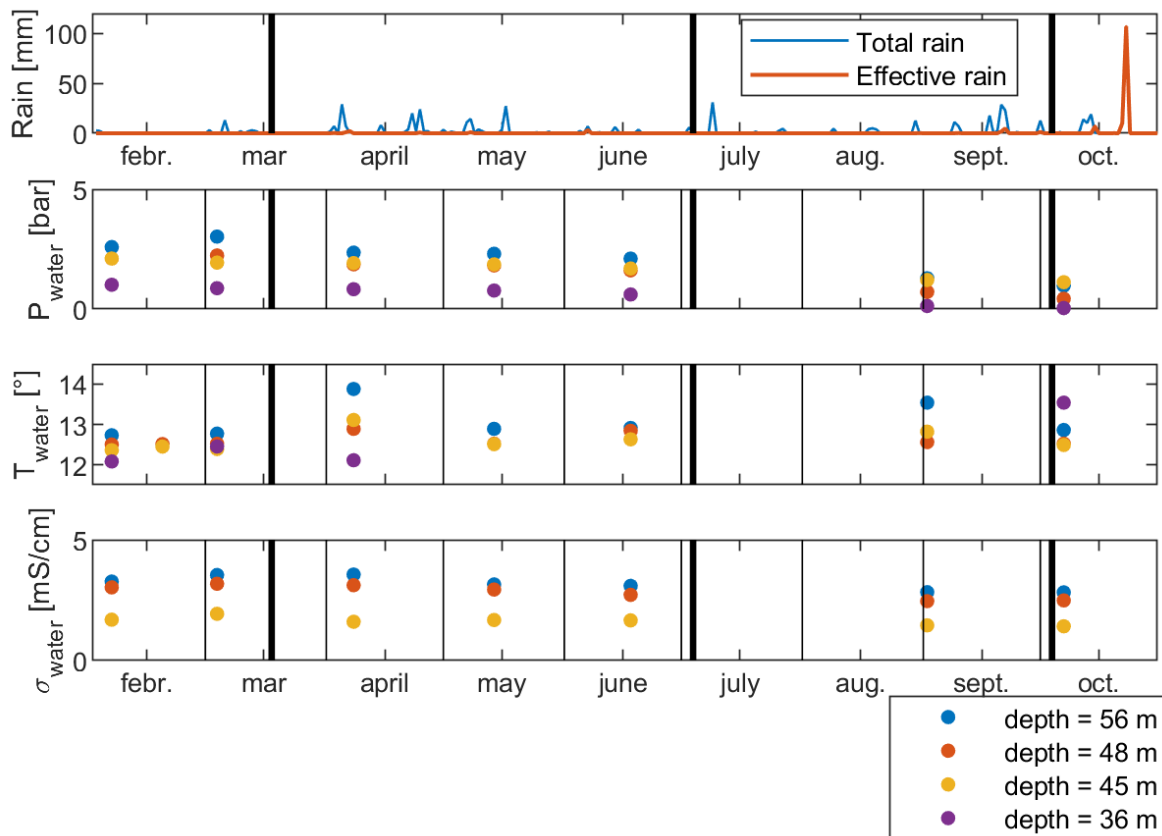


Figure 5.24: Variations of the rainfall at Pégairolles-de-l'Escalette, water pressure and water electrical conductivity during the TDIP time-lapse experiment. The total rain and effective rain computed following [Oudin et al. \[2005\]](#) are presented.

### 5.4.1 TDIP measurements at Lodève landslide

In Mars 2019, two TDIP profiles were installed on the vineyard area forming the lower part of the slide, where the boreholes are located (fig. 5.25). The first profile was installed perpendicular to the slope, in the North/South direction, along a car track that allowed 1/ to keep a good distance (at least 2 m) with the metal stakes holding the vines, and thus limit their impact on the measurement, and 2/ the setting of a long profile (500 m), with a limited tortuosity.

A second profile was installed in the direction of the slope (East/West direction). In this direction, the important topography westward and the road impacted by an important traffic eastward were limiting the spatial extent of the profile. In an attempt at reaching the deep clay and evaporites layers (approximately 60 m depth), the profile was installed along a tortuous path (fig. 5.25), implying the need for a 3D analysis of the profile. Measured only once in March 2019, this profile of 475 m long is expected to be sensitive to 3D variations mainly in the southern part. For this second profile, because of logistic limitations, only 72 electrodes were used, with an electrodes spacing of 5 m in the central part of the profile (electrodes 13 to 59) and of 10 m at both extremities of the profile (electrodes 1 to 13 and 59 to 72) (figure 5.25). Both normal and reciprocal measurements were realized, allowing to evaluate the data error ([Flores Orozco et al. \[2012\]](#)). The complete analysis of this second profile is not presented in this thesis as it could not be completed in time. The main processing steps were however realized, accounting for the local 3D sensitivity of the profile, and the processing and data quality are presented in Appendix A.3.

The position of the electrodes was measured with a differential GPS, to ensure a good accuracy in the geometry of the array.

A Syscal pro was used, without possibility of measuring full decay curves. Instead, only integral chargeabil-

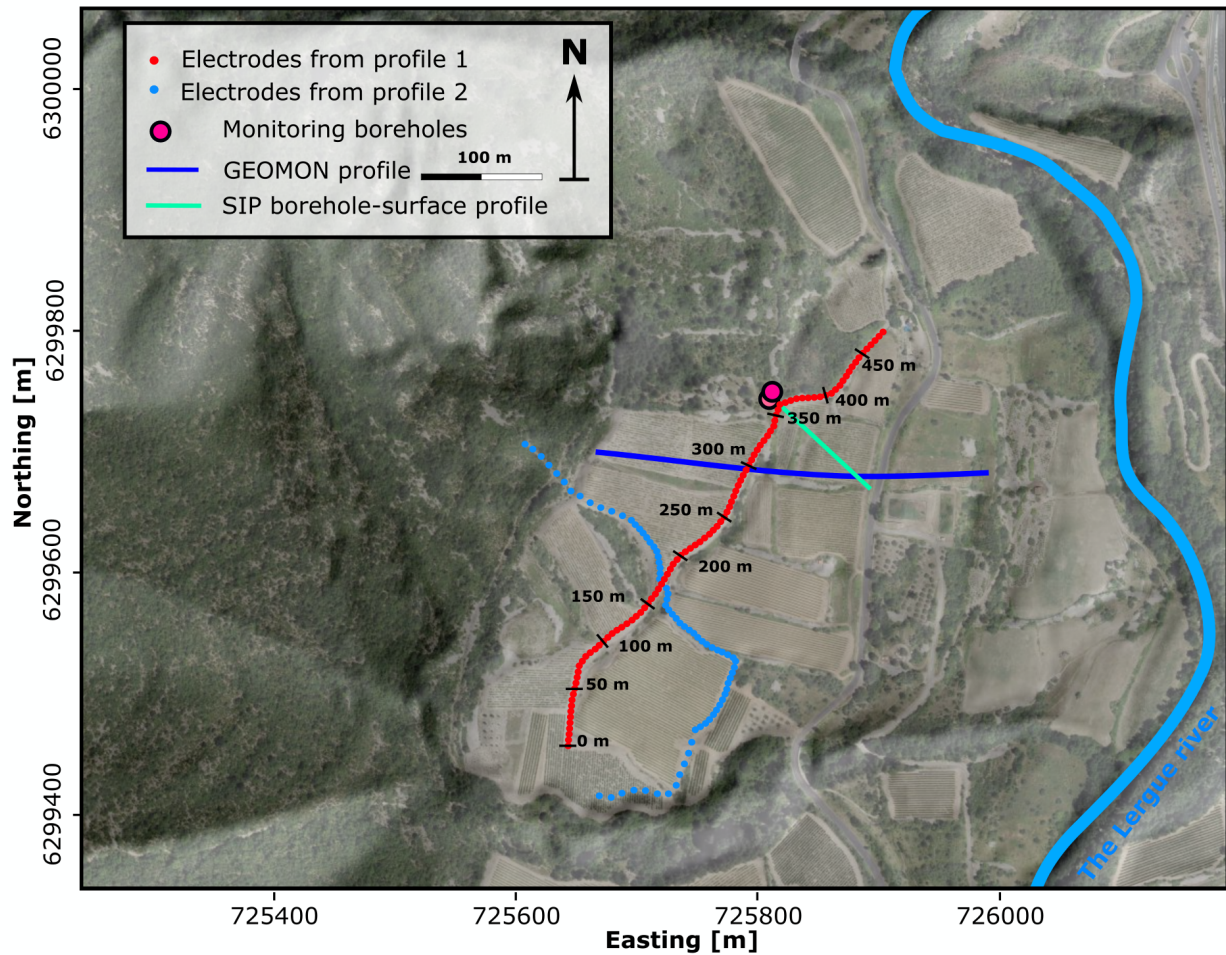


Figure 5.25: Map of the TDIP profiles measured in 2019

ity was measured over a pulse length of 4 s, from which a phase was later computed, following [Kemna et al. \[1997\]](#).

**Repeated measurements:** Profile 1, easy to install and to process, was measured at 3 different time-periods: March 2019, July 2019 and October 2019. During the first period, several experimental settings (spreading sequence and pulse length) were tested:

- Dipole-dipole (DD) array with pulse-length = 500 ms, 1 s, 4 s
- Multiple-gradient (MG) array with pulse length = 4 s

The repetition measurements were both realized with DD and MG arrays and with a pulse length of 4 s.

### 5.4.2 Data quality

The northern part of profile 1 defines two edges (at 360 and 405 m). The apparent resistivity values computed with assumption of an aligned profile are therefore distorted, particularly for the data points near the surface, inducing artifacts in the 2D inversion. If the 3D inversion has the possibility of correcting this artifact, the time-lapse data, interpreted only in 2D, are affected by this flaw. For this reason, the northern part of the profile is ignored in the interpretation.

The data quality, generally satisfying (most electrodes presented low contact resistances), is slightly decreased in the summer period, when the contact resistances were increased by the dry conditions. Electrodes with high contact resistances were salt-watered.

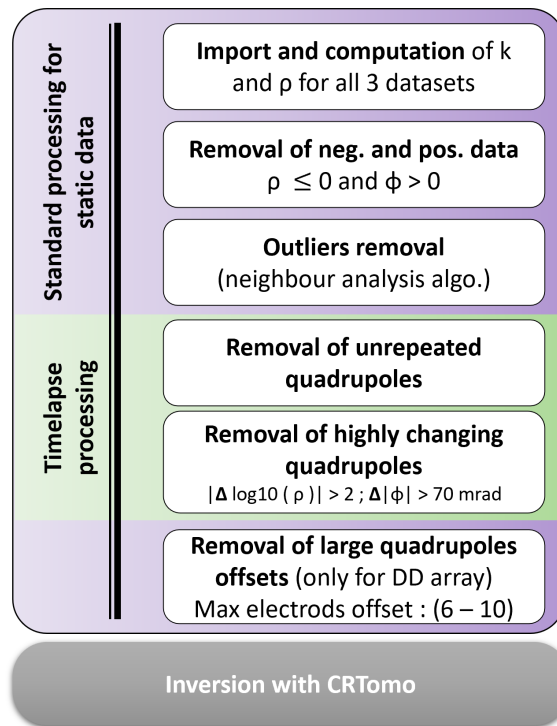


Figure 5.26: Workflow of the TDIP time-lapse processing

### 5.4.3 Data processing

The TDIP processing consists standardly in filtering incoherent data and outliers. Extreme apparent resistivity values are unlikely, and are therefore attributed to erroneous measurements. Additionally, negative resistivities and positive phases are not expected, given the expected dimensionality of the structures. The processing of the time-lapse data includes additional processing steps aiming at removing temporal 'outliers': quadrupoles presenting high temporal variations that are difficult to explain with temporally constrained inversions (fig. 5.26, Flores Orozco et al. [2019]). The data were processed using matlab routines and inverted with CRTomo.

The raw data were extracted and the integral chargeability was converted to a phase value, assuming a constant phase angle model and following Kemna et al. [1997]. The recordings provided a basis of minimum 4703 data for the DD array, and 3923 data for the MG array (Tbl. 5.2). The processing steps for the DCIP data are presented in fig. 5.26.

Because the IP signal was much noisier than the DC signal, the data were first filtered and inverted accounting only for the DC part. A new filtering, much more selective, was realized, including the analysis of the phase shift.

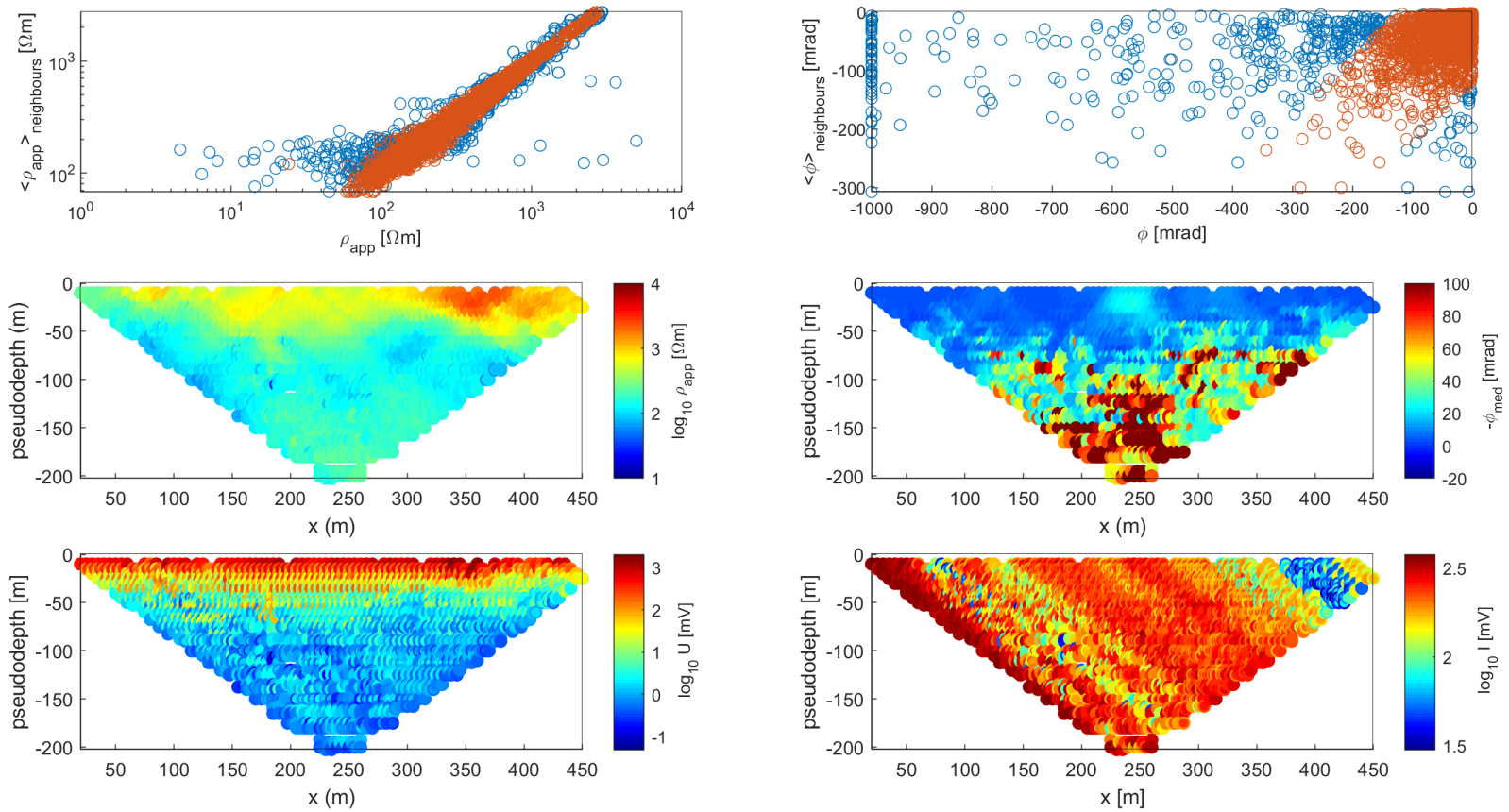


Figure 5.27: Principle of the neighbour analysis algorithm to filter the pseudosections from outliers; scatter plots of the mean resistivity (a.) and phase (b.) values of the nearest 10 neighbours of each data points versus the resistivity and phases values of the data point itself, for all data points in blue, and for the kept data points in orange). Logarithmic apparent resistivity (c.) apparent phase (d.), logarithmic electrical potential (e.) and current intensity (f.) pseudosections.

	Time 1				Time 2				Time 3			
	DD	%	MG	%	DD	%	MG	%	DD	%	MG	%
raw data	9403	100	3923	100	4719	100	3923	100	4703	100	3923	100
removal of $\rho < 0$	8771	93.3	3923	100	3321	70.4	3354	85.5	4570	97.2	3922	99.9
removal of $\phi > 0$	5960	63.4	3427	87.4	1714	36.3	2170	55.3	2955	62.8	3173	80.9
outliers removal	5313	56.5	2778	70.8	1435	30.4	1918	48.9	2561	54.5	2527	64.4
highly changing data removal	793	8.4	1271	32.4	793	16.8	1271	32.4	793	16.9	1271	32.4
removal of large dipoles (8)	711	7.6			711	15.1			711	15.1		
removal of large dipoles (5)	571	6.1			571	12.1			571	12.1		

Table 5.2: Evolution of the number of data (and percentage of remaining data at each step) throughout the processing for the different datasets

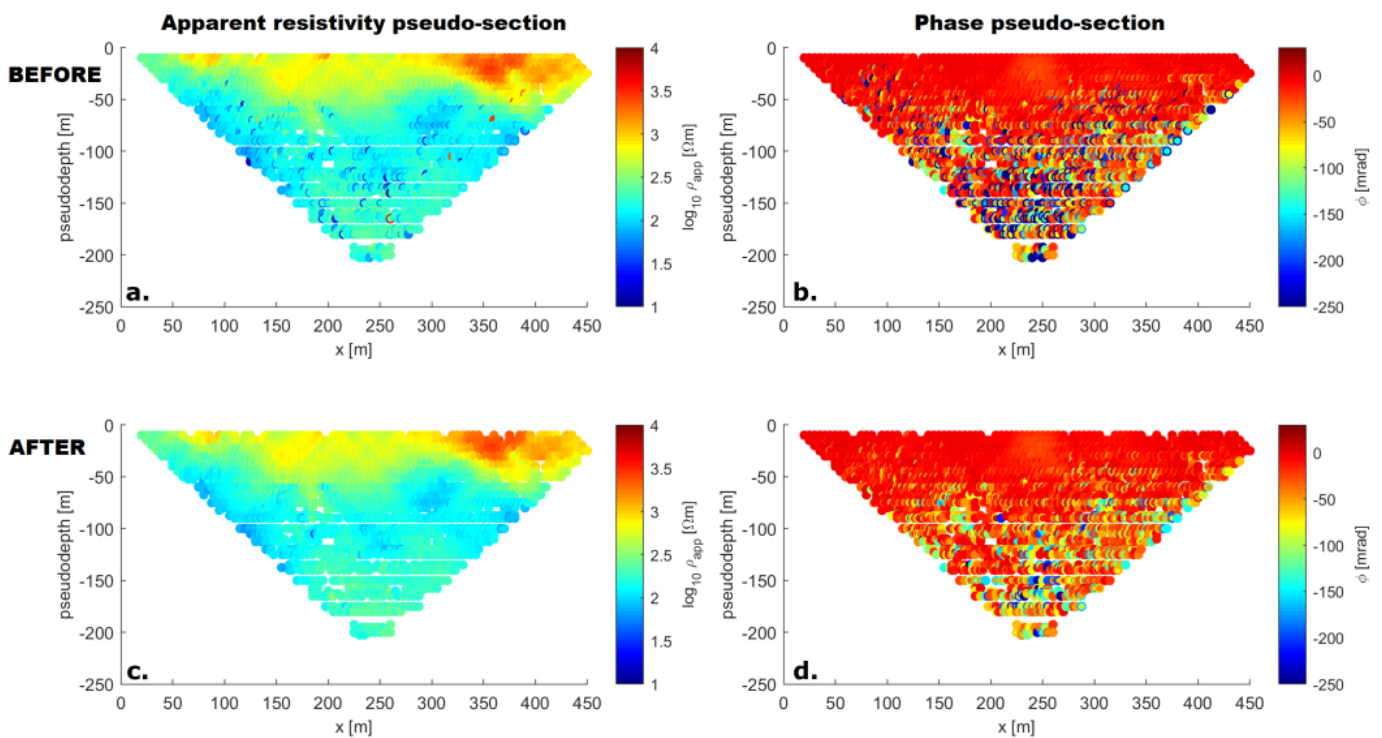


Figure 5.28: Results of the outliers filtering procedure by neighbour analysis of the pseudo-sections: pseudosections previous to outliers filtering (a. and b.) and after outliers filtering (c. and d.)

By definition, the pseudo-section representing any apparent value should be smooth and local variations of an apparent parameter should be limited. Outliers were detected and removed applying a neighbouring analysis scheme to the pseudo-sections of the apparent resistivity and phase. For each data-point, the mean value over the 10 nearest neighbours is computed, and the data-point is kept in the dataset only if its apparent value is close enough to the mean of the 10 neighbouring value such that  $|d - \langle d_{10N} \rangle| < 1.2 \sigma_{10N}(d)$  ( $\sigma$  is the standard deviation).

Fig. 5.27 presents the neighbour filtering procedure, filtered pseudosections of the apparent resistivity and phase and of the logarithmic potential and the current intensity. Fig. 5.28 shows the apparent resistivity and phase before and after outlier filtering.

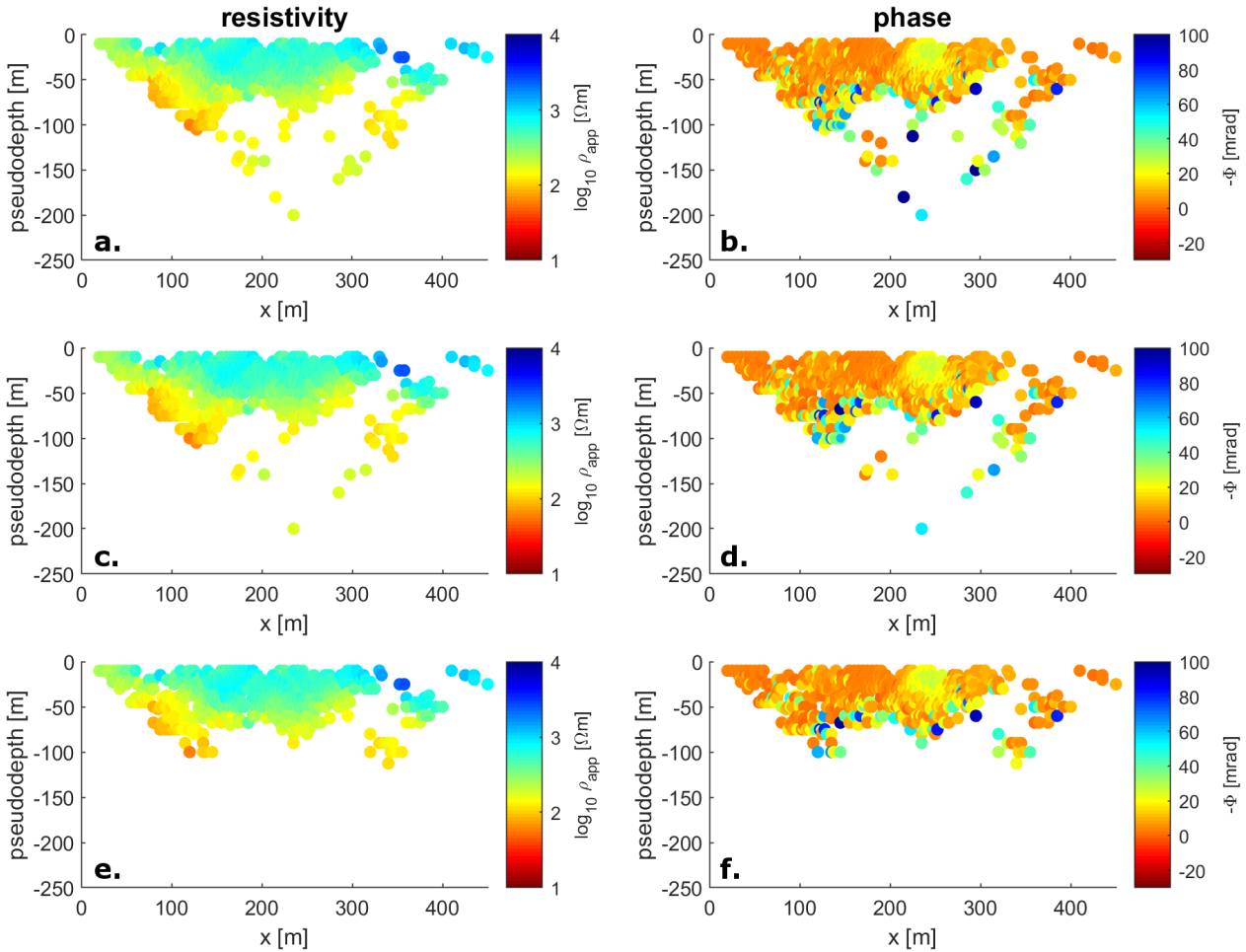


Figure 5.29: Pseudosections of filtered dipole-dipole data with various selectiveness regarding deep apparent data: maximum admitted offsets of 70 m (a. and b.) 40 m (c. and d.) and 25 m (e. and f.)

### Time-lapse processing steps

The application of time-lapse inversion scheme necessitates a few requirements; in particular, certain inversion schemes can only account for repeated quadrupoles. In order to allow the time-lapse inversion to run on the dataset, only the quadrupoles that were repeated and kept in the processing at the three time-periods were selected in the final data. Because a certain stability is expected between the 3 different time-periods, the measurement points that presented very important changes (more than 2 orders of magnitude for the amplitude, and more than 70 mrad for the phase) were removed.

After these processing steps, only few data points remain at depth, providing a very poor sampling and a poor estimation of the error at depth (fig. 5.28). In the dipole-dipole data, the size of the injection and potential dipoles range from 2 to 14 times the electrode-spacing. The largest dipoles provide the deepest data point. For this reason, and to prevent erroneous interpretations of potentially noisy data, the quadrupoles of very large offsets (or high skips) corresponding to the deepest data points, were removed (see fig. 5.29), where different choices of filtering are made for this last step). In the figure 5.29, the apparent resistivity and apparent phase pseudo-sections are compared when keeping all data-points, when removing data-points from dipoles larger than 8 times the electrodes spacing, and when removing data-points from dipoles larger than 5 times the electrodes spacing, showing that the isolated deep data-points are removed by this procedure.

The most decimating steps are the time-lapse processing steps: removal of unrepeated quadrupoles and removal of highly changing quadrupoles.

Figures 5.30 to 5.35 present the filtered data. The histograms of apparent resistivity and phase of both the dipole-dipole (fig. 5.30) and multiple-gradient (fig. 5.33) data reveal a general stability of the distribution of

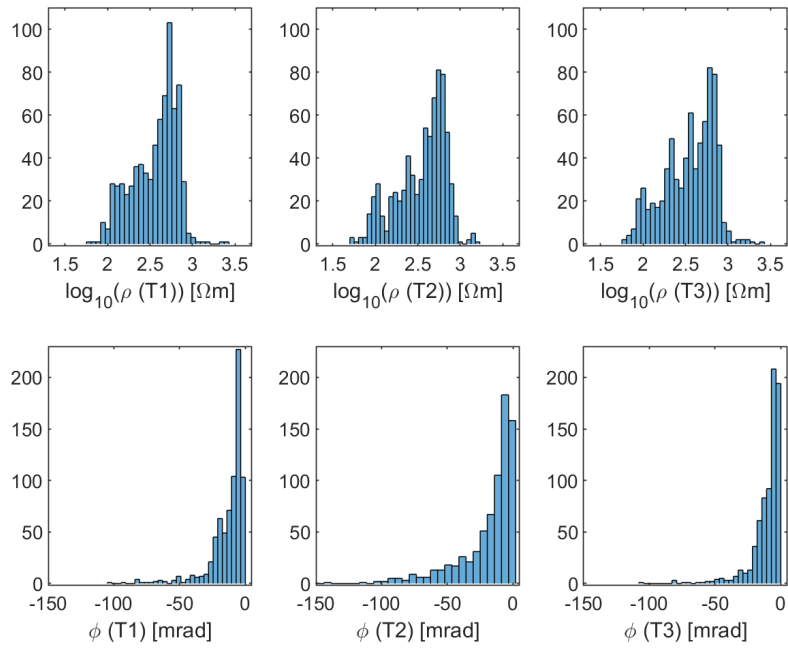


Figure 5.30: Distribution of resistivity values and phases in the 3 dipole-dipole measurements after full data processing (maximum admitted offset in the quadrupoles: 40 m)

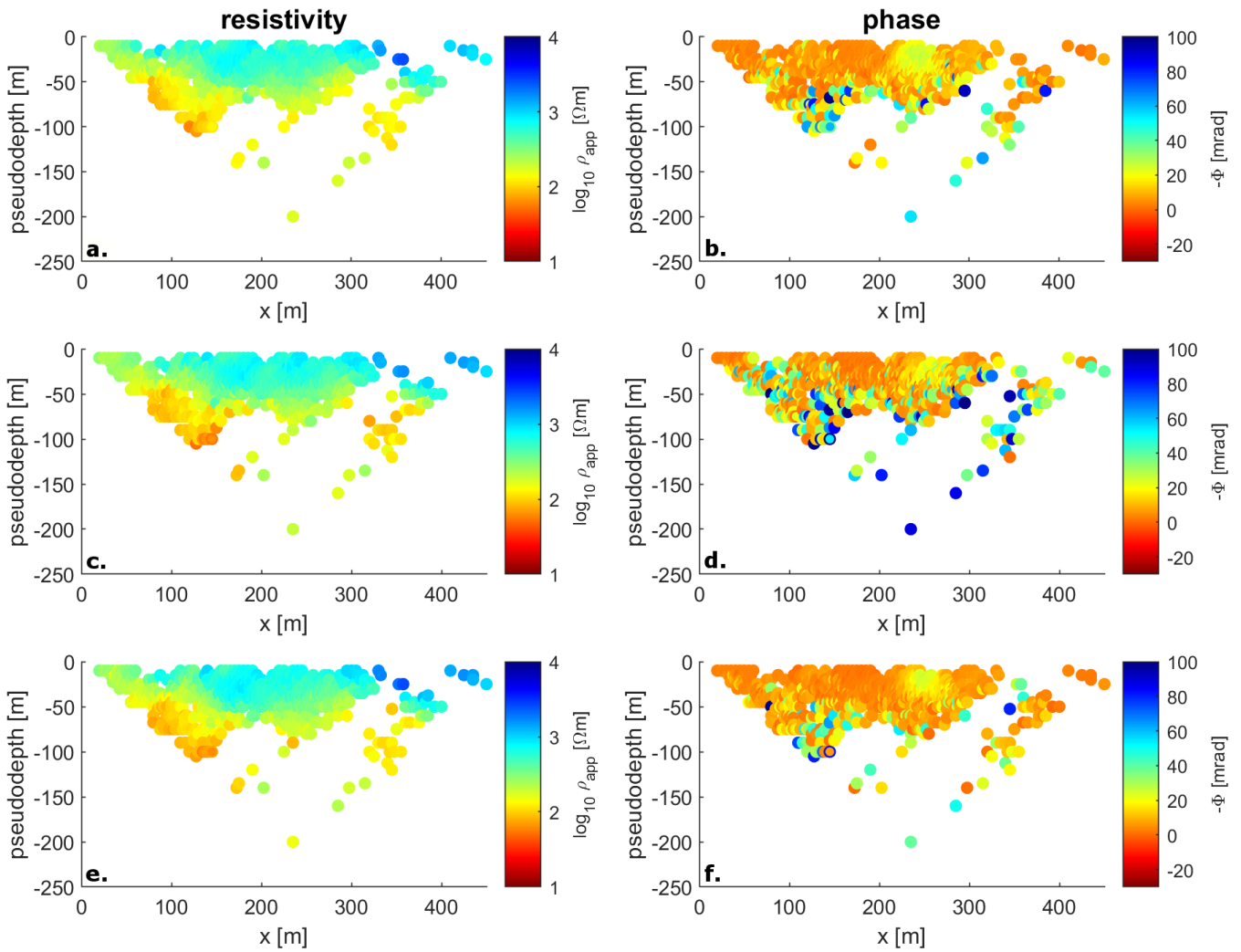


Figure 5.31: Pseudo sections of filtered multiple-gradient data for T1 (a. and b.), T2 (c. and d.) and T3 (e. and f.)

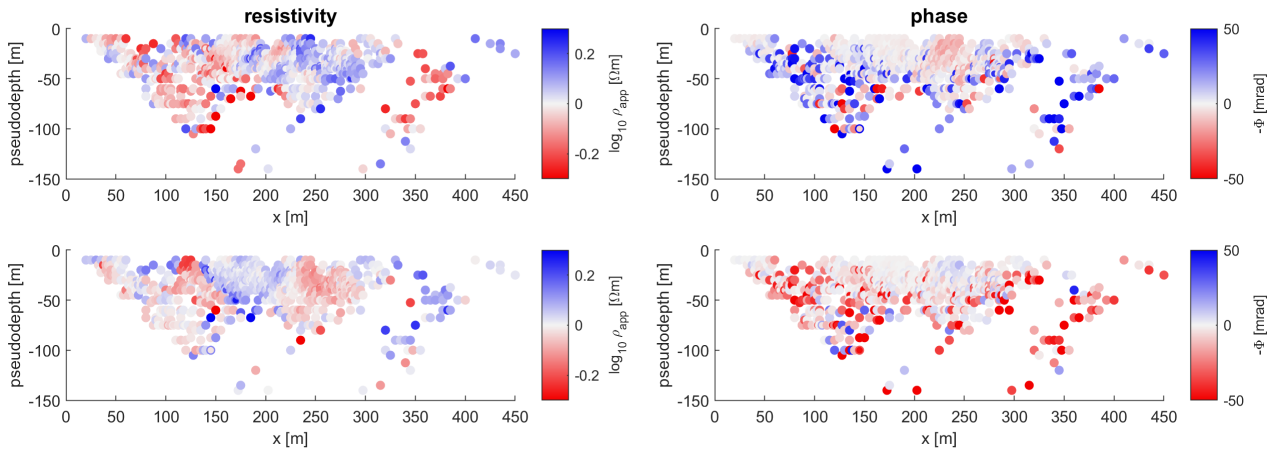


Figure 5.32: Variation of apparent parameters for the dipole-dipole data (maximum admitted offset in the quadrupoles: 40 m) between March (T1), July (T2) and October (T3); ( $\log(\rho(T_{n+1}) - \log(\rho(T_n))$  and  $\phi(T_{n+1}) - \phi(T_n)$ )

apparent resistivity in time. The apparent phase seem to present much important variation of the distribution, including a wider distribution and lower phases in July (T2) than in March (T1) and October (T3). The pseudo-sections of both arrays in fig. 5.31 and 5.34 show that the decrease of phase observed in July mainly concerns the deepest data-point, suggesting variations of the phase at depth. The computed differences in apparent parameters, presented in fig. 5.32 and 5.35, seem to validate that the main variations of the phase are located at depth. The variations of apparent resistivity are of very low amplitude (less than  $0.2 \cdot \Delta \log_{10}(\rho)$ ) and seem laterally discordant.

## 5.4.4 Data inversion

### Inversion scheme

The data were inverted with the software CRTomo (Kemna [2000]). The inversion uses a robust Gauss Newton scheme, with general spatial constraints and in particular strong lateral constraints.

Because no reciprocal data were measured, the error model was simply set by assuming a relative error of 5 % and an absolute error of  $1e^{-3} \Omega.m$  on the resistivity, as well as an absolute error of 10 mrad on the phase. The initial model was set to a resistivity of 500  $\Omega.m$  and a phase of -5 mrad (default values). Several 'static' (i.e. non-time-lapse) inversions were realized with different processings, testing on the restrictiveness of the time-lapse processing steps, and of the removal of large dipole offsets.

**Time-lapse inversion:** An attempt at inverting the data with a time-lapse inversion scheme was made, i.e. with temporal constraints, in order to increase the coherency between the three models, and better isolate the hydrogeological signal. Such inversion scheme is in particular very important to estimate the sensitivity of the methodology (including the measurement array, the chosen processing and the inversion scheme) to variations of the subsurface. This attempt is yet to be improved, as the inversion did not converge properly, probably due to the sparse time-sampling, causing locally important variations which could not be explained by the temporal constraints. For this reason, only independent inversion results are presented and interpreted in this work.

### Inversion results

The many inversions converged with good fit ( $1 > \text{data RMS} > 0.98$ ) within a few (3 to 5) iterations. A logarithmic coverage of -3 was chosen at the limit of interpretability at depth, providing depths on investigation of 80 m at maximum. The inversion results from the dipole-dipole data are presented in the following, however, both array provided very similar observable trends. The features observed and presented in the following are common

to both measurement array and to most inversion tests. Every presented models are cut at depth, where the data sensitivity is estimated to drop (Kemna [2000]).

**Resistivity models:** The resistivity models seem consistent and very stable at the 3 time-periods (fig. 5.36). The variations between the models only appear in figure 5.37, were the difference between each models in presented, and from figure 5.38, were vertical slices of the profiles at  $x = 150$  m,  $x = 200$  m and  $x = 250$  m are compared.

The general features in the resistivity models are: 1/ a top resistive layer at  $1000 \Omega.m$ , 2/ an intermediate transition layer at  $250 \Omega.m$ , 3/ a deep layer at  $100 \Omega.m$ .

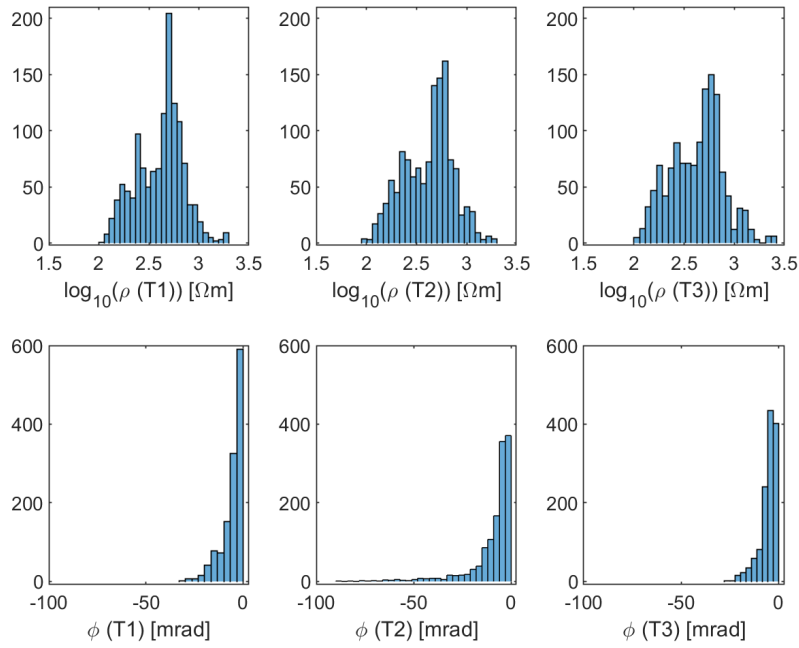


Figure 5.33: Distribution of resistivity values and phases in the 3 multiple-gradient measurements after full data processing.

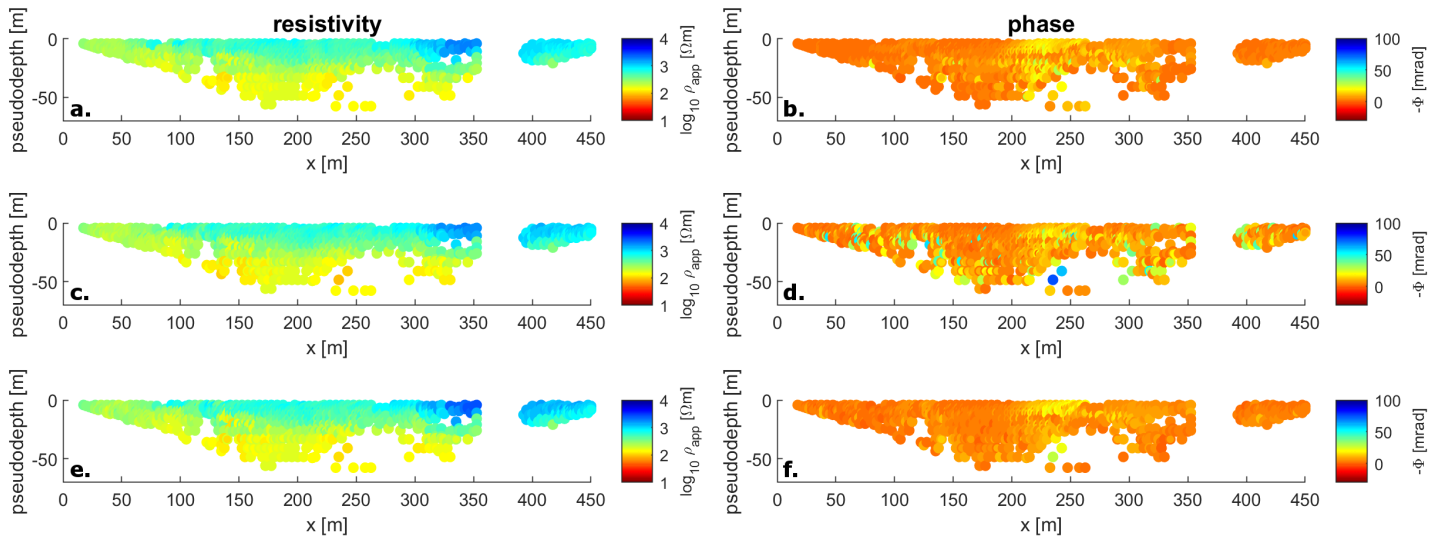


Figure 5.34: Pseudosections of filtered multiple-gradient data for March (a. and b.), July (c. and d.) and October 2019 (e. and f.)

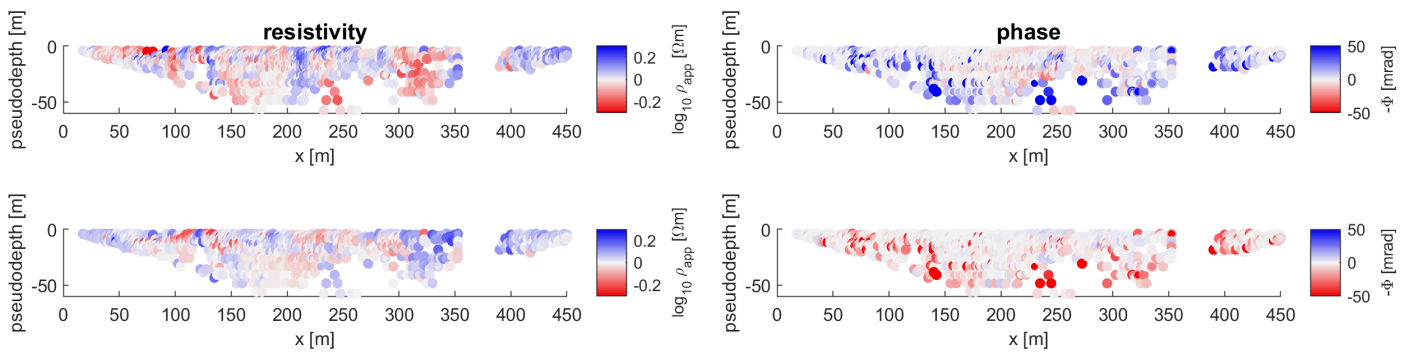


Figure 5.35: Variation of apparent parameters for the multiple-gradient data between March (T1), July (T2) and October (T3); ( $\log(\rho(T_{n+1}) - \log(\rho(T_n)$  and  $\phi(T_{n+1}) - \phi(T_n)$  )

The deep conductive layer correlates well with the expected aquifer, which approximate ( $\pm 5$  m) depth is marked as a black line. The topography of its top interface is not flat, a valley is visible between 160 and 240 m along the profile.

The overall variations in the profiles are below 10 % which very low but still significant (fig.5.37). In the first 30 to 40 m, the time variations of the profiles are mainly vertical trends. At depth, the variations decrease, possibly suggesting that the hydrogeology does not vary at depth during the time experiment. Indeed, no hydrogeological variations are expected at depth below 43 m where the rock is fully saturated: geoelectrical variations could only be produced by a change in the water chemistry.

Extracting vertical logs at specific locations helps understanding the observed variations. Fig. 5.38 shows vertical 'soundings' - or logs - extracted from the 2D profiles located at  $x = 150, 200$  and  $250$  m. The very small variations of resistivity seem very different along the profile. Several discontinuities need to be noted. In fig. 5.38 the discontinuity between the intermediate and the deep layer is very well marked, by a straight discontinuity at  $z = 330$  m for the log at  $x = 150$  m, at  $z = 290$  m for the log at  $x = 200$  m, and at  $z = 310$  m for the log at  $250$  m. Below this depth, that may correspond to a geological discontinuity, the resistivity seem to have increased towards July, and decreased towards October. Above this depth, the variations of resistivity seem very dependant on the location along the profile.

These observations are difficult to correlate with the knowledge from the two boreholes. The lateral variability revealed in the time-lapse profile and the fact that the data are known to be distorted in the vicinity of the boreholes limit the confidence in any comparison. For this reason, the different zones distinguished in the TDIP profiles (fig. 5.36, bottom) cannot be simply attributed to specific units on the basis of the boreholes observations.

**Phase models:** The phase models present values above  $-40$  mrad. The top layers seem generally unpolarizable, with one noticeable small polarizable zone located at  $x = 250$  m.

At T1 and T3, only the deepest part of the profile seems polarizable, below 60 m depth, with phase values of  $-30$  mrad. The rest of the deep conductive layer presents phase values of  $-10$  mrad. At time T2, in July, the polarizable area extends upwards, and occupies the entire deep conductive layer, with values around  $-30$  mrad and the phase in the intermediate layer is decreased to  $-10$  mrad. It can be noted that the increase, at depth, of the phase observed in fig. 5.8, below the polarizable zone, is not observed in these surface measurements.

The temporal variations of the phase seem to occur mainly in the first 40 m of the subsurface. Below this depth, the variations are of very low amplitude, and might be only a consequence of the inversion process. As for the resistivity, variations are mainly expected in the top and unsaturated zone.

The phase soundings in fig. 5.38 show that the main variations are located in the top layers, that are expected to be unsaturated. As for the resistivity soundings, the observed variations are laterally unconsistant. The observed variations are of greater amplitude than thoses observed in the resistivity soudings.

Four zones are marked in fig. 5.38, labeled 1 to 4. The following interpretations and discussions are based partly on these zones. In zone 1, the characteristic decrease of phase observed in July is observable. It is to be noted the decrease of phase in this area is not particularly coupled to a decrease of electrical resistivity. In zone 2, the models from March and July are very similar, and the model from October presents an increased phase and an increase of resistivity. Zone 3 corresponds to a local decrease of phase in the top layer. This decrease, more pronounced in March and October, which present in turn a lower resistivity. Zone 4 presents a clear decrease of phase in October.

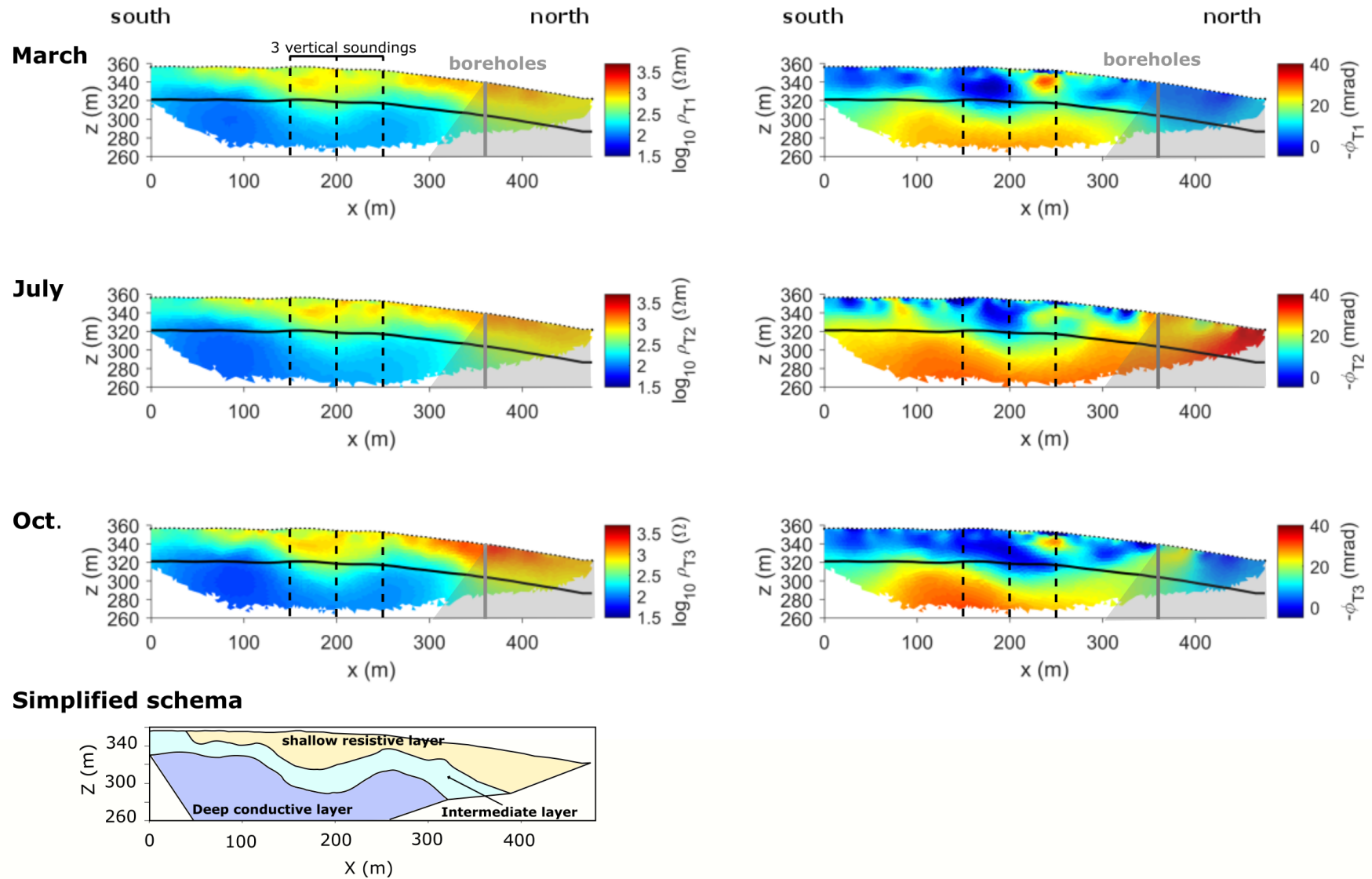


Figure 5.36: Inversion results at the 3 time-periods - the black line on each model represents the line at 40 m below the surface, to roughly locate where to expect the water head; the grey shaded zone corresponds to the area where the profile is not a straight line, and where the data are expected to be slightly distorted. Bottom-left figure: Interpretation scheme related to the resistivity models

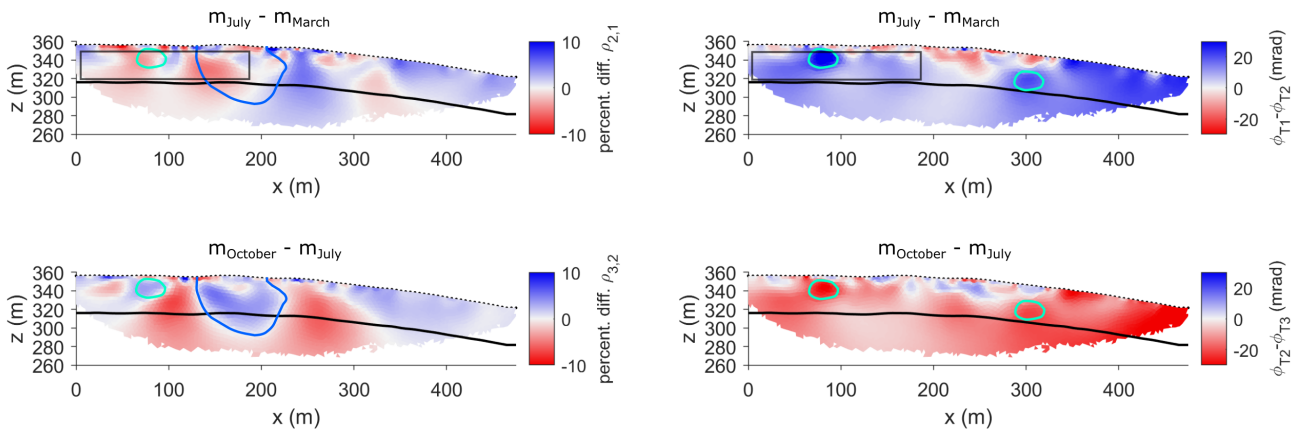


Figure 5.37: Variations in time of the models. The percentage difference of the resistivity in y relative to x (y,x) is  $100 \cdot (\log(\rho_y) - \log(\rho_x)) / \log(\rho_x)$ . An increase of  $\rho$  is expressed in blue, a decrease is expressed in red. An increase of the absolute phase ( $|\phi|$ ) is expressed in blue, a decrease is expressed in red

### 5.4.5 Analysis of temporal variations of the complex resistivity model

#### Structural interpretation

Because of the lateral variability observed in the profile, relating the geological units composing the slope and the water levels observed at the boreholes to features of the TDIP models is hazardous.

The top layer, very resistive (in the order of  $10^3 \Omega \cdot m$ ) can be attributed with high confidence to the top soil, composed of fresh and uncemented scree-slope deposits. The important porosity might produce an important resistivity. This unit, composed of scree slope deposits, was described as very heterogeneous by [Denchik et al. \[2019\]](#), with a notable increase of the cementation with depth, but also with possible lateral variations in the coarseness of the scree and the pore filling. At depth, this unit could potentially contain non-negligible amount of clay in the cement. In particular, in the southern part of the slide, the scree is known to be cemented. The second unit, more conductive, is attributed to the cemented scree slope deposits, partially saturated. The deep conductive layer is attributed to the clay, marls and evaporites layers, partly or fully water-saturated. It seems that the top of the Norian and Carnien units, composed of claystone and evaporites, is not detected in the DCIP profiles. These layers would indeed be expected to be less conductive ([Denchik et al. \[2019\]](#), [Guinea et al. \[2010\]](#)). These units are located below 52 m depth at the location of the two boreholes, and are potentially shallower at the southern part of the profile, where the cemented scree-slope deposits outcrops.

#### Hydrogeological interpretation

The absence of clear temporal variations of the resistivity during the summer, knowing that the water table should change, raises questions. Indeed, the recordings of water pressure at 4 different levels in the boreholes (fig. 5.24) reveals an important variation of the water head throughout the experience. The water pressure at 36 m is observed to vary from 1 bar to 0 bar from February to October. These variations in an unconfined aquifer reveal a variation of water head from 10 to 0 m above the level, by applying the principal of Pascal. Such variations should be recorded and sensed in the TDIP survey.

It can be noticed that the two deepest levels of packer (at a depth of 48 to 56 m) present variations of the water pressure in time that seem inconsistent with the above levels. [Denchik et al. \[2019\]](#) interpreted these results as a decoupling of the water reservoirs from the different units. When looking at the long term series of data, and more specifically at the pressure gradient computed between each packered levels (fig. 5.7) it appears that the gradient between 45 m and 48 m depths is much less stable in time than the gradient between the top levels and between the deepest levels and seems more sensitive to the yearly rainfall cycle. This suggests important variations of the flow dynamics between 45 and 48 m, related to the separation of the two aquifers.

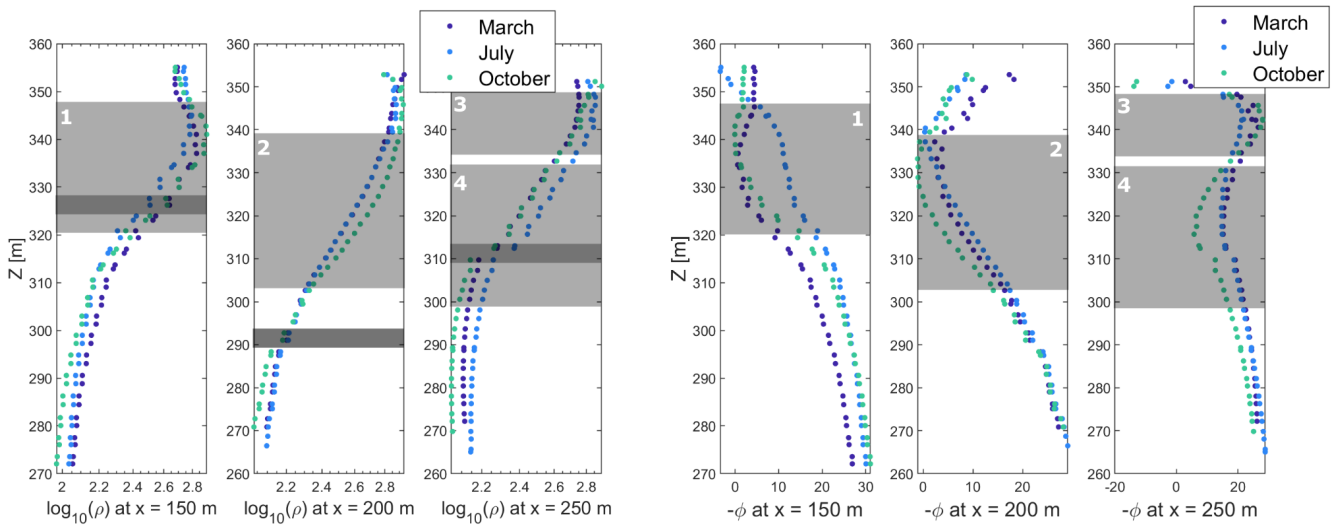


Figure 5.38: Extracted vertical logs from the inverted resistivity (left) and phase (right) models, at  $x = 150, 200$  and  $250$  m.

Fig. 5.39 is a conceptual model proposed to illustrate such trends, where a very permeable unit sandwiched between two impermeable and saturated layers produce such pressure trends.

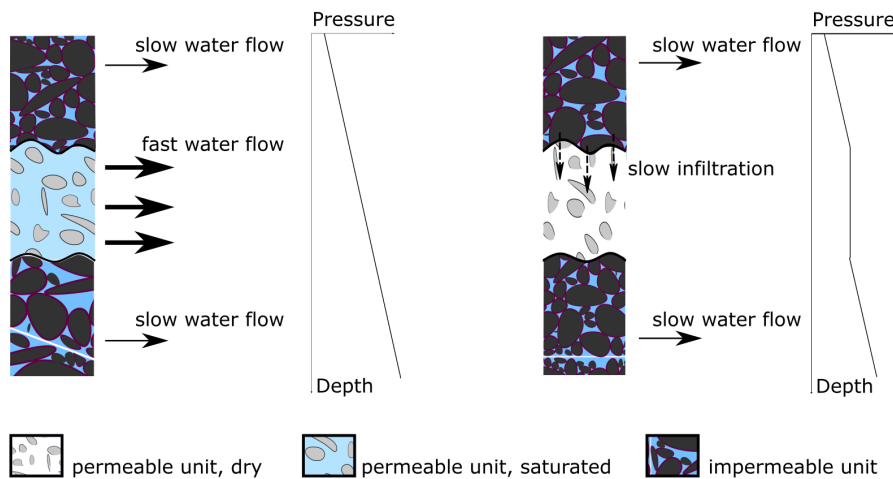


Figure 5.39: Conceptual scheme proposed from the temporal and vertical variations of the pressure at the four levels packered

**Variations of the resistivity:** The stability of the resistivity in time is not consistent with the expected variations of the water head described in the previous subsection. The difference of resistivity in the different models in fig. 5.37 mainly shows vertical trends, close to the surface. Such trends should be attributed to the infiltration of the water through the rock matrix. These trends are particularly observable between July and October. This interpretation could be justified by the presence of small impermeable zones (such as the zone 1 in fig. 5.38), where the meteoric water would infiltrate short after the rain episode, and that would slowly reconstitute the water in time. In such case, very few amount of rain could be sufficient to slightly decrease the resistivity along those path. The effective rain, computed by following Oudin et al. [2005], shows that only 3 mm of rain occurred 27 days before the survey at time T2, as 5 mm of rain fall in the 12 days before the survey at time T3.

The difference between the resistivity at time 2 and 3 highlights as well a channel, above and below which the variations of resistivity are antagonists, suggesting two different hydrogeological responses. This limit is interpreted as a lithological transition from a permeable scree slope deposits and the impermeable levels of mudstone, marls and clays.

The differences in resistivity seem to decrease with depth, either due to an actual stability of the hydrogeological

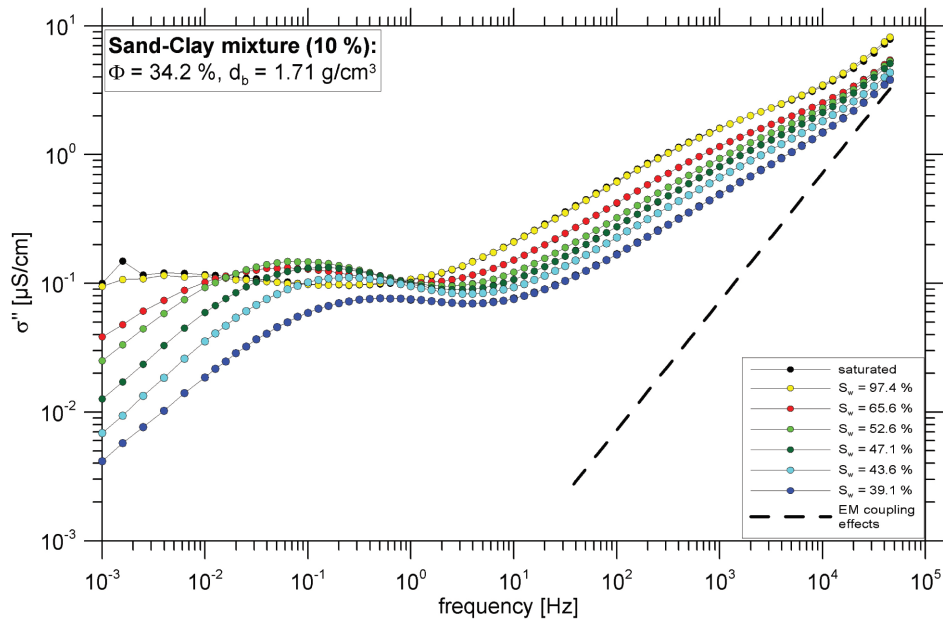


Figure 5.40: Influence of the water saturation on the imaginary part of the complex conductivity in the case of a sand/clay mixture with 10% of clay - by Breede et al. [2012]. In the frequency range between 10 mHz and 1 Hz, the influence of the saturation on the polarization is none linear.

regime, or resulting from a decrease of the resolution with depth. Variations of the hydrogeological regime are expected in the Hettangian, Rhaetian, Norian and Carnien units, as shown and discussed regarding the pressure of the last level of packer (fig. 5.24 and 5.39). Therefore, the lack of resolution might be the correct interpretation. However, no sensitivity analysis were made, no conclusion can therefore be brought.

The generally low amplitude of the resistivity variations suggest that the medium still contains a none-negligible amount of water, that remains trapped in local less permeable zones, but that do not extent laterally as an aquifer. Such isolated filling of water would not contribute in increasing the water pressure in the claystones units, but would take part in the general decrease of the resistivity. Such interpretation would suggest that surface geoelectrical methods might not be as efficient as expected in the hydrogeological monitoring of this type of units, were the complexity of the fluxes cannot be imaged with the required resolution at such depths.

**Variations of the phase:** In a context where the resistivity varies inside a limited range of values in time, the observed variations of the phase are remarkable. The main observations on the variations of the phase are the following ones:

- The deep polarizable area seem to expands towards the top of the clayey units in July (fig. 5.36), resulting in an important decrease of the phase from -5 to -10 mrad in July (fig. 5.38, patch 1).
- Close to the surface, a few small zones seem to concentrate the variations of the phase (fig. 5.37, resulting in incoherent variations of the phase between neighbouring units (fig. 5.38, patches 3 and 4), suggesting local variations of permeability.

The decrease of phase in July is difficult to interpret, as it does not correlate with a clear decrease of the resistivity. It is known that the relation between the soil saturation and the IP response is not linear and depends 1/ on the frequency, 2/ on the clay content, 3/ on the cementation of the rock and 4/ on the range of saturation (Breede et al. [2012], Ulrich and Slater [2004]). As an example, fig. 5.40 shows that, in the particular case of sand-clay mixture containing 10% of clay, between 10 mHz and 1 Hz, the increase of saturation in the domain of  $S < 52\%$  results in an increase of the polarization, but an increase of the saturation at higher saturation would result in a decrease of the polarization response.

**Proposed interpretation of the IP variations:** The chargeability of dry and wet clay at different degrees of saturation was widely studied in the literature, as IP is one of the favored method used, in hydrogeophysics, to

distinguish clay content and water content. On the contrary, the IP response of gypsum and more generally of evaporites is not expected to present any specific characteristic. Very few studies present IP data measured to characterize areas of important evaporitic content. [Guinea et al. \[2010\]](#) presents surface IP measurements realized on a lutite / gypsum subsurface, showing that the chargeability of layers containing an important amount of gypsum can be quite variable. In particular, they remark high chargeability in a unit formed by alternation of gypsum and lutite layers, and argued that such assemblage could favored the accumulation of charges at the many interfaces, producing a capacitance effect, in opposition to pure gypsum layers, presenting low chargeability. At the Lodève landslide, such alternance of clay and evoprites can be observed at the location of the boreholes, below a depth of 52 m, as well as at a depth between 46 and 48 m. In the study from [Guinea et al. \[2010\]](#), no mention of the water head is made, suggesting that the area explored is above the aquifer. In particular, it is not clear how this effect should evolve if such layers are fully saturated.

The influence of the water content, and more precisely the water saturation of the rock matrix on the IP response is complicated as it is non-linear and a decrease of the saturation does not necessarily yield a decrease of the phase or imaginary part ([Ulrich and Slater \[2004\]](#), [Breede et al. \[2012\]](#)). [Breede et al. \[2012\]](#) and [Okay et al. \[2014\]](#) showed that the influence of the water content depends on the frequency, and on the clay content of the rock matrix, by testing the IP response of several sand and clay mixtures at different water saturations. Nevertheless, it seemed from these experiments that at frequencies above 1 Hz, the higher is the clay content, the more linear will be the influence of the water saturation. For high clay contents (>10%), the IP response can be expected to be higher for high saturations. For pure sand however, no general conclusion can be made.

#### **Borehole observations:**

1. The water conductivity (and ions content) does not vary in time.
2. The water pressure progressively decreases throughout the period of the time-lapse experiment related to the progressive decrease of the water head.
3. The effective rain during the experiment period is limited to maximum of 5 mm, very isolated in time.

#### **Basic facts to consider in the interpretation:**

1. The vines are not watered in the summer period, but the roots are expected, particularly in the dry period, to pump some of the shallowest water - no chemical products are disposed in the soil to protect vines from diseases. Only copper and sulphur are disposed in small quantities in the leaves of the vines during Spring.
2. The aquifer might be connected and fed by karstic reservoirs from the Larzac plateau.

An interpretation of the variations of the resistivity and phase observed during this experiment is proposed, in agreement with the borehole observations of the water pressure and the absence of variation of the water conductivity and composition. This interpretation is based on the assumption that the cementation of the scree slope deposits is heterogeneous over the survey area, and locally involves a mix of clay and limestone cement. This cement could retain the water even during dry periods, without being detected in the borehole data, but impacting the DCIP survey. Fig. 5.41 is an electrical resistivity tomography realized in the direction of the slope ('GEOMON profile' in fig. 5.25). It clearly shows lateral variations in the shallow layer, interpreted as local accumulation of clayey cement in the scree slope deposits. In such contexts it could be imagined that even a few quantity of effective rain could contribute to induce small variations of the water content in these areas were the water is stored and rendered slowly. The limited resolution of the survey could miss these small anomalies in the resistivity model. In addition, these areas of low resistivity could focus the injected current and limit the sensitivity to the underlying units. The important increase of the phase observed at the top of the deep conductive layer could then be explained by variations of the water saturation in the unsaturated units, in relation to the dry period. The interpretation drawn on the variations of the resistivity, which lead to the idea that even during the dry period, some areas particularly impermeable still retain a non negligible amount of

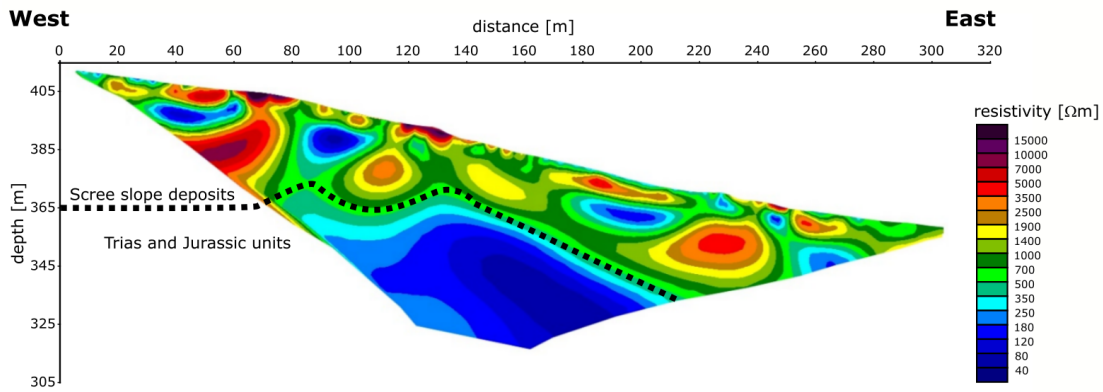


Figure 5.41: Inverted ERT profile measured along the slope in April 2019 with a GEOMON instrument: the lateral variability and bubble shapes of conductive and resistive anomalies in the first 20 to 30 m suggest a high variability in the cementation of the scree slope deposits

water, is validated by the local variations of the phase.

This interpretation suggests that such methodology is insufficient to observe the hydrogeological variations occurring at depth in the clay and evaporites units, during dry periods. Indeed, the small variations occurring in the cement of the scree slope deposits are expected to corner the most important variations observed, masking the variations occurring in the deeper layers.

A second unclarified point is the composition of the cemented scree slope. In particular, the clay content of the cement was not studied, leaving uncertainty in the proposed interpretation of the variations of the phase.

## Conclusion

### CSAMT

Time-lapse CSAMT data were realized at the Lodève landslide in an attempt at characterizing the variations of resistivity of the subsurface relative to the recharge and discharge of the water systems in response to intense seasonal rain events.

The polarization of the magnetic field revealed an important noise content for most stations. In addition, two stations at the East of the slope present very incoherent polarization of the EM fields, potentially because of a ground wire running. The analysis of these unstable polarization revealed that it is in fact only produced by a few outliers for most frequencies. A filtering procedure to remove the data presenting the noisy polarization was successfully applied, and four from the eight stations presented acceptable apparent resistivity curves. The four remaining stations presented important high frequency noise, preventing any analysis of these stations.

Synthetic tests were realized to evaluate the sensitivity of our measurements to variations of the resistivity expected from the hydrogeological variations. These tests demonstrated that CSAMT measurements should be sensitive to such variations but that the interpretation of the soundings by a 1D inversion is limited by the absence of data below the far field limit.

The four interpreted stations display very consistent variations of the apparent resistivity, marked by a decrease of the resistivity with time from November to January. From January to March, the four stations do not present the same variations. The temporal variations seem mostly important at high frequency (above 5000 Hz). Only the apparent resistivity was interpreted. Indeed, no 1D inversion could satisfyingly explain and fit the data. This is attributed to the dimensionality of the subsurface in the first 30 m of the subsurface: it appeared indeed that this layer composed of scree slope deposits is heterogeneously cemented over the site. The lack of time-lapse inversion however limits the interpretation of the variations and do not allow to infer the locations at depth where changes of resistivity occur.

## TDIP

The hydrogeological processes at the Lodève landslide seem quite complex to model as they consist of water flows in units of highly variable permeability. For this reason, a very high vertical resolution is required in order to be captured the variations occurring in the two stacked aquifers of the site.

The TDIP time-lapse experiment revealed that the expected variations cannot be observed with this methodology. The vertical resolution is not high enough to permit observing the variations of water saturation, which seem to be masked in the models by small variations of the signal occurring locally in the shallow layers, composed of more or less cemented scree-slope deposits.

Observing the evolution of the complex resistivity throughout the spring and summer at the Lodève landslide brought however valuable information. The general topography and shape of the main units constituting the slope could be imaged.

The time-lapse observations permitted the identification of infiltration pathways in the first layer of the subsurface, interpreted as the slow discharge of zones where the scree slope deposits is cemented by a clayey cement. At the boundary between the scree-slope deposits and the first Rhaetian unit composed of mudstone, marls and clays, the contrast of permeability resulted in discordant variations of resistivity, interpreted as the accumulation and retention of water in the impermeable Rhaetian layer and on the opposite a fast discharge of the scree slope deposits mainly produced by a vertical flow along the top of the impermeable Rhaetian unit.

Below this depth, no particular variations are observed. The measurements seem indeed unable to image the complex hydrogeological behavior of the Rhaetian, Norian and Carnien units, where vertical contrasts of the permeability are expected, leading in temporal variations in the water content of certain very permeable layers. Sensitivity tests should be realized in order to demonstrate the sensitivity and resolution limits at depth.

This study clearly lacks a time-lapse inversion. A temporally constraint inversion would indeed provide information such as how much does the model at one time explain the data at the next measurement period, and which part of the model must be updated in order to allow the fit of this next measurement. In order to conduct such analysis, a much higher repetition rate should be used (one measurement every two weeks). Without such analysis, we lack of information regarding the sensitivity of the time-lapse data set so actual variations of the model.

In order to improve the time-lapse experiment, another track consists in exploiting the electrodes installations at the ImaGeau borehole, in order to conduct surface/borehole time-lapse measurements, increasing the resolution in the deep layers. Such measurements could, for example, be jointly interpreted with co-located surface measurements.

## General conclusions

The general study of the temporal variations of the hydrogeology from surface measurement was made difficult, in both cases, by the important heterogeneity of the first 30 m, corresponding to scree slope deposits. This first layer appeared to be quite heterogeneous, due to lateral variations in the cementation of the scree slope deposits, which was not anticipated. In both time-lapse studies, this characteristic dramatically reduced the sensitive to the deep variations of the geoelectrical models, produced by changes of water table and water / rock interactions.

In CSAMT, this first heterogeneous layer resulted in 2D and 3D distortion of the apparent resistivity curves, making it difficult to interpret the data with a 1D model.

In TDIP, the heterogeneity in the first layer was particularly observed in the phase models. The temporal variations in the phase models indeed are mainly occurring in this first layer possibly reducing the sensitivity to the variations occurring at largest depths (below 30 m depth).

In surface geophysics, being sensitive to temporal variations of a parameter at large depth when this parameter also varies closer to the surface is generally challenging. Both in CSAMT and in TDIP, more sophisticated

measurement setups and methodologies are required.

- In CSAMT, a 2D or 3D measurement methodology could be employed. 3D CSEM measurements were considered (Appendix I). Applying such a methodology in time-lapse with monthly measurements would be however very time consuming.
- In TDIP, a higher repetition rate (two measurements per month) could allow to conduct a time-lapse inversion, permitting a better constraint on the shallow and the deep variations.
- The use of the electrodes installations in the ImaGeau borehole could as well be exploited in a borehole-surface time-lapse experiment, increasing the resolution at the location of the deep layers of interest.

## Perspectives

These studies leave outstanding issues, which could lead future work. It seems from the TDIP study that evaporitic formations do not present a particular polarization signal. Because no particular variations in the water / rock interactions occurred during the time of the experiment, no conclusion could be drawn on the sensitivity of IP methods to such interactions. This question could be further explored. The simultaneous realization of CSAMT and TDIP measurements could be considered, and the realization of a joint inversion of the two datasets could potentially help to further characterize the site, bringing constraints at depth through CSAMT, and high shallow resolution through TDIP. The possibilities of detecting induced polarization signals through CSAMT measurements could as well be explored. Last, an understanding of the high frequency far field limit obtained in the CSAMT survey is really important before considering further CSAMT measurements.

## 5.5 References

- Archie, G. E. (1942). The electrical resistivity log as an aid in determining some reservoir characteristics. *Transactions of the AIME*, 146(01):54–62.
- Bartel, L. (1982). Potential use of the CSAMT geophysical technique to map UCG processes. Technical report, Sandia National Labs., Albuquerque, NM (USA).
- Blanchet, J. and Creutin, J.-D. (2017). Co-occurrence of extreme daily rainfall in the french Mediterranean region. *Water Resources Research*, 53(11):9330–9349.
- Breede, K., Kemna, A., Esser, O., Zimmermann, E., Vereecken, H., and Huisman, J. (2012). Spectral induced polarization measurements on variably saturated sand-clay mixtures. *Near Surface Geophysics*, 10(6):479–489.
- Darnet, M., Wawrzyniak, P., Coppo, N., Nielsson, S., Schill, E., and Fridleifsson, G. (2018). Monitoring geothermal reservoir developments with the Controlled-Source Electro-Magnetic method—A calibration study on the Reykjanes geothermal field. *Journal of Volcanology and Geothermal Research*.
- Delrieu, G., Kirstetter, P.-E., Nicol, J., and Neppel, L. (2004). L'événement pluvieux des 8-9 septembre 2002 dans le Gard: estimation des précipitations par radars et pluviomètres. *La Houille Blanche*, (6):93–98.
- Denchik, N., Gautier, S., Dupuy, M., Batiot-Guilhe, C., Lopez, M., Léonardi, V., Geeraert, M., Henry, G., Neyens, D., Coudray, P., et al. (2019). In-situ geophysical and hydro-geochemical monitoring to infer landslide dynamics (pégairolles-de-l'Escalette landslide, France). *Engineering Geology*, 254:102–112.
- Falgàs, E., Ledo, J., Benjumea, B., Queralt, P., Marcuello, A., Teixidó, T., and Arango, C. (2006). Imaging ground water resources of a mediterranean coastal aquifer using seismic and csamt data. In *Symposium on the Application of Geophysics to Engineering and Environmental Problems 2006*, pages 863–870. Society of Exploration Geophysicists.
- Flores Orozco, A., Kemna, A., Binley, A., and Cassiani, G. (2019). Analysis of time-lapse data error in complex conductivity imaging to alleviate anthropogenic noise for site characterization. *Geophysics*, 84(2):B181–B193.
- Flores Orozco, A., Kemna, A., and Zimmermann, E. (2012). Data error quantification in spectral induced polarization imaging. *Geophysics*, 77(3):E227–E237.
- Ghorbani, A., Cosenza, P., Revil, A., Zamora, M., Schmutz, M., Florsch, N., and Jougnot, D. (2009). Non-invasive monitoring of water content and textural changes in clay-rocks using spectral induced polarization: A laboratory investigation. *Applied Clay Science*, 43(3-4):493–502.

- Guinea, A., Playà, E., Rivero, L., and Himi, M. (2010). Electrical resistivity tomography and induced polarization techniques applied to the identification of gypsum rocks. *Near Surface Geophysics*, 8(3):249–257.
- Kemna, A. (2000). *Tomographic inversion of complex resistivity: Theory and application*. Der Andere Verlag.
- Kemna, A., Räckers, E., and Binley, A. (1997). Application of complex resistivity tomography to field data from a kerosene-contaminated site. In *3rd EEGS Meeting*, pages cp–95. European Association of Geoscientists & Engineers.
- Lopez, M., Gand, G., Garric, J., Körner, F., and Schneider, J. (2008). The playa environments of the Lodève Permian basin (Languedoc-France). *Journal of Iberian Geology*, 34(1):29–56.
- Maineult, A., Jougnot, D., and Revil, A. (2018). Variations of petrophysical properties and spectral induced polarization in response to drainage and imbibition: a study on a correlated random tube network. *Geophysical Journal International*, 212(2):1398–1411.
- Mitchell, J. K. and Soga, K. (1993). *Fundamentals of Soil Behavior*, John Wiley&Sons. Inc., New York, 422.
- Okay, G., Leroy, P., Ghorbani, A., Cosenza, P., Camerlynck, C., Cabrera, J., Florsch, N., and Revil, A. (2014). Spectral induced polarization of clay-sand mixtures: Experiments and modeling. *Geophysics*, 79(6):E353–E375.
- Oudin, L., Hervieu, F., Michel, C., Perrin, C., Andréassian, V., Anctil, F., and Loumagne, C. (2005). Which potential evapotranspiration input for a lumped rainfall–runoff model?: Part 2—Towards a simple and efficient potential evapotranspiration model for rainfall–runoff modelling. *Journal of Hydrology*, 303(1-4):290–306.
- Ulrich, C. and Slater, L. (2004). Induced polarization measurements on unsaturated, unconsolidated sands. *Geophysics*, 69(3):762–771.
- Vacquier, V., Holmes, C. R., Kintzinger, P. R., and Lavergne, M. (1957). Prospecting for ground water by induced electrical polarization. *Geophysics*, 22(3):660–687.
- Vincent, M. and Zornette, N. (2001). *Projet PACTES - Module cartographie du risque potentiel de mouvements de terrain*. Technical Report 44p, 24fig., BRGM/RP-51327-FR.
- Zonge, K. L. and Hughes, L. J. (1985). Effect of electrode contact resistance on electric field measurements. In *SEG technical program expanded abstracts 1985*, pages 231–234. Society of Exploration Geophysicists.

### 5.5.1 References to internet websites

Imageau © - <https://imageau.eu/products/smd/?lang=en>

## **Chapter 6**

### **Conclusion and perspectives**

## 6.1 Conclusions

The objective of this thesis was to develop, test and validate methodologies for characterizing and modeling three different types of deep water systems: weathered crystalline aquifers, fractured bedrock aquifers, and deep sedimentary aquifers with local high clay content. For each of these contexts, a specific methodology was developed using specific electrical and electromagnetic methods. Both static and time-lapse measurement techniques were considered.

Each method has its own domain of validity (depth of investigation, sensitivity, resolution). Among the chosen methods:

- CSAMT is expected to ensure a good depth of investigation, a particular sensitivity to conductive anomalies and a good vertical resolution, but a poor horizontal resolution. CSAMT measurements can be subject to many potential types of distortion.
- 2D ERT and IP are limited in the depth of investigation due to the limitations imposed by the use of multi-core cables. The lateral sensitivity is however good, and the resolution close to the surface can be very thin. In IP, these limitations are exacerbated because 1/ long cables imply important distortion due to electromagnetic coupling and 2/ the low amplitude of the polarization signal increases the sensitivity to external noise particularly at depth.
- Large-scale 3D electrical measurements, using a network of measurement units permit a great increase in the possibilities of the ERT method. It provides a new sensitivity, restraining in turn the near-surface resolution.

Three study sites, corresponding to the three aquifer types, were selected to develop each methodologies. The general results obtained on the validity of each methodologies for each of the three types of aquifers are presented in the following subsections, as well as the specificity of the realized tests, and the conclusions drawn specifically on the studied sites.

### 6.1.1 Characterization of deep crystalline weathered aquifers

In chapter 3, deep crystalline weathered aquifers were the focus of the hydrogeophysical analysis. Crystalline weathered aquifers consist in crystalline bedrock altered at the top. The water can be stored in the altered rock, which presents a higher porosity. In such aquifers, the water content is expected to decrease with depth as the rock is less and less weathered and the limit of the reservoir at depth is related to the limit of weathering, below which the rock cannot host or conduct the water. In this work, we assume that such aquifers are pseudo-1D structures, that present vertical variations of weathering. The lateral variations are expected to be very smoothed and limited. When such reservoirs extend at depths exceeding 50 or 60 m, it becomes difficult to detect the bottom of the weathered rock.

The methodology proposed in this work was the use of sparse 1D CSAMT soundings to characterize the vertical variations of electrical resistivity, expecting very low horizontal variations. In particular, this assumption can be questioned with regards to surface topography. In order to control the validity of the methodology, extensive numerical modelling tests were enabled by the use of the CSEM computation software *custEM*.

The Strengbach catchment was selected to test the validity of the proposed methodology. This catchment is a small granitic mountainous catchment located in the Vosges mountains. The limit of the catchment at depth could not be imaged by previous geophysical studies, nor by borehole observations, but seems to extend below 80 m depth. Ten soundings were realized over the catchment area, analyzed and inverted in 1D. These soundings were measured with a unique transmitting dipole, limiting the complete resolution of the impedance tensor. Nevertheless, a methodology was proposed to permit the computation of an apparent resistivity curve and to evaluate the importance of none-1D effects. The impact of topography was evaluated, and a correction method was applied to the apparent data. This study allowed to detect the limits at depth of the weathering with a low resolution, providing information on the amount of rock potentially involved in the water storage. The models are expected to be resolved until depths of 400 m.

Some unusual features were observed in the data set, that could not be explained: the high frequency part of each apparent resistivity sounding (above 4 kHz) present an important decrease of the resistivity with increasing frequency (exceeding two orders of magnitudes per decade). Such trend was not observed in the few high frequency AMT measurements that could be processed. This feature seems to originate mainly from the measurement of the electric field and could not be explained in this work.

Although 2D or 3D methodologies could be easily favored in the general study of aquifers (use of airborne TDEM, very popular because allowing a dense and fast sampling), it seems that the depth of investigation obtained with the CSAMT method presents a huge advantage when it comes to imaging deep structures. If a 1D methodology was favorably used at the Strengbach catchment, some of the stations presented clear 2D or 3D bias, and could not be considered with confidence in the analysis. The remaining stations presented very stable trends that could ensure and increase the confidence in the chosen 1D methodology. For this reason, we expect that such methodology should be suited to the study of similar weathered aquifers, but that the dimensionality is a key parameter that should be checked with any available data previous to launching a campaign.

### 6.1.2 Characterization of fractured bedrock aquifers

In chapter 4, the characterization and imaging of fractured bedrock aquifers was studied. Fractured bedrock aquifers are reservoirs that present multiple types of porosity, where fractures constitute discontinuity in the hydrogeological properties. The fractures network constitute a 3D structure that cannot be captured with 1D or 2D measurements.

3D measurements are required to characterize such reservoirs. The proposed methodology is the use of novel measurement system based on the use of a distributed network of 3 channels resistivimeters. These types of systems allow the realization of large-scale 3D resistivity tomography.

The applicability of this method was tested at the S echilienne landslide. It is a large ( $60 \pm 10 \text{ M m}^3$ ) and active landslide of the French Alps, consisting of fractured hard rocks (micaschists) with double permeability and strong spatial heterogeneities. The limits of the fractured hard rock defines the limits of instability, which was estimated in the range of 150 to 200 m by previous 2D ERT measurements. The hydrogeological and hydrochemical processes in the fractured hard rock (water infiltration, chemical alteration) control the deformation of the unstable slope. The S echilienne landslide presents a complex structure with a very heterogeneous fracturation related to the presence of regional faults, leading to important spatial variations of the hydrogeological properties. Strong topographic variations characterize the slope.

A dense network of 21 portable resistivimeters was installed at the S echilienne landslide, covering a large part of the slope, using a novel measurement technique that enable 1/ surveying over a large surface area and 2/ accessing and installing instruments at locations where it is not possible to layout long and heavy cables.

The recorded data were analysed, filtered and inverted, providing a resistivity model of the first 500 m. The evaluation of the sensitivity was realized through direct modeling of ERT data. The model at the surface was compared with 2D resistivity measurements that had been conducted in the past, bringing to light the limits of resolution of the 3D model. A denser network could increase greatly the surface resolution. However, the difficulty of access of the S echilienne landslide limits the possibilities of dense instrumentation, particularly at the most damaged zones. Last, the induced polarization signal was measured, but was not exploited. A thorough processing of the IP decay curves could allow taking them into account and invert the IP signal. The IP signal could in fact bring information on the properties and damaging of the different faults that cross the slope (size of the grains "cementing" or not the faults).

The 3D electrical resistivity model permitted the detection and delineation of the densely fractured rock, as well as the identification of major drains channeling the water of the slope down to the Romanche river. Temporary perched aquifers could be imaged, validating hypothesis on local multi-permeability of the rock material.

At the Séchilienne landslide, the annual hydrogeological cycle is expected to consist mainly in the progressive flow of water from the perched aquifers down to the deep aquifer. This hypothesis, which was partly verified in the 3D model, could be fully validated by repeating such a campaign during the high-flow period.

This methodology seems very promising to study fractured bedrock aquifers located in the first 500 m of the subsurface. Depending on the accessibility of the site, a denser network should easily increase the resolution of the survey.

The flexibility of dense portable networks in electrical resistivity tomography is particularly interesting to study sites where the accessibility is reduced. It presents as a good alternative to airborne TDEM methods, much more expensive, and potentially difficult to realize where the topography changes abruptly.

### 6.1.3 Characterization of deep sedimentary aquifers

In chapter 5, the hydrogeophysical characterization of deep sedimentary aquifers with high clay content was studied. Sedimentary aquifers are usually composed of a succession of sedimentary layers, presenting variable hydrogeological properties. Such structures can therefore produce multiple stacked aquifers in different units. When this type of aquifers are located at important depth, the deep resolution must be thin at depth in order to successfully image and capture the different reservoir units. In this sense, it constitutes a challenge for surface geo-electric acquisitions.

The issue of a good vertical resolution and sensitivity at depth was addressed through two different methodologies: 1D CSAMT soundings and 2D DCIP measurements. A time-lapse methodology was considered as an attempt to isolate the hydrogeological signal and test the sensitivity to temporal variations of water height in the reservoirs.

The landslide of Lodève was selected to apply the methodology. The Lodève landslide is a slow moving (3 to 4 mm/yr) and deep (50 to 60 m) rotational instability on the flanks of a steephead valley marking the southern limit of the Larzac Plateau. The slope is constituted of late Trias to early Jurassic sediments with an important content of clay and evaporites, suspected to react to heavy underground water flow, producing the slide. Because the hydrogeology plays such an important role in the triggering of the instability, such as in many clayey landslides existing in this region, understanding the water flow processes is important to finally model the water / rock interaction and the hydromechanical processes at stake in such landslides.

CSAMT data were recorded at a monthly frequency from November 2018 to March 2019 at 8 CSAMT stations. From the 8 recorded stations, four were systematically affected by very high noise levels particularly at high frequency, which reason could only be suspected. The four remaining stations could be analyzed and clear evolution in time of the apparent resistivity could be observed. These variations were in good agreement with the general trend expected from the meteorology, as intense rainfall events are expected to recharge the aquifer, and decrease the apparent resistivity of the subsurface.

No inversion of the data could satisfactorily be produced, potentially caused by 2D, 3D or metallic distortions. The interpretation was therefore limited to the apparent variations. A second factor limiting the interpretation of the data is the unexpected high frequency transition towards near field. This transition, expected to occur around 400 Hz from the observed apparent resistivity and the distance between transmitter and receivers, was in fact observed between 1 and 2 kHz.

Observing the variations of resistivity through CSAMT sounding is still expected to be a good methodology, because of the deep sensitivity and the good vertical resolution, particularly in conductive layers. However, in order to be efficient, it requires to be set in a real 1D environment. The dimensionality of the subsurface structures should therefore be checked previous to starting such an experiment.

Two TDIP profiles were installed and recorded in March 2019, to permit a characterization of the site. One of the two profiles was repeated twice in July and October, in order to observe the variations of the signal during

the driest period of the year.

Although both profiles presented good data quality, only the repeated one could be inverted. The second profile was indeed recorded over an area where important changes of topography occur, and along a curved line, implying a necessary interpretation through 3D modeling, and the use of a very accurate digital elevation model, which was not available during the time of this work.

The TDIP experiment revealed that the variations of resistivity were of very small amplitude, mainly located in the top layer constituted of scree-slope deposits and located above the aquifer. The analysis of the phase also presented most variations of the models in this same top-layer. The proposed interpretation is that the scree-slope deposits layer, heterogeneously cemented, constitutes small isolated water aquifers, that corner most of the time varying signals, making it difficult to observe the variations related to the hydrogeological evolution in the deep layers. No time-lapse inversion could be successfully realized. The reason is most likely the low temporal repetition rate, producing models that were difficult to relate through temporal constraints. It is very possible that a much higher temporal repetition rate (daily, weekly) would permit a time-lapse inversion, increasing the sensitivity to the variations of the model at depth.

The imaging of deep sedimentary aquifer with high clay content is still challenging. The proposed methodologies could be fruitful if

- the top layers are indeed homogeneous for the CSAMT,
- the repetition frequency was greatly increased for the TDIP.

Obtaining high resolutions at depth remains difficult with both methods. The use of seismic data surely would permit to constrain the models. Joint inversion of ERT and seismic data has proven very helpful in many studies (Bergmann et al. [2014], Hellman et al. [2017], Ronczka et al. [2017]). Similar methodologies implying TDIP and seismics could probably increase the resolution of the geo-electric models at depth. The presence of vineyards at the Lodève landslide obstructed the use of a strong seismic source and such methodology could not be tested.

## 6.2 Perspectives

### 6.2.1 Methodological perspectives in CSAMT

#### **Field methodology: improving the data acquisition**

In this work, all data were recorded using a single transmitting dipole, allowing to compute only a partial impedance tensor. Recording the full magnetotelluric impedance tensor would bring additional valuable information on the dimensionality, and would help in the detection of static shifts. The use of a switch system was considered and developed during the time of the thesis, allowing to change the transmitting dipole without the assistance of a field operator, following a pre-scheduled timing. Two dipoles could be installed, perpendicular to one another, and plugged to the switch box, which could alternatively connect one of the dipoles to the current source. This device could not be tested in the field in the context of this thesis.

#### **Improving the analysis of CSAMT to increase the information content extracted**

In chapter 5, the frequency sampling of the electric and magnetic responses did limit the data quality. This was caused by low signal intensity, reducing the access to harmonic signals, a high frequency transition from near field to far field (2000 Hz), and a frequency rate of 24 kHz, limiting the frequency band to frequencies below 12 kHz.

Increasing the transmission time could be a path towards increasing the quality of apparent resistivity curves. When the measured signal is too weak and too few harmonic signals are recorded, a stacking procedure, ignored in this work, could increase the detectability of the harmonic signals, provide a better error model

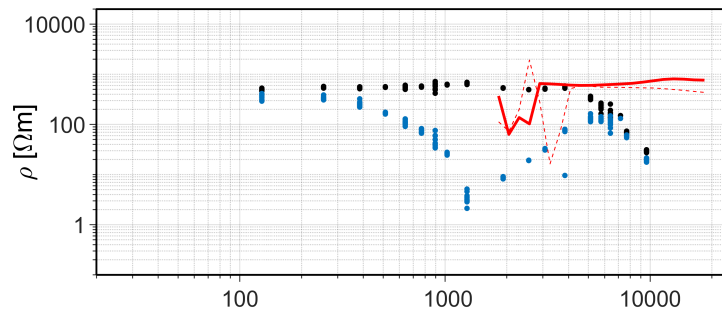


Figure 6.1: Colocated AMT (red curve and red dotted curve - at high frequency) and CSAMT soundings (blue and black dotted curves - at lower frequencies) at the Strengbach catchment

and decrease the data uncertainty.

To supplement the sampled frequency band, AMT data could be jointly interpreted together with CSAMT measurements. The joint interpretation of AMT and CSAMT data was presented in Pedersen et al. [2005], and envisioned in Kalscheuer et al. [2013]. If the theory of both techniques are very close, with the possibility of interpreting (inverting) in the same manner both types of data, the challenge of a joint inversion lies in the frequency sampling of both types of data. The AMT response is interpreted in a much denser manner, as the source signals often cover densely an entire frequency range. The challenge of joint CSAMT and AMT inversion lies in balancing a dense data-set and a sparse one covering different frequency bands. Fig. 6.1 shows the overlap of AMT and CSAMT soundings at the Strengbach catchment. The red curves and red dotted curves are the two apparent resistivity curves from AMT ( $\rho_{xy}$  and  $\rho_{yx}$ ). The black dots are the interpreted apparent resistivity curve from CSAMT,  $\rho_{21}$ . At high frequency, the CSAMT sounding presents an decrease of the amplitude that could not be explained, related to a decrease in amplitude of the electrical response. At low frequency, the AMT response is noisy, due to the lack of signal. A next step in this study is surely to invert jointly the two data.

In a more general case, such type of joint methodology to expand the interpretation of CSAMT at higher frequencies could be also realized with VLF or RMT data.

### Modelling the effect of induced polarization on CSAMT data

Because the frequency at which the polarization phenomena occur superpose with the frequencies investigated in CSAMT surveys, it is expected and known that the polarization effect impacts the EM data (Hohmann [1975], Tang et al. [2014], Liu et al. [2018], García-Fiscal and Flores [2018], García-Fiscal and Flores [2018] fig. 6.2). In time domain EM soundings, the IP can have an obvious signature because it inverts the sense of the EM response. In logarithmic plots, this effects appears on the data as a V shape in the time domain decay (Kaminski and Viezzoli [2017]) corresponding to a change of sign of the measured potential. Kaminski and Viezzoli [2017] comment that a lot of TDEM soundings are expected to contain IP distortions, that are usually simply removed. More importantly, the fact of ignoring such effects and simply invert the data looking for a DC resistivity can reduce the resolution of deep information.

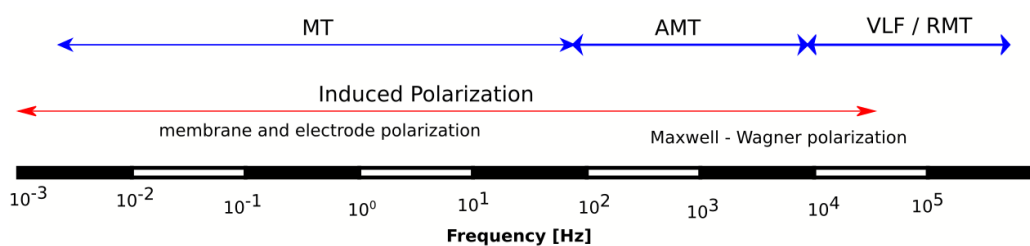


Figure 6.2: Frequency band of the IP phenomena and of plane wave induction EM methods. Inspired from Okay [2011]

In frequency domain EM, this effect was as well investigated. [Tang et al. \[2014\]](#) proposed a synthetic MT apparent resistivity curve affected by a chargeable layer at depth.

[Liu et al. \[2018\]](#) conducted a series of synthetic experiment to model the effect of polarization in CSEM and CSAMT data. In their computation scheme, they injected a complex resistivity in the usual equation of the electric and magnetic field produced by a grounded dipole in a 1D-layered earth. However, only the IP effect on the "Full field" apparent resistivity, hence computed taking the source into account, is presented. Their work showed that the IP could distort importantly the full field apparent resistivity, but that the effect is negligible when the polarizable layer is located at important depths (below 500 m depth).

A few questions are raised here, that deserve attention:

- What is the impact of IP phenomenon on CSAMT data? How much does the IP distort the apparent resistivity curve.
- In CSAMT, the frequency is interpreted as an indicator of the sensitive volume. The frequency in IP has a much different role, which relates to the frequency dependency of the complex resistivity. A question worth asking is: does the IP effect distort significantly the sensitivity of CSAMT data
- How does the IP effect affects the electrical and the magnetic fields individually? [Hohmann \[1975\]](#) showed that a polarizable cube could be detected by the use of a magnetometer, looking at the quadrature part of the magnetic induction. How does this observation translate in far field EM data?
- Is there a way to extract the IP information with confidence from CSAMT or CSEM data in order to correct the data, or even to interpret the IP effect from CSEM, as it is done in TDEM? Plane wave EM methods are frequency domain methods, extracting the IP directly from controlled source data could ease the interpretation by giving directly access to a broad band spectrum, similarly to SIP measurements.

To approach this problem, two different models of induced polarization are considered: a simple complex resistivity ( $\rho = \rho' + i\rho'' = |\rho|e^{i\phi}$ ), including no frequency dependence, and a Cole-Cole model (eq. 6.1), that is usually used to describe the IP measured in the field.

$$\rho = \rho_0 \left( 1 - m_0 \left( 1 - \frac{1}{1 + (i\omega\tau)^c} \right) \right) \quad (6.1)$$

Options could be to explore the signal produced by 1/ an homogeneous polarizable medium and 2/ a layered medium including a polarizable layer at depth.

This could be realized using the two different models of polarization, either by injecting the IP resistivity model in the computation of the impedance (eq. 6.2) or by injecting the IP resistivity model in the computation of the electric and magnetic fields produced by an horizontal grounded dipole.

$$Z = \sqrt{\rho\mu\omega} e^{i\pi/4} = \sqrt{|\rho|\mu\omega} e^{i(\pi/4+\phi/2)} \quad (6.2)$$

with  $\phi < 0$ .

$$\begin{aligned} \rho_{cagniard} &= |\rho| \\ \phi &= \frac{\pi}{4} + \frac{\phi}{2} \\ Sd &= \mathcal{F}(\delta) \end{aligned} \quad (6.3)$$

The function  $\mathcal{F}$  is the function of distortion of  $\delta$ , the skin depth and is yet to be explored.

Studying the IP effect on CSAMT data is the first step towards a joint interpretation of the two methods.

## 6.2.2 Methodological perspectives in DC and IP

### Interpretation of large-scale IP data from R-DAS systems

The new possibilities brought by R-DAS are very promising. The deployment of such stations, easy and fast to install, allows a remarkable increase of the depth of penetration and the surface area investigated by the DCIP

measurements.

In this work, the IP signal recorded by the Fullwaver systems in the study of Séchilienne landslide (chapter 4) could not be analyzed due to low signals, and poor inversion results. Questions remain regarding the sensitivity to the IP signal at depth. Indeed, it is often observed that the polarization at depth in particular below a polarizable body, is difficult to retrieve.

Another direction that requires to be explored is the handling of positive phases, or, in the context of 'full wave' time-domain analysis of the IP signal, of negative chargeability. In IP, effective (i.e. absolute) positive phases are not plausible. In the context of 2D measurements of the IP, positive phases are systematically removed, because attributed to wrong measurements, affected by noise. However, in the context of 3D surveys, and more particularly when the subsurface contains 3D bodies, positive apparent phases can be measured and modeled (Flores Orozco et al. [2018], Dahlin and Loke [2015]). In such context, the data processing must be changed, improved, in order to distinguish plausible positive phases from noisy data. This aspect represent the major perspective on large-scale 3D data analysis of induced polarization data.

### Increasing the resolution at depth

When the use of R-DAS systems is not justified by the TDIP survey (small scale, 2D survey with a high accessibility to the site, few EM inductive coupling problems expected) such that multi-channel instruments are favored (such as in chapter 5), the lack of resolution of a survey at depth can be compensate by taking advantage of borehole electrodes infrastructure, when existing: current injection and potential measurements can be realized both from the surface and on the wall of a borehole (fig. 5.8). In this way, the thin vertical sampling along the borehole could allow to refine the model at depth, in the vicinity of the borehole. This method requires a more complex installation regarding surface measurements, but is very promising, and could be used independently of any additional measurements, or as a supplement to surface measurements.

### Time-lapse measurements in DC and IP

The detection of the hydrogeological changes and water/rock interactions at depth with surface methods was proved to be compromised by variations detected close to the surface. In order to infer the deep variations, generally less resolved, a higher measurement rate might be necessary. High measurement rates might permit to filter the shallow variations. In order to ease the realization of such measurements, instruments were developed to record automatically a profile at a fixed repetition rate. An example of such instruments is the GEOMON<sup>4D</sup> instrument (Supper et al. [2014]). This instrument is used in some studies (Gance et al. [2016]) but only in the context of DC ERT measurements.

## 6.3 References

- Bergmann, P., Ivandic, M., Norden, B., Rücker, C., Kiessling, D., Lüth, S., Schmidt-Hattenberger, C., and Juhlin, C. (2014). Combination of seismic reflection and constrained resistivity inversion with an application to 4d imaging of the CO<sub>2</sub> storage site, Ketzin, Germany. *Geophysics*, 79(2):B37–B50.
- Dahlin, T. and Loke, M. H. (2015). Negative apparent chargeability in time-domain induced polarisation data. *Journal of Applied Geophysics*, 123:322–332.
- Flores Orozco, A., Gallistl, J., Bücken, M., and Williams, K. H. (2018). Decay curve analysis for data error quantification in time-domain induced polarization imaging. *Geophysics*, 83(2):E75–E86.
- Gance, J., Malet, J.-P., Supper, R., Sailhac, P., Ottowitz, D., and Jochum, B. (2016). Permanent electrical resistivity measurements for monitoring water circulation in clayey landslides. *Journal of Applied Geophysics*, 126:98–115.
- García-Fiscal, S. and Flores, C. (2018). Sensitivity of galvanic and inductive induced polarization methods to the Cole-Cole parameters. *Journal of Applied Geophysics*, 158:1–10.
- Hellman, K., Ronczka, M., Günther, T., Wennermark, M., Rücker, C., and Dahlin, T. (2017). Structurally coupled inversion

- of ERT and refraction seismic data combined with cluster-based model integration. *Journal of Applied Geophysics*, 143:169–181.
- Hohmann, G. W. (1975). Three-dimensional induced polarization and electromagnetic modeling. *Geophysics*, 40(2):309–324.
- Kalscheuer, T., Bastani, M., Donohue, S., Persson, L., Pfaffhuber, A. A., Reiser, F., and Ren, Z. (2013). Delineation of a quick clay zone at Smørgrav, Norway, with electromagnetic methods under geotechnical constraints. *Journal of Applied Geophysics*, 92:121–136.
- Kaminski, V. and Viezzoli, A. (2017). Modeling induced polarization effects in helicopter time-domain electromagnetic data: Field case studies heliborne IP effect: Field results. *Geophysics*, 82(2):B49–B61.
- Liu, W., Lin, P., Lü, Q., Li, Y., and Li, J. (2018). Synthetic modelling and analysis of CSEM full-field apparent resistivity response combining EM induction and IP effect for 1d medium. *Exploration Geophysics*, 49(5):609–621.
- Okay, G. (2011). Characterization of textural and hydric heterogeneities in argillaceous geo-materials using induced polarization method: application to the excavation damaged zone (EDZ) of the Tournemire experimental station. *Ecole doctorale ED398 Geosciences et Ressources Naturelles*.
- Pedersen, L. B., Bastani, M., and Dinesius, L. (2005). Groundwater exploration using combined controlled-source and radiomagnetotelluric techniques. *Geophysics*, 70(1):G8–G15.
- Ronczka, M., Hellman, K., Günther, T., Wisén, R., and Dahlin, T. (2017). Electric resistivity and seismic refraction tomography: a challenging joint underwater survey at äspö hard rock laboratory. *Solid Earth*, 8(3):671.
- Supper, R., Ottowitz, D., Jochum, B., Kim, J.-H., Römer, A., Baron, I., Pfeiler, S., Lovisolo, M., Gruber, S., and Vecchiotti, F. (2014). Geoelectrical monitoring: an innovative method to supplement landslide surveillance and early warning. *Near Surface Geophysics*, 12(1):133–150.
- Tang, R., Yu, P., Xiang, Y., and Zhang, X. (2014). The sensitivity analysis of different induced polarization models used in magnetotelluric method. *Acta Geodaetica et Geophysica*, 49(2):225–233.

# Appendix A

This appendix contains three sections. The first section presents the computational basis to characterize the polarization ellipses of the electromagnetic fields, as well as the theoretical phase shift between two orthogonal components of a field in the simple case of an anomaly in a homogeneous flat medium. The second and third sections present work in progress to improve the structural and hydrogeological characterization of the Lodève landslide with TDIP and CSEM methods respectively.

This appendix is written in French in order to fulfill the requirement set by the University of Strasbourg on the writing of English thesis manuscripts.

## A.1 Analyse de la polarisation des champs électromagnétiques

Parce que la théorie du CSAMT est basée sur l'unique existence d'un champ primaire (relatif à un milieu à couches horizontales planes), on peut chercher à isoler, dans les signaux émis, les champs magnétique et électriques primaires, pour baser le calcul du tenseur d'impédance magnétotellurique dessus.

En champ lointain, la théorie nous dit que le champ magnétique primaire (i.e. relatif à un milieu tabulaire plan) est déphasé de  $\pi/4$  par rapport au signal de l'émetteur (chapitre 2, eq. 2.34, Zonge and Hughes [1991]). Le champ électrique, en revanche, ne présente pas ce déphasage.

On peut donc se demander si un traitement possible ne consisterait pas en l'extraction du champ magnétique primaire pour exclusivement le considérer dans le calcul du tenseur d'impédance MT.

Dans un milieu plan homogène, on s'attend à ce que les composantes horizontales de  $\mathbf{H}$  soient déphasés de  $\pi/4$  par rapport à l'émetteur (ce qui revient à une polarisation linéaire). Cependant, lorsque le milieu ne se conforme pas à la théorie (milieu 2D, 3D, variations topographiques), ces considérations peuvent s'avérer incomplètes pour décrire précisément les données. En particulier, dès que l'on sort de ce contexte "idéal", on observe des polarisations elliptiques.

Dans un milieu non tabulaire, les champs décrivent des ellipses (du fait de la complexité du milieu). On démontre ici que la polarisation elliptique s'accompagne, dans certains cas, d'une non-orthogonalité entre les champs en phase et en quadrature respectivement par rapport à l'émetteur. Pour démontrer celà, on montre d'abord que dans un repère orthonormé quelconque, soit une ellipse quelconque, parcourue par un champ magnétique  $\mathbf{H}$ , les projections de ce champ sur les directions définies par une base quelconque orthonormée sont des signaux en phase si et seulement si les vecteurs de bases sont dans la direction du grand et petit axe de l'ellipse (paragraphe "paramétrisation d'une ellipse"). Par contraposée, on en déduit que les directions de projections des signaux en quadrature et en opposition de phase par rapport à l'émetteur sont orthogonales l'une par rapport à l'autre si et seulement si ils sont respectivement dans les directions des grand et petit axes resp.

Pour cette raison, si le signal en quadrature est pivoté d'un angle  $\theta$  par rapport à la direction du grand axe, le signal en opposition de phase par rapport à l'émetteur est selon une direction non orthogonale à celle du signal en quadrature (champ primaire), et il devient délicat et hasardeux de choisir la direction dans laquelle on devrait projeter le champ électrique  $\mathbf{E}$  dans le calcul de  $\mathbf{Z}$ .

### Paramétrisation d'une ellipse :

Soit un repère orthonormé  $\{\vec{e}_G, \vec{e}_p\}$  d'un espace plan, et une ellipse dans le plan  $\{O, \vec{e}_G, \vec{e}_p\}$ , dont le grand axe  $a$  est collinéaire à  $\vec{e}_G$ . Le petit axe  $b$  est donc collinéaire à  $\vec{e}_p$ , et centré en  $O$  (fig. A.1).

Soit une onde EM à la fréquence  $\omega_0$ , polarisée telle que la projection du champ magnétique dans le plan définit par  $\{\vec{e}_G, \vec{e}_p\}$  parcourt de cette ellipse en une période. La projection du champ magnétique ( $\mathbf{H}(t)$  suivant  $\vec{e}_G$  et  $\vec{e}_p$  forment deux signaux périodiques en opposition de phase :  $H_G(t)$  et  $H_p(t)$  respectivement (eq. A.1).

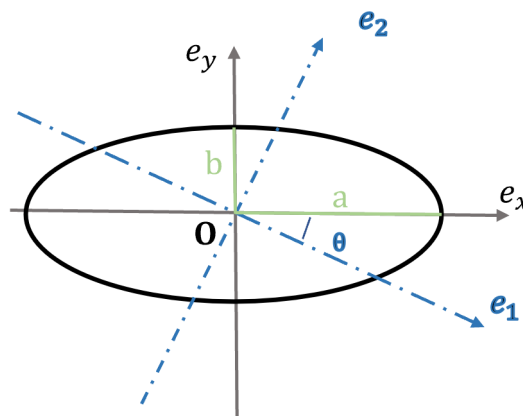


Figure A.1: Ellipse in the plan  $\{O, e_x, e_y\}$

$$\begin{aligned} H_G &= a \cdot \cos(\omega_0 t) \\ H_p &= b \cdot \sin(\omega_0 t) \end{aligned} \quad (\text{A.1})$$

Si les séries temporelles issues de la projection des signaux dans la direction du grand et du petit axe de l'ellipse sont en quadratures. On veut montrer ici que les projections sur un repère quelconque tel que  $\{\vec{e}_1, \vec{e}_2\}$  ne sont pas nécessairement deux signaux en quadrature.

Soit  $H_1$  et  $H_2$  les projections de  $H(t)$  sur  $\vec{e}_1$  et  $\vec{e}_2$  respectivement. On a :

$$\begin{aligned} \vec{e}_1 &= \cos\theta \cdot \vec{e}_G - \sin\theta \cdot \vec{e}_p \\ \vec{e}_2 &= \sin\theta \cdot \vec{e}_G + \cos\theta \cdot \vec{e}_p \end{aligned} \quad (\text{A.2})$$

$$\begin{aligned} H_1 &= a \cdot \cos\theta \cdot \cos(\omega_0 t) - b \cdot \sin\theta \cdot \sin(\omega_0 t) \\ H_2 &= a \cdot \sin\theta \cdot \cos(\omega_0 t) + b \cdot \cos\theta \cdot \sin(\omega_0 t) \end{aligned} \quad (\text{A.3})$$

Il n'est *a priori* pas évident que ces deux signaux ne sont pas en quadrature l'un par rapport à l'autre. Les transformées de fourier de ces deux signaux sont données en eq. A.6.

$$\begin{aligned} \hat{H}_1 &= \frac{a \cos\theta}{2} \cdot [\delta(\omega - \omega_0) + \delta(\omega + \omega_0)] + i \frac{b \sin\theta}{2} \cdot [\delta(\omega - \omega_0) - \delta(\omega + \omega_0)] \\ \hat{H}_2 &= -\frac{a \sin\theta}{2} \cdot [\delta(\omega - \omega_0) + \delta(\omega + \omega_0)] - i \frac{b \cos\theta}{2} \cdot [\delta(\omega - \omega_0) - \delta(\omega + \omega_0)] \end{aligned} \quad (\text{A.4})$$

Par définition, on peut calculer la phase de  $\hat{H}_1$  et  $\hat{H}_2$  :  $\Phi_1$  et  $\Phi_2$ .

$$\begin{aligned} \Phi_1 &= \arctan\left(\frac{b \sin\theta \cdot [\delta(\omega - \omega_0) - \delta(\omega + \omega_0)]}{a \cos\theta \cdot [\delta(\omega - \omega_0) + \delta(\omega + \omega_0)]}\right) \\ \Phi_2 &= \arctan\left(\frac{b \cos\theta \cdot [\delta(\omega - \omega_0) - \delta(\omega + \omega_0)]}{a \sin\theta \cdot [\delta(\omega - \omega_0) + \delta(\omega + \omega_0)]}\right) \end{aligned} \quad (\text{A.5})$$

C'est à dire que :

$$\begin{aligned} \Phi_1 &= \arctan\left(\frac{b \sin\theta}{a \cos\theta}\right) \quad \text{pour } \omega = +\omega_0 \\ \Phi_1 &= \arctan\left(\frac{-b \sin\theta}{a \cos\theta}\right) \quad \text{pour } \omega = -\omega_0 \\ \Phi_2 &= \arctan\left(\frac{b \cos\theta}{a \sin\theta}\right) \quad \text{pour } \omega = +\omega_0 \\ \Phi_2 &= \arctan\left(\frac{-b \cos\theta}{a \sin\theta}\right) \quad \text{pour } \omega = -\omega_0 \end{aligned} \quad (\text{A.6})$$

On se concentre sur la solution  $\omega = \omega_0$ . On a donc les cas particuliers suivant :

$$\Phi_1 = \Phi_2 \text{ ssi } \cos\theta = \sin\theta \text{ i.e. } \theta = \pi/4$$

On sait par définition dla fonction  $\arctan$  que  $\arctan(x) - \arctan(y) = \pi/2$  ssi  $\{x = -1/y; x > 0\}$  ou bien  $\{x = 0, y = -\infty\}$  qui est l'extension de la première condition lorsque l'on fait tendre  $x$  vers 0 . Ainsi, pour que  $\Phi_1$  et  $\Phi_2$  soient en quadrature, il est donc nécessaire que :

$$\frac{b \sin\theta}{a \cos\theta} = \left(\frac{b \cos\theta}{a \sin\theta}\right)^{-1} \quad (\text{A.7})$$

Ce qui n'est le cas que si  $a = b$ ;  $\sin\theta = 0$  et le cas limite  $\cos\theta \rightarrow 0$ . Les deux dernières conditions nous ramène au cas où les vecteurs de base, sur lesquels la projection de l'ellipse est faite, sont dans les directions du petit et grand axes de l'ellipse.  $a = b$  est le cas dégénéré du cercle.

**Extraction et détermination des directions du champ primaire (déphasé de  $\pi/4$  par rapport à l'émetteur) et secondaire**

$$\begin{aligned}\hat{\mathbf{H}}_{primaire} &= \Re \left( [\hat{H}_x, \hat{H}_y] \frac{1}{e^{i(\Phi_{Tx} - \pi/4)}} \right) \\ \hat{\mathbf{H}}_{secondaire} &= \Im \left( [\hat{H}_x, \hat{H}_y] \frac{1}{e^{i(\Phi_{Tx} - 3\pi/4)}} \right)\end{aligned}\quad (\text{A.8})$$

Les directions d'orientation des champs en phase et en quadrature sont données respectivement par la direction de  $\hat{\mathbf{H}}_{primaire}$  et  $\hat{\mathbf{H}}_{secondaire}$ .

### Calculs des champs secondaires selon le formalisme de Grant Caldwell et al. [2002]

On a considéré jusqu'à présent que un champ secondaire est en quadrature par rapport au champ primaire. Cependant, on cherche ici à décrire de manière plus précise ce qui contrôle la phase du champ secondaire, lorsque l'on fait des mesures en champ lointain. Le formalisme utilisé dans les travaux de Grant Caldwell et al. [2002] consiste en une expression tensorielle des fonctions de transfert magnétiques et électriques du milieu, visant à l'identification de paramètres apparents qui soient au plus proche possible de la résistivité apparente au sens de la mesure apparente réalisée dans le cas de mesures DC. Dans cette sous-partie le raisonnement porte sur le champ électrique car sa formulation est plus simple vis-à-vis de l'émetteur, le champ primaire étant en phase avec ce dernier. Le même raisonnement sur le champ magnétique fournirait les mêmes observations.

Dans ce contexte, les équations formulant le vecteur champ électrique  $\mathbf{E}$  en fonction du vecteur densité de courant  $\mathbf{J}$  s'écrivent, dans le domaine fréquentiel, sous la forme :

$$\mathbf{E}(\omega) = \widetilde{\rho}_a(\omega) \mathbf{J} \quad (\text{A.9})$$

avec

$$\mathbf{J} = \frac{I}{2\pi r^3} \mathbf{d} \quad (\text{A.10})$$

$r$  étant la distance source station et  $\mathbf{d}$  étant le vecteur directeur du dipôle émetteur, de norme égal à la dimension du dipôle.  $J$  exprime la densité de courant locale générée en un point donné de l'espace par un dipôle de courant localisé en un second point de l'espace.

$\widetilde{\rho}_a$  est un tenseur d'ordre 2, qui prend la forme général, dans un milieu 1D :

$$\widetilde{\rho}_a = \rho \begin{bmatrix} 1 - g(ikr)/2 & 0 \\ 0 & 1 + g(ikr) \end{bmatrix} \quad (\text{A.11})$$

où  $g$  est la fonction de réponse impulsionnelle en domaine fréquentiel :  $g(ikr) = [1 - (ikr + 1)e^{-ikr}]$ .

Dans le cas du champ proche et du champ lointain, qui sont exprimés dans ce formalisme par les cas asymptotiques  $\omega \rightarrow 0$  et  $\omega \rightarrow \infty$  respectivement,  $g$  prend les valeurs 0 et 1 respectivement. On obtient donc les tenseurs limites suivants :

$$\widetilde{\rho}_a(\omega \rightarrow 0) = \rho \begin{bmatrix} 1 & 0 \\ 0 & 1 \end{bmatrix} \quad (\text{A.12})$$

$$\widetilde{\rho}_a(\omega \rightarrow \infty) = \rho \begin{bmatrix} 1/2 & 0 \\ 0 & 2 \end{bmatrix} \quad (\text{A.13})$$

A partir de ce formalisme, on peut exprimer le champ total généré dans un milieu homogène ou 1D dans lequel se trouve une anomalie. On se place dans le plan représenté en fig. A.2 : un émetteur centré au point O génère le vecteur densité de courant  $\mathbf{J}$  dans le milieu. Le milieu est un milieu homogène de résistivité  $\rho$ , qui contient une anomalie de résistivité  $\rho_s$  localisée en A. La "mesure" est prise au point M. On appelle B1 la base orthonormée de l'espace composée des vecteurs  $\{\vec{e}_{r1}; \vec{e}_{\theta1}\}$ , c'est à dire le repère polaire local en M, centré en O. B2 est la base orthonormée de l'espace composée des vecteurs  $\{\vec{e}_{r2}; \vec{e}_{\theta2}\}$  et B3 celle composée des vecteurs  $\{\vec{e}_{r3}; \vec{e}_{\theta3}\}$ . Dans les formules suivantes, la base dans laquelle les tenseurs et vecteurs sont exprimés est indiquée en indice par B1, B2 ou B3.

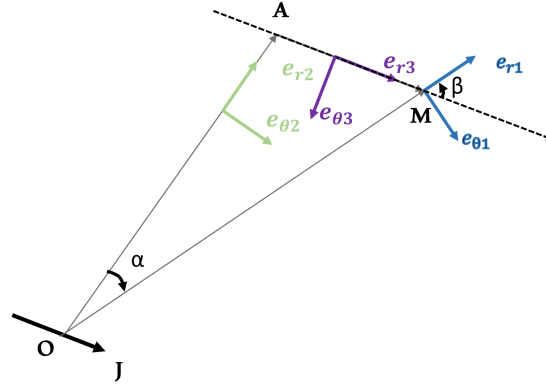


Figure A.2: Schema précisant la géométrie du problème : un dipôle émetteur centré en O génère une densité de courant source  $\mathbf{J}$ , la mesure est réalisée au point M, et une anomalie de résistivité est localisée en A. La base  $\{e_{r1}; e_{\theta1}\}$  est le repère polaire local en M centré en O. De même, on définit le repère local en A :  $\{e_{r3}; e_{\theta3}\}$

On considère exclusivement le cas où M est suffisamment distant de l'émetteur pour que  $kr_M \gg 1$ , avec  $r_M$  la distance entre l'émetteur et M : on se considère en champ lointain, et  $\omega \rightarrow \infty$ . Par ailleurs on suppose que A est relativement proche de M, sans quoi le signal secondaire généré par l'anomalie est négligeable en M.

En M, le champ total est la somme du champ primaire et du champ secondaire généré par l'anomalie en A :

$$\mathbf{E}(M) = \mathbf{E}_p(M) + \mathbf{E}_s(M) \quad (\text{A.14})$$

En suivant l'équation A.9, et parce qu'on considère que M est dans la zone de champ lointain de la source primaire à la fréquence  $\omega$  et pour une résistivité  $\rho$ , on identifie :

$$\mathbf{E}_p(M) = \rho \begin{bmatrix} 1/2 & 0 \\ 0 & 2 \end{bmatrix}_{B1} \cdot \mathbf{J}_{B1}(M) \quad (\text{A.15})$$

En revanche, on n'émet pas d'hypothèse sur le domaine dans lequel le champ secondaire est mesuré. Il pourrait être cohérent de considérer que la station est dans le champ proche de la source secondaire, car si la source secondaire est trop éloignée de la station, il est probable que le signal secondaire ne soit pas mesuré. Cependant, on n'exclue pas le cas où un signal secondaire en "champ transitionnel" est mesuré, on reste donc dans le cas général :

$$\mathbf{E}_s(M) = \rho \begin{bmatrix} 1 - g(ik|AM|)/2 & 0 \\ 0 & 1 + g(ik|AM|) \end{bmatrix}_{B3} \cdot \mathbf{J}_{sB3} \quad (\text{A.16})$$

$\mathbf{J}_s$  est la densité de courant générée en A, et s'exprime de la manière suivante :

$$\mathbf{J}_s = -i\omega\mu \left( \frac{1}{\rho_s} - \frac{1}{\rho} \right) \cdot \mathbf{E}_p(A) \quad (\text{A.17})$$

$\mathbf{E}_p(A)$  s'exprime dans le repère  $\{e_{r2}; e_{\theta2}\}$  de la manière suivante :

$$\mathbf{E}_p(A) = \rho \begin{bmatrix} 1/2 & 0 \\ 0 & 2 \end{bmatrix}_{B2} \cdot \mathbf{J}_{B2}(A) \quad (\text{A.18})$$

On peut donc rassembler les expressions obtenues pour le champ primaire et secondaire, exprimés dans les différents repères en jeu :

$$\mathbf{E}(M) = \left( \rho \begin{bmatrix} 1/2 & 0 \\ 0 & 2 \end{bmatrix}_{B1} \cdot \mathbf{J} \right)_{B1} + \left( \rho \begin{bmatrix} 1 - g(ik|AM|)/2 & 0 \\ 0 & 1 + g(ik|AM|)/2 \end{bmatrix}_{B3} \cdot \left( (-i\omega\mu) \left( \frac{\rho}{\rho_s} - 1 \right) \begin{bmatrix} 1/2 & 0 \\ 0 & 2 \end{bmatrix}_{B2} \cdot \mathbf{J} \right)_{B2} \right) \quad (\text{A.19})$$

En présence de l'anomalie de résistivité  $\rho_s$  dans un endroit quelconque de l'espace, la partie imaginaire des composantes de  $\mathbf{E}$  dans la base  $\{e_{r1}; e_{\theta1}\}$  dépendent de la localisation de l'anomalie. Soit  $\alpha$  l'angle orienté de  $\mathbf{e}_{r2}$  à  $\mathbf{e}_{r1}$  et  $\beta$  l'angle orienté de  $\mathbf{e}_{r3}$  à  $\mathbf{e}_{r1}$  tel que montré en fig. A.2. On applique la rotation :

$$\begin{aligned} \left[ \begin{array}{cc} 1 - g(ikr)/2 & 0 \\ 0 & 1 + g(ikr) \end{array} \right]_{B3 \rightarrow B1} &\Rightarrow \left( \left[ \begin{array}{cc} \cos\beta & \sin\beta \\ -\sin\beta & \cos\beta \end{array} \right] \cdot \left[ \begin{array}{cc} 1 - g(ikr)/2 & 0 \\ 0 & 1 + g(ikr) \end{array} \right]_{B3} \cdot \left[ \begin{array}{cc} \cos\beta & -\sin\beta \\ \sin\beta & \cos\beta \end{array} \right] \right)_{B1} \\ &= \left[ \begin{array}{cc} 1 + g(ikr) \left( \sin^2\beta + \frac{\cos^2\beta}{2} \right) & \cos\beta \sin\beta g(ikr) \frac{3}{2} \\ \cos\beta \sin\beta g(ikr) \frac{3}{2} & 1 + g(ikr) \left( \cos^2\beta + \frac{\sin^2\beta}{2} \right) \end{array} \right]_{B1} \end{aligned} \quad (\text{A.20})$$

Et

$$\mathbf{J}_{B1} = \begin{bmatrix} \cos\alpha & \sin\alpha \\ -\sin\alpha & \cos\alpha \end{bmatrix} \cdot \mathbf{J}_{B2} \quad (\text{A.21})$$

Par ailleurs

$$\begin{aligned} \mathbf{J}_{B1}(\text{M}) &= \frac{\text{I}}{2\pi|\text{OM}|^3} \mathbf{d}_{B1} \\ \mathbf{J}_{B1}(\text{A}) &= \frac{\text{I}}{2\pi|\text{OA}|^3} \mathbf{d}_{B1} \end{aligned} \quad (\text{A.22})$$

ainsi,  $\mathbf{J}_{B1}(\text{M})$  et  $\mathbf{J}_{B1}(\text{A})$  sont collinéaires et égaux à un facteur multiplicatif près sur la norme, qu'on appellera  $c$  :

$$\mathbf{J}_{B1}(\text{M}) = \frac{|\text{OA}|^3}{|\text{OM}|^3} \mathbf{J}_{B1}(\text{A}) = c \mathbf{J}_{B1}(\text{A}) \quad (\text{A.23})$$

Enfin

$$\begin{aligned} \left[ \left[ \begin{array}{cc} 1/2 & 0 \\ 0 & 2 \end{array} \right] \cdot \mathbf{J} \right]_{B2 \rightarrow B1} &\Rightarrow \left( \left[ \begin{array}{cc} \cos\alpha & \sin\alpha \\ -\sin\alpha & \cos\alpha \end{array} \right] \cdot \left[ \begin{array}{cc} 1/2 & 0 \\ 0 & 2 \end{array} \right]_{B2} \cdot \left[ \begin{array}{cc} \cos\alpha & -\sin\alpha \\ \sin\alpha & \cos\alpha \end{array} \right] \cdot \left[ \begin{array}{cc} \cos\alpha & \sin\alpha \\ -\sin\alpha & \cos\alpha \end{array} \right] \cdot \mathbf{J}_{B2} \right)_{B1} \\ &= \left[ \begin{array}{cc} \frac{\cos\alpha}{2} & 2\sin\alpha \\ -\frac{\sin\alpha}{2} & 2\cos\alpha \end{array} \right]_{B1} \cdot \mathbf{J}_{B1} \end{aligned} \quad (\text{A.24})$$

Ainsi, l'expression du champ électrique total dans le repère de base B1 est la formule suivante:

$$\begin{aligned} \mathbf{E}_s(\text{M}) &= \rho \left[ \begin{array}{cc} 1 - g(ik|\text{AM}|)/2 & 0 \\ 0 & 1 + g(ik|\text{AM}|) \end{array} \right]_{B3} \cdot (-i\omega\mu \left( \frac{1}{\rho_s} - \frac{1}{\rho} \right) \rho) \left[ \begin{array}{cc} 1/2 & 0 \\ 0 & 2 \end{array} \right]_{B2} \cdot \mathbf{J}_{B2}(\text{A}) \\ &= -i\omega\mu\rho^2 \left( \frac{1}{\rho_s} - \frac{1}{\rho} \right) \left[ \begin{array}{cc} 1 + g(ik|\text{AM}|) \left( \sin^2\beta + \frac{\cos^2\beta}{2} \right) & \cos\beta \sin\beta g(ik|\text{AM}|) \frac{3}{2} \\ \cos\beta \sin\beta g(ik|\text{AM}|) \frac{3}{2} & 1 + g(ik|\text{AM}|) \left( \cos^2\beta + \frac{\sin^2\beta}{2} \right) \end{array} \right]_{B1} \cdot \left[ \begin{array}{cc} \frac{\cos\alpha}{2} & 2\sin\alpha \\ -\frac{\sin\alpha}{2} & 2\cos\alpha \end{array} \right]_{B1} \cdot \mathbf{J}_{B1}(\text{A}) \end{aligned} \quad (\text{A.25})$$

Dans un premier temps, on se place dans le cas limite  $r \rightarrow 0$  ou, de manière équivalente  $\omega \rightarrow 0$  : on a alors  $g(ikr) \rightarrow 0$ .

$$\mathbf{E}(\text{M}) = \mathbf{E}_p(\text{M}) + \mathbf{E}_s(\text{M})$$

$$= \rho \left[ \begin{array}{cc} 1/2 & 0 \\ 0 & 2 \end{array} \right] \cdot \mathbf{J}_{B1}(\text{M}) + (-i\omega\mu\rho^2 \left( \frac{1}{\rho_s} - \frac{1}{\rho} \right)) \left[ \begin{array}{cc} 1 & 0 \\ 0 & 1 \end{array} \right] \cdot \left[ \begin{array}{cc} \frac{\cos\alpha}{2} & 2\sin\alpha \\ -\frac{\sin\alpha}{2} & 2\cos\alpha \end{array} \right]_{B1} \cdot c \mathbf{J}_{B1}(\text{M}) \quad (\text{A.26})$$

$$= \rho \left[ \begin{array}{cc} \frac{1}{2} - \frac{1}{2}i\omega\mu c \left( \frac{\rho}{\rho_s} - 1 \right) \cos\alpha & -2i\omega\mu c \left( \frac{\rho}{\rho_s} - 1 \right) \sin\alpha \\ \frac{1}{2}i\omega\mu c \left( \frac{\rho}{\rho_s} - 1 \right) \sin\alpha & 2 - 2i\omega\mu c \left( \frac{\rho}{\rho_s} - 1 \right) \cos\alpha \end{array} \right] \cdot \mathbf{J}_{B1}(\text{M})$$

$$\mathbf{E}(M) = \begin{bmatrix} \frac{\rho J_r}{2} - i\left(\frac{\rho J_r}{2}\omega\mu c\left(\frac{\rho}{\rho_s} - 1\right)\cos\alpha + 2\rho J_\theta\omega\mu c\left(\frac{\rho}{\rho_s} - 1\right)\sin\alpha\right) \\ 2\rho J_\theta + i\left(\frac{\rho J_r}{2}\omega\mu c\left(\frac{\rho}{\rho_s} - 1\right)\sin\alpha - 2\rho J_\theta\omega\mu c\left(\frac{\rho}{\rho_s} - 1\right)\cos\alpha\right) \end{bmatrix} \quad (\text{A.27})$$

Sous cette forme, on isole bien le champ primaire du champ secondaire. L'intensité du champ secondaire par rapport au champ primaire dans chacune des directions, et donc les propriétés de l'ellipse de polarisation, dépend fortement de la géométrie du problème : 1/ de l'angle  $\alpha$  2/ de l'angle entre le vecteur directeur du dipôle émetteur  $\mathbf{d}$  et  $e_{r1}$  (ratio entre les deux composantes de  $\mathbf{J}$ ), 3/ des distances  $|\text{OM}|$  et  $|\text{OA}|$  (via le coefficient  $c$ ).

Si maintenant l'hypothèse  $|\text{AM}| \rightarrow 0$  n'est pas valide, l'écriture du champ secondaire, et donc les déphasages des composantes du champ total sur la base B1 fait intervenir en supplément l'angle  $\beta$  ainsi que la distance  $|\text{AM}|$ . Le champ secondaire introduit notamment une composante en phase avec l'émetteur car  $g(\text{ikr})$  devient complexe. Dans une telle situation, le champ secondaire n'est plus dissociable du champ primaire par une simple considération sur la phase.

## A.2 Caractérisation du glissement de terrain de Lodève par mesures TDIP 2D et 3D

En mars 2019, deux profils de TDIP ont été mesurés. Le premier profil, qui a été répété en juillet et octobre 2019, à fait l'objet d'une étude time-lapse présentée dans le chapitre 5. Le second, dont la localisation est présentée dans la fig. 5.25, a été installé de manière non linéique (fig. A.3), imposant son interprétation par inversion 3D des données. Cette inversion 3D n'a pas pu être réalisée dans le contexte de cette thèse. Cependant, une méthode de traitement, prenant en compte la sinuosité du profile, a été imaginée et le traitement complet de ce profile est présenté ci-après.

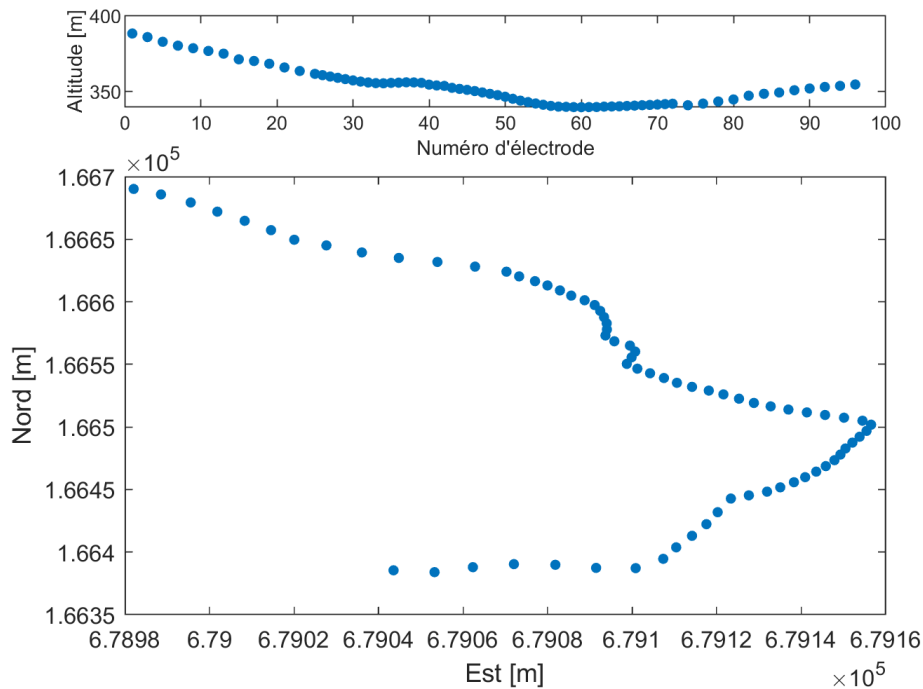


Figure A.3: profile altimétrique et carte horizontale du profile 2

Les étapes du traitement sont celles indiquées comme les "standard processing for static data" (traitements standards pour des données statiques) dans la fig. 5.26 : Importation des données et calcul du facteur géométrique, suppression des données dont la résistivité apparente est négative ou bien dont la phase apparente est positive, et suppression des données aberrantes.

Parce que le profil est sinueux, calculer le facteur géométrique sur la base d'un profil linéique est incorrect. Cependant, car il y a des variations topographiques, le calcul du facteur géométrique n'est possible que par un travail de modélisation 3D (voir chapitre 4). On propose dans l'eq. A.28 une formule pour évaluer  $k$  dans le cas d'électrodes non alignées.

$$k_{2D} = \frac{2\pi}{\frac{1}{\sqrt{(x_A - x_M)^2 + (y_A - y_M)^2}} - \frac{1}{\sqrt{(x_A - x_N)^2 + (y_A - y_N)^2}} - \frac{1}{\sqrt{(x_B - x_M)^2 + (y_B - y_M)^2}} + \frac{1}{\sqrt{(x_B - x_N)^2 + (y_B - y_N)^2}}} \quad (\text{A.28})$$

où  $x$  et  $y$  sont les coordonnées sur une base orthonormée quelconque du plan, les indices A, B, M et N se rapportent aux deux électrodes d'injection aux deux électrodes de potentiel resp..

Par ce calcul, on espère approcher le vrai facteur géométrique 3D aux endroits où le profil est non linéique. En particulier, les distortions attendues, qui peuvent potentiellement générer des changements de signes du potentiel, et qui entraîneraient donc des données non acceptables (telles que  $\rho < 0$ ) seront ainsi en partie corrigées. En effet, même si les variations topographiques rendent le facteur  $2\pi$  largement discutable, calculer un facteur géométrique dans le plan permet tout de même une évaluation correcte du signe de  $k$ , ce qui reste le plus important pour un filtrage correct des données. Fig. A.4 présente les pseudo-sections après suppression des résistivités négatives et phases positives dans le cas du calcul de  $k$  pour des électrodes alignées. De nombreuses anomalies sont observables, qui disparaissent par l'utilisation du facteur géométrique 2D  $k_{2D}$  présenté dans l'équation A.28 (fig. A.5).

Parce que les mesures ont été faites sur ce profil, de manière normale et réciproque (Flores Orozco et al. [2012]), une analyse poussée des incertitudes sur les données pourrait être réalisée, mais cette analyse n'a pas été faite pour ce travail. Cependant, la comparaison visuelle des pseudo-sections des mesures normale et réciproque permet d'apprécier une concordance *a priori* et non quantifiée des deux mesures (fig. A.6 et A.7).

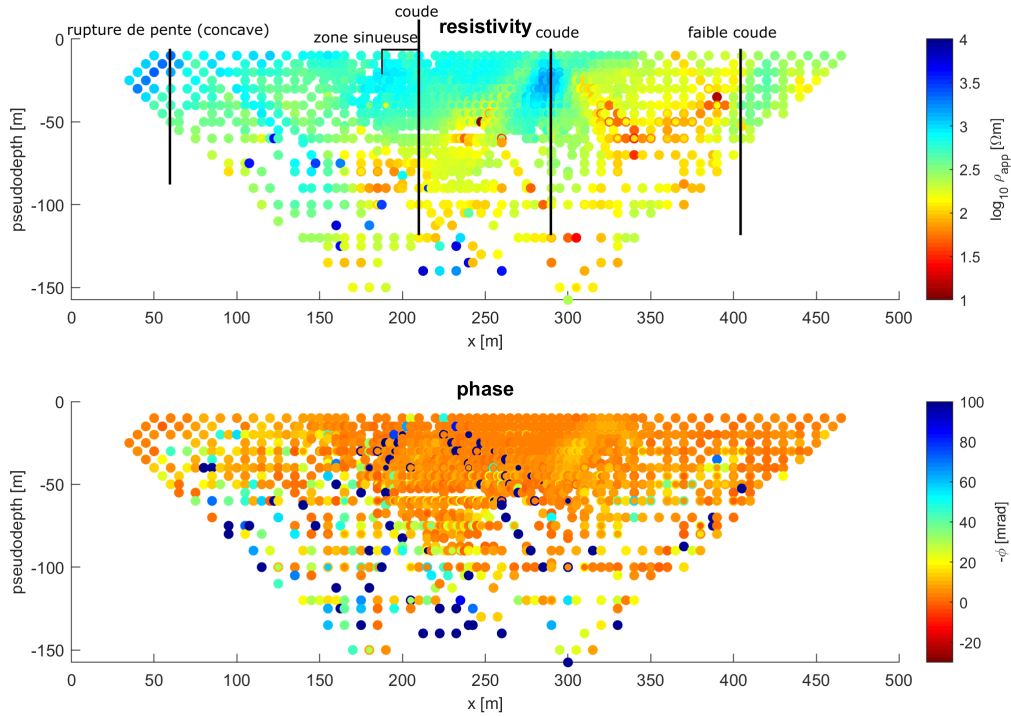


Figure A.4: Pseudo-section des résistivités et phases apparentes, filtrée des résistivités apparentes négatives et des phases positive, sur la base du calcul de  $k$  à une dimension (i.e. en supposant que le profil est linéique). Des anomalies apparaissent clairement, sur la pseudo-section des résistivités apparentes, aux endroits où le profil forme des coude. (mesures réciproques)

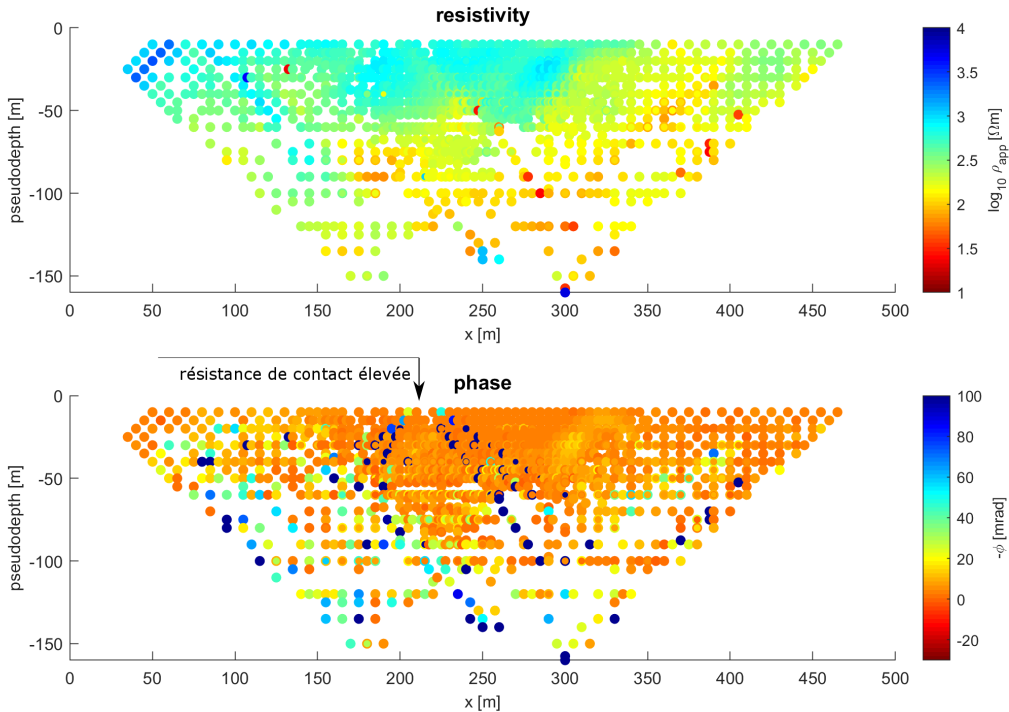


Figure A.5: Pseudo-section des résistivités et phases apparentes, filtrée des résistivités apparentes négatives et des phases positive, sur la base du calcul de  $k_{2D}$ . De nombreuses anomalies de la figure précédente disparaissent. On note sur le profil des phases apparentes un mauvais contact sur une électrode, qui présente systématiquement des polarisations élevées (le long d'une forme en V inversé).

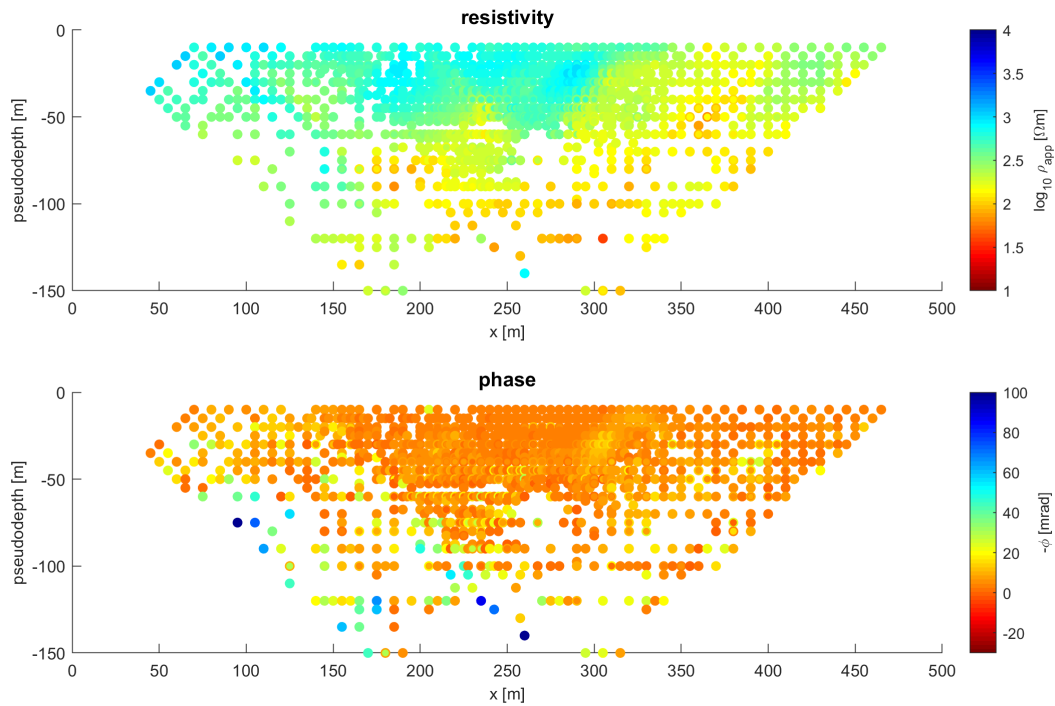


Figure A.6: Pseudo-section des mesures réciproques traitées (calcul de  $k_{2D}$ , suppression des résistivités apparentes négatives et phases apparentes positives et suppression des données aberrantes)

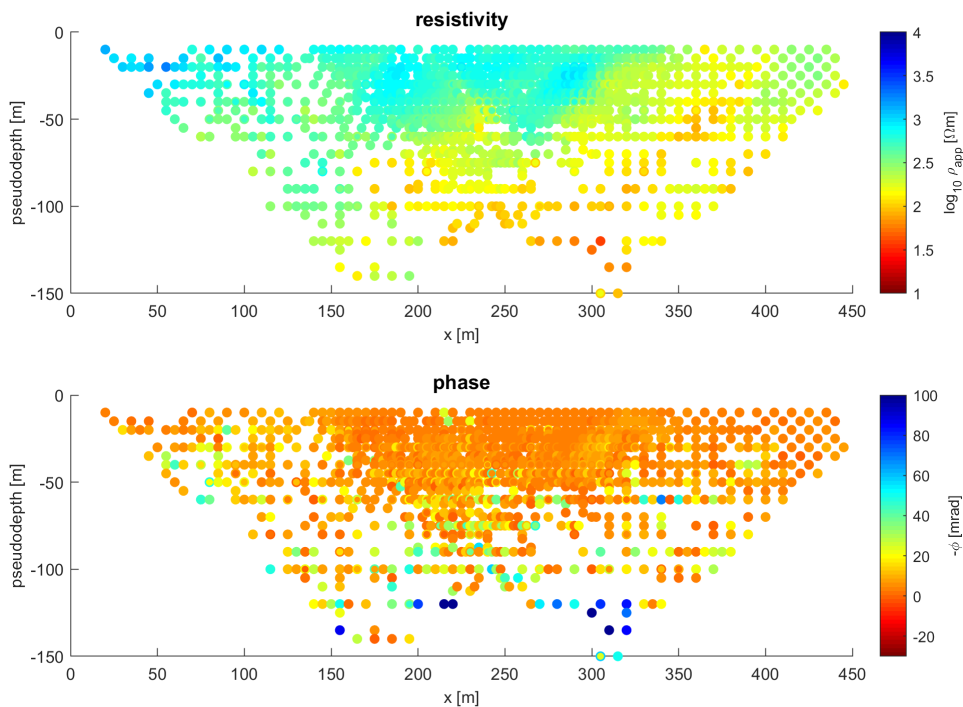


Figure A.7: Pseudo-section des mesures normales traitées (calcul de  $k_{2D}$ , suppression des résistivités apparentes négatives et phases apparentes positives et suppression des données aberrantes)

## A.3 Caractérisation de la structure 3D du glissement de terrain de Lodève par la méthode CSEM

Afin de compléter l'étude time-lapse du glissement de terrain de Lodève par la méthode CSAMT, qui fait l'objet du chapitre 5 de cette thèse, des mesures de CSEM (i.e. CSAMT en champ transitionnel et proche) ont été réalisées sur le site. L'objectif était de fournir un modèle statique de résistivité électrique correspondant à l'état du milieu lors de la première mesure time-lapse. Ce modèle initial pourrait servir de base pour évaluer les éventuels effets 2D et 3D en fournissant les variations latéral de résistivité.

Cette annexe présente les données, les traitements et filtrages réalisés, ainsi qu'une tentative d'inversion des données avec l'outil PolyEM3D.

### A.3.1 Méthodologie de mesure

Des mesures ont été réalisées en Novembre 2018 sur l'ensemble du site (carte en fig. A.8) avec des stations complètes en configuration "vecteur" (champ électriques et magnétiques) et avec des stations électriques. Deux dipôles émetteurs de 200 et ;190 m de longueur ont été utilisés, tout deux situés à 1 km au nord du site, dans un champ relativement plat et conducteur.

Les données 3D ont été acquises avec des équipements de chez Phoenix Geophysics. Le signal source était produit alternativement par deux dipôles électriques au nord du glissement. L'échantillonnage spatiale consiste en 13 stations complètes (2E, 3H) et 9 stations électriques (2E) sur 400x300 m<sup>2</sup>. Cette méthode avait été utilisée dans l'hypothèse que le champ magnétique serait relativement stable sur l'ensemble du site. Les mesures ont été faites pour des fréquences fondamentales comprises entre 512 Hz et 9600 Hz, avec une fréquence d'échantillonnage de 24 kHz maximum.

Les dipôles émetteurs n'ont pas été positionnés suffisamment loin du site pour que les signaux soient en champ lointain sur l'ensemble de la bande de fréquence. Pour cette raison, un traitement et une interprétation basée sur le CSEM (nécessitant la modélisation de l'émetteur) est nécessaire.

### A.3.2 Analyse de la qualité et traitement des données

Parce que les capteurs 3ER semblaient nécessiter une étude de qualité particulière qui n'a pas pu être réalisée pendant cette thèse, seules les données mesurées par le V8 ont été utilisées (mesure du champ magnétique et électrique horizontaux).

Pour évaluer la qualité des données, les cartes de polarisation ont été réalisées, et comparées avec les polarisations théoriques obtenues dans le cas d'un modèle plan homogène. Les fonctions de transfert électriques et magnétiques ont été représentées ainsi que les diagrammes d'Argand, pour évaluer le bruit et la qualité des données.

**Cartes de polarisation:** Les cartes de polarisation ont montré que les données mesurées avec le second dipôle émetteur, orienté dans la direction Nord/Sud, sont beaucoup moins stables spatialement que celles mesurées avec le premier dipôle émetteur. Elles présentent par ailleurs des polarisations relativement loin de ce que la théorie semble prévoir pour un milieu homogène. Pour cette raison, seules les données issues du premier dipôle émetteur ont été analysées et ont été l'objet d'une tentative d'inversion.

**Fonctions de transfert électriques et magnétiques du milieu:** Les fonctions de transfert électriques et magnétiques du milieu ont été calculées, révélant que les mesures réalisées à 9 stations sont de bonne qualité et relativement peu bruitées. La fig. A.11 présente un exemple relativement bruité de fonction de transfert obtenue. Généralement, il a été observé que le champ magnétique est plus bruité que le champ électrique.

#### Diagrammes d'Argand:

Représenter les mesures dans le domaine d'Argand  $\{\Re(E/Tx), \Im(E/Tx)\}$  peut permettre d'évaluer la qualité des mesures (Hannesson and West [1984]). Une donnée de bonne qualité montrera une courbe régulière dont la forme est une spirale autour du centre du repère, qui converge vers zéro aux hautes fréquences (l'amplitude

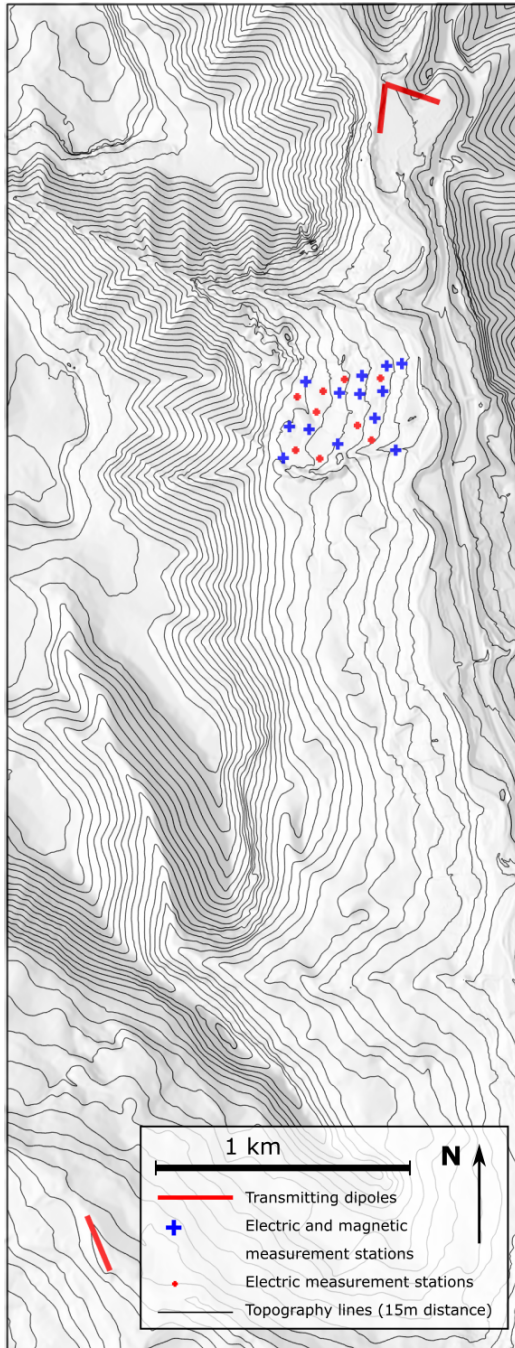


Figure A.8: Carte de la campagne de CSEM en champs proche: stations de mesure et dipôles d'émission

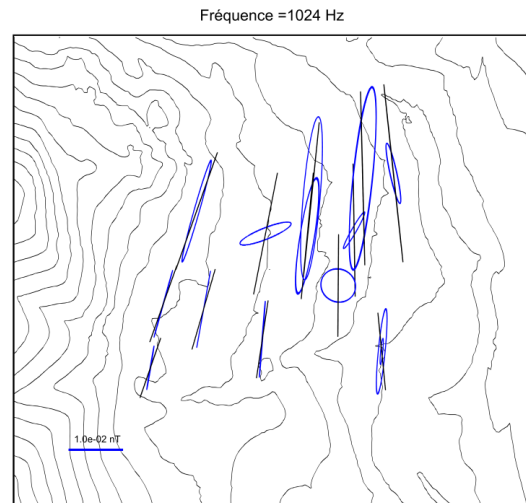


Figure A.9: Carte de polarisation du champ magnétique généré par le dipôle 1 orienté Est-Ouest. Les mesures figurent en bleu, et la modélisation pour un milieu homogène plan à 1000 Ohm.m est représentée en noir.

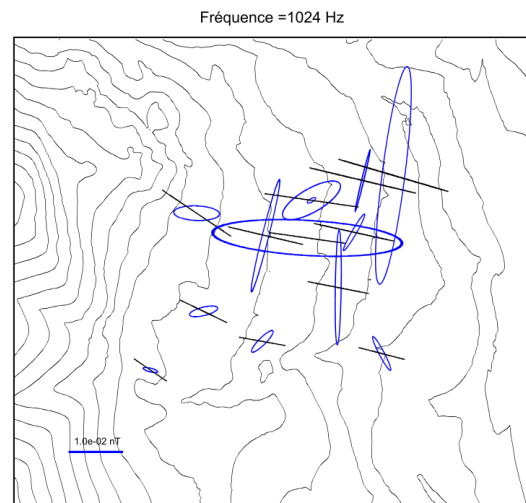


Figure A.10: Carte de polarisation du champ magnétique généré par le dipôle 2 orienté Nord-Sud. Les mesures figurent en bleu, et la modélisation pour un milieu homogène plan à 1000 Ohm.m est représentée en noir.

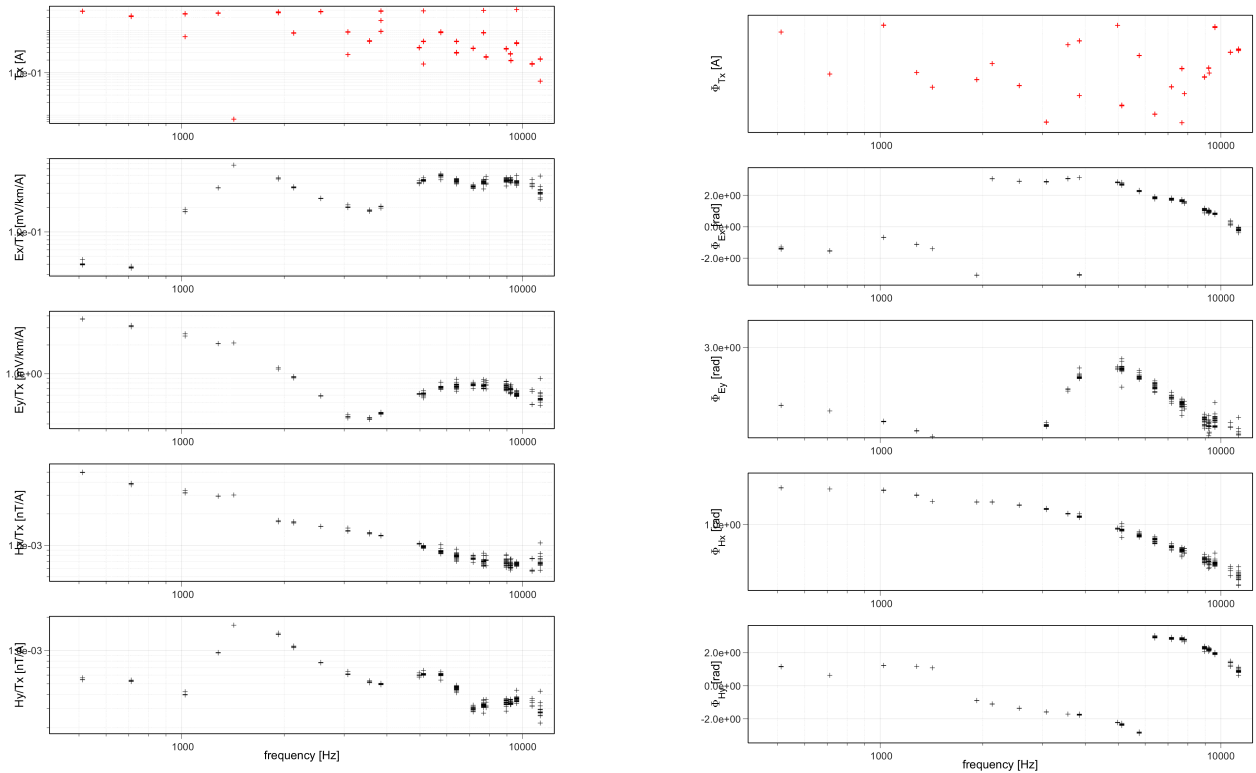


Figure A.11: Signal émis à l'émetteur (en rouge) et fonctions de transfert (amplitude à gauche phase à droite) électriques et magnétiques du milieu

de la réponse diminue), de manière tangente à l'axe des abscisses (la phase vaut zéro en champ lointain). La fig. A.12 représente les diagrammes d'Argand pour la composante Est et Nord sur une station de bonne qualité.

### A.3.3 POLYEM3D : CSEM modeling and inversion software

Une tentative d'inversion des données a été réalisée avec le logiciel d'inversion PolyEM3D (Bretaudeau et al. [2017]), un code de calcul parallèle en différences finies permettant le calcul direct et inverse lié au problème 3D en CSEM. Ce code peut être lancé sur plusieurs solveurs, et a été utilisé sur le super-calculateur du centre Cines.

#### Calcul direct

Le calcul des champs électrique et magnétique générés par une source électromagnétique est fait par le biais d'une formulation en volumes finis du champ électrique. Le calcul direct est basé sur un calcul hybride semi-analytique : le calcul de champ primaire (champ théorique pour un milieu homogène ou milieu en couches horizontales homogènes) est fait par calcul analytique (Streich [2009]) pour lequel le milieu n'a pas besoin d'être discrétisé d'aucune manière que ce soit. La résolution du champ secondaire, provoqué par des anomalies (2D, 3D), se fait par l'intermédiaire du calcul du champ total sur une grille adaptée aux calculs en volumes finis. Le champ secondaire est ensuite obtenu par soustraction du champ primaire, projeté sur la grille aux volumes finis au champ total. Le calcul du champ total se fait par l'inversion de la matrice  $A$  de l'équation (4). Inverser la matrice  $A$  est une opération lourde, pour laquelle il est nécessaire de passer par une parallélisation du calcul. Pour ce faire, deux solveurs sont utilisés : MUMPS et WSMP.

Le champ primaire est calculé, dans POLYEM3D, analytiquement, en suivant Streich [2009]. Ce calcul ne nécessite donc pas de discrétisation particulière de l'espace.

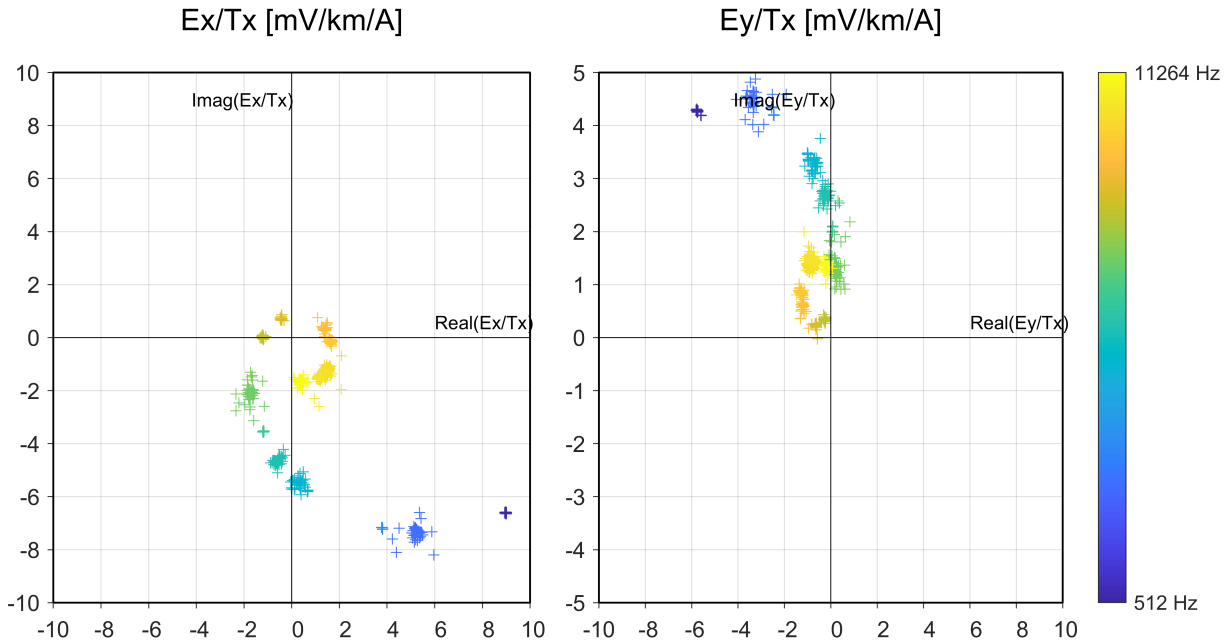


Figure A.12: Diagrammes d'Argand pour une des stations mesurées.

$$\nabla \wedge \nabla \wedge E^p + j\omega\mu\sigma^p E^p = J \quad (\text{A.29})$$

$$\nabla \wedge \nabla \wedge E^s + j\omega\mu\sigma E^s = -j\omega\mu(\sigma - \sigma^p)E^p \quad (\text{A.30})$$

Une fois le champ primaire calculé (Eq. 1), le champ secondaire (Eq.2) est calculé par soustraction du champ primaire dans le champ total. Pour cela, le champ primaire doit être projeté sur la grille de calcul utilisée pour calculer le champ total.

$$\nabla \wedge \nabla \wedge E^T + j\omega\mu\sigma E^T = J \quad (\text{A.31})$$

Résoudre le champ total revient à résoudre le système linéaire :

$$A(\sigma, \omega) E^T = b \quad (\text{A.32})$$

**Reference model** Parce que le calcul se fait par méthode hybride semi-analytique, il est nécessaire de définir un modèle homogène ou 1D, sur lequel le calcul analytique sera fait, puis de définir une ou deux anomalies dans un second modèle.

**Importance de la discrétisation:** L'écart de résistivité entre l'air est la subsurface rend les grandeurs de part-et-d'autre de l'interface extrêmes ( $\nabla E = \frac{\rho}{\epsilon_0}$ ). Il est donc très important de discrétiser correctement les zones à résoudre bien (stations de mesures, station d'émission) pour minimiser les erreurs de calcul. Il est bien de discrétiser en surface à dimension de  $\delta/4$ .

## Calcul inverse

Plusieurs méthodes de résolution itérative du calcul inverse:

- gradient conjugué non-linéaire
- Gauss-Newton

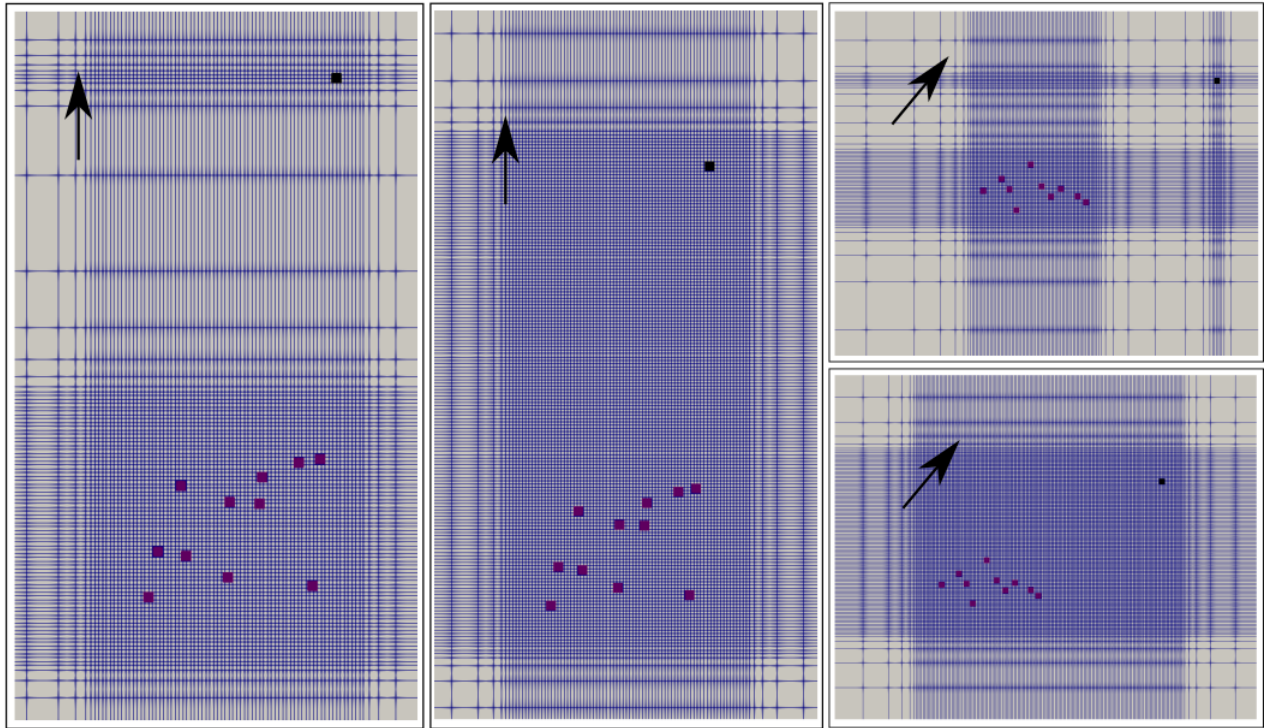


Figure A.13: Les quatre grilles testées pour le calcul direct et inverse. La flèche noire indique la direction du Nord

## Parallélisation : les solveurs

**Mumps** : solveur parallèle très courant, mais finalement assez peu adapté aux grilles vraiment grosses.

**WSMP** (Watson Sparse Matrix Package) : solveur payant proposé par IBM, très bien adapté et parallélisé, et notamment pour les grilles de taille importante.

### A.3.4 Application au jeu de données du glissement de terrain de Lodève

#### Grilles 3D

Quatre grilles ont été réalisées, avec différentes orientations, basées sur des jeux de données variables, et plus ou moins finement discrétisées entre l'émetteur et les stations. Parmi les 4 grilles testées, deux grilles donnent une sensibilité 2D au problème. Ces grilles sont présentées en fig. A.13, et ont fait l'objet de tests à la fois de calcul direct, et d'inversion. A l'issue de ces tests, une 5e grille a été réalisée, présentée dans la fig. A.14

**Grille sélectionnée** Dimension : 70 x 117 x 78 ; Nombre de cellules : 638820

Dans cette dernière grille, la zone centrale est composée de cellule de taille  $5 \times 10 \times 10 \text{ m}^3$ . L'émetteur n'est pas inclus dans le domaine raffiné, mais un raffinement a été réalisé à l'endroit du dipôle d'émission, composé de cellules de dimension  $5 \times 10 \times 10 \text{ m}^3$ .

Cette grille a été faite pour prendre en compte exclusivement, dans l'inversion, la zone la mieux contrainte par les données. Pour cela, une station de mesure a été omise, et le repère de la grille a été pivoté autour de l'axe vertical pour optimiser le maillage.

#### Calcul direct

Avant de réaliser des calculs inverses, des calculs directs ont été réalisés pour évaluer la qualité du calcul direct pour une grille particulière, et orienter le choix de la grille choisie pour l'inversion. Les figures A.15 et A.16 sont deux exemples de calcul direct. On voit clairement que dans le premier cas, la discrétisation grossière de la grille

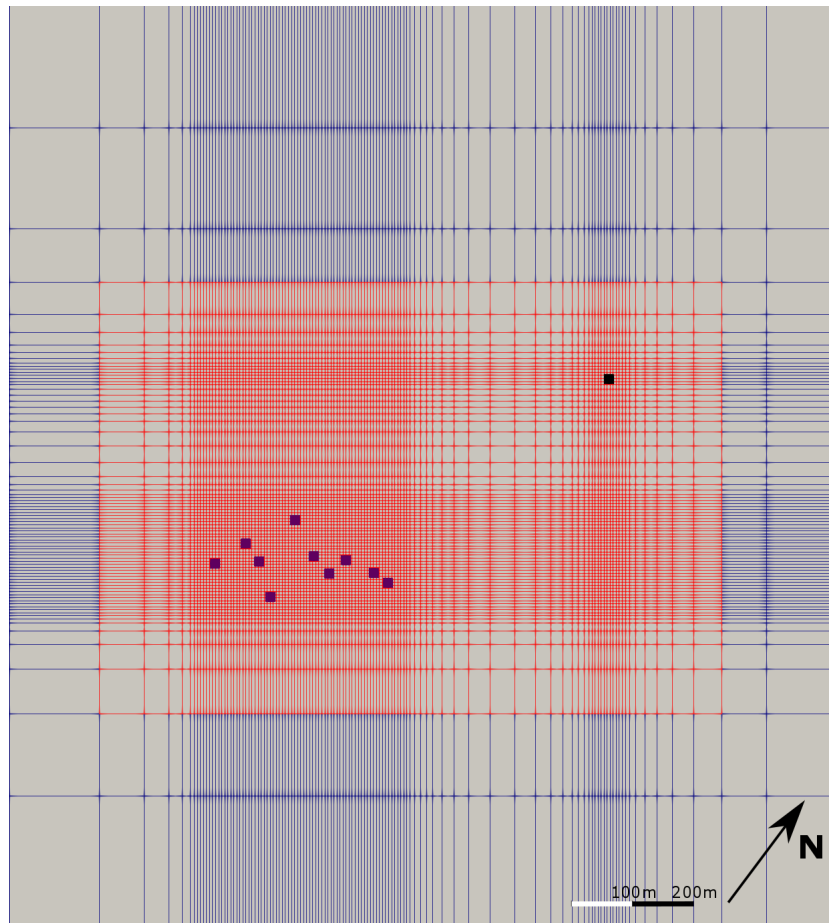


Figure A.14: Grille sélectionnée pour le calcul direct et inverse.

impacte négativement le calcul direct, particulièrement sur la partie réelle de  $E_y$  qui présente des variations de surface en marche d'escalier, alors que le second cas semble beaucoup plus lisse, et donc mieux discrétisé.

### Inversion

Plusieurs tests d'inversion ont été réalisés pour tenter d'identifier un modèle permettant de fitter les données. Cependant, aucun n'a donné de résultat satisfaisant vis-à-vis du fit, ni même des variations de résistivité observées. Le logarithme de base 10 de la résistivité a été inversé.

Une résolution de type Gauss-Newton et une résolution de type gradient conjugué, plus rapide, ont été testés. Une norme  $L_2$  dans le calcul du misfit et de la fonction coût a été utilisée. Des tests ont été faits avec une régularisation donc le coefficient est choisie sur la base du calcul d'une L-curve, mais également sans régularisation, en appliquant à chaque itération un lissage anisotrop au modèle.

Parce qu'il n'y a qu'un unique transmetteur, impliqué dans la mesure de chaque donnée, la sensibilité théorique à l'aplomb de l'émetteur est très élevée. Pour éviter de surinterpréter le modèle à l'aplomb de l'émetteur, la sensibilité y a été artificiellement réduite par le code d'inversion. Les variations topographiques ont délibérément été ignorées car pouvant apporter des biais importants dans le calcul du champ électrique, et car ces variations sont de faible amplitude sur le site.

### A.3.5 Results

Les inversions se sont avérées délicates, et aucune inversion n'a pu converger de manière satisfaisante. La figure A.17 présente un exemple de modèle obtenu après 4 itérations : le modèle présente des patches à la

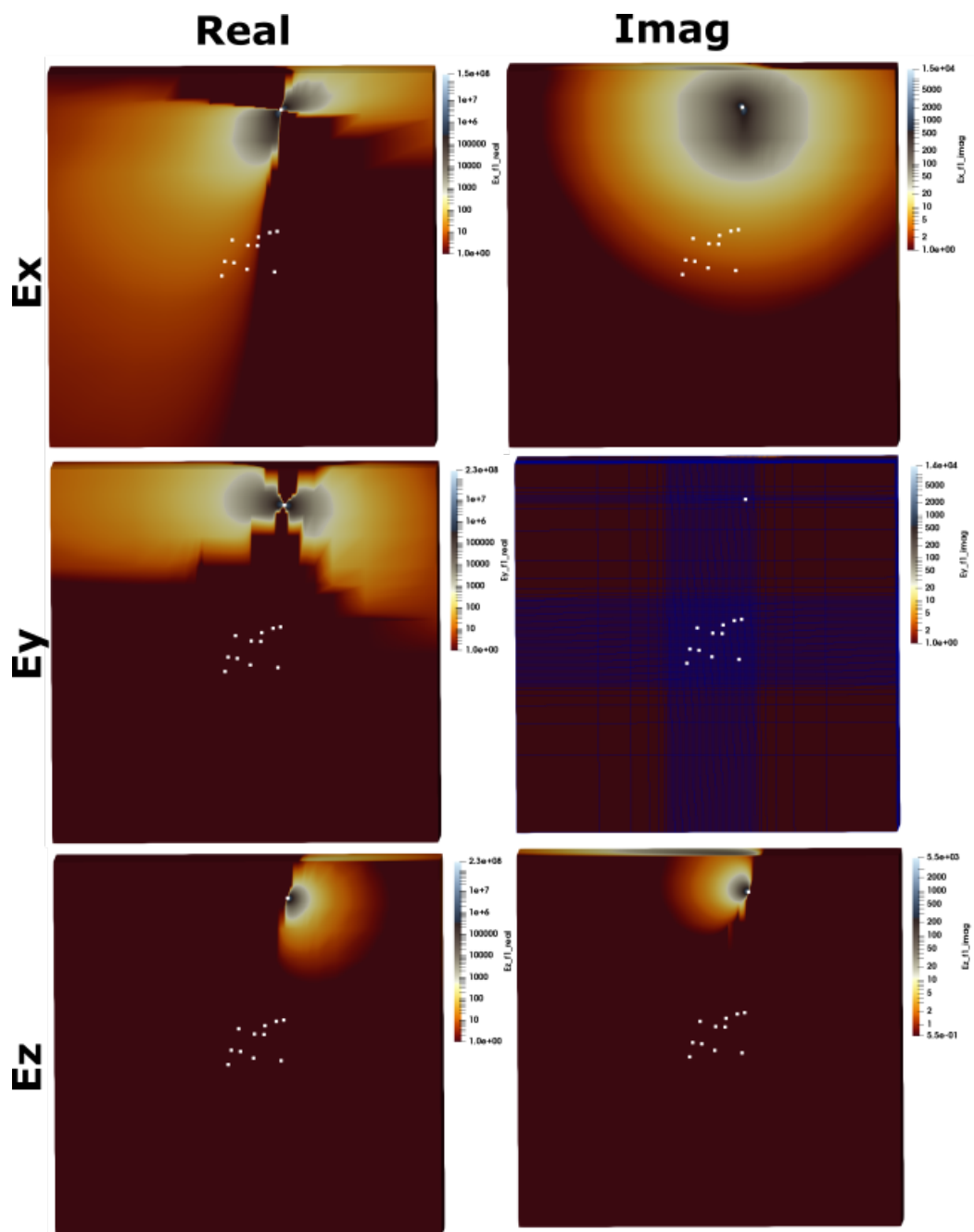


Figure A.15: Exemple de calcul direct sur une grille trop faiblement discrétisée entre l'émetteur et le site (Seules les amplitudes positives apparaissent).

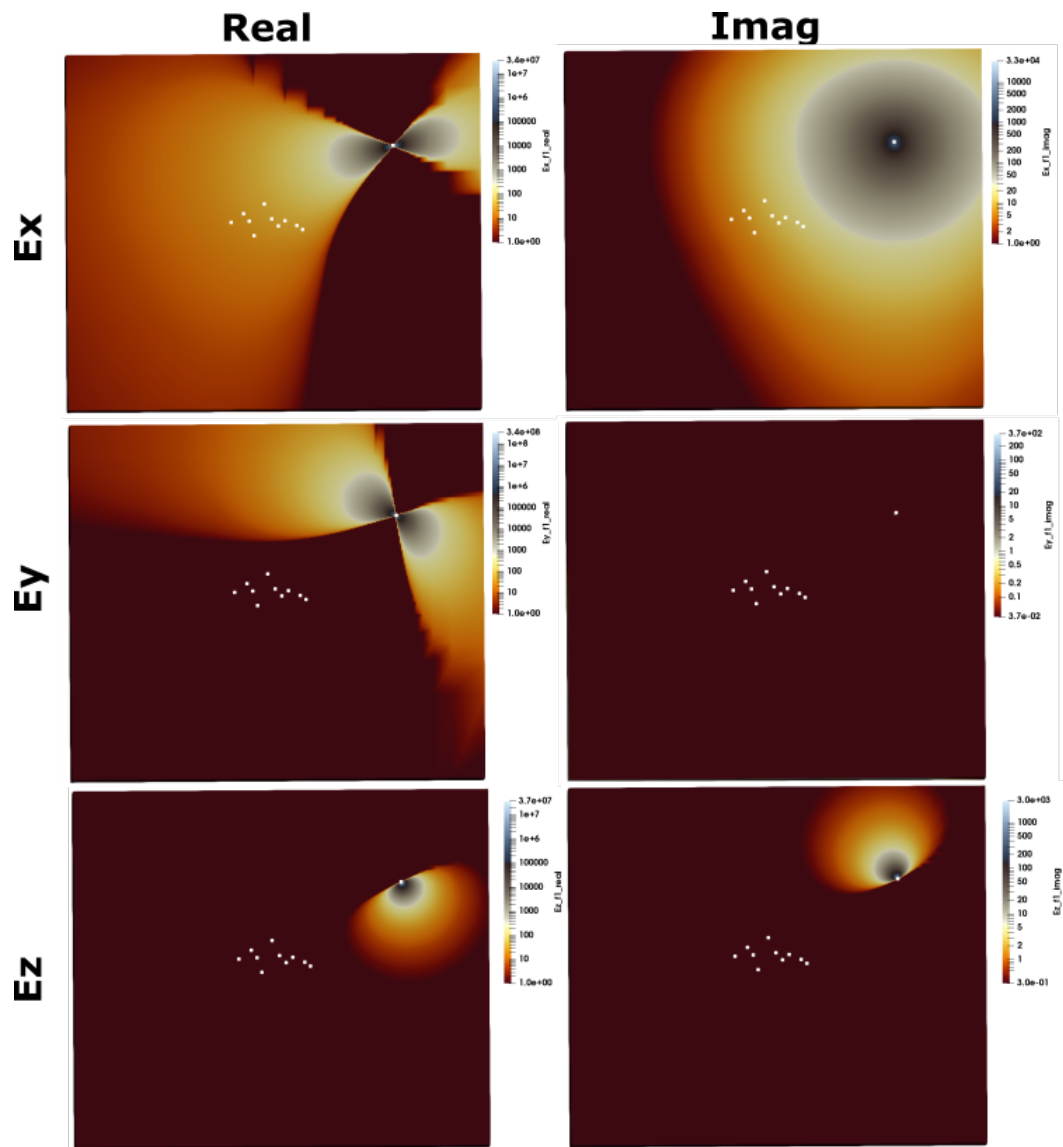


Figure A.16: Exemple de calcul direct sur une grille suffisamment discrétisée entre l'émetteur et le site (Seules les amplitudes positives apparaissent).

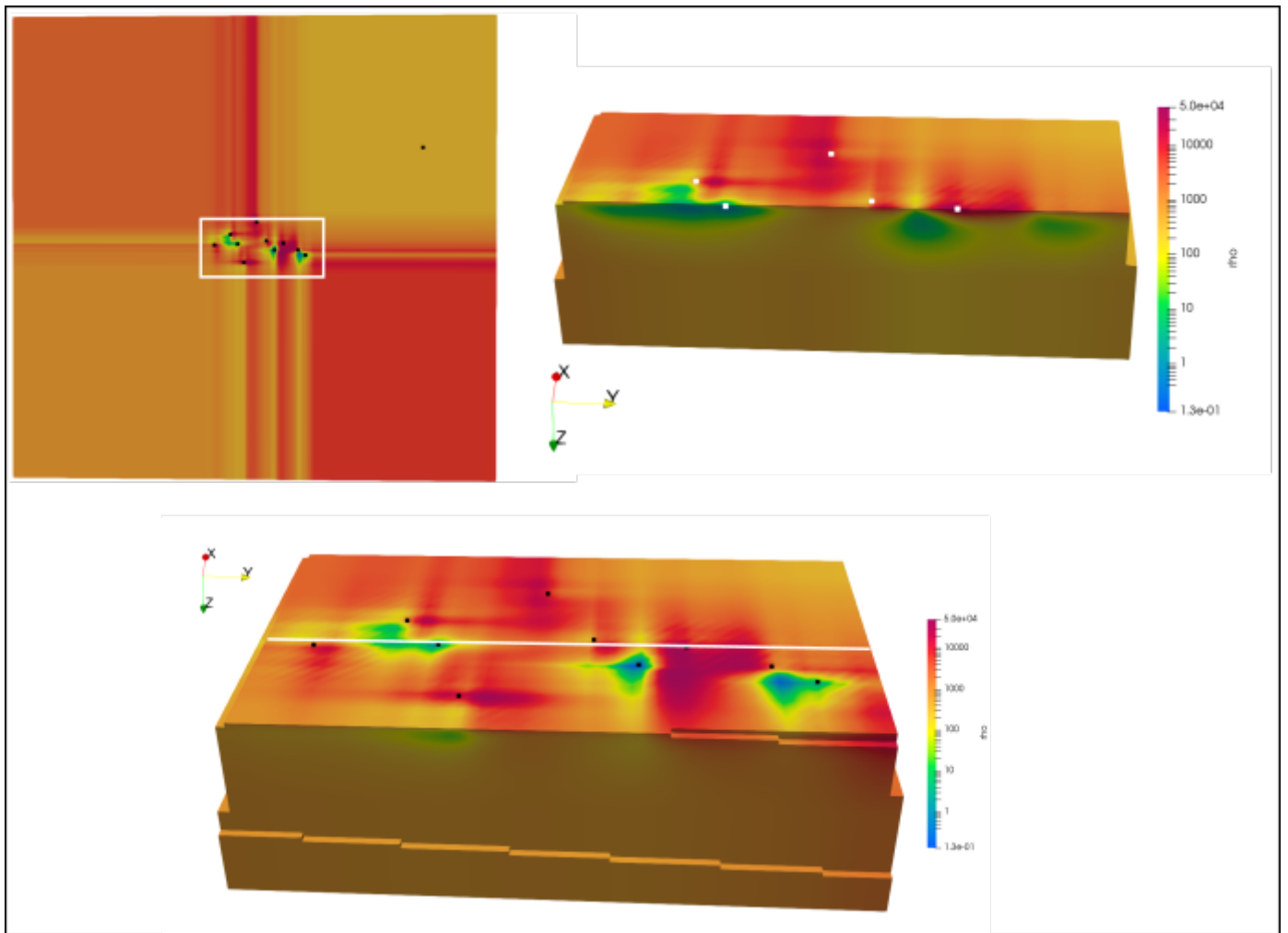


Figure A.17: Exemple de modèle après 4 itérations. Les stations sont représentées par des points.

surface, aux endroits des stations, et les données ne sont pas fittées.

## A.4 References

- Abdelfettah, Y., Sailhac, P., Schill, E., and Larnier, H. (2014). Preliminary magnetotelluric monitoring results at Rittershofen. In *3rd European geothermal workshop, Karlsruhe*, pages 15–16.
- Alfonsi, P. (1997). Relation entre les paramètres hydrologiques et la vitesse dans les glissements de terrains. Exemples de La Clapière et de Séchillienne (France). *Revue française de géotechnique*, (79):3–12.
- Altdorff, D. and Dietrich, P. (2014). Delineation of areas with different temporal behavior of soil properties at a landslide affected Alpine hillside using time-lapse electromagnetic data. *Environmental Earth Sciences*, 72(5):1357–1366.
- Anderson, W. L. (1979). Numerical integration of related hankel transforms of orders 0 and 1 by adaptive digital filtering. *Geophysics*, 44(7):1287–1305.
- Archie, G. E. (1942). The electrical resistivity log as an aid in determining some reservoir characteristics. *Transactions of the AIME*, 146(01):54–62.
- Árnason, K. (2015). The static shift problem in MT soundings. In *Proceedings world geothermal congress*.
- Attwa, M. and Ali, H. (2018). Resistivity characterization of aquifer in coastal semiarid areas: An approach for hydrogeological evaluation. In *Groundwater in the Nile Delta*, pages 213–233. Springer.
- Badea, E. A., Everett, M. E., Newman, G. A., and Biro, O. (2001). Finite-element analysis of controlled-source electromagnetic induction using Coulomb-gauged potentials. *Geophysics*, 66(3):786–799.
- Bannister, P. R. (1966). Quasi-static fields of dipole antennas at the earth's surface. *Radio Science*, 1(11):1321–1332.
- Baranwal, V. C., Franke, A., Börner, R.-U., and Spitzer, K. (2011). Unstructured grid based 2-d inversion of VLF data for models including topography. *Journal of Applied Geophysics*, 75(2):363–372.
- Barfély, J., Bordet, P., Carme, F., Debelmas, J., Meloux, M., Montjuvent, G., Mouterde, R., and Sarrot Reynauld, J. (1972). Carte géologique détaillée de la France (1/50000) n 797 Vizille. *Editions du BRGM*, 38p.
- Bartel, L. (1982). Potential use of the CSAMT geophysical technique to map UCG processes. Technical report, Sandia National Labs., Albuquerque, NM (USA).
- Bartel, L. and Jacobson, R. (1987). Results of a controlled-source audiofrequency magnetotelluric survey at the Puhimau thermal area, Kilauea volcano, Hawaii. *Geophysics*, 52(5):665–677.
- Baudement, C., Bertrand, C., Guglielmi, Y., Viseur, S., Vallet, A., and Cappa, F. (2013). Quantification de la dégradation mécanique et chimique d'un versant instable: approche géologique, hydromécanique et hydrochimique Etude du versant instable de Séchillienne, Isère (38). In *JAG-3èmes journées Aléas Gravitaires*, pages 1–6.
- Bergmann, P., Ivandic, M., Norden, B., Rücker, C., Kiessling, D., Lüth, S., Schmidt-Hattenberger, C., and Juhlin, C. (2014). Combination of seismic reflection and constrained resistivity inversion with an application to 4d imaging of the CO<sub>2</sub> storage site, Ketzin, Germany. *Geophysics*, 79(2):B37–B50.
- Bibby, H. (1977). The apparent resistivity tensor. *Geophysics*, 42(6):1258–1261.
- Binley, A. and Kemna, A. (2005). Dc resistivity and induced polarization methods. In *Hydrogeophysics*, pages 129–156. Springer.
- Blanchet, J. and Creutin, J.-D. (2017). Co-occurrence of extreme daily rainfall in the french Mediterranean region. *Water Resources Research*, 53(11):9330–9349.
- Boerner, D. E. (1992). Controlled source electromagnetic deep sounding: Theory, results and correlation with natural source results. *Surveys in geophysics*, 13(4):435–488.
- Boerner, D. E., Kurtz, R. D., and Jones, A. G. (1993). Orthogonality in CSAMT and MT measurements. *Geophysics*, 58(7):924–934.
- Brakensiek, D. L. (1979). *Field manual for research in agricultural hydrology*. Number 224. Department of Agriculture, Science and Education Administration.
- Breede, K., Kemna, A., Esser, O., Zimmermann, E., Vereecken, H., and Huisman, J. (2012). Spectral induced polarization measurements on variably saturated sand-clay mixtures. *Near Surface Geophysics*, 10(6):479–489.
- Bretonneau, F., Penz, S., Coppo, N., Wawrzyniak, P., and Darnet, M. (2017). Practical inversion of electric resistivity in 3d from frequency-domain land CSEM data. In *23rd European Meeting of Environmental and Engineering Geophysics*, volume 2017, pages 1–5. European Association of Geoscientists & Engineers.

- Cagniard, L. (1953). Basic theory of the magneto-telluric method of geophysical prospecting. *Geophysics*, 18(3):605–635.
- Caldwell, T. G., Bibby, H. M., and Brown, C. (2004). The magnetotelluric phase tensor. *Geophysical Journal International*, 158(2):457–469.
- Cappa, E., Guglielmi, Y., Viseur, S., and Garambois, S. (2014). Deep fluids can facilitate rupture of slow-moving giant landslides as a result of stress transfer and frictional weakening. *Geophysical Research Letters*, 41(1):61–66.
- Carrière, S., Jongmans, D., Chambon, G., Bièvre, G., Lanson, B., Bertello, L., Berti, M., Jaboyedoff, M., Malet, J.-P., and Chambers, J. (2018). Rheological properties of clayey soils originating from flow-like landslides. *Landslides*, 15(8):1615–1630.
- Chanut, M.-A., Dubois, L., Duranthon, J.-P., and Durville, J.-L. (2013). Mouvement de versant de séchilienne: relations entre précipitations et déplacements. In *Acte de colloque, 1ère conférence internationale sur les risques des mouvements de terrain, Ain Draham (Tunisie)*, pages 14–16.
- Chave, A. D. and Jones, A. G. (2012). Introduction to the magnetotelluric method. *The magnetotelluric method: Theory and practice*, pages 1–18.
- Chave, A. D. and Thomson, D. J. (1989). Some comments on magnetotelluric response function estimation. *Journal of Geophysical Research: Solid Earth*, 94(B10):14215–14225.
- Christiansen, A. V. and Auken, E. (2012). A global measure for depth of investigation. *Geophysics*, 77(4):WB171–WB177.
- Collin, J. (1991). Groundwater, a common asset that should be managed in common. Proceedings and review of the colloquium, Paris 1990. *Hydrogeologie (France)*.
- Constable, C. (2007). Geomagnetic spectrum, temporal. *Encyclopedia of Geomagnetism and Paleomagnetism*, Springer, Dordrecht, The Netherlands.
- Constable, C. (2016). Earth's electromagnetic environment. *Surveys in Geophysics*, 37(1):27–45.
- Coppo, N., Darnet, M., Harcouet-Menou, V., Wawrzyniak, P., Manzella, A., Bretaudeau, F., Romano, G., Lagrou, D., and Girard, J.-F. (2016). Characterization of deep geothermal energy resources in low enthalpy sedimentary basins in Belgium using electro-magnetic methods—csem and mt results.
- Dahlin, T. and Loke, M. H. (2015). Negative apparent chargeability in time-domain induced polarisation data. *Journal of Applied Geophysics*, 123:322–332.
- Dambrine, E., Pollier, B., Poszwa, A., Ranger, J., Probst, A., Viville, D., Biron, P., and Granier, A. (1998). Evidence of current soil acidification in spruce stands in the Vosges mountains, north-eastern France. *Water, Air, and Soil Pollution*, 105(1-2):43–52.
- Danielsen, J. E., Auken, E., Jørgensen, E., Søndergaard, V., and Sørensen, K. I. (2003). The application of the transient electromagnetic method in hydrogeophysical surveys. *Journal of applied geophysics*, 53(4):181–198.
- Darnet, M., Dezayes, C., Girard, J., Baltassat, J., Lerouge, C., Reuschlé, T., Coppo, N., Bretaudeau, F., Porte, J., and Lucas, Y. (2019). Geophysical signature of the transition zone between the sedimentary cover and the basement: an analogue approach to help de-risking geothermal prospects. *arXiv preprint arXiv:1905.07897*.
- Darnet, M., Wawrzyniak, P., Coppo, N., Nielsson, S., Schill, E., and Fridleifsson, G. (2018). Monitoring geothermal reservoir developments with the Controlled-Source Electro-Magnetic method—A calibration study on the Reykjanes geothermal field. *Journal of Volcanology and Geothermal Research*.
- Delhaye, R., Rath, V., Jones, A. G., Muller, M. R., and Reay, D. (2017). Correcting for static shift of magnetotelluric data with airborne electromagnetic measurements: a case study from Rathlin basin, northern Ireland. *Solid Earth*, 8(3):637.
- Delrieu, G., Kirstetter, P.-E., Nicol, J., and Neppel, L. (2004). L'événement pluvieux des 8-9 septembre 2002 dans le Gard: estimation des précipitations par radars et pluviomètres. *La Houille Blanche*, (6):93–98.
- Denchik, N., Gautier, S., Dupuy, M., Batiot-Guilhe, C., Lopez, M., Léonardi, V., Geeraert, M., Henry, G., Neyens, D., Coudray, P., et al. (2019). In-situ geophysical and hydro-geochemical monitoring to infer landslide dynamics (pégairolles-de-l'Escalette landslide, France). *Engineering Geology*, 254:102–112.
- Depriester, D., Maynadier, A., Lavernhe-Taillard, K., and Hubert, O. (2014). Thermomechanical modelling of a NiTi SMA sample submitted to displacement-controlled tensile test. *International Journal of Solids and Structures*, 51(10):1901–1922.
- Doetsch, J., Ingeman-Nielsen, T., Christiansen, A. V., Fiandaca, G., Auken, E., and Elberling, B. (2015). Direct current (dc) resistivity and induced polarization (ip) monitoring of active layer dynamics at high temporal resolution. *Cold Regions*

- Science and Technology*, 119:16–28.
- Doetsch, J., Linde, N., Vogt, T., Binley, A., and Green, A. G. (2012). Imaging and quantifying salt-tracer transport in a riparian groundwater system by means of 3d ERT monitoring. *Geophysics*, 77(5):B207–B218.
- Doukoure, F. (2019). Acoustic measurements for the characterisation of the hard rock aquifer at the Strengbach catchment. Master's thesis, Ecole et Observatoire des Sciences de la Terre.
- d'Ozouville, N., Auken, E., Sorensen, K., Violette, S., de Marsily, G., Deffontaines, B., and Merlen, G. (2008). Extensive perched aquifer and structural implications revealed by 3d resistivity mapping in a Galapagos volcano. *Earth and Planetary Science Letters*, 269(3-4):518–522.
- Dubois, L., Chanut, M., and Duranthon, J. (2014). Amélioration continue des dispositifs d'auscultation et de surveillance intégrés dans le suivi du versant instable des Ruines de Séchilienne. *Géologues*, 182:50–55.
- Duranthon, J., Chanut, M., and Dubois, L. (2013). Ruines de Séchilienne, rapport annuel de suivi du site, avril 2012 (mars 2013). *CETE-Centre d'Etudes Techniques de LYON*, 41829(1):119.
- Duranthon, J.-P. and Effendiantz, L. (2004). Le versant instable des "ruines" de Séchilienne: Point sur l'activité du phénomène et présentation du nouveau dispositif de gestion de la télésurveillance. *Bulletin des laboratoires des Ponts et Chaussées*, (252):29–48.
- Duranthon, J. P., Effendiantz, L., Memier, M., and Previtali, I. (2003). Apport des méthodes topographiques et topométriques au suivi du versant rocheux instable des ruines de Séchilienne. *Revue XYZ*, 94:31–38.
- Egbert, G. D. and Kelbert, A. (2012). Computational recipes for electromagnetic inverse problems. *Geophysical Journal International*, 189(1):251–267.
- Falgàs, E., Ledo, J., Benjumea, B., Queralt, P., Marcuello, A., Teixidó, T., and Arango, C. (2006). Imaging ground water resources of a mediterranean coastal aquifer using seismic and csamt data. In *Symposium on the Application of Geophysics to Engineering and Environmental Problems 2006*, pages 863–870. Society of Exploration Geophysicists.
- Falgàs, E., Marquis, G., Sailhac, P., Ledo, J., Queralt, P., and Béhaegel, M. (2005). Aquifer imaging using csamt and ert. In *Near Surface 2005-11th European Meeting of Environmental and Engineering Geophysics*, pages cp–13. European Association of Geoscientists & Engineers.
- Fiandaca, G., Madsen, L. M., and Maurya, P. K. (2018). Re-parameterisations of the Cole–Cole model for improved spectral inversion of induced polarization data. *Near Surface Geophysics*, 16(4):385–399.
- Flores Orozco, A., Bucker, M., Steiner, M., and Malet, J.-P. (2018a). Complex-conductivity imaging for the understanding of landslide architecture. *Engineering geology*, 243:241–252.
- Flores Orozco, A., Gallistl, J., Bucker, M., and Williams, K. H. (2018b). Decay curve analysis for data error quantification in time-domain induced polarization imaging. *Geophysics*, 83(2):E75–E86.
- Flores Orozco, A., Kemna, A., Binley, A., and Cassiani, G. (2019). Analysis of time-lapse data error in complex conductivity imaging to alleviate anthropogenic noise for site characterization. *Geophysics*, 84(2):B181–B193.
- Flores Orozco, A., Kemna, A., and Zimmermann, E. (2012). Data error quantification in spectral induced polarization imaging. *Geophysics*, 77(3):E227–E237.
- Florsch, N., Camerlynck, C., and Revil, A. (2012). Direct estimation of the distribution of relaxation times from induced-polarization spectra using a Fourier transform analysis. *Near Surface Geophysics*, 10(6):517–531.
- Folch, A., Menció, A., Puig, R., Soler, A., and Mas-Pla, J. (2011). Groundwater development effects on different scale hydro-geological systems using head, hydrochemical and isotopic data and implications for water resources management: The Selva basin (ne Spain). *Journal of Hydrology*, 403(1-2):83–102.
- Fox, R. C., Hohmann, G. W., Killpack, T. J., and Rijo, L. (1980). Topographic effects in resistivity and induced-polarization surveys. *Geophysics*, 45(1):75–93.
- Friedel, S., Thielen, A., and Springman, S. M. (2006). Investigation of a slope endangered by rainfall-induced landslides using 3d resistivity tomography and geotechnical testing. *Journal of Applied Geophysics*, 60(2):100–114.
- Gallistl, J., Weigand, M., Stumvoll, M., Ottowitz, D., Glade, T., and Orozco, A. F. (2018). Delineation of subsurface variability in clay-rich landslides through spectral induced polarization imaging and electromagnetic methods. *Engineering Geology*, 245:292–308.
- Gance, J., Leite, O., Texier, B., Bernard, J., and Truffert, C. (2018). The Fullwaver systems: Distributed network of autonomous devices for deep 3d electrical resistivity and induced polarization survey. In *EGU General Assembly Confer-*

- ence Abstracts, volume 20, page 12569.
- Gance, J., Malet, J.-P., Supper, R., Sailhac, P., Ottowitz, D., and Jochum, B. (2016). Permanent electrical resistivity measurements for monitoring water circulation in clayey landslides. *Journal of Applied Geophysics*, 126:98–115.
- Gance, J., Sailhac, P., and Malet, J.-P. (2014). Corrections of surface fissure effect on apparent resistivity measurements. *Geophysical Journal International*, 200(2):1118–1135.
- Gance, J., Sailhac, P., Malet, J.-P., and Viville, D. (2020). Structure of a granitic mountain catchment inferred from electrical resistivity values. *in review*.
- García-Fiscal, S. and Flores, C. (2018). Sensitivity of galvanic and inductive induced polarization methods to the Cole-Cole parameters. *Journal of Applied Geophysics*, 158:1–10.
- Geiermann, J. and Schill, E. (2010). 2-d magnetotellurics at the geothermal site at Soultz-sous-Forêts: Resistivity distribution to about 3000 m depth. *Comptes Rendus Geoscience*, 342(7-8):587–599.
- Gh'Mari, E. et al. (1995). *Etude minéralogique, pétrophysique et géochimique de dynamique d'altération d'un granite soumis aux dépôts atmosphériques acides (bassin versant du Strengbach, Vosges, France). Mécanismes, bilans et modélisation*. PhD thesis, Strasbourg 1.
- Ghorbani, A., Camerlynck, C., and Florsch, N. (2009a). Cr1div: A Matlab program to invert 1d spectral induced polarization data for the Cole–Cole model including electromagnetic effects. *Computers & Geosciences*, 35(2):255–266.
- Ghorbani, A., Cosenza, P., Revil, A., Zamora, M., Schmutz, M., Florsch, N., and Jougnot, D. (2009b). Non-invasive monitoring of water content and textural changes in clay-rocks using spectral induced polarization: A laboratory investigation. *Applied Clay Science*, 43(3-4):493–502.
- Giovannangelis, N. (2014). Structure et dynamique d'un glissement de terrain : exemple du site expérimental de Lodève - Caractéristiques géologiques/hydrogéologiques associées à la semelle savon d'un glissement de terrain. Master's thesis, Géosciences Montpellier.
- Goldstein, M. and Strangway, D. (1975). Audio-frequency magnetotellurics with a grounded electric dipole source. *Geophysics*, 40(4):669–683.
- Grant Caldwell, T., Bibby, H. M., and Brown, C. (2002). Controlled source apparent resistivity tensors and their relationship to the magnetotelluric impedance tensor. *Geophysical Journal International*, 151(3):755–770.
- Guglielmi, Y., Bertrand, C., Compagnon, F., Follacci, J., and Mudry, J. (2000). Acquisition of water chemistry in a mobile fissured basement massif: its role in the hydrogeological knowledge of the La Clapiere landslide (Mercantour massif, southern Alps, France). *Journal of Hydrology*, 229(3-4):138–148.
- Guglielmi, Y., Vengeon, J., Bertrand, C., Mudry, J., Follacci, J., and Giraud, A. (2002). Hydrogeochemistry: an investigation tool to evaluate infiltration into large moving rock masses (case study of La Clapière and Séchilienne alpine landslides). *Bulletin of Engineering Geology and the Environment*, 61(4):311–324.
- Guillemoteau, J. (2012). *Méthodologie d'interprétation en électromagnétisme aéroporté*. PhD thesis, Université de Strasbourg.
- Guinea, A., Playà, E., Rivero, L., and Himi, M. (2010). Electrical resistivity tomography and induced polarization techniques applied to the identification of gypsum rocks. *Near Surface Geophysics*, 8(3):249–257.
- Günther, T., Rücker, C., and Spitzer, K. (2006). Three-dimensional modelling and inversion of DC resistivity data incorporating topography—ii. Inversion. *Geophysical Journal International*, 166(2):506–517.
- Hanneson, J. and West, G. (1984). The horizontal loop electromagnetic response of a thin plate in a conductive earth: Part i—computational method. *Geophysics*, 49(4):411–420.
- Hellman, K., Ronczka, M., Günther, T., Wennermark, M., Rücker, C., and Dahlin, T. (2017). Structurally coupled inversion of ERT and refraction seismic data combined with cluster-based model integration. *Journal of Applied Geophysics*, 143:169–181.
- Helmstetter, A. and Garambois, S. (2010). Seismic monitoring of Séchilienne rockslide (French Alps): Analysis of seismic signals and their correlation with rainfalls. *Journal of Geophysical Research: Earth Surface*, 115(F3).
- Hohmann, G. W. (1975). Three-dimensional induced polarization and electromagnetic modeling. *Geophysics*, 40(2):309–324.
- Jacob, T., Chery, J., Bayer, R., Le Moigne, N., Boy, J.-P., Vernant, P., and Boudin, F. (2009). Time-lapse surface to depth gravity measurements on a karst system reveal the dominant role of the epikarst as a water storage entity. *Geophysical Journal*

- International*, 177(2):347–360.
- Jeanne, P., Rutqvist, J., Vasco, D., Garcia, J., Dobson, P. F., Walters, M., Hartline, C., and Borgia, A. (2014). A 3d hydrogeological and geomechanical model of an enhanced geothermal system at The Geysers, California. *Geothermics*, 51:240–252.
- Jomard, H., Lebourg, T., Guglielmi, Y., and Tric, E. (2010). Electrical imaging of sliding geometry and fluids associated with a deep seated landslide (La Clapière, France). *Earth Surface Processes and Landforms: The Journal of the British Geomorphological Research Group*, 35(5):588–599.
- Jones, A. G., Chave, A. D., Egbert, G., Auld, D., and Bahr, K. (1989). A comparison of techniques for magnetotelluric response function estimation. *Journal of Geophysical Research: Solid Earth*, 94(B10):14201–14213.
- Jongmans, D. and Garambois, S. (2007). Geophysical investigation of landslides: a review. *Bulletin de la Société géologique de France*, 178(2):101–112.
- Jonscher, A. K. (1999). Dielectric relaxation in solids. *Journal of Physics D: Applied Physics*, 32(14):R57.
- Kalscheuer, T., Bastani, M., Donohue, S., Persson, L., Pfaffhuber, A. A., Reiser, F., and Ren, Z. (2013). Delineation of a quick clay zone at Smørgrav, Norway, with electromagnetic methods under geotechnical constraints. *Journal of Applied Geophysics*, 92:121–136.
- Kaminski, V. and Viezzoli, A. (2017). Modeling induced polarization effects in helicopter time-domain electromagnetic data: Field case studies heliborne IP effect: Field results. *Geophysics*, 82(2):B49–B61.
- Kelbert, A., Meqbel, N., Egbert, G. D., and Tandon, K. (2014). Modem: A modular system for inversion of electromagnetic geophysical data. *Computers & Geosciences*, 66:40–53.
- Kemna, A. (2000). *Tomographic inversion of complex resistivity: Theory and application*. Der Andere Verlag.
- Kemna, A., Binley, A., Cassiani, G., Niederleithinger, E., Revil, A., Slater, L., Williams, K. H., Orozco, A. F., Haegel, F.-H., Hördt, A., et al. (2012). An overview of the spectral induced polarization method for near-surface applications. *Near Surface Geophysics*, 10(6):453–468.
- Kemna, A., Räckers, E., and Binley, A. (1997). Application of complex resistivity tomography to field data from a kerosene-contaminated site. In *3rd EEGS Meeting*, pages cp–95. European Association of Geoscientists & Engineers.
- Khaldoun, A., Moller, P., Fall, A., Wegdam, G., De Leeuw, B., Méheust, Y., Fossum, J. O., and Bonn, D. (2009). Quick clay and landslides of clayey soils. *Physical Review Letters*, 103(18):188301.
- Kratzer, T. and Macnae, J. C. (2012). Induced polarization in airborne EM. *Geophysics*, 77(5):E317–E327.
- Lagarias, J. C., Reeds, J. A., Wright, M. H., and Wright, P. E. (1998). Convergence properties of the Nelder–Mead simplex method in low dimensions. *SIAM Journal on optimization*, 9(1):112–147.
- Lajaunie, M., Gance, J., Nevers, P., Malet, J.-P., Bertrand, C., Garin, T., and Ferhat, G. (2019). Structure of the Séchilienne unstable slope from large-scale 3d electrical tomography using a resistivity distributed automated system (R-DAS). *Geophysical Journal International*.
- Larnier, H., Sailhac, P., and Chambodut, A. (2017). Detection and characterization of lightning-based sources using continuous wavelet transform: application to audio-magnetotellurics. *Geophysical Journal International*, 212(1):103–118.
- Le Roux, O., Jongmans, D., Kasperski, J., Schwartz, S., Potherat, P., Lebrouc, V., Lagabrielle, R., and Meric, O. (2011). Deep geophysical investigation of the large Séchilienne landslide (western Alps, France) and calibration with geological data. *Engineering Geology*, 120(1-4):18–31.
- Ledo, J., Queralt, P., Martí, A., and Jones, A. G. (2002). Two-dimensional interpretation of three-dimensional magnetotelluric data: an example of limitations and resolution. *Geophysical Journal International*, 150(1):127–139.
- Legchenko, A., Clément, R., Garambois, S., Maury, E., Mic, L.-M., Laurent, J.-P., Desplanque, C., and Guyard, H. (2011). Investigating water distribution in the Luitel Lake peat bog using MRS, ERT and GPR. *Near Surface Geophysics*, 9(2):201–209.
- Legchenko, A. and Valla, P. (1998). Processing of surface proton magnetic resonance signals using non-linear fitting. *Journal of Applied Geophysics*, 39(2):77–83.
- Lei, D., Fayemi, B., Yang, L., and Meng, X. (2017). The non-static effect of near-surface inhomogeneity on CSAMT data. *Journal of Applied Geophysics*, 139:306–315.
- Lesmes, D. P. and Frye, K. M. (2001). Influence of pore fluid chemistry on the complex conductivity and induced polariz-

- zation responses of Berea sandstone. *Journal of Geophysical Research: Solid Earth*, 106(B3):4079–4090.
- Lin, C., Tan, H., Wang, W., Tong, T., Peng, M., Wang, M., and Zeng, W. (2018a). Three-dimensional inversion of CSAMT data in the presence of topography. *Exploration Geophysics*, 49(3):253–267.
- Lin, C., Zhong, S., Auken, E., Cai, H., Tan, H., Peng, M., and Kong, W. (2018b). The effects of 3d topography on controlled-source audio-frequency magnetotelluric responses. *Geophysics*, 83(2):WB97–WB108.
- Lin, H. (2010). Earth's critical zone and hydrogeology: concepts, characteristics, and advances. *Hydrology and Earth System Sciences*, 14(1):25.
- Liu, W., Lin, P., Lü, Q., Li, Y., and Li, J. (2018). Synthetic modelling and analysis of CSEM full-field apparent resistivity response combining EM induction and IP effect for 1d medium. *Exploration Geophysics*, 49(5):609–621.
- Lofi, J., Pezard, P., Loggia, D., Garel, E., Gautier, S., Merry, C., and Bondabou, K. (2012). Geological discontinuities, main flow path and chemical alteration in a marly hill prone to slope instability: Assessment from petrophysical measurements and borehole image analysis. *Hydrological Processes*, 26(14):2071–2084.
- Loke, M. (2013). Tutorial: 2-d and 3-d electrical imaging survey Revision date: 8th of march 2013. *Geomoto Software*. (<http://www.geomotsoft.com/>).
- Lopez, M., Gand, G., Garric, J., Körner, F., and Schneider, J. (2008). The playa environments of the Lodève Permian basin (Languedoc-France). *Journal of Iberian Geology*, 34(1):29–56.
- Maineult, A., Jougnot, D., and Revil, A. (2018). Variations of petrophysical properties and spectral induced polarization in response to drainage and imbibition: a study on a correlated random tube network. *Geophysical Journal International*, 212(2):1398–1411.
- Malet, J. and Maquaire, O. (2003). Black marl earthflows mobility and long-term seasonal dynamic in southeastern France. In *Proc. 1st Int. Conf. on Fast Slope Movements*, pages 333–340.
- Marescot, L., Monnet, R., and Chapellier, D. (2008). Resistivity and induced polarization surveys for slope instability studies in the Swiss Alps. *Engineering Geology*, 98(1-2):18–28.
- Martínez-Murillo, J., Nadal-Romero, E., Regüés, D., Cerdà, A., and Poesen, J. (2013). Soil erosion and hydrology of the western Mediterranean badlands throughout rainfall simulation experiments: A review. *Catena*, 106:101–112.
- Masson, F., Viville, D., Pierret, M.-C., Mouyen, M., Hecker, L., and Chabaux, F. (2012). Time-lapse microgravity study of the Strengbach catchment (Vosges mountains, France). *Comptes Rendus Geoscience*, 344(6-7):357–365.
- Maurya, P. K., Rønde, V., Fiandaca, G., Balbarini, N., Auken, E., Bjerg, P. L., and Christiansen, A. V. (2017). Detailed landfill leachate plume mapping using 2d and 3d electrical resistivity tomography-with correlation to ionic strength measured in screens. *Journal of Applied Geophysics*, 138:1–8.
- Meric, O., Garambois, S., Jongmans, D., Wathelet, M., Chatelain, J.-L., and Vengeon, J. (2005). Application of geophysical methods for the investigation of the large gravitational mass movement of Séchilienne, France. *Canadian Geotechnical Journal*, 42(4):1105–1115.
- Mitchell, J. K. and Soga, K. (1993). *Fundamentals of Soil Behavior*, John Wiley&Sons. Inc., New York, 422.
- Mohammad, I. H., Srigutomo, W., Sutarno, D., and Sumintadiredja, P. (2013). Interpretation of 1d vector controlled-source audio-magnetotelluric (CSAMT) data using full solution modeling. *Journal of Mathematical and Fundamental Sciences*, 45(2):172–188.
- Mohammad, I. H., Srigutomo, W., Sutarno, D., and Sumintadireja, P. (2012). The modeling of 2d controlled source audio magnetotelluric (CSAMT) responses using finite element method. *Journal of Electromagnetic Analysis and Applications*, 4(07):293.
- Montjuvent, G. and Winistorfer, J. (1980). Glaciations quaternaires dans les Alpes franco-suissees et leur piedmont. *Geol. Alp*, 56:251–282.
- Mudry, J. and Etievant, K. (2007). Synthèse hydrogéologique du versant instable des ruines de Séchilienne. *Unpublished report, UMR Chrono-Environnement, University of Franche-Comté, Franche-Comté*.
- Okay, G. (2011). Characterization of textural and hydric heterogeneities in argillaceous geo-materials using induced polarization method: application to the excavation damaged zone (EDZ) of the Tournemire experimental station. *Ecole doctorale ED398 Geosciences et Ressources Naturelles*.
- Okay, G., Leroy, P., Ghorbani, A., Cosenza, P., Camerlynck, C., Cabrera, J., Florsch, N., and Revil, A. (2014). Spectral induced polarization of clay-sand mixtures: Experiments and modeling. *Geophysics*, 79(6):E353–E375.

- Oldenburg, D. W. and Li, Y. (1994). Inversion of induced polarization data. *Geophysics*, 59(9):1327–1341.
- Oldenburg, D. W. and Li, Y. (1999). Estimating depth of investigation in dc resistivity and ip surveys. *Geophysics*, 64(2):403–416.
- Oudin, L., Hervieu, F., Michel, C., Perrin, C., Andréassian, V., Anctil, F., and Loumagne, C. (2005). Which potential evapotranspiration input for a lumped rainfall–runoff model?: Part 2—Towards a simple and efficient potential evapotranspiration model for rainfall–runoff modelling. *Journal of Hydrology*, 303(1-4):290–306.
- Parsekian, A., Singha, K., Minsley, B. J., Holbrook, W. S., and Slater, L. (2015). Multiscale geophysical imaging of the critical zone. *Reviews of Geophysics*, 53(1):1–26.
- Pedersen, L. B., Bastani, M., and Dinesius, L. (2005). Groundwater exploration using combined controlled-source and radiomagnetotelluric techniques. *Geophysics*, 70(1):G8–G15.
- Pedersen, L. B., Bastani, M., and Dinesius, L. (2006). Some characteristics of the electromagnetic field from radio transmitters in europe. *Geophysics*, 71(6):G279–G284.
- Pelton, W. H., Ward, S., Hallof, P., Sill, W., and Nelson, P. H. (1978). Mineral discrimination and removal of inductive coupling with multifrequency IP. *Geophysics*, 43(3):588–609.
- Petiau, G. and Dupis, A. (1980). Noise, temperature coefficient, and long time stability of electrodes for telluric observations. *Geophysical Prospecting*, 28(5):792–804.
- Pfaffhuber, A. (2001). *Development and test of a controlled source MT method in the frequency range 1 to 50 kHz*. PhD thesis, Diplomarbeit an der Technischen Universität Berlin, Fachbereich für Angewandte Geophysik. Google Scholar.
- Pierret, M., Stille, P., Prunier, J., Viville, D., and Chabaux, F. (2014). Chemical and u–sr isotopic variations in stream and source waters of the Strengbach watershed (Vosges mountains, France). *Hydrology and Earth System Sciences*, 18(10):3969–3985.
- Pierret, M.-C., Cotel, S., Ackerer, P., Beaulieu, E., Benarioumlil, S., Boucher, M., Boutin, R., Chabaux, F., Delay, F., Fournet, C., Friedmann, P., Fritz, B., Gangloff, S., Girard, J.-F., Legtchenko, A., Viville, D., Weill, S., and Probst, A. (2018). The Strengbach catchment: A multidisciplinary environmental sentry for 30 years. *Vadose Zone Journal*, 17(1).
- Raingard, A., Reninger, P.-A., Thiery, Y., Lacquement, F., and Nachbaur, A. (2018). 3d geological modelling coupling AEM with field observations. In *Proceedings of the 7th International Workshop on Airborne Electromagnetics, Kolding, Denmark*, pages 17–20.
- Ranganayaki, R., Fryer, S., and Bartel, L. (1992). Csamt surveys in a heavy oil field to monitor steam-drive enhanced oil recovery process. In *SEG Technical Program Expanded Abstracts 1992*, pages 1384–1384. Society of Exploration Geophysicists.
- Ren, Z., Kalscheuer, T., Greenhalgh, S., and Maurer, H. (2013). A goal-oriented adaptive finite-element approach for plane wave 3-d electromagnetic modelling. *Geophysical Journal International*, 194(2):700–718.
- Revil, A. and Florsch, N. (2010). Determination of permeability from spectral induced polarization in granular media. *Geophysical Journal International*, 181(3):1480–1498.
- Revil, A., Karaoulis, M., Johnson, T., and Kemna, A. (2012). Some low-frequency electrical methods for subsurface characterization and monitoring in hydrogeology. *Hydrogeology Journal*, 20(4):617–658.
- Rochet, L., Giraud, A., Antoine, P., and Evrard, H. (1994). La déformation du versant sud du Mont-Sec dans le secteur des ruines de Séchilienne (Isère). *Bulletin of the International Association of Engineering Geology-Bulletin de l'Association Internationale de Géologie de l'Ingénieur*, 50(1):75–87.
- Rochlitz, R. and Günther, T. (2017). Modeling arbitrary csem setups with the novel FEniCS-based toolbox custEM. In *6th International Symposium on Three-Dimensional Electromagnetics*.
- Rochlitz, R., Skibbe, N., and Günther, T. (2019). custem: Customizable finite-element simulation of complex controlled-source electromagnetic data. *Geophysics*, 84(2):F17–F33.
- Rodriguez, B. D., Stanley, W. D., and Williams, J. M. (1996). Axial structures within the Reelfoot rift delineated with magnetotelluric surveys. Technical report.
- Ronzka, M., Hellman, K., Günther, T., Wisén, R., and Dahlin, T. (2017). Electric resistivity and seismic refraction tomography: a challenging joint underwater survey at äspö hard rock laboratory. *Solid Earth*, 8(3):671.
- Rücker, C., Günther, T., and Spitzer, K. (2006). Three-dimensional modelling and inversion of dc resistivity data incorporating topography—i. Modelling. *Geophysical Journal International*, 166(2):495–505.

- Schamper, C. (2009). *Etude par simulation du suivi d'un réservoir en production par méthodes ElectroMagnétiques*. PhD thesis, Paris 6.
- Schmutz, M., Albouy, Y., Guérin, R., Maquaire, O., Vassal, J., Schott, J.-J., and Descloîtres, M. (2000). Joint electrical and time domain electromagnetism (tdem) data inversion applied to the super sauze earthflow (France). *Surveys in Geophysics*, 21(4):371–390.
- Schmutz, M., Ghorbani, A., Vaudelet, P., and Blondel, A. (2014). Cable arrangement to reduce electromagnetic coupling effects in spectral-induced polarization studies reducing EM coupling effects for SIP. *Geophysics*, 79(2):A1–A5.
- Schmutz, M., Guérin, R., Andrieux, P., and Maquaire, O. (2009). Determination of the 3d structure of an earthflow by geophysical methods: the case of Super Sauze, in the french southern Alps. *Journal of Applied Geophysics*, 68(4):500–507.
- Schulz, W. H., Smith, J. B., Wang, G., Jiang, Y., and Roering, J. J. (2018). Clayey landslide initiation and acceleration strongly modulated by soil swelling. *Geophysical Research Letters*, 45(4):1888–1896.
- Seigel, H. O. (1959). Mathematical formulation and type curves for induced polarization. *Geophysics*, 24(3):547–565.
- Şen, Z. (2014). *Practical and applied hydrogeology*. Elsevier.
- Shan, C., Bastani, M., Malehmir, A., Persson, L., and Engdahl, M. (2014). Integrated 2d modeling and interpretation of geophysical and geotechnical data to delineate quick clays at a landslide site in southwest Sweden. *Geophysics*, 79(4):EN61–EN75.
- Singh, N. and Mogi, T. (2010). Emdpler: A f77 program for modeling the EM response of dipolar sources over the non-magnetic layer earth models. *Computers & Geosciences*, 36(4):430–440.
- Solberg, I.-L., Long, M., Baranwal, V. C., Gylland, A. S., and Rønning, J. S. (2016). Geophysical and geotechnical studies of geology and sediment properties at a quick-clay landslide site at Esp, Trondheim, Norway. *Engineering Geology*, 208:214–230.
- Stalnaker, J. L. (2005). *A finite element approach to the 3D CSEM modeling problem and applications to the study of the effect of target interaction and topography*. PhD thesis, Texas A&M University.
- Sternberg, B. K., Washburne, J. C., and Anderson, R. G. (1985). Investigation of MT static shift correction methods. In *SEG Technical Program Expanded Abstracts 1985*, pages 264–267. Society of Exploration Geophysicists.
- Streich, R. (2009). 3d finite-difference frequency-domain modeling of controlled-source electromagnetic data: Direct solution and optimization for high accuracy. *Geophysics*, 74(5):F95–F105.
- Streich, R., Becken, M., and Ritter, O. (2011). 2.5 d controlled-source EM modeling with general 3d source geometries. *Geophysics*, 76(6):F387–F393.
- Supper, R., Ottowitz, D., Jochum, B., Kim, J.-H., Römer, A., Baron, I., Pfeiler, S., Lovisolò, M., Gruber, S., and Vecchiotti, F. (2014). Geoelectrical monitoring: an innovative method to supplement landslide surveillance and early warning. *Near Surface Geophysics*, 12(1):133–150.
- Szarka, L. and Menvielle, M. (1997). Analysis of rotational invariants of the magnetotelluric impedance tensor. *Geophysical Journal International*, 129(1):133–142.
- Tacher, L., Bonnard, C., Laloui, L., and Parriaux, A. (2005). Modelling the behaviour of a large landslide with respect to hydrogeological and geomechanical parameter heterogeneity. *Landslides*, 2(1):3–14.
- Tang, R., Yu, P., Xiang, Y., and Zhang, X. (2014). The sensitivity analysis of different induced polarization models used in magnetotelluric method. *Acta Geodaetica et Geophysica*, 49(2):225–233.
- Tarasov, A. and Titov, K. (2013). On the use of the Cole–Cole equations in spectral induced polarization. *Geophysical Journal International*, 195(1):352–356.
- Tikhonov, A. (1950). On determining electrical characteristics of the deep layers of the Earth's crust. In *Doklady*, volume 73, pages 295–297.
- Travelletti, J. and Malet, J.-P. (2012). Characterization of the 3d geometry of flow-like landslides: A methodology based on the integration of heterogeneous multi-source data. *Engineering Geology*, 128:30–48.
- Travelletti, J., Sailhac, P., Malet, J.-P., Grandjean, G., and Ponton, J. (2012). Hydrological response of weathered clay-shale slopes: Water infiltration monitoring with time-lapse electrical resistivity tomography. *Hydrological Processes*, 26(14):2106–2119.

- Uhlemann, S., Chambers, J., Wilkinson, P., Maurer, H., Merritt, A., Meldrum, P., Kuras, O., Gunn, D., Smith, A., and Dijkstra, T. (2017). Four-dimensional imaging of moisture dynamics during landslide reactivation. *Journal of Geophysical Research: Earth Surface*, 122(1):398–418.
- Uhlemann, S., Wilkinson, P. B., Chambers, J. E., Maurer, H., Merritt, A. J., Gunn, D. A., and Meldrum, P. I. (2015). Interpolation of landslide movements to improve the accuracy of 4d geoelectrical monitoring. *Journal of Applied Geophysics*, 121:93–105.
- Ulrich, C. and Slater, L. (2004). Induced polarization measurements on unsaturated, unconsolidated sands. *Geophysics*, 69(3):762–771.
- Unsworth, M. J., Lu, X., and Watts, M. D. (2000). Csamt exploration at Sellafield: Characterization of a potential radioactive waste disposal site. *Geophysics*, 65(4):1070–1079.
- Unsworth, M. J., Travis, B. J., and Chave, A. D. (1993). Electromagnetic induction by a finite electric dipole source over a 2-d earth. *Geophysics*, 58(2):198–214.
- Vacquier, V., Holmes, C. R., Kintzinger, P. R., and Lavergne, M. (1957). Prospecting for ground water by induced electrical polarization. *Geophysics*, 22(3):660–687.
- Vallet, A., Bertrand, C., Mudry, J., Bogaard, T., Fabbri, O., Baudement, C., and Régent, B. (2015). Contribution of time-related environmental tracing combined with tracer tests for characterization of a groundwater conceptual model: a case study at the Séchilienne landslide, western Alps (France). *Hydrogeology journal*, 23(8):1761–1779.
- Vallet, A., Charlier, J.-B., Fabbri, O., Bertrand, C., Carry, N., and Mudry, J. (2016a). Functioning and precipitation-displacement modelling of rainfall-induced deep-seated landslides subject to creep deformation. *Landslides*, 13(4):653–670.
- Vallet, A., Charlier, J.-B., Fabbri, O., Bertrand, C., Carry, N., and Mudry, J. (2016b). Functioning and precipitation-displacement modelling of rainfall-induced deep-seated landslides subject to creep deformation. *Landslides*, 13(4):653–670.
- Van Voorhis, G., Nelson, P., and Drake, T. (1973). Complex resistivity spectra of porphyry copper mineralization. *Geophysics*, 38(1):49–60.
- Vengeon, J.-M. (1998). *Déformation et rupture des versants en terrain métamorphique anisotrope. Apport de l'étude des Ruines de Séchilienne*. PhD thesis, Université Joseph-Fourier-Grenoble I.
- Viezzoli, A., Kaminski, V., and Fiandaca, G. (2017). Modeling induced polarization effects in helicopter time domain electromagnetic data: Synthetic case studies. *Geophysics*, 82(2):E31–E50.
- Vincent, M. and Zornette, N. (2001). Projet PACTES - Module cartographie du risque potentiel de mouvements de terrain. Technical Report 44p, 24fig., BRGM/RP-51327-FR.
- Wait, J. R. (1961). The electromagnetic fields of a horizontal dipole in the presence of a conducting half-space. *Canadian Journal of Physics*, 39(7):1017–1028.
- Wannamaker, P. E., Hohmann, G. W., and Ward, S. H. (1984). Magnetotelluric responses of three-dimensional bodies in layered earths. *Geophysics*, 49(9):1517–1533.
- Ward, S. H. and Hohmann, G. W. (1988). Electromagnetic theory for geophysical applications. In *Electromagnetic Methods in Applied Geophysics: Volume 1, Theory*, pages 130–311. Society of Exploration Geophysicists.
- WAWRZYNIAK, P. (2011). *HASH (0x952e130)*. PhD thesis.
- Waxman, M. H. and Smits, L. (1968). Electrical conductivities in oil-bearing shaly sands. *Society of Petroleum Engineers Journal*, 8(02):107–122.
- Weill, S., Delay, F., Pan, Y., and Ackerer, P. (2017). A low-dimensional subsurface model for saturated and unsaturated flow processes: ability to address heterogeneity. *Computational Geosciences*, 21(2):301–314.
- Weill, S., Lesparre, N., Jeannot, B., and Delay, F. (2019). Variability of water transit time distributions at the Strengbach catchment (Vosges mountains, France) inferred through integrated hydrological modeling and particle tracking algorithms. *Water*, 11(12):2637.
- Wild, B., Daval, D., Beaulieu, E., Pierret, M.-C., Viville, D., and Imfeld, G. (2019). In-situ dissolution rates of silicate minerals and associated bacterial communities in the critical zone (Strengbach catchment, France). *Geochimica et Cosmochimica Acta*, 249:95–120.
- Wilkinson, P., Chambers, J., Uhlemann, S., Meldrum, P., Smith, A., Dixon, N., and Loke, M. H. (2016). Reconstruction

- of landslide movements by inversion of 4-d electrical resistivity tomography monitoring data. *Geophysical Research Letters*, 43(3):1166–1174.
- Wynn, J., Mosbrucker, A., Pierce, H., and Spicer, K. (2016). Where is the hot rock and where is the ground water—using CSAMT to map beneath and around Mount St. Helens. *Journal of Environmental and Engineering Geophysics*, 21(2):79–87.
- Yamashita, M., Hallof, P., and Pelton, W. (1985). Csamt case histories with a multichannel CSAMT system and near-field data correction. In *SEG Technical Program Expanded Abstracts 1985*, pages 276–278. Society of Exploration Geophysicists.
- Zonge, K. L. and Hughes, L. J. (1985). Effect of electrode contact resistance on electric field measurements. In *SEG technical program expanded abstracts 1985*, pages 231–234. Society of Exploration Geophysicists.
- Zonge, K. L. and Hughes, L. J. (1991). Controlled source audio-frequency magnetotellurics. In *Electromagnetic Methods in Applied Geophysics: Volume 2, Application, Parts A and B*, pages 713–810. Society of Exploration Geophysicists.

Myriam LAJAUNIE

# Geo-electrical methods for hydrogeological studies – capabilities and limits for the analysis of deep-seated landslides and mountainous watersheds

## Résumé

L'objectif de ce travail de recherche est d'étudier la contribution de plusieurs méthodes géo-électriques pour contraindre les modèles hydrogéologiques des glissements de terrain profond et des bassins versants de montagne (résistivité-DC, audio-magnétotellurie à source contrôlée : CSAMT et polarisation provoquée : IP). Ces applications nécessitent des études à l'échelle de versant, à des profondeurs pouvant aller jusqu'à plusieurs centaines de mètres dans des milieux parfois très hétérogènes et fracturés. Une méthodologie basée sur des mesures 1D de CSAMT a été appliquée à la caractérisation de la structure profonde (450 m) du bassin versant granitique du Strengbach (Vosges France), par l'étude des variations spatiales de l'altération du socle granitique. Une tomographie 3D de résistivité électrique a permis de caractériser les zones fortement endommagées ainsi que les aquifères du glissement de terrain de Séchilienne (Alpes Françaises), permettant de valider des hypothèses sur le fonctionnement hydrogéologique du versant. Enfin, des expériences time-lapses ont été réalisées à la fois par des mesures CSAMT et IP sur le glissement de terrain de Lodève, où des événements météorologiques intenses provoquent une recharge rapide des nappes, entraînant des interactions eau-roche suspectées de déstabiliser le milieu dans les unités argileuses et évaporitiques.

Dans chacun des cas d'étude hydrogéophysiques, la sensibilité des mesures a été évaluée par le biais de modélisation numérique et par utilisation des méthodes inverses. La possibilité de modéliser les données de CSAMT a été en particulier explorée car des hypothèses fortes limitent le domaine d'applicabilité de la méthode. La pertinence de l'imagerie 1D, 2D et 3D est discutée dans le contexte de chaque site, prenant en compte les variations topographiques, ainsi que les structures du sous-sol, et les méthodologies d'étude ont été sélectionnées en conséquence. Des informations hydrogéologiques, géochimiques, géophysique et météorologiques ont systématiquement été intégrées dans l'interprétation et confrontées aux observations géo-électriques.

## Abstract

The objective of our research is to study the contribution of several geo-electric methods (DC-resistivity, controlled source audio-frequency magnetotelluric –CSAMT-, and induced polarization –IP-) for constraining hydro-geological models of deep-seated landslides and small mountainous watersheds. These applications were conducted at the slope-scale up to depths of a few hundreds of meters in highly heterogeneous and fractured media. 1D-CSAMT was used to characterize at depth the structure of the Strengbach granitic catchment (Vosges, France) by inferring the spatial variation of weathering of the granitic basement. 3D electrical resistivity investigation helped characterizing the damaged zones and position of the aquifer of the hard-rock micashistic Séchilienne landslide (French Alps), validating hypothesis on the hydrogeological functioning of the slope. Time-lapse experiments were conducted with both time-domain induced polarization and CSAMT methods at the Lodève landslide where yearly intense meteorological events cause loss of cohesion in clay and evaporite Triassic layers aiming at observing the variations of electrical parameters related to changes in the hydrogeological regime.

The sensitivity of all hydrogeophysical surveys was systematically evaluated through numerical modeling and by inversion. The possibility to model the CSAMT data was particularly explored as strong hypotheses limit the domain of applicability of the method. The pertinence of 1D, 2D and 3D imagery is discussed in the context of the three sites, (topography and subsurface structures) and the methodology was selected and developed accordingly. Hydrogeological, geochemical, geophysical and meteorological information was systematically integrated in the interpretation, either in confrontation to the geo-electrical observations, or as complementary information.